

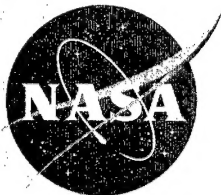
Annual Research Briefs – 1996

Center for Turbulence Research

December 1996

DISTRIBUTION STATEMENT A

Approved for public release;
Distribution Unlimited



Ames Research Center



Stanford University

Annual Research Briefs – 1996

Center for Turbulence Research

December 1996

19970214 042



Ames Research Center



Stanford University

CONTENTS

Preface	1
Simulation of jet impingement heat transfer with the $k - \epsilon - \overline{v^2}$ model. M. BEHNIA, S. PARNEIX and P. DURBIN	3
A new methodology for turbulence modelers using DNS database analysis. S. PARNEIX and P. DURBIN	17
A particle representation model for the deformation of homogeneous turbulence. S. C. KASSINOS and W. C. REYNOLDS	31
Modeling of inhomogeneous compressible turbulence using a two-scale statistical theory. F. HAMBAL	53
Lewis number effects on partially premixed flames. G. R. RUETSCH and J. FERZIGER	67
Conditional moment closure of mixing and reaction in turbulent non- premixed combustion. N. S. A. SMITH	85
Dynamic models for LES of turbulent front propagation with a spec- tral method. H. G. IM, T. S. LUND, and J. H. FERZIGER	101
Jet noise using large eddy simulation. F. BASTIN	115
Towards numerical simulations of trailing-edge aeroacoustics. M. WANG	133
A model for the onset of vortex breakdown. K. MAHESH	143
Compressing an elliptic vortex: transition to turbulence by tumble breakdown. F. S. GODEFERD, N. N. MANSOUR & C. CAMBON	151
A new method for the adaptive control of vortex-wall interactions. P. KOUMOUTSAKOS	165
Symmetries in turbulent boundary layer flows. M. OBERLACK	183
Near-wall models in large eddy simulations of flow behind a backward- facing step. W. CABOT	199
Assessment of the subgrid-scale models at low and high Reynolds numbers. K. HORIUTI	211
Large-eddy simulations of flow around a NACA 4412 airfoil using unstructured grids. K. JANSEN	225
Progress on LES of flow past a circular cylinder. R. MITTAL	233
Experimental investigation of flow through an asymmetric plane dif- fuser. C. U. BUICE and J. K. EATON	243

Progress in the large-eddy simulation of an asymmetric plane diffuser. M. FATICA & R. MITTAL	249
A numerical study of self-similarity in a turbulent plane wake using large-eddy simulation. S. GHOSAL and M. M. ROGERS	257
On the generation of turbulent inflow conditions for boundary layer simulations. T. S. LUND, X. WU, and K. D. SQUIRES	281
A new class of finite difference schemes. K. MAHESH	297
Appendix: Center for Turbulence Research 1996 Roster	307

Preface

This report contains the 1996 annual progress reports of the research fellows and students supported by the Center for Turbulence Research. Last year, CTR hosted twelve resident Postdoctoral Fellows, three Research Associates, four Senior Research Fellows, and supported one doctoral student and ten short term visitors. The major portion of Stanford's doctoral research program in turbulence is sponsored by other support from the United States Office of Naval Research and the Air Force Office of Scientific Research. Many students supported by these programs also conduct their research at the CTR, but their work is not included in this report.

In addition to supporting the work reported in this volume, CTR sponsored its sixth summer program in 1996, its largest ever, with thirty-seven participants. A separate report documenting the findings from the sixth CTR Summer Program was published earlier this year. Both the Annual Research Briefs and Summer Proceedings are available at CTR's site on the world wide web (<http://www-fpc.stanford.edu/CTR/welcome.html>).

The first group of reports in this volume is concerned with turbulence modeling. This is a very important component of the CTR program, owing to its potential impact on engineering applications. A notable study was the demonstration of the excellent prediction capabilities of the $k - \epsilon - v^2$ model (developed earlier at CTR) for impingement cooling used for high-powered electronic chips. The 1996 CTR Summer Program Report contains several other applications of this model to complex flows. The next group of reports is in turbulent combustion, which included an extension of the large eddy simulation methodology to premixed combustion. LES is making successful inroads into the prediction of turbulent combustion. The third group of reports is in the area of computational acoustics and turbulence physics and control. The fundamental computational acoustics program at CTR is now being directed to applications in complex flows. These calculations are very time consuming, but are expected to provide insight into the mechanisms and control of flow generated noise. The final and the largest group of reports is concerned with large eddy simulation of turbulent flows. Recently, CTR's work in this area has been concentrating on the application of dynamic model-based LES (developed earlier at CTR) to complex flows and the assessment of the effects of numerical errors and boundary conditions on the predictive capabilities of this method. Although LES has been shown to be successful in prediction of complex separated flows, it is still taxing the present computational resources, and more effort is being devoted towards making LES more efficient to use.

The CTR's roster for 1996 is provided in the Appendix. Also listed are the members of the Advisory Committee, which meets annually to review the Center's program, and the Steering Committee, which acts on fellowship applications.

In 1996, a new division called Flow Physics and Computation was formed as a joint activity of the Departments of Mechanical Engineering and Aeronautics and

Astronautics at Stanford. The Division consists of eight faculty members and numerous students who are interested in fluid mechanics and computational methods for a variety of flow prediction and control applications. It is expected that this new critical mass activity and the recent positive developments at NASA Ames will lead to enhancement and strengthening of research in fluid mechanics and turbulence. CTR, of course, will be a direct beneficiary of these developments.

It is always a pleasure to use this opportunity to thank Mrs. Debra Spinks for her unrelenting efforts in the daily management of the Center and her compilation of this report.

Parviz Moin
William C. Reynolds
Nagi N. Mansour

Simulation of jet impingement heat transfer with the $k-\varepsilon-v^2$ model

By M. Behnia, S. Parneix AND P. Durbin

1. Motivation and objectives

Jet impingement heating and cooling is used in many engineering and industrial applications (e.g. materials processing, manufacturing, and cooling of computers and electronic equipment). In these applications, normally a turbulent jet of gas or liquid is directed to the target area of interest. The advantages of jet impingement heat transfer process are direct, localized heating or cooling, and increased heat fluxes. This technique is emerging as an attractive cost-effective method of cooling of computers (Nakayama 1995). There are a number of parameters to be considered in the design of such systems. For instance, for optimization of cooling or heating systems, accurate prediction of the local heat transfer coefficient is essential. To this end, the flow and thermal fields must be accurately and economically computed; hence the need for better turbulence models.

Impinging jet flows have several complex features which make them a good test vehicle for evaluation of turbulence models. In the impingement region, the mean flow is perpendicular (or nearly perpendicular) to the surface. It then turns and follows the surface in a wall jet (see Fig. 1). In the stagnation region, the flow is almost irrotational and there is a large total strain along the stagnation streamline. Away from the core of the jet, due to expansion, diffusion, and entrainment, there is substantial curvature in the streamlines. Adjacent to the wall, there are thin stagnation point and wall jet boundary layers on the target plate.

The problem of a normal impinging jet of air striking a flat plate has been considered as a test case by ERCOFTAC. They have adopted the flow and heat transfer measurements of the experiments by Cooper *et al.* (1993) and Baughn and Shimizu (1989), respectively. There are also a number of more recent heat transfer measurements by others (e.g. Baughn *et al.* 1991, Yan 1993, and Lytle and Webb 1994). The experimental data has been used by researchers to test their turbulence models for this demanding case. For instance, Craft *et al.* (1993) used the data of Cooper *et al.* (1993) and Baughn and Shimizu (1989) to examine the $k-\varepsilon$ and three second-moment closure models in an axisymmetric geometry.

The objective of our work has been to compute the flow and thermal fields in an axisymmetric isothermal fully developed turbulent jet perpendicular to a flat uniform heat flux plate using the $k-\varepsilon-\overline{v^2}$ model of Durbin (1995). To this end, the axisymmetric incompressible Navier-Stokes equations in conjunction with the standard $k-\varepsilon$, the $\overline{v^2}$ transport, and the elliptic relaxation equations have been solved on a Cartesian grid. Several turbulent Prandtl numbers and realizability constants are examined. The results are compared with the experimental data of Baughn and Shimizu (1989), Lytle (1990), Baughn *et al.* (1991), Yan (1993),

Cooper *et al.* (1993), and Lytle and Webb (1994). For comparison, computations are also performed with the widely used standard $k - \varepsilon$ model. The local heat transfer behavior of the jet for various jet to target distances is analyzed.

2. Accomplishments

2.1 The $k - \varepsilon - \overline{v^2}$ model

The mean flow satisfies the Reynolds Average Navier-Stokes (RANS) equations, where the turbulent stresses are represented with an eddy-viscosity:

$$D_t U = -\nabla P + \nabla \cdot \{(\nu + \nu_t)(\nabla U + \nabla^t U)\}$$

$$\nabla \cdot U = 0$$

The definition of the turbulent viscosity ν_t needs the evaluation of one time scale, T , and one velocity scale. For the latter, the variable $\overline{v^2}$ has been introduced by Durbin (1993a) instead of the classical turbulent kinetic energy k used in the $k - \varepsilon$ model, i.e. $\nu_t = C_\mu \overline{v^2} T$. Physically, $\overline{v^2}$ might be regarded as the velocity fluctuation normal to the streamlines; note that it is not linked to the y -component of velocity. By arguing that the physical time scale cannot be smaller than the Kolmogorov time scale, Durbin (1991) derived the following expression which prevents $1/T$ becoming infinite at the wall:

$$T' = \min\left(\frac{k}{\varepsilon}; 6\left(\frac{\nu}{\varepsilon}\right)^{1/2}\right)$$

Moreover, Durbin (1996) recently studied the realizability constraint in the context of impinging flows, which is our motivation here, and fixed an upper bound for this time scale:

$$T = \max\left(T', \frac{\alpha}{2\sqrt{3}} \frac{k}{\overline{v^2} C_\mu \sqrt{S^2}}\right),$$

$$\alpha \leq 1, S^2 = S_{ij} S_{ij}$$

α is a model parameter and comparison of our computations with experimental results have indicated an optimum value of 0.5 for the axisymmetric problem studied here.

Three transport equations are used for computing the turbulent kinetic energy, k , the dissipation rate of turbulence, ε , and the new velocity scale, $\overline{v^2}$:

$$D_t k = P - \varepsilon + \nabla \cdot \left(\left(\nu + \frac{\nu_t}{\sigma_k}\right) \nabla k\right)$$

$$D_t \varepsilon = \frac{C'_{\varepsilon_1} P - C_{\varepsilon_2} \varepsilon}{T} + \nabla \cdot \left(\left(\nu + \frac{\nu_t}{\sigma_\varepsilon}\right) \nabla \varepsilon\right)$$

$$D_t \overline{v^2} = k f_{22} - \frac{\overline{v^2}}{k} \varepsilon + \nabla \cdot \left(\left(\nu + \frac{\nu_t}{\sigma_k}\right) \nabla \overline{v^2}\right)$$

P is the rate of production of turbulent kinetic energy, i.e. $P = 2\nu_t S^2$. It should be noted that no damping functions are used in the model equations. The k and ε equations are similar to the $k - \varepsilon$ model, except for the destruction term of ε where ε/k has been replaced by $1/T$. C'_{ε_1} has been chosen as a function of the distance to the closest boundary d in order to give suitable values of C'_{ε_1} for both turbulent boundary layer ($C'_{\varepsilon_1} = 1.55$) and plane mixing layer ($C'_{\varepsilon_1} = 1.3$), i.e. $C'_{\varepsilon_1} = 1.3 + 0.25/[1 + (d/2\ell)^2]^4$. In the channel flow or boundary layer configuration, the term $k f_{22}$ represents the redistribution of turbulent intensity (pressure-strain correlation) from the streamwise and spanwise components. For representing non-local effects, caused by the impermeability of solid boundaries, f_{22} is evaluated through an elliptic equation (Durbin 1991):

$$f_{22} - L^2 \nabla^2 f_{22} = (C_1 - 1) \frac{(2/3 - \overline{v^2}/k)}{T} + C_2 \frac{P}{k}$$

Finally, by using the same approach as for the time scale (Kolmogorov length scale as a lower bound and realizability constraint for the upper bound), the following expression of the turbulent length scale can be derived:

$$L' = C_L \min\left(\frac{k^{3/2}}{\varepsilon}; C_\eta \left(\frac{\nu^3}{\varepsilon}\right)^{1/4}\right)$$

$$L = \max\left(L', \frac{1}{\sqrt{3}} \frac{k^{3/2}}{v^2 C_\mu \sqrt{S^2}}\right)$$

The constants of the model are (Durbin 1995):

$$C_{\varepsilon_2} = 1.9, C_\mu = 0.19, C_1 = 1.4, C_2 = 0.3,$$

$$\sigma_k = 1.0, \sigma_\varepsilon = 1.3, C_L = 0.3, C_\eta = 70.0$$

2.2 Turbulent Prandtl number

In the mean temperature equation, it is customary to substitute the eddy diffusivity of heat by defining a turbulent Prandtl number, which is the ratio of the momentum to heat eddy diffusivity. There is substantial experimental data available on the turbulent Prandtl number (Pr_t). These are primarily based on determining the slope of T^+ in the log-region of a flat plate boundary layer. For air, with a molecular Prandtl number of $Pr = 0.71$, the data ranges between $Pr_t = 0.73$ and 0.92 (Kays 1994). The variation of the molecular Pr in the range of 0.7 to 64 (i.e. gases and most liquids including oils and with the exception of liquid metals) does not strongly affect the turbulent Prandtl number, and according to Kays an approximate value of 0.85 is generally acceptable.

There are also a number of analytically determined relationships for turbulent Prandtl number in the literature. Data from DNS of flow in ducts and external boundary layer flows have also been used to determine Pr_t . For instance, the DNS

results of Kim and Moin (1987) for fully developed flow of air in a duct indicate a $Pr_t \approx 1.2$ at the wall with a non-monotonic decrease to about 0.7 far from the wall. This behavior is in qualitative agreement with data based on experimental measurements in air, which according to Kays and Crawford (1993) can be represented with a relationship of the form

$$Pr_t = \frac{1}{0.5882 + 0.228(\nu_t/\nu) - 0.0441(\nu_t/\nu)^2 [1 - \exp(\frac{-5.165}{(\nu_t/\nu)})]}$$

This formula yields a value of 1.7 at the wall with a sharp decrease in its vicinity and an asymptotic value of 0.85 far from the wall. For the heated flat plate flow, computations of Durbin (1993b) adopting this formula and the widely used constant value of 0.9 have indicated a change of 10% in the Stanton number. In fact, these simulations have shown that the constant Pr_t value yields a marginally better agreement with experiments.

Measurements of Pr_t in other geometries (e.g. jets) are rather rare. Chua and Antonia (1990) made measurements in a circular jet of air and showed a non-monotonic variation of Pr_t between 0.84 at the axis and 1.6 near the jet edge. They suggest a constant value of 0.81 in the region between the axis and the jet half-radius point.

It is noted that there are a number of unresolved issues as far as the concept of turbulent Prandtl number is concerned (Kays 1994). Little work has been done on different geometries. Also, most of the available data is relevant to gases and there are very few measurements for higher Prandtl number liquids (e.g. dielectric liquids used for cooling of computers which have Prandtl numbers of the order of 20). Perhaps DNS of these flows can be used in the future to provide the required data for modeling.

We have examined the effect of Pr_t on the local heat transfer coefficient. We have tested several widely used Pr_t values noted above: 0.73, 0.85, 0.92, and the Kays and Crawford formula.

2.3 Available experimental data

For the turbulent impinging jet, Cooper *et al.* (1993) have recently reported a set of flow measurements at two different Reynolds numbers (i.e. $Re_D = 23,000$ and $74,000$); however, they did not make any heat transfer measurements. They note that the purpose of their experiments was to provide the hydrodynamic data for the heat transfer experiments of Baughn and Shimizu (1989) who measured the local heat transfer coefficient on a constant heat flux impingement plate. Baughn and Shimizu used a fully-developed jet striking a gold-coated plate which was painted by liquid crystals for temperature measurements and mapping of the local heat transfer coefficient. They made their measurements for several jet-to-plate spacings ($H/D \geq 2$). In a later study by Baughn *et al.* (1991), the same test rig was used to study the entrainment effects in a heated jet. They noted that their unheated jet results agreed with the earlier data of Baughn and Shimizu.

Lytle (1990) also made heat transfer and flow measurements in an impinging air jet. He used an infrared thermal imaging system for temperature measurement

and the velocity was measured by an LDV system. The focus of this study was primarily on nozzle-to-plate spacings of less than one nozzle diameter. The results have been partly published in Lytle and Webb (1994). It is noted that the relative size of the impingement plate (compared to the jet diameter) in this study was smaller than that of Baughn's experiments. Yan (1993) developed a preheated-wall transient measurement method using liquid crystals. He made local heat transfer coefficient measurements on the impingement test rig used in previous Baughn's studies. Yan notes that there was good agreement between his measurements and those of Baughn using the steady state method. Lee *et al.* (1995) also used a test rig similar to Baughn's and made measurements at lower Reynolds numbers ($Re_D < 15,000$).

2.4 Simulation results and comparison with experiments

A sketch of the problem and computational domain is shown in Fig. 1. All computations were performed using INS2D, a finite difference code in generalized co-ordinates developed at NASA Ames Research Center. The spatial discretization of convective terms was via the third order QUICK scheme. A fine, non-uniform Cartesian grid of 120×120 cells was used, with a high resolution near the solid regions (i.e. the impingement and pipe walls). A mesh sensitivity was performed by doubling the grid; however, this changed the impingement region Nusselt number by less than 0.5%. Therefore, the 120×120 grid was considered adequate. For high aspect ratios ($H/D \geq 10$), a 160 by 160 grid was used.

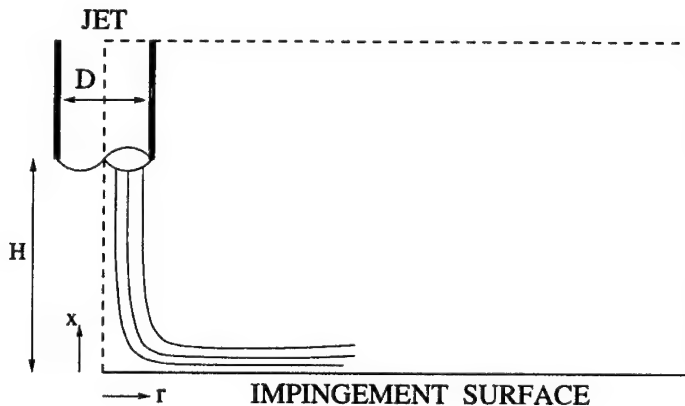


FIGURE 1. The geometry and computational domain.

The computations were performed in two steps. First, a fully-developed pipe flow simulation was performed using 240 grid points in the radial direction. For this computation, the grid spacing was chosen such that there were 5 points located in the region of $y^+ \leq 5$. This solution was then accurately interpolated and used as the inlet condition of the jet. For stability of the solution procedure and accuracy, it was necessary to include a sufficient length of pipe (of the order of 2 pipe diameters) in the computational domain; other investigators have made similar observations

(e.g. Craft *et al.* 1993). This allows the upper computational boundary to be sufficiently distanced from the wall so that it does not affect the flow near the impingement surface. Also, the effect of the jet wall thickness on the flow can be properly modeled. A specified constant static pressure condition was used for the upper and right boundaries. We examined the effect of the right boundary location on the flow and thermal fields. It was noted that once this length was larger than $(H/D+8)$, there was no noticeable effect on the flow field and local Nusselt number. For the thickness of the pipe-wall, we examined two values of $0.112D$ and $0.0313D$ corresponding to the experiments of Baughn and Shimizu (1989) and Cooper *et al.* (1993), respectively, and no noticeable difference was observed. As our main aim was comparison of the computed and measured Nusselt number, the former value was used for the computations.

Simulations were performed for a fixed jet Reynolds number of $Re_D = 23,000$ and various aspect ratios, $0.5 \leq H/D \leq 14$ using both the $k-\varepsilon$ and $k-\varepsilon-\overline{v^2}$ models. The $k-\varepsilon-\overline{v^2}$ simulations required several hundred iterations for convergence (i.e. several minutes of CPU time on the NASA - Cray C90). In general, for the $k-\varepsilon$ simulations, the number of iterations had to be doubled. For the $k-\varepsilon$ model we used a damping function of the form $\nu_t = 0.09kT[1 - \exp(-0.01 |\frac{kT}{\nu}|)]$, which yields similar behavior to the model of Launder and Sharma (1974). Craft *et al.* (1993) used the Launder and Sharma model for the same problem and our $k-\varepsilon$ predictions are similar to theirs.

2.4.1 Preliminary computations

The effect of the realizability constraint parameter α on the computational results was determined by using two different values (i.e. 0.5 and 1). For $H/D = 2$, the computed local Nusselt number is compared with the measured data in Fig. 2a. It is noted that near the impingement region, a somewhat better agreement is obtained for $\alpha = 0.5$, however, downstream of this region and for $r/D \geq 2$, there is very little difference between the two predicted results. In this region, both values yield excellent agreement with the data. The experimental data indicate a dip in the Nusselt number around $r/D = 1.5$ with a second peak at around $r/D = 2$. This behavior seems to be better represented by the simulation with $\alpha = 0.5$, which is the value we chose to use for the computations.

The effect of the turbulent Prandtl number, Pr_t , on the local Nusselt number for $H/D = 6$ is shown in Fig. 2b. The results are not very sensitive to this parameter, in particular downstream of the impingement region. Considering the scatter in the experimental data, it is difficult to say which value of Pr_t more closely fits the data. In the stagnation region, both $Pr_t = 0.92$ and the Kays and Crawford formula are in excellent agreement with the measurements of Lytle and Webb but are slightly higher than the data of Baughn *et al.* Away from this region, as the flow becomes parallel to the plate and forms the wall jet region, the prediction with $Pr_t = 0.73$ follows the data of Baughn and Shimizu, Baughn *et al.*, and Yan. In this region, all predictions are below the measurements of Lytle and Webb. One possible explanation for the higher values of Nusselt number measured by them, in particular in this region, can be their use of a shorter length plate because of

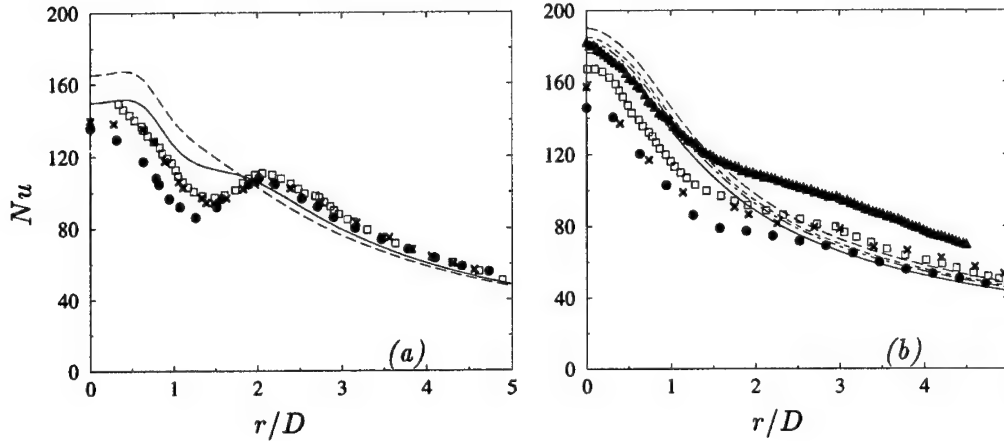


FIGURE 2. Effect of (a) the realizability constant and (b) Pr_t on the local Nusselt number; (a) $H/D = 2$ and different realizability constants, $\alpha = 0.5$ (—), $\alpha = 1.0$ (---); (b) $H/D = 6$ and different Pr_t , Kays & Crawford (—), $Pr_t = 0.73$ (---), $Pr_t = 0.85$ (.....), $Pr_t = 0.92$ (-.-.-). Experimental data: \times Baughn & Shimizu 89 ($Re = 23750$), \square Baughn *et al.* 91 ($Re = 23300$), \bullet Yan 93 ($Re = 23340$), \blacktriangle Lytle & Webb 94 ($Re = 23000$).

their interest in smaller jet to plate spacings (H/D). As the Kays and Crawford Pr_t formula yields a somewhat better agreement in the impingement region, we performed our simulations with this turbulent Prandtl number.

2.4.2 Results for $H/D = 2$

The computed flow field for this case is shown by contours of the Stokes streamlines in Fig. 3 (for clarity, only part of the domain is shown). At the nozzle exit, these are parallel to the jet axis, representing the potential core of the jet. Near the stagnation region, the flow decelerates in the axial direction and turns as exhibited by the sharp curvature in the streamlines. Past this region, and roughly for $r/D > 1.5$, a radial wall jet parallel to the plate begins to form with a developing boundary layer. The ambient fluid outside the jet is entrained into the core with a developing shear layer separating the core and the ambient fluid. The entrainment is clearly evident by the curving of the streamlines outside the pipe towards the core of the jet. This leads to the formation of a recirculation region in the vicinity of the pipe-wall (a magnified view of this region is shown as an inset in Fig. 3). The features of the flow in this region are well captured by our computations, indicating a sufficient grid resolution around the exit of the nozzle and in the shear layer.

Contours of the computed turbulent kinetic energy for both $k - \varepsilon - \overline{v^2}$ and $k - \varepsilon$ models are shown in Fig. 4. The maximum value of k predicted by the $k - \varepsilon$ model is 80% higher than that of $k - \varepsilon - \overline{v^2}$. The location of this maximum, shown by the arrows on the figure, is in the stagnation region for the $k - \varepsilon$, and at about $r/D = 2$ for the $k - \varepsilon - \overline{v^2}$. Further, the $k - \varepsilon - \overline{v^2}$ model predicts that in the shear layer between the jet core and the outer entrainment region, there exists a region of high turbulent kinetic energy. The behavior predicted by the $k - \varepsilon - \overline{v^2}$

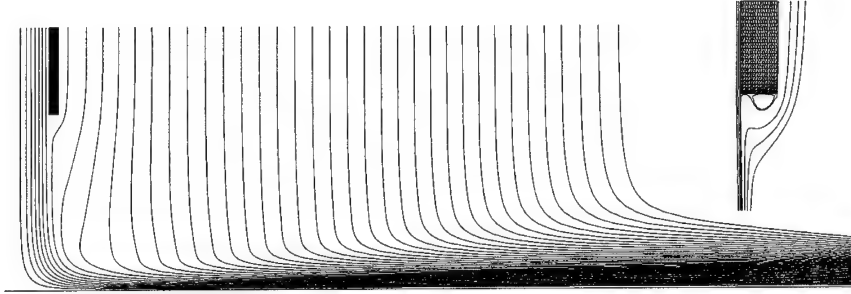


FIGURE 3. Streamlines for $H/D = 2$ computed with the $k - \varepsilon - \overline{v^2}$ model (inset shows the magnified view of the flow near the pipe exit).

model is qualitatively confirmed by the measurements of Lytle and Webb, who also noted an increase in the turbulent intensity away from the stagnation region. They attribute this to the interaction of the accelerating radial flow with the free-stream air. However, our computations suggest that it is due to increased production in the region of streamline convergence.

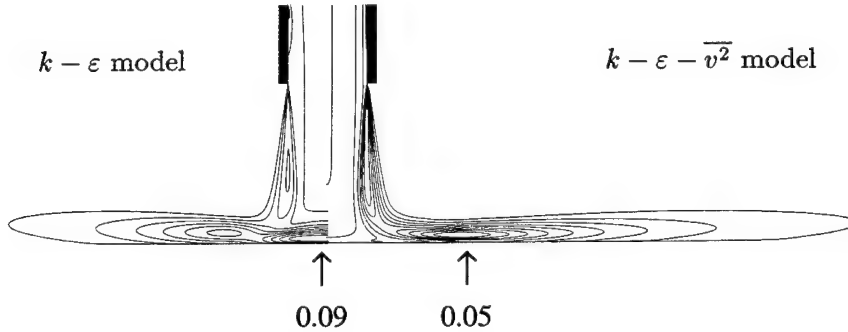


FIGURE 4. Contours of turbulent kinetic energy for $H/D = 2$.

For this aspect ratio, Craft *et al.* 1993 have made velocity measurements at various radial locations (this data was obtained from the ERCOFTAC 1996 database). A comparison of the measured velocity magnitude and our computations with the $k - \varepsilon$ and $k - \varepsilon - \overline{v^2}$ models at four different radial locations are shown in Fig. 5. On the stagnation streamline ($r/D = 0$) there is very little difference between the two predictions, and quite good agreement with the experimental data is noted. At $r/D = 0.5$ the $k - \varepsilon$ model predicts lower velocities than the $k - \varepsilon - \overline{v^2}$, which yields a somewhat better agreement near the wall. However, at this radial location away from the wall, for $x/D \leq 0.25$, the $k - \varepsilon$ predictions are closer to the experimental value, whereas in the outer region, the $k - \varepsilon - \overline{v^2}$ exactly follows the data. In the wall jet region, at $r/D = 1$, the $k - \varepsilon - \overline{v^2}$ model correctly predicts the flow acceleration, and there is excellent agreement with the data near the wall and a slight over-prediction in the outer region. At this radial location, the $k - \varepsilon$ model predicts low velocities in the wall region and high velocities in the outer region. Further

downstream, the flow decelerates, and again the $k - \varepsilon - \overline{v^2}$ model correctly predicts this behavior with a very good agreement with the experiment at $r/D = 2.5$. The $k - \varepsilon$ model does not correctly resolve the development of the boundary layer, leading to an under-prediction of the velocity in the wall region and an over-prediction in the outer region. The failure of the $k - \varepsilon$ model to correctly resolve the behavior of the flow is, perhaps, at least partly due to its prediction of high levels of turbulent kinetic energy in the stagnation region (see Fig. 4).

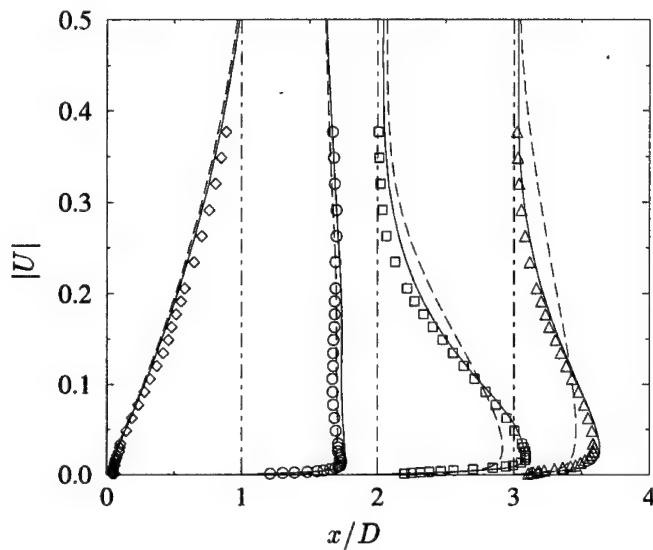


FIGURE 5. Profiles of the velocity magnitude at various radial locations [$r/D = 0$ (\diamond), 0.5 (\circ), 1 (\square), 2.5 (\triangle)] for $H/D = 2$, experimental data (Cooper *et al.*, 1993), — : $k - \varepsilon - \overline{v^2}$ model, --- : $k - \varepsilon$ model.

In the stagnation region, the spuriously high value of k predicted by the $k - \varepsilon$ model results in a significant over-prediction of the local Nusselt number as seen in Fig. 6. In this model, the stagnation Nusselt number is about 200% higher than the measured value, whereas the $k - \varepsilon - \overline{v^2}$ model prediction is only about 9% higher. Downstream of the stagnation region, the $k - \varepsilon$ Nusselt number rapidly decreases and approaches the experimental and $k - \varepsilon - \overline{v^2}$ values. The experimental data indicate a dip in the local Nusselt number distribution around $r/D = 1.4$ and a secondary maximum at around $r/D = 2$. Some investigators (e.g. Lee *et al.* 1995) have attributed the local maximum to transition from a laminar to turbulent boundary layer in the wall jet region. This is not supported by the measurements of Lytle and Webb, who note that there are relatively high levels of turbulence even in the stagnation region. It is believed that the increase in the turbulent kinetic energy away from the stagnation region (as observed by Lytle and Webb and predicted by the $k - \varepsilon - \overline{v^2}$ model), where the shear layer of the jet directly interacts with the flat plate, is responsible for this local increase of the Nusselt number. It appears that the data of Yan indicate a more pronounced local minimum of Nusselt number

compared to the data of Baughn. Also, in the data of Yan, this point is shifted closer to the stagnation point with a somewhat lower value of the local Nusselt number in the region of $r/D < 1.5$. The $k - \varepsilon - \overline{v^2}$ model does not predict a local secondary maximum; however, it does show a deflection in the local Nusselt number distribution. It can be said that the agreement between the data and the $k - \varepsilon - \overline{v^2}$ computation is excellent in the regions of $r/D \leq 1$ and $r/D \geq 1.8$.

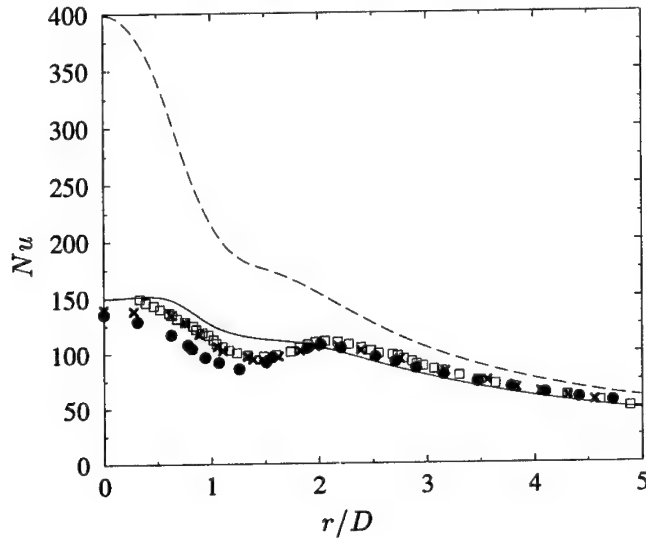


FIGURE 6. Distribution of local wall heat transfer coefficient for $H/D = 2$, — : $k - \varepsilon - \overline{v^2}$ model, --- : $k - \varepsilon$ model, experimental data (for symbol key see Fig. 2).

2.4.3 Results for $H/D = 6$

The contours of the turbulent kinetic energy are shown in Fig. 7. The maximum value of k predicted by the $k - \varepsilon$ model is 66% higher than $k - \varepsilon - \overline{v^2}$. The location of this maximum, shown by the arrows on this figure, is in the stagnation region for the $k - \varepsilon$, and at about $r/D = 1$ for the $k - \varepsilon - \overline{v^2}$.

A comparison of the predicted and measured local Nusselt number is presented in Fig. 8. It is noted that in the impingement region there is a 25% scatter in the experimentally measured Nusselt number. The data of Lytle and Webb is consistently higher than measurements of others. The $k - \varepsilon$ model over-predicts the stagnation Nusselt number by about 150%, but the discrepancy gradually reduces, moving away from the impingement region. The $k - \varepsilon - \overline{v^2}$ model prediction is in excellent agreement with the data of Lytle and Webb in the impingement region; however, in the wall jet region there is better agreement with the data of Yan. It is noted that unlike the lower aspect ratio results ($H/D = 2$), there is no secondary maximum in the Nusselt number distribution. This is believed to be attributed to the fact that as the jet is moved further out from the impingement surface, the location of maximum k moves closer to the jet axis. This is supported by the

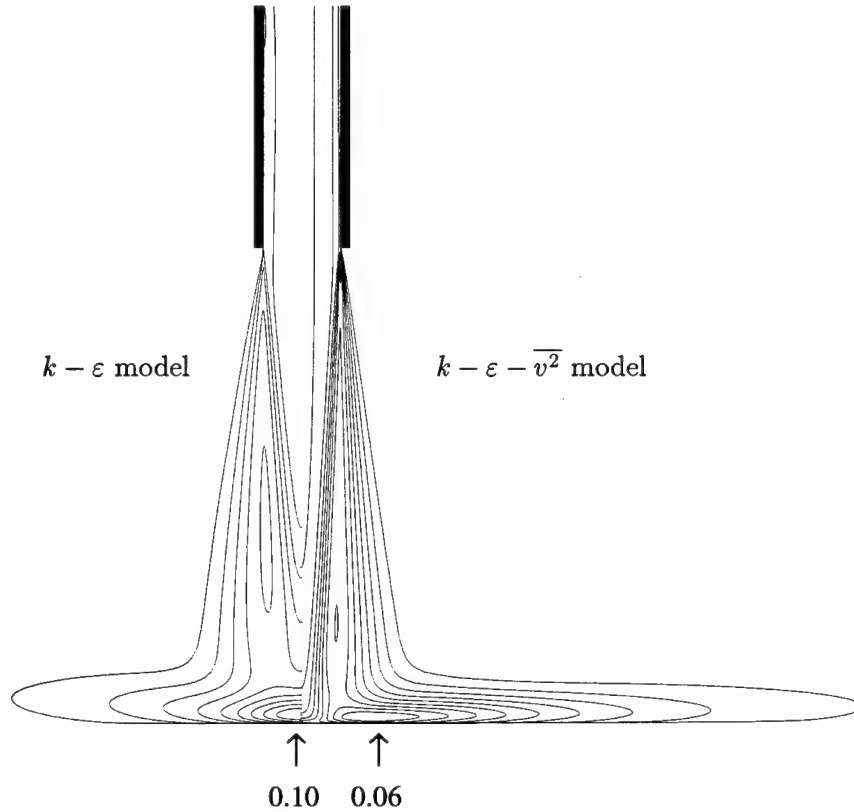


FIGURE 7. Contours of turbulent kinetic energy for $H/D = 6$.

computations with the $k - \varepsilon - \overline{v^2}$ model, which predicts the location of this point at r/D of 2 and 1 for aspect ratios of 2 and 6, respectively.

2.4.4 Stagnation Nusselt number

Simulations have been carried out for a constant Reynolds number ($Re_D = 23,000$) and a wide range of aspect ratios ($0.5 \leq H/D \leq 14$) to determine the dependence of the stagnation Nusselt number on H/D . This dependence is crucial to many applications of impingement cooling. A comparison of the computed values with the experimental data is presented in Fig. 9. The $k - \varepsilon - \overline{v^2}$ model predictions are in good agreement with the data. Also, experimental measurements (e.g. Baughn and Shimizu 1989, Yan 1993 and Lee *et al.* 1995) have indicated that for $H/D > 1$, the stagnation Nusselt number exhibits a maximum value at around $H/D = 6$. Our $k - \varepsilon - \overline{v^2}$ computations confirm this finding and indicate that the maximum stagnation Nusselt number is between H/D of 6 and 7. This is attributed to the increase in the turbulent kinetic energy as the jet is moved away from the impingement surface. For instance, as previously discussed, the maximum of k at $H/D = 6$ is higher than that of $H/D = 2$. This is also supported by Kataoka *et al.* (1987), who show that turbulent intensity reaches a maximum at an aspect ratio of 7. The measurements of Lytle and Webb also indicate that at lower spacing ratios,

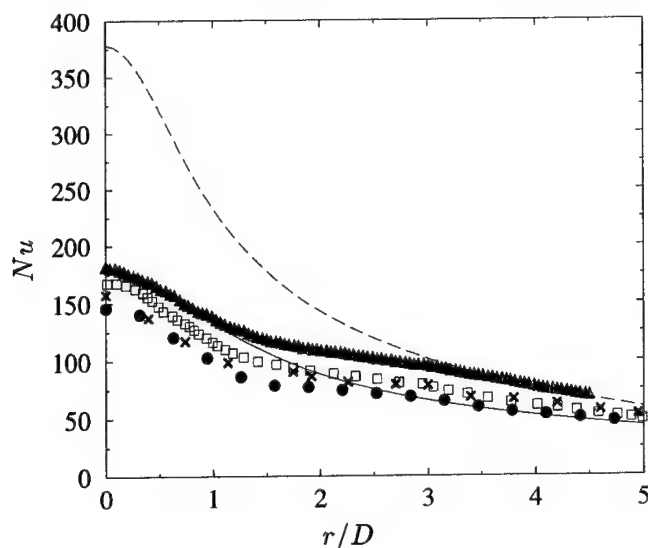


FIGURE 8. Distribution of local wall heat transfer coefficient for $H/D = 6$, — : $k - \varepsilon - \overline{v^2}$ model, --- : $k - \varepsilon$ model, experimental data (for symbol key see Fig. 2).

the stagnation Nusselt number goes through a local minimum at $H/D = 1$, which is also correctly predicted by the $k - \varepsilon - \overline{v^2}$ model.

The $k - \varepsilon$ model substantially over-predicts the stagnation Nusselt number. It also indicates a behavior unlike the trend observed in the experiments and the $k - \varepsilon - \overline{v^2}$ computations. Two local maxima around H/D of 3 and 5 with a local minimum around 4 are noted. At higher aspect ratios, the $k - \varepsilon$ predictions gradually approach the measurements.

3. Future plans

The main aim of this research has been to accurately and economically predict the heat transfer rate in an impinging jet. The computations carried out to date have shown that the $k - \varepsilon - \overline{v^2}$ model predictions agree very well with the experiments, whereas the $k - \varepsilon$ model, in general, does not properly resolve the flow features, highly over-predicts the rate of heat transfer, and yields physically unrealistic behaviors.

It is planned to perform additional two- and three-dimensional computations to cover a wider range of parameters, such as the geometry, Reynolds number, and Prandtl number. In particular, for electronic cooling applications, dielectric liquids in a confined jet geometry need to be explored. There are also some recently obtained experimental measurements of heat transfer from a heated pedestal being cooled by an impinging jet which will be used for comparison with future simulations. The understanding gained and the obtained results can be directly relevant to the design and operation of a number of industrial and engineering applications.

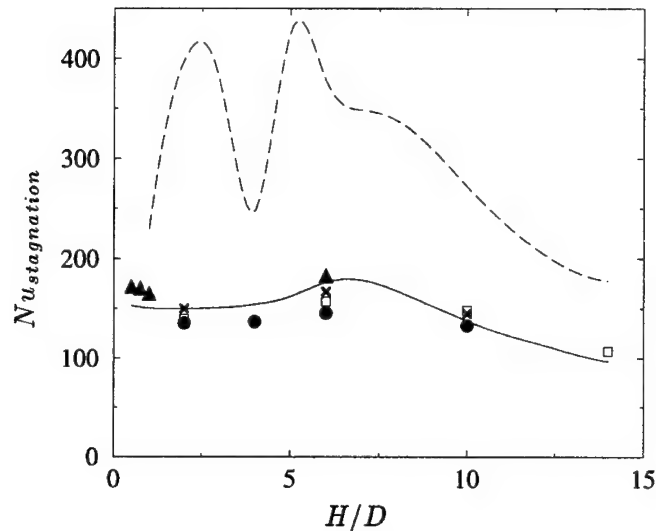


FIGURE 9. Effect of jet distance on the heat transfer at the stagnation point, — : $k - \varepsilon - \overline{v^2}$ model, --- : $k - \varepsilon$ model, experimental data (for symbol key see Fig. 2).

Acknowledgments

We thank Profs. Baughn (UC, Davis), Webb (BYU), and Yan (Southern Illinois) for providing their experimental data.

REFERENCES

- BAUGHN, J., HECHANOVA, A. & YAN, X. 1991 An experimental study of entrainment effects on the heat transfer from a flat surface to a heated circular impinging jet. *J. Heat Transfer*. **113**, 1023-1025.
- BAUGHN, J. & SHIMIZU, S. 1989 Heat transfer measurements from a surface with uniform heat flux and an impinging jet. *J. Heat Transfer*. **111**, 1096-1098.
- COOPER, D., JACKSON, D., LAUNDER, B. & LIAO, G. 1993 Impinging jet studies for turbulence model assessment-I. Flow-field experiments. *Int. J. Heat Mass Transfer*. **36** (10), 2675-2684.
- CRAFT, T., GRAHAM, L. & LAUNDER, B. 1993 Impinging jet studies for turbulence model assessment-II. An examination of the performance of four turbulence models. *Int. J. Heat Mass Transfer*. **36** (10), 2685-2697.
- DURBIN, P. 1991 Near-wall turbulence closure without damping functions. *Theoretical & Comp Fluid Dyn.* **3** (1), 1-13.
- DURBIN, P. 1993a A Reynolds-stress model for near-wall turbulence. *J. Fluid Mech.* **249**, 465-498.
- DURBIN, P. 1993b Application of a near-wall turbulence model to boundary layers and heat transfer. *Int. J. Heat & Fluid Flow*. **14** (4), 316-323.

- DURBIN, P. 1995 Separated flow computations with the $k - \varepsilon - \overline{v^2}$ model. *AIAA J.* **33** (4), 659-664.
- DURBIN, P. 1996 On the $k - \varepsilon$ stagnation point anomaly. *Int. J. Heat & Fluid Flow.* **17**, 89-90.
- ERCOTAC DATABASE 1996 data obtained from <http://fluidigo.mech.surrey.ac.uk/>.
- KATAOKA, K., SUGURO, M., DEGAWA, K., MARUO, K. & MIHATA, I. 1987 The effect of surface renewal due to large-scale eddies on jet impingement heat transfer. *Int. J. Heat Mass Transfer.* **30**, 559-567.
- KAYS, W. M. 1994 Turbulent Prandtl number - Where are we? *J. Heat Transfer.* **116**, 284-295.
- KIM, J. & MOIN, P. 1987 Transport of passive scalars in a turbulent channel flow. *Proceedings of 6th international symposium on turbulent shear flows*, Toulouse, France, September 7-9, 5.2.1-5.2.6.
- LEE, D., GREIF, R., LEE, S. & LEE, J. 1995 Heat transfer from a flat plate to a fully developed axisymmetric impinging jet. *J. Heat Transfer.* **117**, 772-776.
- LYTLE, D. 1990 Air jet impingement heat transfer at low nozzle-to-plate spacings. *MS Thesis*, Brigham Young University.
- LYTLE, D. & WEBB, B. 1994 Air jet impingement heat transfer at low nozzle-plate spacings. *Int. J. Heat Mass Transfer.* **37**(2), 1687-1697.
- NAKAYAMA, W. 1995 Heat transfer engineering in systems integration: outlook for closer coupling of thermal and electrical designs of computers. *IEEE Transactions on Components, Packaging, and Manufacturing Technology-Part A.* **18**(8), 818-826.
- YAN, X. 1993 A preheated-wall transient method using liquid crystals for the measurement of heat transfer on external surfaces and in ducts. *Ph.D. Thesis*, University of California, Davis.

A new methodology for turbulence modelers using DNS database analysis

By S. Parneix AND P. Durbin

1. Motivation and objectives

Many industrial applications in such fields as aeronautical, mechanical, thermal, and environmental engineering involve complex turbulent flows containing global separations and subsequent reattachment zones. Accurate prediction of this phenomena is very important because separations influence the whole fluid flow and may have an even bigger impact on surface heat transfer. In particular, reattaching flows are known to be responsible for large local variations of the local wall heat transfer coefficient as well as modifying the overall heat transfer. For incompressible, non-buoyant situations, the fluid mechanics have to be accurately predicted in order to have a good resolution of the temperature field.

Much previous work on such phenomena has used the case of the backward facing step. The sudden expansion of a channel flow indeed gives rise to a simple geometry, but one that contains complex aerodynamic features such as separation, a spreading shear layer, interaction of this shear layer with a wall, recirculation, and recovery of the reattached boundary layer. Moreover, a lot of databases are available from physical experiments to numerical simulations (DNS and LES): this makes for a good test case on which to validate turbulence models.

In past years, various two-equation turbulence models have been tested and compared with the available experiments. The principal feature of models using wall functions is an underprediction of the recirculation length by about 15%. In fact, recent simulations or experiments show an important departure of the velocity profiles from the law of the wall, not only in the recirculation, but also in the recovery region. A bad prediction of aerodynamics near the wall would have dramatic effects on predictions of heat transfer. The low-Reynolds number cases show strong anisotropies, not only in the boundary layer, but also in the spreading shear layer and in the recirculation; any linear two-equation model would fail to reproduce this important feature of the flow. For this reason, and with the aim of future studies of flows involving buoyancy, curvature, or rotation, we decided to use a Second Moment Closure (SMC) approach, which intrinsically can take into account these phenomena.

The closure of the Reynolds-stress equations consists partially in finding a model for the pressure-strain correlation which acts as a redistribution term between the Reynolds-stress components. Since the *Lauder, Reece and Rodi, 1975* (LRR) paper, a number of models have been proposed especially to take into account specific wall-behavior. However, all these models use a single-point closure and cannot actually represent the well-known non-local effects of the pressure-reflection that occurs near solid boundaries. In order to model these latter effects and to avoid the use

of two-point correlations—which are not viable for non-homogeneous turbulence—Durbin (1993) applied an elliptic operator on the pressure-strain correlations. This approach has been tested on various simple flows and with successful results. Moreover, it does not need the use of either wall functions, whose universality is more and more questionable, or damping functions, which often involve the "ill-behaved" distance to the wall and which can be highly non-linear and numerically stiff.

The aim of this study is to study this modeling methodology by using a SMC-model calibrated in fully-turbulent channel flow to compute the low-Reynolds backward-facing step for which a complete Direct Numerical Simulation (DNS) database is now available (Le, Moin & Kim, 1993). We will see the performance and some discrepancies of the model.

The present report also introduces a new *a priori* test: it consists in freezing some variables for which DNS statistical fields are used and solving differential equations for the others. We think that this technique will be very helpful to turbulence modelers because it is usually difficult to analyze the solution of the whole system of highly coupled equations. Since all the variables are non-linearly coupled, it is difficult, and maybe impossible, to find where problems come from by just looking at the solution of the full computation. At the same time, simple algebraic substitution of DNS data into formulas for pressure-strain, followed by comparison to the pressure-strain data, gives no information on the mathematical and computational properties of the turbulence model. The present approach is better suited to testing analytical closures.

We will also present some ideas for improving the general model.

2. Accomplishments

2.1 Results of the basic model

The flow was computed using a modified version of INS2D, a finite difference code in generalized coordinates written at NASA Ames Research Center. The modifications involve subroutines to solve the turbulence model and the incorporation of Reynolds stress-gradients into the mean flow solver.

A non-uniform grid of 120×120 cells, refined near the walls and around the corner of the step, was used to cover the region $x/h = -3$ to 35 , $x = 0$ being the location of the sudden expansion and h being the step height. Our solution has been checked for grid-independence; a twice finer grid in both directions gave indistinguishable results. Inlet values for the mean velocities, Reynolds stresses, and dissipation were taken from the DNS database. The elliptic relaxation procedure of Durbin (1993) has been combined with the Speziale, Sarkar, Gatski (SSG 1991) pressure strain model in the 'neutral' formulation of Laurence *et al.* (1995). The resulting equations have been calibrated using DNS and experimental data for both channel flow and zero pressure gradient boundary layers. That model was directly applied to the backstep flow without further modification. All the equations and constants used for this computation can be found in the appendix of Parneix *et al.* (1996).

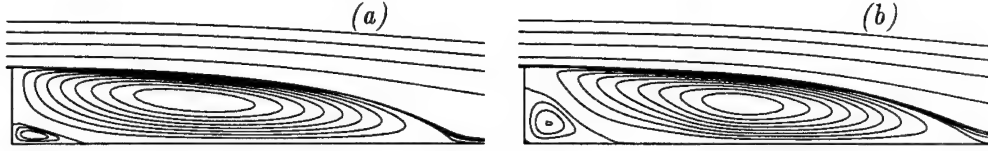


FIGURE 1. Streamlines: (a) Second moment closure; (b) DNS.

Fig. 1 shows the predicted streamlines compared to the DNS data. One can observe that the reattachment length is very well predicted and a secondary bubble is found. The flow seems to have a correct behavior near the reattachment point: it does not show the anomalous streamline pattern that has been found in other computations (Hanjalic 1996). However, the size of this corner bubble is much smaller in the computation than in the data. This defect seems to be linked to an underprediction of the maximum friction coefficient in the backflow (cf Fig. 2a). By looking to the profiles of the streamwise mean velocity (cf Fig. 2b), one can observe that the overall features of the mean flow is reproduced, but the intensity of the backflow is missed by a factor of 2, which could be problematic for the prediction of near-wall heat transfer. Note that this specific problem seems to be common to every existing Second Moment Closure model, whatever near-wall model is used (low-Reynolds model or wall function). Note also that, as with all existing turbulence models including eddy viscosity models, the recovery after reattachment is too slow. The friction coefficient distribution shows similarities (too slow near-wall flow) both upstream and downstream the reattachment point, but we don't know yet if these two problems (too slow backflow and too slow recovery) are linked.

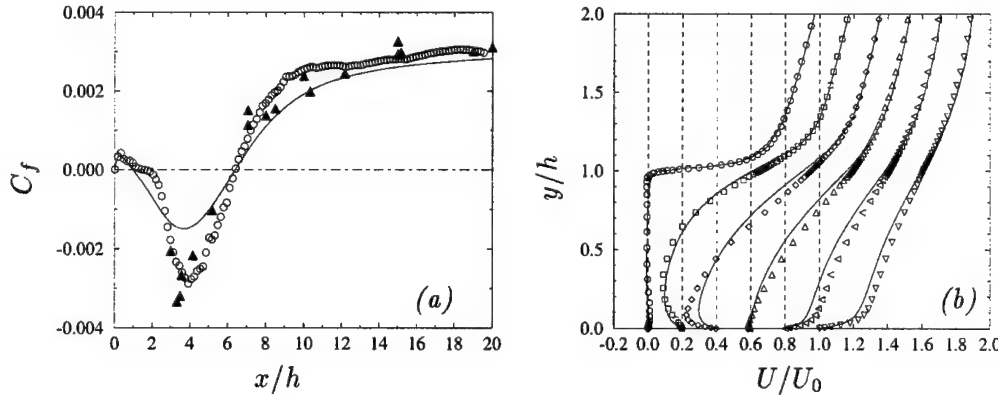


FIGURE 2. (a) Friction coefficient. — : full SMC; \circ : DNS (Le, Moin & Kim, 1993); \blacktriangle : experiment (Jovic & Driver, 1995). (b) U-profiles at locations $x/h = 0.1$ (\circ); 2 (\square); 4 (\diamond); 6 (Δ); 8 (\triangleleft) and 10 (∇); symbols: DNS; lines: full SMC.

Figures 3 to 5 present profiles of the computed normal component of the mean velocity V and statistics (Reynolds stresses $\overline{u_i u_j}$, turbulent kinetic energy k , and dissipation of turbulence ϵ) compared to the DNS data. The V -profiles at $x/h = 0$

and 2 confirm the distribution of the friction coefficient: the intensity of the two bubbles is severely underestimated. By looking at the profiles before reattachment, one can observe that V is also underestimated in the shear layer by about 15%. In fact, all the problems can be linked together by noting that more entrainment in the shear layer would lead to a more intense main recirculation (and maybe also a more rapid recovery), leading to a bigger and more intense secondary bubble. However, a modification of the backflow would also change the pressure distribution and thereby influence the velocity distribution in the shear layer.

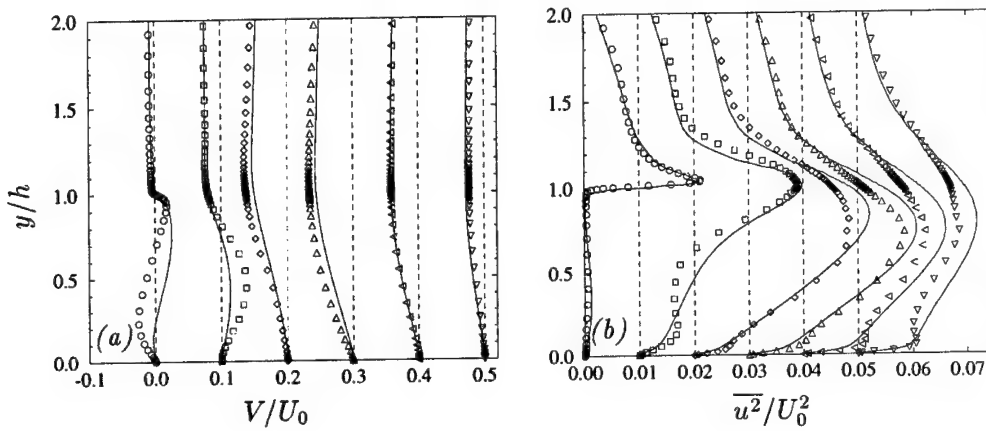


FIGURE 3. (a) V profiles (b) $\overline{u^2}$ profiles (legends similar to Fig. 2b).

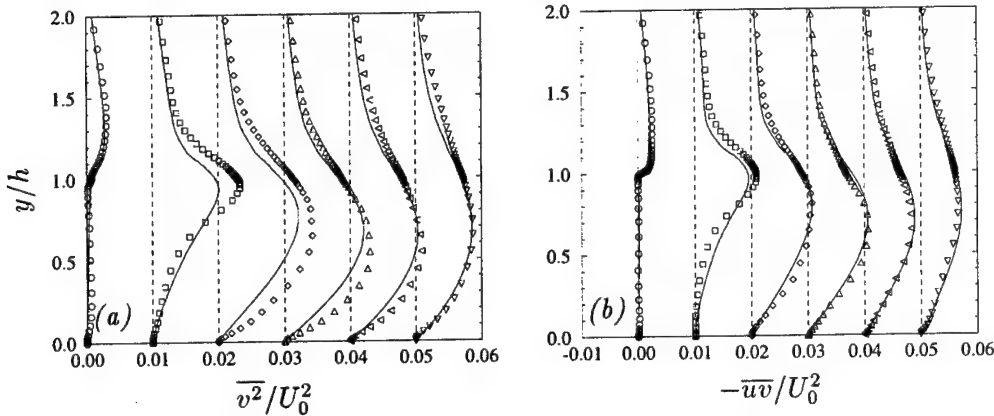


FIGURE 4. (a) $\overline{v^2}$ profiles (b) $-\overline{uv}$ profiles (legends similar to Fig. 2b).

The statistics seem to be reasonably well represented by the model. However, $\overline{u^2}$ shows a too slow recovery: the peak near the wall has not yet appeared at $x/h = 10$. Moreover, the model overestimates the gradients $\partial k/\partial y$ and $\partial \overline{u^2}/\partial y$ at $x/h = 2$. The level of turbulence is too high at this important location, but k and $\overline{u^2}$ do not enter directly into the momentum equations and should have a secondary

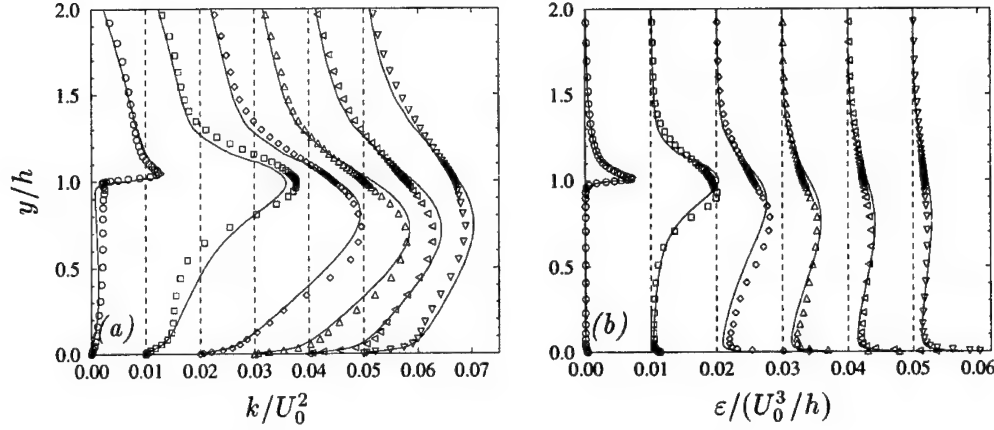


FIGURE 5. (a) k profiles (b) ε profiles (legends similar to Fig. 2b).

effect. Indeed, the main active terms in the turbulent force are $(-\partial \overline{uv}/\partial y)$ for the U -equation and $(-\partial \overline{v^2}/\partial y)$ for the V -equation (cf. Figs. 10 and 11). Figure 4b shows an almost perfect distribution of \overline{uv} , although a slight underestimation of the gradient $(-\partial \overline{uv}/\partial y)$ exists in the shear layer. The primary fault is that $\overline{v^2}$ is underestimated everywhere, especially in the shear layer where $\partial \overline{v^2}/\partial y$ is badly predicted. In fact, if one looks at the results of the following *a priori* tests (cf. Figs. 10 and 11), the conclusion will be exactly in the opposite direction (i.e. the problem comes from the uv -equation instead of the $\overline{v^2}$ -equation). This is because, in the full computation, the gradients of mean flow are badly estimated in some regions, which alters the production term of uv and $\overline{v^2}$. So, without the method presented below for decoupling the model solution from the mean flow solutions, the problem cannot be tracked down.

Finally, the dissipation, ε , is very well simulated except in the near-wall region where one can notice an important underestimation, which is consistent with the fault found in the prediction of $\partial k/\partial y$. Nevertheless, similar comments may be made for ε : a bad production term alters the overall analysis; the present *a priori* method is needed to truly assess the model differential equations.

With all the equations coupled, it is difficult, maybe impossible, to know where the problem comes from by just looking to the solution of the full computation. The analysis of the full solution might suggest that one has to improve both the $\overline{v^2}$ and ε equations. However, the following study will prove that these equations behave sufficiently well, and that the uv -equation is the main problem. It should be pointed out that every other low-Reynolds SMC model or SMC computation with the logarithmic law of the wall underpredicts the backflow intensity. In order to obtain a precise understanding of this and to go further in the study of the DNS database, we generated a new technology for carefully testing each equation of the model.

2.2 A new *a priori* technique for analyzing and improving turbulence models

The standard way of analyzing a DNS database consists in using the full DNS

data to compute the distribution of some important variables like the turbulent Reynolds number Re_t in order to understand the main physical features of the flow and to get some new ideas for modeling. Figure 6, showing Re_t and the budget of the U -momentum equation in the middle of the recirculation ($x/h = 4$), presents an example of such a study. In their experiment, Jovic and Driver (1995) found that the minimum of C_f follows a ‘laminar-like’ law: $C_f = -0.19(Re_h)^{-0.5}$ for Reynolds numbers between 5,000 and 50,000. However, Re_t , which represents about ten times the ratio between the turbulent viscosity and the molecular viscosity (in the $k - \varepsilon$ model), is in the range 200 – 800 in the whole domain, including the bubble (of course, it goes down to 0 at the wall). If one is still not sure of the completely turbulent feature of this recirculation, it becomes obvious by looking at the U -momentum budget: at station $x/h = 4$, the Reynolds stress gradients predominate the viscous force in the whole bubble except very near the wall, far below the maximum of the reverse flow.

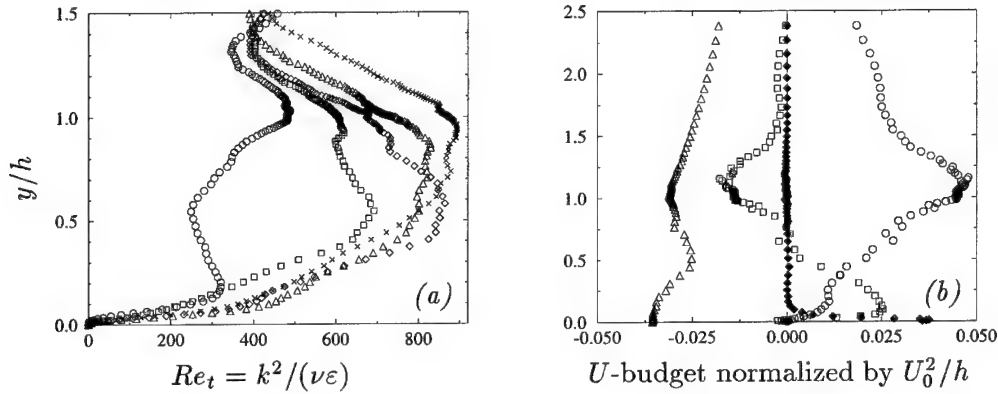


FIGURE 6. Direct analysis of the DNS database (a) Re_t profiles at locations: $x/h = 2$ (\circ); 4 (\square); 6 (\diamond); 8 (\triangle); and 10 (\times). (b) U -momentum budget at station $x/h = 4$ (middle of the recirculation): \circ : convection; \square : turbulent force; \blacklozenge : viscous force; \triangle : pressure force.

It is possible to go further in the investigation of a DNS database. Rodi & Mansour (1993) directly used DNS data for testing turbulence models and looking for improvements. The idea was to introduce the DNS ‘exact’ data into the modeled equations and to analyze the differences with the corresponding ‘exact’ DNS terms. In particular, they showed that it was possible to find some efficient damping functions for improving the behavior of a $k - \varepsilon$ model near the wall. One important problem with such a technique is that, even if a ‘perfect’ equation is found for every term of the global budgets (which means that the modeled equation fits perfectly with the DNS data), the general convergence of the global system has not been included in the study, and the resulting model can be numerically unstable. Moreover, such terms as dissipation or transport of Reynolds stresses are not well enough resolved, even by recent DNS, for an accurate and complete analysis term by term.

In order to avoid these problems, a new set of *a priori* tests has been generated. These consist in solving the full differential equations of each individual variable one by one, while the others are taken directly from the DNS database. This kind of computation allows a finer analysis of the true effects of terms like pressure-strain or transport models; it also permits more confidence in the numerical stability of eventual improved model terms. Moreover, an overall comparison between the full simulation and *a priori* tests explains why an analysis using only the full computation may entail erroneous conclusions. For example, the results presented in the previous section could lead one to believe that the model has some problems in both $\overline{v^2}$ and ε equations (ε is often regarded as the weakest point of turbulence models), whereas the *a priori* tests show that discrepancies are mainly located in the uv -equation. To our knowledge, this idea was first applied by Hanjalic (1994) for 1-D, fully developed channel flow. Although he did not discuss the method, his Fig. 13 was computed using the Reynolds stresses $\overline{u_i u_j}$ and the mean streamwise velocity U from the DNS of a channel flow, solving the ε -equation. Hanjalic then tested different models. His tests were not extended to the other variables. The present report presents the first 2-D use of this technique. We have used the RANS code to obtain the solutions by this *a priori* technique.

A first *a priori* test might concern the mean flow. As soon as the Reynolds stresses are interpolated from the DNS and are assumed to be exact, there is no longer any modelization in the momentum equations. A full RANS solution of the momentum and continuity equations would give 'perfect' mean flow profiles. Unfortunately, the DNS have been conducted with a too short channel (20 step heights downstream of the step) to allow our steady-state computations to converge. In fact, it is well known that, for the kind of outlet boundary conditions formerly used (constant pressure), a channel length of at least 30 step heights is needed to avoid reflections from the outlet boundary, making the computation unstable. However, the mean momentum equation demands that this particular computation will reproduce the DNS mean flow, so there is nothing to be learned from it.

In order to describe in detail the methodology we used to test turbulence models, we will focus first on the k -equation:

$$\frac{\partial k}{\partial t} + U \cdot \nabla k = P - \varepsilon + \nabla \cdot (\nu \nabla k) + D_T \quad (1)$$

P is the rate of production of turbulent kinetic energy: $P = -\overline{u_i u_j} \partial_j U_i$, D_T is the transport term: $D_T = -\partial_k (\overline{k u_k})$. All the other variables (i.e. U , V , ε , and $\overline{u_i u_j}$) are fixed by DNS data in the present test. Thus, $(P - \varepsilon)$ is a fixed source term for the k -equation. The solution of (1) basically will evaluate the efficiency of the model for the transport term D_T (the only term which needs to be modeled). Two models are currently used in SMC computations:

– the Daly-Harlow model (1970) with $0.20 \leq C_\mu^{DH} \leq 0.25$:

$$D_T^{DH} = \frac{\partial}{\partial x_k} (C_\mu^{DH} T_{\overline{u_k u_l}} \frac{\partial k}{\partial x_l}) \quad (2)$$

– the Hanjalic-Launder model (1972) with $C_\mu^{HL} = 0.11$:

$$D_T^{HL} = \frac{\partial}{\partial x_k} (C_\mu^{HL} T \overline{u_k u_l} \frac{\partial k}{\partial x_l}) + \frac{\partial}{\partial x_k} (C_\mu^{HL} T \overline{u_i u_l} \frac{\partial \overline{u_i u_k}}{\partial x_l}) \quad (3)$$

T being the time scale.

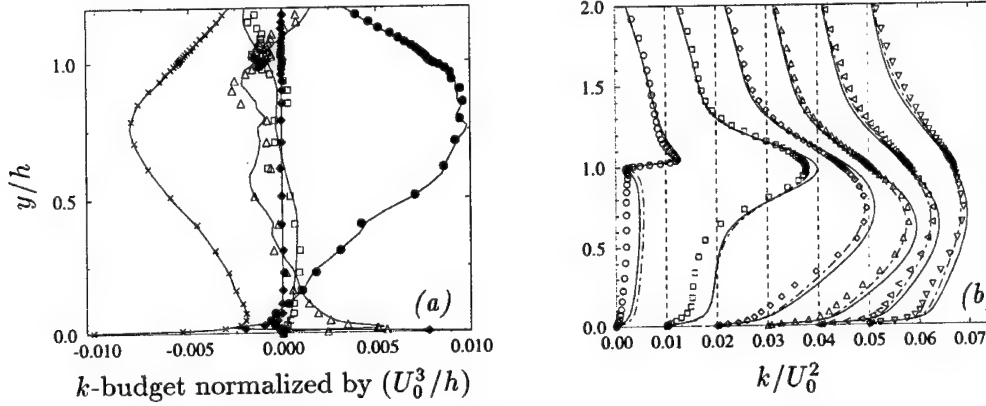


FIGURE 7. *A priori* test of the k -equation. (a) k -budget at $x/h = 4$. \bullet : production; \times : dissipation; \square : convection; \triangle : transport; \blacklozenge : diffusion; — : *a priori* computation. (b) k -profiles. Legend similar to Fig. 2b; — : DH model ($C_\mu^{DH} = 0.2$); --- : DH model ($C_\mu^{DH} = 0.25$).

In the full computation presented in the previous section, we used the DH model with $C_\mu^{DH} = 0.20$. We tested this model by the new *a priori* technique. The budgets (Fig. 7a) look perfect, but this does not mean that the model is accurate because $(P - \varepsilon)$ is fixed; convection is quite small, so at convergence any transport model would balance all the other terms and fall close to the DNS profiles. However, the resulting k -profiles, shown in Fig. 7b, could come out wrong. The figure emphasizes the effectiveness of the transport model. Surprisingly, the behavior of the DH model is excellent in this case (backstep at low Reynolds number), an increase of C_μ^{DH} up to 0.25 giving even better results. In fact, the only discrepancy that has been found concerns the secondary recirculation ($x/h = 0$ and 2) where a severe overprediction has been obtained. This is not improved by modifying the C_μ^{DH} constant. The more elaborated HL-type model improves the behavior in this region but performs poorly after reattachment (see profiles at $x/h = 6$ to 10, Fig. 9a).

Another interesting *a priori* test that has been performed concerns the dissipation ε , which is usually considered as the weak point of any turbulence model. In fact, the generation of the ε -equation relies mainly on intuition, so most of the shortcomings of turbulence models were thought to be in this equation — and most of the modifications of turbulence models were done to it. In this study, we used the ‘primitive’ equation, derived by Hanjalic & Launder (1972) with only two small modifications: ε/k has been replaced by the inverse of the time scale $1/T$ (Durbin 1993), and an extra-production term was included into $C_{\varepsilon 1}$ for taking into account

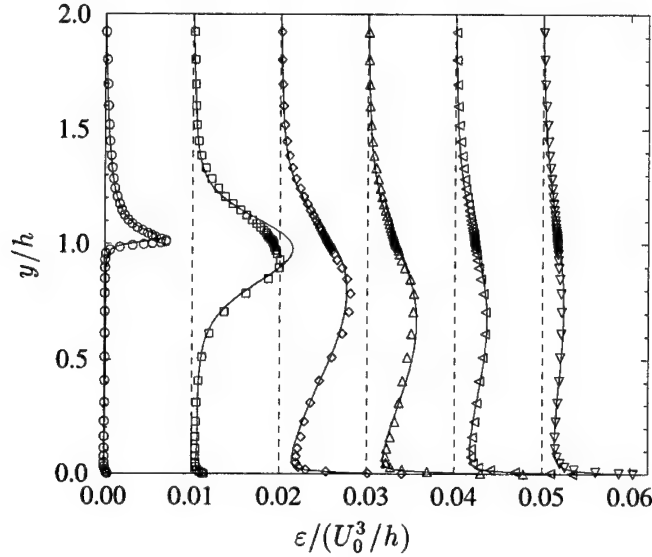


FIGURE 8. *A priori* test of the ε -equation (legend similar to Fig. 2b).

the wall effect (Parneix *et al.* 1996). We fixed all the other variables (i.e. U , V , k , $\overline{u_i u_j}$) and solved this equation. Surprisingly, the results are very good, especially in the recirculation and recovery regions (Fig. 8). In these conditions, it is difficult to believe that only a modification of the ε -equation will cure all the problems, and especially the underprediction of the backflow and the recovery. However, one could argue that the reattachment length is sensitive to the difference $(C_{\varepsilon_2} - C_{\varepsilon_1})$, but this strong dependency seems to lie in the shear layer where the dependence of the growth of the shear layer on $(C_{\varepsilon_2} - C_{\varepsilon_1})$ is well known. Concerning the behavior near the wall, the equation presented above seems to be more than sufficient for this case.

Since we now think that ε is no longer responsible for the backflow and recovery discrepancy, we come back to other modeled terms; first to the transport model. We saw that both DH and HL models perform very well in the shear layer but overpredict the turbulence in the near-wall region, which could affect either backflow or recovery. In these conditions, we tried to improve these predictions by generating a new model. One has then to revisit the third-moment equation:

$$\begin{aligned}
 D_t \overline{u_i u_j u_k} = & -\overline{u_i u_j u_l} \partial_l U_k - \overline{u_i u_k u_l} \partial_l U_j - \overline{u_k u_j u_l} \partial_l U_i \\
 & + \overline{u_i u_k} \partial_l \overline{u_j u_l} + \overline{u_j u_k} \partial_l \overline{u_i u_l} + \overline{u_i u_j} \partial_l \overline{u_k u_l} \\
 & - \partial_l \overline{u_i u_j u_k u_l} \\
 & + \Pi_{ijk} + D_{ijk} - \varepsilon_{ijk}
 \end{aligned} \tag{4}$$

The three last terms (pressure-deformation, viscous diffusion, and dissipation) are usually grouped together in a relaxation term, suggested by the corresponding Rotta approximation for the pressure-deformation in the second-moment equations:

$$\Pi_{ijk} + D_{ijk} - \varepsilon_{ijk} = -\frac{1}{C_s T} \overline{u_i u_j u_k} \tag{5}$$

By recourse to a Gaussianity assumption, the quadruple correlations are approximated in terms of second order correlation:

$$\overline{u_i u_j u_k u_l} = \overline{u_i u_j} \overline{u_k u_l} + \overline{u_i u_k} \overline{u_j u_l} + \overline{u_i u_l} \overline{u_k u_j} \quad (6)$$

By neglecting the convection and production terms, Hanjalic & Launder came up with their algebraic expression of triple correlations (see above). Daly & Harlow only retained the terms involving $\partial_l \overline{u_i u_j}$ and approximated the other terms by modifying the constant. Note that their expression of triple moments itself is not invariant under permutation of the three indices, but the remaining transport model (cf. above) preserves the symmetry on two indices. If one no longer neglects the production terms (note that these latter show the proper slope at the wall, contrary to the DH and HL models), a linear system is then obtained that can be solved analytically. Unfortunately, the derived expression of triple correlations in terms of second moment and gradients of mean flow becomes messy and unfeasible for practical applications. When only $\partial_y U$ is retained (it has been checked to be the most important mean gradient everywhere in the domain), the correction D_T^{cor} (in addition to the HL model) in the k -equation is still too messy, but one main term can be emphasized:

$$D_T^{cor} = \partial_x ((C_s T)^2 [\partial_y U] S_{ii2}) + \dots \quad (7)$$

with $S_{ii2} = 2\overline{u_i u_l} \partial_l \overline{u_i u_k} + \overline{u_k u_l} \partial_l \overline{u_i u_i}$. By doing the same operation as Daly & Harlow (keeping the terms involving $\partial_l \overline{u_i u_j}$; i.e., $\partial_l \overline{u_i u_i}$ for the k -equation), we derived the following expression for the correction of the DH transport model:

$$(D_T)_{ij} = (D_T^{DH})_{ij} + \frac{\partial}{\partial x_k} \left\{ \alpha (C_s T)^2 \frac{\partial U_k}{\partial x_n} \overline{u_n u_l} \frac{\partial \overline{u_i u_j}}{\partial x_l} \right\} \quad (8)$$

which becomes in the k -equation:

$$D_T = D_T^{DH} + \frac{\partial}{\partial x_k} \left\{ \alpha (C_s T)^2 \frac{\partial U_k}{\partial x_n} \overline{u_n u_l} \frac{\partial k}{\partial x_l} \right\} \quad (9)$$

$\alpha = 0$ leads to the classical DH model. Figure 9 presents the results we obtained with $\alpha = -0.8$ and $C_s = 0.25$. An important improvement in the prediction of k in the small bubble region ($0 \leq x/h \leq 2$) can be seen without significant modification of the profiles in the rest of the domain (see the difference between the classical DH model in Fig. 7b and the modified DH model in Fig. 9a). Unfortunately, when this new model was implemented in a computation, only 10% of the discrepancy concerning the friction coefficient minimum was found to have been cured (Fig. 9b). In fact, the flow field is really only improved around $x/h = 2$, where the improvement was also seen to be greatest during the *a priori* test. The backflow and the recovery do not show any specific modification.

In conclusion, these results lead us to think that both k and ε equations seem to represent quite well the physics of the problem (at least in this case!) and that the

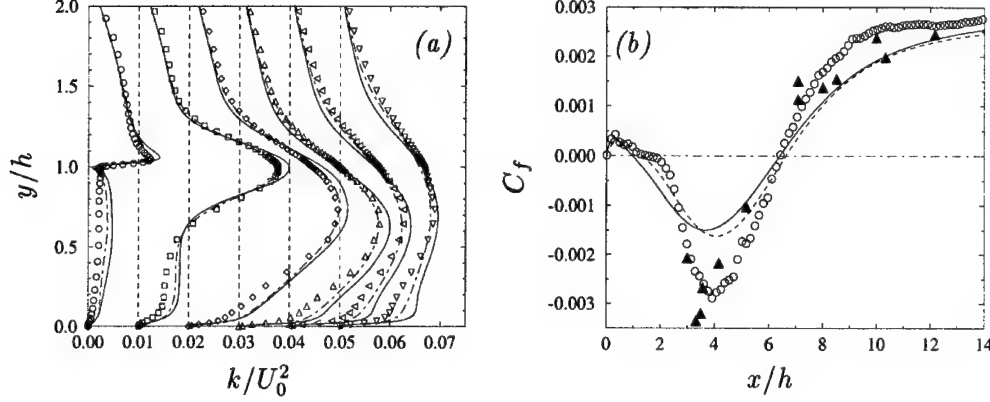


FIGURE 9. A new transport model. (a) *A priori* k -profiles: legends similar to Fig. 2b for symbols; — : HL model; --- : modified DH model. (b) Friction coefficient: legends similar to Fig. 2a; ---- : full computation with modified DH model.

backflow and recovery problems should come from other equations of the model, i.e. the Reynolds-stress equations.

We repeated the same kind of *a priori* tests for each $\overline{u_i u_j}$ -equation, coupled to its associated elliptic operator for the pressure-strain correlation. We have already explained the interest of doing such tests: indeed the \overline{uv} -profiles obtained through the full computation seem to be almost perfect whereas the *a priori* test (with u^2 , v^2 , U , V , k , and ε fixed to their DNS value) shows an overprediction of $-\overline{uv}$ almost everywhere. We tried to be even more pragmatic by computing those *a priori* turbulent stresses that will directly effect the mean flow. So, $\overline{u^2}$ (resp. \overline{uv} and $\overline{v^2}$) have been solved giving the *a priori* turbulent force $-\partial \overline{u^2} / \partial x$ (resp. $-\partial \overline{uv} / \partial x$, $-\partial \overline{uv} / \partial y$ and $-\partial \overline{v^2} / \partial y$).

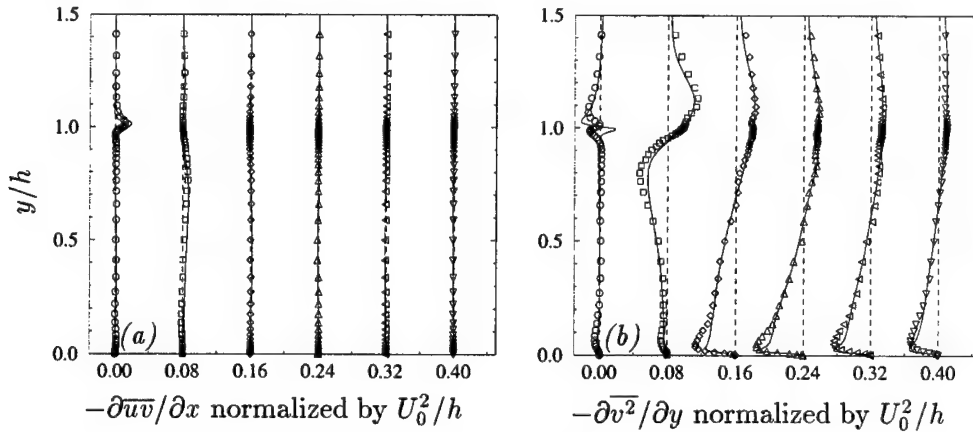


FIGURE 11. *A priori* turbulent force acting in the V -momentum equation (legends similar to Fig. 10). (a) resolution of the \overline{uv} -equation with $\overline{u^2}$, $\overline{v^2}$, k , ε , U and V fixed, (b) resolution of the $\overline{v^2}$ -equation with $\overline{u^2}$, \overline{uv} , k , ε , U and V fixed.

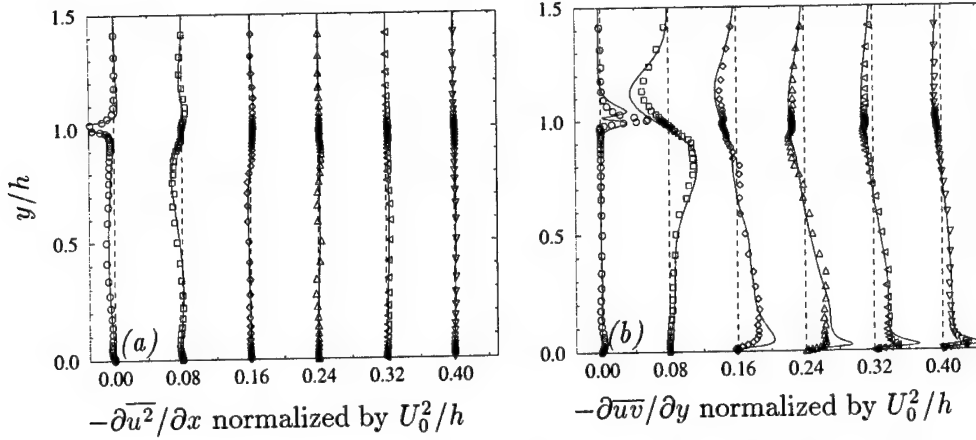


FIGURE 10. *A priori* turbulent force acting in the U -momentum equation at locations: $x/h = 0.1$ (\circ); 2 (\square); 4 (\diamond); 6 (\triangle); 8 (\triangleleft); and 10 (∇). Symbols: DNS, — : *a priori* test. (a) resolution of the u^2 -equation with $\bar{u}v$, v^2 , k , ϵ , U and V fixed, (b) resolution of the $\bar{u}v$ -equation with \bar{u}^2 , v^2 , k , ϵ , U and V fixed.

We kept the same scaling in each figure (10a, 10b, 11a, 11b) in order to be able to compare the effective action of each stress on the momentum budget. At every location (except maybe near the corner of the step), the streamwise gradients are negligible. The turbulent force mainly results in $-\partial\bar{u}v/\partial y$ in the U -equation and $-\partial\bar{v}^2/\partial y$ in the V -equation. One conclusion is that \bar{u}^2 has a secondary effect on the mean flow. By looking at the normal gradients ($\partial/\partial y$), one can notice a peculiar behavior at the corner of the step. The DNS trends are not at all reproduced in this region but this deficiency seems to stay local and to have little influence on the rest of the domain; the kink we can see at location $x/h = 0.1$ has not been transported further ($x/h \geq 2$). Nevertheless, a more careful study should definitely be done in the corner area.

With the exception of this problem, \bar{v}^2 is accurately predicted (cf. Fig. 11b), the only discrepancy can be found near the wall beyond the reattachment point at $x/h = 4$ and 6 (slight underprediction of the gradient), but this should not affect directly the mean flow because, at this location, the flow is nearly parallel to the wall (V is basically equal to 0). However, locations $x/h = 4$, 6 , and 8 of Fig. 10b show an overprediction of the turbulent force acting in the U -momentum by a factor of 2 around the reattachment point in the region where lies most of the backflow ($y/h \leq 0.15$). In this area, U is negative and the turbulent force (which is one of the main terms in the U -momentum budget, see Fig. 6b) acts to slow down the flow, thus the overprediction by a factor of 2 should explain the severe underprediction of backflow we obtained with the full SMC computation. Let us note that the model seems also to be deficient in the recovery region (overprediction of $-\partial\bar{u}v/\partial y$) but this defect appears in a thinner region; moreover, U is positive here and the turbulent stress is then acting as a positive force. In these conditions, a decrease of $-\partial\bar{u}v/\partial y$ should slow down the flow in a region where the flow itself has already

been too slow. The origin of the recovery problem still has to be found.

3. Future plans

A full second moment closure computation has been carried out for evaluating the turbulent flow over a backward-facing step at low Reynolds number ($Re = 5,100$). The model, including elliptic relaxation of pressure-strain to take into account the non-local effects of pressure near to walls, has been calibrated solely with channel flow and zero pressure gradient turbulent boundary layer data at various Reynolds numbers; it has been directly applied to the backstep without any modification. The results show a very good prediction of the recirculation length but an underprediction of the backflow by a factor of 2. The recovery has been seen also to be too slow.

An analysis of the corresponding DNS database proved that the main bubble is definitely turbulent even at this low Reynolds number. A new technique of *a priori* testing with DNS data has been developed; it consists, basically, in evaluating the accuracy of each equation of the model by solving one variable while fixing all the others to their DNS values. It came out that both Daly-Harlow transport model for k , and the ε -equation do surprisingly well, contrary to what is generally thought in the literature.

Regarding the Reynolds stresses, $\overline{u_i u_j}$, $\overline{u^2}$ has a secondary effect on the mean flow because the streamwise gradients occurring in the turbulent force ($-\partial \overline{u^2}/\partial x$ and $-\partial \overline{uv}/\partial x$) are negligible compared to the normal gradients ($-\partial \overline{uv}/\partial y$ and $-\partial \overline{v^2}/\partial y$). In fact, the main problem seems to come from the \overline{uv} -equation, which gives an overprediction of the turbulent force by a factor of 2 in the backflow region.

In the future, we would like to focus on the \overline{uv} -equation in order to find the model term that is deficient and to propose an improved model.

Improving the model with the help of this new testing technique, and getting the right distribution of friction coefficient in the backflow region, will best prove the efficiency of this novel method for turbulence modelers.

In the meantime, we plan to apply the idea of elliptic relaxation on other configurations, including both 2D and 3D geometries. Moreover, at this time, the global numerical stability of Re-stress modeling is still an issue, and some improvements in this domain are still needed.

REFERENCES

- DALY, B. & HARLOW, F. 1970 Transport equations in turbulence. *Physics of Fluids*. **13**(11), 2634-2649.
- DURBIN, P. 1993 A Reynolds-stress model for near-wall turbulence. *J. Fluid Mech.* **249**, 465-498.
- DURBIN, P. A. & LAURENCE, D. 1996 Nonlocal effects in single point closure. *Turbulence Research Associates-96 meeting*. Seoul Korea.
- HANJALIC, K. & LAUNDER, B. E. 1972 A Reynolds stress model of turbulence and its application to thin shear flows. *J. Fluid Mech.* **52**, 609-638.

- HANJALIC, K. 1994 Advanced turbulence closure models: a view of current status and future prospects. *Int. J. Heat and Fluid Flow*. **15**(3), 178-203.
- HANJALIC, K. 1996 Some resolved and unresolved issues in modeling non equilibrium and unsteady turbulent flows. *Engineering Turbulence Modeling and Measurements*, W. Rodi and G. Bergeles Eds., Elsevier Pub. **3**, 3-18.
- JOVIC, S. & DRIVER, D. 1995 Reynolds number effect on the skin friction in separated flows behind a backward-facing step. *Experiments in Fluids*. **18**.
- KASAGI, N. & MATSUNAGA, A. 1995 Three-dimensional particle-tracking velocimetry measurements of turbulence statistics and energy budget in a backward facing step flow. *Int. J. Heat and Fluid Flow*. **16**, 477-485.
- KO, S. & DURBIN, P. 1994 Separated turbulent flows computed with a near-wall Reynolds stress model. *ASME-FED Summer Meeting*. **196**, 83-92.
- LAUNDER, B. E., REECE, G. J. & RODI, W. 1975 Progress in the development of a Re-stress turbulence closure. *J. Fluid Mech.* **68**, 537-566.
- LAUNDER, B. E. 1989 Second-moment closure: present ... and future? *Int. J. Heat and Fluid Flow*. **10**(4), 282-300.
- LAURENCE, D., DURBIN, P. A. & DEMUREN, A. O. 1995 Modeling near wall effects in second moment closures by elliptic relaxation. *10th. Symp. on Turbulent Shear Flows*, Penn State Pennsylvania, 20-1.
- LE, H., MOIN, P. & KIM, J. 1993 Direct numerical simulation of turbulent flow over a backward-facing step. *Proc. 9th Symp. on Turbulent Shear Flows*, Kyoto, Japan, 13.2.1-13.2.6.
- PARNEIX, S., LAURENCE, D. & DURBIN, P. 1996 Second moment closure analysis of the backstep flow database. *Proc. 1996 Summer Program*, Center for Turbulence Research, NASA Ames/Stanford Univ., 47-62.
- RODI, W. & MANSOUR, N. N. 1993 Low Reynolds number $k - \varepsilon$ modeling with the aid of direct simulation data. *J. Fluid Mech.* **250**, 509-529.
- SPEZIALE, C. G., SARKAR, S. & GATSKI, T. B. 1991 Modeling the pressure-strain correlation of turbulence: an invariant dynamical systems approach. *J. Fluid Mech.* **227**, 245-272.

A particle representation model for the deformation of homogeneous turbulence

By S. C. Kassinos AND W. C. Reynolds

1. Motivation and objectives

In simple flows, where the mean deformation rates are mild and the turbulence has time to come to equilibrium with the mean flow, the Reynolds stresses are determined by the applied strain *rate*. Hence in these flows, it is often adequate to use an eddy-viscosity representation. The modern family of k - ϵ models has been very useful in predicting near equilibrium turbulent flows, where the rms deformation rate S is small compared to the reciprocal time scale of the turbulence (ϵ/k).

In modern engineering applications, turbulence models are quite often required to predict flows with very rapid deformations (large Sk/ϵ). In these flows, the structure takes some time to respond and eddy viscosity models are inadequate. The response of turbulence to rapid deformations is given by rapid distortion theory (RDT). Under RDT the nonlinear effects due to turbulence-turbulence interactions are neglected in the governing equations, but even when linearized in this fashion, the governing equations are unclosed at the one-point level due to the non-locality of the pressure fluctuations.

A good turbulence model should have a viscoelastic character, predicting turbulence stresses proportional to the mean strain rate (k - ϵ theory) for slow deformations and stresses determined by the amount of strain (RDT) for rapid deformations. Our goal has been the development of an engineering one-point model of turbulence that has this character. Our belief is that the greater modeling challenge is found in matching RDT when RDT applies. Hence our initial efforts were directed in constructing a good one-point model for RDT (Kassinos and Reynolds 1994).[†] Given a successful RDT model, we believe its blending with k - ϵ theory should be relatively straightforward. The success of the extended particle representation model (PRM) that will be discussed shortly provides justification for this point of view.

In a particle representation method, a number of key properties and their evolution equations are assigned to hypothetical particles. The idea is to follow an ensemble of "particles", determine the statistics of the ensemble, and use those as the representation for the one-point statistics of the corresponding field.

The key innovation in the original PRM approach presented in KR lies in the recognition that the linearity of the RDT governing equations makes it possible to emulate exactly the RDT for homogeneous turbulence using a PRM *without any modeling assumptions*. The non-local pressure effects can be evaluated within the framework of the PRM itself with no modeling assumptions. The PRM can be used

[†] Hereafter denoted by KR.

to evaluate all the one-point tensors needed in turbulence modeling, including the new structure tensors (see KR), but unlike spectral methods provides no two-point information. However, the PRM does provide information about the directional dependence of the real part of the spectrum of homogeneous turbulence. In that sense this method provides closure of RDT at minimum additional expense relative to a one-point approach.

The PRM has been used as the basis for the development of a viscoelastic *one-point* structure-based model of turbulence. Initially, the PRM was restricted to rapid mean deformations because our goal was to use it in developing a one-point model for the RDT of homogeneous turbulence (see KR). The development of the rapid *one-point* structure-based model has been completed with success, and we have recently been working on the extensions of the model to weak deformation rates and inhomogeneous flows. Towards that goal, we have extended the particle representation model to account for the non-linear turbulence-turbulence interactions that are important when the mean deformation is slow. This preliminary report discusses this Interacting Particle Representation Method (IPRM). As will be shown, the IPRM provides surprisingly accurate predictions for the one-point statistics in homogeneous turbulence subjected to a wide range of mean deformations. The IPRM is a viscoelastic structure-based model that bridges successfully RDT with k - ϵ theory. The success of the IPRM provides support to the idea that it should be easy to make a good model of RDT match k - ϵ theory when appropriate, and offers guidance in improving the slow extensions to the *one-point* structure-based model.

2. Accomplishments

In Sections 2.1 and 2.2 we introduce the basic RDT equations and the key ideas behind the PRM for the exact emulation of RDT. Then in Section 2.3, we present the formulation of the model for the non-linear particle-particle interactions (IPRM). In Section 2.4 we evaluate the IPRM for a wide range of mean deformations applied to homogeneous turbulence.

2.1 The basic RDT equations

The discussion is restricted to inviscid RDT because for the large eddies that contribute the most to the Reynolds stresses viscous effects are usually negligible, but this restriction can be removed. For the inviscid RDT of homogeneous turbulence, the fluctuating continuity and momentum equations are given by,

$$\frac{\partial u'_i}{\partial x_i} = 0 \quad (1)$$

and

$$\frac{\partial u'_i}{\partial t} + U_j \frac{\partial u'_i}{\partial x_j} = -G_{ij} u'_j - \frac{1}{\rho} p'_{,i}. \quad (2)$$

Here standard tensor notation is employed (subscripts after commas denote differentiation), U_i is the mean velocity, $G_{ij} = U_{i,j}$ is the mean velocity gradient tensor, and p' is the rapid part of the pressure fluctuations

$$\frac{1}{\rho} p'_{,mm} = -2G_{mn}u'_{n,m}. \quad (3)$$

We introduce the turbulent stream function vector defined by

$$u'_i = \epsilon_{its} \Psi'_{s,t}, \quad \Psi'_{i,i} = 0, \quad \Psi'_{i,nn} = -\omega'_i. \quad (4)$$

We require Ψ'_i to be divergence-free so that the last equality in (4) is valid. This choice is important for the physical meaning of the resulting structure tensors introduced by Kassinos and Reynolds (see KR). Here ω'_i denotes the components of the turbulent vorticity vector. Note that Ψ'_i satisfies a Poisson equation and hence like the fluctuation pressure carries non-local information.

2.1.1 One-point structure tensors

The Reynolds stress tensor and the associated non-dimensional and anisotropy tensors are defined by

$$R_{ij} = \overline{u'_i u'_j} = \epsilon_{ipq} \epsilon_{jts} \overline{\Psi'_{q,p} \Psi'_{s,t}}, \quad r_{ij} = R_{ij}/q^2, \quad \tilde{r}_{ij} = r_{ij} - \frac{1}{3} \delta_{ij}. \quad (5)$$

Here $q^2 = 2k = R_{kk}$. Introducing the isotropic tensor identity (Mahoney 1985)

$$\epsilon_{ipq} \epsilon_{jts} = \delta_{ij} \delta_{pt} \delta_{qs} + \delta_{it} \delta_{ps} \delta_{qj} + \delta_{is} \delta_{pj} \delta_{qt} - \delta_{ij} \delta_{ps} \delta_{qt} - \delta_{it} \delta_{pj} \delta_{qs} - \delta_{is} \delta_{pt} \delta_{qj} \quad (6)$$

and assuming homogeneity, one finds

$$R_{ij} + \underbrace{\overline{\Psi'_{k,i} \Psi'_{k,j}}}_{D_{ij}} + \underbrace{\overline{\Psi'_{i,k} \Psi'_{j,k}}}_{F_{ij}} = \delta_{ij} q^2. \quad (7)$$

The constitutive Eq. (7) shows that for a proper characterization of non-equilibrium turbulence the *componentality* information found in r_{ij} must be supplemented by *structure* information found in the one-point turbulent *structure* tensors D_{ij} and F_{ij} introduced by KR [see Eq. (7)]. In addition to the basic definitions of these tensors that appear in (7), one can use equivalent representations for homogeneous turbulence in terms of the velocity spectrum tensor $E_{ij}(\mathbf{k})$ and vorticity spectrum tensor $W_{ij}(\mathbf{k})$. These are as follows:

- Structure *dimensionality* tensor

$$D_{ij} = \int \frac{k_i k_j}{k^2} E_{nn}(\mathbf{k}) d^3 \mathbf{k} \quad d_{ij} = D_{ij}/q^2 \quad \tilde{d}_{ij} = d_{ij} - \frac{1}{3} \delta_{ij} \quad (8)$$

- Structure *circulicity* tensor

$$F_{ij} = \int \mathcal{F}_{ij}(\mathbf{k}) d^3 \mathbf{k} \quad f_{ij} = F_{ij}/q^2 \quad \tilde{f}_{ij} = f_{ij} - \frac{1}{3} \delta_{ij}. \quad (9)$$

Here $\mathcal{F}_{ij}(\mathbf{k}) = k^2 \overline{\hat{\Psi}_i \hat{\Psi}_j^*}$ is the circulicity spectrum tensor, which is related to the vorticity spectrum tensor $W_{ij}(\mathbf{k}) = \overline{\hat{\omega}_i \hat{\omega}_j^*}$ through the relation

$$\mathcal{F}_{ij}(\mathbf{k}) = \frac{W_{ij}(\mathbf{k})}{k^2}.$$

The familiar rapid pressure–strain-rate term is given by

$$T_{ij} = 2G_{ts}(M_{istj} + M_{jsti}) \quad (10)$$

where the fourth-rank tensor \mathbf{M} is given by

$$M_{ijpq} = \int \frac{k_p k_q}{k^2} E_{ij}(\mathbf{k}) d^3 \mathbf{k}. \quad (11)$$

2.2 A particle representation of the RDT of homogeneous turbulence

The key innovation in the PRM approach of Kassinos and Reynolds (see KR) lies in the recognition that the linearity of the RDT governing equations makes it possible to emulate exactly the RDT for homogeneous turbulence using a PRM *without any modeling assumptions*. The non-local pressure effects can be evaluated within the framework of the PRM thus providing closure. This is unlike traditional particle representation approaches employed by the combustion community. In these traditional particle representations, usually in the form of PDFs, modeling assumptions are introduced at some level, usually to account for the effects of the fluctuating pressure gradient and molecular viscosity on the evolution of the particle velocity. One can take moments of the governing stochastic evolution equations to form equations for one-point statistics, like the Reynolds stresses. To each assumed stochastic model corresponds an equivalent one-point Reynolds Stress Transport (RST) model. Hence, it was common to assume a stochastic model that would produce one of the standard RST models, but in this way modeling was introduced where it was not needed, i.e. in matching RDT.

Next, we present the basic ideas behind the PRM for the emulation the RDT of homogeneous turbulence. A more detailed discussion of the rapid PRM can be found in KR.

2.2.1 Particle properties

We start with a discussion of the properties assigned to each of the hypothetical particles and a geometrical interpretation of the “particles”. The assigned properties are:

- \mathbf{V} velocity vector
- \mathbf{W} vorticity vector
- \mathbf{S} stream function vector
- \mathbf{N} gradient vector
- P pressure.

These hypothetical particles represent an idealized building block for the turbulence structure. As shown in Fig. 1a, each particle corresponds to a plane of

independence. The vector \mathbf{N} , which is normal to the plane of independence, provides a measure of gradients normal to the plane. The remaining vectors lie in the plane of independence. Thus, each particle represents a 1D-1C flow, similar to a vortex-sheet.

2.2.2 Vector identities between properties

We now turn to the vector identities that relate the basic properties assigned to each particle. These identities are motivated by the relationships that exist between the various vectors in a field of turbulence. In fact as it is next shown, a one-to-one correspondence exists between the field and PRM identities.

The three vectors \mathbf{V} , \mathbf{N} , and \mathbf{W} form an orthogonal triad. The stream function vector \mathbf{S} is related to \mathbf{W} through the algebraic equation

$$S_i = -\frac{1}{N^2} W_i, \quad (12)$$

which is motivated by the Poisson Eq. (4). As a result of (12), we will often consider the vectors \mathbf{V} , \mathbf{N} , and \mathbf{S} as the basic orthogonal vector triad (see Fig. 1a).

In a turbulence field, the fluctuation velocity is the curl of the fluctuation stream function [see (4)]; therefore the vector \mathbf{V} is related to \mathbf{S} and \mathbf{N} through the analogous algebraic equation

$$V_i = \epsilon_{ipq} S_q N_p. \quad (13)$$

Equation (13) is a manifestation of the mutual orthogonality of the three vectors and can be used to show that

$$V^2 = S^2 N^2 \quad V_i V_j + S_i S_j N^2 + N_i N_j S^2 = S^2 N^2 \delta_{ij}, \quad (14)$$

where $N^2 = N_i N_i$, $V^2 = V_i V_i$, and $S^2 = S_i S_i$. Note that (14) is the PRM analog of the constitutive Eq. (7).

The corresponding property unit vectors are denoted by lower case letters, that is

$$n_i = \frac{N_i}{N} \quad v_i = \frac{V_i}{V} \quad s_i = \frac{S_i}{S}. \quad (15)$$

Using (15), the constitutive Eq. (14) can be put into the form

$$v_i v_j + s_i s_j + n_i n_j = \delta_{ij}. \quad (16)$$

This is a direct consequence of the orthogonality of the three unit vectors \mathbf{v} , \mathbf{s} , and \mathbf{n} . Equation (16) forms the basis for a number of identities relating higher products of property components.

2.2.3 Property evolution equations

We now turn to the evolution equations for the properties of each particle. The evolutions of \mathbf{W} and \mathbf{N} are governed by ordinary differential equations. The evolutions of \mathbf{V} and \mathbf{S} are determined through the algebraic Eqs. (12) and (13) that relate \mathbf{V} and \mathbf{S} to \mathbf{W} and \mathbf{N} .

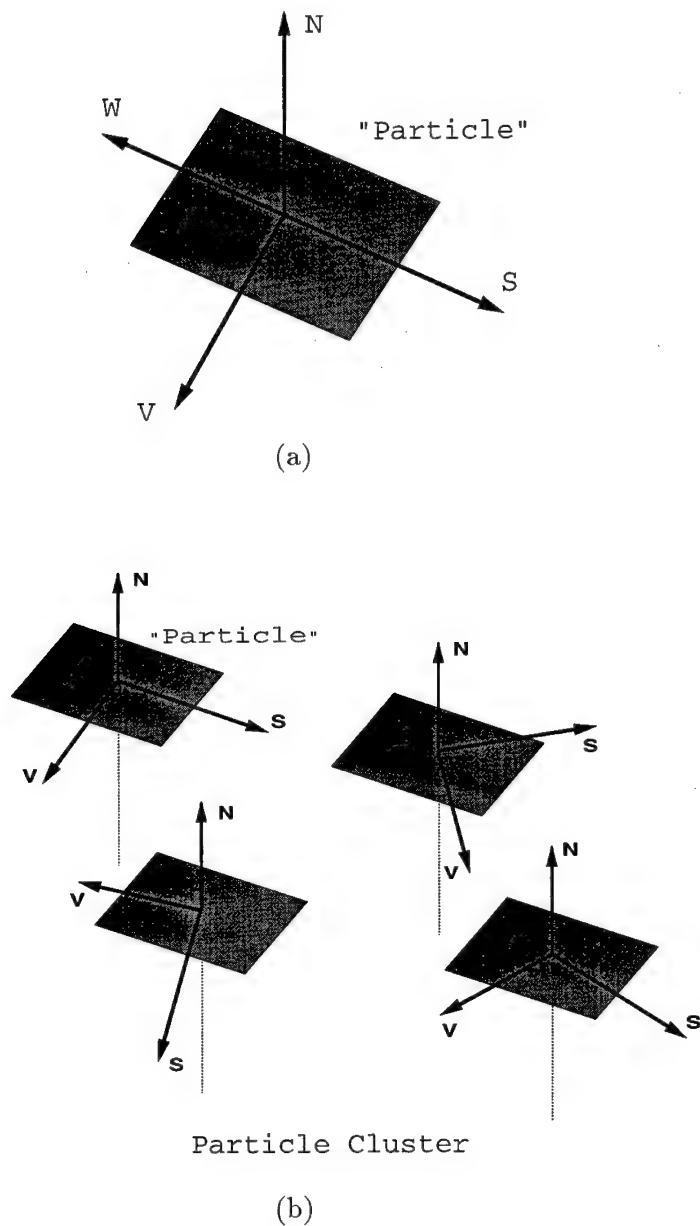


FIGURE 1. Particles used in the PRM: (a) The geometry associated with a hypothetical particle. (b) A cluster of particles forming 1D-2C flow.

A kinematic analysis of the motion of a plane of independence (vortex sheet) in a uniform mean deformation field (see KR) leads to the RDT evolution equation for \mathbf{N}

$$\dot{N}_i = -G_{ki}N_k. \quad (17)$$

The RDT equation for \mathbf{W} is based on the exact RDT equation for the evolution of the fluctuating vorticity in homogeneous turbulence, and is

$$\dot{W}_i = G_{ik}W_k + \Omega_k V_i N_k - G_{kk}W_i. \quad (18)$$

The vector \mathbf{S} is related to \mathbf{W} through (12), which is analogous to the Poisson Eq. (4) connecting the turbulent vector stream function Ψ'_i to the fluctuation vorticity w'_i . Using the definition (12) and the evolution equations (17) and (18), one can derive the evolution equation for \mathbf{S}

$$\dot{S}_i = G_{ik}S_k - \frac{\Omega_k V_i N_k}{N^2} - G_{kk}S_i + 2S_i G_{zk} \frac{N_z N_k}{N^2}. \quad (19)$$

As a consequence of (13), (17), and (19), one finds that the RDT evolution equation for \mathbf{V} is

$$\dot{V}_i = -G_{ik}V_k + 2G_{km} \frac{V_m N_k N_i}{N^2}. \quad (20)$$

The Poisson equation for the rapid pressure (3) is the basis for the analogous definition

$$P = -2G_{km} \frac{V_m N_k}{N^2}, \quad (21)$$

which then allows (20) to be written as

$$\dot{V}_i = -G_{ik}V_k - PN_i \quad (22)$$

by analogy to the mean momentum equation. Note that the definition of a pressure in this context is optional and motivated by the desire to preserve the similarity of the basic PRM evolution equations to their field counterparts.

Equations analogous to the continuity equation and divergence-free vorticity condition,

$$V_i N_i = 0 \quad \text{and} \quad W_i N_i = 0 \quad (23)$$

are satisfied because \mathbf{V} and \mathbf{W} are perpendicular to \mathbf{N} .

Note that one can evolve \mathbf{V} and \mathbf{N} with differential equations independently of any of the remaining variables and that the equations for the particle properties have a one-to-one correspondence with the comparable equations for the fields. The equivalence between the particle representation and the RDT field equations is discussed in detail in KR, where it is shown that \mathbf{N} corresponds to the wavenumber vector \mathbf{k} .

The evolution equations for the normalized gradient vector \mathbf{n} will play an important role in the discussion that follows. This can be derived using the definition (15) along with (17) and is given by

$$\dot{n}_i = -G_{ki}n_k + G_{km}n_k n_m n_i. \quad (24)$$

2.2.4 Representation of one-point statistics

In this section we introduce the representation for the one-point statistics of the turbulence field in the context of the PRM. The Reynolds stress $R_{ij} = \overline{u'_i u'_j}$ is represented as

$$R_{ij} = \langle V_i V_j \rangle = \langle V^2 v_i v_j \rangle, \quad (25)$$

where the angle brackets denote averaging over an ensemble of particles. The structure-dimensionality $D_{ij} = \overline{\Psi'_{n,i} \Psi'_{n,j}}$ and structure circulicity $F_{ij} = \overline{\Psi'_{i,n} \Psi'_{j,n}}$ tensors are represented as

$$D_{ij} = \langle S_n S_n N_i N_j \rangle = \langle V^2 n_i n_j \rangle \quad F_{ij} = \langle N_n N_n S_i S_j \rangle = \langle V^2 s_i s_j \rangle. \quad (26)$$

Similar representations exist for higher-rank tensors. For example, the representation for the fourth-rank tensor \mathbf{M} [see (11)] appearing in the rapid pressure-strain-rate term is given by

$$M_{ijpq} = \langle V_i V_j n_p n_q \rangle = \langle V^2 v_i v_j n_p n_q \rangle. \quad (27)$$

2.2.5 PRM implementation: cluster-averaged method

Unless the evaluation of higher vector moments is required, the cluster-averaged implementation of the PRM described here should be preferred because it offers a better computational efficiency (see KR). The idea in the cluster-averaged method is to do the averaging in two steps, the first step being done analytically.

First, an averaging is done over particles that have the same $\mathbf{n}(t)$, followed by an averaging over all particles with different $\mathbf{n}(t)$. The one-point statistics resulting from the first (cluster) averaging are conditional moments, which will be denoted by

$$R_{ij}^{\text{ln}} \equiv \langle V_i V_j | \mathbf{n} \rangle \quad D_{ij}^{\text{ln}} \equiv \langle V^2 n_i n_j | \mathbf{n} \rangle = \langle V^2 | \mathbf{n} \rangle n_i n_j \quad F_{ij}^{\text{ln}} \equiv \langle V^2 s_i s_j | \mathbf{n} \rangle. \quad (28)$$

The conditionally averaged stress evolution equation

$$\dot{R}_{ij}^{\text{ln}} = -G_{ik} R_{kj}^{\text{ln}} - G_{jk} R_{ki}^{\text{ln}} + 2G_{km} (R_{im}^{\text{ln}} n_k n_j + R_{jm}^{\text{ln}} n_k n_i) \quad (29)$$

is obtained by using the definition (28) along with (21) and (22). Note that (24) and (29) are *closed* for the conditional stress tensor R_{ij}^{ln} and n_i . That is, they can be solved without reference to the other conditioned moments. Thus, to follow the evolution of R_{ij} , instead of following a large number of particles that carry \mathbf{V} and \mathbf{n} with simple evolution equations (direct method), we can follow a smaller number of *particle clusters* that carry \mathbf{R}^{ln} and \mathbf{n} with only slightly more complicated evolution equations. These particle clusters correspond to 1D-2C vortical flows (vortex sheets) as shown in Fig. 1b. The conditioned stresses must satisfy $R_{ip}^{\text{ln}} n_p = 0$ and this property will be maintained by (24) and (29) if it is initially true. Note that it is unnecessary to evolve the conditioned F_{ij}^{ln} equation, since the constitutive Eq. (14) can be used to obtain F_{ij}^{ln} (and hence F_{ij}) from the evolved R_{ij}^{ln} and n_i .

Finally it is important to appreciate that the choice of \mathbf{n} as the *cluster vector* to be evolved in the cluster-averaged method is important. Unlike the evolution equations for the $\langle |\mathbf{n}| \rangle$ conditioned moments, the equations for the $\langle |\mathbf{s}| \rangle$ and $\langle |\mathbf{v}| \rangle$ moments are not closed and require modeling.

2.3. The interacting particle representation model (IPRM)

When the time scale of the mean deformation is large compared to that of the turbulence, the nonlinear turbulence-turbulence interactions become important in the governing field equations. In the context of the IPRM, these nonlinear processes are represented by particle-particle interactions. As in the case of the one-point field equations, the nonlinear processes cannot be evaluated directly and modeling is required. Because some modeling must be introduced, the emulation of the field equations by the IPRM is no longer exact, which was the case for the PRM emulation of RDT.

2.3.1 Formulation of the slow model

Here we present what we have termed the Interacting Particle Representation Method (IPRM). The basic idea behind the IPRM is simple. The overall effect of the background particle-particle interactions on any given particle is modeled in two parts. The first part, which we call the *effective gradient* model, assumes that the background particle-particle interactions provide a gradient acting on the particles in addition to the mean deformation rate. The assumption is that the effective deformation rate can be expressed in terms of the mean deformation rate and statistics based on the particle ensemble thus providing closure.

The second part of the particle-particle interaction model accounts for rotational effects. Mean rotation acting on the particles tends to produce rotational randomization of the \mathbf{V} vectors around the \mathbf{n} vectors (see KR). Effective rotation due to particle-particle interactions should also induce a similar randomization effect. We have found that best results are obtained when this *slow rotational randomization effect* is modeled explicitly.

Different models for the effective eddy deformation tensor are possible, and we are still exploring some of these options. Here we report one such model that we have found to produce excellent results for irrotational mean strain and good results for homogeneous shear, and the elliptic streamline flows (Blaisdell & Shariff 1994). We are using this IPRM as a guide in extending the structure-based model to flows with weak mean deformation.

Direct numerical simulations (see Kassinos & Reynolds 1995) show that under weak strain the structure dimensionality \mathbf{D} remains considerably more isotropic than do the Reynolds stresses \mathbf{R} . Hence we modify the basic equations (17) and (22) for the evolution of the particle properties to account for these effects:

$$dN_i = - \underbrace{G_{ki}^n N_k}_{\text{effective gradient}} dt \quad (30)$$

$$dV_i = - \underbrace{G_{ik}^v V_k}_{\text{effective gradient}} dt + PN_i dt - \underbrace{C_1 V_i dt - C_2 V \epsilon_{ipq} dW_p n_q}_{\text{slow rotational randomization}}. \quad (31)$$

The effective gradients are given by

$$G_{ij}^n = G_{ij} + \frac{C^n}{\tau} r_{ik} d_{kj} \quad G_{ij}^v = G_{ij} + \frac{C^v}{\tau} r_{ik} d_{kj}. \quad (32)$$

Here $G_{ij} = U_{i,j}$ is the mean gradient tensor, and τ is the time scale of the turbulence, which as explained below is evaluated so that the dissipation rate ϵ^{PRM} in the IPRM [Eq. (39)] matches that obtained from a standard model equation for ϵ . The constants C^v and C^n are taken to be $C^n = 2.2C^v = 2.2$. The different values for these two constants account for the different rates of return to isotropy of \mathbf{D} and \mathbf{R} . However, note that the same tensor $r_{ik}d_{kj}$ accounts for the effective eddy deformation rate seen by both N_i and V_i .

The *slow rotational randomization* (SRR) model provides a random rotation of the \mathbf{V} about the \mathbf{n} vector such that the orthogonality of the two vectors is preserved. The “stochastic” character of this correction is introduced through the Wiener process $dW_i(t)$ (see Kassinos and Reynolds 1995, Durbin and Speziale 1994). The increments of the Wiener process are steps of the random walk and provide Gaussian white-noise forcing (Arnold 1974). The properties of these increments are

$$\overline{dW_i} = 0 \quad \overline{dW_i dW_j} = dt \delta_{ij} \quad \overline{V_j dW_i} = 0. \quad (33)$$

The second property in (33) shows that the Wiener process has magnitude $dW = O(dt)^{1/2}$; therefore dW_i/dt is not defined as $dt \rightarrow 0$. Hence, in order to evaluate $d(V_i V_j)/dt$, we first form the product

$$d(V_i V_j) = (V_i + dV_i)(V_j + dV_j) - V_i V_j. \quad (34)$$

One can use (31), (33), and (34) to form the cluster-averaged equations (see Section 2.2.5)

$$\dot{n}_i = -G_{ki}^n n_k + G_{kr}^n n_k n_r n_i \quad (35)$$

$$\begin{aligned} \dot{R}_{ij}^{\text{ln}} &= -G_{ik}^v R_{kj}^{\text{ln}} - G_{jk}^v R_{ki}^{\text{ln}} \\ &+ [G_{km}^n + G_{km}^v](R_{im}^{\text{ln}} n_k n_j + R_{jm}^{\text{ln}} n_k n_i) \\ &- [2C_1 R_{ij}^{\text{ln}} - C_2^2 R_{kk}^{\text{ln}}(\delta_{ij} - n_i n_j)]. \end{aligned} \quad (36)$$

We require the that rotational randomization model leaves the conditional energy unmodified. This requires that $C_1 = C_2^2$, and hence using dimensional considerations we take

$$C_r = C_1 = C_2^2 = \frac{8.5}{\tau} \Omega^* f_{pq} n_p n_q \quad \Omega^* = \sqrt{\Omega_k^* \Omega_k^*} \quad \Omega_i^* = \epsilon_{ipq} r_{qk} d_{kp}. \quad (37)$$

Note that the rotational randomization coefficient C_r is sensitized to the orientation of the \mathbf{n} vector so that the effective rotational randomization vanishes whenever the large-scale circulation is confined in the plane normal to \mathbf{n} . This effect is similar to the material indifference to mean rotation condition, which requires the rotational randomization to vanish whenever $\Omega_k n_k = 0$. By definition $C_r \geq 0$ and this property is satisfied by $f_{pq} n_p n_q > 0$ because f_{ij} is positive definite.

The pressure P is determined by the requirement that $V_k N_k = 0$ is maintained by (35) and (36). This determines the effects of the slow pressure strain-rate-term without the need for further modeling assumptions

$$P = \underbrace{2G_{mk} \frac{V_k N_m}{N^2}}_{\text{rapid}} + \underbrace{\frac{(C^v + C^n)}{\tau} r_{mt} d_{tk}}_{\text{slow}} \frac{V_k N_m}{N^2}. \quad (38)$$

The rate of dissipation of the turbulent kinetic energy $k = \frac{1}{2} q^2$ that is produced by the IPRM Eq. (36) is given by

$$\epsilon^{\text{PRM}} = q^2 \frac{C^v}{\tau} r_{ik} d_{km} r_{mi}. \quad (39)$$

To complete the IPRM we use the standard model equation for the dissipation rate (ϵ) with a rotational modification to account for the suppression of ϵ due to mean rotation,

$$\dot{\epsilon} = -C_0(\epsilon^2/q^2) - C_s S_{pq} r_{pq} \epsilon - C_\Omega \sqrt{\Omega_n \Omega_m d_{nm}} \epsilon. \quad (40)$$

Here Ω_i is the mean vorticity vector, and the constants are taken to be

$$C_0 = -\frac{11}{3} \quad C_s = -3 \quad \text{and} \quad C_\Omega = 0.01.$$

We choose the time scale τ so that $\epsilon^{\text{PRM}} = \epsilon$. This requires that

$$\tau = \left(\frac{q^2}{\epsilon}\right) C^v r_{ik} d_{km} r_{mi}. \quad (41)$$

2.4 Evaluation of the IPRM

In this section, the IPRM given by (35), (36), (40), and (41) is evaluated for five independent homogeneous flows. The evaluation of the IPRM for rapid mean deformation (large Sk/ϵ) is reported in detail in KR, where it is shown that given enough particles, the IPRM reproduces the *exact* RDT results. Therefore, in this section, we report only on the performance of the IPRM for flows involving weak mean deformation (small Sk/ϵ), where the nonlinear interactions are important.

2.4.1 Homogeneous shear in a rotating frame

We first consider the problem of homogeneous shear in a rotating frame. The mean velocity gradient tensor G_{ij} , the frame vorticity Ω_i^f , and frame rotation rate Ω_i are defined by

$$G_{ij} = \begin{pmatrix} 0 & S & 0 \\ 0 & 0 & 0 \\ 0 & 0 & 0 \end{pmatrix}, \quad 2\Omega_i = \Omega_i^f = (0, 0, \Omega^f). \quad (40)$$

We consider initially isotropic turbulence with

$$r_{ij} = \frac{1}{3} \delta_{ij}, \quad k = k_0, \quad \epsilon = \epsilon_0. \quad (41)$$

First, we consider the case of homogeneous shear in a stationary frame ($\Omega^f = 0$) with an initial $Sk_0/\epsilon_0 = 2.36$. The IPRM predictions for the components of the normalized Reynolds stress tensor r_{ij} are shown in Fig. 2. The symbols are from the direct numerical simulation (DNS) of Rogers and Moin (1986), which also had $Sk_0/\epsilon_0 = 2.36$. The agreement between the IPRM predictions and the DNS results is good, but the IPRM somewhat overpredicts r_{11} and underpredicts r_{22} . Figure 3 shows the evolution of the dimensionless parameters P/ϵ and Sk/ϵ . Again, the IPRM predictions (lines) are in good agreement with DNS results (symbols), especially in the period $8 \lesssim St \lesssim 15$ where the DNS was fully developed. The same equilibrium values are predicted for the two dimensionless parameters by both the DNS simulation and the IPRM. As shown in Table 1, the equilibrium state predicted by the model is also in reasonable agreement with the experiments of Tavoularis & Karnik (1989).

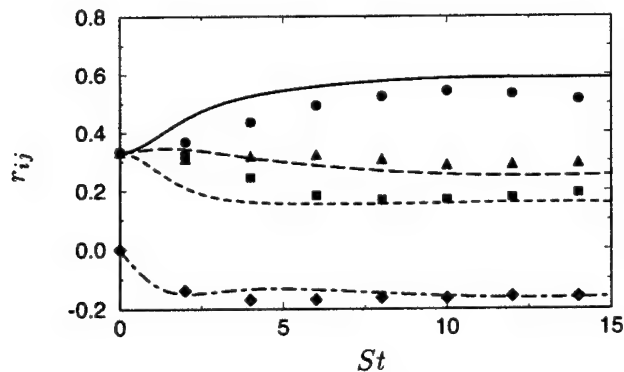


FIGURE 2. Time evolution of the normalized Reynolds stress tensor $r_{ij} = R_{ij}/R_{kk}$ in homogeneous shear flow ($Sk_0/\epsilon_0 = 2.36$). Comparison of the IPRM predictions (lines) with the direct numerical simulations (symbols) of Rogers and Moin (1986); 11 component (—, •), 22 component (---, ■), 33 component (····, ▲), 12 component (-·-·, ◆).

The solution in the case of homogeneous shear in a rotating frame depends on the initial conditions only through the dimensionless parameter Sk_0/ϵ_0 and on the frame vorticity through the dimensionless parameter Ω^f/S (Speziale *et al.* 1991). The value of Ω^f/S determines whether the flow is stable in which case k and ϵ decay in time, or unstable in which case both k and ϵ grow exponentially in time.

The effect of the ratio Ω^f/S on the time evolution of the normalized kinetic energy k/k_0 is shown in Fig. 4. In the absence of DNS or experimental data, we evaluate the model performance using the large-eddy simulations of Bardina *et al.* (1983). Note that the model captures the general trends correctly. For example, it correctly predicts that the highest rate of growth (for both k and ϵ) occurs for $\Omega^f = S/2$, which RDT shows is the most unstable case. It also predicts a weak rate of decay for the case $\Omega^f = S$ and a decay (relaminarization) for $\Omega^f = -S$. The numerical agreement with the LES is reasonable, but the model tends to predict somewhat

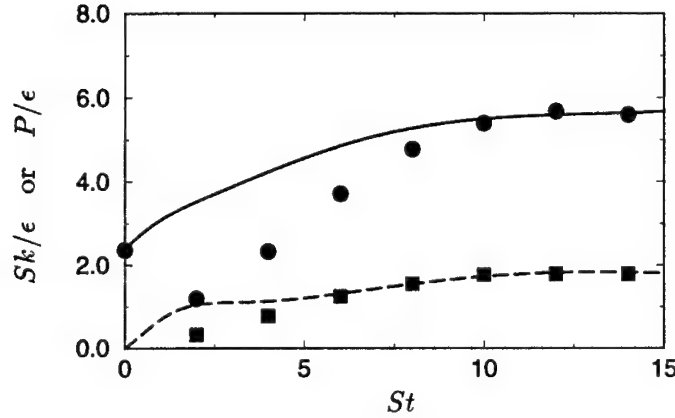


FIGURE 3. Time evolution of the nondimensional parameters Sk/ϵ (—, •) and P/ϵ (---, ■) in homogeneous shear flow. IPRM predictions (lines) are compared to the DNS (symbols) of Rogers and Moin (1986).

lower rates of growth, particularly so in the case $\Omega^f = 0.5S$. This problem is also common to all the currently available second-order closures as noted by Speziale *et al.* (1989). However, a detailed comparison of numerical values is probably not meaningful in this case because the reported LES results came from the filtered field only.

2.4.2 Irrotational axisymmetric strain

Next, we consider the performance of the IPRM for two cases of axisymmetric contraction and two cases of axisymmetric expansion. The mean velocity gradient tensor is given by

$$S_{ij} = \begin{pmatrix} S & 0 & 0 \\ 0 & -S/2 & 0 \\ 0 & 0 & -S/2 \end{pmatrix} \quad (42)$$

with $S > 0$ for contraction and $S < 0$ for expansion. We consider homogeneous turbulence with an initially isotropic state as specified in (41). The solution depends on the initial conditions through the non-dimensional parameter Sk_0/ϵ_0 . Comparisons are made with the DNS of Lee & Reynolds (1985).

The dimensionless strain parameter

$$C^* = \exp\left(\int_0^t |S_{\max}(t')| dt'\right) \quad (43)$$

will serve as the time coordinate for the comparison of the IPRM to the DNS results.

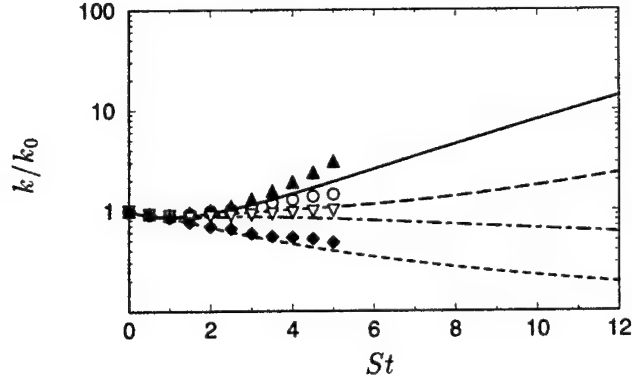


FIGURE 4. Time evolution of the turbulent kinetic energy in rotating shear flows. IPRM predictions (lines) are compared to the LES of Bardina *et al.* (symbols): $\Omega^f/S = 0$ (----, \circ), $\Omega^f/S = 0.5$ (—, \blacktriangle), $\Omega^f/S = 1.0$ (— · —, ∇), and $\Omega^f/S = -1.0$ (····, \blacklozenge).

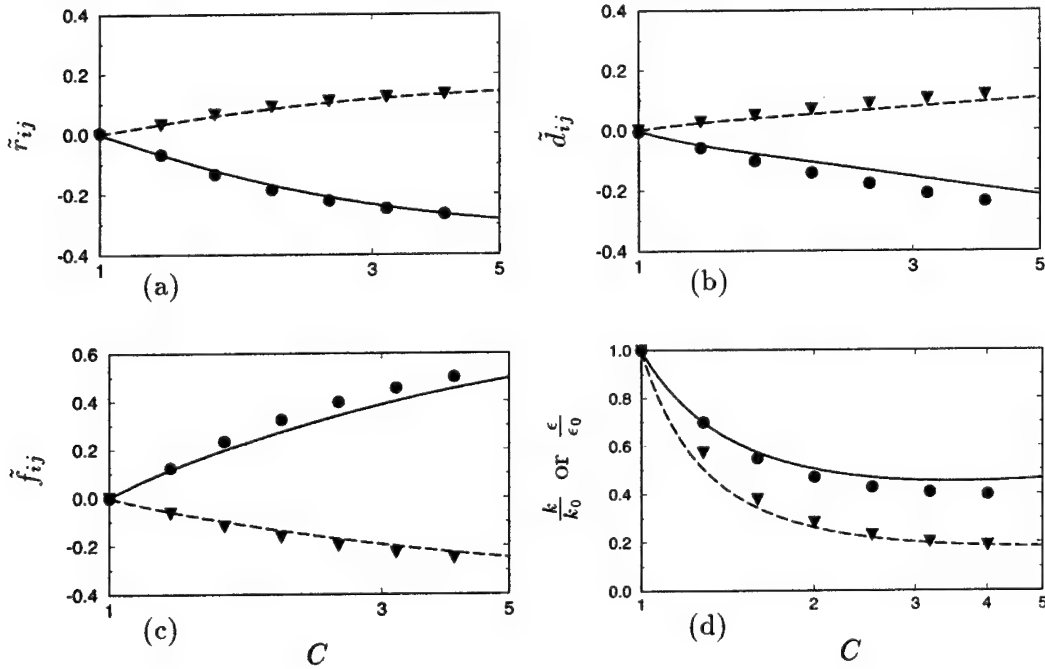


FIGURE 5. Comparison of IPRM predictions (shown as lines) with the DNS of Lee & Reynolds (1985) for axisymmetric contraction case AXK ($Sq_0^2/\epsilon_0 = 1.1$). Evolution of the (a) Reynolds stress, (b) dimensionality, and (c) circulicity anisotropies: 11 component (—, \bullet), 22 and 33 components (----, \blacktriangledown). (d) evolution of the normalized turbulent kinetic energy (—, \bullet) and dissipation rate (----, \blacktriangledown).

Equilibrium Values	IPRM	Experiments
r_{11}	0.59	0.51 ± 0.04
r_{22}	0.16	0.22 ± 0.02
r_{33}	0.25	0.27 ± 0.03
r_{12}	-0.16	-0.16 ± 0.01
Sk/ϵ	5.97	4.60 ± 0.50
P/ϵ	1.86	1.47 ± 0.14

TABLE 1. Equilibrium results for homogeneous shear: comparison with the experiments of Tavoularis & Karnik (1989).

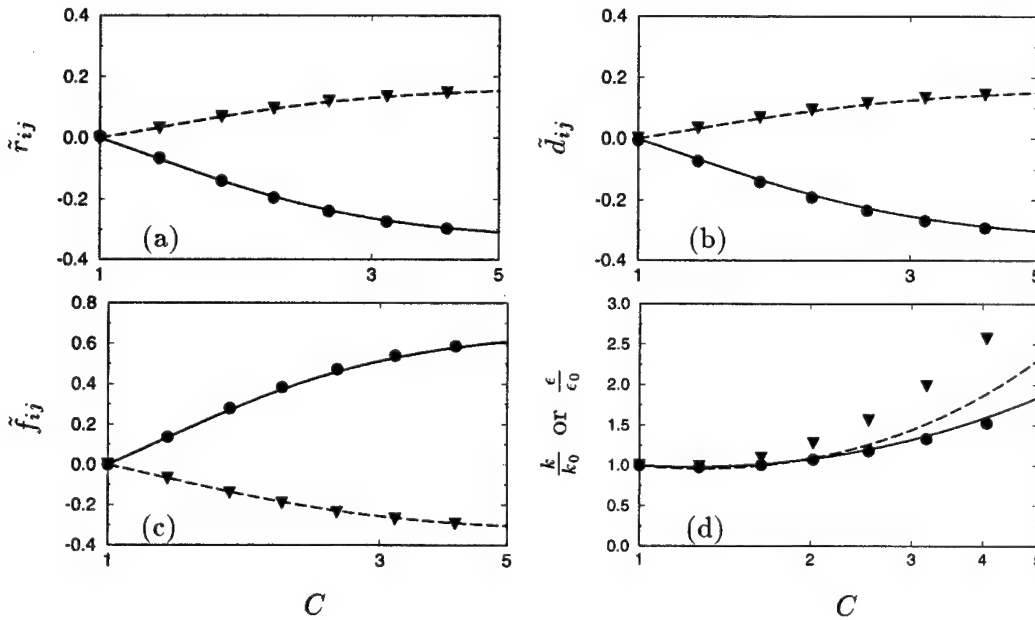


FIGURE 6. Comparison of IPRM predictions with the DNS of Lee & Reynolds (1985) for axisymmetric contraction case AXL ($Sq_0^2/\epsilon_0 = 11.1$). Evolution of (a) the Reynolds stress, (b) dimensionality, and (c) circularity anisotropies. (d) Evolution of the normalized turbulent kinetic energy and dissipation rate. Symbols as in Fig. 5.

Axisymmetric contraction flow

The IPRM predictions for two cases of irrotational axisymmetric contraction are shown in Figs. 5 and 6. In both cases, the IPRM predictions (lines) for the evolution of the anisotropies $\tilde{\mathbf{r}}$, $\tilde{\mathbf{d}}$, and $\tilde{\mathbf{f}}$ are in good agreement with the DNS results (symbols). The IPRM predicts decay of the turbulent kinetic energy k and dissipation rate ϵ for the weaker strain case [$Sq_0^2/\epsilon_0 = 1.1$] and growth in the more rapid run [$Sq_0^2/\epsilon_0 = 11.1$]. This is in agreement with the DNS results; however, the

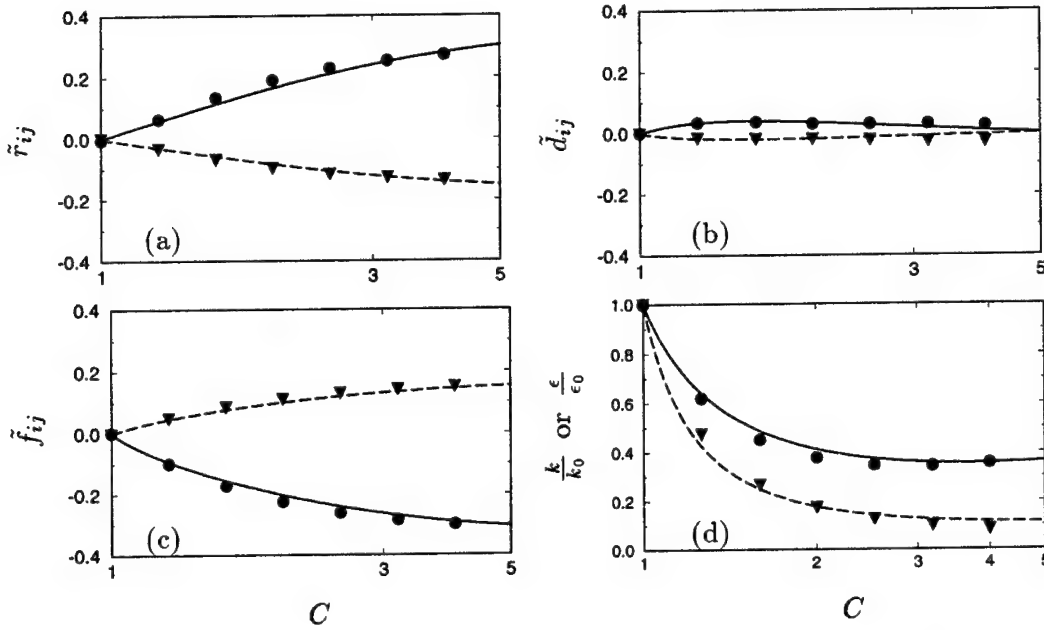


FIGURE 7. Comparison of IPRM predictions (shown as lines) with the DNS of Lee & Reynolds (1985) for axisymmetric expansion case EXO ($Sq_0^2/\epsilon_0 = 0.82$). Evolution of the (a) Reynolds stress, (b) dimensionality, and (c) circulicity anisotropies: 11 component (—, ●), 22 and 33 components (----, ▼). (d) evolution of the normalized turbulent kinetic energy (—, ●) and dissipation rate (----, ▼).

predicted rate of growth for ϵ in this second case is too weak as compared to the DNS result (see Fig. 6d). This difference is related to the model Eq. (40) used for the dissipation rate and not directly to the IPRM equations. We believe that we can improve on this aspect of the IPRM, but feel this refinement should follow once we have investigated various alternative models for the effective eddy deformation $r_{ik}d_{kj}$.

Axisymmetric expansion flow

The IPRM predictions for two cases of irrotational axisymmetric expansion are shown in Fig. 7 for $Sq_0^2/\epsilon_0 = 0.82$ and Fig. 8 for $Sq_0^2/\epsilon_0 = 8.2$. Comparison is again made with the DNS of Lee & Reynolds. As was discussed in Kassinos & Reynolds (1995), the axisymmetric expansion flows exhibit a paradoxical behavior where a weaker mean deformation rate produces a stress anisotropy that exceeds the one produced under RDT. This effect is triggered by the different rates of return to isotropy in \mathbf{r} and \mathbf{d} equations, but it is dynamically controlled by the rapid terms. The net effect is a growth of $\tilde{\mathbf{r}}$ in expense of $\tilde{\mathbf{d}}$, which is strongly suppressed.

As shown in Fig. 7, the IPRM is able to capture these intriguing effects quite accurately despite the relatively simple model used for the particle-particle interactions. This success of the IPRM points to the fact that these unexpected effects, once triggered, are driven by the rapid terms: the IPRM representation of the rapid

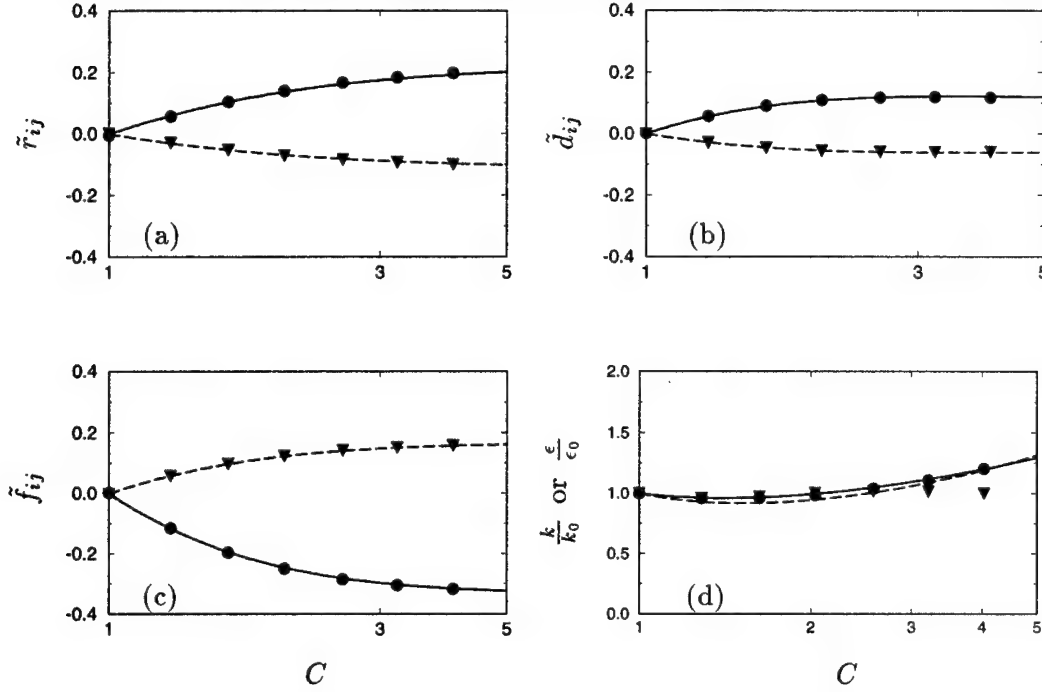


FIGURE 8. Comparison of IPRM predictions with the DNS of Lee & Reynolds (1985) for axisymmetric expansion case EXP ($Sq_0^2/\epsilon_0 = 8.2$). Evolution of (a) the Reynolds stress, (b) dimensionality, and (c) circularity anisotropies. (d) Evolution of the normalized turbulent kinetic energy and dissipation rate. Symbols as in Fig. 7.

terms is exact and this enables it to capture these intriguing effects. The IPRM predictions for the evolution of the turbulent kinetic energy k and dissipation rate ϵ are also quite accurate.

Plane strain

The performance of the IPRM in the case of the irrotational plane strain flows is shown in Fig. 9 for $Sq_0^2/\epsilon_0 = 1.0$ and Fig. 10 for $Sq_0^2/\epsilon_0 = 8.0$. The DNS of Lee & Reynolds (1985) is used for the comparison. The IPRM predictions for the evolution of the anisotropies $\tilde{\mathbf{r}}$, $\tilde{\mathbf{d}}$, and $\tilde{\mathbf{f}}$ are in very good agreement with the DNS results. Note that the value of the initial Sq_0^2/ϵ_0 has a strong effect on the distribution of the \tilde{d}_{ij} components and the IPRM is able to capture these effects quite well. The evolution histories for the normalized turbulent kinetic energy and dissipation rate are shown in Figs. 9d and 10d. The predictions are in good agreement with the DNS results, displaying decay for $Sq_0^2/\epsilon_0 = 1.0$ and growth for $Sq_0^2/\epsilon_0 = 8.0$ at the correct rates.

2.4.3 Elliptic streamline flow

The elliptic streamline flows combine the effects of mean rotation and plane strain and emulate the conditions encountered in the flow through various sections of turbomachinery. These relatively basic flows provide a challenging test case for

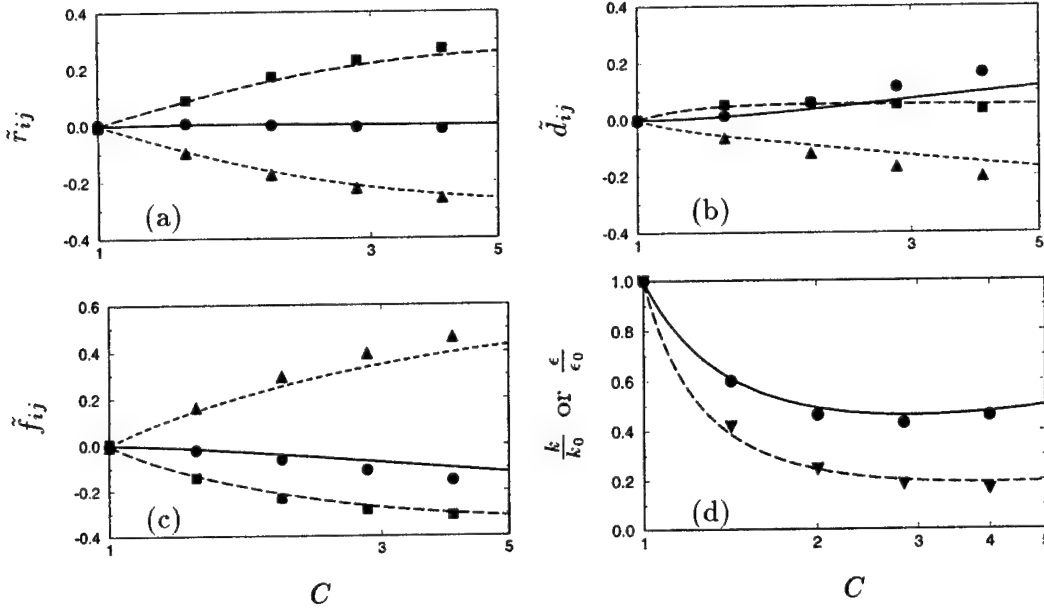


FIGURE 9. Comparison of IPRM predictions (shown as lines) with the DNS of Lee & Reynolds (1985) for plane strain case PXA ($Sq_0^2/\epsilon_0 = 1.0$). Evolution of the (a) Reynolds stress, (b) dimensionality, and (c) circularity anisotropies: 11 component (—, •), 22 component (---, ■), and 33 component (----, ▲). (d) evolution of the normalized turbulent kinetic energy (—, •) and dissipation rate (----, ▼).

turbulence models. For example, direct numerical simulations show exponential growth of the turbulent kinetic energy in elliptic streamline flows, but standard k - ϵ models (as well as most Reynolds stress models) predict decay of the turbulence. The structure-based model (Reynolds & Kassinos 1995) does predict an exponential growth, but not yet at the correct rate.

The elliptic streamline flow corresponds to a mean deformation tensor of the form

$$G_{ij} = \begin{pmatrix} 0 & 0 & -\gamma - e \\ 0 & 0 & 0 \\ \gamma - e & 0 & 0 \end{pmatrix}$$

with $0 < |e| < |\gamma|$. Note that the case $e = 0$ corresponds to pure rotation while the case $|e| = |\gamma|$ corresponds to homogeneous shear. The elliptic streamlines in this flow have an aspect ratio given by $E = \sqrt{(\gamma + e)/(\gamma - e)}$. As explained by Blaisdell and Shariff (1994), the important nondimensional parameters for the elliptic streamline flow are (1) the aspect ratio E of the elliptic streamlines and (2) the ratio of the turbulent time scale to the time scale of the mean deformation. The turbulent Reynolds number is also an important parameter, but the IPRM model is based on a high Reynolds number assumption. The IPRM predictions are shown in Fig. 11 for three different cases, which are summarized in Table 2.

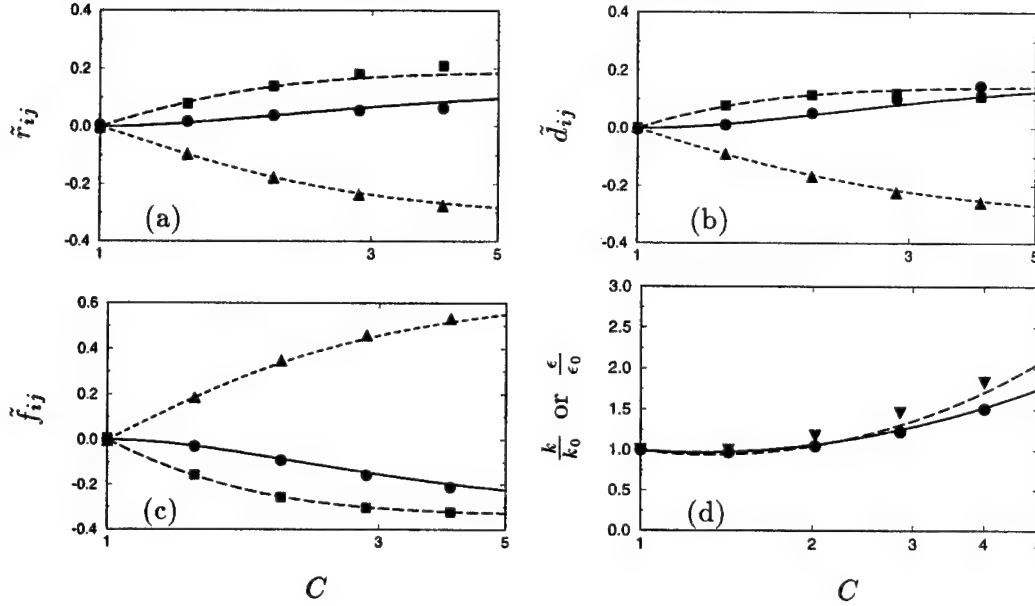


FIGURE 10. Comparison of IPRM predictions with the DNS of Lee & Reynolds (1985) for plane strain case PXD ($Sq_0^2/\epsilon_0 = 8.0$). Evolution of (a) the Reynolds stress, (b) dimensionality, and (c) circularity anisotropies. (d) Evolution of the normalized turbulent kinetic energy and dissipation rate. Symbols as in Fig. 9.

The notation used here is identical to the one introduced by Blaisdell and Shariff (1994). For example, $S_e^* = ek/\epsilon$ represents the ratio of the turbulent time scale to the mean flow time scale based on the mean strain. We have evaluated the IPRM predictions using preliminary results from the simulations of Blaisdell and found its performance to be very good. The IPRM predicts exponential growth for the turbulent kinetic energy and dissipation rate at the correct rates of growth. The IPRM predictions for the individual components of the Reynolds stress anisotropy tensor were also in very good agreement with the corresponding DNS predictions from those preliminary runs. Here we only report the predictions of the IPRM, and postpone any comparison to DNS till final results are available from the simulations of Blaisdell.

Case	E	S_{e0}^*
e3	1.5	1.68691
e4	2.0	1.68691
e2	1.25	1.68691

TABLE 2. Initial conditions for the elliptic streamline cases.

3. Summary and future plans

In simple flows with mild mean deformation rates the turbulence has time to

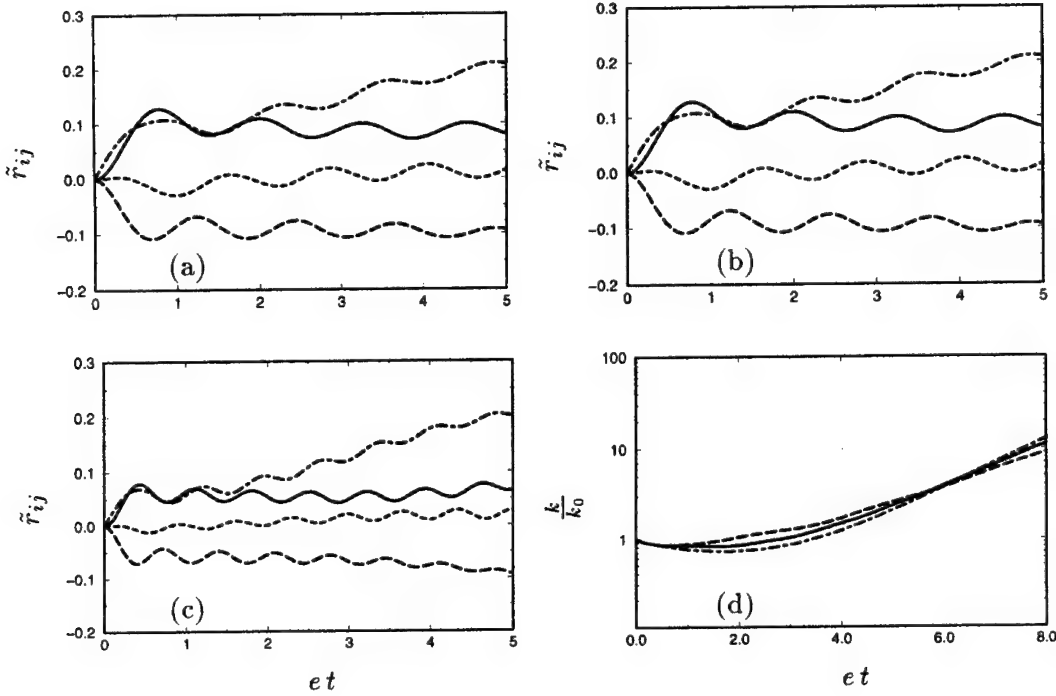


FIGURE 11. IPRM predictions for the evolution of the Reynolds stress anisotropy components in elliptic streamline flow with (a) $E=1.5$, (b) $E=2.0$, and (c) $E=1.25$: 11 component, —; 22 component, ----; 33 component, -.-.-; 13 component, (d) Evolution of the normalized turbulent kinetic energy in elliptic streamline flow: $E=1.5$, —; $E=2.0$, ----; $E=1.25$, -.-.-.

come to equilibrium with mean flow and the Reynolds stresses are determined by the strain *rate*. On the other hand, when the mean deformation is very rapid, the turbulent structure takes some time to respond and the Reynolds stresses are determined by the amount of *total* strain.

A good turbulence model should exhibit this viscoelastic character of turbulence, matching the two limiting behaviors and providing a reasonable blend in between. Our goal has been the development of one-point model for engineering use with the proper viscoelastic character. We have shown that to achieve this goal one needs to include structure information in the tensorial base used in the model because non-equilibrium turbulence is inadequately characterized by the turbulent stresses themselves. We have also argued that the greater challenge in achieving viscoelasticity in a turbulence model is posed by the matching of rapid distortion theory (RDT). Given a good RDT model, we believe its extension to flows with mild deformation rates should be relatively straightforward.

The interacting particle representation model (IPRM) presented here provides strong support for this position. The IPRM is in essence a very good viscoelastic,

structure-based turbulence model. As it was shown here, with a relatively simple model for the nonlinear turbulence-turbulence interactions, the IPRM is able to handle quite successfully a surprising wide range of flows. Some of these flows involve paradoxical effects, and the fact that the IPRM is able to reproduce them suggests that perhaps the model captures a significant part of the underlying physics.

We believe that the success of the IPRM is based on its firm core, that is its exact representation of RDT. We have used the rapid version of the IRPM in constructing a one-point structure-based model for RDT, now completed successfully. We are currently using the IPRM in extending the one-point model to flows with mild deformation rates. We are also investigating further extensions to the IPRM that might enable it to become a valuable engineering tool on its own right.

REFERENCES

- ARNOLD, L. 1974 *Stochastic Differential Equations*. John Wiley and Sons.
- BARDINA, J., FERZIGER, J. H., & REYNOLDS, W. C. 1983 Improved turbulence models based on large eddy simulation of homogeneous, incompressible, turbulent flows. *Report TF-19*, Thermosciences Division, Department of Mechanical Engineering, Stanford University.
- BLAISDELL, G. A. & SHARIFF, K. 1994 Homogeneous turbulence subjected to mean flow with elliptic streamlines. *Proceedings of the 1994 Summer Program*. Center for Turbulence Research, NASA Ames/Stanford Univ., 355-371.
- DURBIN, P. A. & SPEZIALE, C. G. 1994 Realizability of second-moment closures via stochastic analysis. *J. Fluid Mech.* **280**, 395-407.
- LEE, M. J. & REYNOLDS, W. C. 1985 Numerical experiments on the structure of homogeneous turbulence. *Report TF-24*, Thermosciences Division, Department of Mechanical Engineering, Stanford University.
- MAHONEY, J. F. 1985 Tensor and Isotropic Tensor Identities. *The Matrix and Tensor Quarterly*. **34**(5), 85-91.
- KASSINOS, S. C. AND REYNOLDS, W. C. 1994 A structure-based model for the rapid distortion of homogeneous turbulence. *Report TF-61*, Thermosciences Division, Department of Mechanical Engineering, Stanford University.
- KASSINOS, S. C. AND REYNOLDS, W. C. 1995 An extended structure-based model based on a stochastic eddy-axis evolution equation. *Annual Research Briefs 1995*, Center for Turbulence Research, NASA Ames/Stanford Univ., 133-148.
- ROGERS, M. M., MOIN, P. 1987 The structure of the vorticity field in homogeneous turbulent flows. *J. Fluid. Mech.* **176**, 33-66.
- TAVOULARIS, S. & KARNIK, U. 1989 Further experiments on the evolution of turbulent stresses and scales in uniformly sheared turbulence. *J. Fluid. Mech.* **204**, 457-478.

Modeling of inhomogeneous compressible turbulence using a two-scale statistical theory

By Fujihiro Hamba¹

1. Motivation and objectives

Turbulence modeling plays an important role in the study of high-speed flows in engineering and aerodynamic problems; they include flows in supersonic combustion engines and over hypersonic transport aircraft. The enhancement of the kinetic energy dissipation by the dilatational terms is one of the typical compressibility effects. Zeman (1990) and Sarkar *et al.* (1991) proposed that the dilatation dissipation is proportional to the solenoidal dissipation and is a function of the turbulent Mach number. Sarkar (1992) also modeled the pressure-dilatation correlation using the turbulent Mach number. Zeman (1991) related the correlation to the rate of change of the pressure variance.

Using a statistical theory Yoshizawa (1990) pointed out that compressibility effects are tightly linked with density fluctuations. He proposed a three-equation model that consists of transport equations for the kinetic energy, its dissipation, and the density variance (Yoshizawa 1992). Taulbee & VanOsdol (1991) also modeled transport equations for the density variance and the mass flux. Fujiwara & Arakawa (1993) proposed another type of three-equation model involving the sum of the normalized compressible turbulent kinetic energy and the density variance.

Yoshizawa (1990) used a statistical theory called the two-scale direct-interaction approximation (TSDIA) to derive compressible turbulence models. This method was originally developed for incompressible turbulence (Yoshizawa 1984). The TSDIA consists of two main procedures. First, two-scale variables are introduced and the direct-interaction approximation (DIA) is applied to express statistical quantities in terms of two-time velocity correlations in wavenumber space. Second, by using inertial-range spectra, expressions are simplified to derive one-point closure models. However, the second procedure has not been carried out for compressible turbulence because detailed inertial-range spectra are not available. Instead, Yoshizawa (1992) applied dimensional analysis to results of the first procedure. He also proposed an alternative simplified approach that treats the governing equations in physical space (Yoshizawa 1995). Several model expressions were obtained, and an important effect of density fluctuations was clarified by these methods. Some ambiguity still remains; since several nondimensional parameters are involved in compressible turbulence, statistical quantities cannot be uniquely modeled only by dimensional analysis.

¹ Institute of Industrial Science, University of Tokyo, Tokyo 106, Japan

The energy spectrum for compressible turbulence has been examined both theoretically and numerically to some extent. Moiseev *et al.* (1981) theoretically obtained a spectral form that depends on the turbulent Mach number. Kida & Orszag (1990) showed that the spectrum of the solenoidal component in their DNS is very close to that for incompressible flows whereas the spectrum of the compressible component depends strongly on the turbulent Mach number. Bataille & Bertoglio (1993) used eddy-damped quasi-normal Markovian theory to examine inertial-range spectra of weakly compressible turbulence. Although more study needs to be done to understand inertial-range behavior, these findings help us to assume some spectral forms for compressible turbulence.

In this work, we introduce inertial-range spectra of density and velocity variances to simplify results of the first procedure of TSDIA. A deviation from the Kolmogorov spectrum is assumed for the spectrum of the compressible velocity variance. The dependence on nondimensional parameters is systematically obtained by the simplification. We apply the TSDIA to several correlations included in the mean-field equations to propose a three-equation model. We examine models for the dilatation dissipation using DNS of isotropic and homogeneous shear turbulence.

2. Accomplishments

2.1 Fundamental equations and $K - \varepsilon - K_\rho$ model

The motion of a viscous compressible fluid is described by the equations for the density ρ , the velocity u_i , and the internal energy e :

$$\frac{\partial \rho}{\partial t} + \frac{\partial}{\partial x_i}(\rho u_i) = 0, \quad (1)$$

$$\frac{\partial}{\partial t}(\rho u_i) + \frac{\partial}{\partial x_j}(\rho u_j u_i) = -\frac{\partial p}{\partial x_i} + \frac{\partial}{\partial x_j}(\mu s_{ji}), \quad (2)$$

$$\frac{\partial}{\partial t}(\rho e) + \frac{\partial}{\partial x_i}(\rho e u_i) = -p \frac{\partial u_i}{\partial x_i} + \mu s_{ji} \frac{\partial u_i}{\partial x_j} + \frac{\partial}{\partial x_i} \left(\lambda \frac{\partial \theta}{\partial x_i} \right), \quad (3)$$

where μ is the viscosity, λ is the thermal conductivity, and θ is the temperature. The deviatoric part of the strain rate tensor, s_{ij} , is given by

$$s_{ij} = \frac{\partial u_i}{\partial x_j} + \frac{\partial u_j}{\partial x_i} - \frac{2}{3} \frac{\partial u_k}{\partial x_k} \delta_{ij}. \quad (4)$$

For perfect gas, the pressure p and the internal energy e are written as

$$p = \rho R \theta = (\gamma - 1) \rho e, \quad e = c_v \theta, \quad (5)$$

where $\gamma = c_p/c_v$. Here, R is the specific gas constant, and c_v and c_p are the specific heats at constant volume and pressure, respectively.

We divide a physical quantity f into the mean F and the fluctuation f' :

$$f = F + f', \quad F = \langle f \rangle, \quad (6)$$

where f denotes ρ , u_i , e , p , s_{ij} , and θ . Some mean quantities are denoted by an overbar as $\bar{\rho}$. By taking the ensemble average of (1)–(3), we obtain the equations for the mean quantities $\bar{\rho}$, U_i , and E . Those equations contain several correlations such as the mass flux $\langle \rho' u'_i \rangle$ and the Reynolds stress $\langle u'_i u'_j \rangle$. The correlations need to be modeled to close the mean-field equations.

Yoshizawa (1990) pointed out that compressibility effects are tightly linked with the density fluctuations; he proposed a three-equation model that consists of the equations for the turbulent kinetic energy $K (= \langle u'^2 \rangle / 2)$, its dissipation rate ε , and the density variance $K_\rho (= \langle \rho'^2 \rangle)$. The equations for K and K_ρ can be written as

$$\begin{aligned} \frac{DK}{Dt} = & -\langle u'_i u'_j \rangle \frac{\partial U_i}{\partial x_j} - \varepsilon + \frac{1}{\bar{\rho}} \left\langle p' \frac{\partial u'_i}{\partial x_i} \right\rangle - \frac{1}{2} \frac{\partial}{\partial x_j} \langle u'^2 u'_j \rangle - \frac{1}{\bar{\rho}} \frac{\partial}{\partial x_i} \langle p' u'_i \rangle \\ & + \frac{1}{\bar{\rho}^2} \langle \rho' u'_i \rangle \frac{\partial P}{\partial x_i}, \end{aligned} \quad (7)$$

$$\frac{DK_\rho}{Dt} = -2K_\rho \frac{\partial U_i}{\partial x_i} - 2\langle \rho' u'_i \rangle \frac{\partial \bar{\rho}}{\partial x_i} - 2\bar{\rho} \left\langle \rho' \frac{\partial u'_i}{\partial x_i} \right\rangle - \frac{\partial}{\partial x_i} \langle \rho'^2 u'_i \rangle - \left\langle \rho'^2 \frac{\partial u'_i}{\partial x_i} \right\rangle. \quad (8)$$

The correlations included in (7) and (8) as well as the ε equation itself need to be modeled in terms of the mean quantities and the three variables.

Model expressions shown later contain two nondimensional parameters: the turbulent Mach number M_t [$= \sqrt{2K}/\bar{c}$ where \bar{c} is the mean sound speed] and the normalized density variance ρ_n^2 [$= (K_\rho/\bar{\rho}^2)$]. By adopting K_ρ as one of the basic quantities, we can use ρ_n^2 as a parameter independent of M_t . Modeling with the two parameters is expected to be more flexible than that with M_t only.

2.2 Two-scale statistical theory

Here, we give a brief summary of the procedure of the TSDIA. Its mathematical details were given in Yoshizawa (1992).

We first introduce two time and space variables using a small-scale parameter δ as

$$\boldsymbol{\xi} (\equiv \mathbf{x}), \quad \mathbf{X} (\equiv \delta \mathbf{x}), \quad \tau (\equiv t), \quad T (\equiv \delta t). \quad (9)$$

Here, the fast variables $\boldsymbol{\xi}$ and τ describe the rapid variations of the fluctuating field whereas the slow variables \mathbf{X} and T describe the slow variations of the mean field. A quantity f can be written as

$$f = F(\mathbf{X}, T) + f'(\boldsymbol{\xi}, \mathbf{X}, \tau, T). \quad (10)$$

Using the Fourier transform with respect to $\boldsymbol{\xi}$, we express f' as

$$f'(\boldsymbol{\xi}, \mathbf{X}, \tau, T) = \int d\mathbf{k} f(\mathbf{k}, \mathbf{X}, \tau, T) \exp[-i\mathbf{k} \cdot (\boldsymbol{\xi} - \mathbf{U}\tau)]. \quad (11)$$

This representation is equivalent to the viewpoint that the fluctuating motion consists of many small eddies moving with the mean velocity \mathbf{U} . Hereafter, the dependence of $f(\mathbf{k}, \mathbf{X}, \tau, T)$ on \mathbf{X} and T is not written explicitly.

Applying (9)–(11) to the equations for ρ' , u'_i , and p' (or e'), we obtain a system of equations for the fluctuating field in wavenumber space. We expand the fluctuation $f(\mathbf{k}, \tau)$ in powers of δ :

$$f(\mathbf{k}, \tau) = \sum_{n=0}^{\infty} \delta^n f_n(\mathbf{k}, \tau). \quad (12)$$

Substituting (12) into the system of equations and equating quantities in each order of δ , we have an equation for each quantity $f_n(\mathbf{k}, \tau)$. By introducing the Green's functions for ρ_0 , u_{0i} , and p_0 we can formally solve the equations for f_n ($n \geq 1$) in terms of the lower-order quantities.

A correlation included in the mean-field equations can be written as

$$\begin{aligned} \langle f'(\mathbf{x}, t) g'(\mathbf{x}, t) \rangle &= \int d\mathbf{k} \langle f(\mathbf{k}, \tau) g(-\mathbf{k}, \tau) \rangle / \delta(0) \\ &= \int d\mathbf{k} (\langle f_0 g_0 \rangle + \langle f_1 g_0 \rangle + \langle f_0 g_1 \rangle + \cdots) / \delta(0). \end{aligned} \quad (13)$$

Here, $\delta(0)$ denotes the delta function $\delta(k)$ where the one-dimensional wavenumber k equals 0. Substituting the formal solution for f_n and g_n ($n \geq 1$) and applying the DIA, we obtain a model expression for the correlation. It is written in terms of the mean field as well as the basic correlations and the Green's functions defined by

$$Q_\rho(\mathbf{k}, \tau, \tau') = \langle \rho_0(\mathbf{k}, \tau) \rho_0(-\mathbf{k}, \tau') \rangle / \delta(0) = Q_\rho(k, \tau, \tau'), \quad (14)$$

$$\begin{aligned} Q_{ij}(\mathbf{k}, \tau, \tau') &= \langle u_{0i}(\mathbf{k}, \tau) u_{0j}(-\mathbf{k}, \tau') \rangle / \delta(0) \\ &= D_{ij}(\mathbf{k}) Q_s(k, \tau, \tau') + \Pi_{ij}(\mathbf{k}) Q_c(k, \tau, \tau'), \end{aligned} \quad (15)$$

$$G_\rho(\mathbf{k}, \tau, \tau') = \langle \hat{G}_\rho(\mathbf{k}, \tau, \tau') \rangle = G_\rho(k, \tau, \tau'), \quad (16)$$

$$G_{ij}(\mathbf{k}, \tau, \tau') = \langle \hat{G}_{ij}(\mathbf{k}, \tau, \tau') \rangle = D_{ij}(\mathbf{k}) G_s(k, \tau, \tau') + \Pi_{ij}(\mathbf{k}) G_c(k, \tau, \tau'), \quad (17)$$

$$G_e(\mathbf{k}, \tau, \tau') = \langle \hat{G}_e(\mathbf{k}, \tau, \tau') \rangle = G_e(k, \tau, \tau'), \quad (18)$$

where

$$D_{ij}(\mathbf{k}) = \delta_{ij} - \frac{k_i k_j}{k^2}, \quad \Pi_{ij}(\mathbf{k}) = \frac{k_i k_j}{k^2}. \quad (19)$$

For example, the expression for the eddy viscosity can be written as

$$\nu_e \sim \int d\mathbf{k} \int^\tau d\tau' G_s(k, \tau, \tau') Q_s(k, \tau, \tau') + \cdots, \quad (20)$$

The expression includes wavenumber and time integrals of two-time correlations and Green's functions. It is too complicated to be a practical model; some simplifications are necessary.

Following the TSDIA for incompressible turbulence, we assume inertial-range forms for the fundamental statistical quantities as

$$Q_a(k, \tau, \tau') = \sigma_a(k) \exp[-\omega_a(k)|\tau - \tau'|], \quad a = (\rho, s, c), \quad (21)$$

$$G_b(k, \tau, \tau') = H(\tau - \tau') \exp[-\omega'_b(k)(\tau - \tau')], \quad b = (\rho, s, c, e), \quad (22)$$

where

$$\sigma_\rho(k) = C_{\sigma\rho} M_t^2 \bar{\rho}^2 \varepsilon_d \varepsilon^{-1} k^{-3-\alpha-2\beta} k_m^{\alpha+2\beta} H(k - k_m), \quad (23)$$

$$\sigma_s(k) = C_{\sigma s} \varepsilon^{2/3} k^{-11/3} H(k - k_m), \quad (24)$$

$$\sigma_c(k) = C_{\sigma c} \varepsilon_d \varepsilon^{-1/3} k^{-(11/3)-\alpha} k_m^\alpha H(k - k_m), \quad (25)$$

$$[\omega_s(k), \omega'_s(k)] = [C_{\omega s}, C'_{\omega s}] \varepsilon^{1/3} k^{2/3}, \quad (26)$$

$$\begin{aligned} & [\omega_\rho(k), \omega'_\rho(k), \omega_c(k), \omega'_c(k), \omega'_e(k)] \\ &= [C_{\omega\rho}, C'_{\omega\rho}, C_{\omega c}, C'_{\omega c}, C'_{\omega e}] M_t^{-1} \varepsilon^{1/3} k^{(2/3)+\beta} k_m^{-\beta}. \end{aligned} \quad (27)$$

Here, $C_{\sigma a}$, $C_{\omega a}$, and $C'_{\omega b}$ are model constants, $H(k)$ and $H(\tau)$ are the unit step functions, k_m is the wavenumber of the energy-containing range, and ε , ε_d , and M_t are the dissipation, the dilatation dissipation, and the turbulent Mach number defined by

$$\varepsilon = \bar{\nu} \left\langle s'_{ji} \frac{\partial u'_i}{\partial x_j} \right\rangle, \quad \varepsilon_d = \frac{4}{3} \bar{\nu} \left\langle \left(\frac{\partial u'_i}{\partial x_i} \right)^2 \right\rangle, \quad M_t = \frac{\sqrt{2K}}{\bar{c}} = \left(\frac{2\bar{\rho}K}{\gamma P} \right)^{1/2}, \quad (28)$$

respectively. For the solenoidal quantities σ_s , ω_s , and ω'_s , the spectra are the same as those for incompressible turbulence. The compressible part of energy spectrum, σ_c , is set proportional to ε_d . This is because the ratio of the compressible to solenoidal parts of turbulent kinetic energy is shown to be proportional to the ratio of the dilatational to solenoidal dissipations. The spectrum is steeper than the Kolmogorov one by α . Moiseev *et al.* (1981) showed that the deviation α is a function of M_t . Here, we do not include such M_t dependence, but consider α as an unknown numerical parameter. The deviation from the incompressible inertial-range form is also introduced into $\omega(k)$ for compressible quantities. We assume that time scales for compressible quantities are shorter than those for incompressible ones; the ratio is of the order of M_t .

For example, substituting the above spectral forms into (20), we obtain a one-point closure model for the eddy viscosity as a function of k_m and ε . By converting k_m into K and ε , we have a usual expression proportional to K^2/ε .

2.3 Dilatation dissipation

We applied the procedure of the previous section to $\langle \rho' \rho' \rangle$ to obtain an expression for the density variance; it is a function of the mean field $\bar{\rho}$, U_i , and P as well as the quantities K , ε , ε_d , and M_t . Since the transport equation for K_ρ is solved in the $K - \varepsilon - K_\rho$ model, the modeling of K_ρ itself is not necessary. Instead, the expression can be considered a model for ε_d . Expanding ε_d in terms of the other quantities we have

$$\varepsilon_d = C_{\varepsilon d1} \frac{\rho_n^2}{M_t^2} \varepsilon \left[1 + C_{\varepsilon d7} M_t \left(2 \frac{K}{\varepsilon} \frac{\partial U_i}{\partial x_i} + \frac{1}{4} \frac{K}{\varepsilon \bar{\rho}} \frac{D\bar{\rho}}{Dt} - \frac{1}{4} \frac{K}{\varepsilon P} \frac{DP}{Dt} + \frac{3}{2\varepsilon} \frac{DK}{Dt} - \frac{K}{\varepsilon^2} \frac{D\varepsilon}{Dt} + \frac{K}{\varepsilon K_\rho} \frac{DK_\rho}{Dt} \right) \right], \quad (29)$$

where ρ_n^2 is the normalized density variance defined by

$$\rho_n^2 = \frac{K_\rho}{\bar{\rho}^2}, \quad (30)$$

and $C_{\varepsilon d1}$ and $C_{\varepsilon d7}$ are model constants. Hereafter, C_{an} denotes a model constant where a represents a physical quantity and n is the number of the term.

The factor before the square bracket in (29) shows that the ratio $\varepsilon_d/\varepsilon$ is proportional to ρ_n^2/M_t^2 . Yoshizawa (1992) pointed out that this quantity is important in characterizing the compressibility effect and introduced a parameter $\chi (= \rho_n^2/M_t^2)$. Yoshizawa (1995) paid attention to the importance of the parameter χ and proposed the model:

$$\varepsilon_d/\varepsilon_s = C_{\varepsilon dY} \chi, \quad (31)$$

where $\varepsilon_s = \varepsilon - \varepsilon_d$ and $C_{\varepsilon dY}$ is a model constant. This model is the same as (29) to first order.

The modeling of ε_d was originally investigated by Sarkar *et al.* (1991) and Zeman (1990). Sarkar *et al.* (1991) used asymptotic analysis and DNS to model ε_d as follows

$$\varepsilon_d/\varepsilon_s = C_{\varepsilon dS} M_t^2. \quad (32)$$

Zeman (1990) assumed the existence of shock-like structure in flow fields to derive the model

$$\varepsilon_d/\varepsilon_s = C_{\varepsilon dZ} F(M_t, K_{Mt}), \quad (33)$$

where K_{Mt} is the flatness factor of M_t and $F(M_t, K_{Mt})$ is a complicated integral. He also derived a simple algebraic expression for use in practice (Blaisdell & Zeman 1992).

Blaisdell *et al.* (1991) used DNS of decaying isotropic turbulence to examine the above two models. They carried out two simulations that had the same initial values

of M_t but different initial ratios of compressible to solenoidal velocity variances. In spite of the same turbulent Mach number, the two simulations showed different values of $\varepsilon_d/\varepsilon$. They concluded that the development of $\varepsilon_d/\varepsilon$ in isotropic turbulence depends more on its initial values than on the turbulent Mach number and that simulations of isotropic turbulence cannot be used to validate the proposed models. However, Yoshizawa's model as well as the present model show that $\varepsilon_d/\varepsilon$ depends not only on M_t but also on ρ_n^2 . As was pointed out by Yoshizawa (1995), the difference in $\varepsilon_d/\varepsilon$ in the two simulations can be attributed to the difference in ρ_n^2 . The assumption that $\varepsilon_d/\varepsilon$ depends only on M_t seems too restrictive to capture the behavior of decaying isotropic turbulence. In the $K - \varepsilon - K_\rho$ model, we use the two parameters M_t and ρ_n ; the development of ρ_n^2 is obtained from the transport equation for K_ρ .

2.4 Mass flux

Since ensemble averaging is used in this work, the mean-velocity equation contains the mass flux; its modeling is necessary. Taulbee & VanOsdol (1991) examined the transport equation for the mass fluctuating velocity $\langle \rho' u'_i \rangle / \bar{\rho}$ and modeled terms included in the equation. Instead of the transport equation we model the mass flux itself. It can be modeled as

$$\begin{aligned} \langle \rho' u'_i \rangle = & -C_{\rho u1} M_t \frac{K^2}{\varepsilon} \frac{\partial \bar{\rho}}{\partial x_i} \left[1 - 2 \frac{\rho_n^2}{M_t^2} + C_{\rho u3} \left(\frac{K}{\varepsilon} \frac{\partial U_i}{\partial x_i} + \frac{3}{\varepsilon} \frac{DK}{Dt} - \frac{5}{4} \frac{K}{\varepsilon^2} \frac{D\varepsilon}{Dt} \right) \right] \\ & - \frac{10 + 15\alpha}{10 + 6\alpha} C_{\rho u1} \frac{\rho_n^2}{M_t} \frac{K^2}{\varepsilon} \left[-\frac{17}{8} \frac{\partial \bar{\rho}}{\partial x_i} + \left(\frac{17}{8} - \frac{5}{2\gamma} \right) \frac{\bar{\rho}}{P} \frac{\partial P}{\partial x_i} + \frac{9}{4} \frac{\bar{\rho}}{K} \frac{\partial K}{\partial x_i} \right. \\ & \left. - \frac{3}{2} \frac{\bar{\rho}}{\varepsilon} \frac{\partial \varepsilon}{\partial x_i} + \frac{3}{2} \frac{\bar{\rho}}{K_\rho} \frac{\partial K_\rho}{\partial x_i} \right]. \end{aligned} \quad (34)$$

The term with the first square bracket depends on the gradient of mean density; it corresponds to the gradient-diffusion approximation. The eddy diffusivity is proportional to $M_t K^2 / \varepsilon$. It is smaller than the eddy diffusivity in incompressible flows by a factor of M_t . The eddy diffusivity for the mass flux includes nonequilibrium effects due to DK/Dt and $D\varepsilon/Dt$ as well as compressibility effects due to ρ_n^2/M_t^2 and $\partial U_i / \partial x_i$.

On the other hand, the term with the second square bracket also depends on the gradients of mean quantities other than $\bar{\rho}$; this effect is called cross diffusion. For example, when the gradients of $\bar{\rho}$ and P are small and the isentropic relations hold, the profile of P is proportional to that of $\bar{\rho}$; the pressure gradient term simply represents the modification of the eddy diffusivity. However, when the temperature changes rapidly due to heat release, the profiles of density and pressure may be different; in such a case the cross diffusion effect due to the pressure gradient can be important in the mass flux model.

Using the simplified approach Yoshizawa (1995) derived a model for the mass flux as follows

$$\langle \rho' u'_i \rangle = - \left[1 + \frac{3(\gamma - 1)}{\gamma} \frac{\sigma_\rho^2}{\sigma_\epsilon} \chi \right] \frac{\nu_T}{\sigma_\rho} \frac{\partial \bar{\rho}}{\partial x_i} - \frac{3}{\gamma} \chi \nu_T \bar{\rho} \frac{1}{E} \frac{\partial E}{\partial x_i} - \frac{3}{2} \frac{K_\rho}{\bar{\rho}} \frac{\nu_T}{K} \frac{DU_i}{Dt}, \quad (35)$$

where $\nu_T = (2/3)C_u(K^2/\epsilon)$ and σ_ρ , σ_ϵ , and C_u are model constants. If we assume that $P = (\gamma - 1)\bar{\rho}E$ and $DU_i/Dt = -(1/\bar{\rho})\partial P/\partial x_i$, we can see that the second and third terms on the right-hand side correspond to the cross-diffusion term due to the mean pressure in (34). The major difference between (34) and (35) lies in the dependence of the eddy-diffusivity on M_t ; the diffusivity of the former is of $O(M_t)$ whereas that of the latter is of $O(1)$. This difference stems from the different dependence of the time scale for density fluctuations on M_t .

2.5 Reynolds stress

Yoshizawa (1995) pointed out that compressibility effects are not incorporated into the Reynolds stress up to the order of δ ; this order corresponds to the eddy-viscosity approximation. We calculated the Reynolds stress up to the order of δ^2 to obtain

$$\begin{aligned} \langle u'_i u'_j \rangle &= \frac{2}{3} K \delta_{ij} \\ &- C_{uu1} \frac{K^2}{\epsilon} \left(\frac{\partial U_i}{\partial x_j} + \frac{\partial U_j}{\partial x_i} \right)^* \left[1 - 2 \frac{\rho_n^2}{M_t^2} + C_{uu4} \left(\frac{23}{49} \frac{K}{\epsilon} \frac{\partial U_i}{\partial x_i} + \frac{1}{\epsilon} \frac{DK}{Dt} - \frac{5}{12} \frac{K}{\epsilon^2} \frac{D\epsilon}{Dt} \right) \right] \\ &+ C_{uuA} \frac{K^3}{\epsilon^2} \left[\frac{62}{105} \left(\frac{\partial U_i}{\partial x_k} \frac{\partial U_j}{\partial x_k} \right)^* + \frac{2}{35} \left(\frac{\partial U_k}{\partial x_i} \frac{\partial U_k}{\partial x_j} \right)^* + \frac{34}{105} \left(\frac{\partial U_i}{\partial x_k} \frac{\partial U_k}{\partial x_j} + \frac{\partial U_j}{\partial x_k} \frac{\partial U_k}{\partial x_i} \right)^* \right. \\ &\left. + \frac{7}{15} \frac{D}{Dt} \left(\frac{\partial U_i}{\partial x_j} + \frac{\partial U_j}{\partial x_i} \right)^* \right] + C_{uu10} M_t \frac{K^3}{\epsilon^2} \left[\frac{\partial}{\partial x_i} \left(\frac{1}{\bar{\rho}} \frac{\partial P}{\partial x_j} \right) + \frac{\partial}{\partial x_j} \left(\frac{1}{\bar{\rho}} \frac{\partial P}{\partial x_i} \right) \right]^*, \quad (36) \end{aligned}$$

where

$$(f_{ij})^* \equiv f_{ij} - \frac{1}{3} f_{kk} \delta_{ij}. \quad (37)$$

Except for the isotropic part, $(2/3)K\delta_{ij}$, the expression consists of three parts. The first part represents the modification of the eddy viscosity due to compressibility and nonequilibrium effects. The second part corresponds to nonlinear models that have already been investigated for incompressible flows (Speziale 1987). The third part represents the compressibility effect due to a mean pressure gradient.

The modification of the eddy viscosity due to DK/Dt and $D\epsilon/Dt$ has already been proposed for incompressible flows (Yoshizawa & Nisizima 1993). Yoshizawa (1995) also mentioned its importance for compressible flows. Expression (36) suggests that we should take into account not only the nonequilibrium effect but also the compressibility effects due to the density variance and mean-velocity divergence.

Sarkar (1995) showed that the reduced growth rate of turbulence energy in homogeneous shear flows is primarily due to the decrease in turbulence production. Since the production term includes the Reynolds stress, compressibility effects on the Reynolds stress need to be modeled appropriately. In the present model the direct effect of compressibility on the eddy viscosity is expressed by ρ_n^2/M_t^2 in (36) because the mean-velocity divergence vanishes for homogeneous shear flows. For inhomogeneous turbulence the mean-velocity divergence can play an important role when the flow speed rapidly changes in the streamwise direction as in a shock wave. If the flow speed decreases and the divergence is negative, the eddy viscosity becomes smaller than the usual estimate, K^2/ε .

Although the third part is smaller than the second part by a factor of M_t , its expression is interesting in the sense that it does not include the mean velocity. Each term in the square bracket can be divided into the two terms: $(1/\bar{\rho})\partial^2 P/\partial x_i^2$ and $-(1/\bar{\rho}^2)(\partial\bar{\rho}/\partial x_i)(\partial P/\partial x_i)$. A term similar to the latter can be seen in the K equation (7). The importance of this term in the K equation was discussed by Yoshizawa (1995). Similarly the transport equation for the Reynolds stress contains such a term. Therefore, the gradients of mean density and pressure can affect the Reynolds stress.

2.6 Pressure-dilatation correlation

The pressure-dilatation correlation has been investigated as a typical compressibility effect. In this work we obtained a model expression as

$$\begin{aligned} \left\langle p' \frac{\partial u_i'}{\partial x_i} \right\rangle &= C_{pd1} \frac{\rho_n^2}{M_t} \gamma P \frac{\varepsilon}{K} + C_{pd2} \frac{\rho_n^4}{M_t^3} \gamma P \frac{\varepsilon}{K} \\ &\quad - C_{pd3} \frac{\rho_n^2}{M_t} \left(\gamma P \frac{\partial U_i}{\partial x_i} + 3 \frac{\gamma P}{K} \frac{DK}{Dt} - \frac{5}{4} \frac{\gamma P}{\varepsilon} \frac{D\varepsilon}{Dt} \right) + 2 \rho_n^2 \frac{\gamma P}{\bar{\rho}} \frac{D\bar{\rho}}{Dt} \\ &\quad - \rho_n^2 \gamma \frac{DP}{Dt} + C_{pd8} \frac{\rho_n^2}{M_t} \frac{K^2}{\varepsilon} \gamma \bar{\rho}^2 \frac{\partial}{\partial x_i} \left(\frac{P}{\bar{\rho}^3} \frac{\partial \bar{\rho}}{\partial x_i} - \frac{\gamma-1}{\gamma} \frac{1}{\bar{\rho}^2} \frac{\partial P}{\partial x_i} \right). \end{aligned} \quad (38)$$

By assuming some relations for basic model constants such as $C_{\omega\rho}$ and $C_{\omega c}$, we found that the constant C_{pd1} vanishes. If the assumption does not hold exactly, the constant can have a small nonzero value.

Using the simplified approach Yoshizawa (1995) proposed a model as

$$\left\langle p' \frac{\partial u_i'}{\partial x_i} \right\rangle = -C_{pdY1} \bar{\rho} \varepsilon \chi + C_{pdY2} \bar{\rho} K \chi \frac{\partial U_i}{\partial x_i} + C_{pdY3} \bar{\rho} K \chi \frac{1}{E} \frac{DE}{Dt}. \quad (39)$$

The third term on the right-hand side corresponds to the two terms that include $D\bar{\rho}/Dt$ and DP/Dt in the present model. Each term in (39) is proportional to χ whereas terms in (38) show a different dependence on ρ_n and M_t . Using the first and third terms in his model, Yoshizawa (1995) explained the property of the pressure-dilatation correlation whose value is positive for decaying isotropic turbulence and negative for homogeneous shear turbulence. The present model contains terms with

Dk/Dt and $D\varepsilon/Dt$. The terms can also explain the different sign of the correlation because of the difference in the development of energy in the two flows.

Sarkar (1992) modeled the pressure dilatation in the form of a power series in M_t as follows

$$\begin{aligned} \left\langle p' \frac{\partial u'_i}{\partial x_i} \right\rangle = & C_{pdS1} M_t \bar{\rho} \left(\langle u'_i u'_j \rangle - \frac{2}{3} K \delta_{ij} \right) \frac{\partial U_i}{\partial x_j} + C_{pdS2} M_t^2 \bar{\rho} \varepsilon_s \\ & + C_{pdS3} M_t^2 \bar{\rho} K \frac{\partial U_i}{\partial x_i}. \end{aligned} \quad (40)$$

This model is different from the above two models in that it does not contain the density variance. The first term on the right-hand side has a similar factor to the production term in the K equation. Yoshizawa (1995) illustrated that such a term can overestimate the pressure-dilatation correlation in a turbulent channel flow in which the shear is strong but the correlation is very small. On the other hand, the present and Yoshizawa's models contain the density variance; it is expected to explain the small value of the correlation.

2.7 Comparison to DNS data

Blaisdell *et al.* (1991) performed DNS of decaying isotropic and homogeneous shear turbulence. Using the DNS data we compare models for the dilatation dissipation. Although the TSDIA assumes inertial-range spectra, the simulations are at low Reynolds numbers and do not show an inertial range. The DNS results must include some low Reynolds number effects. The values of model constants in this paper may change for higher Reynolds number flows. Nonetheless, we believe that by comparing the models to the DNS we can better understand compressible turbulence.

We examined four simulations of isotropic turbulence and nine simulations of homogeneous shear flow. Here, we will show results of three simulations; their initial conditions are given in Table I. The parameter χ_c in Table I denotes the ratio of the compressible to total velocity variance $\langle u'_{ci} u'_{ci} \rangle / \langle u'_j u'_j \rangle$.

Case	Flow	M_t	ρ_n	χ_c
idc128	isotropic	0.3	0	0
ie128	isotropic	0.3	0.15	0.25
sha192	shear	0.4	0	0

Table 1. Initial conditions for DNS of isotropic and homogeneous shear turbulence by Blaisdell *et al.* (1991).

Figures 1 and 2 show the time history of the ratio $\varepsilon_d/\varepsilon$ for cases idc128 and ie128. The initial values of M_t are the same for the two cases whereas those of ρ_n and χ_c are different. The solid lines denote the DNS results, the dashed lines denote the values predicted by Sarkar's model (32), and the dotted lines denote those by the present model (29). The model constant in Sarkar's model is given by $C_{edS} = 1$.

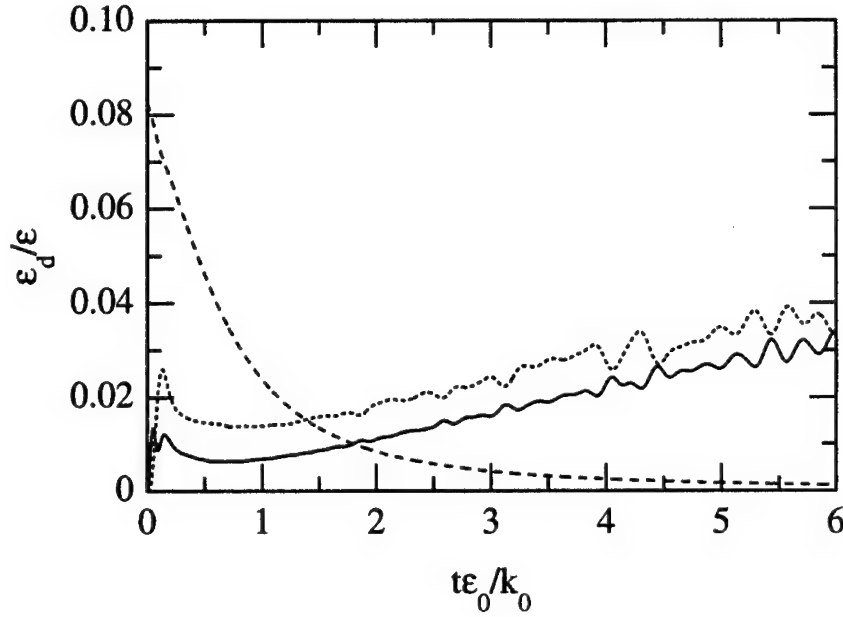


FIGURE 1. Time history of the ratio of dilatation dissipation to total dissipation for case idc128: —, DNS; ----, Sarkar's model; ·····, present model.

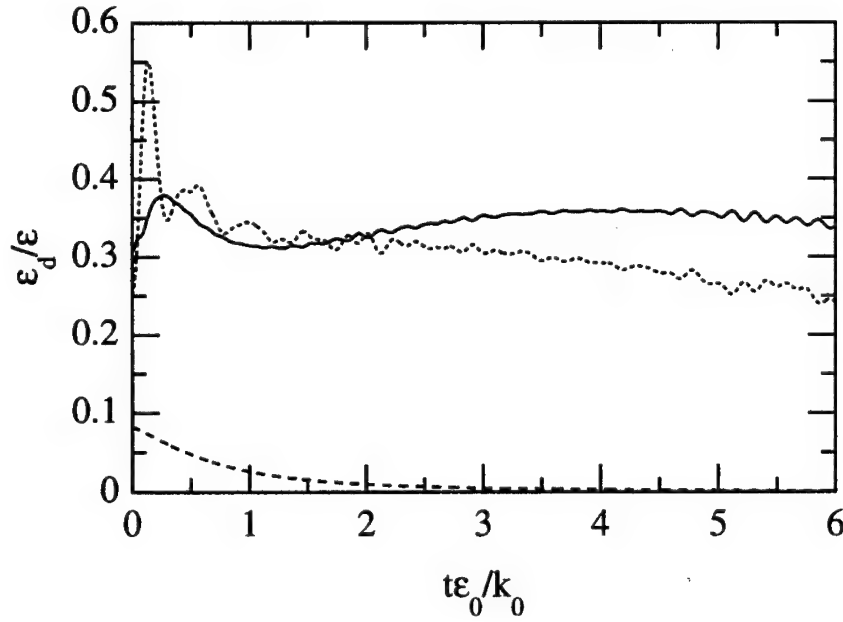


FIGURE 2. Time history of the ratio of dilatation dissipation to total dissipation for case ie128: —, DNS; ----, Sarkar's model; ·····, present model.

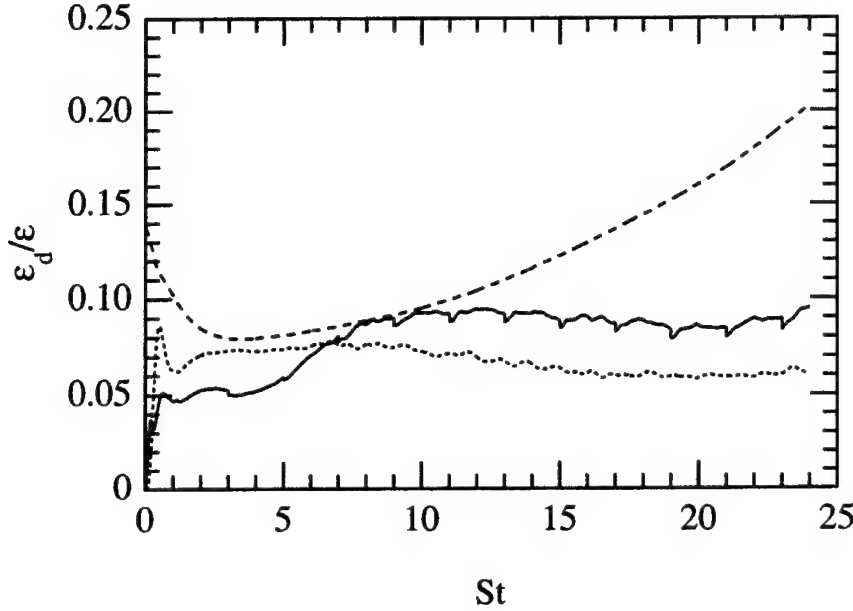


FIGURE 3. Time history of the ratio of dilatation dissipation to total dissipation for case sha192: —, DNS; ----, Sarkar's model; ·····, present model.

On the other hand, values of constants in the present model have not been obtained yet because the values of the basic constants, such as $C_{\sigma c}$ and α , are not known. Here, to examine overall agreement with DNS data, the model constants are set at $C_{ed1} = 1$ and $C_{ed7} = 0$ in (29). In Figs. 1 and 2 the DNS results for the two cases are very different; the value of $\varepsilon_d/\varepsilon$ for icl28 in Fig. 2 is much greater than that for idcl28 in Fig. 1. Since Sarkar's model contains only M_t , the predicted values for the two cases are almost the same; they decrease in time monotonically. On the other hand, the present model contains M_t and ρ_n^2 ; it predicts different values of $\varepsilon_d/\varepsilon$ for the two cases. The value for idcl28 increases in time like the DNS result. The model explains the effect of the initial condition in terms of the density variance. Similar results were obtained for the other two simulations using a higher turbulent Mach number, $M_t = 0.7$ (not shown). Fujiwara (1996) also illustrated the initial condition effects solving the $K - \varepsilon - F$ model where F is the sum of the nondimensional density variance and compressible kinetic energy.

Contrary to isotropic turbulence the effect of initial conditions were shown to disappear for homogeneous shear turbulence. Time histories of $\varepsilon_d/\varepsilon$ for simulations with different initial conditions tend to overlap as time increases. Here, we show results of a case denoted sha192; in this case the largest number of grid points was used and its results are considered the most reliable. Figure 3 shows the time history of $\varepsilon_d/\varepsilon$ for case sha192. The difference between the present and Sarkar's models is smaller than that for isotropic turbulence. However, the DNS result shows almost a constant value after $St = 10$ whereas Sarkar's model predicts a continually

increasing value after $St = 3$. The present model shows the same tendency as the DNS although the value is smaller. Other simulations with $M_t = 0.5$ extend to $St = 15$ and show qualitatively similar profiles as in Fig. 3. Therefore, the parameter ρ_n is concluded to be important for modeling the dilatation dissipation.

3. Future plans

Model expressions obtained in this work need to be examined further by comparing to DNS of homogeneous and inhomogeneous turbulence. Since the TSDIA is a method based on derivative expansions, expressions contain several terms including higher-order terms. Some terms should be selected so that model expressions are simple but contain essential compressibility effects. Model constants also should be estimated by DNS.

We assumed inertial-range spectra of the density and velocity variances. The spectral forms are not as established as those for incompressible flows. If details of inertial-range spectra are obtained in other theories or experiments, we can include them into this analysis. The relationship to incompressible models in the limit of zero Mach number also needs to be considered to improve the models.

Acknowledgment

I would like to thank Dr. N. N. Mansour for his support and valuable comments and Prof. G. A. Blaisdell for providing his DNS data. My stay at CTR was supported by a research fellowship from the Japanese government.

REFERENCES

- BATAILLE, F. & BERTOGLIO, J.-P. 1993 Short and long term behaviour of weakly compressible turbulence. In FED-Vol. 151, *Transitional and Turbulent Compressible Flows*, ASME, 139-145.
- BLAISDELL, G. A., MANSOUR, N. N., & REYNOLDS, W. C. 1991 Numerical simulations of compressible homogeneous turbulence. *Rep. TF-50*. Dept. of Mech. Engr., Stanford University.
- BLAISDELL, G. A. & ZEMAN, O. 1992 Investigation of the dilatational dissipation in compressible homogeneous shear flow. *Proc. of Summer Program*. Center for Turbulence Research, NASA Ames/Stanford Univ., 231-245.
- FUJIWARA, H. 1996 Compressibility effects on shear turbulence. Ph.D. thesis, University of Tokyo.
- FUJIWARA, H. & ARAKAWA, C. 1993 Direct numerical simulation and modeling of compressible isotropic turbulence. In *Ninth Symp. on Turbulent Shear Flows*, Kyoto, 22-2-1.
- KIDA, S. & ORSZAG, S. A. 1990 Energy and spectral dynamics in forced compressible turbulence. *J. Sci. Comp.* **5**, 85-125.
- MOISEEV, S. S., PETVIASHVILY, V. I., TOOR, A. V., & YANOVSKY, V. V. 1981 The influence of compressibility on the selfsimilar spectrum of subsonic turbulence. *Physica*. **2D**, 218-223.

- SARKAR, S. 1992 The pressure-dilatation correlation in compressible flows. *Phys. Fluids A*, **4**, 2674-2682.
- SARKAR, S. 1995 The stabilizing effect of compressibility in turbulent shear flow. *J. Fluid Mech.* **282**, 163-186.
- SARKAR, S., ERLEBACHER, G., HUSSAINI, M. Y., & KREISS, H. O. 1991 The analysis and modelling of dilatational terms in compressible turbulence. *J. Fluid Mech.* **227**, 473-493.
- SPEZIALE, C. G. 1987 On nonlinear $K - \ell$ and $K - \varepsilon$ models of turbulence. *J. Fluid Mech.* **178**, 459-475.
- TAULBEE, D. & VANOSDOL, J. 1991 Modeling turbulent compressible flows: The mass fluctuating velocity and squared density. AIAA Paper, No. 91-0524.
- YOSHIZAWA, A. 1984 Statistical analysis of the deviation of the Reynolds stress from its eddy-viscosity representation. *Phys. Fluids*, **27**, 1377-1387.
- YOSHIZAWA, A. 1990 Three-equation modeling of inhomogeneous compressible turbulence based on a two-scale direct-interaction approximation. *Phys. Fluids A*, **2**, 838-850.
- YOSHIZAWA, A. 1992 Statistical analysis of compressible turbulent shear flows with special emphasis on turbulence modeling. *Phys. Rev. A*, **46**, 3292-3306.
- YOSHIZAWA, A. 1995 Simplified statistical approach to complex turbulent flows and ensemble-mean compressible turbulence modeling. *Phys. Fluids*, **7**, 3105-3117.
- YOSHIZAWA, A. & NISIZIMA, S. 1993 A nonequilibrium representation of the turbulent viscosity based on a two-scale turbulence theory. *Phys. Fluids A*, **5**, 3302-3304.
- ZEMAN, O. 1990 Dilatation dissipation: The concept and application in modeling compressible mixing layers. *Phys. Fluids A*, **2**, 178-188.
- ZEMAN, O. 1991 On the decay of compressible isotropic turbulence. *Phys. Fluids A*, **3**, 951-955.

Lewis number effects on partially premixed flames

By G. R. Ruetsch AND J. Ferziger

1. Motivation and objectives

Combustion is generally categorized as either premixed, where flames propagate into homogeneous mixtures of reactants, or as nonpremixed, where initially separated reactants diffuse into the reaction zones. Although these approaches are applicable to many combustion devices, there are cases not in either of these two limiting regimes. Under such circumstances, one must consider partially premixed combustion.

In partially premixed combustion, mechanisms from both premixed and non-premixed regimes coexist and, as a result, some interesting phenomena arise. One such phenomenon is flame stabilization in laminar mixing layers by triple flames. These flames were first observed by Phillips (1965) in a methane mixing layer. Additional studies of triple flames are contained in Kioni *et al.* (1993), Dold (1989), Dold *et al.* (1991), Hartley and Dold 1991, Müller *et al.* (1994), and Ruetsch *et al.* (1995).

Triple flames may be thought of as an approach to partially premixed combustion from the nonpremixed limit. We can also approach the regime of partially premixed combustion from the premixed limit, where we consider inhomogeneously premixed flames. This regime has been addressed in Ruetsch and Broadwell (1995), where premixed flames were subjected to weak perturbations in mixture fraction.

One interesting feature of both triple and inhomogeneously premixed flames is the high curvature they possess. It is important to distinguish this type of curvature from that which arises from velocity fluctuations in the premixed case. Curvature of a flame due to velocity fluctuations is limited by various mechanisms which damp small wavenumber disturbances. In the partially premixed case, however, flame curvature is a consequence of the mixture fraction gradient which can be arbitrarily large. Aside from these geometrical aspects, this curvature plays a significant role in flame propagation. As an example, triple flames have propagation speeds that exceed the premixed flame speed by a factor of the square root of the density ratio. When the flames are confined laterally, as in the case of the inhomogeneously premixed flames, this mechanism for enhanced propagation speed due to heat release effects is greatly inhibited.

Another aspect of flame speed dependence on curvature is through the Lewis number, the ratio of thermal to mass diffusivities. This dependence of flame speed on the Lewis number relates to the thermal-diffusive instability, which has been extensively studied in the premixed case. Partially premixed combustion differs from the premixed case since the curvature in partially premixed cases can become very large and can be maintained by fixing the gradients in the approaching reactant field. This suggests that the partially premixed case provides a unique opportunity

to study Lewis number effects on flame speed. To this date, the topic of partially premixed combustion coupled with nonunity Lewis numbers has not been investigated. The present study addresses this issue.

We begin by reviewing the thermal-diffusive instability in premixed combustion and then discuss the configuration for studying similar behavior in the partially premixed case. This is followed by results of the numerical solutions and then by a set of model equations developed to evaluate and analyze the processes occurring in the simulations.

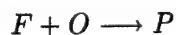
1.1 Thermal-diffusive instability

The thermal-diffusive instability is well documented for premixed flames (Williams 1986). Although we are considering partially premixed combustion, we expect and observe similarities with the premixed case. This thermal-diffusive mechanism relies on the strong influence of the temperature in the burnt gases on the reaction rate, and hence burning velocity. In turn, the temperature in the burnt gases increases with enhanced diffusion of reactant species into the flame and reduced diffusion of heat into the approaching flow. These diffusion rates are affected by the gradients in the species and temperature fields and by the values of the mass and thermal diffusivities. The ratio of the mass and thermal diffusivities is the Lewis number; the gradients in the profiles are modified by the differential diffusion of thermal energy and species. As a planar flame is perturbed slightly, the gradients of the reactant and temperature fields steepen or broaden. For unity Lewis number, the changes in mass and heat diffusion offset one another and the temperature in the burnt gases remains unchanged, as does the burning velocity. For Lewis numbers larger than unity, where the thermal diffusivity exceeds the mass diffusivity, the heat transfer out of the flame is dominant in the forward sections of the flame where the gradients are steeper. Likewise, the mass diffusion into the flame is dominant in the trough. This results in a stabilizing effect due to the temperature and burning velocity decreasing in the forward sections of the flame and increasing in the troughs. The opposite is true for Lewis numbers less than unity, where the flame becomes unstable to small perturbations.

1.2 Numerical simulation and flow configuration

We use direct numerical simulations to solve the fully compressible Navier-Stokes equations. The simulation uses a two-dimensional version of the code developed by Trounev (1991). This code uses the high-order compact finite difference scheme of Lele (1992) for spatial differentiation, the third order Runge-Kutta scheme of Wray for time advancement, and the Navier-Stokes characteristic boundary conditions of Poinso and Lele (1992). Below we summarize some of the important features and assumptions of the code relevant to this work; for further details on the numerical method readers are referred to Lele (1992) and Poinso and Lele (1992).

The chemical scheme we consider is represented by a one-step global reaction between a fuel and oxidizer:



where we have assumed unity stoichiometric coefficients for simplicity. The reaction rate follows the Arrhenius form:

$$\dot{\omega} = K \rho Y_F \rho Y_O \exp\left(-\frac{T_{ac}}{T}\right)$$

where ρ is the density, T_{ac} is the activation temperature, K is the pre-exponential factor, and Y_F and Y_O are the fuel and oxidizer mass fractions. Following Williams (1986), we write this reaction rate as

$$\dot{\omega} = \Lambda \rho Y_F \rho Y_O \exp\left(-\frac{\beta(1-\theta)}{1-\alpha(1-\theta)}\right)$$

where the reduced pre-exponential factor (Λ), heat release parameter (α), Zel'dovich number (β), and reduced temperature (θ) are defined by:

$$\Lambda = K \exp(-\beta/\alpha); \quad \alpha = \frac{T_f - T_0}{T_f}; \quad \beta = \frac{\alpha T_{ac}}{T_f}; \quad \theta = \frac{T - T_0}{T_f - T_0}$$

with T_f being the adiabatic flame temperature and T_0 taken in the ambient flow. In this study we hold the Zel'dovich number constant at $\beta = 8$ and use a heat release parameter of $\alpha = 0.75$.

The transport coefficients in the simulations are temperature dependent. This temperature dependence is expressed through the molecular viscosity, μ , given by:

$$\mu = \mu_0 \left(\frac{T}{T_0}\right)^a$$

with $a = 0.76$. The temperature dependence of the thermal conductivity, λ , and the mass diffusivities, \mathcal{D}_k , is obtained by requiring the Lewis, Prandtl, and Schmidt numbers to be constant:

$$Le_k = \frac{\lambda}{\rho \mathcal{D}_k c_p}, \quad Pr = \frac{\mu c_p}{\lambda}, \quad Sc_k = \frac{\mu}{\rho \mathcal{D}_k}$$

where $k = F, O$ refers to the fuel or oxidizer species. Although we are concerned with variations in the Lewis number, we do not want to consider differential diffusion in this study. Therefore, we allow the Lewis number to vary from simulation to simulation, but require that all species have equal Lewis numbers. We modify the Lewis number by changing the mass diffusivity, or Schmidt number, while maintaining a constant thermal diffusivity in the cold gases. We also maintain constant planar premixed laminar flame speed by modifying the pre-exponential factor Λ .

We solve the compressible Navier-Stokes equations in the two-dimensional domain depicted in Fig. 1. At the boundaries in the horizontal direction we use an inflow boundary condition on the left and nearly-perfect reflective boundary conditions, required to avoid pressure drift, at the outflow. In the lateral direction, we use

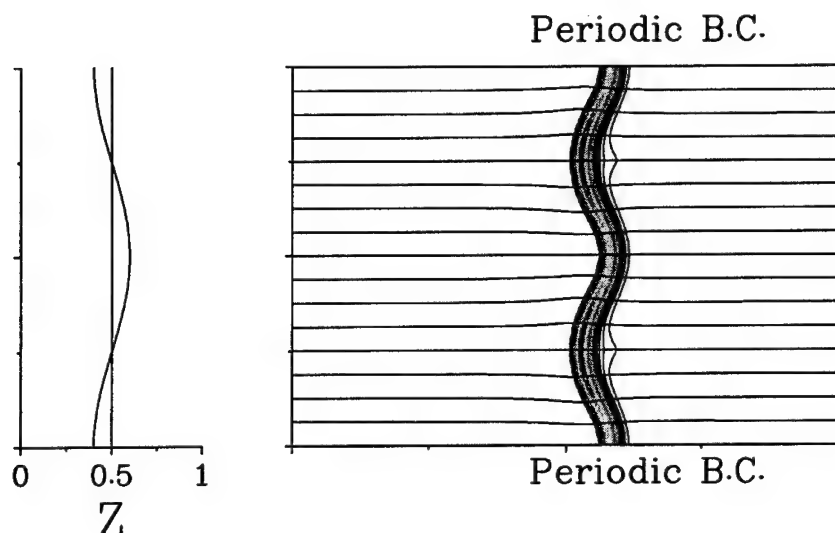


FIGURE 1. Computational domain used in the simulations. The left boundary is the inlet where the flow is uniform and the mixture fraction variation is given on the left. The lateral boundaries are periodic and represent the effects of confinement on the flame. The streamlines and reaction rate are shown within the domain. The inlet velocity, although always uniform, is adjusted to stabilize the flame within the domain.

periodic boundary conditions. This is in contrast to previous work on triple flames, which used nonreflecting boundary conditions in the lateral direction.

Within this domain we initialize the flow as a planar premixed flame, in which the mixture fraction, defined as

$$Z = \frac{1 + Y_F - Y_O}{2},$$

is everywhere equal to its stoichiometric value, $Z_{ST} = 0.5$. The incoming flow is uniform and set equal to the premixed laminar flame speed, S_L^0 . Also associated with the flame is the premixed flame thickness, δ_L^0 .

After the flow and flame are initialized, a sinusoidal perturbation is added to the uniform stoichiometric mixture fraction, specified by:

$$Z = Z_{ST} + \frac{\Delta Z}{2} \cos(2\pi y/L_{\Delta Z})$$

where $L_{\Delta Z}$ is the height of the domain in Fig. 1. In all cases, we maintain stoichiometric conditions on average. It should be noted that we are not dealing with a stability problem, in which a small perturbation is either damped or amplified. Rather, we introduce a finite disturbance in one field which produces finite changes

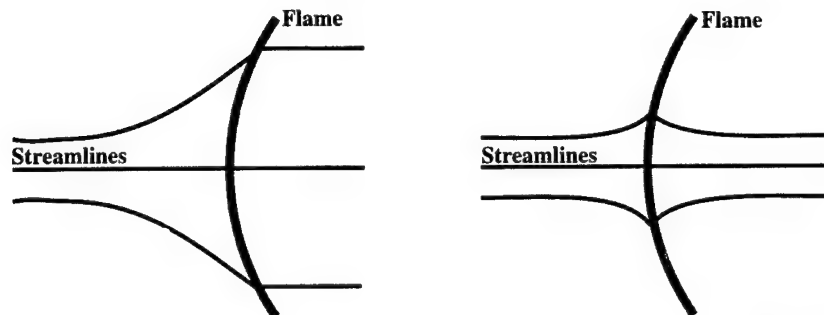


FIGURE 2. Streamline patterns for unconfined (left) and confined (right) flames. A redirection of the velocity vectors is observed across the flame front due to heat release effects. This redirection occurs upstream of the flame in the unconfined case, causing a divergence of the streamlines thus decelerating the horizontal velocity before the flame. As a result the propagation or upstream speed increases in order to maintain the premixed flames speed locally. In the confined case, the redirection of velocity vectors occurs both in front of and behind the flame. The increase in flame speed is much smaller in the confined cases and may be negligible for small wavelengths of lateral perturbations.

in the other fields. As this perturbation reaches the flame, the flame shape and propagation speed change, so the inlet velocity must be adjusted in order to achieve a steady-state solution. Because the variation in mixture fraction at the inlet has two stoichiometric points, two leading-edge flames occur. The range of mixture fraction is small enough, with $\Delta Z = 0.2$, that the diffusion flame is weak and is not apparent in the figure. In addition to the reaction rate, streamlines are also shown in the figure. Although we do observe streamline divergence in front of the flame, the propagation speed of the flame in Fig. 1, where $Le = 1$, remains equal to the planar premixed flame speed, S_L^0 .

The use of periodic or confined rather than free lateral boundaries greatly affects the flame's propagation. For unconfined unity Lewis number flames, it has been shown that the ratio of the propagation speed relative to the plane laminar premixed flame varies with the square root of the density ratio across the flame. Depending on the wavelength of the mixture fraction perturbation in the confined case, this effect may be absent. A schematic representation of why this occurs presented in Fig. 2. In both cases, there is a redirection of velocity vectors across the flame front resulting from heat release effects. However, in the unconfined case this redirection occurs in front of the flame resulting in a strong divergence of streamlines in the unburnt region of the flow field. This divergence in streamlines results in a decrease in horizontal velocity prior to the flame. As a result, in order for the local flame speed to maintain a velocity equal to the premixed flame speed, the upstream or propagation speed must increase. In the confined case, the redirection of velocity vectors across the flame occurs both in front of and behind the flame, hence the increase in propagation speed is smaller than that of the unconfined case.

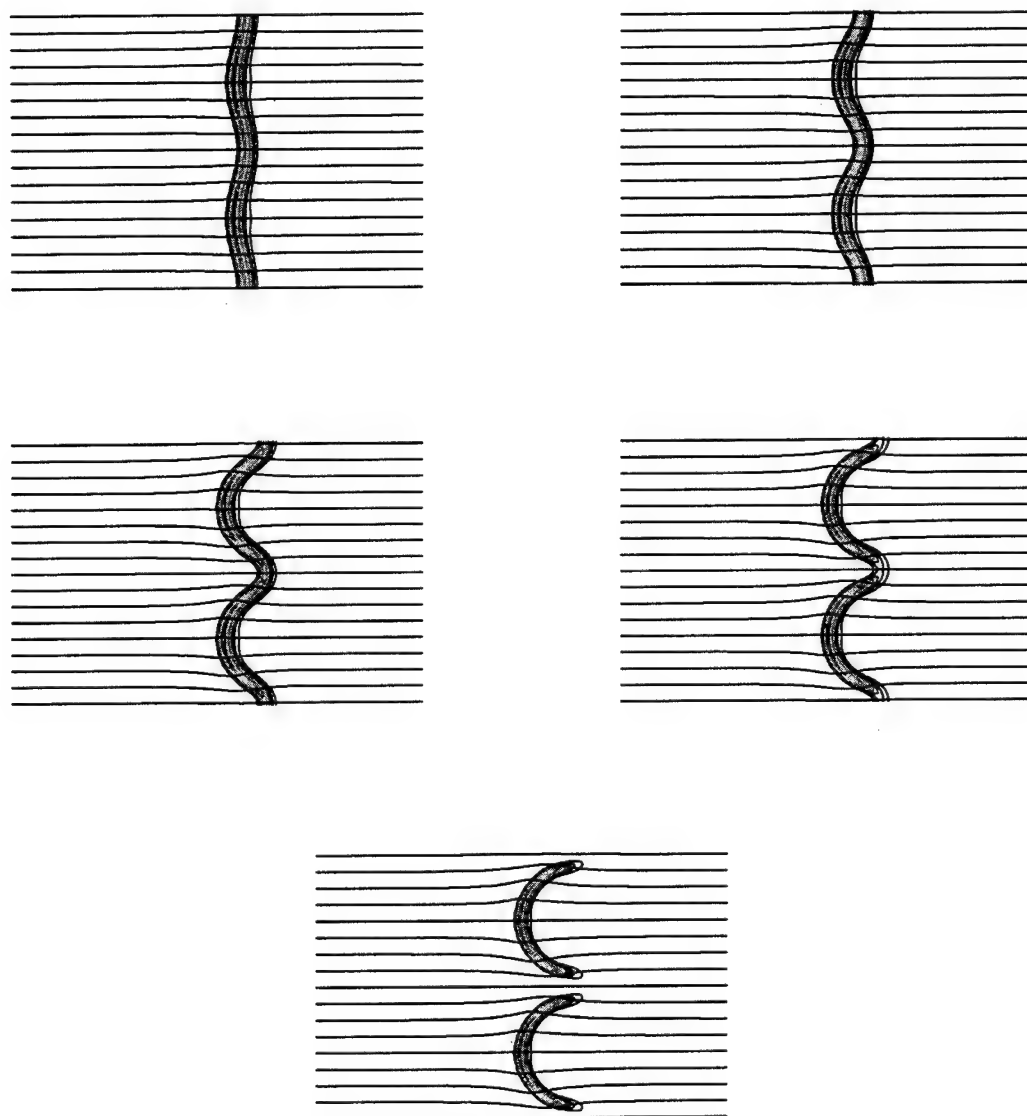


FIGURE 3. Reaction rate and streamlines for different Lewis number cases: $Le = 1.2$ top left, $Le = 1.0$ top right, $Le = 0.8$ center left, $Le = 0.6$ center right, and $Le = 0.4$ bottom. Flame surface area increases as the Lewis number becomes smaller. For the $Le = 0.4$ case, the flame trough opens due to leakage of reactants, similar to the case of a Bunsen flame.

2. Accomplishments

In this section we present results from simulations of nonunity Lewis number

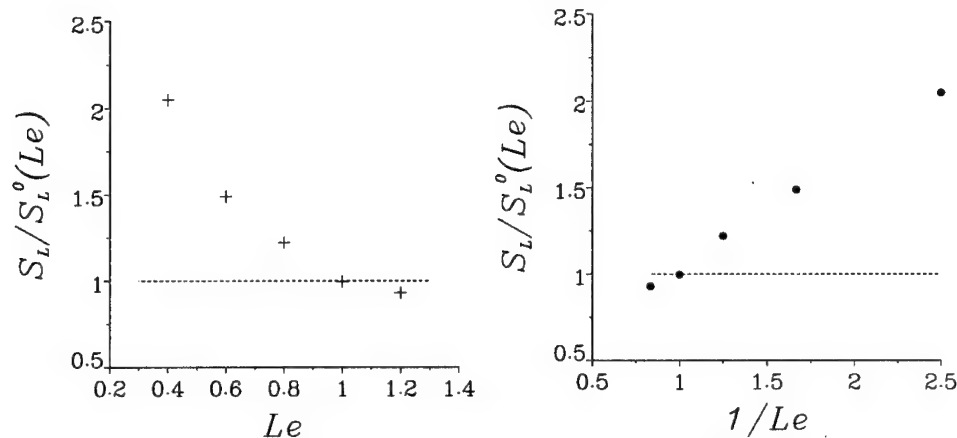


FIGURE 4. Flame speed as a function of Lewis number (left) and inverse Lewis number (right) Due to the strong confinement effects, the flame speed of the unity Lewis number case is that of the premixed flame speed. The flame speed increases with decreasing Lewis number, consistent with the thermal diffusive mechanism. Flame speeds are normalized by the planar premixed flame speed at stoichiometric conditions for the various Lewis numbers.

flames, followed by a discussion of a set of model equations used to analyze the flame's behavior. We start by discussing how the thermal-diffusive instability, in the context of partially premixed flames, modifies the flame shape.

The thermal-diffusive instability has been discussed thus far in terms of premixed flames. We now apply these concepts to our partially premixed case. The fundamental ideas mentioned above hold for the partially premixed case. In partially premixed combustion, however, the reaction rate is not constant along the flame front as in the premixed case. It is this gradient in reaction rate along the flame front that creates the perturbation in flame shape: the sections of the flame with mixture fractions closest to stoichiometry burn the fastest. Thus, to some degree the flame shape is determined by the approaching mixture fraction field. The thermal-diffusive mechanism then modifies this basic shape.

The modification of the basic flame shape due to the thermal diffusive mechanism is apparent from the flames in Fig. 3, where the reaction rate and streamlines are displayed for flames with Lewis numbers ranging from 0.4 to 1.2. Consistent with the thermal-diffusive mechanism, we observe that as the Lewis number decreases, the surface area of the flame increases. We should emphasize that the flame shapes in Fig. 3 are converged steady-state solutions. Although the thermal-diffusive instability accentuates the perturbation due to the variable mixture fraction field for Lewis numbers less than unity, the flame does reach a steady condition as nonlinear effects come into play (Williams 1996).

In addition to the modification of flame shape with Lewis number, we also observe an increase in flame speed, as shown in Fig. 4. The flame speed increases dramatically when the Lewis number drops below unity. We observe a flame speed more than twice the planar flame speed for $Le = 0.4$, which is larger than any flame

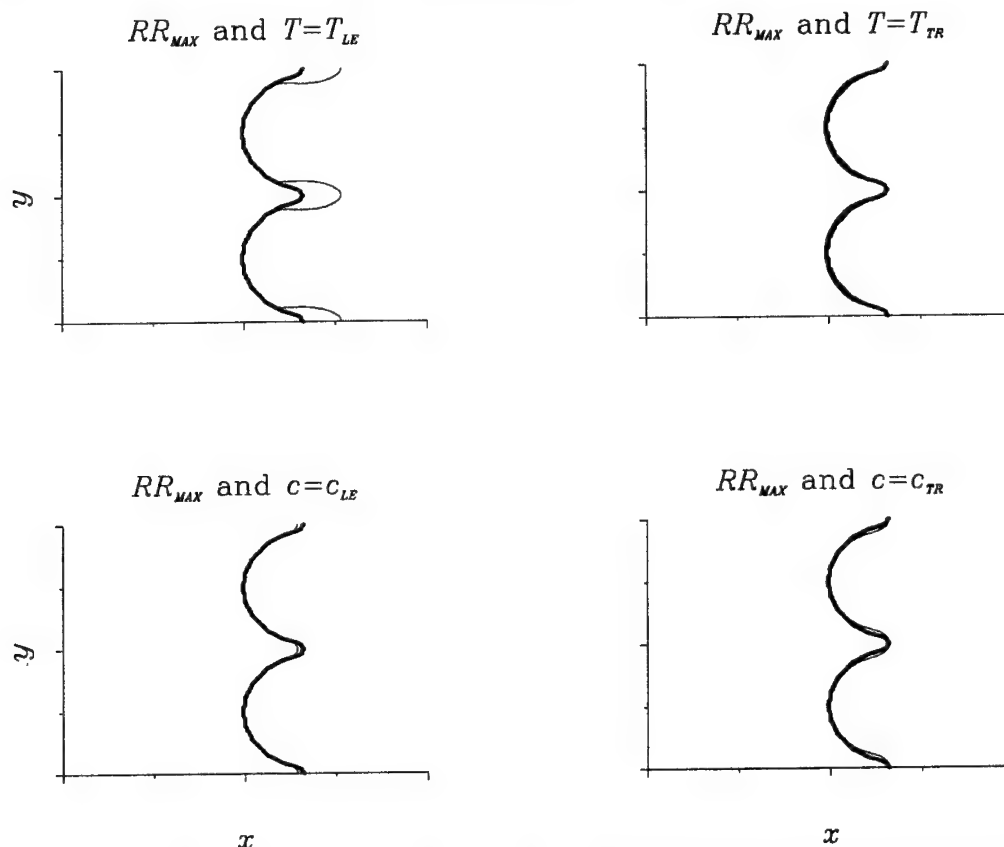


FIGURE 5. Flame surface (bold line), determined by maximum reaction rate on horizontal lines through the flame, and isocontours (thin line) of T and c for $Le = 0.4$ flames. Isovalues of T and c are chosen from the values along the flame surface at the leading edge (LE) and trough (TR). Although both fields have isocontours that track the flame surface reasonable well, the variable c is more reliable and is used as the progress variable.

speed observed in the unconfined configuration for $Le = 1$ flames (Ruetsch *et al.* 1995). One must also keep in mind that the mixture fraction range is $0.4 < Z < 0.6$ at the inlet and decreases before the mixture reaches the flame. Since the unconfined case has a much larger range in mixture fraction, $0 < Z < 1$, but produces a smaller increase in flame speed, it is evident that the Lewis number plays a strong role in the propagation characteristics of partially premixed flames. Also depicted in Fig. 4, we observe a good linear correlation of flame speed with the inverse of the Lewis number.

2.1 Progress variable

A necessary ingredient for further analysis of flame behavior is a definition of a progress variable which indicates the mixture's degree of reactedness. Together with the mixture fraction, the progress variable replaces the fuel and oxidizer mass fractions as independent variables. In premixed combustion, the progress variable

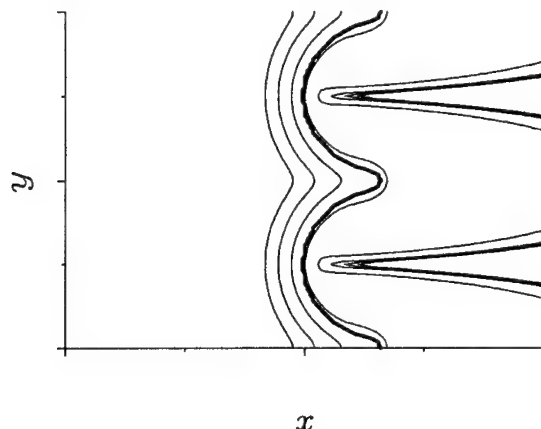


FIGURE 6. Flame surface (bold line) and various isovalue contours of the progress variable c . Before the premixed portion of the flame, the curvature of c and the flame surface are comparable. After the premixed flame, the radii of curvature of the c contours more closely resemble the thickness of the trailing diffusion flame.

can either be the reactant species mass fraction or the temperature. In partially premixed combustion, the issue is more complicated. We would like an isopleth of the progress variable to coincide with the flame surface. In partially premixed combustion, we define the flame surface as the curve connecting the horizontal extrema of the reaction rate. This curve is plotted in Fig. 5 for the $Le = 0.4$ flame along with temperature contours and the variable c given by:

$$c = 1 - Y_F - Y_O,$$

which is also the product mass fraction. The values of T and c used to obtain the isocontours are chosen to coincide with the flame surface at both the leading edge and trough.

From Fig. 5 we see that both quantities track the flame surface reasonably well. However, c follows the contour more closely, especially in the trough. We should point out that c reaches a value of unity only when neither fuel nor oxidizer are present. Therefore, in regions not at stoichiometric conditions, it is possible to burn one reactant completely and not have $c = 1$. In this respect, c does not have the traditional property of being unity when no further burning is possible. In spite of this shortcoming, we choose c as our progress variable for its ability to track the flame front and its linear dependence on the mass fractions of the reactant species.

The characteristics of c change considerably as we cross the flame surface, as indicated in Fig. 6. Prior to reaching the flame, the radius of curvature of c isocontours scale with the lateral thickness, $L_{\Delta Z}$. After passing through the flame surface, the radius of curvature scales with the thickness of the trailing diffusion flame. This has a large effect on the flame stretch, \mathcal{K} , defined as

$$\mathcal{K} = \nabla_T \cdot \mathbf{u} + S_L(Z)\kappa$$

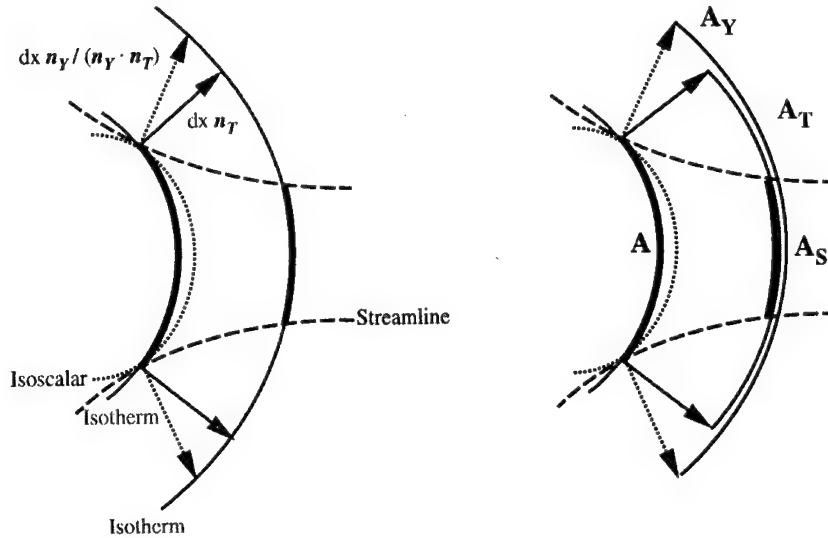


FIGURE 7. Control volumes for the one dimensional equation formulation. The control volume is bounded laterally by streamlines and by isotherms in the flow direction. The areas A_T and A_Y are used to define leakage of heat and species through the streamtube.

where ∇_T is the tangential gradient operator and $\kappa = \nabla_T \cdot \mathbf{n}_T$ is the curvature. Profiles of flame stretch through the flame surface indicate that stretch is dominated by curvature effects as expected and that no reasonable value can be assigned to the stretch as the change in the curvature through the flame is quite dramatic.

The inability to define a single value for curvature and thus flame stretch does not invalidate the use of c as a progress variable. One must remember that the concept of a progress variable strictly applies only to a premixed combustion. The fact that this quantity behaves differently in a region undergoing nonpremixed combustion does not invalidate its usefulness.

Because of the inability to define flame stretch accurately, the analysis of these partially premixed flames must proceed along an alternative path, which we discuss in the next section.

2.2 Model equations for partially premixed combustion

We now discuss a set of one-dimensional equations for analyzing the behavior of curved partially premixed flames. This method is based on the work of Echekki (1992) and Echekki (1996) for premixed combustion, which was used in analysis of the laminar flame tip by Poinot *et al.* (1992). This approach reduces the Navier-Stokes equations to a set of one-dimensional equations while maintaining aspects of the flame's multidimensional nature through terms representing various isopleth curvatures. This approach differs from conventional models that handle the geometrical aspects exactly, while the physical processes are approximated. In our case, the terms representing the physical processes remain intact, and the geometrical aspects are approximated.

We begin by examining the control volume of Fig. 7, which is bounded laterally

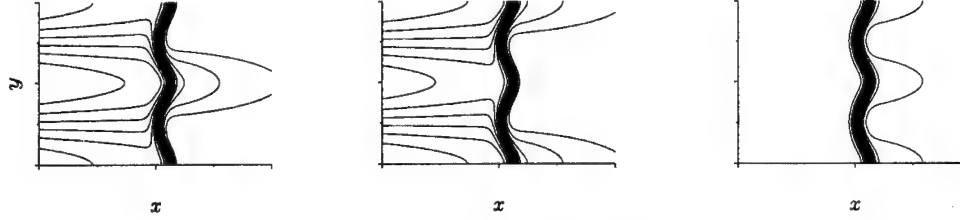


FIGURE 8. Fuel mass fraction (left), oxidizer mass fraction (center), and temperature (right) contour plots for $Le = 1$ case. For this partially premixed case, the need to account for a difference between the normals of the individual species and temperature fields is evident. The differences become stronger as one considers nonunity Lewis numbers and larger perturbations to the mixture fraction.

by streamlines and by isotherms in the streamwise direction. We define normals pointing in the flow direction for the temperature and various scalar fields as:

$$\mathbf{n}_T = \frac{\nabla T}{|\nabla T|}; \quad \mathbf{n}_{Y_F} = -\frac{\nabla Y_F}{|\nabla Y_F|}; \quad \mathbf{n}_{Y_O} = -\frac{\nabla Y_O}{|\nabla Y_O|}; \quad \mathbf{n}_c = \frac{\nabla c}{|\nabla c|}$$

The distance between the two isotherms along the normal \mathbf{n}_T is δx . We use the area of the first isotherm A as the base area, and define three surfaces along the second isotherm: the streamtube area, A_S ; the area between the intersection of the two isotherm normals emanating from the boundaries of A with the second isotherm surface, A_T ; and the area between the intersection of the two isoscalar normals, \mathbf{n}_{Y_i} , emanating from the boundaries of A with the second isotherm surface, A_{Y_i} . These latter two areas are used to account for the cross-stream diffusion of species and heat. The distance along \mathbf{n}_{Y_i} between the two isotherm surfaces is given by:

$$\delta x_{Y_i} \mathbf{n}_{Y_i} = \frac{\delta x}{\mathbf{n}_{Y_i} \cdot \mathbf{n}_T} \mathbf{n}_{Y_i}.$$

This control volume differs from the one used by Echehki (1992) in that the normals to the isotherms and isopleths are not colinear. This is a necessity for partially premixed combustion, as demonstrated in Fig. 8, where contours of the fuel and oxidizer mass fractions, along with the temperature, are shown. It is desirable to use the progress variable c in place of the individual reactant species, and a transport equation for c is developed later in this paper. It suffices to mention here that \mathbf{n}_c and \mathbf{n}_T are not necessarily colinear, even for unity Lewis number. Figure 9 shows this clearly; $\mathbf{n}_c \cdot \mathbf{n}_T$ deviates from unity in the flame trough.

2.2.1 Area relations

In this section we develop relations between the reference areas A and A_S , used in defining our control volume, and the auxiliary areas A_T and A_{Y_i} , used in our analysis to account for cross-stream diffusion. A useful relation in obtaining such relations is the identity from Chung and Law (1988) in their integral analysis of stretched premixed flames:

$$A_2 = A_1(1 + \nabla_T \cdot \mathbf{a})$$

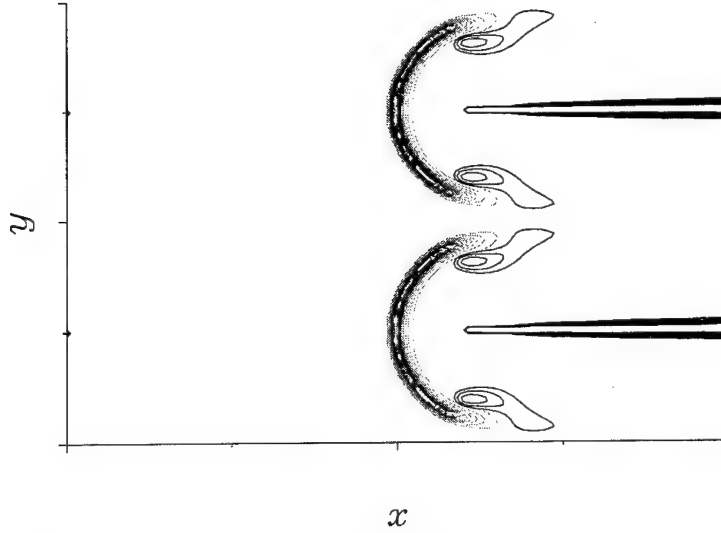


FIGURE 9. Alignment of progress variable and temperature normals for $Le = 0.4$ case. The reaction rate is shown in grey, and the dark contours show levels of $1 - \mathbf{n}_c \cdot \mathbf{n}_T$, thus departures from alignment. The greatest departure from alignment occurs in the trailing diffusion flame, but there are regions near the flame trough where the alignment of \mathbf{n}_c and \mathbf{n}_T is not preserved.

where \mathbf{a} is any vector from a point on A_1 to A_2 and the gradient operator ∇_T represents the divergence on the plane tangent to A_1 :

$$\nabla_T \cdot \mathbf{a} = \nabla \cdot \mathbf{a} - \mathbf{n}_T \mathbf{n}_T : \nabla \mathbf{a}$$

According to this relation we have:

$$A_T = A [1 + \delta x \nabla_T \cdot \mathbf{n}_T],$$

$$A_{Y_i} = A \left[1 + \delta x \nabla_T \cdot \left(\frac{\mathbf{n}_{Y_i}}{\mathbf{n}_{Y_i} \cdot \mathbf{n}_T} \right) \right],$$

and we express the streamtube area as

$$A_S = A + \delta A.$$

The term $\nabla_T \cdot \mathbf{n}_T$ is the curvature of the isotherm. The similar term in the equation for A_{Y_i} reduces to the isotherm curvature only if $\mathbf{n}_T = \mathbf{n}_{Y_i}$, in which case $A_T = A_{Y_i}$. We also define the differences between these areas as

$$\delta A_{TS} \equiv A_T - A_S = A \delta x \nabla_T \cdot \mathbf{n}_T - \delta A$$

and

$$\delta A_{Y_i S} \equiv A_{Y_i} - A_S = A \delta x \nabla_T \cdot \left(\frac{\mathbf{n}_{Y_i}}{\mathbf{n}_{Y_i} \cdot \mathbf{n}_T} \right) - \delta A$$

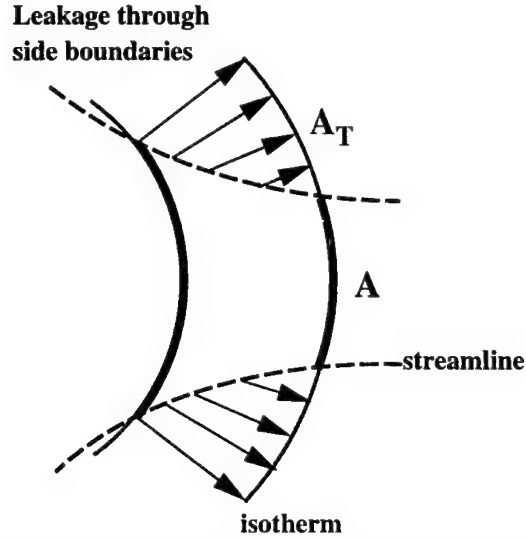


FIGURE 10. Lateral diffusion of heat through the streamtube. This leakage can be accounted for by measuring the flux through the expanded area in the downstream isotherm. (This diagram demonstrates the method used to account for thermal leakage, but the same concept applies to mass leakage through the streamtube.)

where in the limit of small δx we obtain:

$$\frac{dA_{TS}}{dx} = A \nabla_T \cdot \mathbf{n}_T - \frac{dA}{dx}$$

and

$$\frac{dA_{Y_i S}}{dx} = A \nabla_T \cdot \left(\frac{\mathbf{n}_{Y_i}}{\mathbf{n}_{Y_i} \cdot \mathbf{n}_T} \right) - \frac{dA}{dx}.$$

These relations provide a crucial link between the basic governing equations and our model equations. Since we are developing a set of one-dimensional equations, we need to include information regarding the other spatial dimensions. It is the behavior of the normal terms in these area relations that provide the multidimensional information required for adequate representation of the geometrical aspects of the problem.

2.2.2 Governing equations

With the area relations defined, we now consider conservation laws applied to the control volume. Since our control volume is bounded by streamlines, continuity is simply:

$$\delta[m] = 0$$

where m is the mass flow rate in the streamtube. The difference between values at the outlet and inlet isotherms is denoted as $\delta[\] = [\]_{x+\delta x} - [\]_x$. The species equation is:

$$\delta[mY_i + \mathcal{M}_i] + \mathcal{F}_i \delta A_{Y_i S} = \dot{\omega}_{Y_i} \delta x A$$

where $\mathcal{M}_i = -\rho A \mathcal{D}_i dY_i/dx$, $\mathcal{F}_i = -\rho \mathcal{D}_i dY_i/dx$, and $\dot{\omega}_{Y_i}$ are the diffusive flow rate, diffusive flux, and rate of production of species i . The term $\mathcal{F}_i \delta A_{Y_i,S}$ represents the leakage of species i across the streamtube, which is equivalent to the heat that crosses the area $\delta A_{Y_i,S}$ as indicated in Fig. 10. In the limit of small δx this becomes:

$$m \frac{dY_i}{dx} + \frac{d\mathcal{M}_i}{dx} + \left[A \nabla_T \cdot \left(\frac{\mathbf{n}_{Y_i}}{\mathbf{n}_{Y_i} \cdot \mathbf{n}_T} \right) - \frac{dA}{dx} \right] \mathcal{F}_i = \dot{\omega}_{Y_i} A$$

or by substituting for \mathcal{M}_i and \mathcal{F}_i :

$$m \frac{dY_i}{dx} - \frac{d}{dx} \left(\rho A \mathcal{D}_i \frac{dY_i}{dx} \right) - \rho \mathcal{D}_i \left[A \nabla_T \cdot \left(\frac{\mathbf{n}_{Y_i}}{\mathbf{n}_{Y_i} \cdot \mathbf{n}_T} \right) - \frac{dA}{dx} \right] \frac{dY_i}{dx} = \dot{\omega}_{Y_i} A \quad (1)$$

The first and second terms in this equation represent the convection and diffusion processes across the isotherms. The term in square brackets, representing the leakage of reactants across the streamtube, contains information about the multi-dimensional nature of the flame.

Equation (1) can be used for each species so that, although this study uses a simple chemical scheme, the method can be applied to complex reaction mechanisms. In our case, we are more interested in the progress variable c and the mixture fraction Z than the mass fractions. We can obtain these equations by combining the equations for the individual species and substituting for c :

$$m \frac{dc}{dx} - \frac{d}{dx} \left(\rho A \mathcal{D} \frac{dc}{dx} \right) + \rho \mathcal{D} \frac{dA}{dx} \frac{dc}{dx} + \rho \mathcal{D} A \left[\nabla_T \cdot \left(\frac{\mathbf{n}_{Y_F}}{\mathbf{n}_{Y_F} \cdot \mathbf{n}_T} \right) \frac{dY_F}{dx} + \nabla_T \cdot \left(\frac{\mathbf{n}_{Y_O}}{\mathbf{n}_{Y_O} \cdot \mathbf{n}_T} \right) \frac{dY_O}{dx} \right] = \dot{\omega}_c A$$

where $\dot{\omega}_c = -(\dot{\omega}_{Y_F} + \dot{\omega}_{Y_O})$. To eliminate Y_F and Y_O from the equations, we use the relations

$$Y_F = Z - \frac{c}{2}; \quad Y_O = 1 - Z - \frac{c}{2}$$

and obtain:

$$m \frac{dc}{dx} - \frac{d}{dx} \left(\rho A \mathcal{D} \frac{dc}{dx} \right) + \rho \mathcal{D} \left[\frac{dA}{dx} \frac{dc}{dx} + A \frac{dZ}{dx} \nabla_T \cdot \left(\frac{\mathbf{n}_{Y_F}}{\mathbf{n}_{Y_F} \cdot \mathbf{n}_T} - \frac{\mathbf{n}_{Y_O}}{\mathbf{n}_{Y_O} \cdot \mathbf{n}_T} \right) - \frac{1}{2} A \frac{dc}{dx} \nabla_T \cdot \left(\frac{\mathbf{n}_{Y_F}}{\mathbf{n}_{Y_F} \cdot \mathbf{n}_T} + \frac{\mathbf{n}_{Y_O}}{\mathbf{n}_{Y_O} \cdot \mathbf{n}_T} \right) \right] = \dot{\omega}_c A. \quad (2)$$

In a similar fashion, we can develop an equation for Z :

$$m \frac{dZ}{dx} - \frac{d}{dx} \left(\rho A \mathcal{D} \frac{dZ}{dx} \right) + \frac{1}{2} \rho \mathcal{D} \left[2 \frac{dA}{dx} \frac{dZ}{dx} + A \frac{dZ}{dx} \nabla_T \cdot \left(\frac{\mathbf{n}_{Y_F}}{\mathbf{n}_{Y_F} \cdot \mathbf{n}_T} + \frac{\mathbf{n}_{Y_O}}{\mathbf{n}_{Y_O} \cdot \mathbf{n}_T} \right) - \frac{1}{2} A \frac{dc}{dx} \nabla_T \cdot \left(\frac{\mathbf{n}_{Y_F}}{\mathbf{n}_{Y_F} \cdot \mathbf{n}_T} - \frac{\mathbf{n}_{Y_O}}{\mathbf{n}_{Y_O} \cdot \mathbf{n}_T} \right) \right] = 0 \quad (3)$$

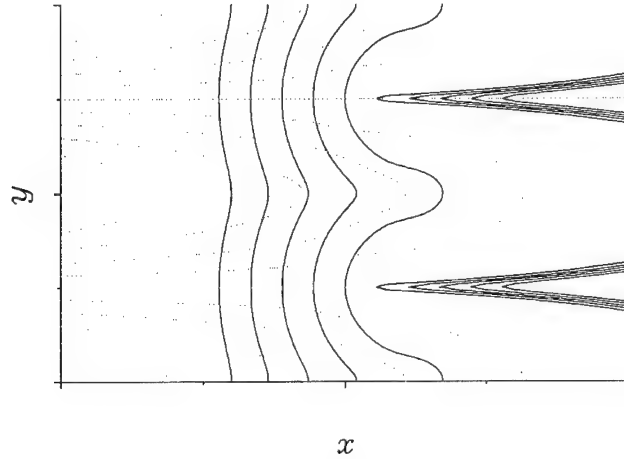


FIGURE 11. Alignment of progress variable and mixture fraction. Progress variable c (dark lines) and mixture fraction Z (grey scale) isopleths are shown for the $Le = 0.4$ case. Along the line through the leading edge \mathbf{n}_c and \mathbf{n}_Z are orthogonal; however, this is not the case as one moves from this line of symmetry.

Equation (2) clearly shows the effect of partial premixing on the evolution of the progress variable. To contrast Eq. (2) with the premixed case, we can write the evolution equation for c in premixed combustion for which $\mathbf{n}_{Y_F} = \mathbf{n}_{Y_O} = \mathbf{n}_T$, giving:

$$m \frac{dc}{dx} - \frac{d}{dx} \left(\rho A \mathcal{D} \frac{dc}{dx} \right) + \rho \mathcal{D} \frac{dc}{dx} \left[\frac{dA}{dx} - A \nabla_T \cdot \mathbf{n}_T \right] = \dot{\omega}_c A, \quad (4)$$

which is identical to the species equation of Echehki (1992). Equation (2) shows an explicit dependence on mixture fraction through the dZ/dx term, which modifies the equation when the isopleths of the fuel and oxidizer differ.

We have eliminated Y_F and Y_O in Eqs. (2) and (3), except for their implicit occurrence in the normal vectors. We can replace these by forming the normal vectors from our transformation equations:

$$\mathbf{n}_{Y_F} = \frac{\frac{1}{2} \nabla c - \nabla Z}{|\frac{1}{2} \nabla c - \nabla Z|}; \quad \mathbf{n}_{Y_O} = \frac{\frac{1}{2} \nabla c + \nabla Z}{|\frac{1}{2} \nabla c + \nabla Z|} \quad (5)$$

Substitution of these quantities into Eqs. (2) and (3), in general, leads to complicated expressions but there are cases where simplifying assumptions can be made. These cases occur when the gradients of the progress variable and mixture fraction are either colinear or orthogonal.

In general, as demonstrated by Fig. 11, we cannot make assumptions about the alignment of \mathbf{n}_c and \mathbf{n}_Z . However, along the line through the leading edge we find that $\mathbf{n}_c \cdot \mathbf{n}_Z = 0$. It is not sufficient that these normal vectors are orthogonal along this line of symmetry. Due to the ∇_T operator, we must also require that these normal vectors remain orthogonal as we move laterally. In cases where a substantial

region with $\mathbf{n}_c \cdot \mathbf{n}_Z \sim 0$ exists, the expressions in Eq. (5) simplify greatly. When \mathbf{n}_c and \mathbf{n}_T are collinear and \mathbf{n}_Z and \mathbf{n}_T are orthogonal, we can write:

$$\frac{\mathbf{n}_{Y_F}}{\mathbf{n}_{Y_F} \cdot \mathbf{n}_T} = \frac{\frac{1}{2}\nabla c - \nabla Z}{\frac{1}{2}\nabla c \cdot \mathbf{n}_T}; \quad \frac{\mathbf{n}_{Y_O}}{\mathbf{n}_{Y_O} \cdot \mathbf{n}_T} = \frac{\frac{1}{2}\nabla c + \nabla Z}{\frac{1}{2}\nabla c \cdot \mathbf{n}_T}$$

Furthermore, along the leading edge streamtube $Z = 0.5$, thus $dZ/dx = 0$, which upon substitution in the conservation equation for c once again recovers the equation obtained for a premixed flame, which can be written as:

$$m \frac{dc}{dx} - A \left[\frac{d}{dx} \left(\rho \mathcal{D} \frac{dc}{dx} \right) + \rho \mathcal{D} \frac{dc}{dx} \nabla_T \cdot \mathbf{n}_c \right] = \dot{\omega}_c A. \quad (6)$$

We can determine the local streamwise velocity by manipulation of Eq. 6 to obtain:

$$u \sim \frac{m}{\rho A} = \mathcal{D} \left[\frac{d}{dx} \ln \left(\rho \mathcal{D} \frac{dc}{dx} \right) + \kappa + \frac{\dot{\omega}_c}{\rho \mathcal{D} dc/dx} \right]$$

where $\kappa = \nabla_T \cdot \mathbf{n}_T$ is the local curvature. The fact that we have a local curvature in this equation is desirable due to its rapid rate of change. It is instructive to contrast this equation with the multidimensional equation used in calculating the propagation velocity (Ruetsch and Broadwell 1995):

$$V = \frac{1}{\rho |\nabla c|} \frac{\partial}{\partial x_i} \left(\rho \mathcal{D} \frac{\partial c}{\partial x_i} \right) + \frac{1}{\rho |\nabla c|} \dot{\omega}_c.$$

The first term in the multidimensional equation corresponds to the first and second terms in the 1D equation, where the multidimensional diffusion term is broken up into streamwise and lateral, through curvature, components.

Through examination of Eq. (2) we have learned when partial premixing must be considered and under what circumstances the problem can be analyzed from a premixed standpoint: $\mathbf{n}_c \cdot \mathbf{n}_T = 1$ and $\mathbf{n}_c \cdot \mathbf{n}_Z = 0$ in a neighborhood of the streamtube. Under weak gradients of the mixture fraction, the leading edges of partially premixed flames to some degree fall in this category.

Up to this point, the issue of Lewis number effects has not been discussed in regards to the one-dimensional equations. In order for the Lewis number to come into play, we need to include both thermal and mass diffusion. Therefore, we look to energy conservation. The energy equation can be written in differential form as:

$$\delta \left[\sum_i (mY_i + \mathcal{M}_i) h_i + \mathcal{Q} \right] + \sum_i \delta A_{Y_i S} \mathcal{F}_i h_i + \delta A_{TS} q = \dot{\omega}_c Q_c A \delta x \quad (7)$$

where $\mathcal{Q} = -A\lambda dT/dx$, $q = -\lambda dT/dx$, and Q_c is the heat release from the chemical reaction per unit change in progress variable. The terms in brackets represent the flow of enthalpy across the isotherms due to convection and mass diffusion, as well

as heat conduction across the isotherms. The remaining terms represent the leakage of energy across the streamtube due to mass diffusion and heat conduction, along with heat release through chemical reactions. Defining $h = \sum Y_i h_i$ and assuming $h_i = h = c_p T$ for all i we have, after taking the limit of small δx :

$$m \frac{dT}{dx} - Le \frac{d}{dx} \left(\rho \mathcal{D} A \frac{dT}{dx} \right) - \rho \mathcal{D} T \sum_i \frac{dA_{Y_i S}}{dx} \frac{dY_i}{dx} - Le \rho \mathcal{D} \frac{dA_{TS}}{dx} \frac{dT}{dx} = \frac{Q_c}{c_p} \dot{\omega}_c A. \quad (8)$$

where we have represented all diffusion terms through the mass diffusion coefficient and use the Lewis number to effectively convert to the thermal diffusivity when required. After some manipulation, Eq. 8 becomes:

$$\begin{aligned} m \frac{dT}{dx} - Le A \left[\frac{d}{dx} \left(\rho \mathcal{D} \frac{dT}{dx} \right) + \rho \mathcal{D} \frac{dT}{dx} \nabla_T \cdot \mathbf{n}_T \right] \\ - \rho \mathcal{D} A T \left[\frac{dZ}{dx} \nabla_T \cdot \left(\frac{\mathbf{n}_{Y_F}}{\mathbf{n}_{Y_F} \cdot \mathbf{n}_T} - \frac{\mathbf{n}_{Y_O}}{\mathbf{n}_{Y_O} \cdot \mathbf{n}_T} \right) \right. \\ \left. + \frac{dc}{dx} \nabla_T \cdot \left(\frac{\mathbf{n}_c}{\mathbf{n}_c \cdot \mathbf{n}_T} - \frac{1}{2} \frac{\mathbf{n}_{Y_F}}{\mathbf{n}_{Y_F} \cdot \mathbf{n}_T} - \frac{1}{2} \frac{\mathbf{n}_{Y_O}}{\mathbf{n}_{Y_O} \cdot \mathbf{n}_T} \right) \right] = \frac{Q_c}{c_p} \dot{\omega}_c A. \end{aligned} \quad (9)$$

The first line of Eq. 9 contains the convective and thermal diffusion terms. The last two lines represent the energy change via mass diffusion through the lateral boundaries and the chemical source.

In the premixed limit, Eq. 9 reduces to:

$$m \frac{dT}{dx} - Le A \left[\frac{d}{dx} \left(\rho \mathcal{D} \frac{dT}{dx} \right) + \rho \mathcal{D} \frac{dT}{dx} \nabla_T \cdot \mathbf{n}_T \right] = \frac{Q_c}{c_p} \dot{\omega}_c A,$$

which holds not only in the premixed limit but also for the streamtube passing through the leading edge under the conditions used to obtain Eq. 6.

3. Future work

Up to this point, efforts have been concentrated on the development of the model equations described above. Future work will concern applying these equations to simulation data in order to determine the significance of certain processes and to obtain scaling behavior regarding flame propagation. In particular, we would like to recover the linear relation of flame speed with the inverse of the Lewis number depicted in Fig. 4.

One aspect of flame propagation that can be addressed using these equations is the process by which the flame trough is stabilized. The weak reaction rate and convergence of streamlines would suggest that the trough region doesn't stabilize, but simulations indicate that the flame does reach a steady state. Leakage of heat and species is evidently important in this region and can be analyzed using the model equations.

This laminar study allows one to develop an understanding of how fluctuations in the reactant composition alone affects flame behavior. Once the behavior of

these flames is understood, data from partially premixed turbulent simulations can be analyzed, where contributions from both velocity and mixture fraction fields modify flame behavior.

REFERENCES

- CHUNG, S. H. AND LAW, C. K. 1988 An integral analysis of the structure and propagation of stretched premixed flames. *Combust. & Flame*. **72**, 325.
- DOLD, J. W. 1989 Flame propagation in a nonuniform mixture: analysis of a slowly varying triple flame. *Combust. & Flame*. **76**, 71.
- DOLD, J. W., HARTLEY, L. J., AND GREEN, D. 1991 Dynamics of laminar triple-flamelet structures in non-premixed turbulent combustion. *Dynamical Issues in Combustion Theory*. Springer-Verlag, 83.
- ECHEKKI, T. 1992 Studies of curvature, strain, and unsteady effects on premixed flames. *Ph. D. Thesis*, Stanford University.
- ECHEKKI, T. 1996 A quasi-one dimensional premixed flame model with cross-stream diffusion. To appear in *Combust. & Flame*.
- HARTLEY, L. J., AND DOLD, W. 1991 Flame propagation in a nonuniform mixture: analysis of a propagating triple-flame. *Comb. Sci. & Tech.* **80**, 23.
- KIONI, P. N., ROGG, B., BRAY, K. N. C., AND LIÑÁN, A. 1993 Flame spread in laminar mixing layers: the triple flame. *Combust. & Flame*. **95**, 276.
- LELE, S. 1992 Compact finite difference schemes with spectral-like resolution. *J. Comp. Phys.* **103**, 16.
- MÜLLER, C. M., BRIETBACH, H., AND PETERS, N. 1994 Partially premixed turbulent flame propagation in jet flames. *25th International Symposium on Combustion*. p. 1099
- PHILLIPS, H. 1965 Flame in a buoyant methane layer. *10th International Symposium on Combustion*. p. 1277
- POINSOT, T., AND LELE, S. 1992 Boundary conditions for direct simulations of compressible viscous flows. *J. Comp. Phys.* **101**, 104.
- POINSOT, T., ECHEKKI, T., AND MUNGAL, M. G. 1992 A study of the laminar flame tip and implications for premixed turbulent combustion. *Comb. Sci. & Tech.* **81**, 45.
- RUETSCH, G. R., VERVISCH, L., AND LIÑÁN, A. 1995 Effects of heat release on triple flames. *Phys. Fluids*. **7**, 1447.
- TROUVÉ, A. 1991 Simulation of flame-turbulence interaction in premixed combustion. *Annual Research Briefs 1991*. CTR, Stanford University/Nasa Ames., 273-286.
- WILLIAMS, F. A. *Combustion Theory* Addison-Wesley, NY, 1986.
- WRAY, A. A. Private communication.

Conditional moment closure of mixing and reaction in turbulent nonpremixed combustion

By Nigel S. A. Smith¹

1. Motivation

Nonpremixed combustion is the process whereby fuel and oxidizer species, which are each nonflammable in isolation, concurrently mix to form a flammable mixture, and chemically react in the flammable mixture. In cases of practical industrial interest, the bulk of nonpremixed combustion occurs in a turbulent mixing regime where enhanced mass transfer rates allow the maximum power density to be achieved in any given thermochemical device.

Conventional moment closure techniques are inapplicable in modeling turbulent combustion because of the nonlinear dependence of chemical reactions upon small scale fluctuations in species concentrations and temperature. More sophisticated closures are required so as to model turbulent nonpremixed combustion systems of practical interest, such as in gas turbine combustors and diesel engines.

A number of sophisticated models can be found in the literature, notably the laminar flamelet method (see Peters 1984), and the joint probability density function method (see Pope 1985). Some of the issues surrounding the latter method were investigated in a recent study at the Center for Turbulence Research (see Frolov *et al.* 1996), while others have investigated the former method (see Mell *et al.* 1994).

Another model of substantial merit is the conditional moment closure (CMC) method, which was proposed independently by Klimenko (1990) and Bilger (1993). This method has been successfully compared with turbulent jet flame experiments (Smith *et al.* 1995, Smith 1994), isothermal reacting mixing layers in an atmospheric wind tunnel (Li & Bilger 1993), isothermal direct numerical simulations (Mell *et al.* 1993), and in reacting DNS with heat release and complex chemistry (Smith 1995).

The results of the most recent DNS study incorporating realistic chemistry in a direct numerical simulation indicated a sensitivity of the method to the choice of chemical mechanism used to describe the thermochemical system. The choice of mechanism was found to have an impact on the accuracy of the chemical closure itself.

Work carried out at the CTR, in the six months following Smith (1995), has been aimed at improving the mixing submodel as well as understanding the deficiencies in the chemical closure for in a generic combustor chemical system.

¹ Present address: Aeronautical & Maritime Research Lab., Australia

1.1 Conditional moment closure method

The classical difficulty faced in modeling turbulent nonpremixed combustion is that of closing the averaged equations for chemically reactive species. The instantaneous equation for the evolution of the mass fraction Y_α of a reactive species α is the following,

$$\frac{\partial}{\partial t}(\rho Y_\alpha) + \frac{\partial}{\partial x_i}(\rho u_i Y_\alpha) = \frac{\partial}{\partial x_j}(\rho D_\alpha \frac{\partial Y_\alpha}{\partial x_j}) + \rho \dot{w}_\alpha \quad (1)$$

where \dot{w}_α is the net chemical production rate of the species α , and D_α is the corresponding molecular diffusivity where a simplified Fickian approximation has been made to model molecular transport. Applying a traditional averaging scheme, such as density-weighted (Favre) unconditional ensemble averaging, yields the following,

$$\frac{\partial}{\partial t}(\bar{\rho} \tilde{Y}_\alpha) + \frac{\partial}{\partial x_i}(\bar{\rho} \tilde{u}_i \tilde{Y}_\alpha) = \frac{\partial}{\partial x_j}(\bar{\rho} D_\alpha \frac{\partial \tilde{Y}_\alpha}{\partial x_j}) + \bar{\rho} \tilde{\dot{w}}_\alpha. \quad (2)$$

In order to close the averaged species equation, a model must be provided for the averaged source term $\tilde{\dot{w}}_\alpha$. First order closures that evaluate the instantaneous chemical rate expressions with averaged species concentrations and temperature,

$$\tilde{\dot{w}}_\alpha(Y_1, Y_2, \dots, Y_N, T) \approx \dot{w}_\alpha(\tilde{Y}_1, \tilde{Y}_2, \dots, \tilde{Y}_N, \tilde{T}) \quad (3)$$

are known to be highly inaccurate in combustion cases of practical interest. The chemical reactions encountered in combustion processes are highly nonlinear, and thus small perturbations in the input parameters can cause very large changes in the computed reaction rate.

Under the Conditional Moment Closure (CMC) method, the level of perturbations from the modeled mean data is reduced by averaging the reactive species equations *conditionally* upon a conserved scalar mass fraction.

At the expense of adding an additional computational dimension to the modeling problem, conditional averaging allows chemical closure to be effected in many cases of nonpremixed turbulent combustion.

The average of a fluctuating turbulent quantity A , conditional upon the conserved scalar mixture fraction $\xi(x_i, t)$ being equal to a sample value η , is the following (see Klimenko (1990)):

$$\langle A(x_i, t) | \xi(x_i, t) = \eta \rangle \equiv \frac{1}{P_\eta} \int \int A(x_i, t) \delta(\xi(x_i, t) - \eta) dx_i dt \quad (4)$$

In the above definition, P_η is the probability density function of the conserved scalar at the location x_i and time t , and δ denotes the Dirac delta function. In all that follows, the full conditional averaging operator $\langle \dots | \xi(x_i, t) = \eta \rangle$ will be abbreviated to $\langle \dots | \eta \rangle$ for the sake of brevity.

The evolution of the conditional mean mass fraction $Q_\alpha \equiv \langle Y_\alpha | \eta \rangle$ of a reactive species α is governed by the following,

$$\langle \rho | \eta \rangle \frac{\partial Q_\alpha}{\partial t} + \langle \rho u_i | \eta \rangle \frac{\partial Q_\alpha}{\partial x_i} = \frac{1}{2} \langle \rho \chi | \eta \rangle \frac{\partial^2 Q_\alpha}{\partial \eta^2} + \langle \rho \dot{w}_\alpha | \eta \rangle + e_q + e_y \quad (5)$$

where the molecular diffusivities of all species are assumed uniform. The residual terms, e_q and e_y , contained unclosed expressions involving the conditional means and variations from the conditional means. These terms are presumed small in the cases studied here.

The symbol χ denotes the instantaneous scalar dissipation rate and is defined (below) in terms of the mixture fraction ξ .

$$\chi \equiv 2D_\xi \left(\frac{\partial \xi}{\partial x_i} \right)^2 \quad (6)$$

In order to close the CMC scalar equation, means of determining $\langle \rho \chi | \eta \rangle$ and $\langle \dot{w}_\alpha | \eta \rangle$ are required. The conditional mean scalar dissipation rate, $\langle \rho \chi | \eta \rangle$, is determined from the conserved scalar PDF equation so as to ensure conservation of mass. The calculation of this quantity is discussed in a later section.

1.2 Chemical source terms

The net volumetric chemical formation rate (dimensions of $mol/(L^3T)$) of a reactive species is most commonly described as a linear combination of Arrhenius type expressions, as given below:

$$\dot{w}_\alpha = \sum_{\beta=1}^{N_r} c_{\alpha,\beta} [K_\beta(T) \prod_{\gamma=1}^{N_s} Y_\gamma^{\nu_{\gamma,\beta}}]. \quad (7)$$

The net production rate of the species α is equal to the weighted sum of the production by all chemical reactions ($\beta = 1, \dots, N_r$). The weighting factor for species α and reaction β , $c_{\alpha,\beta}$, is an integer in the case of elementary reactions and may be positive or negative or zero (no net effect).

Each individual reaction is governed by the law of mass action, and a so-called reaction rate "constant," K_β , as given below:

$$K_\beta(T) = \rho^{n_\beta} k_\beta(T) = \left(\frac{P}{R} \right)^{n_\beta} \lambda_\beta T^{a_\beta} \exp -\theta_\beta/T. \quad (8)$$

Reaction rate constants are typically strongly nonlinear functions of temperature, T , and to a lesser extent pressure. The activation temperature is denoted by θ_β , the reaction order by n_β , and the pre-exponential coefficient by λ_β .

A Taylor series expansion in terms of temperature and the participating reactants in each reaction can easily be derived. Neglecting terms third order and higher, an expression for the conditional mean source term for a species α can be written in

terms of conditional mean species mass fractions Q_γ , as well as the first and second conditional moments of temperature and the reactant mass fractions.

$$\langle \dot{w}_\alpha | \eta \rangle \approx \sum_{\beta=1}^{N_r} c_{\alpha,\beta} K_\beta(\langle T | \eta \rangle) r_\beta \prod_{\gamma=1}^{N_s} Q_\gamma^{\nu_{\gamma,\beta}} \quad (9)$$

The modifying function r_β from the above equation is defined as follows for a bimolecular reaction with reactant species Y_1 and Y_2 ,

$$r_\beta = 1 + B_\beta \frac{\langle (T')^2 | \eta \rangle}{\langle T | \eta \rangle^2} \left(1 + \frac{\sigma_{1,2}}{Q_1 Q_2}\right) + A_\beta \left(\frac{\sigma_{1,T}}{Q_1 \langle T | \eta \rangle} + \frac{\sigma_{2,T}}{Q_2 \langle T | \eta \rangle}\right) \quad (10)$$

where,

$$B_\beta = \frac{1}{2}((a_\beta + \theta_\beta / \langle T | \eta \rangle)^2 - a_\beta - 2\theta_\beta / \langle T | \eta \rangle) \quad (11)$$

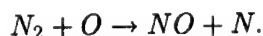
and

$$A_\beta = a_\beta + \theta_\beta / \langle T | \eta \rangle \quad (12)$$

In the majority of previous CMC modeling efforts, the function r_β has been assumed to equal unity. It is, however, clear that in instances where the activation temperature θ_β , or the temperature exponent a_β are large, chemical closure is sensitive to even small levels of conditional variance.

2. Objectives

The objective of the most recent work has been to evaluate the level of departure of the modifying function r_β away from unity, over a range of reaction types within a turbulent nonpremixed combustion system. Of particular interest is the behavior of the modifying function for the rate controlling reaction for the thermal production of nitric oxide (NO) given below:



The reaction above has a very high activation temperature and would seem susceptible to errors which might arise from assuming a unit modifying function. This is of particular significance to existing comparisons between experiment and simple first-order closure CMC calculations (see Smith *et al.* 1995) in turbulent jet flames of hydrogen. In those cases, the model appears to consistently overpredict NO levels while more or less accurately predicting the major reaction products.

In order to evaluate the advantage that might be gained by allowing for non-unity modifying functions, direct numerical simulations of weakly turbulent nonpremixed combustion of methane in air were performed. The chemical mechanism employed included NO formation through prompt and thermal reaction pathways, in addition to major species production.

The simulation conditions were arranged as much as possible to make best use of the limited number of grid points in the domain in collecting a statistical sample. The simulation was organized such that a substantial portion of the domain could be treated as statistically similar.

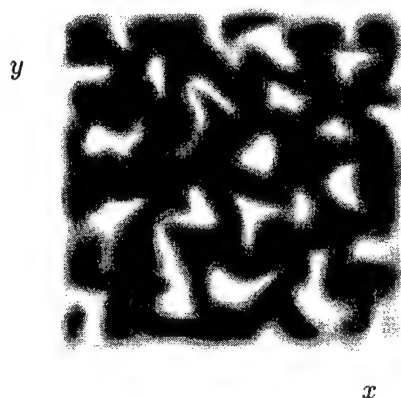


FIGURE 1. Initial distribution of the conserved scalar. White regions denote $\xi = 1$ while black regions denote $\xi = 0$. Initial conserved scalar unmixedness $\Omega = 0.64$.

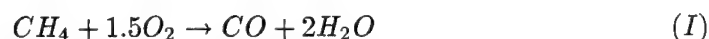
2.1 Simulation conditions

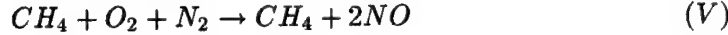
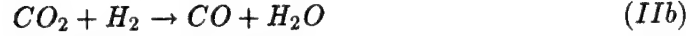
The DNS code that was used is little changed from that described previously (see Smith 1995, Ruetsch & Broadwell 1995). The code features a the high-order compact finite differencing scheme, as described by Lele (1992), for spatial differencing, and the third order Runge-Kutta timestepping algorithm of Wray. The Navier-Stokes characteristic boundary conditions described by Poinso and Lele (1992) are also included.

All simulations performed to date have been two dimensional with sizes ranging up to 257^2 . It is desirable to perform three dimensional simulations of the same nature, but as yet computational resources have been insufficient to allow a reasonable Reynolds number in the calculation while carrying realistic chemistry.

2.1.1 Chemical reaction mechanism

A novel eight step reduced chemical mechanism for methane combustion (Frolov 1996) has been devised which allows substantial savings in resolution requirements over more orthodox mechanisms, while purporting to provide reasonable agreement with experiment. The mechanism consists of global steps which do not make explicit use of any radical species, such as hydroxyl (OH), methyl (CH_3), and so on, but instead employs tuning factors for the fuel oxidation and prompt NO_x steps. These tuning factors are incorporated into the pre-exponential coefficients in the Arrhenius expressions and make allowance for variations in local equivalence ratio, fuel species, and pressure. The tuning constants were derived by Frolov (1996) from comparison of the reduced mechanism with full mechanism calculations in counterflow laminar premixed flames.





The Arrhenius rate constants corresponding to the above reaction steps are given below where λ_β , a_β and E_β denote the pre-exponential factor, temperature index, and activation energy for reaction number β , and p is the local pressure in bar.

No.	$\lambda_\beta(\text{mol}, L, s)$	a_β	$E_i(\text{kcal/mol})$
I	A_1/p	0.0	50.0
II f	$1.0 \times 10^{12}/p$	0.0	41.5
II b	$3.1 \times 10^{13}/p$	0.0	49.1
III	$7.0 \times 10^{13}/p^2$	0.0	21.0
IV	$8.5 \times 10^{12}/p^2$	0.0	21.0
V	A_5/p^2	0.0	50.0
VI f	1.7×10^{17}	-0.5	136.0
VI b	4.1×10^{15}	-0.5	93.3

The pre-exponential factors for reactions I and V are functions of the local equivalence ratio β . Frolov (1996) determined the appropriate values of λ_1 and λ_5 at a range of equivalence ratios from $\beta = 0.67$ up to $\beta = 1.54$. The pre-exponential factors vary nonlinearly over the range such that the lean limit values are orders of magnitude greater than the rich limit values. The values under stoichiometric conditions for each is $\lambda_1 = 2.57 \times 10^{15} L/(\text{mol} \cdot s)$ and $\lambda_5 = 7.03 \times 10^{13} L^2/(\text{mol}^2 s)$. At the suggestion of Frolov (1996), linear interpolation between the known values for λ_1 and λ_5 was used to determine values for intermediate mixing states.

2.1.2 Domain initialization

The turbulent field was initialized using an incompressible phase scrambled kinetic energy spectrum for the velocity components and a conserved scalar. The initialized conserved scalar field can be seen Fig. 1, where black regions denote pure oxidizer zones and white regions denote pure fuel zones. Scalar *normalized unmixedness* can be defined as:

$$\Omega \equiv \frac{\langle \xi^2 \rangle}{\langle \xi \rangle (1 - \langle \xi \rangle)}, \quad (13)$$

which can be seen to be a normalized measure of the fluctuation level. Unmixedness varies between zero, where the scalar field is homogeneous, and unity where only

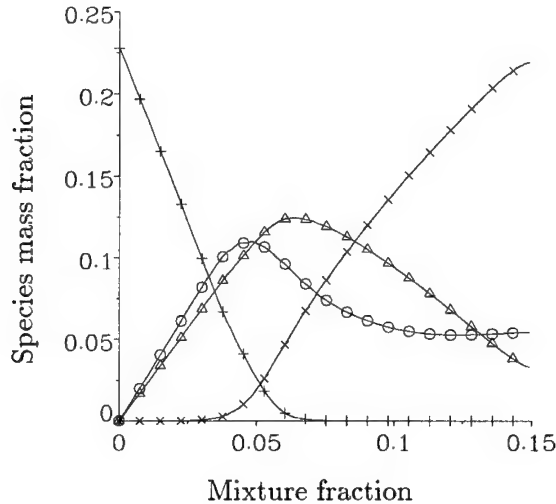


FIGURE 2. Adiabatic equilibrium species mass fraction profiles in mixture fraction space. Symbol key : + - O_2 , \times - CO , \circ - CO_2 , Δ - H_2O .

pure fuel and pure oxidizer zones exist with no mixing at all. The initial conserved scalar fields used here had initial unmixednesses of $\Omega \approx 0.8$ in all cases.

Reactive species' mass fractions and internal energy were mapped onto the conserved scalar field using adiabatic chemical equilibrium relationships between mixture fraction (conserved scalar) and the reactive scalars. The adiabatic equilibrium reactive scalar mass fraction profiles are plotted versus conserved scalar mixture fraction in Fig. 2.

Note that the chemical conditions in the richest permissible mixture corresponded to a state with an equivalence ratio of approximately three. This mixture fraction is beyond the rich flammability limit of methane-air mixtures at standard temperature and pressure. Of all the species present in the simulation, only nitric oxide (NO) was initialized as being zero at all mixture fractions.

By initializing the simulation using the method described above, the flame zones were effectively ignited simultaneously, albeit artificially, prior to run time. This was done to avoid a potentially long transient period where (presumably) triple flames would propagate along the unburnt flammable ribbons between the fuel and oxidizer pockets away from the ignition points.

In order to avoid the establishment of intense pressure waves as a result of mapping flame zone temperatures onto an initial cold flow field, the local densities were adjusted everywhere to maintain a uniform initial pressure field. The existence of large density gradients after initialization caused a short period where the flow field reorganized to preserve continuity. It is difficult to draw a parallel in behavior between the decay of turbulent motions in the reacting case and the well known trends in inert grid turbulence. The former case is subject to dilatation, variable viscosity, and baroclinic torque effects that are absent in the latter.

Unfortunately, it was further found that it was not possible to perform simulations

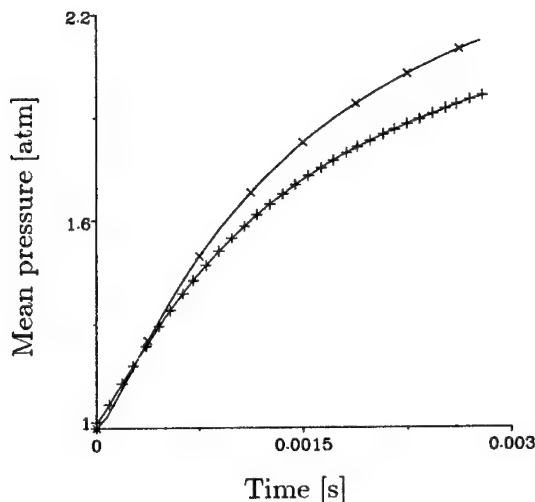


FIGURE 3. Simulated and modeled mean pressure as a function of time. Symbol key : + - DNS, x - CMC model

with a combination of periodic boundary conditions and the initialization technique described above. No satisfactory explanation for this restriction has been found. It was found, however, that the calculation could proceed without hindrance if the domain was instead bounded by adiabatic slip walls encompassing a small filter zone with initially damped wall-normal velocity.

Under the simulation conditions described above, the flow and mixing fields on a central portion of the grid (210^2) were found to be statistically homogeneous. All of these points were then used in each of the statistical samples taken periodically throughout the temporal evolution of the simulation. With the passage of time, turbulent motions caused parcels of fuel and oxidizer to be convected into close proximity while molecular diffusion fed the reaction zones present at the fuel/oxidizer interfaces.

2.2 Modeling method

Conditional moment closure model calculations were made for the same conditions as were present in the simulation. These calculations were made with unit chemical modifying functions r_β (see Eq. 10).

The spatially degenerate CMC and PDF equations corresponding to statistically isotropic conditions with uniform molecular diffusivities are given below,

$$\langle \rho | \eta \rangle \frac{\partial Q_\alpha}{\partial t} = \frac{1}{2} \langle \rho \chi | \eta \rangle \frac{\partial^2 Q_\alpha}{\partial \eta^2} + \langle \rho \dot{w}_\alpha | \eta \rangle \quad (14)$$

$$\frac{\partial}{\partial t} (\langle \rho | \eta \rangle P_\eta) = -\frac{1}{2} \frac{\partial^2}{\partial \eta^2} (\langle \rho \chi | \eta \rangle P_\eta) \quad (15)$$

where the conditional averages are taken over the entire domain and residual terms have been neglected.

The CMC equation (Eq. 5) was solved with the conditional mean scalar dissipation rate profile being given by the PDF equation in the following manner:

$$\langle \rho \chi \mid \eta \rangle = \frac{-2}{P_\eta} \int \int \frac{\partial}{\partial t} (\langle \rho \mid \eta' \rangle P_{\eta'}) d\eta' d\eta' \quad (16)$$

In this study it is possible to use PDF information from the simulation to determine the conditional mean scalar dissipation rate, but in practice this information will not typically be available to the modeler.

The form of the density-weighted PDF, $(\langle \rho \mid \eta \rangle P_\eta / \langle \rho \rangle)$, was assumed to be a Beta function. This assumption reduces the number of degrees of freedom in the PDF to two, namely specification of the conserved scalar mean and variance. The conditional mean density-weighted scalar dissipation rate was calculated using the time history of conserved scalar density-weighted mean and variance from the simulation, and the Beta function assumed form.

Beta functions have the useful characteristic of being able to change in gross shape, according to changes in variance. Thus where the variance is high, a beta function will have singularities at the fully mixed and fully unmixed states. Where the variance is low, the beta function form allows for the possibility of a singularity at only one of the end mixing states (depending on the value of the mean). For very low variance the beta function forms a mono-modal Gaussian-like distribution about the mean.

The effectiveness of the Beta function as an assumed form PDF has been discussed by Girimaji (1991) in relation to passive scalar mixing in isothermal isotropic turbulence.

3. Results

Over the course of the simulation, the Favre averaged mixture fraction unmixedness (see Eq. 13) decreased from near 0.65 down to 0.093. In this same period the simulated mean pressure rose from an initial pressure of one atmosphere to a final value of nearly two atmospheres. Around 56% of the available CO and 42% of the available CH_4 fuel species were consumed during the simulated burn. The total amount of CO_2 mass present increased by 138%, while the total mass of H_2O increased by 155%. Slightly more than 60 ppm of NO (by mass) was produced from an initial zero level over the course of the burn.

The effectiveness of the CMC model in predicting the mean simulated trends can be gauged from Figs. 3 & 4. It is evident that the CMC model consistently overpredicts the mean pressure during the course of the burn to the point where it is in excess by 10% at the end. The model also tends to overpredict NO mass fraction levels, but to a greater degree. The NO mass fraction discrepancy is on the order of 150% towards the end of the burn.

Figure 5 provides a comparison of the simulated and predicted conditional mean temperature profiles at two different stages of the burn. In the figure, the temperature has been normalized by the adiabatic equilibrium temperature of a stoichiometric mixture at one atmosphere (2216 K). At the earlier time, some 0.28

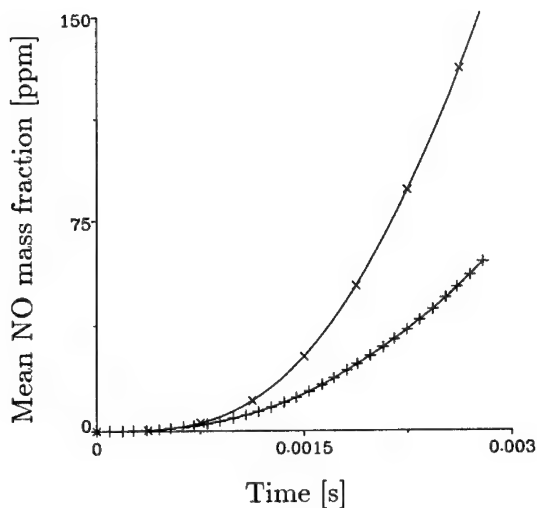


FIGURE 4. Simulated and modeled mean NO mass fraction as a function of time. Symbol key : + - DNS, \times - CMC model

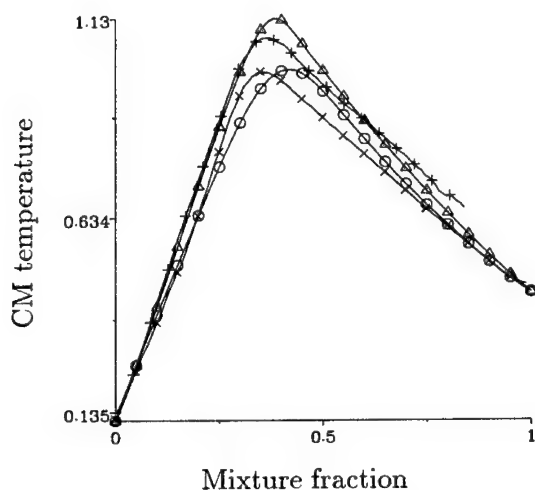


FIGURE 5. Simulated and modeled conditional mean (normalized) temperature as a function of mixture fraction for two different times. Symbol key : \times - DNS at $0.28ms$, + - DNS at $2.0ms$, o - CMC at $0.28ms$, Δ - CMC at $2.0ms$.

milliseconds into the burn, the location of the CMC predicted peak conditional mean temperature is clearly shifted towards the rich side compared to the corresponding simulated profile. At that time, the actual values of the predicted and simulated profiles agree quite closely.

At the later time of 2 milliseconds, the rich shift in the predicted peak temperature location is much less pronounced, but still discernible. The overprediction of the peak temperature by the model at this time is consistent with the level of mean

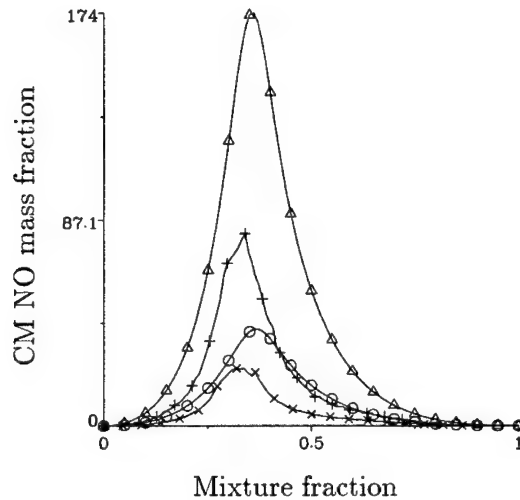


FIGURE 6. Simulated and modeled conditional mean NO mass fraction (ppm) as a function of mixture fraction for two different times. Symbol key : \times - DNS at $1.2ms$, $+$ - DNS at $2.0ms$, o - CMC at $1.2ms$, Δ - CMC at $2.0ms$.

pressure discrepancy seen in Fig. 3.

Simulated and predicted conditional mean NO mass fractions (in parts per million) are plotted for comparison in Fig. 6. The predicted profiles are substantially elevated over the corresponding simulated profiles at all times. The level of overprediction of the peak conditional mean NO mass fraction increases with time, both in relative and absolute terms. It is apparent that at the earlier time, the location of the model's peak mass fraction is shifted compared to the simulation's peak. At the later time, there is no significant shift in location between the modeled and simulated peak mass fractions.

4. Discussion

The results presented above serve to illustrate some of the current difficulties that can face CMC modelers when they seek to apply the model to problems of practical interest.

4.1 Conditional mean scalar dissipation rate

As was mentioned in section 2.2, the practical determination of conditional mean scalar dissipation rate currently relies on the assumption that the actual mixture fraction PDF conforms closely to a convenient assumed form. It is fairly clear that in the instance of isothermal mixing in isotropic turbulence, the usage of a beta function assumed form is most likely adequate (see Girimaji 1991).

However, there is a question as to whether these assumed forms, which are used in isothermal cases, remain accurate when used to embody density-weighted PDFs in cases with variable density.

The difference between the modeled and simulated conditional mean scalar dissipation rate profiles can be determined from Fig. 7. It is clear that the modeled

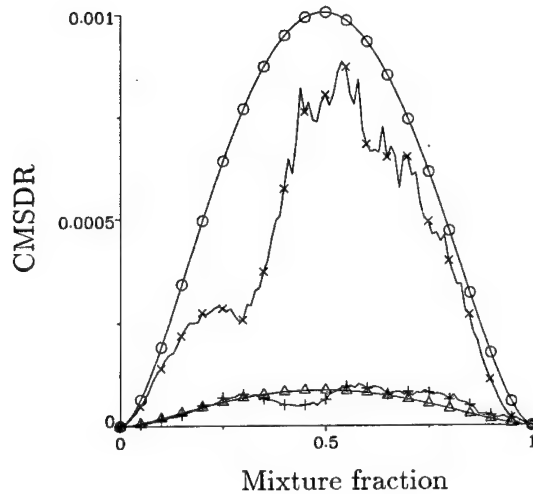


FIGURE 7. Simulated and modeled conditional mean scalar dissipation rate $\langle \chi | \eta \rangle$ as a function of mixture fraction for two different times. Symbol key : \times - DNS at 0.28ms, $+$ - DNS at 2.0ms, o - CMC at 0.28ms, Δ - CMC at 2.0ms.

profiles agree quite well in terms of general magnitude with the simulated profiles, at both time points.

There are however, significant differences in shape between the modeled and predicted profiles that are particularly present at early times in the burn. The modeled profiles invariably tend to approximate inverted parabolas under the range of mixture fraction variance studied here. The simulated profiles tend to have a cleft at or near the location of maximum heat release.

The existence of this departure from a simple parabolic form, is coincident with the type of unexpected lean shift seen in the simulated conditional mean temperature profiles at early times in the burn (see Fig. 5). The presence of a low region in the conditional mean scalar dissipation rate profile on the lean side of the stoichiometric mixture fraction (~ 0.367) would locally minimize the level of temperature depression below chemical equilibrium. The mixture on the rich side of stoichiometric is subject to more intense local mixing and so would tend to exhibit greater temperature depression.

A possible explanation for the asymmetric shape of the simulated conditional mean scalar dissipation rate profiles can be gleaned from a rearrangement of Eq. 15.

$$\langle \rho | \eta \rangle \frac{\partial P_\eta}{\partial t} + P_\eta \frac{\partial}{\partial t} (\langle \rho | \eta \rangle) = -\frac{1}{2} \frac{\partial^2}{\partial \eta^2} (\langle \rho \chi | \eta \rangle P_\eta) \quad (17)$$

Bearing in mind that conditional mean scalar dissipation rate is obtained from this equation through the double integration of both sides, then it would appear that wherever the local change in conditional mean density is particularly rapid, it could have an unusual influence on the form of $\langle \rho \chi | \eta \rangle$.

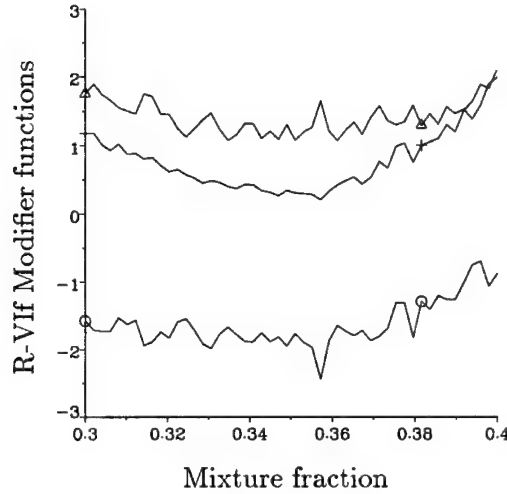


FIGURE 8. Chemical modifier functions for thermal NO formation reaction (R-Vif) determined from DNS data, 2.0ms into the burn. Symbol key : + - r_β , o - B_β grouping, Δ - A_β grouping.

For cases where pressure is assumed to be uniform across all mixture fractions, the conditional mean density is linked inversely to the conditional mean specific thermal energy ($\langle e | \eta \rangle$). An expression for the time rate of change of conditional mean density can be written as,

$$\frac{\partial \langle \rho | \eta \rangle}{\partial t} = \frac{1}{\langle e | \eta \rangle} \left[\int_0^1 P_{\eta'} \langle \dot{s}_e | \eta' \rangle d\eta' - \langle \rho | \eta \rangle \frac{\partial \langle e | \eta \rangle}{\partial t} \right] \quad (18)$$

where $\langle \dot{s}_e | \eta \rangle$ is the conditional mean chemical energy production rate. Both the chemical source term and the entire time rate of change in conditional mean thermal energy are required in any case for the solution of the full set of CMC equations.

It may be possible to employ some kind of assumed form for the *unweighted* mixture fraction PDF (P_η), and use the above pair of equations to determine $\langle \rho \chi | \eta \rangle$. This method is practically difficult since the energy derivative term requires $\langle \rho \chi | \eta \rangle$ in order to be evaluated in the first place, and thus would entail the iterative solution of an integro-differential equation. Furthermore, it is not clear that the unweighted PDF should conform to an easily parameterized assumed form such as the beta function. Such an approach risks inconsistency between the derivative of the arbitrary assumed form PDF and the computed conditional mean density derivative, which may lead to unphysical $\langle \rho \chi | \eta \rangle$ profiles.

4.2 Second order chemical closure

It is evident that the CMC model prediction for the rate of nitric oxide formation greatly exceeds the simulated rate. In part, this is no doubt due to the overprediction of conditional mean temperature by the CMC model. An additional 100 – 200K in peak conditional mean temperature in can double or triple the rate of NO formation via thermal reaction pathways.

It is instructive to also examine the chemical modifier functions r_β , A_β and B_β (see Eqs. 10-12) for the thermal NO formation reaction (R-VIf) as determined from the simulation.

The effect of neglecting second order terms in the conditional mean chemical closure can be determined from Fig. 8. The lower trace corresponds to the A_β grouping of terms, containing the conditional covariances between species and temperature. The upper trace corresponds to the B_β grouping, containing covariances between the reactant species, and the variance of temperature. The middle trace corresponds to the modifier function r_β and is equal to unity plus the sum of the other two traces.

In the reactive section of mixture fraction space around stoichiometric, the modifier function dips below the unit line by as much as $\sim 50\%$. This indicates that simple first order chemical closures, which assume a unit modifier function at all mixture fractions, will overpredict the thermal formation rate of NO by as much as 100% even given the correct conditional mean species and temperature distributions to begin with.

Fortunately, the bulk of the key reactions in typical combustion chemistry do not have as high activation energies as the thermal NO formation step and as such are not so difficult to model.

The prognosis for improved NO prediction by the CMC model is not terribly good. Short of a full second order closure scheme involving the equations for all key species variances and covariances, there is little that can be done. A partial second order closure, tracking just temperature variance or species variances alone, would not succeed since it is clear that the true r_β profile is the small difference between these two large quantities.

5. Conclusions

A study of the effectiveness of the conditional moment closure model in predicting turbulent nonpremixed combustion of methane in air has been undertaken. On the whole, the model has provided quite good agreement with the simulation for all unconditional mean species yields, with the exception of nitric oxide.

Predicted conditional mean species mass fractions and temperature were found to differ more significantly from the simulation due to small differences in the density-weighted PDF and its temporal evolution.

Large discrepancies were found in the case of nitric oxide, where higher temperatures in the model calculations and a natural tendency of the first order chemical closure to overpredict NO formation were cited as contributing factors.

Wherever practicable, future CMC model applications that seek to accurately predict NO formation should include some form of partial second order chemical closure. This should involve temperature, and the nitrogen and oxygen bearing reactant species. This is particularly desirable in combusting systems where instantaneous deviations from conditional means are expected to be large.

REFERENCES

- BILGER, R. W. 1993 Conditional Moment Methods for Turbulent Reacting Flow. *Phys. Fluids*, **5**, 436-444.
- FROLOV, S. M. 1996 Private communication.
- FROLOV, S. M., SMITH, N. S. A., BOWMAN, C. T. 1996 Evaluation of joint probability density function models for turbulent nonpremixed combustion with complex chemistry. *Proceedings of the 1996 Summer Program*, CTR, NASA Ames/Stanford Univ., 167-186.
- GIRIMAJI, S. S. 1991 Assumed Beta-pdf Model for Turbulent Mixing: Validation and Extension to Multiple Scalar Mixing. *Combust. Sci. Tech.* **78**, 177-196.
- KLIMENKO, A. YU. 1990 Multicomponent Diffusion of Various Admixtures in Turbulent Flow. *Fluid Dynamics*, **25**, 327-334.
- LELE, S. 1992 Compact finite difference schemes with spectral-like resolution. *J. Comp. Phys.* **103**, 16.
- LI, J. D., BILGER, R. W. 1993 Measurement and Predictions of the Conditional Variance in a Turbulent Reactive-Scalar Mixing Layer. *Phys. Fluids*, **5**, 3255-3264.
- MELL, W. E., NILSEN, V., KOSALY, G., RILEY, J. J. 1993 Direct Numerical Simulation Investigation of the Conditional Moment Closure Model for Nonpremixed Turbulent Reacting Flows. *Combust. Sci. Tech.*, **91**, 179-186.
- MELL, W., KOSALY, G., RILEY, J. J. 1994 An Investigation of Closure Models for Nonpremixed Turbulent Reacting Flows. *Phys. Fluids*, **6**, 1331-1356.
- PETERS, N. 1984 Laminar diffusion flamelet models in nonpremixed turbulent combustion. *Prog. Energy Comb. Sci.*, **10**, 319-339.
- POINSOT, T., LELE, S. 1992 Boundary conditions for direct simulations of compressible viscous flows. *J. Comp. Phys.*, **101**, 104.
- POPE, S. B. 1985 PDF Methods for Turbulent Flows. *Prog. Energy Combust. Sci.*, **11**, 119-192.
- RUETSCH, G. R., & BROADWELL, J. E. 1995 Effects of confinement on partially premixed flames. *Annual Research Briefs - 1995*, CTR, NASA Ames/Stanford Univ., 323-333.
- SMITH, N. S. A. 1994 *Development of the Conditional Moment Closure Method for Modelling Turbulent Combustion*. PhD Thesis, University of Sydney.
- SMITH, N. S. A. 1995 Modeling complex chemical effects in turbulent nonpremixed combustion. *Annual Research Briefs - 1995*, CTR, NASA Ames/Stanford Univ., 301-321.
- SMITH, N. S. A., BILGER R. W., CARTER C. D., BARLOW R. S., CHEN, J.-Y. 1995 A Comparison of CMC and PDF Modelling Predictions with Experimental Nitric Oxide LIF/Raman Measurements in a Turbulent H_2 Jet Flame. *Combust. Sci. Tech.*, **105**, 357-375.

Dynamic models for LES of turbulent front propagation with a spectral method

By H. G. Im¹, T. S. Lund, AND J. H. Ferziger

1. Motivation and objectives

Direct numerical simulation of turbulent reacting flows places extreme demands on computational resources. At the present time, simulations can be performed only for greatly simplified reaction systems and for very low Reynolds numbers. Direct simulation of more realistic cases occurring at higher Reynolds number and including multiple species and numerous chemical reactions will exceed available computational resources far into the future. Because of this, there is a clear need to develop the technique of large eddy simulation for reacting flows. Unfortunately this task is complicated by the fact that combustion arises from chemical reactions that occur at the smallest scales of the flow. Capturing the large-scale behavior without resolving the small-scale details is extremely difficult in combustion problems. Thus LES modeling for turbulent combustion encounters difficulties not present in modeling momentum transport, in which the main effect of the small scales is to provide dissipation. The difficulty is more pronounced in premixed combustion, where detailed chemistry plays an essential role in determining the flame speed (or overall burning rate); in nonpremixed combustion infinite rate chemistry can be assumed, eliminating the small scale features to a first approximation.

One of the practically relevant and better understood types of turbulent premixed combustion is the laminar flamelet regime, in which the characteristic chemical time is much shorter than the characteristic flow time (Liñán & Williams 1993). Under this condition, combustion can be represented in terms of the propagation of laminar flamelets corrugated by turbulent eddies. It has been suggested (Kerstein *et al.* 1988) that such a propagating front may be captured by defining the front as a level contour of a continuous function G , whose governing equation is

$$\frac{\partial G}{\partial t} + u_j \frac{\partial G}{\partial x_j} = S_L |\nabla G|. \quad (1)$$

In this equation, all information about the flame structure is carried by the flame speed S_L . This provides a convenient opening for large eddy simulation; the flame structure need not be modeled. Since the flame retains its laminar structure, explicit expressions for S_L as a function of the flow variables may be taken from asymptotic studies (e.g., Clavin 1985) or computations.

In LES, only *filtered* flame fronts are resolved. These fronts can be viewed as flame brushes that propagate at a speed, \bar{S} , higher than the laminar flame speed.

¹ Present address: Sandia National Laboratories

The problem is closed if one can provide an explicit expression for \bar{S} as a function of available quantities. Several previous studies have attempted to derive relationships between \bar{S} and the turbulence intensity u' (Clavin & Williams 1979, Yakhot 1988a, Kerstein and Ashurst 1992, Pocheau 1992). However, the existing theoretical and empirical results for $\bar{S}(u')$ do not agree with one another, so the functional form of $\bar{S}(u')$ remains an open question. Even if the question is resolved, there will be a constant or function to be determined.

In this study, we present an attempt at LES using a dynamic subgrid-scale model that has been successfully applied to a variety of turbulent flows (Germano *et al.* 1991). The basic formulation was derived earlier (Im 1995), but the model is modified to incorporate the effect of subgrid transport. In contrast to previous LES approaches for the G -equation (Menon *et al.* 1993), the model constants are computed dynamically as a part of the calculation procedure rather than being prescribed. Dynamic modeling for turbulent flow has been shown to exhibit correct behavior, for example, in the near-wall region of boundary layers, without the need for additional modification. The LES models for the G -equation suggested in this study have these features, allowing the possibility of application to practical combustion systems.

2. Accomplishments

2.1 Some remarks on the G -equation

Before we proceed with LES modeling, some numerical issues related to the G -equation should be pointed out. If one wishes to solve Eq. (1) in the Huygens' limit, i.e. $S_L = S_L^\circ$, numerical difficulties arise due to the formation of cusps as the front propagates. Cusps are a natural consequence of the Huygens' process in much the same way as shocks are a characteristic feature of Burger's equation. To overcome the numerical difficulty associated with cusps, previous studies introduced various types of diffusive terms (e.g. Kerstein *et al.* 1988). These terms are not entirely *ad hoc*, however; they can be shown to represent the effect of thermal relaxation under transverse heat diffusion in the preheat zone of a wrinkled front (Clavin 1985). Using the asymptotic relation for S_L , Eq. (1) can be written as

$$\frac{\partial G}{\partial t} + u_j \frac{\partial G}{\partial x_j} = S_L^\circ |\nabla G| + \mathcal{D} \nabla^2 G, \quad (2)$$

where only the leading term has been kept; this is a reasonable approximation provided the flame thickness is sufficiently smaller than the hydrodynamic scale. In the above relation, $\mathcal{D} = S_L^\circ \mathcal{L}$ is the Markstein diffusivity, where the Markstein length, \mathcal{L} , is typically normalized by the flame thickness ℓ_F . Since

$$\ell_F = \alpha / S_L^\circ = (1/S_L^\circ)(\nu/Pr),$$

we find

$$\mathcal{D} = (\nu/Pr)Ma$$

where ν is the molecular viscosity, Pr the Prandtl number, and $Ma = \mathcal{L}/\ell_F$ the Markstein number, which is $O(1)$ in practical flames (Searby & Quinard 1990).

We attempt to solve Eq. (2) with a given value of \mathcal{D} ; the results depend on this parameter. Numerical realization of the Huygens' limit (i.e. $\mathcal{D} \rightarrow 0$) is extremely difficult, if not impossible. Our numerical simulations of the passive G -equation in isotropic turbulence revealed that the overall flame speed depends significantly on the size of the diffusion term in the G -equation. This is not surprising; it demonstrates that one must be careful about choosing this term, especially when comparing the flame speed with experiments. Accurate estimation of the Markstein number is mandatory for such comparisons.

Due to the lack of experimental results, in this study LES models are validated by comparing with DNS results based on Eq. (2) with 64^3 resolution. Most of the LES are performed in 32^3 resolution using the filtered DNS fields as initial conditions.

2.2 Subgrid-scale models for the G -equation

We now describe the dynamic subgrid-scale models for the passive G -equation. As in turbulence, we assume scale invariance of the G -equation in the inertial range of turbulence, which has been shown to exist by Yakhot (1988b) and Pocheau (1992). We define the grid filter \bar{G} and the test filter \hat{G} respectively as

$$\bar{f}(\mathbf{x}) = \int f(\mathbf{x}') \bar{G}(\mathbf{x}, \mathbf{x}') d\mathbf{x}', \quad \hat{f}(\mathbf{x}) = \int f(\mathbf{x}') \hat{G}(\mathbf{x}, \mathbf{x}') d\mathbf{x}',$$

where the width of the test filter, $\hat{\Delta}$, is larger than that of the grid filter, Δ . Applying the grid filter to Eq. (2), we obtain

$$\frac{\partial \bar{G}}{\partial t} + \frac{\partial}{\partial x_j} (\bar{u}_j \bar{G}) = -\frac{\partial}{\partial x_j} (\overline{u_j G} - \bar{u}_j \bar{G}) + S_L^0 |\nabla \bar{G}| + \mathcal{D} \frac{\partial^2 \bar{G}}{\partial x_j^2}. \quad (3)$$

Here both the subgrid scalar flux $\overline{u_j G} - \bar{u}_j \bar{G}$ and the filtered modulus term $|\nabla \bar{G}|$ need to be modeled. In the previous study (Im 1995), these two terms were modeled by a single *filtered* propagation term, $\bar{S} |\nabla \bar{G}|$. This model, however, suffered from numerical instability since no subgrid dissipation was provided. In this study, the subgrid flux term is modeled by an eddy diffusivity model analogous to the Smagorinsky model, i.e.:

$$\gamma_k = \overline{u_k G} - \bar{u}_k \bar{G} = -\alpha_t \frac{\partial \bar{G}}{\partial x_k}, \quad \alpha_t = C_G \Delta^2 |\bar{\Sigma}|, \quad (4)$$

where $|\bar{\Sigma}|$ is the magnitude of the strain rate tensor:

$$|\bar{\Sigma}| = (2\bar{\Sigma}_{ij}\bar{\Sigma}_{ij})^{1/2}, \quad \bar{\Sigma}_{ij} = \frac{1}{2} \left(\frac{\partial \bar{u}_i}{\partial x_j} + \frac{\partial \bar{u}_j}{\partial x_i} \right). \quad (5)$$

Similarly, at the test filter level, we obtain

$$\Gamma_k = \widehat{\overline{u_k G}} - \hat{u}_k \hat{G} = -\hat{\alpha}_t \frac{\partial \hat{G}}{\partial x_k}, \quad \hat{\alpha}_t = C_G \hat{\Delta}^2 |\hat{\Sigma}|. \quad (6)$$

and a generalization of Germano's identity

$$\mathcal{F}_k = \Gamma_k - \hat{\gamma}_k = \widehat{\bar{u}_k \tilde{G}} - \hat{\bar{u}}_k \tilde{G} \quad (7)$$

can be used to determine the constant C_G . Using Eqs. (4), (6), and (7) with the least-square contraction (Lilly 1992), we obtain

$$C_G \Delta^2 = -\frac{\mathcal{F}_i \mathcal{H}_i}{\mathcal{H}_j \mathcal{H}_j}, \quad (8)$$

where

$$\mathcal{H}_k = (\hat{\Delta}/\Delta)^2 |\hat{\Sigma}| \frac{\partial \hat{\tilde{G}}}{\partial x_k} - |\hat{\Sigma}| \frac{\partial \tilde{G}}{\partial x_k}. \quad (9)$$

Next we consider the modeling of the propagation term, $S_L^\circ |\nabla G|$. This requires a special treatment as it contains a nonlinear modulus. We adopt the following model

$$S_L^\circ |\nabla G| = \bar{S} |\nabla \tilde{G}|. \quad (10)$$

The effective flame speed, \bar{S} , can be related to the laminar flame speed by requiring that the filtered equations maintain the correct overall burning rate. This constraint gives rise to the notion of representing the "filtered propagation term" as "propagation of the filtered front at higher speed", and may be characterized by writing

$$S_L^\circ A_L = \bar{S} \bar{A}, \quad (11)$$

where A_L is the laminar flame area that would be computed in a direct simulation, and \bar{A} is the area of the filtered flame front. For incompressible isotropic turbulence, the flame area can be readily computed as (Kerstein *et al.* 1988)

$$A_L = \langle |\nabla G| \rangle, \quad \bar{A} = \langle |\nabla \tilde{G}| \rangle, \quad (12)$$

where the bracket denotes the volume average. Furthermore, it is necessary to determine \bar{S} as a function of turbulence intensity. Theoretical studies suggest the functional form

$$\bar{S}/S_L^\circ = 1 + C_S (q/S_L^\circ)^p \quad (13)$$

where $q = [(u_i - \bar{u}_i)(u_i - \bar{u}_i)]^{1/2}$ is the square-root of the subgrid kinetic energy in the filter volume. Previous studies (Clavin & Williams 1979, Pocheau 1992) show that quadratic ($p = 2$) and linear ($p = 1$) behaviors are expected in the weak and strong turbulence limits, respectively. In the next section, this functional relation will be examined using an *a priori* test based on DNS data.

Given the value of p , the constant C_S can be determined by a dynamic procedure. Combining (11), (12), (13) and applying the same model to the test-filtered quantities, we obtain

$$\frac{\bar{S}}{S_L^\circ} = \frac{A_L}{\bar{A}} = \frac{\langle |\nabla G| \rangle}{\langle |\nabla \tilde{G}| \rangle} = \left\langle 1 + C_S \left(\frac{q}{S_L^\circ} \right)^p \right\rangle, \quad (14)$$

$$\frac{\hat{S}}{S_L^\circ} = \frac{A_L}{\hat{A}} = \frac{\langle |\nabla G| \rangle}{\langle |\nabla \hat{G}| \rangle} = \left\langle 1 + C_S \left(\frac{Q}{S_L^\circ} \right)^p \right\rangle, \quad (15)$$

where $Q = [(u_i - \hat{u}_i)(u_i - \hat{u}_i)]^{1/2}$ is the square-root of the subgrid kinetic energy associated with the test filter. It is readily seen that there are two unknowns, $\langle |\nabla G| \rangle$ and C_S , and two equations, provided the subgrid kinetic energies, q and Q , are available. This requires an additional model for the subgrid kinetic energy as a function of the large-scale quantities. As will be seen later, unlike the case of Smagorinsky's model, the model for the subgrid kinetic energy is crucial to accurate prediction of the flame speed. We shall consider the following three models:

1. $q \sim \Delta |\bar{S}|$, deduced from dimensional reasoning similar to that used in Smagorinsky's model. Since \bar{S} can be computed, this model is applicable with any numerical method. Unfortunately, this model overpredicts the turbulent flame speed when the turbulence is not in the inertial subrange, as will be shown later.
2. Spectral curve fit, which can be used with spectral methods. The turbulence energy spectrum is described by an algebraic power relation

$$E(k) = C_k k^{-m}, \quad (16)$$

or an exponential

$$E(k) = C_k \exp(-mk). \quad (17)$$

The two unknowns C_k and m can be determined from $E(\bar{k})$ and $E(\hat{k})$. The subgrid kinetic energy can then be computed as

$$q(\bar{k}) = \int_{\bar{k}}^{\infty} E(k) dk. \quad (18)$$

3. Since the spectral curve fit has limited application, we suggest another model similar to that of Bardina *et al.* (1983). We define a new filter with size $\tilde{\Delta}$, where $\Delta < \tilde{\Delta} < \hat{\Delta}$. Then the subgrid kinetic energies are estimated by

$$q^2 = \bar{u}_i \bar{u}_i - \tilde{u}_i \tilde{u}_i, \quad (19)$$

and

$$Q^2 = \hat{u}_i \hat{u}_i - \tilde{u}_i \tilde{u}_i, \quad (20)$$

where $\tilde{\Delta}/\Delta = \hat{\Delta}/\tilde{\Delta} = 1.4 \approx \sqrt{2}$ are used in the present calculation.

In the following section, *a priori* tests are performed by applying these models (referred to as Models 1, 2, and 3) for the propagation term, combined with the Smagorinsky-type subgrid transport model.

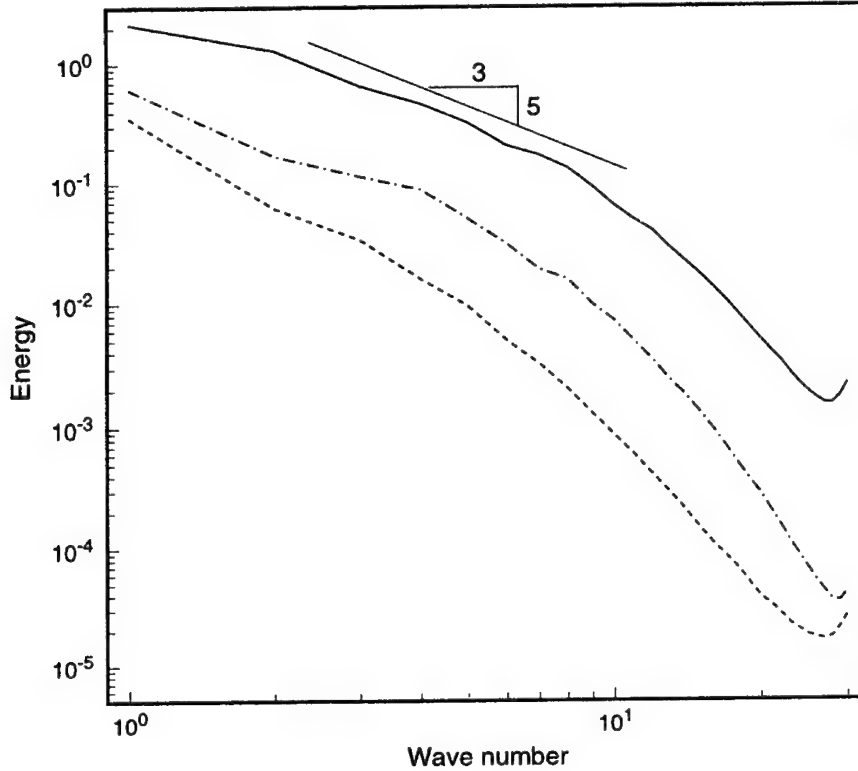


FIGURE 1. Energy spectra obtained from the DNS, 3.6 large-eddy turnover times after the g -field was initialized. Turbulence energy: — ; scalar energy ($g'^2/2$) for $u'/S_L^o = 0.5$: ---- ; energy in g fluctuations for $u'/S_L^o = 2$: -.-.

2.3 *A priori tests of the models*

The subgrid models proposed in §2.2 are tested by post-processing DNS results. We performed DNS based on Eq. (2) with incompressible homogeneous isotropic turbulence. The turbulence is forced at the lowest wavenumbers in order to hold the total kinetic energy approximately constant. The numerical method is pseudo-spectral in space with second order Runge-Kutta time integration (Rogallo 1981). A developed flow field is used as the initial condition and the G -field is initialized as a linear function $G = x$. To make the G -field homogeneous, we define $g = G - x$ and solve for g . Following initialization of the g field, the simulation is run for 3.6 large-scale eddy turn over times, at which point the g field is fully-developed. The Reynolds number based on Taylor microscale is about 75 and $Ma/Pr = 4$, so $D = 4\nu$. Two cases were computed; $u'/S_L^o = 0.5$ and 2, which was accomplished by adjusting S_L^o for the same turbulence field.

Figure 1 shows the DNS results for the turbulence and scalar energy (g'^2) spectra for both values of u'/S_L^o . The slope $-5/3$ is also shown. It is seen that the turbulence spectrum has a slope $-5/3$ over a limited range of k due to the low Reynolds number

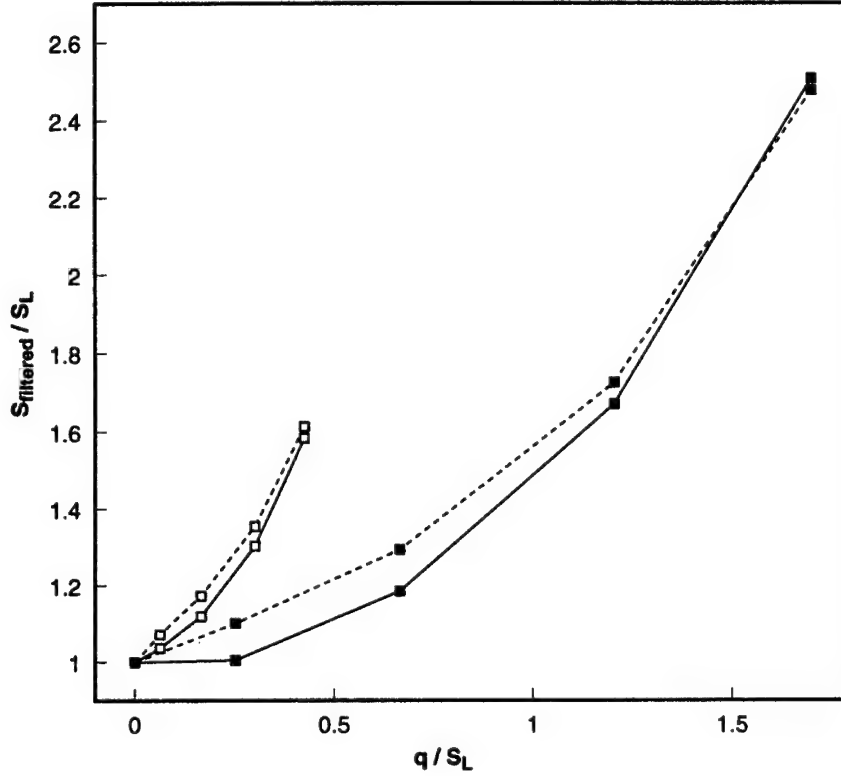


FIGURE 2. Enhanced filtered flame speed \bar{S}/S_L° vs. normalized subgrid kinetic energy q/S_L° . Cutoff filter: —; Gaussian filter: ----; $u'/S_L^\circ = 0.5$: \square ; $u'/S_L^\circ = 2$: \blacksquare .

of the flow.

Since the Smagorinsky-type transport model has been established in previous LES studies, the main emphasis in this work is on the modeling of the propagation term. We first examine the functional relation of \bar{S}/S_L° and q/S_L° . These quantities are computed from the DNS spectrum by using

$$q = \int_{\bar{k}}^{\infty} 2E(k)dk, \quad (20)$$

$$\bar{S}/S_L^\circ = \langle |\nabla \bar{G}| \rangle / \langle |\nabla \bar{G}| \rangle. \quad (21)$$

To obtain the filtered field \bar{G} , we use (a) the cutoff filter in the Fourier space, and (b) the Gaussian filter $\mathcal{G}(k) = \exp(-k^2\Delta/24)$. Although the cutoff filter is more relevant with the spectral method, the Gaussian filter is more practical with finite difference techniques.

Figure 2 shows \bar{S}/S_L° as a function of q/S_L° for various filter sizes; increased abscissa corresponds to increased filter size. It is seen that while the Gaussian filter

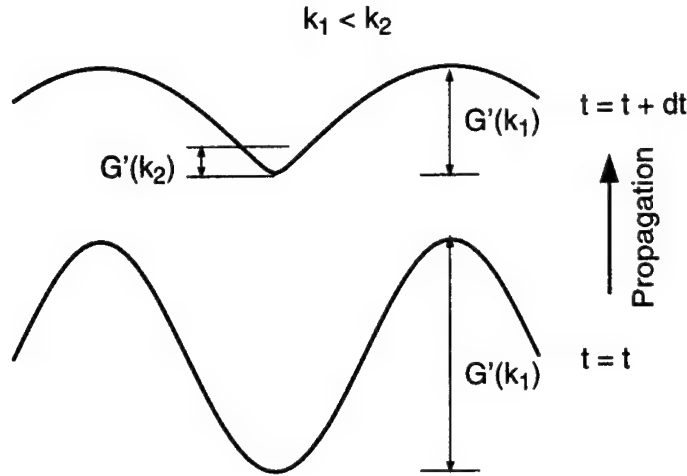


FIGURE 3. Schematic showing the mechanism of kinematic restoration by the flame propagation.

gives approximately linear behavior at very small q/S_L° , with the cutoff filter the increase in \bar{S}/S_L° is much less significant and the curves exhibit quadratic behavior from the start. This observation is in contrast to an earlier result that showed linear behavior (Bourlioux *et al.* 1996). Incidentally, the quadratic behavior is consistent with a theoretical prediction of Clavin & Williams (1979) for weak turbulence.

It is noted that the nonlinear behavior shown in Fig. 2 is more prominent in the stronger turbulence case, $u'/S_L^\circ = 2$. The reason can be found from Fig. 1; for stronger turbulence ($u'/S_L^\circ = 2$) the fluctuations in the G -function are controlled more by the turbulence than by the propagation and there is more scalar energy at low wavenumbers. Physically, as shown schematically in Fig. 3, propagation diminishes front corrugation, which is called “kinematic restoration” by Peters (1992), while small-scale wrinkles are formed at the trough, which will lead to cusp formation in the Huygens’ limit. Therefore, one effect of propagation is to transfer energy from low to high wave-numbers. Consequently, the higher u'/S_L° , i.e. the less significant the propagation, the more the nonlinearity in Fig. 2, because less energy is present at high wavenumbers. Since the cutoff filter is used in the present spectral calculation, we choose $p = 2$ for most of our calculations.

Next we use the DNS data to check the accuracy of the model for the effective propagation defined in section 2.2. To do this, the 64^3 DNS field is used to compute the actual flame speed, taken as the volume average of $|\nabla G|$. Then the DNS field is filtered to 32^3 by truncating the high wavenumbers. This cutoff-filtered field is then used to compute the filtered flame speed, which is the target for the model.

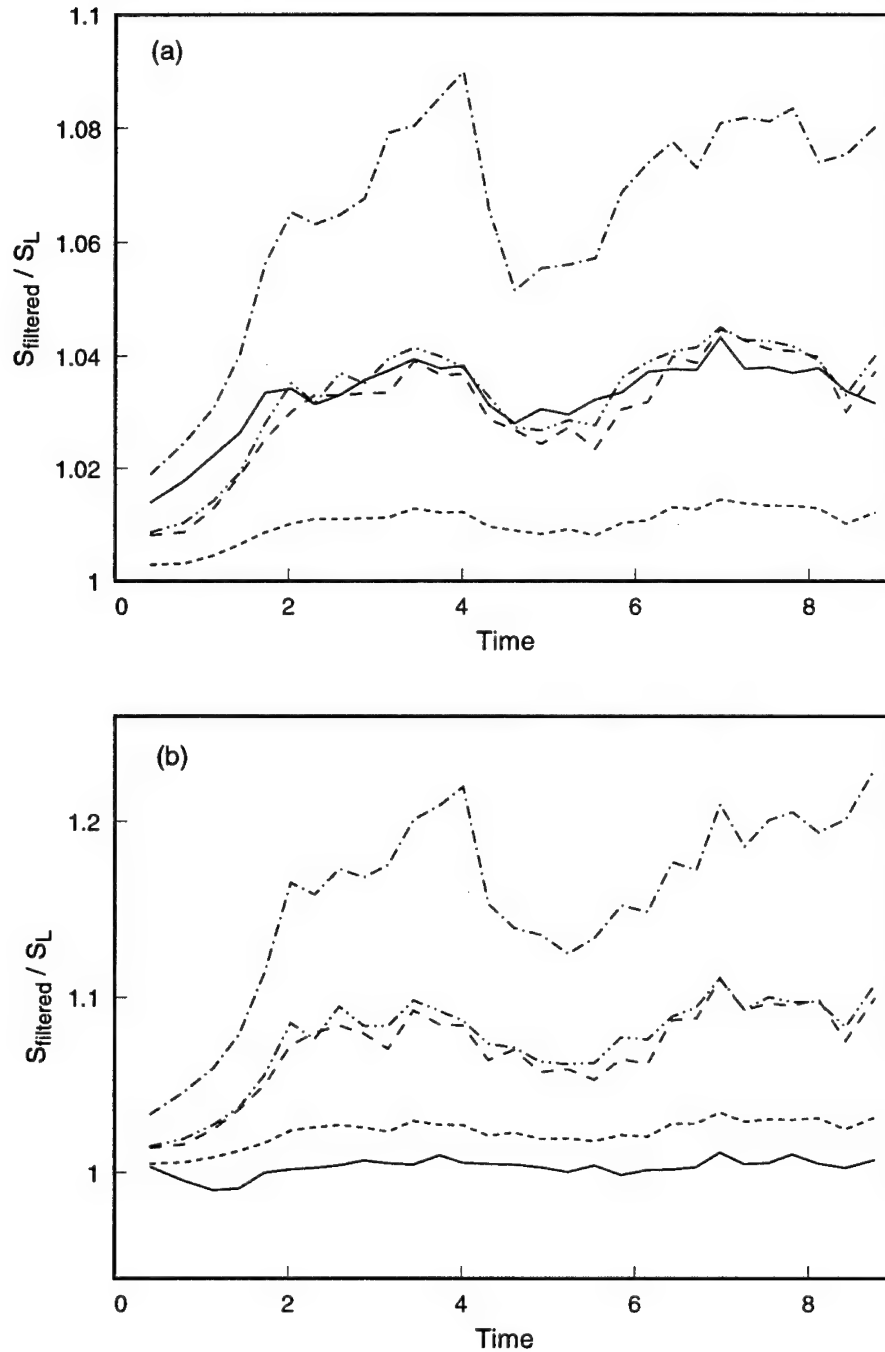


FIGURE 4. *A priori* tests of the filtered flame speed \bar{S} for various models; (a) $u'/S_L^o = 0.5$, (b) $u'/S_L^o = 2$. Direct DNS result: —; Model 1: ---; Model 2 with the power law: - - -; Model 2 with the exponential law: - · - ·; Model 3: · · ·.

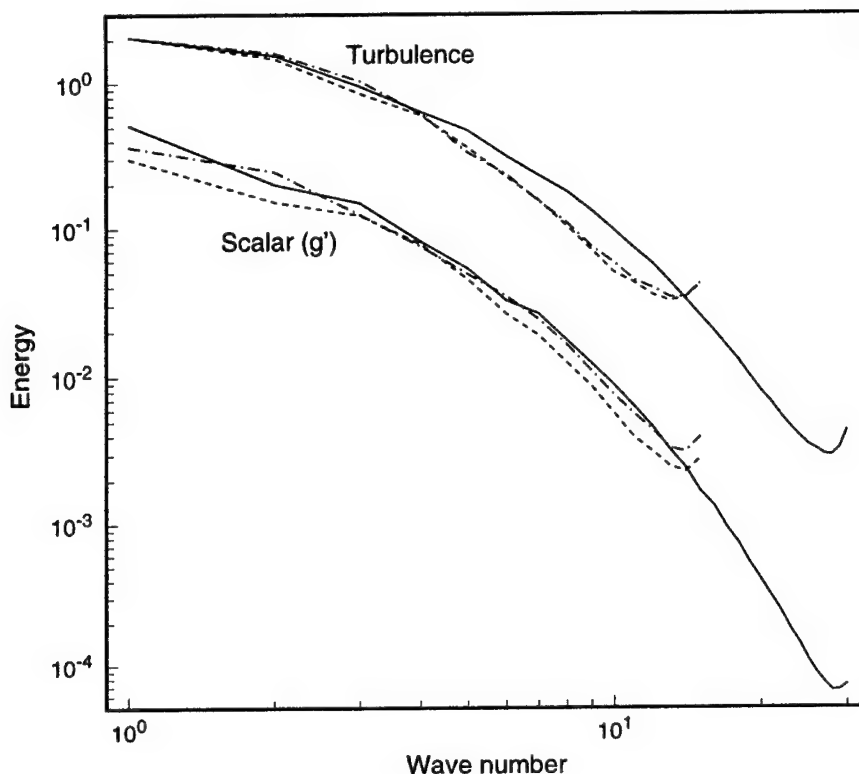


FIGURE 5. Comparison of energy spectra obtained from DNS and various LES models for $u'/S_L^\circ = 2$ at 3.6 eddy turnover time after the g -field was initialized; DNS: —; LES with Model 1: ---; LES with Model 2 with the exponential law: -.-.

Using only the filtered information, Eqs. (14) and (15) are solved for \bar{S}/S_L , for each of the three models for the subgrid kinetic energy. In order to test the validity of Eq. (15), a second “test filtering” of the DNS data is made by truncating to 16^3 modes. Finally the procedure is repeated at each time step in the DNS from the initialization of the g field to the end of the run, 3.6 large-scale turnover times later.

Figures 4(a) and (b) show \bar{S}/S_L° computed from various subgrid kinetic energy models at various times during the DNS, for $u'/S_L^\circ = 0.5$ and 2, respectively. A quadratic functional relation ($p = 2$) was assumed. In both cases, it is clear that Model 1 overpredicts the filtered flame speed. This may be due to the low Reynolds number of this flow. For $u'/S_L^\circ = 0.5$, both model 2 with the power law and model 3 give good results. On the other hand, for $u'/S_L^\circ = 2$, for which less energy is contained in the subgrid scales, the actual \bar{S}/S_L° is much smaller than that predicted by Model 2 with the power law and Model 3, but Model 2 with the exponential law gives better agreement. These results indicate that the prediction of turbulent flame speed using LES of the G -equation depends strongly on accurate estimation of subgrid turbulent kinetic energy.

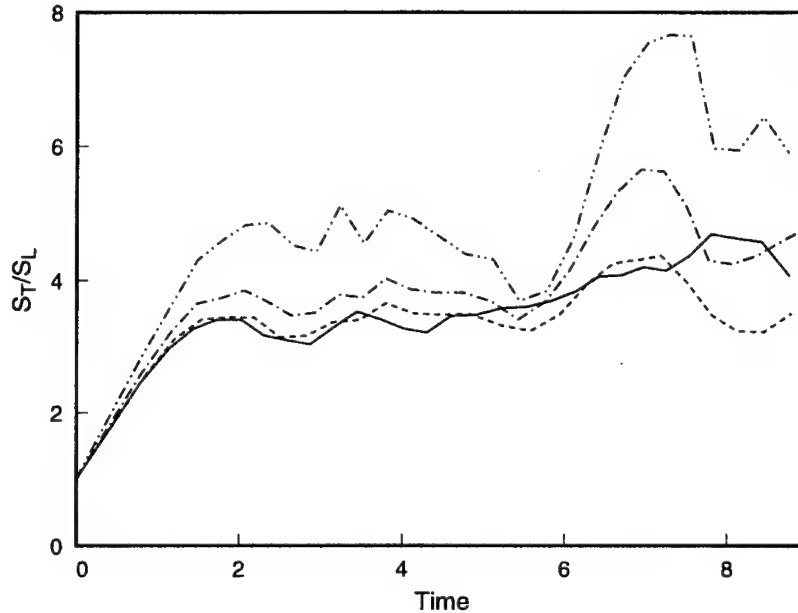


FIGURE 6. Volume averaged turbulent flame speed as a function of time, for $u'/S_L^0 = 2$; DNS: — ; LES with Model 1, $p = 1$: - - - ; LES with Model 1, $p = 2$: - · - · ; LES with Model 2, exponential law and $p = 2$: - · - · . Time is scaled by 0.4 large-scale eddy turnover times.

2.4 Results of LES runs

We now present results of actual LES using the suggested dynamic models; this is sometimes called *a posteriori* testing. The initial flow field of the DNS is truncated to 32^3 resolution and used as the initial field for \bar{u} , and $\bar{G} = x$ initially.

Figure 5 shows the turbulence and scalar energy spectra of DNS and various LES results at a time 3 large-scale eddy turnover times after initialization of the g field. Two subgrid kinetic energy models are tested: Model 1 (a poor model) and the exponential fit version of Model 2 (the best model). The LES energy spectrum is in fair agreement with the DNS, although it appears that the subgrid-scale model is slightly over-dissipative. The scalar energies of both LES cases agree fairly well with the DNS, while the energy of Model 1 is higher than the exponential spectral fit model, as might be expected from Fig. 4.

Finally, the volume-averaged turbulent flame speed, represented by $\bar{S}(|\nabla \bar{G}|)$, is plotted as a function of time in Fig. 6. Results from the DNS are plotted as the solid line. To illustrate the effects of the improvements in the model, results for Model 1 with $p = 1$ are also shown. This simple model may overpredict the turbulent front speed by as much as a factor of two; significant improvement is obtained by merely switching to the quadratic relation ($p = 2$). Model 2 with the exponential curve fit gives the best result in this case since the scalar spectrum falls more rapidly with wavenumber for stronger turbulence.

3. Conclusions and future work

Dynamic models for LES of the G -equation of turbulent premixed combustion have been proposed and tested. Several such models were tested in forced homogeneous isotropic turbulence. The results indicate that, unlike the case for Smagorinsky's model applied to the momentum equation, the estimate of the subgrid kinetic energy is crucial to accurate prediction of turbulent flame speed. For the cases studied here, the extended Smagorinsky model overpredicts the flame speed. Furthermore, \bar{S}/S_L° is not necessarily a linear function of q/S_L° ; quadratic dependence seems to fit the results more accurately.

From the differences between the cases with $u'/S_L^\circ = .5$ and 2, it appears that the inability to fit \bar{S}/S_L° as a function of q/S_L° with a fixed value of p is mainly due to the non-similarity between the turbulence and scalar energy spectra in Fig. 1. A modification is proposed to improve the model; one can free the exponent p and use the dynamic procedure to determine it. This requires two levels of test-filters and complicates the numerical procedure.

Finally, we remark that although in the present work G is treated as a passive scalar, the concept can be extended to include heat release. The challenge is a numerical issue of how to capture discontinuities across highly corrugated flames while resolving the small-scale turbulence. Methods designed to resolve this issue have been proposed (Klein 1995, Bourlioux et al. 1996), but further work is still needed.

Acknowledgments

The authors would like to thank Prof. A. Bourlioux at CERCA, Université de Montréal for the stimulating discussions during the CTR Summer Program in 1996, and Drs. G. R. Ruetsch and N. S. A. Smith for helpful comments.

REFERENCES

- BARDINA, J., FERZIGER, J. H. & REYNOLDS, W. C. 1983 Improved subgrid-scale models based on large eddy simulation of homogeneous, incompressible, turbulent flows. *Report TF-19* Dept. Mech. Eng., Stanford University, Stanford, CA.
- BOURLIOUX, A., KLEIN, R. & MOSER, V. 1996 A dynamic subgrid scale model for turbulent premixed flames. *Technical report, CERCA, Montreal*.
- BOURLIOUX, A., IM, H. G. AND FERZIGER, J. H. 1996 A dynamic subgrid-scale model for LES of the G -equation, *Proceedings of the 1996 Summer Program*. Center for Turbulence Research, NASA Ames/Stanford Univ., 137-148.
- CLAVIN, P. 1985 Dynamic behavior of premixed flame fronts in laminar and turbulent flows. *Prog. Energy Combust. Sci.* **11**, 1.
- CLAVIN, P. & WILLIAMS, F. A. 1979 Theory of premixed-flame propagation in large-scale turbulence. *J. Fluid Mech.* **90**, 589.

- GERMANO, M., PIOMELLI, U., MOIN, P. & CABOT, W. H. 1991 A dynamic subgrid-scale eddy viscosity model. *Phys. Fluids A*, **3**, 1760.
- IM, H. G. 1995 Study of turbulent premixed flame propagation using a laminar flamelet model. *Annual Research Briefs*, Center for Turbulence Research, NASA Ames/Stanford Univ., 347-358.
- KERSTEIN, A. R. & ASHURST, WM. T. 1992 Propagation rate of growing interfaces in stirred fluids. *Phys. Rev. Lett.* **68**, 934.
- KERSTEIN, A. R., ASHURST, WM. T., & WILLIAMS, F. A. 1988 Field equation for interface propagation in an unsteady homogeneous flow field. *Phys. Rev. A*, **37**, 2728.
- KLEIN, R. 1995 The level set approach to premixed turbulent combustion in the flamelet regime: theory and numerical implementation. *Lecture Notes, Euroconference on Premixed Combustion, Aachen*.
- LILLY, D. K. 1992 A proposed modification of the Germano subgrid-scale closure method. *Phys. Fluids A*, **4**, 633.
- LIÑÁN, A. & WILLIAMS, F. A. 1993 *Fundamental Aspects of Combustion*, Oxford University Press.
- MENON, S. AND KERSTEIN, A. R. 1992 Stochastic simulation of the structure and propagation rate of turbulent premixed flames. *24th Symp. (Int'l) on Combustion*, The Combustion Institute, 443-450.
- PETERS, N. 1992 A spectral closure for premixed turbulent combustion in the flamelet regime. *J. Fluid Mech.* **242**, 611.
- POCHEAU, A. 1992 Front propagation in a turbulent medium. *Europhysics Letters*, **20**, 401.
- ROGALLO, R. 1981 Numerical experiments in homogeneous turbulence, *NASA Tech. Memo.*, TM81315.
- SEARBY, G. & QUINARD, J. 1990 Direct and indirect measurements of Markstein numbers of premixed flames. *Comb. Flame.* **82**, 298.
- YAKHOT, V. 1988a Propagation velocity of premixed turbulent flames. *Comb. Sci. Tech.* **60**, 191.
- YAKHOT, V. 1988b Scale invariant solutions of the theory of thin turbulent flame propagation. *Comb. Sci. Tech.* **62**, 127.

Jet noise using large eddy simulation

By F. Bastin

1. Motivation and objectives

With the advent of high-supersonic transport aircraft, supersonic jet noise becomes a major technological problem and there is a strong need for a reliable prediction approach. Our present interest is the *mixing noise* component induced by the turbulent flow itself. The physics of *shock-associated noise* is very different and must be treated in another context (see Tam 1995).

Traditional jet mixing noise predictions are based on a *steady* statistical description of the turbulent flow, which may be obtained using analytical models as in Ribner (1969) or more recently in Béchara *et al.* (1995) from a steady Reynolds averaged computation (RANS). Some interesting aspects of the problem can be predicted, such as the decrease of the acoustic emission for a coaxial jet, but this approach provides little insight about the nature of the acoustic sources and necessarily relies on strong modeling assumptions which limit its generality.

A more difficult but promising method consists in directly using the history of the turbulent fluctuations obtained from a numerical simulation. The task is not trivial since the constraint of capturing the wide range of acoustic space and time scales adds to the already complex problem of a turbulent flow computation. Depending on the method chosen to obtain the acoustic radiation, it may be necessary to also represent a weak amplitude acoustic near-field very sensitive to dissipation and dispersion errors. This is why this difficult problem has been tackled progressively at both ends of the Reynolds number range. At Stanford a sequence of projects of increasing complexity led Mitchell, Lele & Moin (1995) to treat the case of an excited laminar axisymmetric jet by directly simulating Navier-Stokes equations (DNS). They compare different methods to derive the acoustic field, which is also directly represented in the simulation. At the other end, Bastin, Lafon & Candel (1995) considered unsteady RANS of high-Reynolds-number two-dimensional plane jets and obtained the radiated noise using exclusively Lighthill's (1952) aeroacoustic analogy.

It is now time to take the next step and treat a real configuration where results could be compared to an experiment. This will provide the first opportunity to directly evaluate the suitability of the whole approach for prediction purposes. For this we selected the case of a supersonic circular jet at Mach number $M = 1.37$, for which both flow and acoustic measurements are available, respectively by Lau *et al.* (1979) and Tanna *et al.* (1976). The experiment was designed to produce a fully expanded jet near ambient temperature ($T_J/T_0 = 0.94$) so that the "acoustic" Mach number, defined as $M_a = U_J/c_0$, is 1.33. The Reynolds number based on the jet diameter and exit velocity is 1.5×10^6 . For such a case, large eddy simulation (LES) seems the only technique that may provide a realistic description of the turbulent

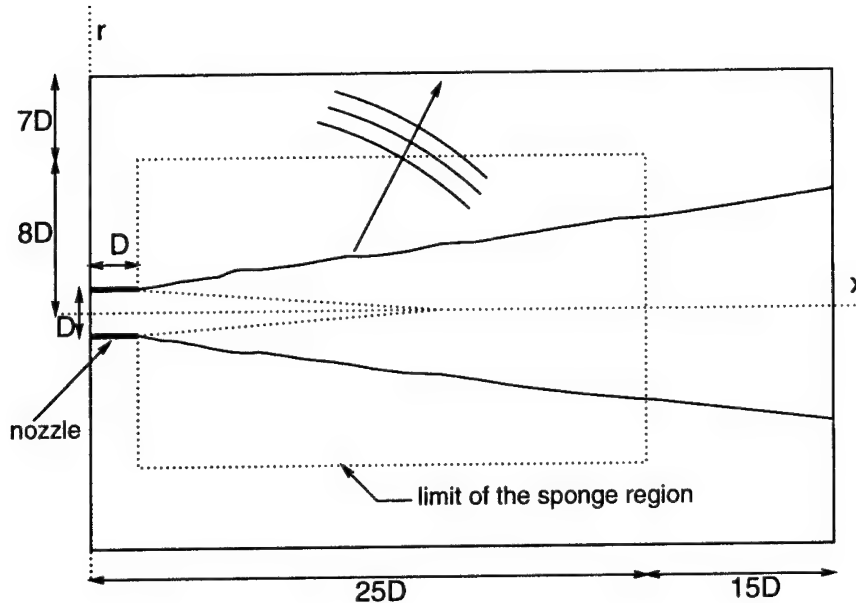


FIGURE 1. Schematic section of the flow and computational domain.

fluctuations contributing to the radiated noise. Therefore, the first objective of this project is to set up the large eddy simulation of a “real” (i.e. high-Reynolds-number and spatially developing) supersonic jet. The configuration of the computational problem is presented in Fig. 1. Note that a part of the nozzle is included in the computational domain: indeed it is intended *not* to provide any artificial excitation of the flow, which is a major difference with previous studies. We hope to obtain a natural flow by letting the intrinsic spatial instabilities develop on a well designed grid. The second part of the project consists in applying different known methods to obtain the acoustic field radiated by the computed flow, then analyzing the results in the light of the experimental data. The present brief describes the activity of the past year, which was entirely devoted to preparing the simulation of the flow.

In the following, the length, velocity, and time scales are respectively the jet exit diameter D , the ambient speed of sound c_0 , and D/c_0 . x , r , and ϕ are the coordinates of the cylindrical system associated with the jet, with the x origin at the nozzle exit. x_i refers to the cartesian coordinate system.

2. Accomplishments

2.1 Choice of the method - feasibility

It was decided that the starting point for the simulation would be a finite element code solving the compressible Navier-Stokes equations, developed by various contributors in the group of Prof. T. Hughes at Stanford (see e.g. Shakib 1988, Johan *et al.* 1992 or Jansen *et al.* 1993), and which was recently used by Jansen (1995) to perform the large eddy simulation of the flow around an airfoil at high angle of attack ($\alpha = 12^\circ$). Two issues were addressed before making this choice. First the

use of an unstructured grid allows an easy representation of a three-dimensional configuration while reducing the number of grid points by taking advantage of the inhomogeneous grid resolution requirements. However, finite element methods are more expensive per grid point than finite differences. Therefore, we had to verify that the savings in terms of grid points are enough to justify the use of finite elements. Second, recent work by Beaudan & Moin (1994) has shown that numerical dissipation can easily overwhelm the effect of the subgrid-scale model, giving little reliability to any large eddy simulation. It was therefore useful to assess the dissipation of the present method.

To obtain an estimate of the number of grid points necessary for this simulation, the resolution requirements were defined as follows. It seems from experimental observations that the internal boundary layer is laminarized by the favorable pressure gradient in the nozzle, so that the grid only needs to resolve the mean velocity gradient. Consequently the nozzle interior represents a negligible fraction of the whole grid. In the mixing layer region, previous LES studies of temporally evolving free shear flows by Ragab & Sheen (1993), Vreman *et al.* (1994), or Fatica *et al.* (1994) led us to opt for an isotropic grid with 5 points in the radial direction across each vorticity thickness δ_ω . Using the experimental growth rate of the jet, this defines a grid that is very fine at the tip of the nozzle and coarsens linearly with the streamwise distance:

$$\Delta x_i = 0.016 x.$$

This must be modified at the nozzle exit ($x = 0$), where the relevant length scale is the internal boundary layer thickness. This parameter is not given in the experimental data, but it is expected to have a negligible influence on the further development of the shear layer. From similar experiments, the 99% thickness δ was set at 4% of the jet diameter.

Another constraint is to capture the acoustic sources in the jet. The acoustic near field must also be captured if a method such as Kirchhoff's formulation is to be used to obtain the acoustic radiation. This restriction implies

$$\Delta x_i \leq \frac{1}{n M_a St},$$

where n is the number of points per wavelength, M_a the acoustic Mach number (here 1.33), and St the Strouhal number (based on the jet exit velocity and the jet diameter) of the highest frequency to be captured. The experimental data suggest $St = 1$, and it is interesting to see that with $n = 8$ this constraint takes over the previous condition at $x \simeq 6$, meaning that the grid requirements are governed by the jet dynamics along the potential core (which is roughly 6 diameters long) and by the acoustic sources thereafter. In other words (and putting aside the complex and still controversial mechanisms of interaction between the nozzle and the acoustic field), the finer structures captured by the simulation during the first few diameters downstream from the nozzle are necessary to obtain a realistic further development of the jet, but they are negligible acoustic sources *per se*.

With these conditions the size of the grid can be estimated for both structured and unstructured grids. As a result the latter requires about 17 times less grid points than the former. The ratio varies somewhat when the parameters of the resolution requirements are varied, and it depends on whether the acoustic near field is represented or not, but it is never less than 15. The main reason for such a high ratio, which is enough to justify the choice of an unstructured grid method, lies in the azimuthal resolution which is very high at the nozzle lip. A structured grid is forced to carry this resolution everywhere.

The second question to investigate is the dissipation properties of the numerical scheme. The present finite element method is based on a Galerkin formulation in space stabilized with the SUPG operator described by Hughes & Mallet (1986). This finite element formulation can be combined with any time-stepping scheme. In all this report, the second-order accurate trapezoidal rule in time was used. The spatial formulation is illustrated on the simple example of the one-dimensional advection equation:

$$\frac{\partial U}{\partial t} + a \frac{\partial U}{\partial x} = 0,$$

where a is the advection velocity. In this case the weighted residual R is given by

$$R_l = \int W_l \frac{\partial U}{\partial t} + [W_l a U] - \int \frac{\partial W_l}{\partial x} a U + \int (a \frac{\partial W_l}{\partial x}) \tau (\frac{\partial U}{\partial t} + a \frac{\partial U}{\partial x}),$$

where W_l is a weighting function. The stabilizing dissipation error is entirely due to the last integral of the residual, where τ is a controlled local parameter. This is precisely what makes the scheme very different from standard upwind spatial differences, where the dissipation is an intrinsic non-adjustable feature of the method. In the present work we use first-order elements, which makes the dissipation error fourth-order, and the finite element method can be made, at any point in space and time, *arbitrarily close to the non-dissipative fourth-order accurate Padé scheme* (obtained for $\tau = 0$).

In the current version of the code, the dissipation of the method (i.e. τ) is a function of the *local* CFL number, given by $\text{CFL} = a \Delta t / \Delta x$. This CFL number is local because in the general case the maximum characteristic velocity (here a) and the grid spacing Δx vary in space. The non-dimensional relevant parameter characterizing the dissipation is in fact $\tilde{\tau} = a\tau / \Delta x$ and we have presently

$$\tilde{\tau} = \frac{1}{2}(1 + \text{CFL}^{-2})^{-1/2}.$$

The expression extended for the system of Navier-Stokes equations in three dimensions can be found in Shakib (1988) and was never modified throughout the present work. This relation makes the dissipation error small when the local CFL number is small, which is the case practically everywhere in our computational problem. Indeed, the time step is determined with a local CFL number of order 1 by the highest velocity and smallest mesh spacing that occur at the same place at the nozzle lip. As the time step is constant in the whole computational domain, the local

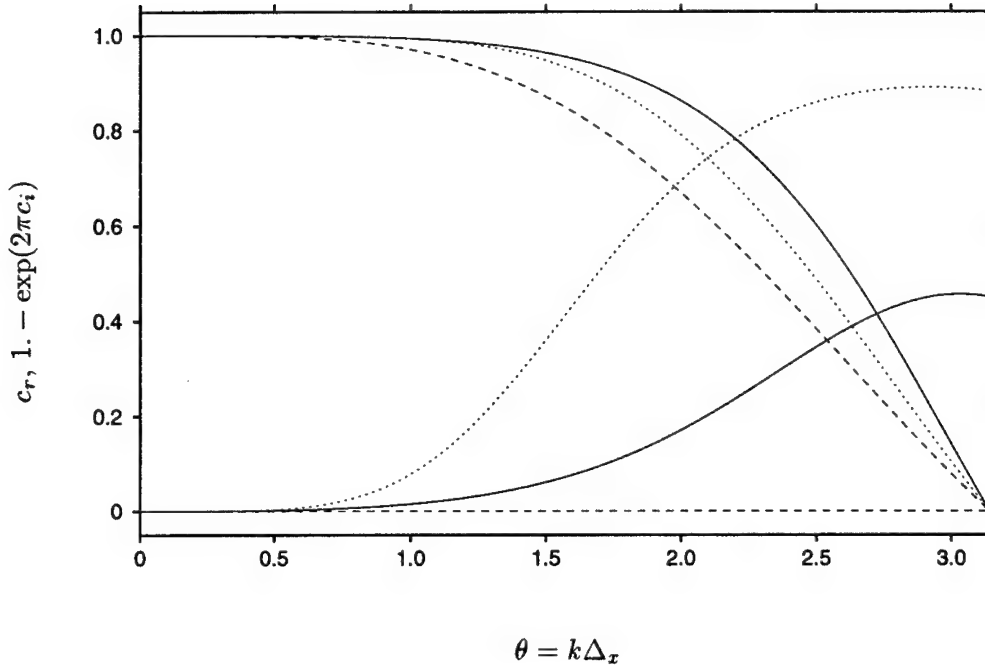


FIGURE 2. Dispersion and dissipation of the present finite element method compared with reference finite difference schemes. Analysis on the pure advection equation with the trapezoidal rule temporal scheme and $CFL = 0.05$. Dispersion is indicated by c_r , which tends to its exact value of 1 (no dispersion) in the limit of zero wavenumber ($\theta = 0$). Dissipation over one period of the exact wave is given by $1 - \exp(2\pi c_i)$ and tends to 0 (no dissipation) in the same limit. — Present FEM; ---- fourth order central-differences; fifth order upwind-differences.

CFL number is much smaller everywhere else. To change the point of view, free shear flows, in contrast to boundary layers, have the property that the grid spacing is minimum precisely where the velocity is maximum, which defines the shortest time scale to be captured by the simulation. The relative time step (or the local CFL number) is therefore small in most of the computational domain.

To complete this theoretical analysis, we consider the same advection equation with $a = 1$ and write classically the numerical solution $U = \exp[ik(x - ct)]$ where k is a fixed real wavenumber and $c = c_r + ic_i$ the complex numerical propagation velocity. c_i represents the dissipation error while the difference of c_r to 1 accounts for the dispersion error. The spatial scheme is combined with the trapezoidal rule in time with $CFL = 0.05$, and we compare the dissipation and dispersion of the present finite element formulation to the central fourth-order and one point upwind-biased fifth-order differences. It is seen in Fig. 2 that the finite element method is already less dissipative than this high-order upwind scheme, especially with more than 4 points per wavelength ($\theta < \pi/2$). Moreover, the dissipation of the finite element

formulation could be decreased at will if deemed necessary simply by modifying the expression for $\tilde{\tau}$. Finally, the dispersion error behavior is excellent, which results from the proximity to a Padé scheme.

To confirm these analytical results, numerical tests were conducted, with the same three-dimensional code that is used later, on two cases that are relevant to the main simulation, namely the propagation of an acoustic wave in subsonic flow at $M = 0.5$ and the growth of temporal axisymmetric instabilities of a supersonic jet at $M = 1.4$ with $\delta_\theta/R = 0.05$. As everywhere else the trapezoidal rule is used in time. The CFL number and resolution are also matched to the main simulation. It was observed that with $CFL = 0.02$ and no more than 8 points per wavelength, an acoustic wave propagates with 0.3% amplitude attenuation per period and -0.2% phase error. Correspondingly, at $CFL = 0.08$ and with 32 points per wavelength, the error on the growth rate of the jet instability was -0.6% with 0.2% phase error. These numerical results are consistent with the one-dimensional theoretical analysis.

2.2 Parallelization

Finite element codes are naturally good candidates for data parallelism, since most of the time is spent performing local computations on elements. Parallel machines are also at the high-end of modern supercomputers: for example 64 processors of the IBM SP2 outperform a single processor of the CRAY C90 by an order of magnitude. Thus the initial code was ported by Johan *et al.* (1992) on the Connection Machine 512-nodes CM5, where the computational domain is partitioned in physical space, so as to affect an equal number of elements to each processor. Parallelization on the CM5 was based on the use of a high-level language (CM-Fortran, similar to the emerging standard HPF), where the actual detection and organization of inter-processor communications is completely controlled by a "smart" compiler. This makes programming practically as easy as in the serial world, which is an important advantage. On the other hand, performance is generally not optimal, portability is still mediocre, and in our specific case the future of the CM5 is uncertain. For these reasons we decided to move to the completely different approach of message passing with the interface standard MPI, which allows us to run on a variety of platforms, but specifically the IBM SP2. With this technique, a suitable strategy must be constructed to communicate data between processors, which requires a real programming effort, but gives full control on the actual parallelization.

In the present finite element code, the bulk of the data that must be communicated is the residual at the nodes shared by several processors, i.e. the nodes at the boundary of each piece of the domain partition among the processors. The main idea to optimize communications consists of renumbering the nodes before the computation so that the data that must be shared are stored contiguously in main memory, which avoids inefficient indirect addressing. To accomplish this, an elaborate preprocessing step was developed where, given the partition, nodes are relabeled and the exact sequence of communications is determined to minimize waiting times. The partition itself is produced by the program *Metis* developed by Karypis & Kumar (1995). The preprocessing is done only once before the actual

simulation, during which communications then take place following the same fixed pattern.

The performance and scalability of the new code justify the effort. The two tests presented in Table 1 show that the parallelization itself is cheap (as seen from the speedup between the *serial* version and 4 processors) and that scalability (here between 4 and 16 processors) is very good. Correspondingly the wall-clock time taken by communications is about 3% of the total CPU time. As a comparison the same ratio for the previous CM5 version is in the order of 15%. It is not easy to give exact figures for larger numbers of processors because the SP2 that we are using (at MHPCC, Maui) provides a mixture of processors of different performance, but it seems the communication time does not exceed 5% of the CPU time, with still a good scalability between 32 and 64 processors.

20000 nodes		50000 nodes	
1 proc (serial):	1421.	4 proc:	493.
4 proc:	366.	16 proc:	128.
speedup:	97%	speedup:	96%

TABLE 1. Cpu time for test problems

2.3 Dynamic model

Since it was first formulated by Germano *et al.* (1991), it was often shown that the dynamic subgrid-scale model has very attractive properties, such as its robustness and the removal of any ad hoc tuning or damping near solid boundaries. For the present large eddy simulation we select the compressible version described by Moin *et al.* (1991). More precisely only the trace-free part of the subgrid-scale stress tensor τ_{ij} is represented with a Smagorinsky eddy viscosity model. The Smagorinsky coefficient is determined during the computation by the dynamic procedure. The trace of τ_{ij} , i.e. the subgrid-scale energy, is neglected ($C_I = 0$ with the notations of Moin *et al.* 1991). Finally, the turbulent Prandtl number is set to 0.7 and is not determined dynamically. To implement the dynamic model in the finite element code, we followed the approach of Jansen (1994), who develops a top-hat test filter generalized for an unstructured grid. For the present jet case the dynamic coefficient is averaged in the homogeneous azimuthal direction, which requires additional communications between processors.

The present implementation was tested on the case of isotropic homogeneous turbulence decay. The simulation was run on a 32^3 periodic grid and aimed at reproducing the results of the experiment conducted by Comte-Bellot & Corrsin (1971). For a fair comparison the initial velocity field of the simulation must match the *filtered* spectrum given at the first experimental station, corresponding to $t = 42$ with the conventions of the reference. The grid filter is assumed here to be a “box” filter of width equal to the computational mesh spacing Δx . Furthermore, the initial field must have realistic phase information, for which the skewness of the velocity gradient is a good indicator. To satisfy these requirements the initial field is adjusted by letting the simulation run for a few eddy turnover times and renormalizing the

spectrum. This procedure is iterated until convergence of the skewness. Once the initial field is determined and matches the experiment at $t = 42$, the actual decay is simulated and results are compared to the experimental data given at $t = 98$ and 171. During this computation, the time step is constant with initially 45 time steps per eddy turnover time at the first experimental station ($t = 42$). Correspondingly, the initial CFL number based on the r.m.s. velocity is 0.03.

Figure 3a shows the decay of the kinetic turbulent energy obtained with the dynamic model, with the Smagorinsky coefficient fixed at $C_s = 0.17$, or when no subgrid-scale model is used. The relative position of the three curves was expected, but the variations observed are important since they show that the numerical dissipation does not take over the subgrid-scale model. Indeed the main argument of Beaudan & Moin (1994) to dismiss the fifth-order upwind-differences in space was the observation that it produced the same results regardless of the subgrid-scale model, or even when the model was switched off. It may also be noted that the decay obtained with the dynamic model is reasonable, while fixing the Smagorinsky coefficient seems to provide even better results. However, the velocity spectra presented in Fig. 3b show that this would be a premature conclusion: if we focus for example on the slope of the velocity spectrum obtained at the last experimental station ($t = 171$), it is clear that the dynamic model nicely matches the experiment, while the fixed coefficient spectrum drops off at high wavenumber, indicating that the model provides excessive dissipation. The very good decay shown in Fig. 3a with fixed coefficient is the result of errors cancellation. Finally the spectrum obtained with no model is flatter, which indicates that the numerical dissipation inherent to the scheme is not dominant.

2.4 Grid generation

The object is to obtain a three-dimensional grid composed of tetrahedral elements which satisfy the highly inhomogeneous resolution requirements that were discussed in section 2.1. The grids produced by commercial software may be appropriate for steady computations, but they fail to provide the quality and smoothness desirable for large eddy simulations in non-trivial geometries. Hence, it was necessary to develop a grid generator specific to the present case.

A triangular two-dimensional grid which maps an azimuthal section of the jet ($\phi = 0$) is first generated. This grid is shown in Fig. 4a and is itself designed in two steps. First the shear layer region is covered with a "pseudo-structured" grid which can be precisely controlled. Due to technical reasons it is not possible to extend this grid indefinitely away from the line $r = 0.5$ and therefore we use an advancing front method to map the rest of the two-dimensional section. A careful eye will detect the transition between these two approaches on the magnified view in Fig. 4b, where the nozzle lip is also clearly seen. The three-dimensional grid is then obtained schematically by rotating each triangle in the two-dimensional grid to create a three-faced toroid, then generating tetrahedral elements, complying to varying azimuthal resolution requirements for each toroid. The result can be observed on the streamwise section of Fig. 4c. The present grid was designed this way and has about 600,000 nodes and 3,500,000 elements. This multi-step grid

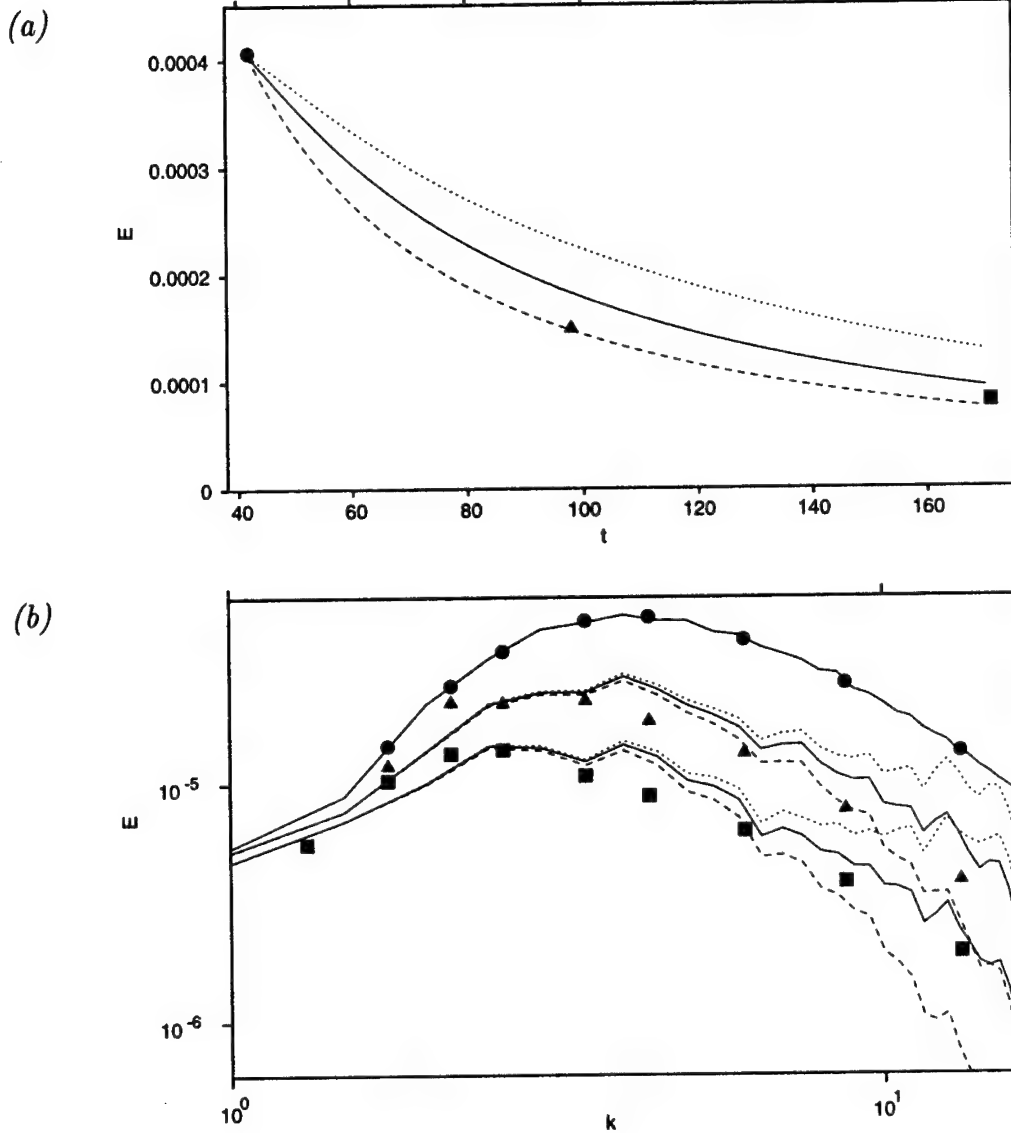


FIGURE 3. Test of the subgrid-scale model in a LES of decaying isotropic turbulence on a 32^3 grid, with comparison to filtered experimental data of Comte-Bellot & Corrsin (1971). (a) Decay of resolved kinetic turbulent energy; (b) filtered velocity spectra where the wavenumber ranges from 1 to 16 (normalization by $2\pi/L$, where L is the size of the computational box). — Present dynamic model; ---- fixed coefficient Smagorinsky model ($C_s = 0.17$); no model. ●, ▲, ■ Experiment at $t = 42, 98$ and 171 respectively.

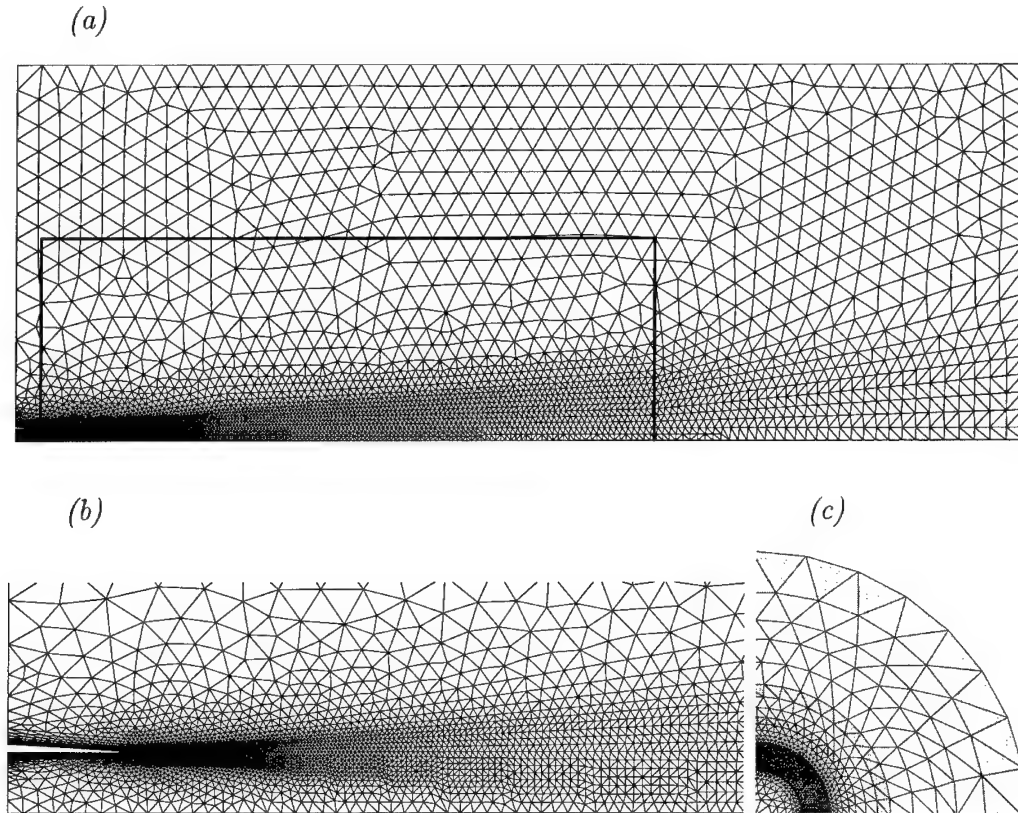


FIGURE 4. Sections of the present grid. (a) Generating two-dimensional grid, or azimuthal section ($\phi = 0$), of the full three-dimensional grid. The jet is going from left to right, and the grid (including the sponge) is 41 diameters long and 15 diameters in radius. The thick boundary indicates the limit of the sponge, starting 25 diameters downstream and 8 diameters in radius. (b) Magnified view of the same azimuthal section. The portion presented here is 6 diameters long and 2 diameters in radius. The nozzle can be seen on the left. (c) Quarter streamwise section at $x = 1$ (one diameter downstream from the nozzle) with the same scale as (b). Apparent faces of the elements are shown up to $r = 2.3$. Note the clustering of elements in the shear layer (around $r = 0.5$).

generator has been made robust and is now general in the sense that the only input is the resolution requirements as a function of space. Therefore, should resolution needs change, a new grid can be obtained very simply in a few minutes.

2.5 Boundary and initial conditions

The boundary conditions for a compressible jet with no co-flow involve some difficulties. The outflow ($x = x_{\max}$) is subsonic, which means that one physical boundary condition must be specified. This condition should reflect as little as

possible of outgoing vortical structures. Moreover, the flow is unsteady so that the velocity on the edges of the jet may be temporarily negative, which is a potential source of numerical instability. There should be an entrainment associated with the jet, implying an "external inflow" ($x = x_{\min}$ and $r > D/2$), parallel to the nozzle, as opposed to the main internal inflow through the nozzle ($x = x_{\min}$ and $r < D/2$). The entrainment is unknown *a priori* and must develop naturally, which means that the corresponding boundary conditions must allow for a modification of the mean flow. Because there is no co-flow, the mean flow is weak (the entrainment typically peaks at one or two percent of the jet exit velocity) so there is again a risk of having a local outflow where an inflow is expected. The radial velocity on the lateral boundary ($r = r_{\max}$) naturally changes sign, with an inflow in early sections followed downstream by an outflow. In the rest of this section we present boundary conditions which bring a satisfactory solution to these problems. They have been obtained partly on the main turbulent simulation, and partly on a preliminary two-dimensional laminar simulation.

Previous experience has shown that a "sponge" region, where the basic equations are modified in a suitable way, can be very helpful in making boundary conditions less critically sensitive. The sponge must also be smooth so as to minimize the impact on the physical part of the flow. A systematic investigation of sponge techniques has been carried out by Israeli & Orszag (1981), who propose different solutions. An attractive one, referred to as "cooling", can be implemented by adding to the evolution equation for the generic variable Φ a source term $-A(\mathbf{x})[\Phi - \Phi_0(\mathbf{x})]$. In this expression, $A(\mathbf{x})$ is the local amplitude of the sponge and $\Phi_0(\mathbf{x})$ a steady solution, which can be considered as the target. As the strength A of the sponge increases in space, Φ is driven to the target Φ_0 . This technique has the advantage that the solution is known at the end of the sponge (it should be almost identical to Φ_0) so that any boundary conditions compatible with Φ_0 can be applied. Furthermore, excellent results were obtained on the simple cases of the subsonic convection of a vortex, or the propagation of an acoustic wave in subsonic flow, with an error an order of magnitude lower than with characteristic-type boundary conditions alone. It turned out, however, that the necessity to prescribe the target solution is a major drawback in the case of the supersonic jet. Even with a long computational domain, the flow is still far from being at rest at the outflow boundary: consider that 40 diameters downstream from the nozzle, the maximum Mach number is still 0.3. It is therefore not possible to set Φ_0 to the ambient conditions, and unless the sponge was made so weak that it became useless, we observed a strong numerical instability of the jet in reaction to any "guessed" Φ_0 , for example based on experimental data. The cooling sponge indeed violates the characteristic nature of the flow, and after these observations it seems undesirable to use this technique even if a suitable Φ_0 could be found. Given the sensitivity of the simulation to the imposed target, it could be argued that the sponge indirectly enforces the flow upstream, which would be a flaw of a prediction approach. Therefore we came back to a more classical filtering sponge. This option, which was already used by Mitchell *et al.* (1995) or

Bastin *et al.* (1995), does not fully release the constraint to have low reflection outflow boundary conditions, which are discussed in the next paragraph. In practice, if Φ is the solution at the end of a time step, a filtered solution $\hat{\Phi}$ is obtained by convolution with the same top-hat generalized filter that is used for the dynamic model. The filter width is therefore equal to the mesh spacing. The solution Φ is then replaced by a weighted combination $(1 - \beta)\Phi + \beta\hat{\Phi}$, where β is a coefficient that varies smoothly in space from zero outside the sponge (no filtering) to 1% at the boundary of the computational domain, where the sponge effect is maximum.

The outflow boundary condition was chosen to be the characteristic-based form detailed by Poinso & Lele (1992), where the amplitude of the incoming characteristic wave is replaced following the suggestion of Rudy & Strikwerda (1980) by a term conveying the influence of the ambient pressure. The principle of this condition is simple, but it involves a precise modification of Navier-Stokes equations at boundary nodes, which fits poorly in the frame of the finite element method, where boundary conditions are naturally expressed in terms of boundary integrals. To implement this boundary condition efficiently, i.e. without inserting expensive tests everywhere in the standard volume treatment, it was necessary to develop a new data structure in the code, indicating the elements with boundary nodes where the residual must be altered. Once the regular residual is assembled, these elements are re-processed and the term to be modified is extracted and replaced.

For the external inflow which was defined above, four conditions must be specified. A first condition to prescribe is no swirl ($u_\phi = 0$). Two additional physical conditions compatible with a modification of the mean flow associated to entrainment are obtained by assuming that the flow is coming from an upstream reservoir with no entropy variations. From thermodynamical relations and the compressible Bernoulli equation, these two conditions are written as constant total temperature and pressure. They were implemented in the finite element code, where it is relatively simple to impose zeroth order conditions on variables at the boundary nodes. A fourth condition must be specified. The most physical condition would be to prescribe that no free-stream azimuthal vorticity comes into the domain. However, we were not able to implement this in a stable way. As there is no unique and obvious approach to impose this condition in the finite element formulation, it is hard at this stage to say if the problem is due to the implementation itself or comes from the compatibility with other boundary conditions. The boundary condition was therefore replaced by setting the radial velocity u_r to zero. This assumption of parallel incoming streamlines is not strictly right, but the radial velocity is expected to be an order of magnitude lower than the streamwise entrainment velocity, so that the error is minimal. On the lateral boundary, no-slip conditions are imposed. This simple choice is again justified by steady $k-\epsilon$ computations which showed that the velocity on this boundary would be under 0.1% of the jet exit velocity.

On the nozzle itself, no-slip conditions and constant temperature are prescribed. The internal supersonic inflow is completely specified with *steady* conditions. Pressure and temperature are constant across the flow, while a laminar boundary layer

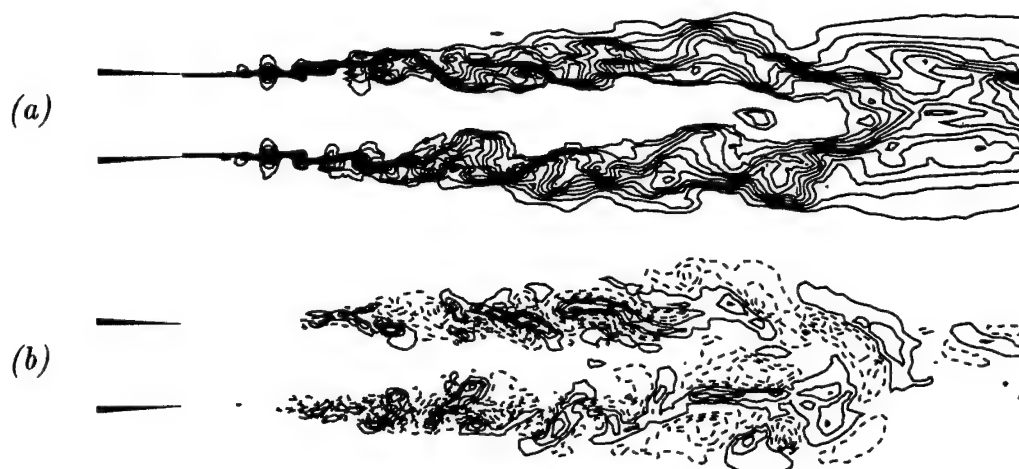


FIGURE 5. Instantaneous planar view of the jet ($\phi = 0$) at $t = 12.1$. The scale can be inferred from the nozzle, which is drawn on the left. The present section is 10 diameters long. (a) Streamwise velocity, with contours drawn from 0.1 to 1.3 in increments of 0.1; (b) azimuthal velocity, with contours drawn from -0.45 to 0.45 in increments of 0.1. Dotted contours indicate negative values.

velocity profile is prescribed with the 99% thickness δ equal to 4% of the jet diameter. It is an essential feature of the present simulation that the flow is not explicitly excited. The grid is finest at the tip of the nozzle to allow a natural "ignition" of the flow.

Finally, the simulation is initialized with the result of a steady axisymmetric $k-\epsilon$ computation of the same flow, obtained on a structured grid with a different code. The fact that no perturbations are superimposed on this initial field can again be emphasized. Although the initial field is rapidly changed by the LES equations, less realistic initializations led to numerical instabilities.

2.6 Preliminary results

Upon completion of the steps described in the previous sections, the final code was obtained. At the time of the present brief, the main turbulent simulation has just begun and the physical time was advanced by only 12.5 time units. It is useful to keep in mind that during one time unit (D/c_0) the shear layer primary (axisymmetric Kelvin-Helmholtz) instability propagates about 0.8 diameter downstream.

An instantaneous azimuthal section of the jet at $t = 12.1$ is presented in Fig. 5. The first coherent structure, which in this convectively unstable flow originates from the tip of the nozzle, has barely reached the downstream boundary of this view (10 diameters downstream from the nozzle). At least qualitatively, the shear layer identified by the streamwise velocity contours (Fig. 5a) is reasonable. It is also clearly not axisymmetric, which is a desirable feature of a realistic turbulent jet. The fact that the grid itself is not perfectly axisymmetric (as can be checked in Fig. 4c) is sufficient to induce the first three-dimensional disturbances to which the flow is

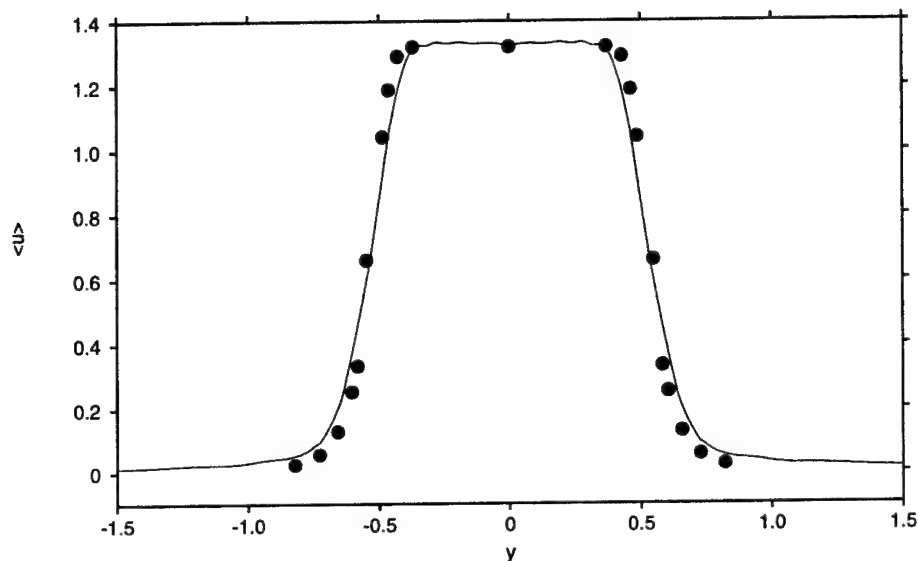


FIGURE 6. Mean radial profile of the streamwise velocity at $x = 2$. — computed; ● experiment. The profile is symmetrized for clarity.

naturally unstable. The three-dimensionality of the flow can also be estimated from the azimuthal velocity shown in Fig. 5b. As expected there is no mean swirl motion of the jet, but the amplitude of the azimuthal velocity fluctuations peaks at more than 30% of the exit streamwise velocity, which represents strong three-dimensional structures.

It is also interesting to note that significant levels of azimuthal velocity are not observed before one diameter downstream from the nozzle, which appears as the distance necessary for the initial symmetry to break down. The flow is also two-dimensional in the region where initial conditions are still being convected out, which corresponds to the downstream extremity of the present view. The numerical mechanism for onset of three-dimensionality is therefore clearly identified as an instability operating from the nozzle lip.

It is still too early at this stage to obtain converged statistics of the flow anywhere but very close to the nozzle, where the local time scale is smallest. Thus only the radial profile of streamwise velocity two diameters downstream from the nozzle is presented and compared to experimental data (see Fig. 6). Although the spreading rate appears slightly too high, the agreement is reasonable for this location where the state of the internal boundary layer or the exact shape of the nozzle (which is unknown to us) may still have an influence.

Finally it is interesting to look more into the detail of the transition to three-dimensionality in this computation, since this is one of the crucial aspects which will give confidence in the simulation. For this we consider the jet at some point in time and take three sections perpendicular to its axis. The first section is taken at

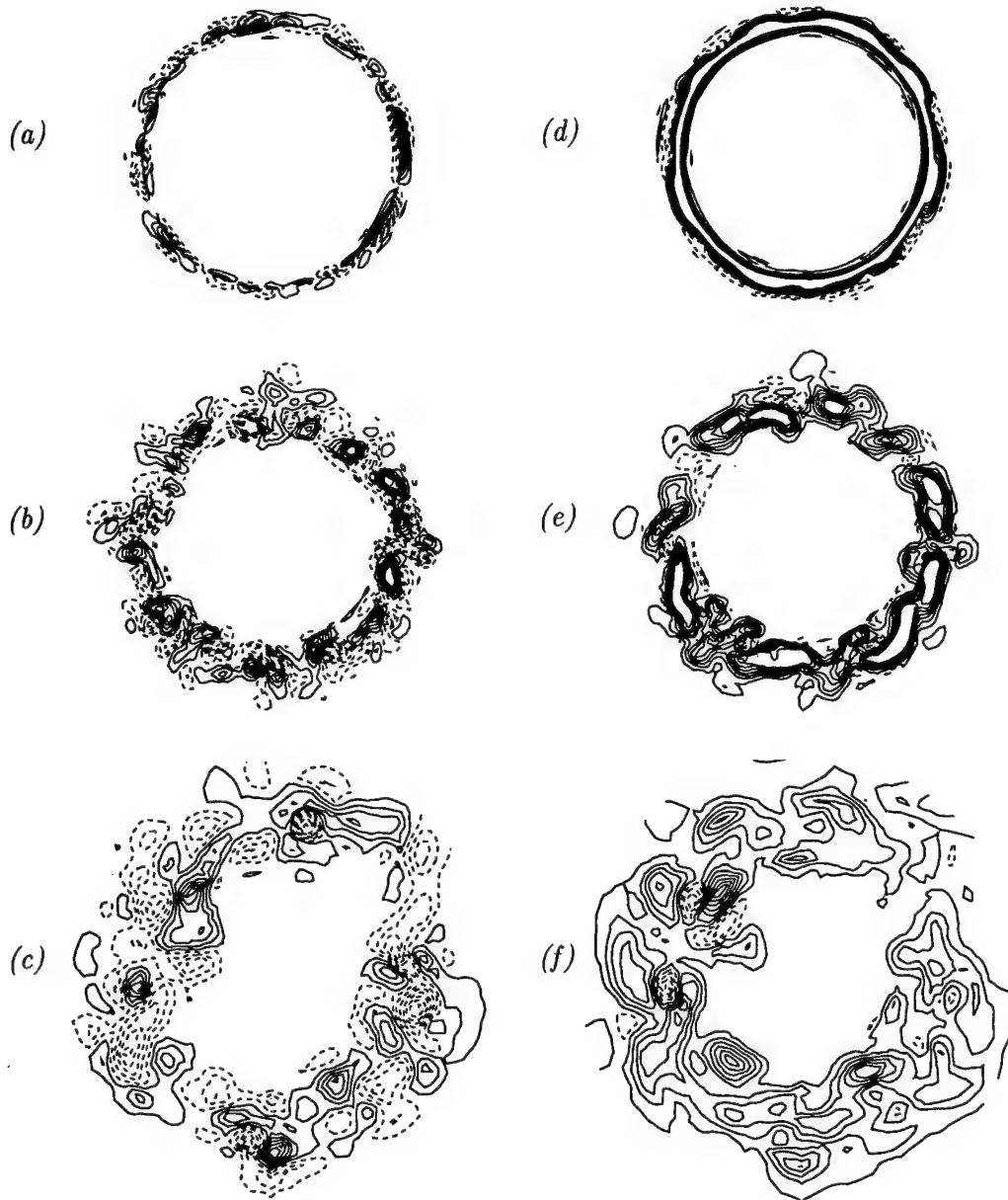


FIGURE 7. Spatial vortex breakdown at $t = 9.7$. (a-c) Streamwise vorticity ω_x ; (d-f) azimuthal vorticity ω_ϕ . (a,d) $x = 1$; (b,e) $x = 1.5$; (c,f) $x = 2.5$. Contours are drawn from -15 to 15 in increments of 2. Dotted contours indicate negative values.

$x = 1$, which was seen in Fig. 5b to correspond to the beginning of an observable transition, and two more sections are taken at $x = 1.5$ and $x = 2.5$. Figure 7 shows the streamwise and azimuthal vorticities at these locations. At $x = 1$, Fig. 7d

shows a vortex ring with small azimuthal fluctuations, corresponding in Fig. 7a to low levels of streamwise vorticity. Only half a diameter downstream, the vortex ring now shows strong azimuthal oscillations (Fig. 7e). At this stage the streamwise vorticity has reached the intensity level of its azimuthal counterpart (Fig. 7b). One diameter further, the vortex ring has completely broken down (Fig. 7f) though it can still be noted that the azimuthal vorticity remains mostly positive. At the same time Fig. 7c shows well-developed streamwise structures of smaller spatial scale and same or higher amplitude.

It is difficult to make quantitative comparisons with the numerous studies on vortex breakdown available in the literature. These generally deal with an idealized configuration of one or a few incompressible vortex rings, a different situation from this supersonic spatially developing jet. Nevertheless, the process of small-scale streamwise structures progressively building up and taking over the initial axisymmetric motion has been analyzed e.g. by Shariff *et al.* (1994), who performed direct simulations of a single vortex ring, or visualized by Liepmann & Gharib (1992) in an incompressible round jet. The present simulation appears to reproduce this evolution very well.

3. Future plans

The advancement of this compressible turbulent jet is still subject to occasional numerical problems, but the main simulation is finally on its way. As progress is made and statistics are accumulated, it will be possible to extensively compare the computed flow to experimental data.

Acoustic results are expected to be obtained in the near future. The numerical approach to derive the acoustic field via Lighthill's analogy has been designed, and the corresponding acoustic routines are essentially ready. To keep data storage requirements affordable, the contribution of turbulent fluctuations to acoustic sources is accumulated as the solution progresses. Because of their smaller time scale, the high-frequency components of the radiated noise should converge first.

Several theoretical aspects of the noise radiation problem can also be worked upon, such as estimating the error associated to refraction effects, which are neglected by Lighthill's analogy.

REFERENCES

- BASTIN, F., LAFON, P. & CANDEL, S. 1995 Computation of jet mixing noise from unsteady coherent structures. *CEAS/AIAA Paper 95-039*.
- BEAUDAN, P. & MOIN, P. 1994 Numerical experiments on the flow past a circular cylinder at sub-critical Reynolds numbers. *Report No. TF-62*, Thermosciences Div., Dept. of Mech. Engr., Stanford Univ.
- BÉCHARA, W., LAFON, P., BAILLY, C. & CANDEL, S. 1995 Application of a $k-\epsilon$ model to the prediction of noise for simple and coaxial free jets. *J. Acoust. Soc. Am.* **97**, 3518-3531.

- COMTE-BELLOT, G. & CORRSIN, S. 1971 Simple Eulerian time-correlation full- and narrow-band velocity signals in grid-generated 'isotropic' turbulence. *J. Fluid Mech.* **48**, 273-337.
- FATICA, M., ORLANDI, P. & VERZICCO, R. 1994 Direct and large eddy simulations of round jets. In *Direct and large-eddy simulation I* (eds P. R. Voke, L. Kleiser & J.-P. Chollet), Kluwer Academic Publishers, Dordrecht, 49-60.
- GERMANO, M., PIOMELLI, U., MOIN, P. & CABOT, W. H. 1991 A dynamic subgrid-scale eddy viscosity model. *Phys. Fluids A*, **3**, 1760-1765.
- HUGHES, T. J. R. & MALLET, M. 1986 A new finite element formulation for computational fluid dynamics: III. The generalized streamline operator for multidimensional advective-diffusive systems. *Comp. Meth. Appl. Mech. Eng.* **58**, 305-328.
- ISRAELI, M. & ORSZAG, S. A. 1981 Approximation of radiation boundary conditions. *J. Comput. Phys.* **41**, 115-135.
- JANSEN, K., JOHAN, Z. & HUGHES, T. J. R. 1993 Implementation of a one-equation turbulence model within a stabilized finite element formulation of a symmetric advective-diffusive system. *Comp. Meth. Appl. Mech. Eng.* **105**, 405.
- JANSEN, K. 1994 Unstructured-grid large-eddy simulation of flow over an airfoil. *Annual Research Briefs*. Center for Turbulence Research, NASA Ames/Stanford Univ., 161-173.
- JANSEN, K. 1995 Preliminary large-eddy simulations of flow around a NACA 4412 airfoil using unstructured grids. *Annual Research Briefs*. Center for Turbulence Research, NASA Ames/Stanford Univ., 61-72.
- JOHAN, Z., HUGHES, T. J. R., MATHUR, K. K. & JOHNSON, S. L. 1992 A data parallel finite element method for computational fluid dynamics on the Connection Machine system. *Comp. Meth. Appl. Mech. Eng.* **99**, 113.
- KARYPIS, G. & KUMAR, V. 1995 A fast and high quality multilevel scheme for partitioning irregular graphs. *Technical Report TR 95-035*, Department of Computer Science, University of Minnesota.
- LAU, J. C., MORRIS, P. J. & FISHER, M. J. 1979 Measurements in subsonic and supersonic jets using a laser velocimeter. *J. Fluid Mech.* **93**, 1-27.
- LIEPMANN, D. & GHARIB, M. 1992 The role of streamwise vorticity in the near-field entrainment of round jets. *J. Fluid Mech.* **245**, 643-668.
- LIGHTHILL, M. J. 1952 On sound generated aerodynamically. I. General theory. *Proc. Roy. Soc. Lond. A*, **211**, 564-587.
- MITCHELL, B. E., LELE, S. K. & MOIN, P. 1995 Direct computation of the sound generated by vortex pairing in an axisymmetric jet. *AIAA Paper 95-0504*.
- MOIN, P., SQUIRES, K., CABOT, W. & LEE, S. 1991 A dynamic subgrid-scale model for compressible turbulence and scalar transport. *Phys. Fluids A*, **3**, 2746-2757.

- POINSOT, T. J. & LELE, S. K. 1992 Boundary conditions for direct simulations of compressible viscous flows. *J. Comput. Phys.* **101**, 104-129.
- RAGAB, S. A. & SHEEN, S.-C. 1993 Large eddy simulation of mixing layers. In *Large eddy simulation of complex engineering and geophysical flows* (eds B. Galerpin & S. A. Orszag), Cambridge University Press, p 255.
- RUDY, D. H. & STRIKWERDA, J. C. 1980 A nonreflecting outflow boundary condition for subsonic Navier-Stokes calculations. *J. Comput. Phys.* **36**, 55-70.
- RIBNER, H. S. 1969 Quadrupole correlations governing the pattern of jet noise. *J. Fluid Mech.* **38**, 1-24.
- SHAKIB, F. 1988 Finite element analysis of the compressible Euler and Navier-Stokes equations. Ph.D. Thesis, Stanford.
- SHARIFF, K., VERZICCO, R. & ORLANDI, P. 1994 A numerical study of three-dimensional vortex ring instabilities: viscous corrections and early non linear stage. *J. Fluid Mech.* **279**, 351-375.
- TAM, C. K. W. 1995 Supersonic jet noise. *Ann. Rev. Fluid Mech.* **27**, 17-43.
- TANNA, H. K., DEAN, P. D. & BURRIN, R. H. 1976 The generation and radiation of supersonic jet noise. Vol. III Turbulent mixing noise data. *AFAPL TR 76-65*.
- VREMAN, A. W., GEURTS, B. J. & KUERTEN, J. G. M. 1994 Subgrid-modelling in LES of compressible flow. In *Direct and large-eddy simulation I* (eds P. R. Voke, L. Kleiser & J.-P. Chollet), Kluwer Academic Publishers, Dordrecht, 133-144.

Towards numerical simulations of trailing-edge aeroacoustics

By Meng Wang

1. Motivation and objectives

The aeroacoustics of flow-hydrofoil interactions exhibits distinct characteristics depending on the physical length scales involved. In the small-foil (relative to acoustic wavelength) limit characteristic of the noise generated by large-scale vortex shedding at low flow Mach number, the noise calculation is facilitated by the use of the Lighthill analogy (Lighthill 1952) in conjunction with a free-space Green's function, in the sense of Curle's formulation (Curle 1955). A methodology for computing the vortex-shedding noise using the Curle formulation, including both surface-induced dipole sources and volume quadrupole sources, has been developed. The completed work, emphasizing the importance of an adequate outflow boundary treatment for accurate volume source calculation, can be found in Wang (1995) and Wang, Lele & Moin (1996).

A more fascinating aspect of the hydrofoil noise is the aeroacoustic scattering by the trailing edge, or the interaction of turbulent-boundary-layer eddies with the trailing edge. This occurs at the large-body limit, i.e., when the hydrofoil chord is comparable with or exceeds the dominant acoustic wavelength, and is the source of intense, broad-band noise (Brooks & Hodgson 1981; Blake & Gershfeld 1988). Our ongoing research is focused on this flow regime. The presence of a sharp trailing edge enhances the acoustic-energy radiation to the far-field by altering the source characteristics; for instance, turbulent eddies, known as quadrupole sources in free space, behave in a non-multipole (sometimes termed "3/2-pole") fashion in the vicinity of a semi-infinite flat-plate edge (Ffowcs Williams & Hall 1970). Crighton & Leppington (1971) show that the non-multipole character of the radiated field is caused by the fact that the scattering surface is noncompact relative to the acoustic wavelength. To account for the surface reflection effect, a hard-wall Green's function, whose normal derivative vanishes on the surface, must be employed in an integral solution to the Lighthill equation. Howe (1978) gives an extensive review of the theoretical developments in trailing-edge noise prediction methods.

In addition to the directly radiated aerodynamic noise, the fluctuating wall-pressure (pseudo-sound) field is of importance in practical applications since it tends to excite structural vibrations and low frequency noise (Blake 1986). The space-time characteristics of wall-pressure fluctuations are frequently required as a forcing-function input for various structural models. The rapid changes in surface pressure near the trailing edge provides an efficient mechanism for generating the detrimental lower-frequency content of the wall-pressure wavenumber spectrum. The problem is often further complicated by the presence of adverse pressure gradient, boundary-layer separation, and vortex shedding in the trailing-edge region.

Blake (1975) and Blake & Gershfeld (1988) conducted a series of aeroacoustic experiments with lifting hydrofoils which have asymmetrically beveled trailing edges. The asymmetric edge shape produced a separated flow on the low-pressure side, and an attached boundary layer on the high-pressure side. Measurements were made of the turbulent velocity fields near the trailing edge, fluctuating surface pressures, and radiated noise signals. Correlation and cross-spectral analyses were conducted between the velocity and pressure signals in an attempt to determine the physical mechanisms for generating unsteady surface pressure and radiated noise. Brooks & Hodgson (1981) measured the scattered surface pressure fields near the trailing edges and the radiated fields, of flows past a NACA 0012 airfoil at several angles of attack and with varying degrees of edge bluntness. The cross-spectral analysis of the measured noise data pointed to the trailing edge region as the dominant noise source. In the case of a sharp edge, excellent agreement with theoretical predictions in terms of the U_∞^5 -dependence (U_∞ is the free-stream velocity) of sound intensity and the $\sin^2(\theta/2)$ (θ is defined in Fig. 5) directivity was obtained.

Well designed experiments are invaluable in validating theory and providing insight into the complex edge-noise phenomena. However, they are limited in terms of providing detailed, global information about the flow field, and frequently resort to *a priori* assumptions regarding acoustic source mechanisms in order to reduce the amount of data to be collected. There is a pressing need for developing numerical simulation capabilities and accurate numerical databases to facilitate the acoustic source analysis. As a preliminary attempt, Zawadzki *et al.* (1996) used the database of Na & Moin (1996) for a separated, flat-plate turbulent boundary layer to examine the acoustic forcing functions, arguing that the separated boundary layer has characteristics similar to those of the boundary layer incident to a hydrofoil trailing-edge on the suction side. There are, however, important aspects of the trailing edge flow, such as pressure scattering, that the flat-plate boundary layer does not include.

The objectives of the present work are twofold. First, we aim to develop a computational method for the prediction of trailing-edge noise and wall-pressure fluctuations. The general approach consists of a large eddy simulation (LES) of the turbulent near-field (the boundary layers and the near wake), in combination with a suitable formulation of aeroacoustic theory for the evaluation of the acoustic source functions and the radiated field. The second goal is to study the physical mechanisms for the generation of sound and pseudosound. Besides the edge scattering effect, we are also interested in the roles played by pressure gradients, boundary-layer separation, and the lifted shear-layer.

2. Accomplishments

2.1 LES of trailing-edge turbulence

The flow configuration corresponds to one of Blake's experiments (Blake 1975). As shown in Fig. 1, where the contour lines denote the mean streamwise velocity from a Reynolds Averaged Navier-Stokes (RANS) calculation (to be discussed later), a two-dimensional hydrofoil with a beveled, 25-degree trailing edge is placed in a

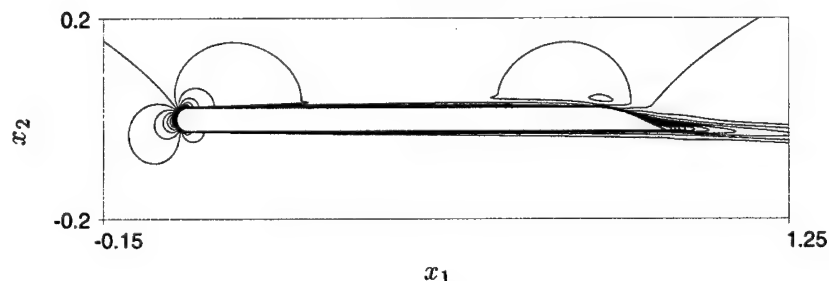


FIGURE 1. Flow past a hydrofoil with a 25-deg beveled trailing edge (the contour lines represent streamwise velocity obtained from a RANS calculation).

uniform stream at zero-degree angle of attack. The hydrofoil has a circular leading edge and a chord/thickness ratio of 21.125. The chord-based free-stream Reynolds number is 2.15×10^6 . A more detailed definition of the geometry and experimental conditions can be found in Blake (1975).

Past experiences with airfoils at high Reynolds number (Jansen 1995, Kaltenbach & Choi 1995) indicate that a full-scale LES with the entire foil would be too costly and suffer from inadequate grid resolution. In particular, laminar separation near the nose and the ensuing transition to turbulence pose an extremely stringent resolution requirement. Since the major interest in the present study is the trailing-edge region, we opted for a simulation which includes only the aft section ($\sim 38\%$ chord length) of the foil and the near wake. The computational grid for a preliminary simulation is depicted in Fig. 2. For clarity, only one in every four grid lines is plotted, and the domain has been truncated in the vertical direction. The actual domain size, in terms of maximum thickness of the hydrofoil, is approximately $20 \times 82 \times 0.5$ in the streamwise (x_1), normal (x_2), and spanwise (x_3) directions, respectively. A total of $288 \times 160 \times 32$ effective computational cells are employed, with mesh refinements near the surface and the trailing edge.

The numerical method employed in the present study is described in Choi (1993) and Mittal (1996). Second-order central difference is used for spatial discretization on a staggered mesh in curvilinear coordinates in the x_1 - x_2 plane, and Fourier collocation with dealiasing is used for discretization in the Cartesian x_3 direction. The time-advancement is of the fractional step type, in combination with the Crank-Nicolson method for viscous terms and third order Runge-Kutta scheme for convective terms. The continuity constraint is imposed through a pressure Poisson equation, which is solved at each Runge-Kutta sub-step using a multi-grid iterative procedure. The subgrid-scale stress is modeled using the dynamic SGS model (Germano *et al.* 1991) in combination with least-square contraction (Lilly 1992), spanwise averaging, and a clipping operation to limit the total viscosity to positive values.

The numerical code, originally written for the C -type mesh, has been modified to accommodate an inflow-outflow configuration with a splitting wedge, as shown in Fig. 2. The modified code has been validated under simpler laminar flow conditions,

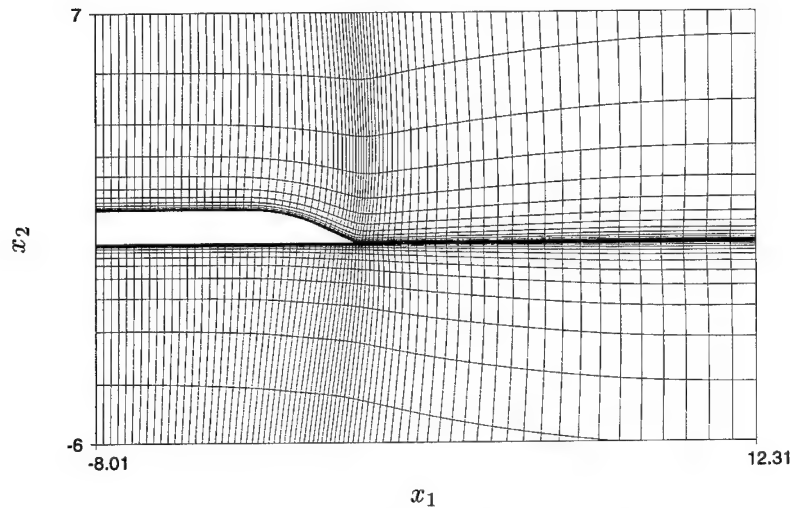


FIGURE 2. Computational grid for LES of trailing-edge flow. For clarity only one in every four grid lines is plotted.

including double (upper and lower surface) Blasius boundary layers, and linear amplifications of Tollmien-Schlichting waves.

The inflow boundary conditions pose a particular problem not encountered in a full-scale airfoil simulation. The mean velocity profiles at the upper and lower inlets differ from those of a flat-plate boundary layer due to flow acceleration. They are also affected by the presence of a mean circulation associated with a lifting surface. Unfortunately, the experimental measurements made by Blake (1975) were limited to the upper-side of the foil, and even there the available data are insufficient for boundary condition specification. As a result, we resorted to an auxiliary RANS calculation, using the $k-\epsilon-v^2$ turbulence model (Durbin 1995) in a large domain enclosing the full hydrofoil. The resulting mean velocity data are used in setting up the velocity boundary conditions outside the boundary layers. As demonstrated in Fig. 3, the mean streamwise velocities at the inlets on two sides of the edge indeed deviate significantly from each other and from the free-stream velocity of unity. Serious errors will arise if the uniform free-stream velocity is imposed at both inlets.

The turbulent-boundary-layer inflow data are generated from two separate LES of flat-plate boundary layers with zero pressure gradient, on the basis that the pressure gradients from experiments and the RANS calculation are small at the given chord station. The inflow-generation procedure is described by Lund (1994). The inflow-generation LES employs an identical mesh resolution as the trailing-edge flow LES at the inlets and matches the local boundary layer properties, including the momentum thickness and Reynolds number, with those from the RANS simulation. A discrete time series of the three velocity components in an appropriate x_2 - x_3 plane are saved to be later fed into the inflow boundaries of the main simulation.

A no-slip condition is applied to the surface of the foil. The top and bottom

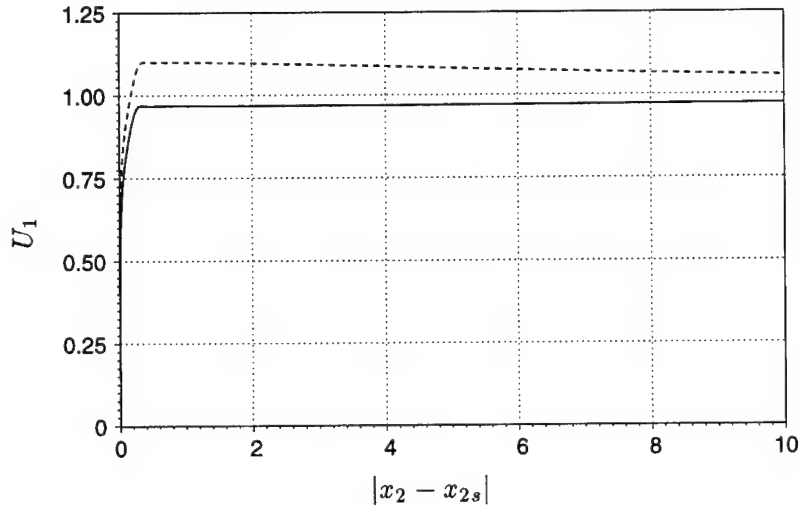


FIGURE 3. Mean streamwise velocities at LES inlets as a function of vertical distance from the foil surface, obtained from a RANS calculation. — lower inlet; ---- upper inlet.

boundaries are placed far (41 foil thicknesses) away from the foil to minimize the impact of velocities imposed along these boundaries. We used the velocity distributions from the RANS calculation, which deviate from the free-stream velocity by less than two percent. At the downstream boundary the convective outflow condition (Pauley, Moin & Reynolds 1988) is applied to allow the vortical disturbances in the wake to leave the computational domain smoothly.

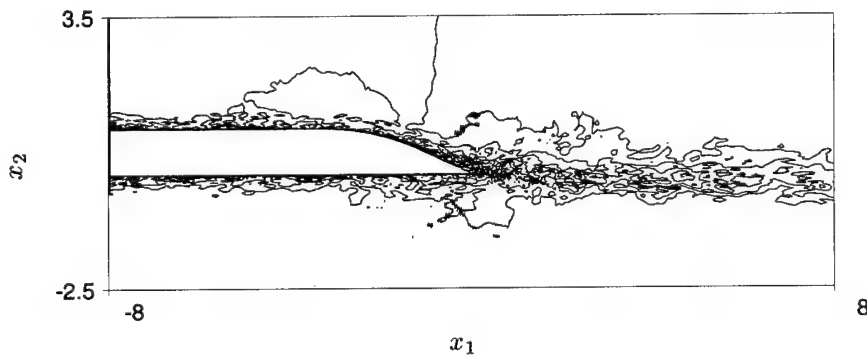


FIGURE 4. Contours of streamwise velocity u_1 in a constant x_3 plane, at $t = 29.2$. Contour levels from -0.1 to 1.3 , increment 0.1 .

The trailing-edge LES is presently in progress. As of this date the numerical integration has advanced approximately 1.5 flow-through times based on the free-stream velocity. It is too early to collect meaningful statistics. An instantaneous streamwise velocity field in mid-span is plotted in Fig. 4. One notices that there is

no visible flow separation on the suction side of the edge. This could be caused either by the initial transients still present at this stage of simulation or by insufficient spatial resolution in this preliminary run. The grid spacing in wall units is estimated to be $\Delta x_{2min}^+ \approx 2$, $\Delta x_3^+ \approx 55$, and $\Delta x_1^+ \approx 220$ at inlets and 100 near the trailing edge. Thus, the resolution is quite poor compared with that of typical wall-bounded LES practices.

2.2 Acoustic formulation

A solution to the Lighthill equation in frequency domain can be expressed in terms of convolution integrals with an appropriate Green's function (Goldstein 1976),

$$\begin{aligned} \hat{\rho}_a(\mathbf{x}, \omega) = & M^2 \int_V \hat{T}_{ij}(\mathbf{y}, \omega) \frac{\partial^2 G}{\partial y_i \partial y_j}(\mathbf{x}, \mathbf{y}, \omega) d^3 \mathbf{y} \\ & + M^2 \int_S n_j \hat{p}_{ij}(\mathbf{y}, \omega) \frac{\partial G}{\partial y_i}(\mathbf{x}, \mathbf{y}, \omega) d^2 \mathbf{y}, \end{aligned} \quad (1)$$

where ρ_a denotes the density perturbation and the caret denotes temporal Fourier transform. $T_{ij} = \rho v_i v_j + \delta_{ij} (p - \rho/M^2) - \tau_{ij}$ is the Lighthill stress tensor defined in terms of the fluctuating velocity relative to the free-stream value ($v_i = u_i - \delta_{i1}$), the entropy (second term), and the viscous stress tensor τ_{ij} . $p_{ij} = p \delta_{ij} - \tau_{ij}$ is the compressive stress tensor, \mathbf{x} and \mathbf{y} are the coordinates of the observation point and the source point, respectively, and n_i denotes the directional cosine of the outward normal (into the fluid) to the rigid surface S over which the surface integration takes place. The volume integral is taken over the entire unsteady flow region V external to the body. G is the Green's function which satisfies the modified wave (Helmholtz) equation

$$\left(\frac{\partial^2}{\partial x_j \partial x_j} + k^2 \right) G(\mathbf{x}, \mathbf{y}, \omega) = -\delta(\mathbf{x}, \mathbf{y}) \quad (2)$$

and the appropriate boundary conditions. Equations (1) and (2) are written in a dimensionless form. The velocity, density, and pressure are nondimensionalized by the undisturbed free-stream values U'_∞ , ρ'_∞ , and $\rho'_\infty U'^2_\infty$, respectively. The spatial coordinates are normalized by the hydrofoil thickness h' . The frequency (ω) is normalized by U'_∞/h' . Re and M denote respectively the free-stream Reynolds number based on h' and the free-stream Mach number. δ_{ij} is the Kronecker delta, and the usual summation convention applies for repeated subscripts.

Except for the neglect of $O(M)$ bulk convection effect, (1) is exact and may serve as the starting point for studying the aeroacoustics of arbitrary flow-body interactions. For instance, the Curle integral (Curle 1955) is obtained if the free-space Green's function is used. A hard-wall Green's function, which satisfies $\partial G / \partial \mathbf{n} = 0$, is required for the calculation of acoustic scattering phenomenon. In general, an analytical expression for Green's function tailored to the complex, acoustically non-compact geometry such as the hydrofoil is nonexistent. Under certain asymptotic limits, however, one may use a known Green's function for a simpler geometry as an approximation.

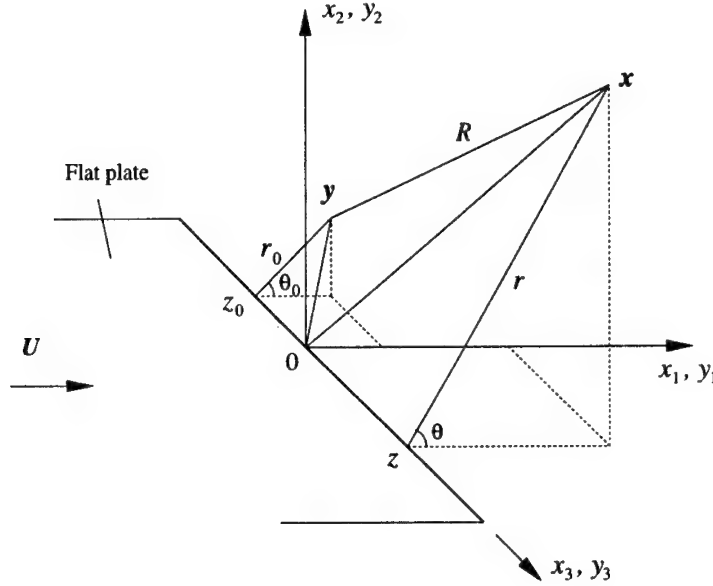


FIGURE 5. Coordinate system for calculating the radiated noise of flow past the trailing-edge of a semi-infinite flat plate.

In the limit that the hydrofoil thickness is much smaller than the acoustic wavelength ($h \ll \lambda_a$), the foil is reasonably approximated by a half-plane with zero thickness, for which the far-field Green's function is known (Ffowcs Williams & Hall 1970; Goldstein 1976):

$$G = \frac{e^{ikR}}{4\pi R} \left(\frac{1}{2} + \frac{e^{-i\frac{\pi}{4}}}{\sqrt{\pi}} \int_0^a e^{iu^2} du \right) + \frac{e^{ikR^*}}{4\pi R^*} \left(\frac{1}{2} + \frac{e^{-i\frac{\pi}{4}}}{\sqrt{\pi}} \int_0^{a^*} e^{iu^2} du \right). \quad (3)$$

In the above equation, the wavenumber $k = M\omega$, and the distances $R = |\mathbf{x} - \mathbf{y}|$ and $R^* = |\mathbf{x} - \mathbf{y}^*|$, where $\mathbf{y}^* = (y_1, -y_2, y_3)$. In the cylindrical coordinate system defined in Fig. 5,

$$R = [r^2 + r_0^2 - 2rr_0 \cos(\theta - \theta_0) + (z - z_0)^2]^{\frac{1}{2}}, \quad (4)$$

$$R^* = [r^2 + r_0^2 - 2rr_0 \cos(\theta + \theta_0) + (z - z_0)^2]^{\frac{1}{2}}, \quad (5)$$

$$a = (2kr_0 \sin \phi)^{\frac{1}{2}} \cos \left(\frac{\theta - \theta_0}{2} \right), \quad (6)$$

$$a^* = -(2kr_0 \sin \phi)^{\frac{1}{2}} \cos \left(\frac{\theta + \theta_0}{2} \right), \quad (7)$$

$$\sin \phi = \frac{r}{[r^2 + (z - z_0)^2]^{\frac{1}{2}}}. \quad (8)$$

For high Reynolds number flows, the viscous stress, entropy, and hence the surface integral are frequently neglected. Substituting (3)-(8) into (1) and retaining only the lowest order terms in M and R^{-1} lead to

$$\begin{aligned} \hat{\rho}_a(\mathbf{x}, \omega) \approx & M^{\frac{5}{2}} \frac{e^{-i\frac{\pi}{4}}}{\pi^{\frac{1}{2}}} \int_V \frac{1}{4\pi R} \frac{(\omega \sin \phi)^{\frac{1}{2}}}{(2r_0)^{\frac{3}{2}}} \\ & \times \left\{ \left(\widehat{v_\theta^2} - \widehat{v_r^2} \right) \left[e^{i(kR+a^2)} \cos\left(\frac{\theta-\theta_0}{2}\right) - e^{i(kR^*+a^{*2})} \cos\left(\frac{\theta+\theta_0}{2}\right) \right] \right. \\ & \left. - 2\widehat{v_r v_\theta} \left[e^{i(kR+a^2)} \sin\left(\frac{\theta-\theta_0}{2}\right) + e^{i(kR^*+a^{*2})} \sin\left(\frac{\theta+\theta_0}{2}\right) \right] \right\} d^3\mathbf{y}. \quad (9) \end{aligned}$$

The strongest far-field noise is generated by the fluctuating Reynolds stress components normal to the scattering edge in a cylindrical region of radius much smaller than the acoustic wavelength ($r_0 \ll \lambda_a$). Within this region, $e^{i(kR+a^2)} \approx e^{i(kR^*+a^{*2})} \approx e^{ikR}$, and the simpler, more familiar form (Goldstein 1976) is recovered. Equation (9) is more suitable for numerical evaluations in that it allows the volume integration to be carried out to larger r_0 values. Since the integrand decays as $r_0^{-3/2}$, a large r_0 bound is beneficial in minimizing the spurious boundary noise caused by nonvanishing source terms at the computational boundary. As demonstrated by Wang *et al.* (1996), boundary errors can severely compromise the accuracy of an acoustic analogy based calculation.

The thin-foil limit ($h \ll \lambda_a$) discussed above covers the relatively low frequency (wavenumber) range of the radiated noise. Since $\lambda_a \sim l_e/M$, where l_e is the eddy size, the approximation is valid for $l_e/h \gg M$, a condition likely to be met by the range of eddies resolvable in the source-field LES, at typical Mach numbers in naval applications.

On the other hand, if $h \gg \lambda_a$, the trailing edge is approximately equivalent to a triangular wedge on the acoustic length scale. By using a conformal mapping technique, Crighton & Leppington (1971) showed that $\hat{\rho}_a \sim M^{2+q/p}$ for a wedge of exterior angle $(p/q)\pi$.

3. Future plans

First, we will continue the LES of the trailing edge flow, and at the same time improve the numerical scheme to achieve higher computational efficiency. Grid-refinement studies will be carried out. Once a reliable, statistically convergent near-field solution is established, the velocity and wall-pressure statistics will be calculated and compared with the experimental measurements of Blake (1975). Cross-correlation and spectral analyses will be conducted to investigate the wall-pressure generation and scattering mechanisms.

The radiated far-field noise will be calculated following the framework outlined in Section 2.2. A remaining formulation issue to be addressed in the course of investigation is the treatment of the infinite, homogeneous spanwise direction in the source integral.

Acknowledgment

This work was supported by ONR grant N00014-95-1-0221.

REFERENCES

- BLAKE, W. K. 1975 *A Statistical Description of Pressure and Velocity Fields at the Trailing Edge of a Flat Strut*, DTNSRDC Report 4241, David Taylor Naval Ship R & D Center, Bethesda, Maryland.
- BLAKE, W. K. 1986 *Mechanics of Flow-Induced Sound and Vibration*, Vol. I and II, Academic Press, London.
- BLAKE, W. K. & GERSHFELD, J. L. 1988 The aeroacoustics of trailing edges. In *Frontiers in Experimental Fluid Mechanics*, Chap. 10, (Gad-el-Hak, M. Eds.), Springer-Verlag.
- BROOKS, T. F. & HODGSON, T. H. 1981 Trailing edge noise prediction from measured surface pressures. *J. Sound & Vib.* **78**, 69-117.
- CHOI, H. 1993 Toward large eddy simulation of turbulent flow over an airfoil. *Annual Research Briefs-1993*, Center for Turbulence Research, Stanford University/NASA Ames, 145-149.
- CRIGHTON, D. G. & LEPPINGTON, F. G. 1971 On the scattering of aerodynamic noise. *J. Fluid Mech.* **46**, 577-597.
- CURLE, N. 1955 The influence of solid boundaries upon aerodynamic sound. *Proc. Royal Soc. Lond. A.* **231**, 505-514.
- DURBIN, P. A. 1995 Separated flow computations with the $k-\epsilon-v^2$ model. *AIAA J.* **44**, 659-664.
- FFOWCS WILLIAMS, J. E. & HALL, L. H. 1970 Aerodynamic sound generation by turbulent flow in the vicinity of a scattering half plane. *J. Fluid Mech.* **40**, 657-670.
- GERMANO, M., PIOMELLI, U., MOIN, P. & CABOT, W. H. 1991 A dynamic subgrid-scale eddy viscosity model. *Phys. Fluids A.* **3**, 1760-1765.
- GOLDSTEIN, M. E. 1976 *Aeroacoustics*, Chap. 4, McGraw-Hill.
- HOWE, M. S. 1978 A review of the theory of trailing edge noise. *J. Sound & Vib.* **61**, 437-465.
- JANSEN K. 1995 Preliminary large-eddy simulations of flow around a NACA 4412 airfoil using unstructured grids. *Annual Research Briefs-1995*, Center for Turbulence Research, Stanford Univ./NASA Ames, 61-72.
- KALTENBACH, H.-J. & CHOI H. 1995 Large-eddy simulation of flow around an airfoil on a structured mesh. *Annual Research Briefs-1995*, Center for Turbulence Research, Stanford Univ./NASA Ames, 51-60.
- LIGHTHILL, M. J. 1952 On sound generated aerodynamically; I. General theory. *Proc. R. Soc. Lond. A.* **211**, 564-587.

- LILLY, D. K. 1992 A proposed modification of the Germano subgrid scale closure method. *Phys. Fluids A*, **3**, 2746-2757.
- LUND T. S. 1994 Large-eddy simulation of a boundary layer with concave stream-wise curvature. *Annual Research Briefs-1994*, Center for Turbulence Research, Stanford Univ./NASA Ames, 185-195.
- MITTAL R. 1996 Progress in LES of flow past a circular cylinder. Article in this volume.
- NA, Y. & MOIN, P. 1996 Direct Numerical Simulation of Turbulent Boundary Layers With Adverse Pressure Gradient and Separation. *Report No. TF-68*, Dept. of Mech. Engr., Stanford Univ.
- PAULEY, L. L., MOIN, P. & REYNOLDS, W. C. 1988 *Numerical Study of Unsteady Laminar Boundary Layer Separation*, Report No. TF-34, Dept. of Mech. Engr., Stanford Univ.
- WANG, M. 1995 Aerodynamic sound of flow past an airfoil . *Annual Research Briefs-1995*, Center for Turbulence Research, Stanford Univ./NASA Ames, 257-271.
- WANG, M., LELE, S. K. & MOIN, P 1996 Computation of quadrupole noise using acoustic analogy. *AIAA J.* **34**, 2247-2254.
- ZAWADZKI, I., GERSHFELD, J. L., NA, Y. & WANG M. 1996 Hydroacoustic forcing function modeling using DNS database. *Proc. 1996 Summer Program*, Center for Turbulence Research, Stanford Univ./NASA Ames, 369-382.

A model for the onset of vortex breakdown

By K. Mahesh

1. Motivation and objectives

A large body of information exists on the breakdown of incompressible streamwise vortices. Less is known about vortex breakdown at high speeds. An interesting example of supersonic vortex breakdown is the breakdown induced by the interaction of vortices with shock waves. The flow in supersonic engine inlets and over high-speed delta wings constitute technologically important examples of this phenomenon, which is termed 'shock-induced vortex breakdown'.

In this report, we propose a model to predict the onset of shock-induced vortex breakdown. The proposed model has no adjustable constants, and is compared to both experiment and computation. The model is then extended to consider two other problems: the breakdown of a free compressible vortex, and free incompressible vortex breakdown. The same breakdown criterion is used in all three problems to predict the onset of breakdown. Finally, a new breakdown map is proposed that allows the simultaneous comparison of data from flows ranging from incompressible breakdown to breakdown induced by a shock wave.

This work is described in detail by Mahesh (1996); only the prominent results are presented in this report.

2. Accomplishments

2.1 Shock-induced breakdown

Figure 1 shows a schematic of the interaction between a streamwise vortex and a normal shock wave. The axial flow is from left to right. The variables x and r are used to denote the axial and radial coordinate respectively. The axial and swirl components of velocity are denoted by U and v_θ respectively, and p , ρ , and T represent the pressure, density, and temperature. The subscripts ' ∞ ' and ' c ' correspond to values in the free-stream and the centerline of the vortex, and the states upstream and downstream of the shock wave are respectively denoted by the subscripts '1' and '2' (e.g., $p_{\infty 2}$ denotes the free-stream pressure downstream of the shock wave). This report will occasionally refer to the variables, γ , Γ , and M_∞ . γ denotes the ratio of specific heats and is taken as 1.4. Γ is the swirl number of the vortex and is defined as $\Gamma = v_{\theta m}/U_\infty$ where $v_{\theta m}$ denotes the maximum swirl velocity. M_∞ is the free-stream Mach number, defined as $M_\infty = U_\infty/c_\infty$.

The model is obtained as follows. First, a simple criterion for breakdown of the upstream vortex is proposed. The properties of the upstream vortex are then substituted into the criterion. The resulting equation is then rearranged to obtain an expression for the critical swirl number above which the vortex would break down.

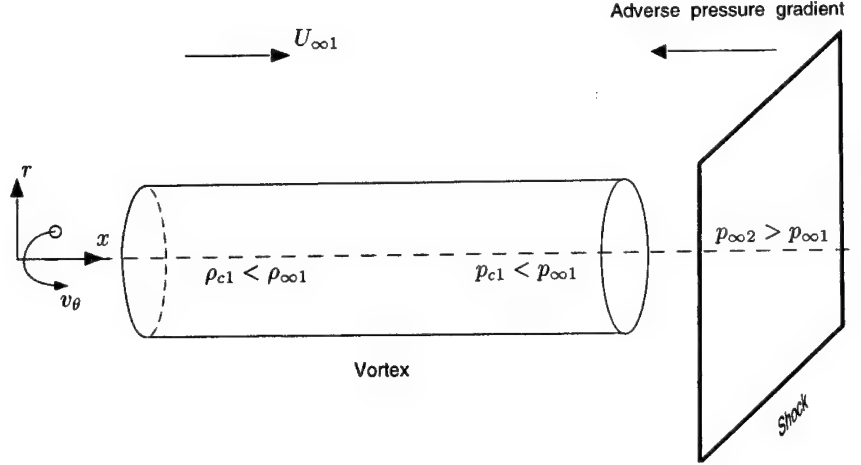


FIGURE 1. Schematic of the interaction between a streamwise vortex and a normal shock wave.

The breakdown criterion is based upon an approximation to the axial momentum equation at the centerline of the vortex. Consider the vortex impinging upon the shock wave. The vortex experiences an adverse streamwise pressure rise, which may be quantified by the pressure difference, $p_{\infty 2} - p_{c1}$. The fluid in the vortex has a certain inertia in the streamwise direction, which may be quantified by the streamwise momentum flux, $\rho_{c1} U_{c1}^2$. Breakdown is assumed to occur if the axial pressure rise exceeds the upstream streamwise momentum flux, thereby stagnating the flow; i.e., if

$$\begin{aligned} p_{\infty 2} - p_{c1} &\geq \rho_{c1} U_{c1}^2 \\ &\geq \rho_{c1} U_{\infty 1}^2 \left(1 + \frac{\Delta U}{U_{\infty 1}} \right)^2 \end{aligned} \quad (1)$$

where ΔU denotes the upstream excess in axial velocity at the centerline. If the axial velocity is uniform, then $\Delta U = 0$. Using $p_{\infty 1}$, $\rho_{\infty 1}$ and $T_{\infty 1}$ to non-dimensionalize the pressure, density, and temperature respectively, Eq. 1 may be rewritten for uniform axial velocity as

$$\tilde{p}_{\infty 2} - \tilde{p}_{c1} = \gamma \tilde{\rho}_{c1} M_{\infty 1}^2, \quad (2)$$

where the 'tilde' is used to denote non-dimensional variables.

The Rankine vortex is used to approximate the swirl velocity in the upstream vortex. Two different idealizations of the thermodynamic field in the upstream vortex are considered: spatially uniform stagnation temperature and spatially uniform entropy. The radial momentum equation is then easily integrated to obtain the density and pressure at the centerline of the upstream vortex, i.e. \tilde{p}_{c1} and $\tilde{\rho}_{c1}$, are obtained in terms of Γ and $M_{\infty 1}$. The Rankine-Hugoniot equations for a normal shock express $\tilde{p}_{\infty 2}$ in terms of the upstream Mach number, $M_{\infty 1}$. Substituting for

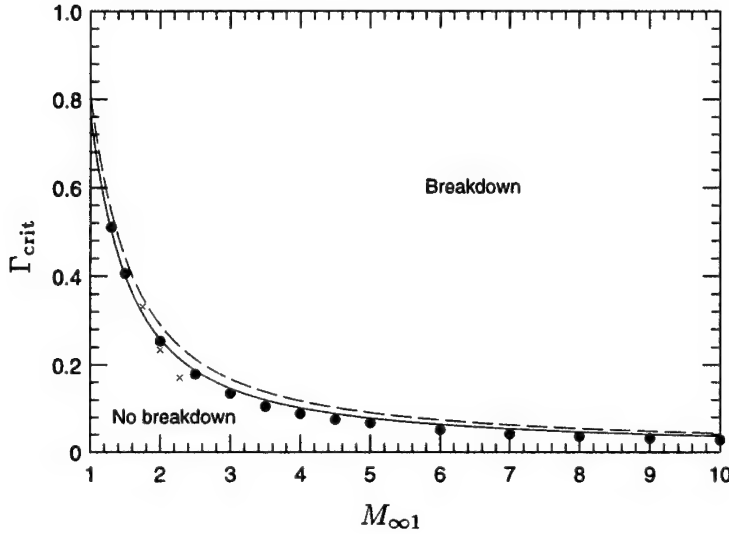


FIGURE 2. Comparison of predicted critical swirl number to experiment and computation of shock-induced vortex breakdown. — (Prediction: uniform stagnation temperature), ---- (Prediction: uniform entropy), • (Computation), × (Experiment).

\tilde{p}_{c1} , $\tilde{\rho}_{c1}$, and $\tilde{p}_{\infty 2}$ into the above breakdown criterion will therefore yield an expression for the critical swirl number Γ_{crit} in terms of Mach number of the shock wave. This expression is given below.

Uniform stagnation temperature vortex

The critical swirl number is given by:

$$\Gamma_{crit} = \frac{1}{M_{\infty 1}} \sqrt{\frac{2}{\gamma - 1} \left\{ 1 - \left(\frac{1}{1 + \gamma M_{\infty 1}^2} \left[1 + \frac{2\gamma}{\gamma + 1} (M_{\infty 1}^2 - 1) \right] \right)^{\frac{\gamma - 1}{2\gamma}} \right\}}. \quad (3)$$

Uniform entropy vortex

The critical swirl number is given by the following implicit equation:

$$1 + \frac{2\gamma}{\gamma + 1} (M_{\infty 1}^2 - 1) - [1 - (\gamma - 1) \Gamma_{crit}^2 M_{\infty 1}^2]^{\frac{\gamma}{\gamma - 1}} = \gamma M_{\infty 1}^2 [1 - (\gamma - 1) \Gamma_{crit}^2 M_{\infty 1}^2]^{\frac{1}{\gamma - 1}}. \quad (4)$$

Results for the critical swirl number are presented for the case where the axial velocity is uniform. Figure 2 shows the predicted values of the critical swirl number as a function of the Mach number of the shock. The predicted values are compared to the experimental values reported by Delery *et al.* (1984) and the computations by Erlebacher *et al.* (1996). Good agreement is seen. The critical swirl number is predicted to decrease with increasing Mach number as observed. According to the proposed criterion, this decrease in Γ_{crit} is due to a combination of two factors:

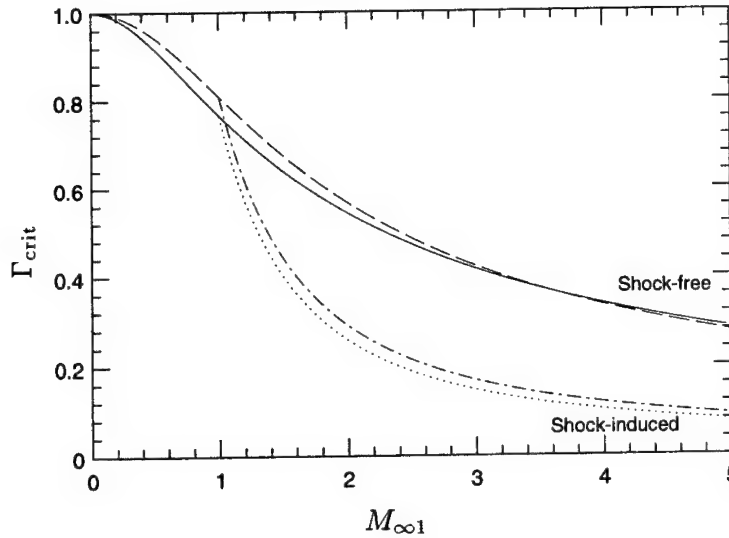


FIGURE 3. Predicted critical swirl number for shock-free vortex breakdown compared to the prediction for shock-induced breakdown. — (Shock-free: uniform stagnation temperature), ---- (Shock-free: uniform entropy), (Shock-induced: uniform stagnation temperature), -.-.- (Shock-induced: uniform entropy).

increase in the adverse pressure rise (due to $\tilde{p}_{\infty 2}$ increasing while \tilde{p}_{c1} decreases) and decrease in streamwise momentum flux (due to $\tilde{\rho}_{c1}$ decreasing) with increasing Mach number.

The ability of the model to predict the onset of shock-induced breakdown was further evaluated (Mahesh 1996) by comparing to the experimental data of Metwally *et al.* (1989). The 'strong interactions' observed experimentally were seen to lie in the region where the model predicts breakdown, while the 'weak interaction' regions were seen to lie in the predicted region of non-breakdown. Also, the influence of an excess/deficit in the centerline axial velocity, and obliquity of the shock wave on the critical swirl number was considered (Mahesh 1996). Jet-like profiles of the axial velocity were observed to delay breakdown, while a wake-like profile made the vortex more susceptible to breakdown. For fixed upstream Mach number, Γ_{crit} was predicted to increase as the shock became increasingly oblique.

2.2 Shock-free breakdown of a compressible vortex

The breakdown of a free axisymmetric vortex, i.e. breakdown in the absence of an externally imposed pressure gradient, is considered in this section. The arguments used are identical to those in breakdown induced by a shock. In the absence of the shock, the vortex discharges into the atmosphere. The difference between atmospheric pressure, ($p_{\infty 1}$), and the pressure at the vortex centerline, (p_{c1}), provides the adverse pressure rise that causes breakdown. Breakdown of the vortex is therefore assumed to occur when

$$1 - \tilde{p}_{c1} = \gamma \tilde{\rho}_{c1} M_{\infty 1}^2 \quad (5)$$

S_{crit}	
Quasi-cylindrical	1.41
Axisymmetric N-S	1.35
Bossel	1.12
Squire	1.4
Benjamin	1.4
Num. simulation	1.28
Spall <i>et al.</i>	1.37
Present	1.4

TABLE 1. Prediction of critical swirl number for incompressible vortex breakdown compared to other approaches. All data other than the present reproduced from review article by Delery (1993).

which is identical to the expression obtained when $\tilde{p}_{\infty 2}$ is set equal to one in Eq. 2. The corresponding expressions for the critical swirl number are given below.

Uniform stagnation temperature vortex

$$\Gamma_{\text{crit}} = \frac{1}{M_{\infty 1}} \sqrt{\frac{2}{\gamma - 1} \left[1 - \left(\frac{1}{1 + \gamma M_{\infty 1}^2} \right)^{\frac{\gamma - 1}{2\gamma}} \right]}. \quad (6)$$

Uniform entropy vortex

$$1 - [1 - (\gamma - 1)\Gamma_{\text{crit}}^2 M_{\infty 1}^2]^{\frac{\gamma}{\gamma - 1}} = \gamma M_{\infty 1}^2 [1 - (\gamma - 1)\Gamma_{\text{crit}}^2 M_{\infty 1}^2]^{\frac{1}{\gamma - 1}}. \quad (7)$$

Figure 3 shows the predicted values of the critical swirl number as a function of the free-stream Mach number. Also shown (for supersonic flow) are the values obtained for breakdown induced by a shock wave at the same Mach number. Compressibility is seen to make the vortex more susceptible to breakdown. A similar trend was noted by Keller (1994). This trend may be explained by noting that increasing the free-stream Mach number decreases the centerline pressure and density, thereby increasing the adverse pressure rise while decreasing the axial momentum flux. The predicted values of Γ_{crit} in the absence of the shock are seen to be greater than those predicted for shock-induced breakdown. This trend can be explained by noting that the pressure rise across the shock wave produces a larger adverse pressure rise for the same upstream momentum flux.

2.3 Incompressible vortex breakdown

Figure 3 shows that as $M_{\infty 1}$ tends towards 0, Γ_{crit} tends towards 1. An incompressible vortex in the absence of externally imposed adverse pressure gradients is

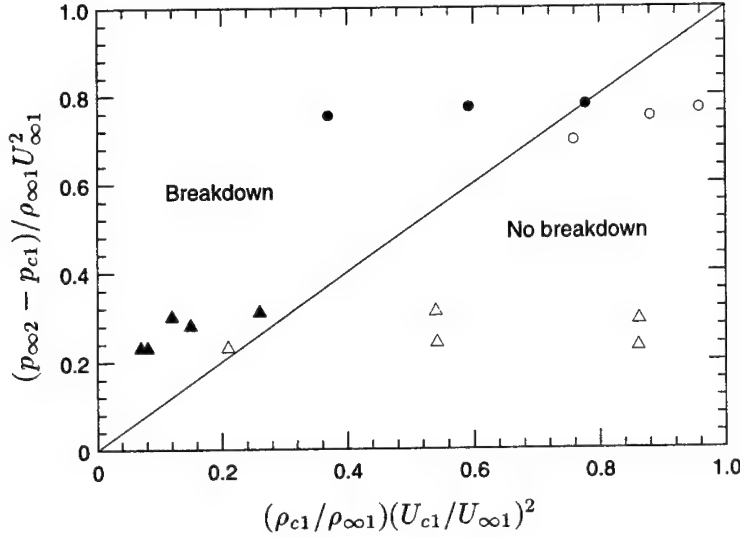


FIGURE 4. Evaluation of the proposed breakdown map in predicting the onset of vortex breakdown. • (Experiment: breakdown), ◦ (Experiment: no breakdown), ▲ (Computations: breakdown), △ (Computations: no breakdown).

therefore predicted to undergo breakdown at a critical swirl number of one. In a recent review article, Delery (1993) documents (section 3.4.5 of his paper) critical swirl numbers for incompressible vortex breakdown as predicted by different theories. He considers a Burger's vortex and defines a swirl parameter S , which is related to the swirl number Γ by,

$$S = \frac{\Gamma}{1 - e^{-1.256}} = 1.398 \Gamma. \quad (8)$$

Thus $\Gamma_{\text{crit}} = 1$ corresponds to $S_{\text{crit}} = 1.398 \sim 1.4$. Table 1 reproduces from Delery's paper the critical swirl numbers obtained by different approaches. Our simple criterion is seen to agree well with the other data.

2.4 A 'universal' breakdown map

The preceding sections presented results for the onset of vortex breakdown by plotting the critical swirl number as a function of Mach number. The curve $\Gamma_{\text{crit}} = \Gamma_{\text{crit}}(M_{\infty 1})$ defined the boundary between the regimes of breakdown and non-breakdown. However, the critical swirl number is not universal (as also observed by Delery, 1993). Different curves were obtained for Γ_{crit} for the different problems. In this section, a breakdown map that allows a common breakdown boundary to be defined for all of the above mentioned problems is proposed. It is suggested that a plot of $p_{\infty 2} - p_{c1}$ against $\rho_{c1} U_{c1}^2$ could be used to map the onset of vortex breakdown. The proposed map could even be used for incompressible vortex breakdown, and would be expected to adequately represent the onset of breakdown induced by pressure gradients acting over distances that are small as compared to a characteristic lengthscale of the vortex. The curve $p_{\infty 2} - p_{c1} = \rho_{c1} U_{c1}^2$ (the 45° line) would act as

the boundary between the breakdown and non-breakdown regimes. The proposed map is illustrated in Fig. 4. Note that the pressure rise and momentum flux are non-dimensionalized by $\rho_{\infty 1} U_{\infty 1}^2$ to allow incompressible data to be plotted. Experimental data on normal shock/vortex interaction from Metwally *et al.* (1989) is also shown. The breakdown and non-breakdown cases are seen to be appropriately delineated. Also plotted are data on oblique shock/vortex interaction from the recent computations by Nedungadi and Lewis (1996). Numerical solutions of the constant stagnation temperature Burger's vortex were used to obtain the centerline pressure and density since the vortices considered had a velocity deficit. With the exception of one point (run 8 in their paper), the proposed map appropriately delineates the 'strong' and 'weak' interactions observed in the computations.

3. Conclusions

A simple inviscid model was proposed to predict the onset of breakdown in an axisymmetric vortex. Three problems were considered: shock-induced breakdown, free compressible breakdown, and free incompressible breakdown. A formula with no adjustable constants was derived for the critical swirl number in all three problems. Comparison to experimental and computational data showed good agreement. Finally, a new breakdown map that allows a common breakdown boundary to be defined for a wide range of flows was proposed.

Acknowledgments

This work was supported by the AFOSR under Contract F49620-92-J-0128 with Dr. Len Sakell as technical monitor. I am thankful to Mr. Keith Lucas and Profs. Sanjiva Lele, Parviz Moin, and Peter Bradshaw for helpful discussions.

REFERENCES

- DELERY, J.M. 1993 Aspects of vortex breakdown. *Prog. Aerosp. Sci.* **30**, 1-59.
- DELERY, J.M., HOROWITZ, E., LEUCHTER, O. & SOLIGNAC, J.L. 1984 Fundamental studies on vortex flows. *La Recherche Aeronautique*. **2**, 1-24.
- ERLEBACHER, G., HUSSAINI, M.Y. & SHU, C-W 1996 Interaction of a shock with a longitudinal vortex. *NASA CR-198332, ICASE Report 96-31*.
- KELLER, J.J. 1994 On the practical application of vortex breakdown theory to axially symmetric and three-dimensional compressible flow. *Physics of Fluids*. **6**, 1515-1523.
- MAHESH, K. 1996 A model for the onset of breakdown in an axisymmetric compressible vortex. *Physics of Fluids*. **8**, 3338-3345. Also CTR Manuscript 161.
- METWALLY, O., SETTLES, G.S. & HORSTMAN, C. 1989 An experimental study of shock/vortex interaction. *AIAA Paper 89-0082*.
- NEDUNGADI, A. & LEWIS, M.J. 1996 Computational study of the flowfields associated with oblique shock/vortex interactions. *AIAA J.* **34**, 2545-2553.

Compressing an elliptic vortex: transition to turbulence by tumble breakdown

By Fabien S. Godeferd¹, Nagi N. Mansour² AND Claude Cambon¹

1. Motivations and objectives

Stability of the elliptic vortex attracted interest in the past decade. Cambon (1982), and Cambon, Teissèdre and Jeandel (1985) have studied the stability of such flows with spatially uniform velocity gradient, and have provided RDT solutions for a wide range of the parameter S/Ω (where the strain rate S and the vorticity 2Ω define the velocity gradient matrix). The range studied included those of hyperbolic streamlines (strain dominated, $S/\Omega > 1$), linear streamlines (simple shear, $S/\Omega = 1$), and elliptical streamlines (vorticity dominated, $S/\Omega < 1$). The latter class has more recently attracted interest and several studies appeared (Pierrehumbert 1986, Bayly 1986, Craik and Criminale 1986). These studies will be collectively referred to as PBCC. Recent review of the subject of instability of elliptic flows and significant progress in this area can be found in Waleffe (1990).

Background linear instability (in the elliptic core of actual eddies) was shown to be the active mechanism in several complex transitional and turbulent flows, including mixing layers, wakes, trailing vortices, etc. This was the primary motivation for the study of stability and transition to turbulence using Direct Numerical Simulations (DNS) by Blaisdell and Shariff (1994) and by Lundgren and Mansour (1996) for a confined elliptic vortex. Linear stability analysis of an unbounded elliptic vortex, stretched along its axis, was analytically performed by Le Dizès, Rossi and Moffat (1996, hereafter referred to as L-DRM). The case of a circular unbounded vortex, periodically compressed along its axis, was studied by Mansour & Lundgren (1990). This study showed that the flow displays a parametric instability due to the interaction between vorticity and periodic compression, *in the absence of ellipticity, or additional weak planar strain*. The present paper shares the motivations of these previous works regarding fundamental aspects of transition to turbulence, and is particularly connected to the latter three papers. Another specific motivation, however, comes from the dynamics of turbulence in reciprocating engines, as presented hereafter.

During the compression stroke, both *swirl* (axis parallel to the direction of compression) and *tumble* (axis perpendicular to the direction of compression) mean vortices are present. These vortices evolve in different ways. The swirling motion is stabilized by the compression (even if potential instabilities exist, as shown by Mansour & Lundgren 1990), whereas the tumble motion (created by the off-set

¹ LMFA UMR 5509 – École Centrale de Lyon – France

² NASA Ames Research Center

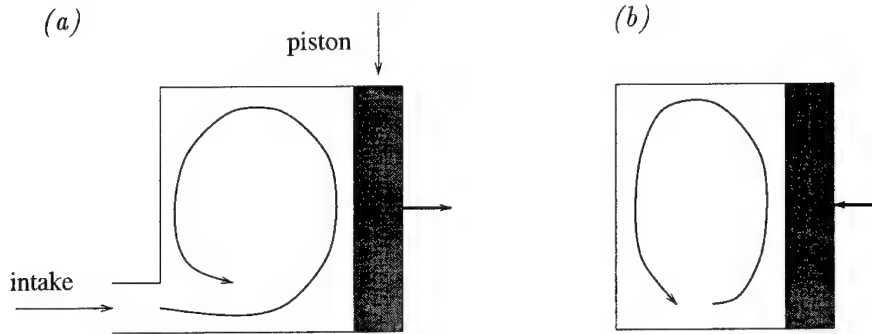


FIGURE 1. Sketch (a) of the generation of the tumble by injection in the experiment, (b) and the following compression of the tumble.

from the symmetry axis of the intake-valve jet) is often observed to break down. Such a breakdown is desirable near the end of the compression stroke, since it could enhance turbulence and mixing at the beginning of the combustion stroke. This problem has motivated research projects which involve both an experimental study of a compressed tumble (Marc *et al.*, 1996) and a related numerical approach using single-point closures (Leroy and Le Penven, 1996). A sketch of the experimental setup is shown in Fig. 1.

The three-dimensional character of the disturbances within a parametric instability of the elliptical-type was not addressed in previous studies.

2. Linear stability and RDT approach to the unbounded flow

Rapid Distortion Theory (RDT) and linear stability analysis start from the same equations in the case of background (or mean) flow with uniform velocity gradient. The background (mean) velocity field is a solution of the Euler equations. The disturbance (or fluctuating) field can be sought under the form of time-dependent three-dimensional Fourier modes. On the one hand, considering a single-mode disturbance field, the solutions of the linearized equations are exact solutions (as pointed out by Craik and Criminale, 1986). On the other hand, RDT considers a sum over all of the Fourier modes, nonlinear coupling terms are neglected through the RDT assumption. This approach has the advantage that the computation of statistics is possible. Statistical homogeneity, in the sense of ensemble average, for the disturbance field is preserved by the space-uniform mean distortion, and, in turn, is consistent with the decoupling of the 'mean' flow (solution of Euler equations) in the absence of feedback from the Reynolds stress gradient.

2.1 The background flow

In three dimensions, we are concerned with the following mean velocity gradient matrix:

$$U_{i,j} \rightarrow \begin{pmatrix} -S(t) & -\Omega(t) & 0 \\ \Omega(t) & 0 & 0 \\ 0 & 0 & 0 \end{pmatrix} \quad (1)$$

where the mean velocity field $U_i = \lambda_{ij}(t)x_j$ is a superposition of a pure compression flow of rate $S(t)$ and a pure rotation flow of angular velocity $\Omega(t)$, or vorticity $2\Omega(t)$, where t is the time variable. The compression is chosen along the axis 1, and the vorticity vector is along the axis 3, in agreement with a 'tumble' flow pattern. The compression rate S is calculated given a uniform lengthscale variation law in the x_1 direction

$$L(t)/L(0) = \frac{(1 + 1/r)}{2} + \frac{(1 - 1/r)}{2} \cos(2\omega t) \quad (2)$$

so that

$$S(t) = -\dot{L}/L \quad \text{and} \quad \Omega(t) = \Omega_0 L(0)/L(t), \quad (3)$$

where $\dot{\{ \}}$ indicates the time derivative. The latter equation ensures that the mean velocity field is a solution of the Euler equations and reflects the conservation of angular momentum. The compression law (2), or equivalently the volumetric law, is roughly similar to the one in an actual engine, where r is the maximum volumetric ratio which is reached when $2\omega t = \pi$ (see also Mansour & Lundgren 1990). Hence the three parameters r , ω , and Ω_0 completely characterize the background flow. Of course, different $L(t)$ -laws can be used in Eqs. (3) and (1) if necessary.

Elliptic stream-functions corresponding to Eq. (1) are more classically formulated in a system where the axes are rotated ($\alpha = \pi/4$) around the x_3 direction, so that

$$U_{i,j} \rightarrow \begin{pmatrix} -S/2 & -S/2 - \Omega & 0 \\ -S/2 + \Omega & -S/2 & 0 \\ 0 & 0 & 0 \end{pmatrix} \quad (1')$$

and the extra-diagonal part is the same as the one considered by PBCC, but with time-dependent coefficients. Splitting the matrix into trace and deviator, one finds

$$\begin{pmatrix} -S/3 & 0 & 0 \\ 0 & -S/3 & 0 \\ 0 & 0 & -S/3 \end{pmatrix} + \begin{pmatrix} -S/6 & -S/2 - \Omega & 0 \\ -S/2 + \Omega & -S/6 & 0 \\ 0 & 0 & S/3 \end{pmatrix} \quad (1'')$$

in which the trace-free (incompressible) part is similar to the one considered by L-DRM.

2.2 Linear stability and RDT

After splitting the velocity and pressure field into a background (capital letters) and a disturbance part (lower case letters), namely $U_i + u_i$ and $P + p$, the linearized equations for the disturbances are solved using three-dimensional Fourier modes in the coordinate system that follows the background field. Note that this approach is Lagrangian with respect to the mean trajectories. With the method used by Cambon and coworkers since the early eighties (see Cambon *et al.*, 1994, for an up-to-date presentation in English), the linear problem amounts to solving a system of two coupled differential equations for two solenoidal components of the disturbance velocity field, along trajectories in Fourier space. The numerical code (denoted MITHRA) is basically the same as the one used by Cambon (1982) and Cambon

et al. (1985) to study the effects of the elliptical flow instability on the turbulence statistics.

The linear solutions are computed under the form of two matrices:

- The first one is the Lagrangian displacement tensor $F_{ij}(t, 0) = \partial x_i / \partial X_j$ which characterizes the background flow trajectories in physical and spectral space, or:

$$x_i = F_{ij}(t, 0)X_j \quad k_i = F_{ji}^{-1}(t, 0)K_j \quad k_i x_i = K_i X_i \quad (4)$$

where space coordinates and wavevectors in capital letters stand for Lagrangian ones with respect to the mean. Similar formalism used in DNS is often referred to as 'Rogallo space' (Rogallo, 1981).

- The second one, denoted $g_{\alpha\beta}(\mathbf{k}/k, t, 0)$, characterizes the linear inviscid response of the disturbance field. The number of components is minimal (rank-two matrix), when taking into account the solenoidal property. This is equivalent to the fact that the velocity Fourier amplitude vector lies in the plane normal to the wave vector. More details are summarized in the appendix.

These two matrices completely characterize the inviscid linear stability problem. In addition, the viscous contribution can be obtained easily, as recently recovered by Landman and Saffman (1987) in the particular case of the elliptic flow. The statistics of homogeneous turbulence can be computed as well, given an initial form for the velocity statistical moments (e.g. isotropic), as has been done in classic RDT for over forty years (Batchelor and Proudman, 1954).

Compared to previous linear stability and RDT studies, the case of the compressed tumble presents some original features as follows:

- The background flow is compressible. An important parameter is the volumetric ratio $J = \det \mathbf{F}$, equal to $L(t)/L(0)$ for a one-dimensional compression. This brings only a few changes since the disturbance field is solenoidal, meaning that we deal here with *compressed*, but not compressible turbulence. This type of approximation is justified at low Mach number, as discussed by Mansour & Lundgren (1990). Note that the spherical part of the mean velocity gradient matrix, as in Eq. (1''), could be removed from consideration by a rescaling of the disturbance field (Cambon *et al.*, 1992).
- The ellipticity and vorticity are continuously varying in a very different way from that in the study by L-DRM, even though axial stretching and the related increase of the axial vorticity were similar, looking at the incompressible part of (1''). In the compressed case addressed by Mansour & Lundgren, the axial vorticity was steady and there was no ellipticity.

Typical results for stability analysis are presented as a function of the angular distribution of the matrix \mathbf{g} in wave-space. Since, indeed, in the unbounded inviscid case, it depends only on the orientation of the wave vector and not on its modulus.

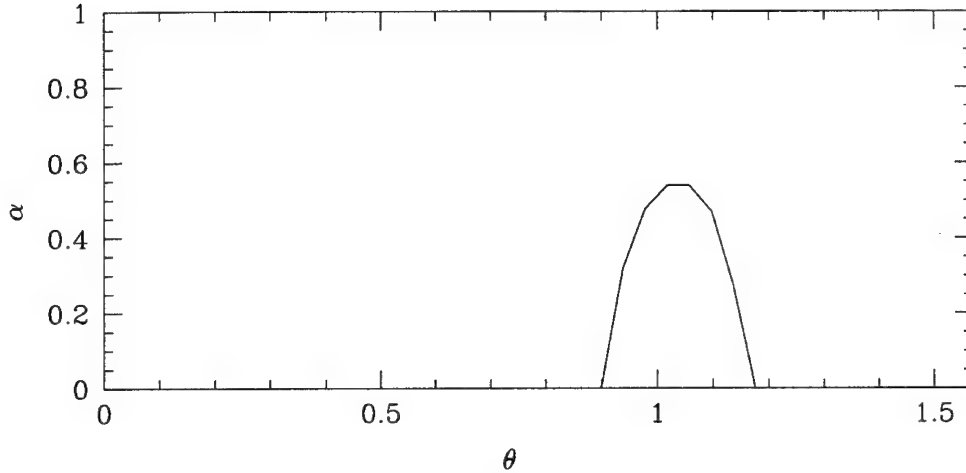


FIGURE 2. Elliptic vortex: Floquet parameter α as a function of the orientation θ of the Fourier mode \mathbf{k} . The peak value is located around $\theta = \pi/3$ with a maximum close to $9/16$ (see e.g. Waleffe, 1990).

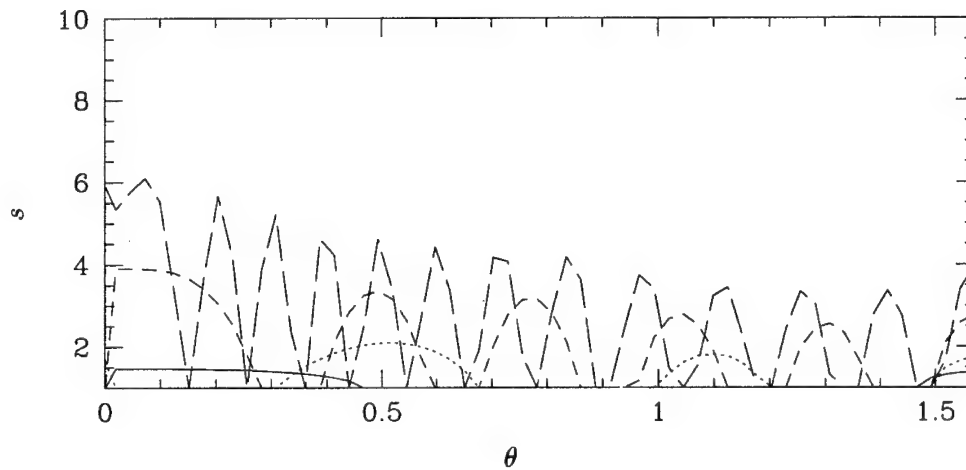
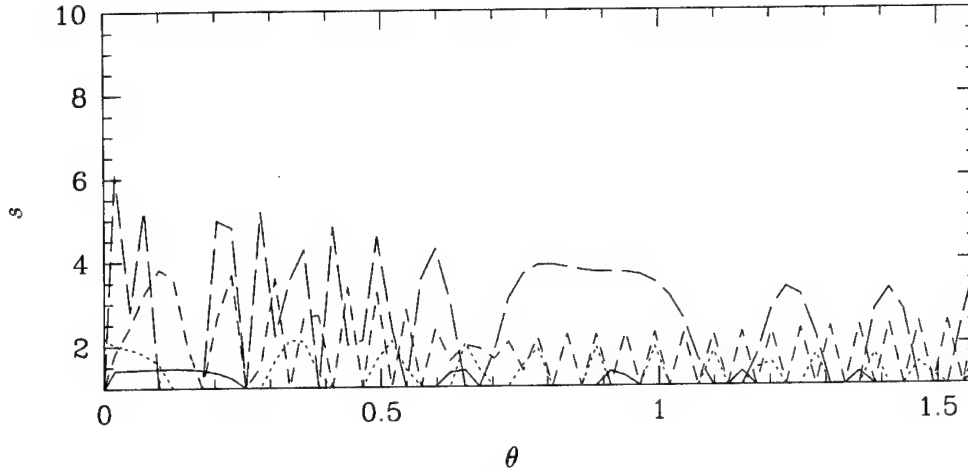
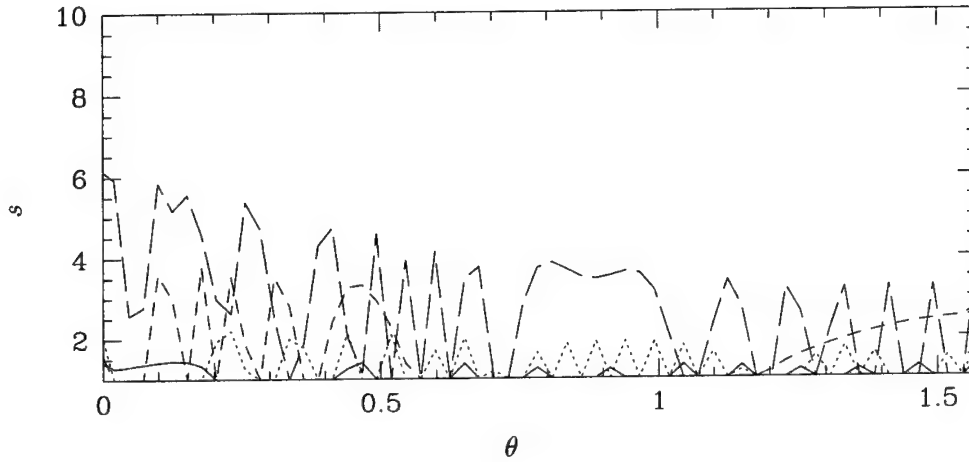


FIGURE 3. Same as Fig. 6 with $\Omega_0 = 100$.

Figure 2 shows the case of the classic elliptic instability (the diagonal terms are not present in Eq. (1')) and S and Ω are chosen constants. The maximum eigenvalue s of \mathbf{g} is computed after a period $T = 2\pi/\sqrt{\Omega^2 - S^2}$, which with respect to \mathbf{F} corresponds to the time needed for closing elliptic trajectories. Under the form of a non-dimensional Floquet coefficient α defined from $s = \exp(\alpha ST)$, the classic distribution is recovered when the angle of \mathbf{K} with the axis of the vortex (x_3) varies from 0 to $\pi/2$ at $K_1 = 0$. Accordingly, a single peak of instability emerges around $\pi/3$, with a maximum close to $9/16$ (Waleffe, 1989, Cambon *et al.*, 1994).

Figures 3, 4, and 5 show the corresponding case for the compressed tumble at

FIGURE 4. Same as Fig. 6 with $\Omega_0 = 500$.FIGURE 5. Same as Fig. 6 with $\Omega_0 = 1000$.

four different non-dimensional times (or crank angles) ($2\omega t = \pi/4, \pi/2, 3\pi/2, \pi$ in Eq. (2)). The tumble is assumed to be circular at the initial time since $S = 0$, and to have the maximum aspect ratio r at the final time. A convenient 'realistic' choice of parameters in the context of reciprocating engines is $r = 10$, $2\omega = 52 \text{ s}^{-1}$, with different values for $\Omega_0 = 100$ (Fig. 3), $\Omega_0 = 500$ (Fig. 4), $\Omega_0 = 1000$ (Fig. 5).

Compared to the case of the stationary elliptic vortex where a single instability peak is exhibited and to the elongated elliptic vortex (Le Dizès *et al.*, 1996) where the instability growth is inhibited by a sufficiently rapid stretching rate, the present results are completely different and particularly important regarding a possible 'explosive' instability. The case of pure compression ($\Omega_0 = 0$) is also shown in Fig. 6 to contrast with the tumble case. The only case where a number of instability

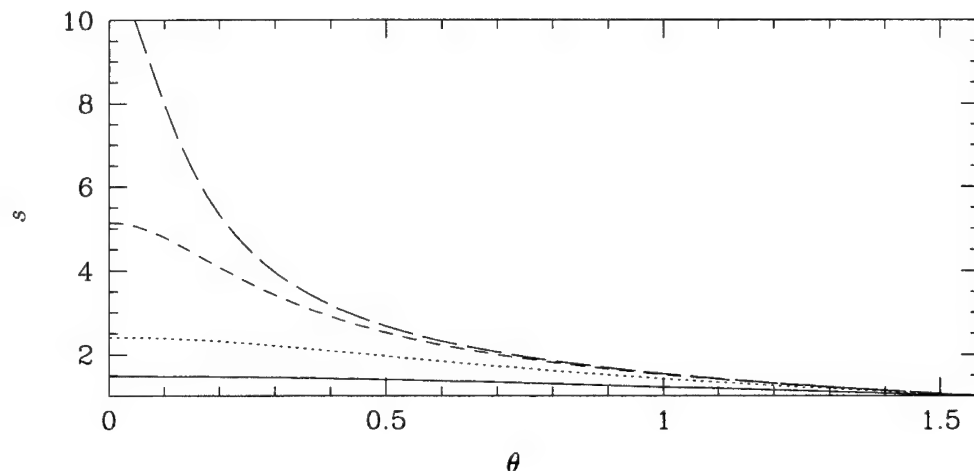


FIGURE 6. Maximum eigenvalue s of the amplification matrix \mathbf{g} for different orientations θ of the Fourier mode \mathbf{k} . This case with no vorticity $\Omega_0 = 0$, at different crank angles: —, $\omega t = \pi/4$; ·····, $\omega t = \pi/2$; ----, $\omega t = 3\pi/4$; -·-·-, $\omega t = \pi$.

bands were found is the periodically compressed swirl flow (Mansour & Lundgren 1990), but our results display an unexpected number of unstable thin bands. The most general analytical results for the steady elliptical flow and the periodically compressed swirl flow, which are based on Hill's equations, are summarized in the appendix.

Figure 7 shows that the kinetic energy history is weakly affected by the complex instability distribution. The growth of the turbulent kinetic energy reflects the scrambling effect of rotation, which diminishes the Reynolds stress anisotropy and, therefore, the energy production. As a result, the energy growth rate is reduced by the presence of rotation.

3. Future plans

Linear analysis has shown that tumble will play an important role in the evolution of turbulence which is subjected to compression. We plan to carry out a DNS of this flow. The DNS will follow the approach of Lundgren and Mansour (1996) where a confined elliptic flow was studied. The velocity field will be expanded in sine and cosine series in x - and y -directions and Fourier series in the z -direction. The y -coordinate will move in time following a one-dimensional compression.

Appendix A. A short review of the analytical works using Hill's equations

In this appendix we develop the linearized equations for a general uniform deformation tensor and summarize the various studies used to analyze the instability of flows under rotation and strain.

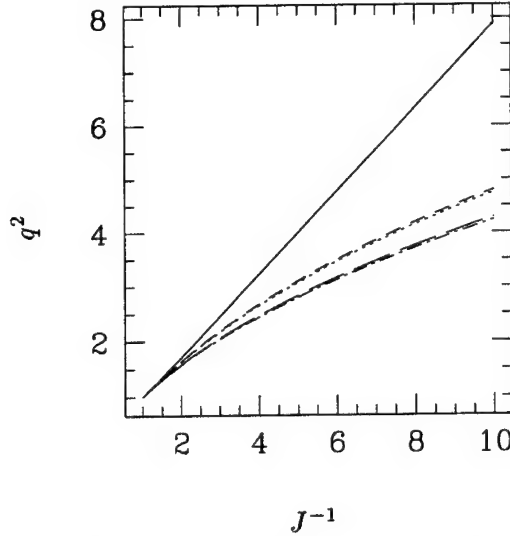


FIGURE 7. Evolution of the normalized kinetic energy for the compressed tumble vortex, as a function of the volumetric ratio J^{-1} , with $J^{-1} = 10$ at the end of the compression. —, $\Omega_0 = 0$; ·····, $\Omega_0 = 10$; ----, $\Omega_0 = 100$; — — —, $\Omega_0 = 500$; — — — —, $\Omega_0 = 1000$.

A.1. Linear equations and generic solutions for disturbances

In the presence of a background (or mean) velocity field $U_i = U_{i,j}(t)x_j \equiv \lambda_{ij}(t)x_j$, possibly divergent ($U_{l,l} = \dot{J}/J$), linearized equations for the amplitudes of velocity disturbances are

$$\dot{\hat{u}}_i + \lambda_{il}\hat{u}_i + \nu k^2 \hat{u}_i = - \left(\delta_{il} - 2 \frac{k_i k_l}{k^2} \right) \lambda_{lj} \hat{u}_j \quad (\text{A.1})$$

where velocity and pressure disturbances are expressed in terms of 3D Fourier modes, or

$$[u_i, p] = [\hat{u}_i(\mathbf{k}, t), \hat{p}(\mathbf{k}, t)] e^{i\mathbf{k} \cdot \mathbf{x}},$$

and the wavevector \mathbf{k} is considered as time-dependent, following the characteristic curves (second Eq. (4)), that are solutions of

$$\dot{k}_i = -\lambda_{ji} k_j \quad \text{and} \quad k_i(t=0) = K_i. \quad (\text{A.2})$$

The overdot $\dot{\{ \}}$ denotes a time derivative *at fixed* $\mathbf{K} = \mathbf{k}(t=0)$, which is similar to the substantial derivative in physical space. Eq. (A.1) is valid for any unbounded *solenoidal* velocity disturbance field ($k_i \hat{u}_i = 0$), in agreement with the closed expression

$$p' = k_j \lambda_{jl} \hat{u}_l \quad (\text{A.3})$$

for a term proportional to the Fourier transform of the pressure Laplacian. The background field is a particular solution of the Euler equations if $\dot{\lambda} + \lambda^2$ is a symmetric tensor, or equivalently if the mean vorticity obeys the Helmholtz equations. Without lack of generality, Eqs. (A.1) and (A.2) for the initial value problem have solutions of the form

$$k_i = M_{ij}(t, 0)K_j \quad \text{with} \quad \mathbf{M} = \mathbf{F}^{-1} \quad \text{and} \quad M_{ij}(t = 0, 0) = F_{ij}(t = 0, 0) = \delta_{ij} \quad (\text{A.4})$$

and

$$\begin{aligned} \hat{u}_i(\mathbf{k}, t) &= G_{ij}(\mathbf{k}/k, t, 0) \exp[-\nu V_{ln}(\mathbf{k}/k, t, 0)k_l k_n] \hat{u}_j(\mathbf{K}, 0) \\ &\quad \text{with} \quad G_{ij}(t = 0) = \delta_{ij} - K_i K_j / K^2 \end{aligned} \quad (\text{A.5})$$

where the matrices \mathbf{F} , as in Eq. (4) (or \mathbf{M}), \mathbf{G} , and \mathbf{V} are deterministic and can be tabulated once for all for a given background velocity field. For the sake of simplicity, the exponential viscous factor will no longer be considered in the following. The two-time argument $(t, 0)$ reflects that we are concerned with linear transfer operators from an initial $(t = 0)$ state to an instantaneous one, as for Green's functions. Of course \mathbf{F} and \mathbf{G} are the basis for the most general linear stability analysis. The main difficulty comes from the implicit time-dependence of the orientation of \mathbf{k} in the linear system for \mathbf{G} , or equivalently in inviscid Eq. (A.1). Optional subsequent prediction of statistics (e.g. $\langle \hat{u}_i^* \hat{u}_j \rangle$) is obtained in terms of initial statistics and products of \mathbf{G} matrices.

A final reduction of the number of dependent deterministic functions that generate the linear solutions is to use a rank-2 matrix (the \mathbf{g} matrix) rather than \mathbf{G} , considering only the two nonzero components ($\hat{\varphi}^\alpha$, $\alpha = 1, 2$) of \hat{u}_i in a plane normal to \mathbf{k} , in accordance with the solenoidal property. The linear combinations $\hat{\varphi}^2 \pm i\hat{\varphi}^1$ are the amplitudes of the 'helical modes', useful in any problem involving rotation.

In addition to analytical solutions discussed in previous works, the code MITHRA can numerically solve the linear problem in the most general way as follows. The input is the initial mean vorticity vector $2\Omega_i(t = 0) = \epsilon_{ijk}\lambda_{kj}(t = 0)$, the time-dependent symmetric part $\lambda_{ij}(t) + \lambda_{ji}(t)$, and data about discretisation of the initial wavevector. In addition, one can introduce given initial statistical velocity moments. The actual time evolution for the eventually unsteady vortical part of the mean, in agreement with Helmholtz equation, is automatically ensured, and \mathbf{F} , \mathbf{V} and \mathbf{g} are numerically computed using a fourth-order Runge-Kutta method. Given a periodic history of \mathbf{F} , hence a periodic wavevector motion as considered below, diagonalization of \mathbf{g} after a time-period yields values and spectral distributions of the Floquet parameter, but this is only a very peculiar application of MITHRA.

Hill's equations considered in subsequent subsections can be found starting from a special set of two components that generates \hat{u}_i for the solenoidal velocity field. These two components are similar to the $\hat{\varphi}^\alpha$, $\alpha = 1, 2$ addressed by Cambon and coworkers (used in MITHRA for computing \mathbf{g}), and also proportional to the amplitudes of the Laplacian of vertical velocity ($\nabla^2 u_3$ used in classic Orr-Sommerfeld equation) and vertical vorticity ($\omega_3 = \epsilon_{3ij}u_{j,i}$ used in classic Squires equation).

A.2. The basic elliptical flow

The planar ($\alpha, \beta = 1, 2$) background flow is characterized by

$$\lambda_{\alpha\beta} \rightarrow \begin{pmatrix} 0 & S_0 - \Omega_0 \\ S_0 + \Omega_0 & 0 \end{pmatrix} \quad (A.6)$$

Starting from Eqs. (A.1) and (A.2) a linear system for \hat{u}_3 and p' (Eq. (A.3)) is found,

$$(k^2 p') = 2(S_0^2 - \Omega_0^2)k^2 k_3 \hat{u}_3$$

and

$$k^2(\dot{\hat{u}}_3) = 2k_3 p'.$$

By elimination of p' in the previous system, one finds a second order ODE:

$$(k^2 \ddot{\hat{u}}_3) = 4[-\Omega_0^2 k_3^2 + S_0^2 k^2 + S_0 \Omega_0 (k_2^2 - k_1^2)] \hat{u}_3 \quad (A.7)$$

which is valid for any case (hyperbolic $S_0 > \Omega_0$, pure shear $S_0 = \Omega_0$, and elliptic $S_0 < \Omega_0$) addressed by Cambon and coworkers. In the elliptical case ($S_0 < \Omega_0$), the motion of \mathbf{k} is periodic, in agreement with $\ddot{F}_{\alpha\beta} = (S_0^2 - \Omega_0^2)F_{\alpha\beta}$ so that $\ddot{k}_i = (S_0^2 - \Omega_0^2)(k_i - k_3 \delta_{i3})$. In this case only, the above Eq. (A.7) is the specific Hill's equation addressed by Waleffe (1990), up to a slightly different choice (not K_i , $i = 1, 2, 3$ as in (4) and (A2)) to initialize \mathbf{k} . When the specific periodic motion of \mathbf{k} is accounted for, the above equation is parameterized by the two angular-dependent (in terms of the orientation of \mathbf{K}) parameters a and c below that define the configuration plane in which to plot isovalues of the Floquet parameter. This is used to have a complete and synoptic representation of the linear stability problem. Waleffe found

$$(1 - a \cos(2\phi)) \ddot{Z} + (c^2 - 4a \cos(2\phi)) Z = 0$$

with $Z = k^2 \hat{u}_3$, $\phi = \sqrt{\Omega_0^2 - S_0^2}(t - t_0)$, and he plotted the neutral curve in the (a, c) -plane.

A.3. The periodically compressed circular (swirl) flow

The *compressing* background flow is given by

$$\lambda_{ij} = \begin{pmatrix} 0 & -\Omega_0 & 0 \\ \Omega_0 & 0 & 0 \\ 0 & 0 & S(t) \end{pmatrix}$$

where the axial strain-rate $S = \dot{L}/L$ is given by a periodic law, similar to (2) for $L(t)$, and the vorticity is constant since the mean flow is compressible (no amplification by vortex stretching). In this case, the two relevant components used by Mansour & Lundgren are proportional to horizontal (or vertical) divergence ($\Phi = k_1 \hat{u}_1 + k_2 \hat{u}_2 = -k_3 \hat{u}_3$) and vertical axial vorticity ($\Psi = k_1 \hat{u}_2 - k_2 \hat{u}_1$). The corresponding Hill's

equation is finally found by eliminating Ψ , and working with $\xi = L^2(t)k^2(t)\Phi$, so that

$$[1 - a \sin(2t^*) + 0.5\eta a \sin^2(2t^*)] \ddot{\xi} = -\sigma^2 \xi$$

where $t^* = \omega t$ is the non-dimensional time and $\eta = (r - 1)/(r + 1)$, as in (2). In terms of the two angular parameters that parameterize this Hill's equation, namely $\sigma = 2(\Omega_0/\omega) \cos \theta$ and $a = 2\eta \sin^2 \theta$, the relevant representation plane was found in which isovalues of the Floquet parameter were numerically plotted, not only the neutral curves. Different instability bands were shown in the (a, σ) -plane that correspond to different instability bands in terms of θ , as shown in the present Figures 2-6. In order to contrast the results in Fig. 1 (Mansour & Lundgren) and the results delivered by MITHRA, we have computed a typical RDT history of \mathbf{g} in the same conditions.

For a compression ratio $r = 8$ and a swirl ratio $\Omega_0/\omega = 2$, the parabolic dashed line, which gives in the (a, σ) -plane the variation in θ at fixed compression and swirl ratios (the Mansour-Lundgren Fig. 1), predicts three unstable angular bands. These bands are accurately recovered when looking at the angular θ distribution of the maximum eigenvalue of \mathbf{g} after a period ($t = T = \pi/\omega$).

A.4. Relevance of the Floquet analysis to the compressed tumble case

The mean flow gradient matrix corresponding to Eq. (1-3) yields a more complex problem than the two cases reported above. Even if it were possible to derive a unique second order ODE from the two-equations linear system (from A.1) in terms of either

- $(\hat{\varphi}^1, \hat{\varphi}^2)$ (Cambon and coworkers),
- (\hat{u}_3, p') (Waleffe) or
- $(-k_3 \hat{u}_3, -i\hat{\omega}_3)$ (Mansour & Lundgren),

the specific time dependence induced by the motion of \mathbf{k} would remain analytically unknown in the coefficients of such a second order ODE. Even the solution (4) of Eq. (A.2) cannot be simply expressed. In fact k_1 and k_2 are themselves governed by a Hill- type equation!).

Regarding, now, the Floquet problem, which can always be numerically treated by computing the \mathbf{g} -angular distribution after a period, we obtained the following preliminary information:

- The angular distribution after a complete period depends on the initial phase or initial crank angle when using either (2) or the compression history of Mansour-Lundgren compression law. No instability is found, reflecting a complete reversibility of the \mathbf{g} history, when using (2) (where $\dot{L} = 0$ initially), whereas a number of instability peaks is found when starting from an extremum of \dot{L} , as Mansour-Lundgren did.
- The distribution of instability peaks obtained at the end of the compression stroke (Figs. 2-5) has nothing to do with the distribution obtained after a complete period.

- Even if a non-periodic law is used for reaching the end of the compression stroke (e.g. a constant strain-rate and exponential decrease for $L(t)$ were checked), a 'forest' of instability peaks is still obtained, but its distribution is different from the one corresponding to (2).

This refined numerical analysis illustrates that the results from a Floquet analysis should be treated with caution since in general such an analysis is strongly dependent on the form of the compression law.

REFERENCES

- BACHELOR, G. K. & PROUDMAN, I. 1954 The effect of rapid distortion on a fluid in turbulent motion. *Q. J. Mech. Appl. Maths.* **7**, 83-103.
- BAYLY, B. J. 1986 Three-dimensional instability of elliptical flow. *Phys. Rev. Lett.* **57**, 2160-2171.
- BLAISDELL, G. A. & SHARIFF, K. 1994 Homogeneous turbulence subjected to mean flow with elliptic streamlines. *Proceedings of the 1994 Summer Program*, Center for Turbulence Research, Stanford, CA., 355-371.
- CAMBON, C. 1982 Étude spectrale d'un champ turbulent incompressible soumis à des effets couplés de déformation et de rotation imposés extérieurement. *Thèse de doctorat d'état*, Université Claude Bernard-Lyon I.
- CAMBON, C., BENOIT, J. P., SHAO, L. & JACQUIN, L. 1994 Stability analysis and large eddy simulation of rotating turbulence with organized eddies. *J. Fluid Mech.* **278**, 175-200.
- CAMBON, C., COLEMAN, G. N. & MANSOUR, N. N. 1993 Rapid distortion analysis and direct simulation of compressible homogeneous turbulence at finite Mach number. *J. Fluid Mech.* **257**, 641-665.
- CAMBON, C., MAO, Y. & JEANDEL, D. 1992 On the application of time dependent scaling to the modelling of turbulence undergoing compression. *Eur. J. Mech. B/Fluids.* **11**(6), 683-703.
- CAMBON, C., TEISSÈDRE, C. & JEANDEL, D. 1985 Étude d'effets couplés de déformation et de rotation sur une turbulence homogène. *J. Méc. Théor. Appl.* **4**, 629-657.
- CRAIK, A. D. D. & CRIMINALE, W. O. 1986 Evolution of wavelike disturbances in shear flows: a class of exact solutions of the Navier-Stokes equations. *Proc. R. Soc. Lond. A.* **406**, 13-26.
- LANDMAN, M. J. & SAFFMAN, P. G. 1987 The three-dimensional instability of strained vortices in a viscous fluid. *Phys. Fluids.* **30**, 2339-2342.
- LE DIZÈS, S., ROSSI, M. & MOFFATT, H. K. 1996 On the three-dimensional instability of elliptical vortex subjected to stretching. *Phys. Fluids.* **8**(8), 2084-2090.

- LEROY, O., LE PENVEN, L., CAMBON, C. & SCOTT, J. 1996 Combustion dans les moteurs à piston. *Rapport ARC CNRS/ECOTECH/GIE PSA-RENAULT*. Rapport 1995-96, LMFA Ecole Centrale de Lyon, France.
- LUNDGREN, T. S. & MANSOUR, N. N. 1996 Transition to turbulence in an elliptic vortex. *J. Fluid Mech.* **307**, 43-62.
- MANSOUR, N. N. & LUNDGREN, T. S. 1990 Three-dimensional instability of rotating flows with oscillating axial strain. *Phys. of Fluids A*. **12**(2), 2089-2091.
- MARC, D., BORÉE, J., BAZILE, R., CHARNAY, G., TRINITÉ, M. & LECERF, A. 1996 Étude expérimentale modèle de l'aérodynamique interne des moteurs: cas de l'écoulement de rouleau. 5^{ème} congrès francophone de vélocimétrie laser, Rouen, France. 24-27 Sept. 1996.
- PIERREHUMBERT, T. J. 1986 Universal short-wave instability of two-dimensional eddies in an inviscid fluid. *Phys. Rev. Lett.* **57**, 2157-2159.
- ROGALLO, R. S. 1981 Numerical experiments in homogeneous turbulence. *NASA Tech. Mem.* 81315.
- WALEFFE, F. 1989 The three-dimensional instability of a strained vortex and its relation to turbulence. *PhD thesis*. MIT.
- WALEFFE, F. 1990 On the three-dimensional instability of strained vortices. *Phys. of Fluids A*. **2**(1), 76-80.

A new method for the adaptive control of vortex-wall interactions

By P. Koumoutsakos

1. Motivation and objectives

The control of vortical flows is gaining significance in the design of aeronautical and marine structures. While passive devices have been used effectively in the past, active control strategies have the potential of allowing a leap in the performance of future configurations. The efficiency of control schemes is strongly dependent on the development of accurate flow models that can be devised using information that is available not only from numerical solutions of the governing Navier-Stokes equations but also can be measured experimentally. In that context it is desirable to construct adaptive control schemes using information that can be measured at the wall.

The objective of this study is to propose an efficient methodology for the adaptive control of vortical, wall bounded flows. The present scheme is based on sensing wall pressure and calculating the wall vorticity flux from this information. This information is used to determine the amount of unsteady, spatially varying mass transpiration needed as the actuating mechanism. The amount of suction and blowing is determined explicitly in order to achieve a desired vorticity flux at the wall. The closed form control law is obtained by formulating the physical mechanism of vorticity generation at a no-slip wall.

The control scheme is tested on the model problem of a vortex dipole impinging on a wall. It is shown that by using information at the wall, we are able to reproduce efficiently the effects obtained by other control schemes that rely on off-wall information. The proposed methodology is based on explicit formulation of physical processes, and its simplicity allows its incorporation to flow control both computationally as well as in actual applications.

The control scheme is discussed in more detail in Koumoutsakos (1996); only representative results are presented in this report.

2. Accomplishments

2.1 Wall-vorticity flux

In wall bounded flows, the tangential velocity of fluid elements relative to the boundary establishes velocity gradients. With the definition of vorticity (ω) as the curl of velocity ($\omega = \nabla \times \mathbf{u}$), this may be equivalently described in terms of the vorticity that is acquired by the fluid elements near the wall. Lighthill (1963) envisioned the wall as a system of sources and sinks of vorticity. He drew an analogy between the way vorticity is produced at the wall and enters the flow and the way temperatures are established near a heat conducting boundary.

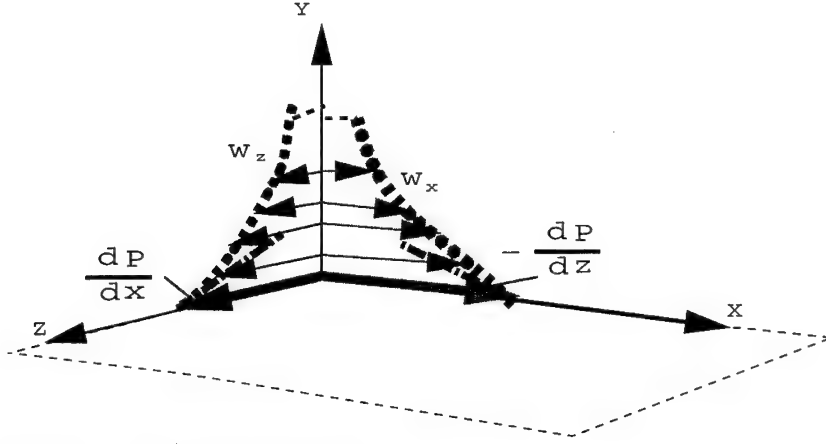


FIGURE 1. Definition sketch.

Following Hornung (1990) we identify the *diffusive vorticity flux tensor at the wall* as:

$$J_w = -(\nu \nabla \omega)_w \quad (1)$$

where ν is the kinematic viscosity of the fluid and the subscript w denotes quantities measured at the wall.

The normal component of the diffusive vorticity flux tensor is defined as the wall vorticity flux (Panton 1984, Hornung 1990).

$$\sigma = -(\nu \mathbf{n} \cdot \nabla \vec{\omega})_w \quad (2)$$

where ω is the vorticity and \mathbf{n} is the outward normal at the wall.

In the rest of this work we consider for simplicity a Cartesian coordinate system and flow over a flat wall identified with the xOz plane (Fig. 1) with a unit normal \hat{j} . The vorticity flux is then expressed as

$$\sigma = -\left(\nu \frac{\partial \omega}{\partial y}\right)_w \quad (3)$$

Hornung (1990) has presented a formula for the local vorticity flux for a general fluid material:

$$\sigma = -\hat{j} \times \left(\frac{d\vec{V}_w}{dt} + \frac{(\nabla p)_w}{\rho_w} \right) - \frac{1}{\rho_w} \hat{j} \left(\hat{j} \cdot (\nabla \times \tau_w) \right) + \frac{1}{\rho_w} \hat{j} \times \begin{bmatrix} \frac{\partial \sigma_x}{\partial x} \\ \frac{\partial \sigma_z}{\partial z} \\ 0 \end{bmatrix} \quad (4)$$

where $\vec{V}_w(t)$ is the local wall velocity, τ_w is the shear stress tensor, and σ_x, σ_z are the components of the normal stress components along the wall.

For an incompressible viscous flow over a stationary wall, the vorticity flux is directly proportional to the pressure gradients, as Eq. 4 reduces to:

$$\nu \left(\frac{\partial \omega_x}{\partial y} \right)_w = \frac{1}{\rho} \left(\frac{\partial p}{\partial z} \right)_w \quad \text{and} \quad -\nu \left(\frac{\partial \omega_z}{\partial y} \right)_w = \frac{1}{\rho} \left(\frac{\partial p}{\partial x} \right)_w \quad (5)$$

where p is the pressure and ω_x and ω_z are the streamwise and spanwise vorticity components (Fig. 1). The flux of the wall normal vorticity, ω_y , may be determined from the kinematic condition ($\nabla \cdot \boldsymbol{\omega} = 0$) as:

$$-\left(\frac{\partial \omega_y}{\partial y}\right)_w = \left(\frac{\partial \omega_x}{\partial x}\right)_w + \left(\frac{\partial \omega_z}{\partial z}\right)_w \quad (6)$$

Thus one may obtain the wall flux of all three vorticity components as a function of time by measuring the instantaneous pressure at the wall and calculating its gradient.

Wall pressure fluctuations measurements are often reported in the literature (see for example Johanson *et al.* 1987) and have revealed a strong coupling between the vortical structures near the wall and the pressure field on the wall. Similar observations have been made in flow fields obtained in direct numerical simulations of wall bounded flows (Moin and Kim, 1985). However, measurements of pressure gradients at a wall are not common. An exception is the work of Andreopoulos and Agui (1996) (referred to as AA from here on). They use high frequency response transducers to measure fluctuating wall pressure gradients and then compute the vorticity flux in a two-dimensional turbulent boundary layer. Their measurements demonstrated the significance of vorticity flux in describing near wall processes. They made an attempt to correlate vorticity flux signals with physical phenomena such as bursting-sweep processes in the boundary layer. They observed that fluid acquires or loses vorticity at the wall during rather violent events followed by periods of small fluctuations. During these events they observed a predominant orientation at 45° for the wall vorticity flux, implying an equal vorticity flux for the streamwise and the spanwise vorticity components. This may be linked with the observations of Orlandi and Jiménez (1994), who studied the role of spanwise vorticity in the redistribution of streamwise vortices and the formation of streaks of high and low skin friction in the boundary layer.

AA demonstrated that the major contributions to the vorticity flux come from the uncorrelated part of the pressure signals at two adjacent locations which contain a wide range of vortical scales. As the degree of correlation is smaller between the small scales, their contribution to the vorticity flux is more pronounced. This imposes a severe requirement on the spatial resolution of the pressure gradients/vorticity flux measurements. Practical applications would require actuators and sensors with sizes in the order of $50\mu\text{m}$ and actuator frequencies of 1MHz (Moin and Bewley, 1994). However, recent advances in micro pressure sensor fabrication technology (Ho and Yui 1996) give us an opportunity to overcome these difficulties. Löfdahl *et al.*, (1996) presented measurements in a two-dimensional flat plate boundary layer with a resolution of eddies with wave numbers less than ten viscous units using microscopic silicon pressure transducers. It appears that by using this new technology one may be able to describe in detail physical processes in terms of the flow vorticity and the wall vorticity flux.

The role of the vorticity flux from oscillating walls as a mechanism for the control of unsteady separated flows was discussed by Wu, Wu and Wu (1993). They

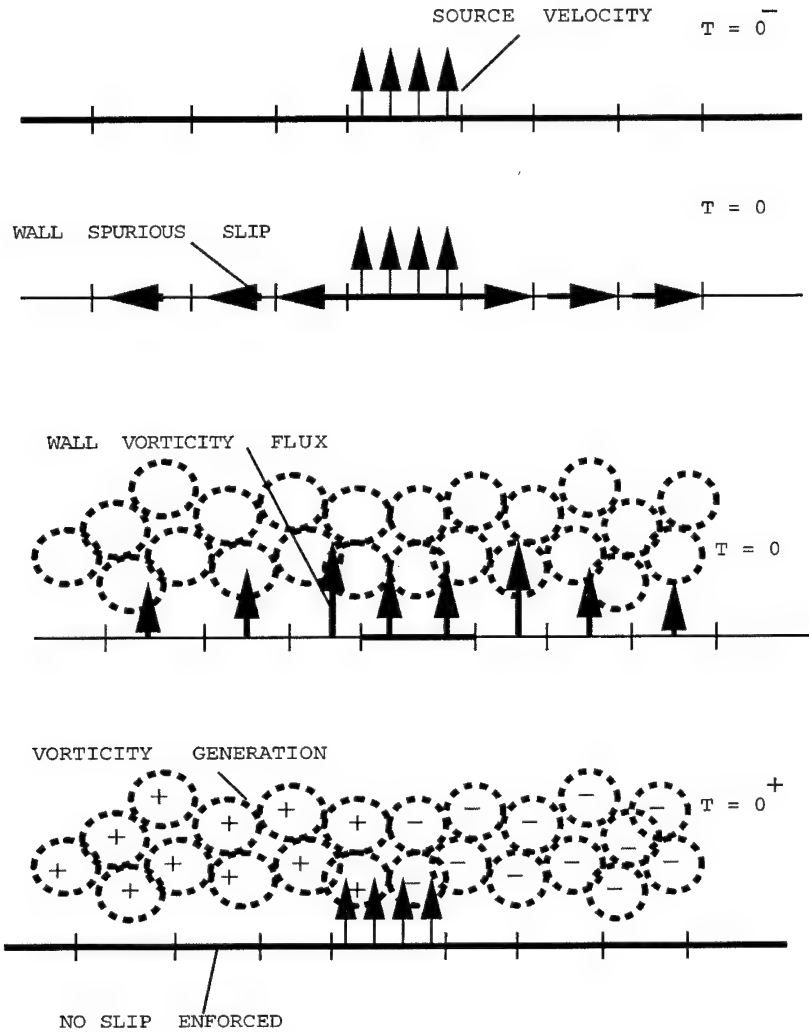


FIGURE 2. Slip cancellation algorithm.

concluded that wall oscillations can produce a mean vorticity flux that is partially responsible for phenomena of vortex flow control by waves. Gad-El-Hak has shown that the vorticity flux can be affected by wall transpiration as well as by wall-normal variation of the kinematic viscosity (ν) as a result of surface heating, film boiling, cavitation, sublimation, chemical reaction, wall injection of higher/lower viscosity fluid, or in the presence of shear thinning/thickening additive.

However these works do not provide us with an explicit formulation for the actuator strength necessary to induce a desired vorticity flux at the wall. In that direction, recently Lee, Kim, Babcock and Goodman (1996) used non-linear neural networks to obtain a simple expression for the wall blowing and suction needed to reduce the skin friction of turbulent channel flow.

In this article we propose the use of vorticity flux for effective, adaptive control

mechanisms in wall bounded flows. For a general fluid material the wall vorticity flux may be affected by appropriately selecting the type, magnitude, and location of the controlling devices so as to modify the fluid stresses near the wall (Eq. 9). For the present scheme using a formulation based on Lighthill's (1963) conceptual model of vorticity generation at the wall, we obtain in closed form the magnitude of the blowing/suction necessary to manipulate the vorticity field. The present control scheme relies on information that can be obtained experimentally as well as computationally. It is applied to the model problem (Choi, Moin and Kim, 1994 and referred to as CMK from here on) of a vortex dipole interacting with a wall. It is shown that the present strategy, using wall only information, reproduces efficiently phenomena that have been obtained previously using off wall information.

2.2 Vorticity flux induced by blowing and suction at the wall

We proceed to describe our methodology by considering two-dimensional configurations. The present analysis and the results discussed herein are readily extendable to three-dimensional flows.

Following Lighthill (1963) we consider the generation of vorticity at the wall as a fractional step algorithm. During the first substep an inviscid field is established, and it induces a spurious slip velocity (or equivalently a vortex sheet) at the boundary. The production of vorticity is materialized then at the following substep as the vortex sheet enters diffusively into the flow, eliminating the spurious velocity at the wall and enforcing the no-slip boundary condition. To illustrate this process consider the generation of vorticity over a wall segment due to the instantaneous blowing at one location (Fig. 2). According to Lighthill's model there is a slip velocity at the wall for an instant. A simple calculation shows that over an elementary wall segment δs we may calculate a circulation of $\delta\Gamma = U_{slip}\delta s$. The spurious slip velocity U_{slip} may be easily determined from inviscid flow theory, and at each location it is proportional to the inverse distance from the source. This spurious slip velocity is then nullified via the diffusive generation of vorticity at the wall so that the no-slip boundary condition is enforced. The amount of circulation that enters the flow over each time step δt , over each segment, is then $\delta\Gamma$ and it is related to a vorticity flux as $\delta\Gamma = \nu\partial\omega/\partial y\delta t\delta s$. Thus the instantaneous vorticity flux at each location over the wall due to the instantaneous blowing is expressed as:

$$\nu \left(\frac{\partial\omega}{\partial y} \right)_w = - \frac{U_{slip}}{\delta t} \quad (7)$$

We consider now a system of sources/sinks at the wall of strength q_j that are distributed uniformly over a panel of size d_j , centered at locations $x'_j, j = 1, 2, 3, \dots, N$. The induced tangential velocity at point x_i on the wall and the corresponding vorticity flux may be determined as:

$$\nu \delta t \frac{\partial\omega}{\partial y}(x_i) = \sum_{j=1}^N \frac{q_j}{2\pi} \int_{-d_j/2}^{d_j/2} \frac{x-s}{(x-s)^2} ds \quad (8)$$

where $x = x_i - x'_j$. Similar expressions relate the vorticity flux at a location on the wall with the tangential acceleration of wall elements. It is also clear that via the present formulation the velocity gradients at the wall induced by the actuators may be determined as well and, ultimately, they can be used to affect the wall shear stresses.

For the purposes of our control scheme we consider a series of vorticity flux (or equivalently pressure gradient) sensors on the wall at locations $x_i, i = 1, 2, 3, \dots, M$. Using the formulas described above we can explicitly determine the actuator strengths necessary to achieve a desired vorticity flux profile at the wall, at a time instant k , by solving the linear set of equations:

$$B u_k + X_{k-1} = D_k \quad (9)$$

where $D_k = (\frac{\partial \omega^k}{\partial y}(x_1), \frac{\partial \omega^k}{\partial y}(x_2), \dots, \frac{\partial \omega^k}{\partial y}(x_M))$ is an $M \times 1$ vector of the *desired* vorticity flux at the sensor locations, $X_{k-1} = (\frac{\partial \omega^{k-1}}{\partial y}(x_1), \frac{\partial \omega^{k-1}}{\partial y}(x_2), \dots, \frac{\partial \omega^{k-1}}{\partial y}(x_M))$

is an $M \times 1$ vector of the *measured* vorticity flux at the sensor locations and $u_k = (q_1^k(x'_1), q_2^k(x'_2), \dots, q_N^k(x'_N))$ is an $N \times 1$ vector of the source strengths at the actuator locations, B is an $M \times N$ matrix whose elements B_{ij} are determined by evaluating the integrals in Eq. 8 as:

$$B_{ij} = \frac{1}{2\pi} \text{Log} \frac{|x'_j - x_i - d_j/2|}{|x'_j - x_i + d_j/2|} \quad (10)$$

Matrix B is a sparse matrix, and when large numbers of sensors and actuators are employed one may use multipole expansions to reduce the computational cost. Furthermore if the relative locations of the sensors and actuators remain constant, matrix B need be inverted only once, thus minimizing the computational cost of the method. Note that the location of sensors and actuators may be selected in such a way that the matrix B is *symmetric, positive definite*. By setting $D_k = (1 + \alpha)X_k$, the solution of the above system of equations then implies the minimization of the functional

$$P(u_k) = \frac{1}{2} u_k^T B u_k - \alpha u_k^T X_k \quad (11)$$

The present technique gives us flexibility over the specific constraints that we wish to impose on the actuator strengths. Practical considerations may impose that control is performed only by jet-like actuators, $q_j \geq 0, j = 1, \dots, N$ or that the blowing and suction configuration should result in a net zero mass flux;

$$\sum_{j=1}^N q_j = 0 \quad (12)$$

Such constraints may be easily incorporated in the above scheme by appropriately adjusting matrix B . A square matrix is always possible by modifying accordingly the number of sensors and actuators. In the present example the zero mass constraint was implemented so that $B_{Mj} = 1, j = 1, \dots, N$.

Sensors and actuators are not in the same locations. The simplicity of the present scheme allows for a number of different placement of sensors and actuators and the *active* selection of the optimal locations by suitable optimization algorithms. Here we chose the locations of sensors and actuators to be collocated. Physically this may be understood as a favorable situation as the sensors are able to sense the vorticity field induced by the actuators, allowing for the control scheme to suitably compensate for it.

2.3 Control of vortex dipole interactions with a wall

To illustrate the effects of the present control strategy on vortex-wall interactions, we consider the idealized situation of a two-dimensional vortex dipole interacting with a wall. This model has been used in the past by CMK and it allows us to compare our scheme with previous well established control strategies and draw some conclusions as to its efficiency.

We consider a Lamb's vortex dipole of radius R , traveling with velocity U . The Reynolds number of the initial vortex dipole is defined as $Re = UR/\nu$ and in all simulations discussed herein $Re = 400$, and the vortex is initially located at a distance of $2.5R$ above the wall. For the simulations presented herein we employ a fast high resolution viscous vortex method (Koumoutsakos and Leonard, 1995). No symmetry constraint is imposed on the evolution of the vorticity field, the time step is chosen as $\delta t = 0.01$, and the size of the Lagrangian vortex particles is chosen as $\epsilon^2 = 0.0002$. A maximum of 200,000 Lagrangian computational elements were used for these simulations. For more details on the implementation of fast viscous vortex methods and the selection of numerical parameters, the reader is referred to Koumoutsakos and Shiels (1996).

The sensors and actuators have a finite size. In our computational experiments we found that the sensed vorticity flux is more accurately described when we calculate its average over a finite segment of the wall and that the finite size of the actuators allows for a more well conditioned description of the velocity field near the wall. The effect of different actuator and sensor arrangements is assessed by considering here the following four configurations:

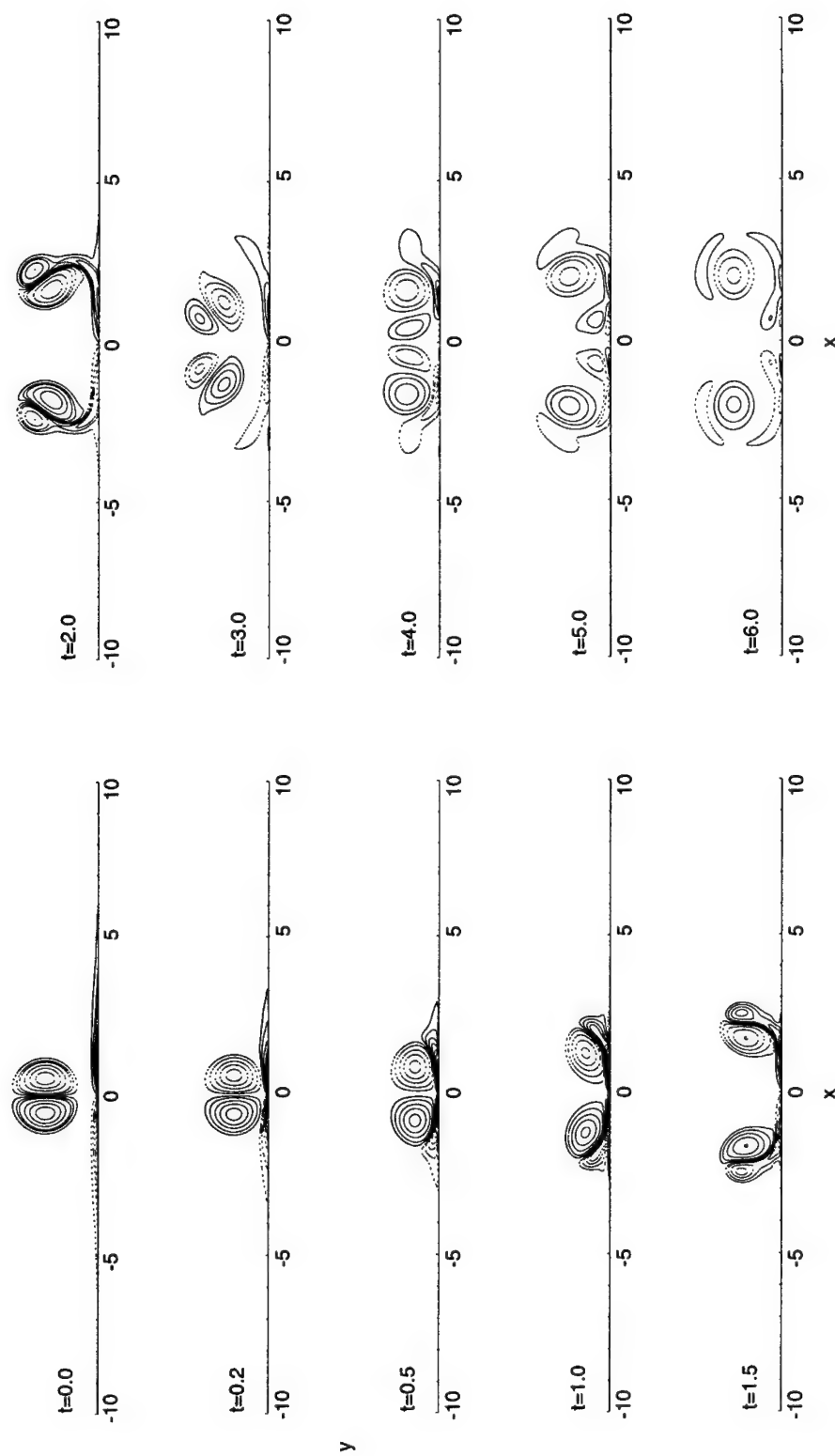
Configuration 1: Sensors of size 0.1 at $\pm(0.15 + 0.4i)$, $i = 0, \dots, 10$ for a total of 22 sensors and actuators at: $\pm(0.05 + 0.4i)$, $i = 0, \dots, 11$ for a total of 24 actuators.

Configuration 2: Sensors of size 0.1 at $\pm(0.15 + 0.2I)$, $I = 0, \dots, 19$ or a total of 40 sensors. Actuators, of size 0.1, at $\pm(0.05 + 0.2I)$, $I = 0, \dots, 20$ for a total of 42 actuators.

Note that in order to enforce the zero mass flux constraint one needs at least one more actuator than sensors. Because the present calculations are of a left-right symmetric flow, we enforce symmetry in the blowing/suction magnitude of the actuators. Hence the number of sensors and actuators in all configurations are related by $N/2 = M/2 + 1$.

Representative animations of the simulations discussed in the following section may be found at the www address:

<http://www.galcit.caltech.edu/~petros/RESEARCH/dipole.html>.

FIGURE 3. *Uncontrolled* interactions of a vortex dipole with a wall.

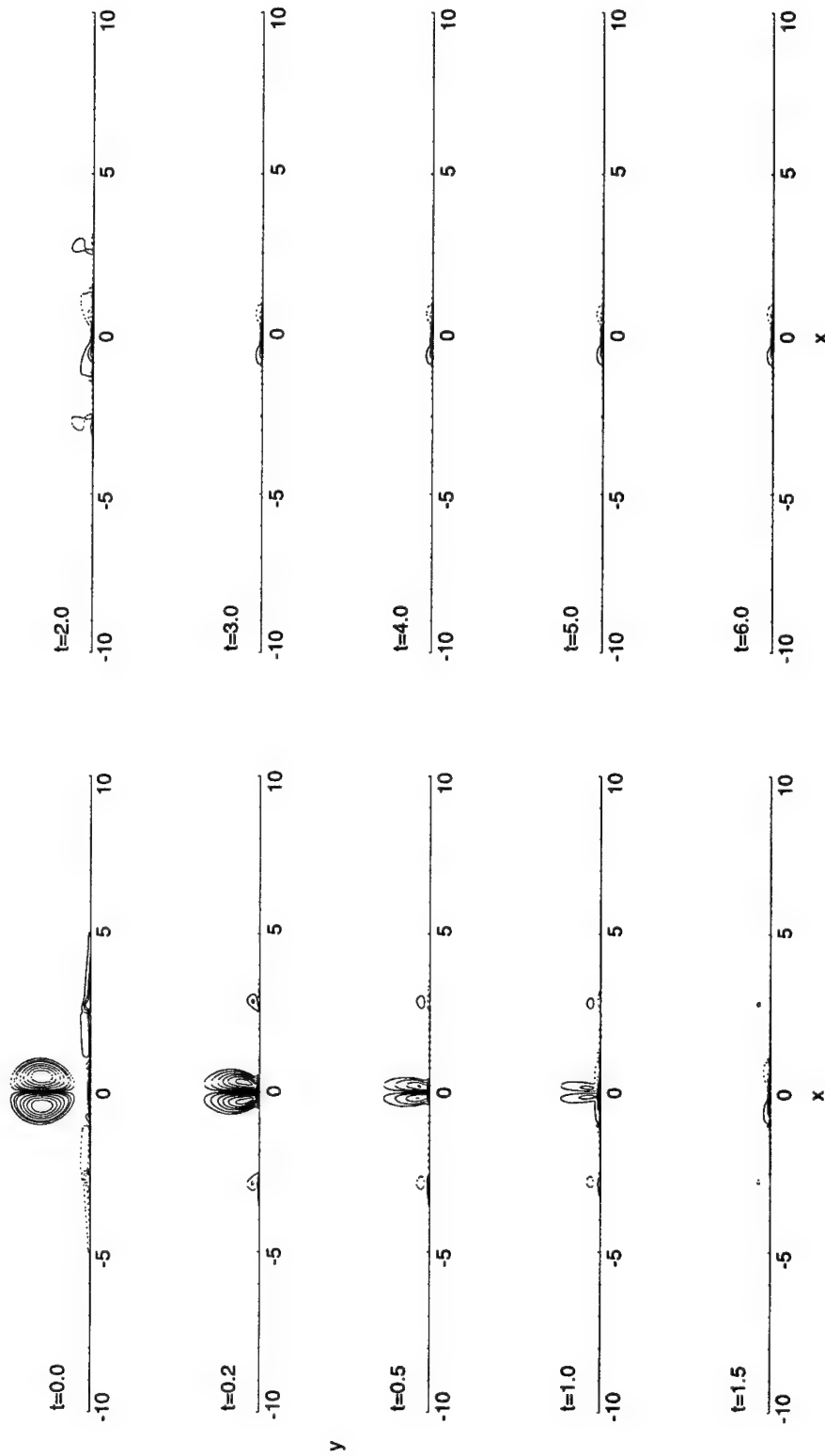


FIGURE 4. Configuration 1: Controlled wall-vortex interaction.

2.4 Simulations of a vortex dipole interactions with a wall

No Control: In Fig. 3 we present contour plots of the vorticity field of the uncontrolled interaction of a vortex dipole with a wall. The vortex dipole propagates towards the wall generating vorticity of opposite sign on its surface. As the primary vortex approaches the wall, it interacts with this secondary vorticity generating two new dipoles that propagate outwards ($T=0$ to 1.5). When the initial components of the dipole are far apart, the new dipolar structures are lifted from the wall ($T=1.5$ to 2.0). The lifted secondary vorticity is weaker than the respective primary vorticity field. Thus, the preferential direction of the new dipoles results in an interaction between the original dipole components so that the vortical structures propagate again towards the wall ($T=2$ to 4). New secondary vorticity is generated and the process described before is repeated ($T=4$ to 5). However, due to the action of diffusion, the vorticity field is weakened ($T=5$ to 6), resulting in a quasi-steady pattern that is eventually eroded.

The results of the present simulations are in excellent agreement with the results of Orlandi (1990) to which the reader is referred for a thorough discussion and quantification of this dipole wall interaction.

Control canceling the wall flux: In Fig. 4 we present contour plots of the vorticity field of the controlled interaction of a vortex dipole with a wall. In this type of control we eliminate the vorticity flux at the sensor locations (i.e. set $D_k = 0$). The vorticity flux is measured at each instant and at the following time step we appropriately adjust the strength of the actuators by solving

$$B u_k = -X_{k-1} \quad (13)$$

for u_k .

As the vortex descends towards the wall, the cancellation of the vorticity flux in the sensor locations results in a pattern where sinks are distributed in the middle of the wall. Respective blowing is established in the outer actuators so that the zero net mass flux is enforced (see also Fig. 5). As the control scheme acts to eliminate the secondary vorticity generated at the wall the primary vortex dipole 'sees' a permeable wall. At time $T = 1.0$ the primary vortex dipole has been drawn into the wall.

We examine here the effect of actuator placement in this type of control by using the sets of sensors and actuators locations described in Configuration 1 above. The locations of sensors and actuators are collocated and adjacent to each other. This allows for the sensors to account for the vorticity field generated by the actuators. As the present control strategy requires the elimination of the vorticity flux at the sensor locations, the actuator strengths are adjusted so that blowing/suction compensates to eliminate even the vortical structures generated by the actuators. The effect of sensor and actuator placement is discussed further in Koumoutsakos (1996).

The time invariance of the source/sink patterns at the wall suggests a weak time-correlation of the flow induced wall vorticity flux signals. The control scheme identifies the oncoming vortical structures and takes appropriate action to cancel the

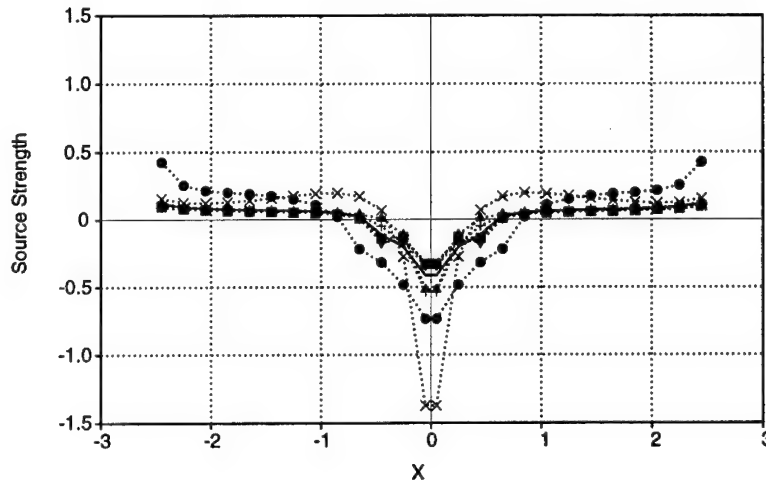


FIGURE 5. Configuration 1. Source strengths at times: \bullet 0.2, \times 0.5, \blacktriangle 1.0, \blacktriangledown 2.0, \blacklozenge 3.0, \blacksquare 4.0, $+$ 5.0, — 6.0.

vorticity flux so that the dynamics of the flow are eventually governed by the dynamics of the actuators.

Control enhancing the wall flux: In Fig. 6 we present contour plots of the vorticity field of another type of controlled interaction of a vortex dipole with a wall. In this case the desired vorticity flux is such that the *secondary vorticity is enhanced* and the lift-off, observed in the uncontrolled case, is prevented. To achieve this, we require that the actuator strengths are adjusted so as to maintain the sensed vorticity flux (or equivalently $D_k = 2X_{k-1}$) via the solution of the system:

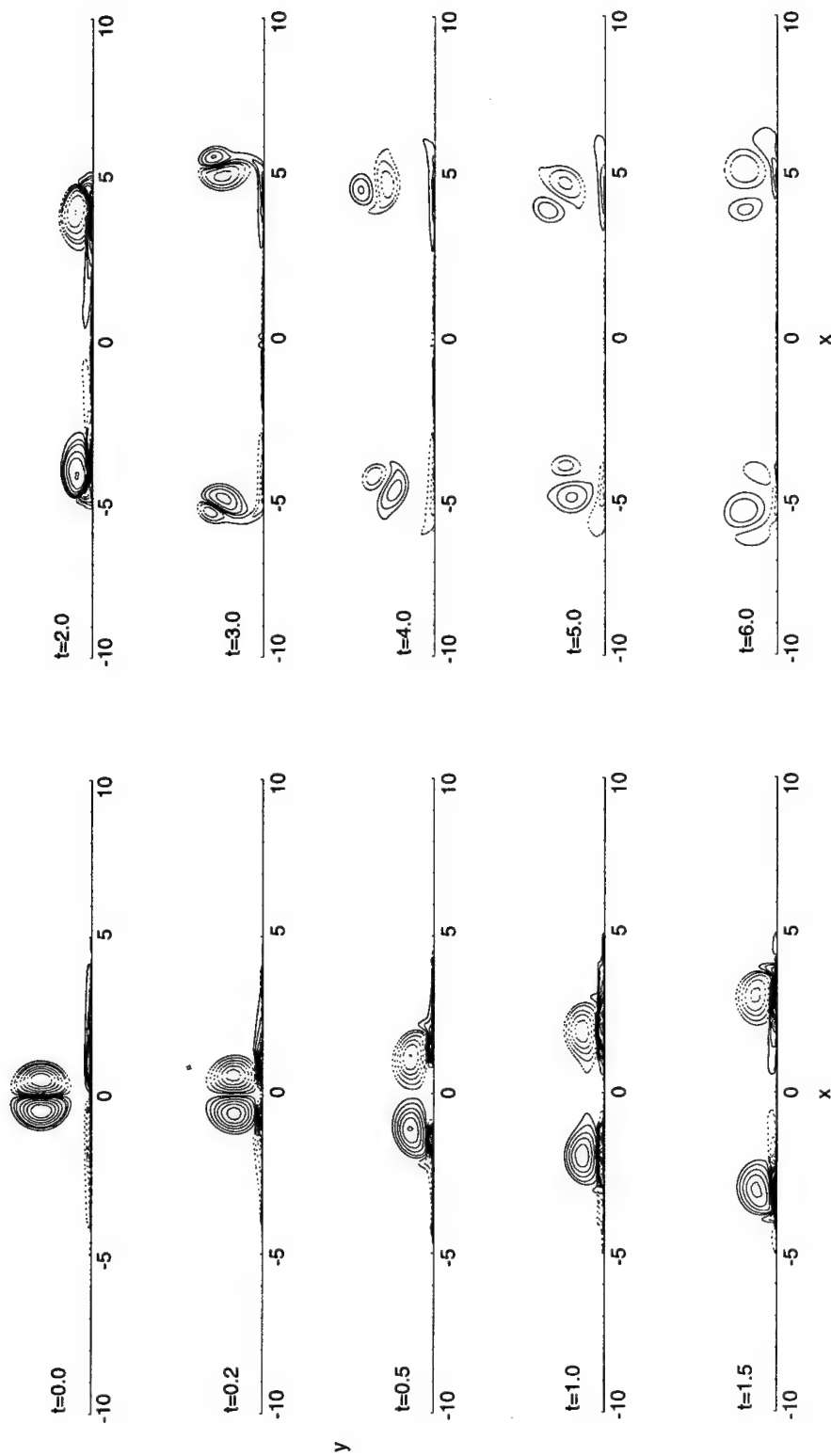
$$B \vec{u}_k = \vec{X}_{k-1} \quad (14)$$

Note that a simple sign change distinguishes Eq.13 and Eq.14.

The vorticity flux induced by the actuators at each time step is enforced to be equal to the vorticity flux induced by the flow at the previous time step. Hence the control scheme tries to maintain a steady profile of wall vorticity flux. The sensor and actuator locations are adjacent and collocated. They occupy segments of the wall up to ± 4.05 , outside of which there are no sensors and actuators.

As the vortex dipole approaches the wall, it interacts with secondary vorticity. In this case, the primary vortex components roll on the sheet of secondary vorticity that the actuators try to maintain. Lift-off is prevented as the primary vortex components 'surf' the controlled portion of the wall. The vortical structures eventually lift off outside the controlled region, as the primary vortices have not lost enough of their strength by the act of diffusion. The lift-off process outside the controlled region is seemingly unaffected by the enhancement of the secondary vorticity. For example compare the last frame in Fig. 6 with the last frame in Fig. 3.

In Fig. 7 we present the actuator strengths for a series of time instances. Initially the actuator strengths are such that they oppose the descend of the vortex dipole.

FIGURE 6. Configuration 2: *Controlled* wall-vortex interaction.

As the secondary vorticity is enhanced and the primary vortices roll over the layer of secondary vorticity, the actuator strength is diminished.

Further studies of the effect of actuator and sensor placement is discussed in Koumoutsakos (1996).

We make here a comparison of the present active control strategy and the 'v-control', discussed by CMK. In their simulations of control of a vortex dipole impinging at a wall, the flow velocity normal to the wall is sensed at a distance $y^+ = 10$ off the wall. Blowing/suction is adjusted so as to oppose this velocity. As the primary vortex descends towards the wall, the blowing/suction counteracts this motion, enhancing the generation of secondary vorticity. This secondary vorticity in turn pairs off with the primary vortex, resulting in a vortex dipole propagating parallel to the wall. It appears that the center of the newly formed dipoles is near the $y^+ = 10$ location. This may explain also why the control scheme is not as effective, at say $y^+ = 25$, as then the sensed velocity field would not be that of the dipolar structure, but that of the primary vortex itself.

In CMK's simulations sensors and actuators are distributed throughout the wall and the lift-off of the secondary vorticity field is completely prevented. The behavior of the vorticity field is strikingly similar to the vorticity field presented here (Figs. 9, 10) over the controlled part of the wall. This strongly suggests that CMK's control strategy and the one discussed in the previous section are *equivalent*. Although they rely on two different descriptions of the same underlying physical mechanisms, they induce the same behavior to the vortical structures.

The two schemes differ in the way in which they sense the vorticity field that is approaching and adjust the necessary blowing/suction at the wall. As the present adaptive control strategy relies on the sensing of the wall pressure and the calculation of the vorticity flux, it appears more suitable to experimental applications and seems a more promising method for practical applications. The equivalence of the two schemes suggests that the successful results that have been obtained using the 'v-control' scheme in more complex flows (CMK, Lee *et al.* 1996) can be obtained more efficiently by the present strategy.

2.5 Formulation of adaptive control

The proposed adaptive control methodology relies on measurements of the wall vorticity flux at one time step and the immediate adjustment of the actuator strengths at the following time step to achieve a desired vorticity flux. This process may be improved either by considering earlier time signals of the vorticity flux in a systematic way or by identifying the time correlation of the vorticity flux signals at the sensor locations. Such correlations can then be conceptually represented by a nonlinear mapping as follows:

$$X_{k+1} = F(X_k, k) + Q(u_k, k) \quad (15)$$

where $F(\cdot)$ and $Q(\cdot)$ are the nonlinear maps of the vorticity flux and the control input respectively between the time instances $t = k\delta t$ and $t = (k + 1)\delta t$.

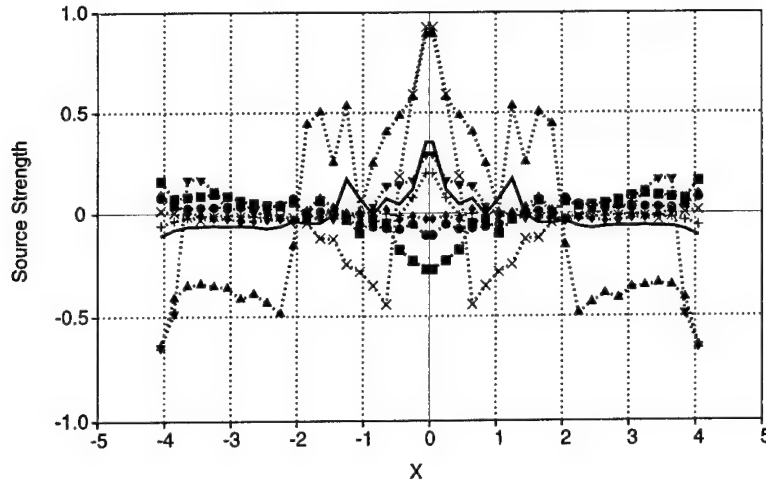


FIGURE 7. Configuration 2. For symbol captions see Fig. 5.

Taking advantage of the explicit relationship between the distributed mass sources and the vorticity flux (as was discussed in the previous sections) Eq. 15 may be expressed as:

$$X_{k+1} = F(X_k, k) + Bu_k \quad (16)$$

Then if $F(\cdot)$ is known, stabilization of the system becomes trivial by appropriately choosing the location of sensors and actuators as well as the number of constraints on the strength of the actuators to obtain a square and invertible matrix B . For example, one can use the feedback control $u_k = -B^{-1}F(X_k, k) + GX_k$ where G is a $n \times n$ matrix with all its eigenvalues inside the unit disk in the complex plane. The closed-loop system then is simply $X_{k+1} = GX_k$ which is asymptotically stable since all its eigenvalues have magnitude less than one.

The problem is then reduced to the *identification* of $F(\cdot)$. In Fig. 8 we present the function F for the uncontrolled case and for the controlled case 2b at a sensor location. It appears that after an initial transient, corresponding to the time that the primary vortex dipole is away from the wall, the dynamics of the system are determined by the dynamics of the actuators as F tends asymptotically to zero (or $F(X_k, k) \ll Bu_k$). On a related study Faller *et al.* (1994) have observed no strong time correlation of wall pressure signals in unsteady separated flows. This suggests that the identification of $F(\cdot)$ is not necessary and that one could proceed with the strategy discussed in the previous sections. We believe, however, that in order to account for experimental uncertainties and numerical errors and to increase the applicability of our scheme, the approximation/identification of the nonlinear map F is necessary.

There are two major approaches which can be used in order to achieve this. The *first* approach is based on approximating the nonlinear map at each instant by its first order, linear expansion according to $F(X_k, k) = A(k)X_k + \dots$

The *second* approach is based on identification of $F(\cdot)$ using a non-linear neural

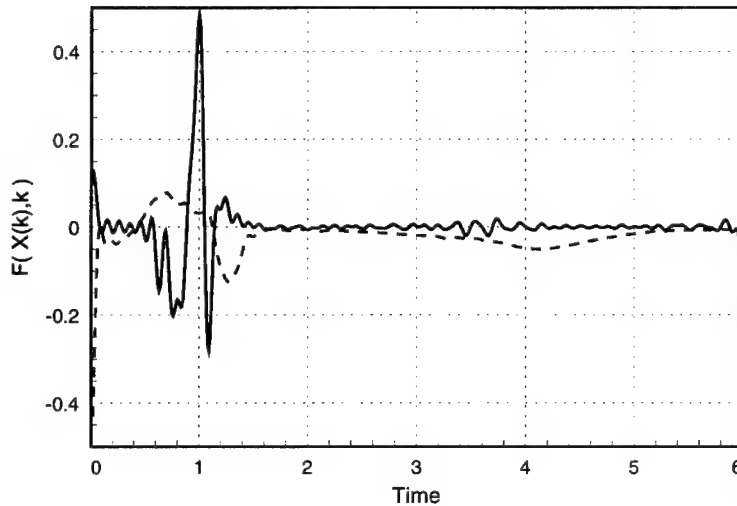


FIGURE 8. Residual function at location 1.15. — Controlled. Case 2, ---- No control.

network. Using past input and output data we can use neural network techniques to approximate the function $F(\cdot)$ adaptively. This approach is not as simple as the one in the linear approach, but it has the additional advantage of encompassing problems which require *shaping of the system response*.

Schreck *et al.* (1995) have demonstrated the ability of neural networks to capture and create simple models of the wall pressure field in unsteady separated flows of three dimensional airfoils. Moreover, they observed that the resulting model exhibits a strongly linear behavior.

3. Conclusions and future work

We have presented an active control technique that is based on the physical mechanism of vorticity generation at the wall. The wall vorticity flux may be used to describe the effects of several control devices such as (but not limited to) blowing and suction at the wall.

In the present scheme the vorticity flux is sensed at the wall via the measurement of wall pressure. A simple control strategy is described that allows calculation of the strength of wall transpiration in closed form to achieve a desired wall vorticity flux. The efficiency of the control scheme is demonstrated in simulations of the model problem of vortex dipole interactions with a wall. Using information available at the wall, the present control scheme is able to reproduce phenomena that were previously obtained computationally using off-wall information.

The implementation of the control scheme does not depend on a particular numerical method or flow configuration, making it suitable for practical applications. The simplicity of the technique and the explicit relationship between sensor and actuator outputs allows one to concentrate on issues such as devising strategies for optimal sensor and actuator placement. It may also be efficiently implemented

in control schemes employing large numbers of micro sensors and actuators as its computational cost is minimal. The present scheme may be easily applied to the control of a variety of wall bounded flows, and we believe that it could be effective in experimental control strategies.

Work is underway to implement the proposed strategy in the control of turbulent channel flow and in the control of unsteady separated bluff body flows.

REFERENCES

- ANDREOPOULOS, J. & AGUI, J. H. 1996 Wall-vorticity flux dynamics in a two-dimensional turbulent boundary layer. *J. of Fluid Mech.* **309**, 45-84.
- CHOI, H., MOIN, P. & KIM, J. 1994 Active turbulence control for drag reduction in wall bounded flows. *J. of Fluid Mech.* **262**, 75-110.
- FALLER, W., SCHRECK, S. & LUTTGES, M. 1994 Real time prediction and control of three-dimensional unsteady separated flow fields using neural networks. *AIAA Paper 94-0532*.
- GAD-EL-HAK, M. 1990 Control of low-speed airfoil aerodynamics. *AIAA J.* **118**, 1537-1552.
- HO, C. & TAI, Y. 1996 Review: MEMS and its applications for flow control. *J. of Fluids Engr.* **118**, 437-447.
- HORNUNG, H. 1990 *Sources of Vorticity*. Ae 232. Class notes, California Institute of Technology.
- JOHANSSON, A. V., ALFREDSSON, P. H. & HARITONIDIS, J. H. 1987 Evolution and dynamics of shear-layer structures in near-wall turbulence. *J. of Fluid Mech.* **224**, 579.
- KOUMOUTSAKOS, P., & LEONARD, J. 1995 High resolution simulations of the flow around an impulsively started cylinder using vortex methods. *J. of Fluid Mech.* **296**, 1-38.
- KOUMOUTSAKOS, P., & SHIELS, D. 1996 Simulations of the flow normal to an impulsively started and uniformly accelerated flat plate. *J. of Fluid Mech.* **328**, 177-227.
- KOUMOUTSAKOS, P. 1996 Active control of vortex-wall interactions. (Submitted to *Phys. Fluids A*.)
- LEE, C., KIM, J., BABCOCK, D. & GOODMAN, R. 1996 Application of neural network to turbulence control for drag reduction. (Submitted for publication.)
- LIGHTHILL, M. J. 1963 *Introduction to boundary layer theory*. J. Rosenhead (editor) - Oxford University Press, New York. 54-61.
- LÖFDAHL, L., KÄLVESTEN, E. & STEMME, G. 1996 Small silicon pressure transducers for space-time correlation measurements in a flat plate boundary layer. *J. of Fluids Engr.* **118**, 457-463.
- MOIN, P. & BEWLEY, T. R. 1994 Feedback control of turbulence. *Appl. Mech. Rev.* **47**, S3-S13.

- MOIN, P. & KIM, J. 1985 The structure of vorticity fields in turbulent channel flow. Part 1. Analysis of instantaneous field and statistical correlations. *J. Fluid Mech.* **155**, 441-464.
- ORLANDI, P. 1990 Vortex dipole rebound from a wall. *Phys. Fluids A.* **1429**, 75-110.
- PANTON, R. L. 1984 *Incompressible Flow*. John Wiley and Sons, Inc.
- SCHRECK, S., FALLER, W., & LUTTGES, M. 1995 Neural network prediction prediction of three-dimensional unsteady separated flow fields. *J. of Aircraft.* **32**, 178-185.
- WU, J. Z., WU, X. H., & WU, J. M. 1993 Streaming vorticity flux from oscillating walls with finite amplitude. *Phys. of Fluids A.* **5**, 1933-1938.

Symmetries in turbulent boundary layer flows

By M. Oberlack

1. Motivation and objectives

The motivation for the present analysis was the finding in Oberlack (1995) that the logarithmic mean profile is a self-similar solution of the two-point correlation equation. The latter can be achieved by introducing the similarity variable $\tilde{r}_i = \frac{r_i}{x_2}$ in the correlation equation. As a result the coordinate x_2 disappears in the two-point correlation equation which finally only depends on \tilde{r}_i . This simple scaling may appear trivial. However, it is worth noticing that in the two-point correlation equation non-local terms like $(\bar{u}_k(\mathbf{x} + \mathbf{r}) - \bar{u}_k(\mathbf{x})) \frac{\partial R_{ij}}{\partial r_k}$ appear which makes guessing of other similarity solutions a non-trivial task.

The objective is the development of a new theory which enables the algorithmic computation of *all* self-similar mean velocity profiles. The theory is based on Lie-group analysis and unifies a large set of self-similar solutions for the mean velocity of stationary parallel turbulent shear flows. The results include the logarithmic law of the wall, an algebraic law, the viscous sublayer, the linear region in the middle of a Couette flow and in the middle of a rotating channel flow, and a new exponential mean velocity profile not previously reported. Experimental results taken in the outer parts of a high Reynolds number flat-plate boundary layer, strongly support the exponential profile. From experimental as well as from DNS data of a turbulent channel flow the algebraic scaling law could be confirmed in both the center region and in the near wall region. In the case of the logarithmic law of the wall, the scaling with the wall distance arises as a result of the analysis and has not been assumed in the derivation. The crucial part of the derivation of all the different mean velocity profiles is to consider the invariance of the equation for the velocity fluctuations at the same time as the invariance of the equation for the velocity product equations. The latter is the dyad product of the velocity fluctuations with the equation for the velocity fluctuations. It has been proven that all the invariant solutions are also consistent with similarity of all velocity moment equations up to any arbitrary order.

2. Governing equations

The bases for the following analysis are the incompressible Navier-Stokes equations in a rotating frame. Using the standard Reynolds decomposition, $U_i = \bar{u}_i + u_i$ and $P = \bar{p} + p$, where the overbar denotes a time or ensemble average, the Reynolds averaged Navier-Stokes equations for a parallel flow are

$$K + \nu \frac{\partial^2 \bar{u}_1}{\partial x_2^2} - \frac{\partial \overline{u_1 u_2}}{\partial x_2} = 0 \quad (1)$$

$$-\frac{\partial \bar{p}}{\partial x_2} - \frac{\partial \overline{u_2 u_2}}{\partial x_2} - 2\Omega \bar{u}_1 = 0 \quad (2)$$

$$\frac{\partial \overline{u_3 u_2}}{\partial x_2} = 0 \quad (3)$$

and the fluctuation equations are

$$\frac{\partial u_i}{\partial t} + \bar{u}_1 \frac{\partial u_i}{\partial x_1} + \delta_{i1} u_2 \frac{d\bar{u}_1}{dx_2} - \frac{d\overline{u_i u_2}}{dx_2} + \frac{\partial u_i u_k}{\partial x_k} + \frac{\partial p}{\partial x_i} - \nu \frac{\partial^2 u_i}{\partial x_k^2} + 2\Omega \epsilon_{i3l} u_l = 0. \quad (4)$$

The corresponding continuity equation for u_i is

$$\mathcal{C} = \frac{\partial u_k}{\partial x_k} = 0 \quad (5)$$

In (1)-(4) and subsequently the density has been absorbed with the pressure. In the case of a pressure driven flow in the x_1 direction the mean pressure \bar{p} has been replaced by $-x_1 K + \bar{p}(x_2)$, where K is a constant. The only axis of rotation is normal to the mean shear in x_3 -direction, and hence we take $\Omega = \Omega_3$.

Equations (1)-(3) can be rewritten and unified with the equation for the fluctuation (4) by solving (1) and (2) for the gradient of the Reynolds stresses and using the result in (4),

$$\begin{aligned} \mathcal{N}_i(\mathbf{x}) = & \frac{\partial u_i}{\partial t} + \bar{u}_1 \frac{\partial u_i}{\partial x_1} + \delta_{i1} u_2 \frac{d\bar{u}_1}{dx_2} - \delta_{i1} \left(K + \nu \frac{\partial^2 \bar{u}_1}{\partial x_2^2} \right) \\ & + \delta_{i2} \left(\frac{\partial \bar{p}}{\partial x_2} + 2\Omega \bar{u}_1 \right) + \frac{\partial u_i u_k}{\partial x_k} + \frac{\partial p}{\partial x_i} - \nu \frac{\partial^2 u_i}{\partial x_k^2} + 2\Omega \epsilon_{i3l} u_l = 0. \end{aligned} \quad (6)$$

The present analysis is restricted to stationary parallel shear flows

$$\frac{\partial \bar{u}_1}{\partial x_1} = \frac{\partial \bar{u}_1}{\partial x_3} = \frac{\partial \bar{u}_1}{\partial t} = \frac{\partial \bar{p}}{\partial x_1} = \frac{\partial \bar{p}}{\partial x_3} = \frac{\partial \bar{p}}{\partial t} = 0, \quad (7)$$

and hence \bar{u}_1 and \bar{p} are only functions of the remaining spatial coordinate x_2 .

From a wide variety of different experiments it is well known that high Reynolds number turbulent flows are Reynolds number invariant. Cantwell (1981) has already investigated this from a group theoretical point of view. Using this, we impose an additional restriction on the viscosity dependence in the mean quantities. In the limit of large Reynolds numbers, the leading order \bar{u}_1 and \bar{p} are assumed to be independent of viscosity and hence

$$\frac{\partial \bar{u}_1}{\partial \nu} = \frac{\partial \bar{p}}{\partial \nu} = 0. \quad (8)$$

The latter assumption does not restrict the number or the functional form of the self-similar solutions to be computed later. It only limits the appearing constants

in the self-similar solutions to be independent of viscosity. An explicit Reynolds number dependence in the scaling laws will be investigated in a future approach since the functional dependence can not be captured with the present analysis.

The system of Eqs. (6) describes the fluctuation and mean of an arbitrary parallel turbulent shear flow. The set of equations is underdetermined. In the classical approach of finding turbulent scaling laws the latter difficulty has motivated the introduction of second moment equations. However, in the next section the above set of equations will be analyzed with regard to its symmetry properties, without any further introduction of higher correlation equations which contain more unclosed terms.

In order to do that, an equation is introduced, which can be directly derived from Eq. (6) without introducing further unclosed terms. It is the velocity product equation, which is the dyad product of \mathcal{N}_i and u_j

$$\mathcal{N}_i u_j + \mathcal{N}_j u_i = 0. \quad (9)$$

The set of Eqs. (5)-(9) to be analyzed result to three mayor differences between the present and the classical similarity approach using the Reynolds stress transport equations. Firstly, in the present approach only the Reynolds stresses appear as unclosed terms in the equations and no higher order correlations as the pressure-strain correlation, the dissipation or the triple correlation need to be considered. Hence, in the present approach only a finite number of variables are present in the system to be analyzed.

Secondly, it is easy to see that any scaling law valid for the mean and the fluctuation velocities obtained from the velocity product Eqs. (9) still holds for the Reynolds stress equations. This fact is crucial for the present approach to obtain scaling laws which are consistent with averaged quantities. The averaging procedure applied to the velocity product equations does not affect the scaling properties of the equation.

Thirdly, it has been proven by Oberlack (1996a) that any scaling law for the velocity fluctuation and the second order velocity product Eqs. (9) is also a scaling law for all n^{th} order velocity product equations. The n^{th} order velocity product equations are defined as the n^{th} order dyadic product of the velocity fluctuations with the equation for the velocity fluctuations. Since the averaging procedure does not change the scaling properties of the n^{th} order velocity product equations, it is also consistent with all n^{th} order correlation equations. In the classical approach using correlation functions, it may not be possible to show that all higher order velocity correlations are consistent with the scaling in the Reynolds stress equations. The Reynolds stress equations is the first in a row of an infinite number of correlation equations which need to be considered in principle in the classical approach.

3. Lie point symmetries in turbulent parallel shear flows

A set of differential equations is said to admit a symmetry if a transformation to a new set of variables exists which leaves the equations unchanged. If the symmetries are computed all self-similar solutions can be obtained as will be pointed out below.

The set of variables considered in the subsequent transformation consist of

$$\mathbf{y} = \{x_1, x_2, x_3, t, \nu, u_1, u_2, u_3, p, \bar{u}_1, \bar{p}\}. \quad (10)$$

The purpose of the symmetry analysis is to find all those transformations

$$\tilde{\mathbf{y}} = \mathbf{f}(\mathbf{y}; \varepsilon) \quad (11)$$

which, under consideration of (7) and (8), satisfy

$$\mathcal{C}(\mathbf{y}) = \mathcal{C}(\tilde{\mathbf{y}}), \quad \mathcal{N}_i(\mathbf{y}) = \mathcal{N}_i(\tilde{\mathbf{y}}) \quad (12)$$

and the extended system also including (9)

$$(\mathcal{N}_i u_j + \mathcal{N}_j u_i)(\mathbf{y}) = (\mathcal{N}_i u_j + \mathcal{N}_j u_i)(\tilde{\mathbf{y}}). \quad (13)$$

Lie gave an infinitesimal form of the transformation (11)

$$\tilde{\mathbf{y}} = \mathbf{y} + \varepsilon \boldsymbol{\zeta} + \mathcal{O}(\varepsilon^2) \quad \text{with} \quad \boldsymbol{\zeta} = \left. \frac{\partial \mathbf{f}}{\partial \varepsilon} \right|_{\varepsilon=0} \quad (14)$$

where, instead of \mathbf{f} , all the infinitesimal generators $\boldsymbol{\zeta}$ need to be calculated, each element depending on \mathbf{y} .

It can be proven that the infinitesimal transformation (14) is *fully equivalent* to the global transformation (11) (see Bluman (1989)). The direct approach finding \mathbf{f} only from (12) and (13) using the global transformation (11) would have been almost impossible.

The calculation of $\boldsymbol{\zeta}$ is fully algorithmic and results in more than a hundred linear overdetermined PDE's for $\boldsymbol{\zeta}$. Its derivation has been aided by SYMMGRP.MAX, a software package for MACSYMA (1993) written by Champagne (1991). The solution has been calculated by hand. The complete set of solutions is given in Oberlack (1996a).

For the present approach, the global transformation (12) is not needed since only the self-similar solutions for the mean flow will be investigated. The equation for the self-similar solutions is the invariant surface condition (ISC). In the present case of parallel flow, the ISC for the mean flow is given by

$$\frac{dx_2}{\xi_{x_2}} = \frac{d\bar{u}_1}{\eta_{\bar{u}_1}} \quad (15)$$

where

$$\xi_{x_2} = a_1 x_2 + a_3 \quad \text{and} \quad \eta_{\bar{u}_1} = [a_1 - a_4] \bar{u}_1 + a_2 \quad (16)$$

are the infinitesimal generators.

Four different solutions for different combinations of parameter $a_1 - a_4$ have to be distinguished. Each case has a specific meaning for the corresponding turbulent

flow in terms of an external time, length, or velocity scale which may break some of the scaling symmetries as has been pointed out by Jiménez (1996).

A non-zero angular rotation rate will be considered only in the subsection (3.2). In this case the set of transformations to be obtained later contain a reduced number of parameters. The rotation rate will be considered as a branching parameter for the two different cases of $\Omega = 0$ and $\Omega \neq 0$.

3.1 Turbulent shear flows with zero system rotation

Algebraic mean velocity profile: ($a_1 \neq a_4 \neq 0$ and $a_2 \neq 0$)

The present case is the most general of all. No scaling symmetry is broken. As a result the mean velocity \bar{u}_1 has the following form

$$\bar{u}_1 = C_1 \left(x_2 + \frac{a_3}{a_1} \right)^{1 - \frac{a_4}{a_1}} - \frac{\frac{a_2}{a_1}}{1 - \frac{a_4}{a_1}}. \quad (17)$$

In the domain where the algebraic mean velocity profile is valid there can be no external length and velocity scale acting directly on the flow since non-zero and unequal parameters a_1 and a_4 are needed for its derivation. It will be pointed out in section (4) that the case of an algebraic scaling law applies both in the vicinity of the wall and in the center region of a channel flow.

Barenblatt (1993) developed an algebraic scaling law based on the idea of incomplete similarity with respect to the local Reynolds number. The proposed scaling law involves a special Reynolds number dependence of the power exponent and the multiplicative factor. It emerges that the familiar logarithmic law is closely related to the envelope of a family of power-type curves. George (1993) proposed an asymptotic invariance principle for zero pressure-gradient turbulent boundary layer flows. They found that the profiles in an overlap region between the inner and outer regions are power laws. Using the limit of infinite Reynolds number, the usual logarithmic law of the wall is recovered in the inner region.

Logarithmic mean velocity profile: ($a_1 = a_4 \neq 0$ and $a_2 \neq 0$)

For the present combination of parameters we can see in the infinitesimals (16) that no scaling symmetry with respect to the velocity \bar{u}_1 exists and hence an external velocity scale is symmetry breaking. The mean velocity \bar{u}_1 can be integrated to

$$\bar{u}_1 = \frac{a_2}{a_1} \log \left(x_2 + \frac{a_3}{a_1} \right) + C_2. \quad (18)$$

In case of the classical logarithmic law of the wall it is the friction velocity u_τ , which breaks the scaling symmetry for the velocities. The present case coincides with the usual derivation of the logarithmic law of the wall as first given by von Kármán (1930) where the friction velocity u_τ is the only velocity scale in the near wall region. So far a logarithmic scaling law has only been found in the vicinity of the wall. The wall breaks the translational symmetry with respect to x_2 and hence a_3 has to be zero.

Exponential mean velocity profile: ($a_1 = 0$ and $a_4 \neq a_2 \neq 0$)

Since a_1 is zero in the present case there is an external length scale which breaks the symmetry in (16) with respect to the spatial coordinates. As a result the spatial coordinate is an invariant with only a constant added to the infinitesimal in (16) resulting from the frame invariance in the x_2 direction.

The mean velocity \bar{u}_1 turns out to have the following form

$$\bar{u}_1 = \frac{a_2}{a_4} + \exp\left(-\frac{a_4}{a_3}x_2\right)C_3. \quad (19)$$

It will be shown in section (4) that (19) applies to the flat plate high Reynolds number boundary layer flow. It appears that the boundary layer thickness is the external length scale which is symmetry breaking.

Linear mean velocity profile: ($a_1 = a_4 = 0$ and $b_1 \neq a_3 \neq 0$)

In the present case there is an external velocity and length scale symmetry breaking. Only the linear mean velocity profile is a self-similar solution

$$\bar{u}_1 = \frac{a_2}{a_3}x_2 + C_4. \quad (20)$$

The latter profiles may apply in the viscous sublayer where ν/u_τ and u_τ are the symmetry breaking length and velocity scales respectively. Another example is the center region of a turbulent Couette flow where the symmetry is broken due to the moving wall velocity and channel height (see Bech (1995) and Robertson (1970)).

3.2 Turbulent shear flows with non-zero system rotation

Here we consider the symmetries of the Eqs. (6)-(9) with $\Omega \neq 0$. The infinitesimal generators to be obtained are very similar to those in non-rotating case but with one important difference: $a_4 = 0$ and hence the scaling symmetry with respect to the time has been lost.

The rotation rate Ω scales with x_2 and only the linear profile is a self-similar solution

$$\bar{u}_1 = C_5\Omega x_2 + C_6. \quad (21)$$

The present case is distinguished from the previous linear mean velocity profiles since a scaling of the spatial coordinates still holds ($a_1 \neq 0$). The present linear law applies in the center region of a rotating turbulent channel flow where the time scale is the inverse of the rotation rate Ω .

4. Experimental and numerical verification of the scaling laws

Some of the mean velocity profiles derived in the previous section have been already obtained by means of other methods and verified in several experiments and DNS data. The best known result is von Kármán's (1930) logarithmic law of the wall which has been verified in a large number of experiments since its derivation.

Another well known mean velocity profile, derived in the previous section, is the linear mean velocity which can be found in the viscous sublayer of the universal law of the wall, and it is valid up to about $y^+ = 3$. May be less well known is the linear mean velocity profile which covers a broad region in the center of a turbulent Couette flow. This has been shown by the experimental study of Robertson (1970) and in the DNS of Bech (1995) to name only two. In both of the latter two cases there is a length and a velocity scale dominating the flow and hence break two scaling symmetries. In the viscous sublayer the length and the velocity scale are ν/u_τ and u_τ and in the turbulent Couette flow it is b and u_w , the channel width and the wall velocity respectively. As a consequence, no scaling symmetry exists as has been already pointed out in the previous section and only the linear mean velocity profile is a self-similar solution.

A third linear mean velocity profile, which from a similarity point of view is distinct from the previous two cases, can be found in the center region of a rotating channel flow. Here the external time scale Ω^{-1} acts on the flow and hence it is symmetry breaking which results in $a_4 = 0$. However, in contrary to the previous case a scaling symmetry with respect to the spatial coordinates still exists. The linear mean velocity as given by Eq. (21) is well documented in the experimental data of Johnston (1972) and in the DNS results of Kristoffersen (1993). In both investigations they found the value C_5 to be approximately 2.

In order to avoid the duplication of well documented invariant solutions, we will focus on basically two cases. The first one is the verification of the exponential law, which has never been reported in the literature. This has been found to match a broad region in the outer part of a turbulent boundary layer flow. The second one is the algebraic law which fits about 80% of the core region of the turbulent channel flow. In addition the algebraic scaling law has also been identified in the vicinity of the wall in low Reynolds DNS data of a turbulent channel flow.

Zero pressure-gradient turbulent boundary layer flow

There is a considerable amount of data available for canonical boundary layer flows but the Reynolds number is usually low and some of the data contain too much scatter. For the present purpose the data need to be very smooth.

Three sets of experimental data have been chosen for comparison with the exponential velocity profile. These data are at medium to high Reynolds numbers, and we believe that they have been taken very carefully. The data of DeGraaff (1996) are very smooth and cover the Reynolds number range $Re_\theta = 1500 - 20000$, where $\theta = \int_0^\infty (1 - \bar{u}/\bar{u}_\infty)\bar{u}/\bar{u}_\infty dy$ is the momentum thickness and \bar{u}_∞ is the free stream velocity. The second set of data are from Fernholz (1995) with the highest Reynolds number of $Re_\theta = 60000$. The third data set of Saddoughi (1994) reaches the unchallenged Reynolds number of $Re_\theta = 370000$.

Figure 1 shows DeGraaff's data for the mean velocity profiles taken at six different Reynolds numbers, in the usual wall variables in semi-log scaling. The extension of the viscous subregion and the logarithmic region are visible, with extension depending on the Reynolds number. In outer scaling the log-region extends approximately to $y/\Delta = 0.025$ where $\Delta = \int_0^\infty (\bar{u}_\infty - \bar{u})/u_\tau dy$ is the Rotta-Clauser length scale and

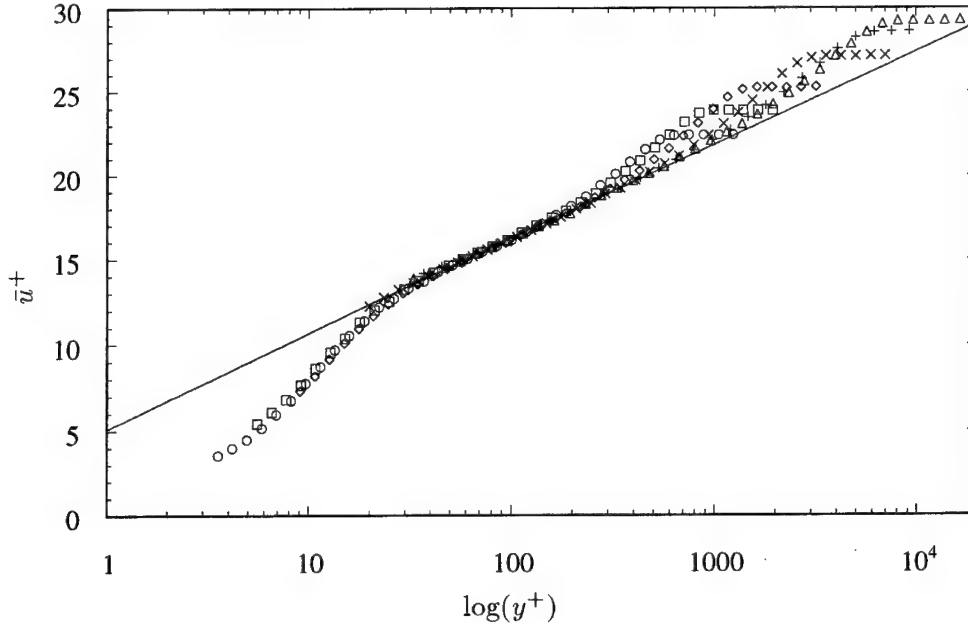


FIGURE 1. Mean velocity of the zero-pressure gradient turbulent boundary layer in log-linear scaling from DeGraaff (1996): \circ , $Re_\theta = 1500$; \square , $Re_\theta = 2300$; \diamond , $Re_\theta = 3800$; \times , $Re_\theta = 8600$; $+$, $Re_\theta = 15000$; \triangle , $Re_\theta = 20000$; —, $2.41 \ln(y^+) + 5.1$.

u_τ is the friction velocity.

As has been pointed out above, it appears that the exponential law (19) matches the outer part of a high Reynolds number flat plate boundary layer flow. In order to match the theory and the data, the mean velocity profile in Eq. (19) will be re-written in outer scaling

$$\frac{\bar{u}_\infty - \bar{u}}{u_\tau} = \alpha \exp\left(-\beta \frac{y}{\Delta}\right) \quad (22)$$

where α and β are universal constants.

In Fig. 2 the turbulent boundary layer data are plotted as $\log\left[\frac{\bar{u}_\infty - \bar{u}}{u_\tau}\right]$ vs. $\frac{y}{\Delta}$. If the data match the scaling law given by (22) a straight line is visible. In the scaling of Fig. 2 the log region is valid up to $y/\Delta \approx 0.025$ and does not follow the exponential (22). For all Reynolds number cases, there is no Reynolds number dependence within the measurement accuracy, and all the data appear to converge to a straight line in the region $y/\Delta \approx 0.025 - 0.15$. The data of Saddoughi (1994) show an extended region for the exponential law up to about $y/\Delta \approx 0.23$. With increasing Reynolds number the applicability of the exponential law appears to increase. For the medium Reynolds number cases, the applicability is approximately five times longer than the logarithmic law and for the high Reynolds number case it is about eight times longer.

The outer part of the boundary layer does not match the exponential (22) and

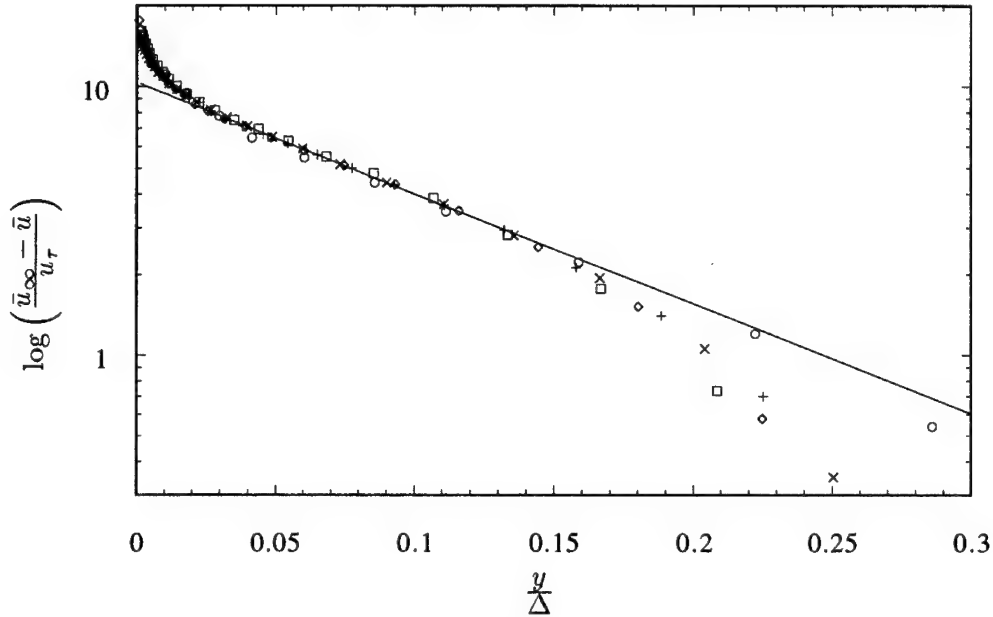


FIGURE 2. Mean velocity of the zero-pressure gradient turbulent boundary layer in lin-log scaling of the defect law: \circ , $Re_\theta = 370000$ (Saddoughi (1994)); \square , and \diamond , $Re_\theta = 60000$ (Fernholz (1995)); $+$, $Re_\theta = 15000$ and \times , $Re_\theta = 20000$ (DeGraaff 1996)); —, $10.34 \exp(-9.46y/\Delta)$.

it appears that a weak Reynolds number dependence exists. This seems to be in contradiction to Coles (1962) who found the wake parameter to be constant for $Re_\theta > 5000$. However, several explanations can be given for this behavior. It is common to have a few percent of error in experimental data. Since the data are plotted in log coordinates, and the free stream velocity is subtracted, a few percent error in the free stream velocity has a large impact on the lower part of the curve. This is almost invisible in the upper part. In fact from $y/\Delta \approx 0.3$ the data for the medium Reynolds number flows exhibit no clear trend. This is due to the error accumulation coming from the difference of two almost equally large numerical values.

$y/\Delta \approx 0.3$ corresponds approximately to the boundary layer edge. It is also possible that the outer-region large-scale intermittency plays a dominant role for the scaling of the mean velocity.

If the exponential velocity profile (22) were valid over the entire boundary layer, an integration of (22) from zero to infinity would give $\alpha = \beta$. A least square fit of the presented data leads to approximately the latter equivalence with $\alpha = 10.34$ and $\beta = 9.46$.

Even though the exponential (22) in Fig. 2 shows an excellent agreement with the experimental data, one may object that, unlike the channel flow, boundary layer flows are not strictly fully parallel flows. However, since the stream line curvature is usually very small, locally the flow can be considered as parallel. The dependence

on the streamwise position is hidden in the Rotta-Clauser length Δ and hence does not appear in the experimental results explicitly. Recently Oberlack (1996c) has derived the exponential mean velocity by a group analysis of the two-point correlation equation for a two-dimensional mean flow. It corresponds to a linear growth rate of the boundary layer thickness.

The two dimensional turbulent channel flow

Most data for the turbulent channel flow exhibits too much scatter and cannot be used for the present purpose. A fair comparison between data and algebraic law can only be made in double log plots. Here the experimental data of Niederschulte (1996), Wei (1989) and the low Reynolds number DNS data of Kim (1987) will be used for the investigation of the algebraic scaling law.

Beside the classical wall based scaling laws, here we found another algebraic regime which scales on a wall normal coordinate with its origin in the center of the channel. The validity of an algebraic scaling law based on the center-line appears to be more clear than for the near wall region. The reason for that can be found in the infinitesimal generators (16). Since for the algebraic scaling law both constants a_1 and a_4 have to be non-zero and different from each other, the region where the algebraic scaling law applies has the highest degree of symmetry. The center region seems to be more suitable for that because in the near wall region u_τ is symmetry breaking which results to $a_1 = a_4$ and eventually leads to the log law.

Regarding the algebraic law in the center of the channel we find the appropriate outer scaling for the channel is similar to the turbulent boundary layer flow

$$\frac{\bar{u}_c - \bar{u}}{u_\tau} = \varphi \left(\frac{y}{b} \right)^\gamma, \quad (23)$$

where φ and γ are constants, y originates on the channel center line, \bar{u}_c is the center line velocity and b is the channel half width.

In Fig. 3 the data of Wei (1989) and Niederschulte (1996) have been plotted in double log scaling for the Reynolds number range $Re_c = 18000 - 40000$, where Re_c is based on the center line velocity and channel half width. Even though the data exhibit some scatter, there is some obvious indication that the center region up to about $y/b = 0.8$ closely follows an algebraic scaling law given by (23). The unknown constants in (23) have been fitted to $\varphi = 5.83$ and $\gamma = 1.69$ using Niederschulte's data. We believe Niederschulte's experiment has been done very carefully and the algebraic scaling law has a large extension towards the center line.

An even more profound indication regarding the algebraic law can be obtained from the DNS data of Kim (1987). In Fig. 4 the data are plotted in double log scaling and an almost perfectly straight line is visible for both $Re_c = 3300$ and 7900 from the centerline up to about $y/b = 0.75$. The scaling extends slightly further out for the $Re_c = 7900$ case. Since both Reynolds numbers in the DNS are low, a weak Reynolds number dependence of both φ and γ exists.

At this point it may be instructive to refer to a recent result of Oberlack (1996b) who analyzed circular parallel turbulent shear flows with respect to the self-similarity using the present theory. For this case he also found the existence of an algebraic

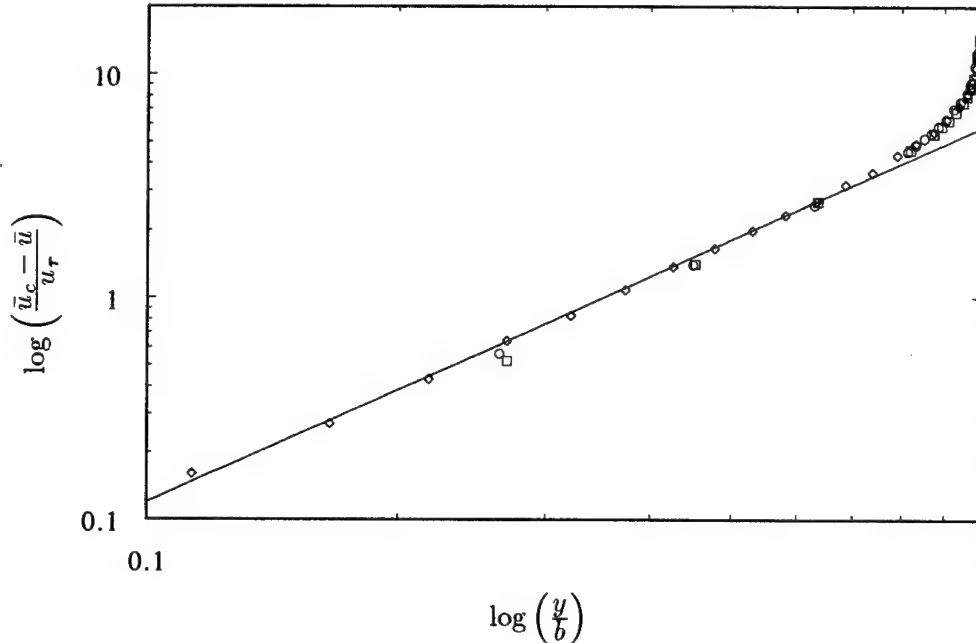


FIGURE 3. Mean velocity of the turbulent channel flow in double-log defect law scaling: \circ , $Re_c = 40000$; \square , $Re_c = 23000$ Wei (1989); \diamond , $Re_c = 18000$ Niederschulte (1996); —, $5.83(y/b)^{1.69}$.

scaling law. Oberlack analyzed the high Reynolds number data of Zagarola (1996) and here also he found an almost perfect fit, covering 80% of the center of the pipe.

It has been mentioned earlier that in appendix of Oberlack (1996a) the two-point correlation equations have been analyzed with respect to its self-similarity of a parallel shear flow. The resulting equation for the mean flow derived there is fully equivalent to the Eqs. (15)/(16). Further more scaling laws for the two-point correlations could be obtained.

Hunt (1987) have analyzed the two-point correlations with respect to self-similarity using the data of Kim (1987). They investigated the near wall region assuming the logarithmic law to hold. The surprising result here is that the self-similarity of R_{22} has a much longer extension towards the centerline as could be expected from the fairly short log region in the mean flow. The result could be clarified using the fact that the near wall region does not follow a log, but rather an algebraic scaling law. Figure 5 shows the mean velocity of the channel flow data in double log coordinates. Up to about $y^+ = 3$ the linear law of the viscous sublayer is valid. In the range $50 < y^+ < 250$ for $Re_c = 7900$ an almost perfectly straight line is visible and a least square fit of an algebraic law in this range results in a much higher correlation coefficient than a least square fit of a logarithmic function. Since the algebraic law extends much further than a logarithmic law, we can also expect the self-similarity of the two-point correlation R_{22} to hold much further. The only difference for R_{22} regarding the two different scaling laws is that in case of the algebraic scaling law

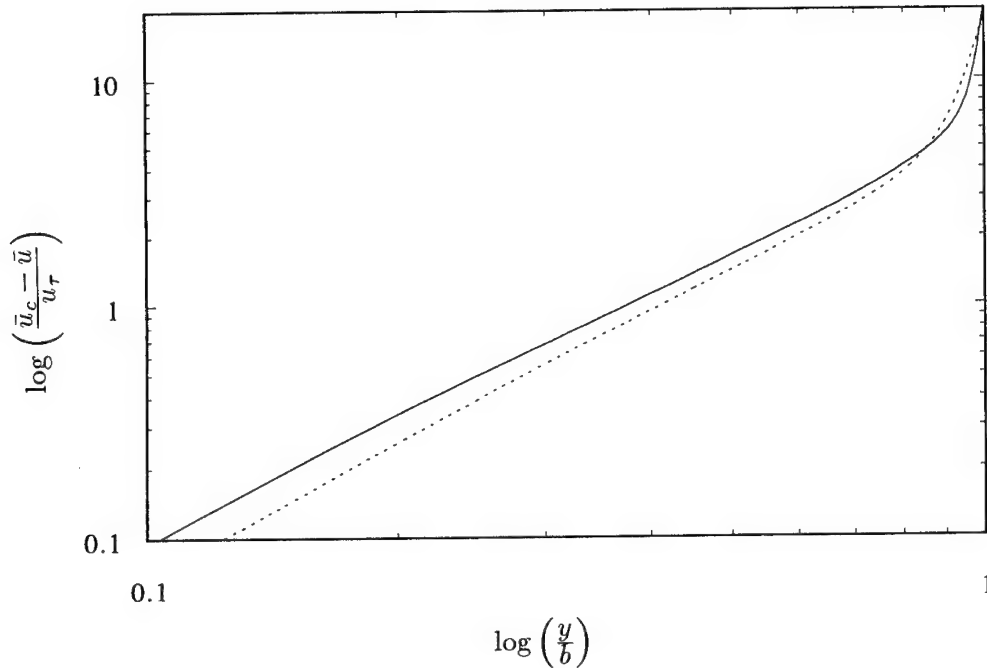


FIGURE 4. Mean velocity of the turbulent channel flow in double-log defect law scaling from Kim, Moin & Moser (1987): —, $Re_c = 7900$; ---, $Re_c = 3300$.

R_{22} also scales with the wall distance, while for the log law this is not the case.

5. Future plans

In the near future the theory presented herein will be applied to turbulent flows with higher dimensions up to 3D time dependent ones. If possible, all self-similar flows will be empirically validated using experimental and DNS data.

An important application of the present theory is in turbulence modeling. Common statistical turbulence models may not be consistent with all the symmetries calculated in the present theory and hence can not capture the associated scaling laws. As an example, consider the standard k - ε model which, interesting enough, formally admits all the symmetries of the unaveraged Euler equations (see Pukhnachev (1972)). This is somewhat misleading since it has been shown in the previous sections that turbulence has different symmetry properties than the unaveraged Navier-Stokes equations.

The standard k - ε model captures some non-trivial scaling laws like the exponential law. However, it can be shown in the case of a turbulent channel flow that the symmetry groups of the k - ε are not consistent with the present finding. As a result, k - ε misses the correct exponent for the algebraic mean velocity profile in the center of the channel.

The present theory can be used as an guide to develop new or improve existing turbulence models. It is proposed that turbulence models should have all of the symmetry properties computed in the present analysis. This is a necessary condition

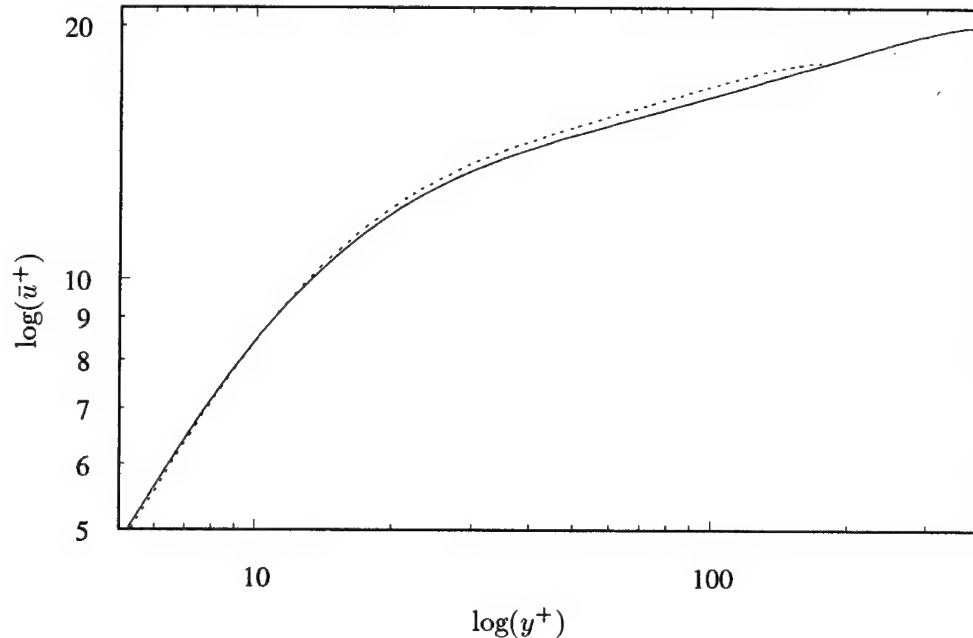


FIGURE 5. Mean velocity of the turbulent channel flow in double log scaling from Kim, Moin & Moser (1987): —, $Re_c = 7900$; ----, $Re_c = 3300$.

in order to capture the turbulent scaling laws and the associated turbulent flows. The presented symmetry properties in turbulent flows can be considered as a new realizability concept. A more general theory on symmetries in turbulence models is now under investigation and will be published elsewhere.

Acknowledgment

The author is sincerely grateful to Peter Bradshaw, Brian J. Cantwell, Nail H. Ibragimov, William C. Reynolds and Seyed G. Saddoughi for reading the manuscript at several stages of its development and giving valuable comments. The author is in particular thankful to Javier Jiménez for discussing some physical interpretation of the symmetry groups. Furthermore he thanks Dave Degraaff, Robert D. Moser, Seyed G. Saddoughi, Martin Schober and Timothy Wei for the kind cooperation and their cession of the data. Finally, I would like to thank Willy Hereman who was extremely patient in answering all my questions regarding the Lie group package SYMMGRP.MAX. The work was in part supported by the Deutsche Forschungsgemeinschaft.

REFERENCES

- BARENBLATT, G. 1993 Scaling laws for fully developed turbulent shear flows. Part 1. Basic hypotheses and analysis. *J. Fluid Mech.* **248**, 513-520.
- BECH, K. H., TILLMARK N., ALFREDSSON, P. H. & ANDERSSON, H. I. 1995 An investigation of turbulent plane Couette flow at low Reynolds numbers. *J.*

Fluid Mech. **286**, 291-325.

BLUMAN, G. W. & KUMEI S. 1989 *Symmetries and Differential Equations*. Applied mathematical sciences, **81**, Springer.

CANTWELL, B. J. 1981 Organized motion in turbulent flow. *Ann. Rev. Fluid Mech.* **13**, 457-515.

CHAMPAGNE, B., HEREMAN, W. & WINTERNITZ, P. 1991 The computer calculation of Lie point symmetries of large systems of differential equations. *Comp. Phys. Comm.* **66**, 319-340.

COLES, D. 1962 *The turbulent boundary layer in a compressible fluid*. Report, R-403-PR., The Rand Corporation, Santa Monica, CA.

DEGRAAFF, D. 1996 Private communication.

FERNHOLZ, H. H., KRAUSE, E., NOCKEMANN M. & SCHÖBER, M. 1995 Comparative measurements in the canonical boundary layer at $Re_{\delta_2} \leq 6 \times 10^4$ on the wall of the German-Dutch wind tunnel. *Phys. Fluids*. **7**, (6), 1275-1281.

GEORGE, W. K., CASTILLO, L. & KNECHT, P. 1993 The zero pressure-gradient turbulent boundary layer. *Reynolds Symposium on Turbulence*, Asilomar, CA.

HUNT, J. C. R., MOIN, P., MOSER, R. D. & SPALART, P. R. 1987 Self similarity of two-point correlation in wall bounded turbulent flows. *CTR Summer Program Proceedings, Center for Turbulence Research, Stanford Univ./NASA Ames*, 25-36.

JIMÉNEZ, J. 1996 Private communication.

JOHNSTON, J. P., HALLEEN, R. M. & LAZIUS D. K. 1972 Effects of spanwise rotation on the structure of two-dimensional fully developed turbulent channel flow. *J. Fluid Mech.* **56**, 533-557.

VON KÁRMÁN, TH. 1930 Mechanische Ähnlichkeit und Turbulenz. *Nachr. Ges. Wiss. Göttingen*. **68**.

KIM, J., MOIN, P. & MOSER, R. 1987 Turbulence statistics in fully developed channel flow at low Reynolds number. *J. Fluid Mech.* **177**, 133-166.

KRISTOFFERSEN, R. & ANDERSSON H. I. 1993 Direct simulations of low-Reynolds-number turbulent flow in a rotating channel. *J. Fluid Mech.* **256**, 163-197.

MACSYMA 1993 Mathematics Reference Manual. *Macsyma Inc.*

NIEDERSCHULTE, G. L. 1996 Turbulent flow through a rectangular channel. *Ph. D. thesis at University of Illinois, Department of Theoretical and Applied Mechanics*.

OBERLACK, M. 1995 Analysis of the two-point velocity correlations in turbulent boundary layer flows. *Annual Research Briefs 1995* Center for Turbulence NASA Ames/Stanford Univ., 209-220.

OBERLACK, M. 1996a Unified theory for symmetries in plane parallel turbulent shear flows. To be submitted to *J. Fluid Mech.*

- OBERLACK, M. 1996b Similarity in rotating and non-rotating turbulent pipe flows. To be submitted to *J. Fluid Mech.*
- OBERLACK, M. 1996c Symmetries in the two-point correlation equation for plane turbulent flows. Unpublished.
- PUKHNACHEV, V. V. 1972 Invariant solutions of Navier-Stokes equations describing motions with free boundary. *Dokl. Akad. Nauk.* **202**, 302.
- ROBERTSON, J. M. & JOHANSON, H. F. 1970 Turbulence structure in plane Couette flow. *J. Engng. Mech. Div. ASCE.* **96**, 1171.
- SADDOUGHI, S. G. & VEERAVALLI S. V. 1994 Local isotropy in turbulent boundary layers at high Reynolds number. *J. Fluid Mech.* **268**, 333-372.
- WEI, T. & WILLMARTH, W. W. 1989 Reynolds-number effects on the structure of a turbulent channel flow. *J. Fluid Mech.* **204**, 57-95.
- ZAGAROLA, M. V. 1996 Mean-flow scaling of turbulent pipe flow. Dissertation at Princeton University.

Near-wall models in large eddy simulations of flow behind a backward-facing step

By W. Cabot

1. Motivation & objectives

Accurate large eddy simulation (LES) of a wall-bounded flow generally requires a near-wall resolution comparable to that in direct numerical simulation (DNS). As much as 50% of the total grid points — and computational cost — are expended in the near-wall regions in a typical simulation. This limits LES to fairly low Reynolds numbers on current computers. To perform practical flow applications at realistically high Reynolds numbers, such as flow over an airfoil, it is desirable to replace very thin, near-wall regions in the LES with easily and inexpensively computed wall models to specify the near-wall boundary conditions.

This approach is expected to be feasible in simple flows with well developed boundary layers where local equilibrium conditions are expected to hold and known, empirical law-of-the-wall scalings can be exploited. Cabot (1995) found that LES of channel flow, with wall stresses predicted by either an instantaneous log law or by integration of simple boundary layer equations, produced accurate low-order statistics. Piomelli *et al.* (1989) used modified log law models for the wall stress in channel flow. Using the same models, Arnal & Friedrich (1993) obtained mean flow statistics in high Reynolds number flow over a backward-facing step in fair agreement with experimental measurements. Balaras *et al.* (1996) used simple boundary layer equations to successfully simulate channel flow and flow in a square duct.

In practical applications the flow is usually more complicated and can feature large adverse pressure gradients and extensive regions of separation, reattachment, and recovery. Such is the case in the flow over a backward-facing step. The objective of this work is to study the applicability of the simple near-wall models, similar to those used in channel flow, to the flow over a step, even though equilibrium conditions will not be valid in the reattachment region and turbulent models may be invalid in the separated region. If these wall models fail to give satisfactory results, different near-wall modeling schemes that can handle a wider range of flow conditions will need to be formulated and tested; the tests performed here may provide some insight into what physical ingredients these more general wall models need to incorporate.

2. Accomplishments

In this study of the flow over a backward-facing step, only the bottom wall behind the step was modeled, since this is where the most complex flow behavior occurs (Fig. 1). Differential boundary layer equations were used as the basis of the near-wall model in a thin “sublayer” region, in the hope that they would be flexible enough to treat local flow and pressure variations in a more accurate manner than

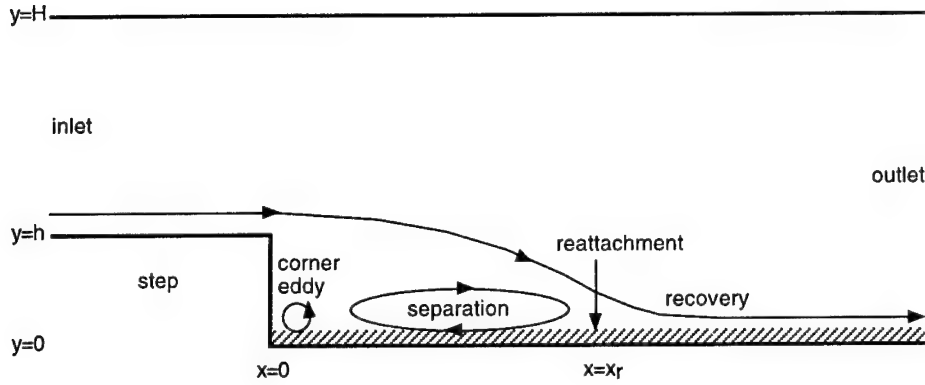


FIGURE 1. Sketch of the flow over a step (*not to scale*). The cross-hatched region along the lower wall behind the step is replaced by a near-wall model.

algebraic relations. Results from LES with wall models were compared with results from LES with resolved walls at moderately high Reynolds numbers by Akselvoll & Moin (1995), referred to hereafter as “the full LES”. The results were also compared with experimental measurements for nearly the same flow configuration by Adams *et al.* (1984) and Vogel & Eaton (1985).

The flow has a Reynolds number Re_h (based on the inlet centerline velocity U_c and step height h) of 28,000, and the outlet-to-inlet expansion ratio is 1.25. The flow is separated from $x/h \approx 2-7$ (where x is the streamwise location past the step). Reattachment occurs in the mean at $x_r \approx 7h$, beyond which the flow recovers (almost) to a standard boundary layer by the time it reaches the outlet at $x \approx 20h$.

2.1 Near-wall momentum balance

A preliminary look at the complexity of the flow behind the step is provided by calculating the balance of terms in the streamwise momentum equation in the near-wall region. The time- and span-averaged flow field from the full LES is used for this purpose. The streamwise component of the Navier-Stokes equation is integrated from the wall to a height $y = 0.08h$ (corresponding to $y^+ \approx 60$ in wall units near the outlet). This gives

$$\begin{aligned}
 & \underbrace{-\int_0^y (\partial \langle u^2 \rangle / \partial x) dy}_1 - \underbrace{\langle uv \rangle}_2 - \underbrace{\int_0^y (\partial P / \partial x) dy}_3 \\
 & \quad + \underbrace{(\nu \partial U / \partial y - \tau_w)}_4 + \int_0^y (\nu \partial^2 U / \partial x^2) dy \approx 0,
 \end{aligned} \tag{1}$$

where $\langle \dots \rangle$ denotes the average, and where $U = \langle u \rangle$ and $P = \langle p \rangle$. The streamwise wall stress, $\tau_w = \nu \partial U / \partial y$ at $y = 0$, is the term that one is most interested in predicting from the wall model. The first term is dominated by the mean velocity

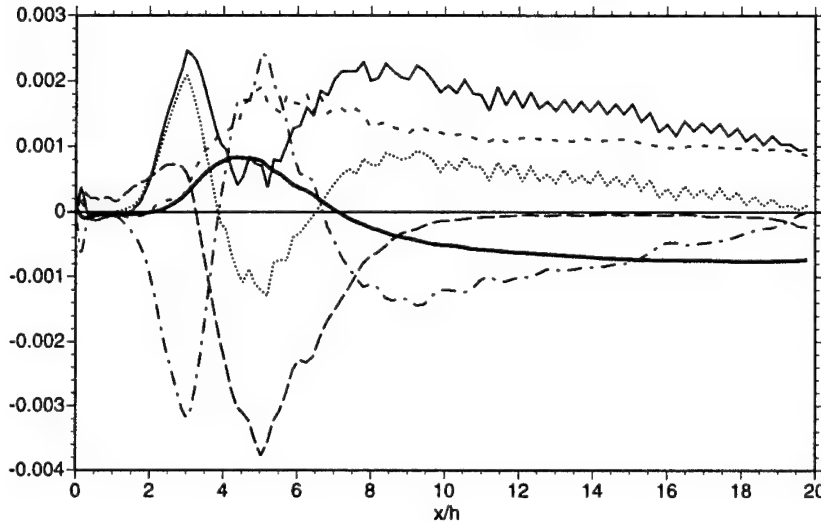


FIGURE 2. Streamwise momentum balance terms from Eqs. (1) and (2) in the region near the bottom wall behind a step from Akselvoll & Moin's (1995) $Re_h = 28000$ LES: — streamwise advection (term 1); — wall-normal advection (term 2); --- streamwise pressure gradient (term 3); — viscous stress (term 4). Term 2 is also decomposed into mean momentum flux (term 2a) and ---- Reynolds stress (term 2b).

component ($\langle u^2 \rangle \approx U^2$) and the lattermost viscous term is completely negligible. Further, the wall-normal momentum flux $\langle uv \rangle$ can be decomposed into a mean part (UV , where $V = \langle v \rangle$) and a Reynolds stress part ($\langle u'v' \rangle$, which includes the contribution from the subgrid-scale model). This gives

$$-\int_0^y (\partial U^2 / \partial x) dy - \underbrace{UV}_{2a} - \underbrace{\langle u'v' \rangle}_{2b} - \int_0^y (\partial P / \partial x) dy + (\nu \partial U / \partial y - \tau_w) \approx 0. \quad (2)$$

These terms are shown in Fig. 2. It is seen that the viscous stress roughly balances the Reynolds stress only far downstream in outlet region ($x/h \approx 20$), where the flow begins to resemble a well developed, zero-pressure-gradient boundary layer. In the separated region ($x/h \approx 2-7$), however, the large advection and adverse pressure gradient terms are very important in the momentum balance. One might therefore suspect *ab initio* that wall models based simply on stress balance would not perform well in this flow.

The presence of relatively large Reynolds stresses in the separated region seems to contradict the common notion that this is an inherently two-dimensional, laminar roller. Although it is possible that the Reynolds stress here is not a measure of turbulence so much as a measure of spanwise oscillations and streamwise movement of the unsteady roller structure, it is evident from the LES results of Le & Moin (1993) that a large amount of turbulence is transported to the reattachment and

separated regions from the overlying shear layer (also see the article by Parneix & Durbin in this volume).

2.2 Large eddy simulations with near-wall boundary layer equations

The boundary layer equations are derived from the Navier-Stokes equations under the assumption that, in the very thin wall region, the horizontal (x and z) length scales are much greater than the wall-normal (y) scales, and that y derivatives are much greater than x, z derivatives. For this reason viscous terms involving horizontal gradients are neglected, and the wall-normal pressure gradient is assumed to be negligible. These resulting equations for the horizontal velocity components, in which $\tilde{\cdot}$ denotes a space and/or time filter, are

$$\frac{\partial \tilde{u}_\ell}{\partial t} + \frac{\partial(\tilde{u}_\ell \tilde{u}_j)}{\partial x_j} = -\frac{\partial \tilde{p}}{\partial x_\ell} + \nu \frac{\partial^2 \tilde{u}_\ell}{\partial y^2}, \quad \ell = 1, 3; \quad (3)$$

the wall-normal velocity component v is found from the continuity equation,

$$\tilde{v} = - \int_0^y \left(\frac{\partial \tilde{u}}{\partial x} + \frac{\partial \tilde{w}}{\partial z} \right) dy. \quad (4)$$

The standard procedure is to integrate these equations on a fine wall-normal mesh with a fixed horizontal pressure gradient that is set at the base of the overlying interior flow. The boundary conditions for the horizontal velocity components are that they vanish at the wall and match the corresponding interior velocity components at the top of the sublayer. The matching horizontal velocity and pressure gradient from the interior flow are filtered to the same resolution as sublayer calculation. Note that there is no pressure solution required in the sublayer, which simplifies the calculation considerably. The wall-normal derivatives of \tilde{u}_ℓ at the walls are computed from the sublayer solution to give the wall stress components, $\tilde{\tau}_{w\ell} = \nu \partial \tilde{u}_\ell / \partial y$, which are used as boundary conditions by the interior flow solution.

The term $\tilde{u}_\ell \tilde{u}_j$ must be modeled, just as in the filtered equations for LES or Reynolds-averaged Navier-Stokes (RANS) equations. For the sublayer, near-wall eddy viscosity models based on the law-of-the-wall have been generally used, similar to RANS models (cf. Menter, 1991):

$$\tilde{u}_\ell \tilde{v} \sim \tilde{u}_\ell \tilde{v} - \nu_t \frac{\partial \tilde{u}_\ell}{\partial y}, \quad \nu_t = \kappa y u_s D^2, \quad D = 1 - \exp(-y u_d / \nu A), \quad (5)$$

where κ is the von Kármán constant (≈ 0.4), u_s is a velocity scale, and D is an *ad hoc* damping function for the viscous layer, where u_d is another velocity scale and $A = 19$ is a damping constant. In a standard law-of-the-wall model, the model velocity scales are just the friction velocity, $u_s = u_d = u_\tau \equiv (\tilde{\tau}_{w1}^2 + \tilde{\tau}_{w3}^2)^{1/4}$. In the Johnson-King model (Johnson & Coakley, 1990), u_s and u_d are different melds of u_τ and the square root of the maximum Reynolds stress; this model gives good results in flows with mild adverse pressure gradients and separation (Menter, 1991). No models are used for the horizontal momentum flux in the sublayer, viz.,

$$\frac{\partial \tilde{u}_\ell \tilde{u}}{\partial x} \sim \frac{\partial \tilde{u}_\ell \tilde{u}}{\partial x}, \quad \frac{\partial \tilde{u}_\ell \tilde{w}}{\partial z} \sim \frac{\partial \tilde{u}_\ell \tilde{w}}{\partial z}; \quad (6)$$

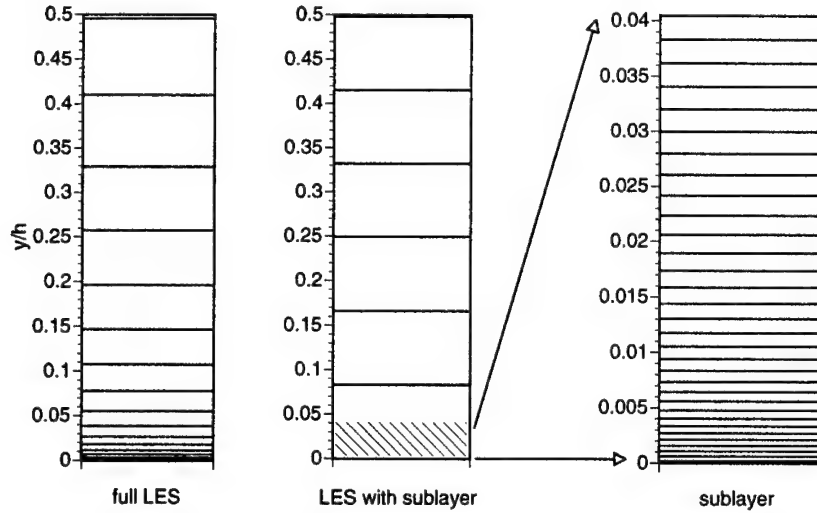


FIGURE 3. Wall-normal grid behind the step in the full LES and the LES with the wall model sublayer (cross-hatched region) embedded in the lower half of the wall cell.

adding the corresponding eddy viscosity models for these terms has not been found to give significantly different statistics. The boundary layer equations for the near-wall sublayer become

$$\frac{\partial \tilde{u}_\ell}{\partial t} + \frac{\partial(\tilde{u}_\ell \tilde{u}_j)}{\partial x_j} + \frac{\partial \tilde{p}}{\partial x_\ell} = \frac{\partial}{\partial y} \left[(\nu + \nu_t) \frac{\partial \tilde{u}_\ell}{\partial y} \right], \quad \ell = 1, 3. \quad (7)$$

Because the Reynolds stress model is based on RANS models, which assume an ensemble average (or an equivalently broad filter in space and/or time), the sublayer is computed on a horizontal mesh that is twice as coarse as the interior mesh; the matching velocities and pressure gradients are further filtered in time with a running time average, which is exponentially damped with an ϵ -folding time of h/U_c .

Equation (7) is used all the way into the corner behind the step, although at some point the neglected streamwise gradients must become important. As will become evident, this improper treatment may lead to some aberrant flow behavior in the corner.

The LES used in this study is identical to the $Re = 28000$ backstep simulation of Akselvoll & Moin (1995), except for the removal of grid points from the interior LES domain along the bottom wall behind the step. The wall-normal stretching in the original grid behind the lower half of the step was also removed to prevent numerical instability. The original and modified wall-normal meshes are compared in Fig. 3. The LES uses a second-order central finite difference scheme on a staggered grid with a compact, third-order Runge-Kutta time advancement and fractional step method for the pressure solution (Le & Moin, 1991). The original (x, y, z) grid

TABLE 1. Wall model cases

case	$\nabla \cdot \tilde{u}\tilde{u}$	$(\nabla \tilde{p})_m$	κ	u_s, u_d
LW0	no	no	0.4	u_τ
LW0p	no	yes	0.4	u_τ
LW1A	$(\text{yes})_m$	yes	0.4	u_τ
LW1	yes	yes	0.4	u_τ
DLW1	yes	yes	0–0.2*	u_τ
JK1	yes	yes	0.4	$\{u_\tau, u_m\}$

* “dynamic”

behind the step used a $146 \times 33 \times 96$ mesh on a $20h \times h \times 3h$ domain. The LES with the sublayer uses a $146 \times 23 \times 96$ interior mesh on the same domain; the sublayer itself uses a $74 \times 33 \times 48$ mesh between the wall up to the first off-wall nodes of the horizontal velocities at $y \approx 0.04h$.

A number of different variations of boundary layer Eqs. (7), with continuity (4) and eddy viscosity model (5), were used in the LES, a sample of which are presented here (summarized in Table 1). The simplest law-of-the-wall, stress-balance model, LW0, neglects advection and pressure gradient terms of the left-hand side of (7) altogether, and, with $u_s = u_d = u_\tau$ and $\kappa = 0.4$, gives a meld between the standard log law and viscous layer. Model LW0p includes only the pressure gradient fixed at the matching height, and LW1A included both advection and pressure gradient terms fixed at the matching height. Model LW1 includes all the terms on the left-hand side of (7), with the advection terms computed internally in the sublayer using the same integration scheme as the interior mesh. Model JK1 is the same as LW1 but uses the inner Johnson-King model (Menter, 1991) to calculate u_s and u_d ; the maximal shear stress used to evaluate the velocity scales is found from the interior and sublayer flow field behind the step, which significantly increases the expense of the calculation. It was found that the JK1 model predicted eddy viscosity values 2–3 times larger than the law-of-the-wall model. Because some of the Reynolds stress is retained in the advection terms on the left-hand side of (7) on the sublayer mesh, any RANS model for eddy viscosity is likely to overpredict the amount of Reynolds stress in the sublayer; thus another model, DLW1, was used in which the coefficient κ was estimated “dynamically” by matching the Reynolds stress $(\tilde{u}\tilde{v} - \tilde{u}\tilde{v})$ in the interior flow just above the sublayer to the law-of-the-wall model. As expected, this generally results in values of κ substantially lower than 0.4, as seen in Fig. 4.

The LES results show that the flow behind the step is much more sensitive to the wall model than was the case in channel flow, especially in the separated region. The steady-state wall stress predicted by the different models is shown in Fig. 5 and the pressure coefficient is shown in Fig. 6. Experimental results for a similar flow configuration are also shown for comparison. The LW0 model underpredicts the magnitude of the wall stress in the recovery region ($x/h \approx 7$ –15) as well as in the separated region ($x/h \approx 2$ –7) compared with the full LES results. Note, however, that the experimental wall stress is also about half the magnitude of the full LES in the separated region. Similar results have been found in other

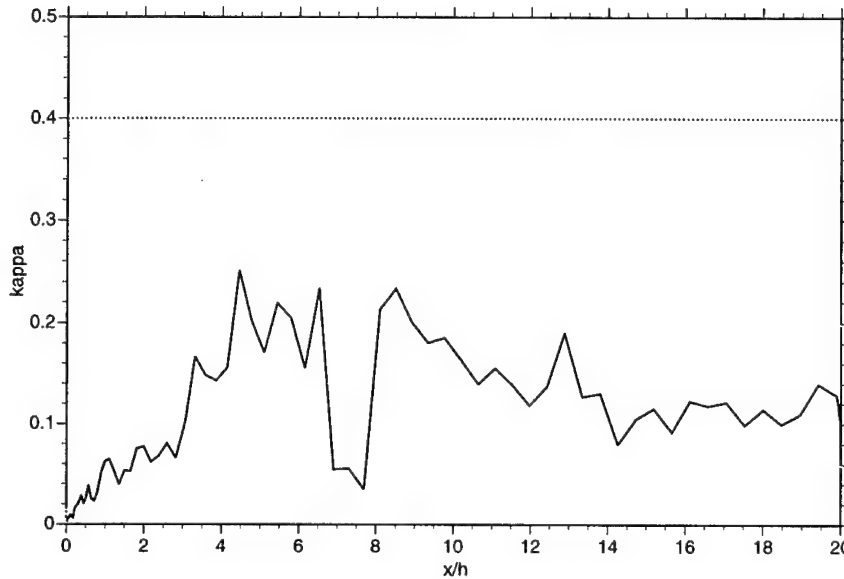


FIGURE 4. The near-wall eddy viscosity coefficient κ (averaged in z and over a short time) determined by a fit to the stress above the sublayer (—) is used in the DLW1 case, and its standard RANS value, the von Kármán constant (.....) is used in the LW1 case.

high Reynolds number experiments (Driver & Seegmiller, 1985); the LES results of Akselvoll & Moin (1995), in fact, resemble low Reynolds results (Le & Moin, 1993). The cause of this discrepancy is not known. But it obviously leads to confusion in attempting to gauge the performance of these wall model results. The JK1 model clearly overpredicts the wall stress everywhere due to its excessively large eddy viscosity. The LW1 case does a reasonable job in the recovery and outflow region, but overpredicts the wall stress in the separated region with excessively rapid backflow and low pressure (Fig. 6). There is little difference between DLW1 and LW1 cases, even though the eddy viscosity is more than halved (Fig. 4) in the former case; the magnitude of the wall stress is slightly less in the separated region, but the separated region spreads farther out from the step with reattachment moving from $x_r/h \approx 7.0$ – 7.2 . In fact, when the eddy viscosity is set to zero, there is little change in the results from the DLW1 case, indicating that the large pressure gradient and advection terms dominate the balances in the sublayer equations in these cases.

The corner regions in LES using any of the wall models all compare poorly with the full LES (although the comparison is somewhat better with the experimental results). Instead of forming a well developed corner eddy, the flow rushes straight into the corner and up the step. Large fluctuations in pressure and velocities are often observed in the corner. It is likely that the haphazard treatment of the corner region in the near-wall model, both in terms of the governing equations and grid resolution, may lead to the ill behavior of the flow. Also unanswered at this time is

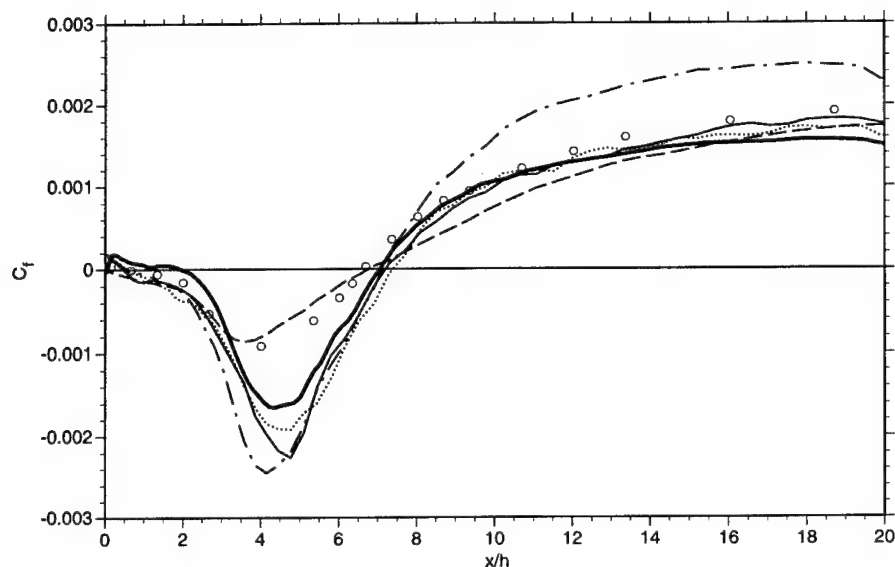


FIGURE 5. The friction coefficient $C_f = 2\tau_w/U_c^2$ on the bottom wall behind the step for the full LES (—) and LES with wall models: cases --- LW0, — LW1, DLW1, and —·— JK1; compared with Vogel & Eaton's (1985) experimental data (ooo).

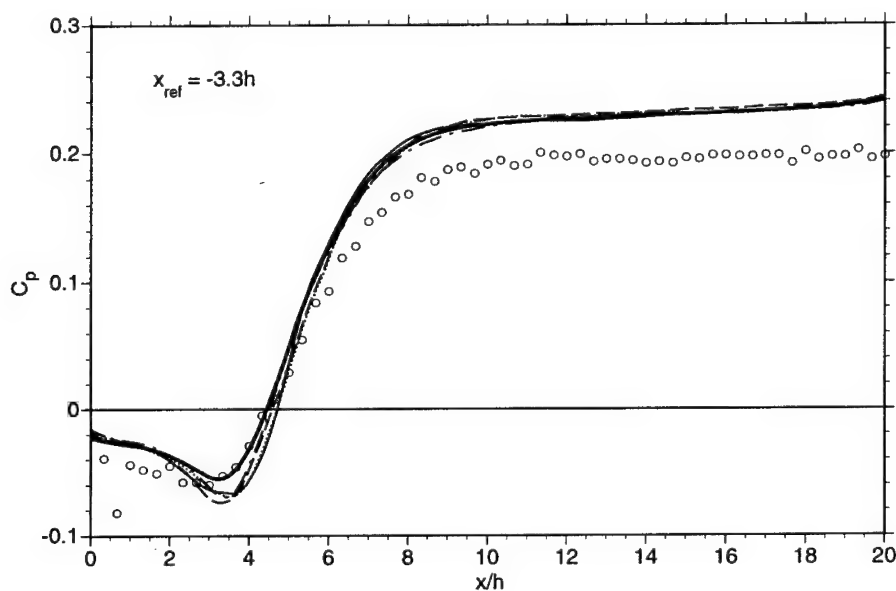


FIGURE 6. The pressure coefficient $C_p = 2(p_w - p_{\text{ref}})/U_c^2$ along the bottom wall behind the step for the full LES (—) and LES with wall models: cases --- LW0, — LW1, DLW1, and —·— JK1; compared with Adams *et al.*'s (1984) experimental data (ooo).

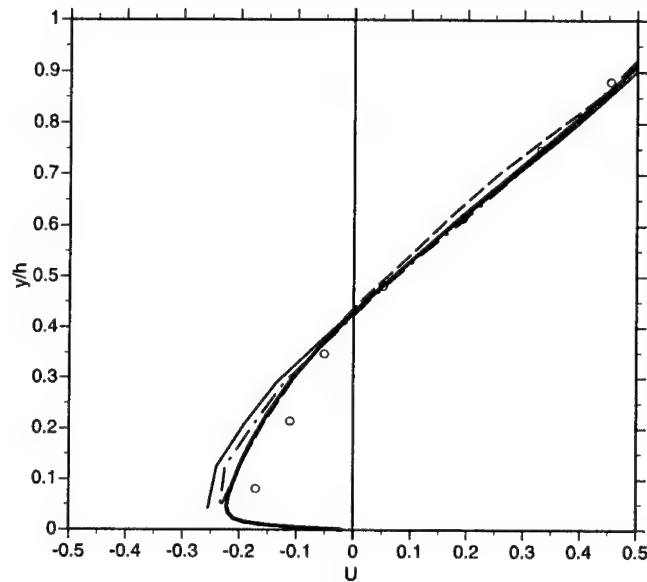


FIGURE 7. Mean streamwise velocity profile in the middle of the separated region for the full LES (—) and LES with wall models: cases --- LW0, —·— LW1, and ···· JK1; compared with Adams *et al.*'s (1984) experimental data (○ ○ ○).

whether the corner eddy fails to form because of the excessive speed of the backflow into the corner, or if it is the absence of the corner eddy (due to deficiencies in the wall model implementation) that allows the strong backflow to develop in the first place.

Mean streamwise velocity profiles appear to be rather insensitive to the different wall stresses predicted by the models. In general, the agreement between LES with wall models and the full LES is quite good, which in turn are in good agreement with experiments (see Akselvoll & Moin, 1995). The largest difference occurs in the separated region, where the LW1 model gives a noticeably larger backflow at $x/h = 4.5$ than in the full LES (Fig. 7). (All of the LES results in fact show a substantially larger backflow than the experiment.) Surprisingly, the mean flows for LW0 and JK1, which show the greatest deviation from the full LES in terms of wall stress, have the best overall agreement in term of mean streamwise velocity above the wall layer, even in the separated region.

The mean reattachment point of $x_r/h \approx 7.0$ is found for most of the wall model cases presented so far, in fair agreement with the full LES and experiments, due to a proper cancellation of (or in the case of LW0, a fortuitous absence of) terms in the sublayer. The simulation with a wall model that neglected the advection terms but retained the pressure gradient in (7) (case LW0p in Table 1) gave $x_r/h \approx 8.5$, and another that fixed both the pressure gradient and advection terms from the overlying interior flow (case LW1A in Table 1) gave $x_r/h \approx 7.5$; the wall stress

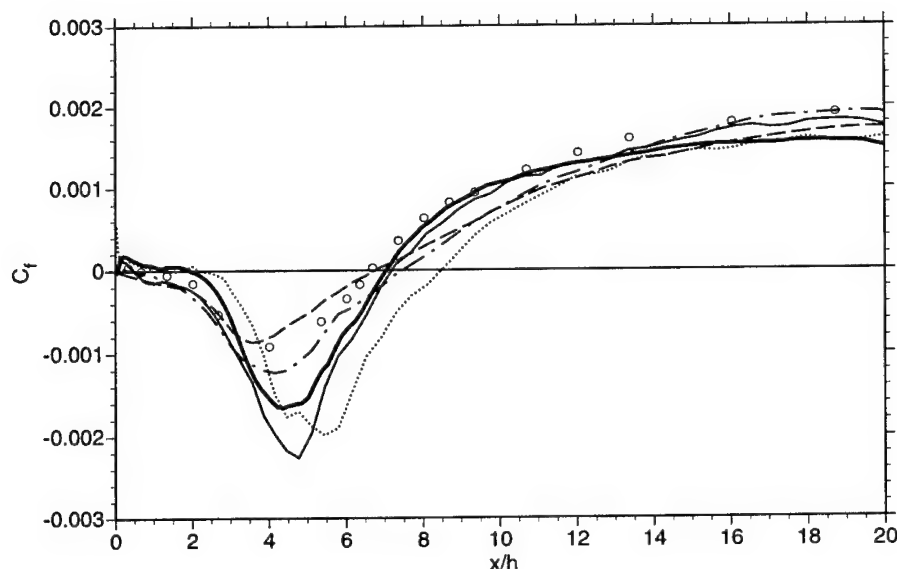


FIGURE 8. The friction coefficient on the bottom wall behind the step for the full LES (—) and LES with wall models: cases --- LW0, LW0p, — · — LW1A, and — — — LW1; compared with Vogel & Eaton's (1985) experimental data (o o o).

for these cases are shown in Fig. 8. These results suggest that the separation and reattachment regions are very sensitive to the near-wall balance between pressure gradients and advection terms in the sublayer.

3. Future plans

The cause of the sometimes poor results with the wall model behind the step needs to be ascertained. This is especially true of the separated and corner regions: Flows with boundary layer wall models develop overly rapid backflow (along with lower pressure) in the separated region than in the full LES, and they lack a well developed corner eddy. In broad terms, the culprit could be deficiencies in implementation of the wall model and/or in the equations representing the sublayer region. Many of these issues, outlined below, will be addressed in the future.

Implementation issues. Sensitivity to the sublayer mesh grid — in both horizontal and wall-normal directions — should be established. In the wall-normal direction, a strategy of overlapping the sublayer and interior zones is being explored, which will allow more flexibility in matching the two solutions. It may be proven to be more important to match things like the wall-normal momentum or stress than the streamwise velocity. The corner region requires special treatment, and it will need to be replaced with a different grid meshing and governing equations, or a different "corner" model (as yet undetermined). In principle, the wall model should be applied along all walls, including the corner, the face of the step, and around the

step's edge. A consistent treatment of the whole "near-step" problem will therefore be explored. A realistic cost appraisal of these methods will also then be possible. Wall models may also be implemented in an alternative flow, the diffuser, which features separation and adverse pressure gradients without the severe step geometry; both LES and experimental data exist for this flow as well.

Modeling issues. Modifications need to be made to the governing equations for the near-wall sublayer since the boundary layer equations are known to be inappropriate for the reattachment region where wall-normal scales are comparable to horizontal scales. The eddy viscosity model for the unresolved sublayer stress, based on RANS models, needs improvement. It has been tuned for well developed turbulent boundary layers, but is inappropriate for the nonequilibrium conditions behind the step in the separated and reattachment regions where turbulence is largely transported from high shear layers above. Alternative models that better describe this situation need to be formulated and tested; they can perhaps be merged smoothly to the standard stress model depending on flow conditions. The ability of the outer flow to communicate to the sublayer which type of flow to model may need to be developed in terms of global criteria rather than simple, local diagnostics. The *ad hoc* damping function in the law-of-the-wall eddy viscosity model (5) needs to be replaced with a more physical near-wall condition, perhaps based on the wall-normal velocity. The eddy viscosity model of the Reynolds stress in the separated region will likely need to be augmented or replaced altogether.

The discrepancy between the full LES and experimental results in the flow over the backward-facing step at high Reynolds numbers, particularly in the separated region, makes comparisons with LES with wall models rather ambiguous. For testing models that are intended to handle the separated region correctly, it may be better to use lower Reynolds number DNS and LES results (Le & Moin, 1993; Akselvoll & Moin, 1995), which agree very well with experiments.

REFERENCES

- ADAMS, E. W., JOHNSTON, J. P., & EATON, J. K. 1984 Experiments on the structure of turbulent reattaching flow. Dept. of Mech. Engr. Tech. Rep. MD-43, Stanford Univ.
- AKSELVOLL, K., & MOIN, P. 1995 Large eddy simulation of turbulent confined coannular jets and turbulent flow over a backward facing step. Dept. of Mech. Engr. Tech. Rep. TF-63, Stanford Univ.
- ARNAL, M., & FRIEDRICH, R. 1993 Large-eddy simulation of a turbulent flow with separation. In *Turbulent Shear Flows 8*, ed. by F. Durst *et al.*, Springer-Verlag (Berlin), 169-187.
- BALARAS, E., BENOCCHI, C., & PIOMELLI, U. 1996 Two-layer approximate boundary conditions for large-eddy simulations. *AIAA J.* **34**, 1111-1119.
- CABOT, W. 1995 Large-eddy simulations with wall models. *Annual Research Briefs 1995*, Center for Turbulence Research, NASA Ames/Stanford Univ., 41-50.

- DRIVER, D. M., & SEEGMILLER, H. L. 1985 Features of a reattaching turbulent shear layer in divergent channel flow. *AIAA J.* **23**, 163-171.
- JOHNSON, D. A., & COAKLEY, T. J. 1990 Improvements to a nonequilibrium algebraic turbulence model. *AIAA J.* **28**, 2000-2002.
- LE, H., & MOIN, P. 1991 An improvement of fractional step methods for the incompressible Navier-Stokes equations. *J. Comp. Phys.* **92**, 369-379.
- LE, H., & MOIN, P. 1993 Direct numerical simulation of turbulent flow over a backward-facing step. In *Annual Research Briefs 1992*, Center for Turbulence Research, NASA Ames/Stanford Univ. 161-173.
- MENTER, F. R. 1991 Performance of popular turbulence models for attached and separated adverse pressure gradient flows. *AIAA Paper.* **91-1784**.
- PIOMELLI, U., FERZIGER, J., MOIN, P., & KIM, J. 1989 New approximate boundary conditions for large eddy simulations of wall-bounded flows. *Phys. Fluids A.* **1**, 1061-1068.
- VOGEL, J. C., & EATON, J. K. 1985 Combined heat transfer and fluid dynamic measurements downstream of a backward-facing step. *ASME J. Heat Trans.* **107**, 922-929.

Assessment of the subgrid-scale models at low and high Reynolds numbers

By K. Horiuti¹

1. Motivation and objectives

Large-eddy simulation (LES) is a turbulence simulation method in which the large scale (grid-scale or GS) field is directly calculated, while the small scale (subgrid-scale or SGS) field is modeled. The velocity and pressure fields (f) are decomposed into GS component (\bar{f}) and SGS component ($f' = f - \bar{f}$) using a filtering procedure. A decomposition of the SGS stress tensor, τ_{ij} , which results from filtering the Navier-Stokes equations, consists of three terms (Bardina 1983):

$$\tau_{ij} = L_{ij} + C_{ij} + R_{ij}, \quad (1)$$

$$L_{ij} = \overline{\bar{u}_i \bar{u}_j} - \bar{u}_i \bar{u}_j, \quad C_{ij} = \overline{\bar{u}_i u'_j + u'_i \bar{u}_j}, \quad R_{ij} = \overline{u'_i u'_j}.$$

L_{ij} is the Leonard term, C_{ij} is the cross term, and R_{ij} is the SGS Reynolds stress. The indices $i = 1, 2$, and 3 correspond to the directions x , y , and z , respectively, where x is the streamwise direction, y is the wall-normal or cross-stream direction, and z is the spanwise direction. In the present study, we consider fields which are homogeneous in two directions (x and z). We apply the Gaussian filter in the homogeneous directions because scale-similarity models are used to approximate the SGS stress tensors. No filter was applied in the inhomogeneous direction, but the same numerical discretization method was used in the y -direction in both the direct numerical simulation (DNS) data generation and assessing the LES models. In the following, $\langle \rangle$ denotes the average in the $x - z$ plane.

Our investigation is mostly focused on the SGS Reynolds stress R_{ij} . The SGS models commonly used for LES to represent the effects of the SGS on the GS are divided into two groups; SGS eddy viscosity coefficient models (EVM) and scale-similarity models.

Accurate SGS models must be capable of correctly representing the energy transfer between GS and SGS. Recent direct assessment of the energy transfer carried out using direct numerical simulation (DNS) data for wall-bounded flows (Piomelli *et al.* 1990, 1991) revealed that the energy exchange is not unidirectional. Although GS kinetic energy is transferred to the SGS (forward scatter (F-scatter) on average, SGS energy is also transferred to the GS. The latter energy exchange (backward scatter (B-scatter) is very significant, i.e., the local energy exchange can be backward nearly as often as forward and the local rate of B-scatter is considerably higher than the net rate of energy dissipation (Piomelli *et al.* 1991). Moreover, a mean

¹ Department of Mechano-Aerospace Engineering, Tokyo Institute of Technology

reverse flow of energy from SGS to GS fluctuating turbulent motions was observed in the buffer layer region of the channel (Horiuti 1989, Härtel *et al.* 1994). In free shear flows, a greater degree of B-scatter was observed in the mixing layer (Horiuti 1997)

EVM relates the SGS stress to the GS velocity deformation via the eddy viscosity. All SGS EVMs are derived from the Smagorinsky model (Smagorinsky 1963). In general, an EVM is adequate for approximating the interaction between given turbulent scales and distinctly smaller scales, in which the main function of the SGS is to remove energy from the GS, but it is inadequate for representing the B-scatter. A dynamic Smagorinsky model (Germano *et al.* 1991) can be used to model partial B-scatter in regions of reduced eddy viscosity, but strong B-scatter would require a negative eddy viscosity, which would lead to numerically unstable solutions, although a recent dynamic localization model (Ghosal *et al.* 1995a) may avoid this instability.

An alternative SGS model for EVM is the scale-similarity model (Bardina 1983). A representative model is the Bardina model in which the SGS Reynolds stress term is approximated as (Bardina 1983, Horiuti 1993a):

$$R_{ij} \simeq R_{ij}^B = C_B(\bar{u}_i - \bar{\bar{u}}_i)(\bar{u}_j - \bar{\bar{u}}_j). \quad (2)$$

Note that the model constant C_B cannot be determined using only the Galilean invariance constraint (Speziale 1985), but needs to be optimized (Horiuti 1993a, 1994, 1997). We have optimized C_B using several DNS data for incompressible channel and mixing layer flows so that the root-mean-square (rms) value of the modeled SGS Reynolds stress term approaches its value based on DNS data. Representative optimized values of C_B were in the range between 2.0 and 9.0 (Horiuti 1993a, 1993b, 1997).

The Bardina model for the SGS Reynolds stress (Eq. 2) gave better agreement between the exact and modeled SGS Reynolds stresses than the Smagorinsky model (Bardina 1983, Horiuti 1989, 1993a). This model, in which the SGS stress is no longer aligned with the GS strain rate, can exhibit B-scatter (Horiuti 1989, 1997).

The drawback inherent in the Bardina model, however, is that the predicted magnitude of the B-scatter contribution is larger than the exact DNS value. To overcome this problem, the filtered Bardina (F-Bardina) model

$$R_{ij} \simeq C_B \overline{(\bar{u}_i - \bar{\bar{u}}_i)(\bar{u}_j - \bar{\bar{u}}_j)}, \quad (3)$$

was proposed (Horiuti 1997). This model was obtained by utilizing the elliptic relaxation model procedure (Durbin 1993) to incorporate the nonlocal effect in physical space into the Bardina model. A marked improvement was obtained using the F-Bardina model compared with the Bardina model. The SGS Reynolds stress tensor approximated using the F-Bardina model was much closer to the exact DNS value than that obtained using the Bardina model. Also, the overestimation of the B-scatter obtained using the Bardina model was significantly reduced when the F-Bardina model was used.

High Re		
(i, j)	Bardina	F-Bardina
(1,1)	0.63	0.81
(1,2)	0.55	0.71
(2,2)	0.53	0.71
(3,3)	0.56	0.74

TABLE I: Correlation coefficients between the exact SGS Reynolds stresses and the those obtained using the different models for the high Reynolds number channel flow.

The testing of Horiuti (1997), however, was conducted using DNS data from a low Reynolds number channel and mixing layer flows. It was felt that further testing at higher Reynolds numbers was a necessary step needed to establish the validity of the new model. This is the primary motivation of the present study. The objective is to test the new model using DNS databases of high Reynolds number, fully developed turbulent channel and mixing layer flows.

2. Accomplishments

In the present study, we make use of direct numerical simulation flow fields available at CTR to directly test the various approximations. To compute the large-eddy flow fields, we filter the DNS fields by applying a two-dimensional Gaussian filter in the $i = 1, 3$ -directions.

The high Reynolds number DNS databases were for the fully developed incompressible channel and the time-developing mixing layer flows. The channel flow DNS data was generated at $Re_\tau = 590$ (Reynolds number based on the wall-friction velocity, u_τ , and the half-channel height, δ) using $384 \times 257 \times 384$ grid points in the $x \times y \times z$ -directions (Mansour 1996). The incompressible mixing layer DNS data was at $Re_\theta = 2400$ (the Reynolds number based on the momentum thickness, δ_m , and the velocity difference, ΔU) using $512 \times 180 \times 192$ grid points in the $x \times y \times z$ -directions (TBL case; Rogers & Moser 1994). The results are compared with the previous assessment for low Reynolds numbers ($Re_\tau = 180$ for channel flow, and $Re_\theta = 200$ for mixing layer, Horiuti 1997).

2.1 Model assessment for channel flow

The high Reynolds number channel flow field was filtered to $64 \times 257 \times 64$ grid points in the x -, y -, and z -directions, respectively. The low Reynolds number channel flow field (with $128 \times 129 \times 128$ grid points) was filtered to $32 \times 129 \times 32$ grid points. These numbers of LES grid points were chosen so that the turbulent kinetic energy retained in the SGS components is large. This is necessary to make a fair assessment of the SGS models.

Table I lists the correlation coefficients between the exact SGS Reynolds stress tensor and those obtained using the Bardina and F-Bardina models for the high Re_τ case. For comparison, the previous results obtained for the low Reynolds number are

Low Re		
(i, j)	Bardina	F-Bardina
(1,1)	0.71	0.86
(1,2)	0.66	0.77
(2,2)	0.64	0.81
(3,3)	0.65	0.81

TABLE II: Correlation coefficients between the exact SGS Reynolds stresses and the those obtained using the different models for the low Reynolds number channel flow.

listed in Table II. The results obtained using the F-Bardina model are remarkably improved compared with those obtained using the Bardina model.

The GS and SGS fields interact via the SGS production term P due to the SGS Reynolds stress R_{ij} , i.e., $P = -\overline{u'_i u'_j} (\partial \bar{u}_i / \partial x_j + \partial \bar{u}_j / \partial x_i) / 2$. The accuracy of the models is assessed by considering the prediction of the GS-SGS energy transfer. Figure 1 shows the y -distribution of the fraction of grid points in each $x - z$ plane where the B-scatter occurs in the P term. The optimized C_B values for the Bardina and F-Bardina models were, respectively, 3.5 and 4.3 for the low Re_τ case. For the high Re_τ case, the C_B value was approximately 9.0 for both models. In Fig. 1, R_{ij} is estimated from the exact SGS Reynolds stress. The results obtained by using the Bardina and F-Bardina models for the R_{ij} term are also included.

Approximately 30% of the grid points experience the B-scatter in the region $y_+ > 50$ for the low Re_τ case, but the fraction for the high Re_τ case is generally smaller than that for the low Re_τ case. A sharp decrease occurs at $y_+ \approx 10$, where the maximum (net) SGS production ($\langle P \rangle$) is the largest, for both Re_τ . This decrease is more considerable for the high Re_τ case. This decrease was not discernible in the results of Piomelli *et al.* (1991) in which a spectral cutoff filter was used instead of the Gaussian filter. Leslie and Quarini (1979) analytically found that when the Gaussian filter is used, the B-scatter contribution to the wave-number-dependent eddy viscosity is greatly reduced compared with that of the cutoff filter, which is consistent with the present results.

Throughout the channel, the fraction predicted using the Bardina model is much larger than the DNS exact value for both Reynolds numbers. Marked improvement is obtained by using the F-Bardina model.

The production term P is decomposed into the forward scatter part (defined as $(P + |P|)/2$, denoted by P_+) and the backward scatter part ($(P - |P|)/2$, denoted by P_-). In Fig. 2, we compare the y -distributions of the plane-averaged P_+ and P_- values obtained using the models with the exact values obtained from the DNS data for the low Re_τ case. The Bardina model overestimates the B-scatter term, whereas the results obtained using the F-Bardina model are in good agreement with the exact DNS data. These results are consistent with those observed in the fraction profiles shown in Fig. 1.

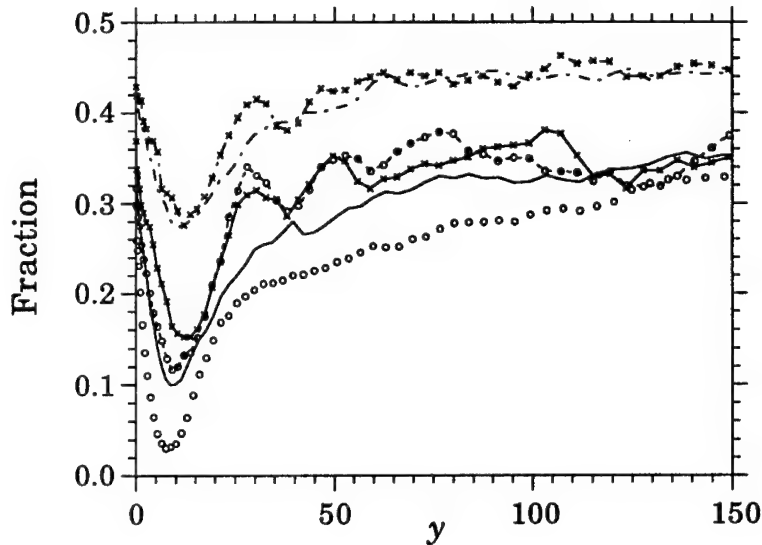


FIGURE 1. y -profiles of the fraction of grid points in each $x-z$ plane where the SGS production term, $P < 0$ from channel flow. $\cdots \circ \cdots$, Exact (low); $-\times-$, Bardina (low); $-\times-$, F-Bardina (low); \circ , Exact (high); $---$, Bardina (high); $---$, F-Bardina (high).

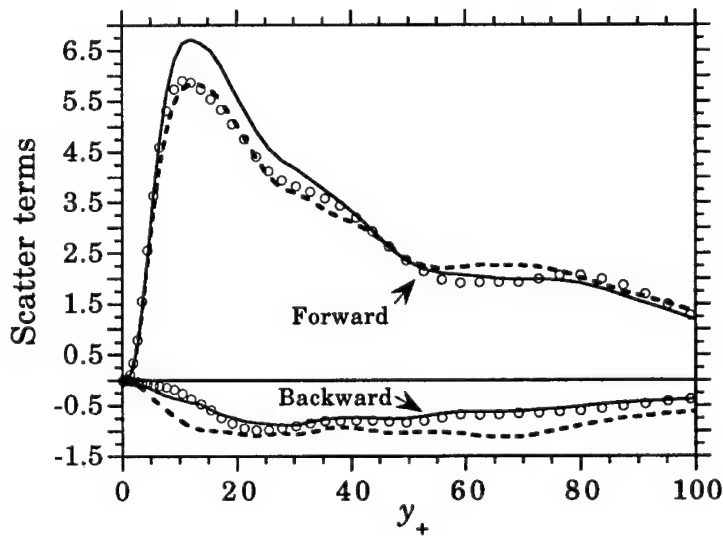


FIGURE 2. Decomposition of the plane-averaged SGS production term P obtained from the DNS exact data and obtained using different models from low Re_τ channel flow. Symbols: \circ , Exact; $---$, Bardina; $---$, F-Bardina.

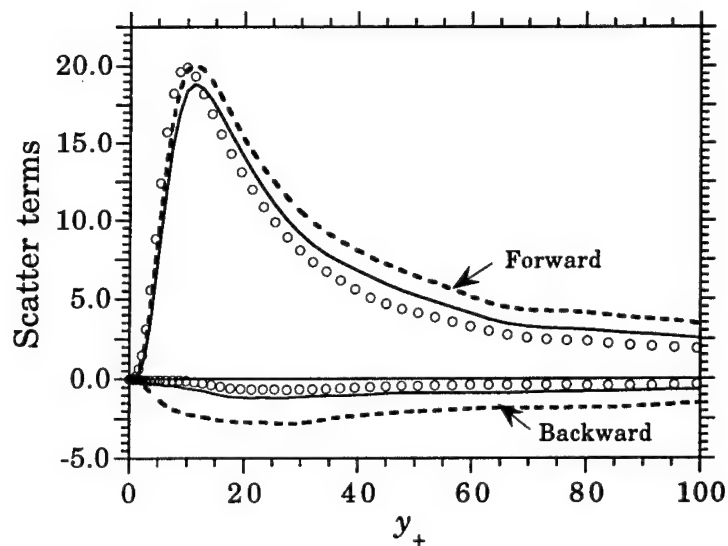


FIGURE 3. Decomposition of the plane-averaged SGS production term P obtained from the DNS exact data and obtained using different models from high Re_τ channel flow. Symbols as in Fig. 2.

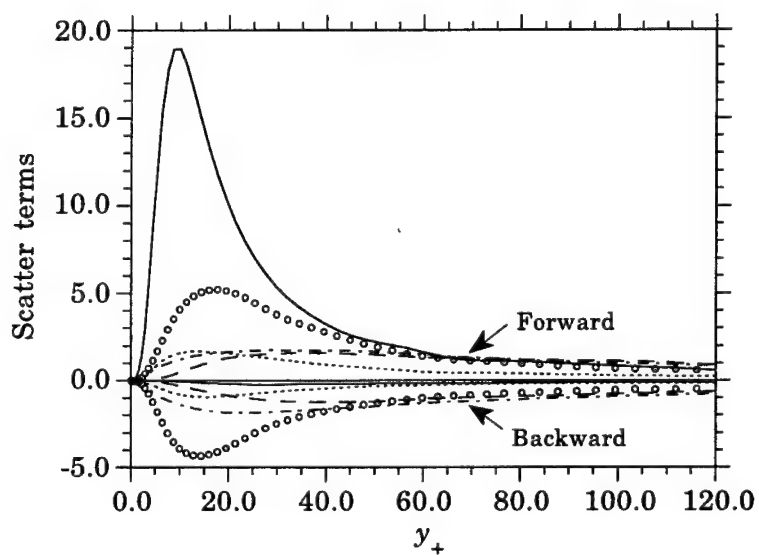


FIGURE 4. Decomposition of the plane-averaged P_{ij} terms obtained from DNS of high Re_τ channel flow. Symbols: \circ , (1,1); —, (1,2); ·····, (1,3); ----, (2,2); - · - ·, (3,3).

The corresponding result for the high Re_τ case is shown in Fig. 3. The exact values show that the energy transfer is predominantly forward near the wall as was found in Fig. 1. An overestimate of the B-scatter term for the Bardina model is more pronounced than in the low Re_τ case, whereas the F-Bardina model does not yield the excessive prediction of the B-scatter observed in the Bardina model. The F-Bardina model gives a sufficient GS energy drain when C_B is properly chosen, with an accurate prediction of the B-scatter being yielded concurrently (Horiuti 1997) for both Reynolds numbers, which implies that this model may be used as an alternative to the SGS EVM.

To determine the local rate of SGS production, we have examined the root-mean-square (rms) value of P (figure not shown). It was found that the local variance of P was two to six times larger than the plane-averaged value as was pointed out in Piomelli (1991).

Figure 4 shows the plane-averaged profiles of the individual components of the SGS production term $P_{ij} = -(\overline{u'_i u'_k} \partial \bar{u}_j / \partial x_k + \overline{u'_j u'_k} \partial \bar{u}_i / \partial x_k)$, in which R_{ij} is estimated from the exact SGS Reynolds stress of the high Re_τ channel flow. These terms are decomposed into two-parts that contribute to F- ($P_{ij} > 0$) and B- ($P_{ij} < 0$) scatters. It is found that the shear production term, P_{12} , is dominant in the region at $y_+ \approx 10$. The energy transfer arising in this term is predominantly forward due to the presence of the large mean shear rate near the wall. Away from the wall, however, the P_{12} term becomes gradually small and instead the normal production term, particularly the P_{11} term, becomes dominant. It can be seen that the magnitudes of the F- and B- scatter terms in P_{11} are very close to each other, with the total sum of P_{11} being slightly positive, but the sum becomes negative in the region at $y_+ \approx 15$. Correlations of the occurrence of this B-scatter event with the coherent vortical structure, which is oriented perpendicular to the wall, are discussed in Horiuti (1995).

An almost equal occurrence of F- and B- scatter is found similarly in other components. We note that the individual components, P_{ij} , were better approximated by using the F-Bardina model than by the Bardina model (figure not shown). Additionally, we found that the transfer between SGS and the fluctuating GS was predominantly backward as was previously pointed out by Horiuti (1997, figure not shown). Similar results were obtained for the low Re_τ channel flow.

2.2 Model assessment for mixing layer

The high Reynolds number mixing layer field was filtered to $128 \times 180 \times 48$ grid points in the x -, y - and z -directions. The low Reynolds number mixing layer flow field (with $192 \times 129 \times 128$ grid points) was filtered to $96 \times 129 \times 64$ grid points.

Table III lists the correlation coefficients between the exact SGS Reynolds stress tensor and those obtained using the Bardina and F-Bardina models for the high Re_θ case. Table IV lists the results for the low Reynolds number case. As in the channel flow, the results obtained using the F-Bardina model are significantly improved compared with those obtained using the Bardina model. We note, however, that the values of the correlation coefficients are generally lower for the high Reynolds number case than for the low Reynolds number case in both flows.

High Re		
(i, j)	Bardina	F-Bardina
(1,1)	0.66	0.82
(1,2)	0.55	0.68
(2,2)	0.63	0.81
(3,3)	0.63	0.80

TABLE III: Correlation coefficients between the exact SGS Reynolds stresses and the those obtained using the different models for the high Reynolds number mixing layer.

Low Re		
(i, j)	Bardina	F-Bardina
(1,1)	0.87	0.93
(1,2)	0.85	0.92
(2,2)	0.87	0.94
(3,3)	0.88	0.94

TABLE IV: Correlation coefficients between the exact SGS Reynolds stresses and the those obtained using the different models for the low Reynolds number mixing layer.

The optimized C_B values in the Bardina and F-Bardina models were 5.0 and 7.0, respectively, for the high Re_θ case. For the low Re_θ case, the optimized C_B values in the Bardina and F-Bardina models were 2.0 and 2.5, respectively. All of the optimized C_B values are between 2.0 and 9.0, and are rather independent of the type of flow.

Figure 5 shows the fraction of grid points at which the B-scatter occurs in P estimated from the exact SGS Reynolds stress for low and high Reynolds numbers. For the low Re_θ case, the fraction is over 40% throughout the vortical region of the mixing layer, and is generally larger than in the low Reynolds number channel flow (Fig. 1). The fraction, however, is significantly decreased for the high Re_θ case (approximately 30% throughout the vortical region). The fraction profiles implied by the Bardina and F-Bardina models for the R_{ij} term in P are also included in Fig. 5. The overestimate of the fraction in the results obtained using the Bardina model is more pronounced for the high Re_θ case than for the low Re_θ case.

Plane-averaged F- and B-scatter term values are shown in Figs. 6 and 7, respectively, for the low and high Re_θ cases. It can be seen that the magnitudes of these two terms are very close to each other for the low Re_θ case, indicating that F- and B-scatters occur almost evenly, with the total sum of P being slightly positive. For the high Re_θ case, the magnitude of the B-scatter contribution is decreased. This is consistent with the fraction profiles shown in Fig. 5.

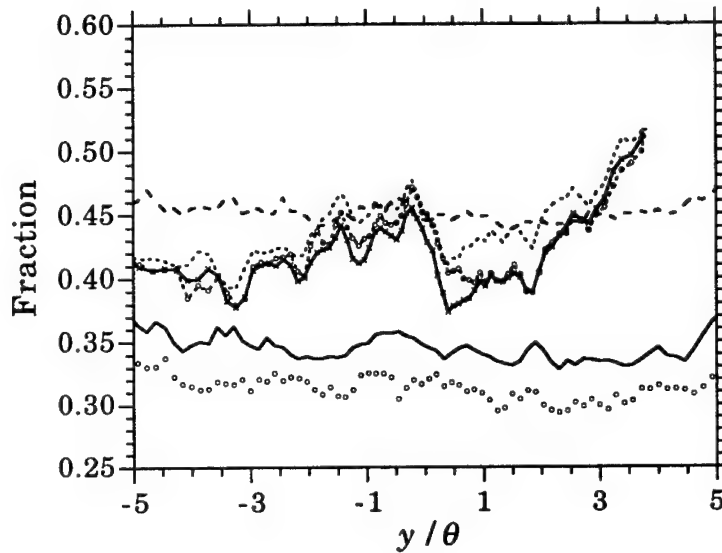


FIGURE 5. y -profiles of the fraction of grid points in each $x-z$ plane where the SGS production term $P < 0$ from mixing layer. $\cdots \circ \cdots$, Exact (low); \cdots , Bardina (low); $-- \times --$, F-Bardina (low); \circ , Exact (high); $----$, Bardina (high); $---$, F-Bardina (high).

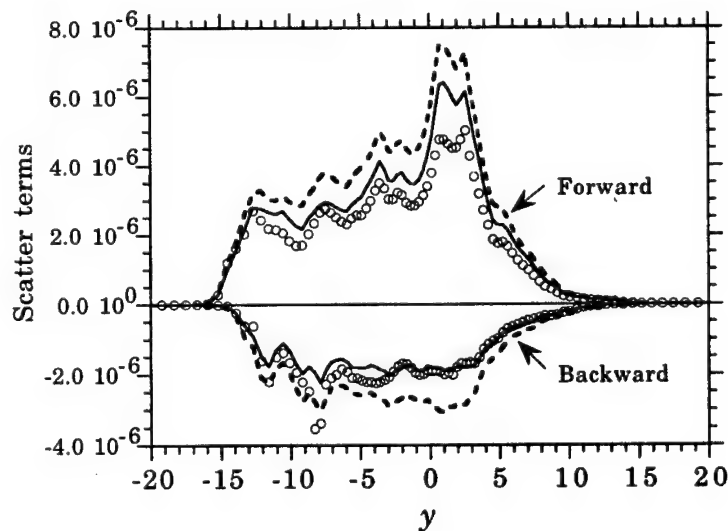


FIGURE 6. Decomposition of the plane-averaged SGS production term P obtained from the DNS exact data and obtained using different models from low Re_τ channel flow. Symbols as in Fig. 2.

In the spatial distributions of P that were estimated from the low Re_θ DNS data, it was found that a large SGS energy production occurs in the braid region of the mixing layer. At the time which the test was conducted, the roll-up of the Kelvin-Helmholtz (K-H) vortices was complete, and these two eddies started to merge. The predominantly streamwise vortices ("rib" vortices) resided in the braid region between the K-H rollers (Rogers & Moser 1994). The distribution of the production term was characterized by a very intermittent appearance of the strong F- and B-scatter regions that took place side by side with a quadruple-like structure (Horiuti 1997).

This quadruple structure was highly aligned with the rib vortices. The vorticity distribution in the cross section of the rib vortices was not exactly circular, but rather elliptic. The F-scatter event occurred in the 1st and 3rd quadrants of the rib vortices, and B-scatter was generated in the 2nd and 4th quadrants of the rib vortices. We consider that the presence of these rib vortices is the primary cause of the almost equal occurrence of F- and B- scatters in the low Re_θ mixing layer. The present results indicate that the B-scatter events may occur in a deterministic manner rather than in a stochastic manner.

The major axis of the elliptic vortex, the circulation of which was counterclockwise, was making a positive angle with the cross-stream (y) axis. As a result, the area of 1st and 3rd quadrants was larger than that of the 2nd and 4th quadrants. Subsequently, the magnitude of F-scatter was larger than the B-scatter. Similarly, in the clockwise elliptic vortices, their major axis was making a negative angle with the y axis, the resultant net-scatter was also forward.

This finding may be a result of the low Reynolds number of the DNS. The distributions of the SGS production term P for the high Re_θ case also exhibited the quadruple-like structure, but the four quadrants were not as distinctive as for the low Re_θ case, i.e., the 1st and 3rd quadrants of the F-scatter regions were dominant, taking over the 2nd and 4th quadrants.

Figure 8 shows the plane-averaged profiles of the individual components of the SGS production term P_{ij} , in which R_{ij} is estimated from the exact SGS Reynolds stress from the high Re_θ mixing layer. These terms are decomposed into the F- and B- scatter contributions.

In the low Re_θ case, the quadruple structure of the SGS production term distribution primarily arose in the P_{22} term. In the high Re_θ case, it can be seen that large contributions result from the normal production terms, P_{22} and P_{33} , but it was found that the correlation coefficient between the P_{22} term and the P_{33} term was negative, thus they almost canceled each other out. Although, unlike the channel flow (Fig. 4), the magnitude of the shear stress production terms of P_{23} and P_{12} is smaller than the normal production terms, F-scatter contributions are larger than the B-scatter contributions in the P_{23} and P_{12} terms. As a result, the total summation of the production term P became predominantly forward.

Although the four quadrants of the quadruple-like structure in the total production term P distribution for the high Re_θ case were not distinctive as in the low Re_θ case, the distributions of the P_{22} and P_{33} terms exhibited distinctive quadruple-like

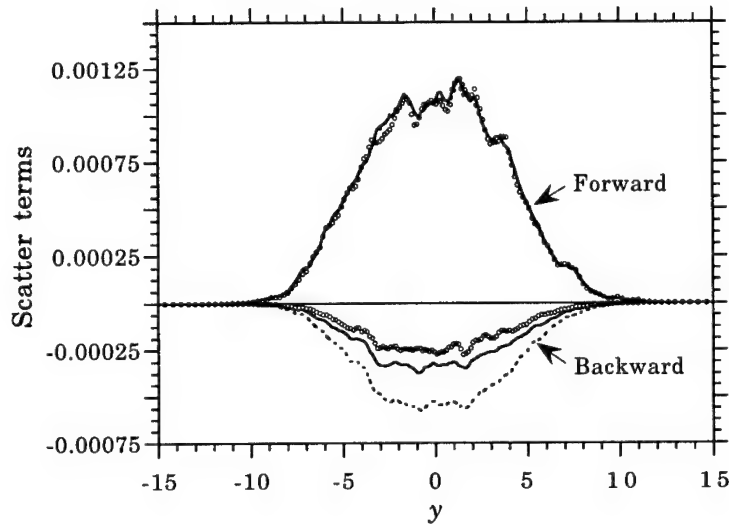


FIGURE 7. Decomposition of the plane-averaged SGS production term P obtained from the DNS exact data and obtained using different models from high Re_τ mixing layer. Symbols as in Fig. 2.

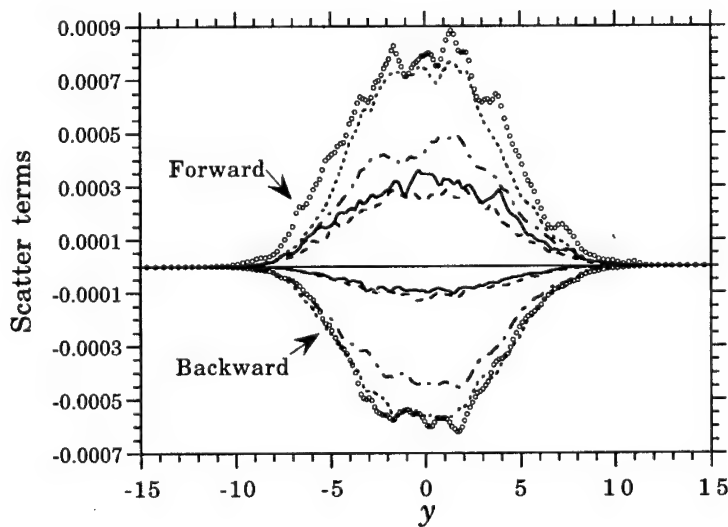


FIGURE 8. Decomposition of the plane-averaged P_{ij} terms obtained from the DNS exact data from high Re_τ mixing layer. —, (1,1); ---, (1,2); ○, (2,2); ····, (2,3); - · - ·, (3,3).

structures. This fact indicates that the rib vortices reside in the high Reynolds number mixing layer on average as in the low Reynolds number case and that the generation of a large SGS energy production occurs along the rib vortices. A negative correlation of the P_{22} term and the P_{33} term, however, was not depicted in the low Re_θ case.

3. Future plans

We have assessed the SGS models from the point of view of energy transfer between the grid scale (GS) and the subgrid-scale (SGS) via a correlation with the filtered DNS data ('a priori' test).

The energy transfer was directly analyzed using DNS data for fully developed turbulent channel and mixing layer flows for both high and low Reynolds numbers. A significant reduction of the B-scatter effect was found for the high Reynolds number case compared with the low Reynolds number case. We note, however, that the occurrence of F- and B-scatters may depend on grid resolution. For example, the rib vortices formed in the low Reynolds number mixing layer were only coarsely resolved (approximately 6 grid points for a single rib vortex), thus the SGS was significantly affected by the large GS motions. When the rib vortices are more finely resolved, the contributions of the B-scatter will decrease.

A capability of the scale-similarity models for the SGS Reynolds stress to represent the transfer was further tested. It was shown that the Bardina model is, in general, an inaccurate model for the SGS Reynolds stress. Its inaccuracy was greater for the high Reynolds number case for both flows. In a new scale-similarity model (filtered-Bardina, F-Bardina, model), the correlation with the DNS data was shown to be substantially improved compared to that of the Bardina model, and an excessively high prediction of B-scatter in the Bardina model was substantially improved for both Reynolds numbers and both flows.

The validity of the F-Bardina model was established for two different flows and low/high Reynolds numbers. Further development of the present work is directed in two ways.

One is to investigate the correlation of the SGS energy production mechanism with the coherent vortical structures that reside in the turbulence. Preliminary results are reported in Horiuti (1995), but that study was conducted at the low Reynolds numbers. More refined and detailed examination of the high Reynolds number DNS data is necessary.

Another direction is to develop the SGS models based on the filtered-Bardina model. We must note that, although the F-Bardina model yielded very high correlation with the exact DNS data, its high correlation is decreased as the Reynolds number is increased as can be seen in Tables I-IV.

In fact, as the Reynolds number is increased, it is expected that the interscale interaction of GS with the distinctively smaller SGS will become significant as well as the interaction of GS with the larger SGS. An SGS model, which can be used to represent these two GS-SGS interactions, i.e., the local interaction between adjacent wave number bands and the nonlocal interaction between GS and very small

SGS, is desirable. The former interaction can be adequately represented using the F-Bardina model. In order to adequately represent the latter interaction, it is necessary to add the SGS EVM part to the model. That is, a mixed model of F-Bardina and Smagorinsky models is considered to be a more desirable and general model. A new dynamic two-parameter mixed model in which the two model parameters contained in the model were determined consistently with the dynamic SGS procedure (Germano *et al.* 1991) was proposed as an extension of the F-Bardina model (Horiuti 1996). Further refinement of the proposed model is currently underway.

Acknowledgments

I am grateful to the Center for Turbulence Research for its hospitality. Drs. N. N. Mansour and M. M. Rogers provided me with the DNS database. I am also grateful to Profs. P. Moin, and J. H. Ferziger for valuable discussions. This work was partially supported by the overseas research program, Ministry of Education, Science and Culture.

REFERENCES

- BARDINA, J. 1983 Improved turbulence models based on large eddy simulation of homogeneous, incompressible turbulent flows. *Ph.D. dissertation*. Stanford University, Stanford, California.
- DURBIN, P. A. 1993 A Reynolds stress model for near-wall turbulence. *J. Fluid Mech.* **249**, 465.
- GERMANO, M., PIOMELLI, U., MOIN, P. & CABOT, W. H. 1991 A dynamic subgrid-scale eddy viscosity model. *Phys. Fluids*. **A3**, 1760.
- GHOSAL, S., LUND, T. S., MOIN, P. & AKSELVOLL, K. 1995 A dynamic localization model for large-eddy simulation of turbulent flows. *J. Fluid Mech.* **286**, 229.
- GHOSAL, S. & MOIN, P. 1995 The basic equations for the large eddy simulation of turbulent flow in complex geometry. *J. Comp. Physics*. **118**, 24.
- HÄRTEL, C., KLEISER, L., FRIEDEMANN, U., & FRIEDRICH, R. 1994 Subgrid-scale energy transfer in the near-wall region of turbulent flows. *Phys. Fluids*. **6**, 3130.
- HORIUTI, K. 1989 The role of the Bardina model in large eddy simulation of turbulent channel flow. *Phys. Fluids*. **A1**, 426.
- HORIUTI K. 1993a A proper velocity scale for modeling subgrid-scale eddy viscosity in large eddy simulation. *Phys. Fluids*. **A5**, 146.
- HORIUTI, K., MANSOUR, N. N., & KIM, J. 1993b A normal stress subgrid-scale eddy viscosity model in large eddy simulation. *Annual Research Briefs 1992* Center for Turbulence Research, NASA Ames/Stanford Univ., 61-71.
- HORIUTI, K. 1994 Assessment of the generalized normal stress and the Bardina Reynolds stress subgrid-scale models in large eddy simulation. *Direct and Large*

- Eddy Simulation I*, Ed. by P. R. Voke, L. Kleiser and J.-P. Chollet, Kluwer Acad. Pub., 85.
- HORIUTI, K. 1995 Subgrid-scale energy production mechanism in large eddy simulation. *Proc. of the International Symposium on Mathematical Modeling of Turbulent Flows*, Tokyo. 164.
- HORIUTI K. 1996 A new dynamic two-parameter mixed model for large-eddy simulation. Submitted to *Phys. Fluids*.
- HORIUTI, K. 1997 Backward scatter of subgrid-scale energy in wall-bounded and free shear turbulence. *J. Phys. Soc. Japan*. **66** (1).
- LESLIE, D. C. & QUARINI, G. L. 1979 The application of turbulence theory to the formulation of subgrid modeling procedures. *J. Fluid Mech.* **91**, 65.
- MANSOUR, N. N. 1996 Unpublished data.
- ROGERS, M. M. & MOSER, R. D. 1994 Direct simulation of a self-similar turbulent mixing layer. *Phys. Fluids*. **6**, 903.
- PIOMELLI, U., ZANG, T. A., SPEZIALE, C. G., & M. Y. HUSSAINI 1990 On the large-eddy simulation of transitional wall-bounded flows. *Phys. Fluids*. **A2**, 257.
- PIOMELLI, U., CABOT, W. H., MOIN, P. & LEE, S. 1991 Subgrid-scale backscatter in turbulent and transitional flows. *Phys. Fluids*. **A3**, 1766.
- SMAGORINSKY, J. 1963 General circulation experiments with the primitive equations. I. The basic experiment. *Monthly Weather Review*. **91**, 99.
- SPEZIALE, C. G. 1985 Galilean invariance of subgrid-scale stress in large eddy simulation. *J. Fluid Mech.* **156**, 55.

Large-eddy simulation of flow around a NACA 4412 airfoil using unstructured grids

By Kenneth Jansen¹

1. Motivation and objectives

Large-eddy simulation (LES) has matured to the point where application to complex flows is desirable. The extension to higher Reynolds numbers leads to an impractical number of grid points with existing structured-grid methods. Furthermore, most real world flows are rather difficult to represent geometrically with structured grids. Unstructured-grid methods offer a release from both of these constraints. However, just as it took many years for structured-grid methods to be well understood and reliable tools for LES, unstructured-grid methods must be carefully studied before we can expect them to attain their full potential.

In the past three years, important building blocks have been put into place, making possible a careful study of LES on unstructured grids. The first building block was an efficient mesh generator which allowed the placement of points according to smooth variation of physical length scales. This variation of length scales is in all three directions independently, which allows a large reduction in points when compared to structured-grid methods, which can only vary length scales in one direction at a time. The second building block was the development of a dynamic model appropriate for unstructured grids. The principle obstacle was the development of an unstructured-grid filtering operator. New filtering operators were developed in Jansen (1994). In the past year, some of these filters have been implemented into a highly parallelized finite element code based on the Galerkin/least-squares finite element method (see Jansen *et al.* 1993 and Johan *et al.* 1992).

We have chosen the NACA 4412 airfoil at maximum lift as the first simulation for a variety of reasons. First, it is a problem of significant interest since it would be the first LES of an aircraft component. Second, this flow has been the subject of three experimental studies (Coles and Wadcock 1979, Hasting and Williams 1987, and Wadcock 1987). The first study found the maximum lift angle to be 13.87° . The later studies found the angle to be 12° . Wadcock reports in the later study that the early data agree very well with his new data at 12° , suggesting that the early experiment suffered from a non-parallel mean flow in the Caltech wind tunnel. It should be pointed out that the Reynolds-averaged simulations are usually run at 13.87° and do not agree with the data when run at 12° as was shown in Jansen (1995). It is hoped that LES can clarify this controversy. The third reason for considering this flow is the variety of flow features which provide an important test of the dynamic model. Starting from the nose where the flow stagnates, thin laminar

¹ Present address: Rensselaer Polytechnic Institute, Troy, NY

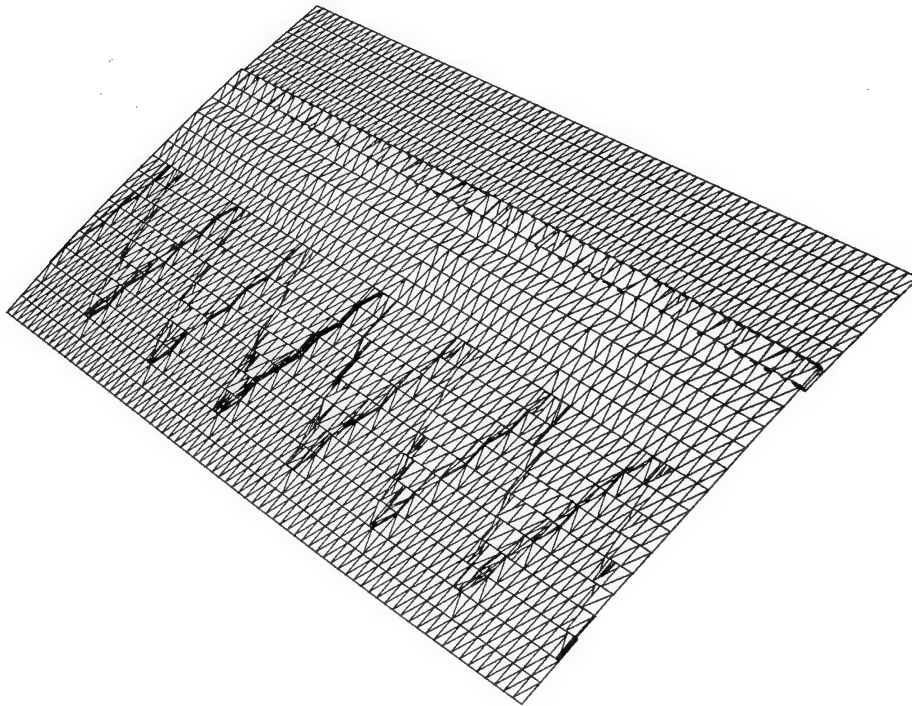


FIGURE 1. A transition strip is modeled geometrically by applying a no-slip boundary condition to the nodes which form a surface of height, shape, and position equivalent to Wadcock's serrated tape which was applied to the airfoil surface.

boundary layers are formed in a very favorable pressure gradient. This pressure gradient soon turns adverse, driving the flow toward a leading edge separation. Only the onset of turbulence can cause the flow to remain attached or to reattach if it did separate. The persistent adverse pressure gradient eventually drives the turbulent flow to separate in the last 20 percent of chord. The separation bubble is closed near the trailing edge as the retarded upper surface boundary layer interacts with the very thin lower surface boundary layer. The large difference in boundary layers creates a challenging wake to simulate. Only the dynamic model can be expected to perform satisfactorily in this variety of situations: from the laminar regions where it must not modify the flow at all to the turbulent boundary layers and wake where it must represent a wide variety of subgrid-scale structures.

The flow configuration we have chosen is that of Wadcock (1987) at Reynolds number based on chord $Re_c = u_\infty c / \nu = 1.64 \times 10^6$, Mach number $M = 0.2$, and 12° angle of attack.

2. Accomplishments

2.1 Effect of wind tunnel walls and transition strip

In Jansen (1995) a grid independent solution was obtained which did not agree well with the experiments in the separated region. This was not completely surprising since two important effects of the experiment were not accounted for in the simulation: the wind tunnel walls and the transition strip.

Wadcock used a strip of tape with serrations cut into the edge on the upstream side. The serrated tape has been modeled in a coarse fashion by our current simulation as can be seen in Fig. 1. The tape is effectively a forward facing step (with serrations) of height $\delta_{99}/4$, followed by a backward facing step.

The blockage effect of the wind tunnel walls has also been included in the recent calculations. Note that the boundary layers on the walls are not simulated; rather, slip boundary conditions are applied on the wind tunnel walls as can be seen in Fig. 2.

These two effects were studied separately for a short period of time (not sufficient for converged statistics in the trailing edge region) and agreement with experiments was seen to improve in both cases. The effect of the walls was somewhat greater than that of the transition strip. This discussion is left qualitative because the enormous cost of these calculations led us to abandon the individual effect studies in favor of using our limited resources on converging the combined effect simulation. The results of this simulation can be seen in Fig. 3 where the velocity profiles of the new simulation (with wind tunnel walls and transition strip) are compared to the original simulation. Note the large increase in the degree of separation.

Though the new simulation is in better agreement with the experiment, new problems were created. As can be seen in Fig. 4, there is a reduction in the three-dimensionality of the turbulence in the separated region. A similar story is told by the two-point correlation in this region, which shows very little decay. While some reduction is to be expected, concern developed as to whether the periodic boundary condition, which is applied in the spanwise direction, was promoting spanwise coherent vortices due to insufficient spanwise extent. From Fig. 3 it is apparent that the boundary layer is significantly thicker in the new simulation. With a spanwise domain width, W of 2.5% of chord the spanwise domain becomes less than a boundary layer height at about two-thirds of the chord length.

2.2 Wider domain simulation

The most obvious choice of doubling the domain while maintaining the current resolution was postponed in lieu of a doubling of the domain by doubling the spanwise size of each element. The rationale for this decision was that the refinement studies of Jansen (1995) showed only a small change from the current grid to the twice coarser grid. The new simulation would also not engender an increased cost since the number of nodes remained the same. It was assumed that changes in the first half of the airfoil would suggest inadequate resolution while changes in the trailing edge region would address the domain width question.

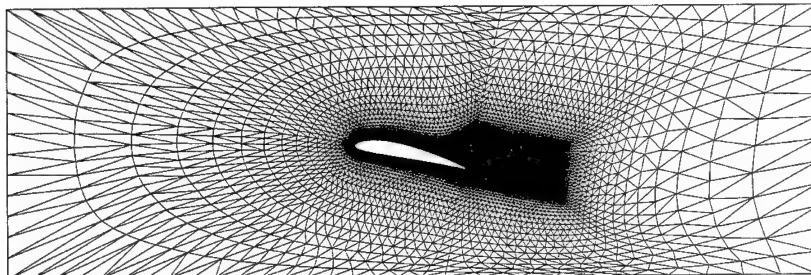


FIGURE 2. The cross sectional plane of an unstructured mesh which accounts for the inviscid effects of the wind tunnel walls.

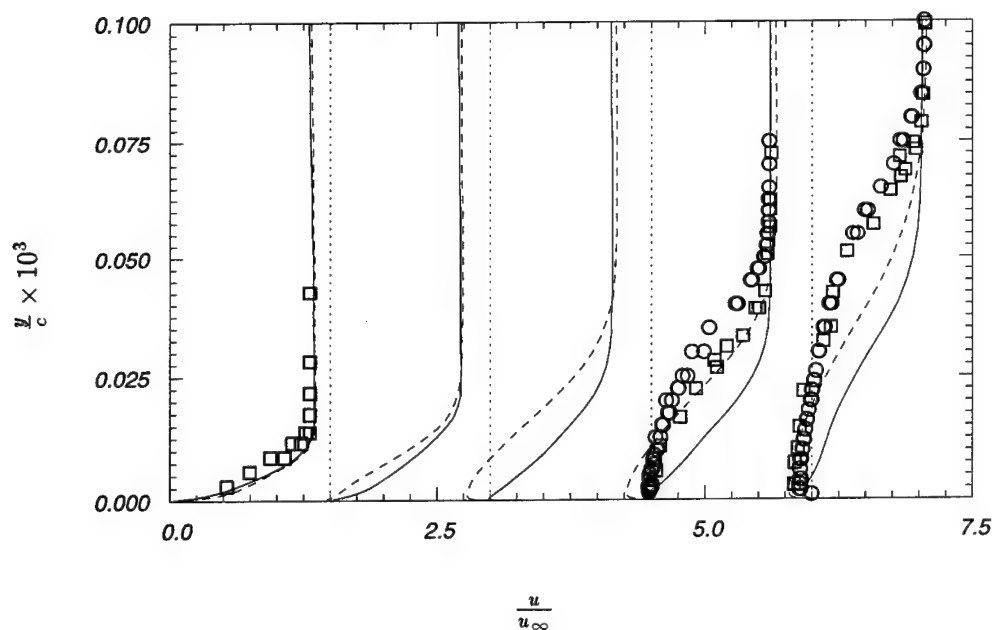


FIGURE 3. Profiles of tangential velocity component at various positions along the airfoil surface ($x/c = 0.59, 0.66, 0.78, 0.82, 0.95$). Solutions correspond to: without wind tunnel walls or transition strip —, with wind tunnel walls and transition strip ----, Wadcock \square , Hastings and Williams \circ .

The times-series from the new simulation are presented in Fig. 5 where the three-dimensionality can be seen to return to the separated region. The amount of separation is reduced, causing some departure from the experimental data as can be seen in Fig. 6. This is to be expected because the presence of three-dimensional vortical structures in the separated region pump high momentum fluid down to the

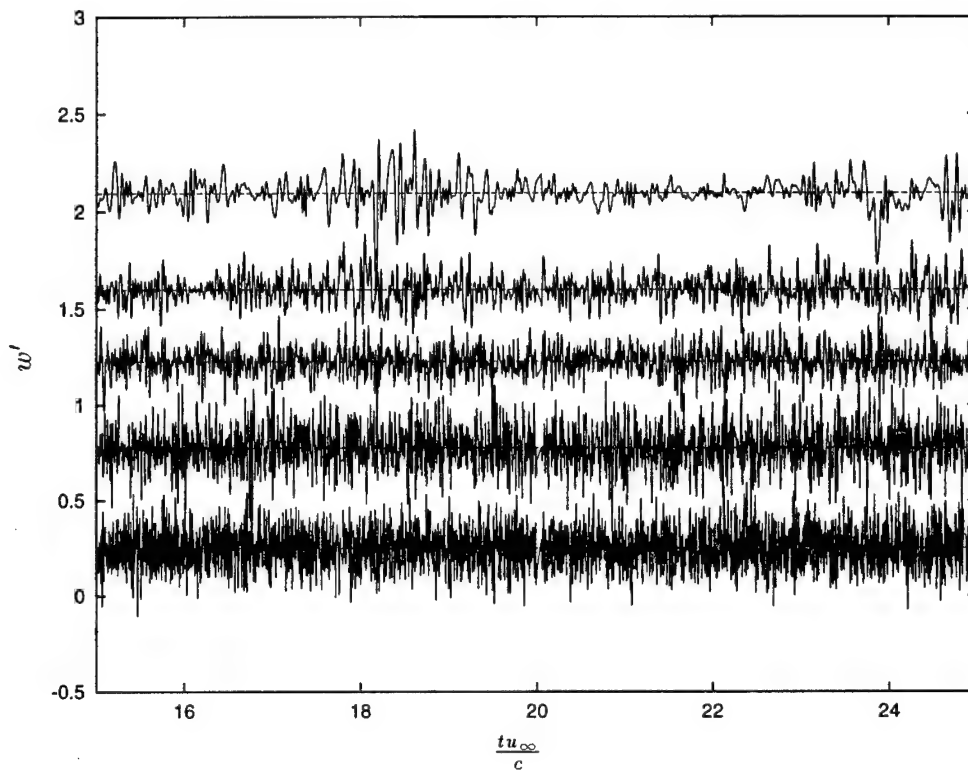


FIGURE 4. Time series of the spanwise velocity fluctuation at various positions along the chord length, approximately half a boundary layer height off of the wall. From the bottom up ($x/c = 0.1, 0.3, 0.529, 0.66, 0.815, 0.95$). Note that the top curve ($x/c = 0.95$) indicates a loss of three-dimensionality in the separated region.

wall, reducing the magnitude of the separation. Fig. 6 also illustrates that the first half of the airfoil is nearly grid independent.

3. Future plans

3.1 More spanwise domain studies

Based on the findings in the previous section more attention will be given to the spanwise domain effects. Since the resolution changed at the same time as the expansion of the domain, it is difficult to isolate the two effects. For this reason the first study will maintain the 5% chord domain width and improve the resolution in the second half of the airfoil where the solution has shown some change. A grid has already been generated to accomplish this task, and a simulation has just begun. The number of nodes has gone up by 70%, making this simulation significantly more expensive than the others described in this report.

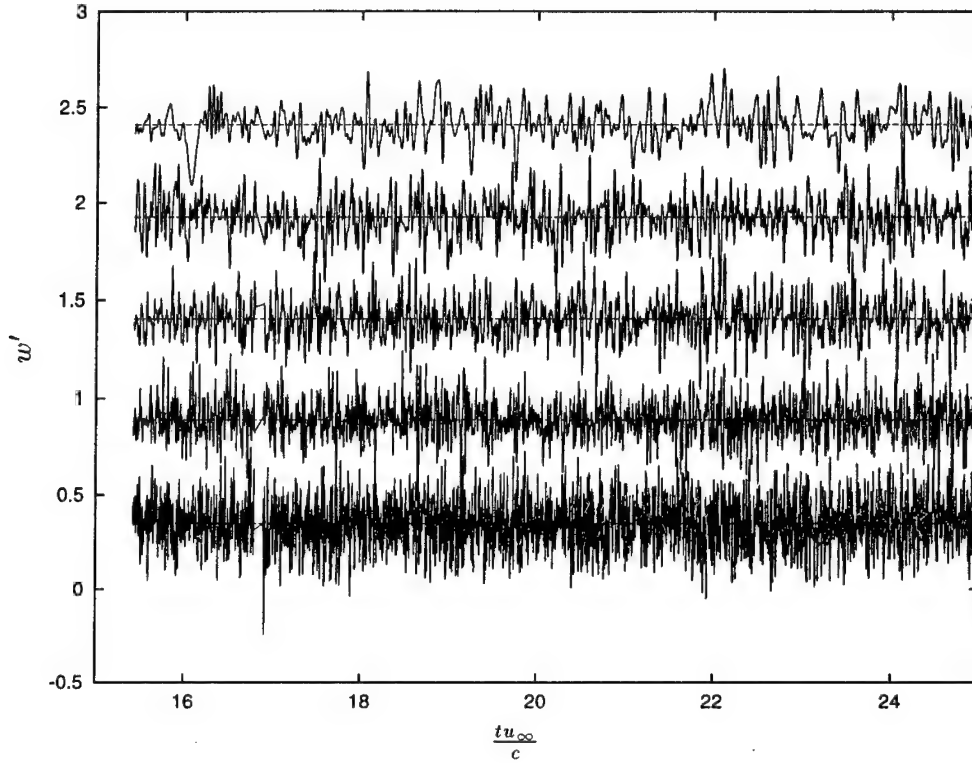


FIGURE 5. Time series of the spanwise velocity fluctuation as described in Fig. 4. Note that the top curve ($x/c = 0.95$) has a strong signal indicating a return of three-dimensionality in the separated region with the increased domain width.

3.2 Higher order methods

Given the number of points that are required to obtain a grid-independent solution, it seems clear that higher order methods should be explored. This is straightforward, but non-trivial, to do with the finite element method. There are two benefits to higher order methods besides the obvious one of higher accuracy. First, the higher order methods will have a more complete representation of the residual error of the discrete approximation and, therefore, the scheme will be less dissipative. Second, alternative filters, described in Jansen (1994), can be implemented and tested. It is difficult to predict at this time if the method will lose computational efficiency when extended to higher order.

3.3 Computational platform change

In the past year the code has been ported to the IBM SP2 (see Bastin 1996 for details). This port involved the use of MPI, a communication standard that is more widely used than that of the original code, which should make the port to other platforms reasonably simple. In the coming year more effort will be applied in this area to try to take advantage of the changing computational resources available for

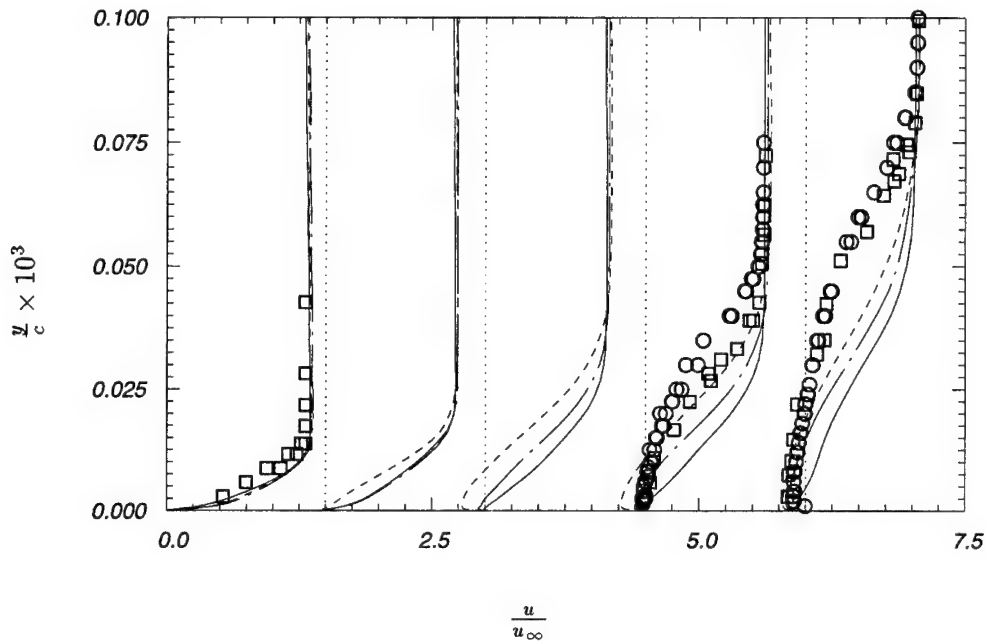


FIGURE 6. Profiles of tangential velocity component at various positions along the airfoil surface ($x/c = 0.59, 0.066, 0.78, 0.82, 0.95$). Solutions correspond to: without wind tunnel walls or transition strip —, with wind tunnel walls and transition strip ($W/c = 0.025$) ----, with wind tunnel walls and transition strip ($W/c = 0.05$) — · —, Wadcock \square , Hastings and Williams \circ .

this type of simulation, thereby expediting its progress.

REFERENCES

- BASTIN, F. 1996 Jet noise using large eddy simulation. *Annual Research Briefs 1996*. Center for Turbulence Research, NASA Ames/Stanford Univ.
- COLES, D., & WADCOCK, A. J. 1979 A flying-hot-wire study of two-dimensional mean flow past an NACA 4412 airfoil at maximum lift. *AIAA J.* **17**, 321.
- HASTINGS, R. C. & WILLIAMS, B. R. 1987 Studies of the flow field near a NACA 4412 aerofoil at nearly maximum lift. *Aero. J.* **91**, 29.
- JANSEN, K. 1994 Unstructured grid large eddy simulation of flow over an airfoil. *Annual Research Briefs 1994*. Center for Turbulence Research, NASA Ames/Stanford Univ., 161-174.
- JANSEN, K. 1995 Preliminary large-eddy simulations of flow around a NACA 4412 airfoil using unstructured grids. *Annual Research Briefs 1995*. Center for Turbulence Research, NASA Ames/Stanford Univ., 61-72.
- JANSEN, K., JOHAN, Z., & HUGHES, T. J. R. 1993 Implementation of a one-equation turbulence model within a stabilized finite element formulation of a

- symmetric advective-diffusive system. *Comp Meth Appl Mech Eng.* **105**, 405.
- JOHAN, Z., HUGHES, T. J. R., MATHUR, K. K., & JOHNSON, S. L. 1992 A data parallel finite element method for computational fluid dynamics on the Connection Machine system. *Comp. Meth. Appl. Mech. Eng.* **99**, 113.
- WADCOCK, A. J. 1987 Investigation of low-speed turbulent separated flow around airfoils. *NACA CR 177450*.

Progress on LES of flow past a circular cylinder

By R. Mittal¹

1. Motivation and objectives

The objective of the present research is to assess the usefulness of large-eddy simulation (LES) methodology for flows in complex geometries. Flow past a circular cylinder has been calculated using a central-difference based solver, and the results have been compared to those obtained by a solver that employs higher-order upwind biased schemes (Beaudan & Moin, 1994). This comparison allows us to assess the suitability of these schemes for LES in complex geometry flows.

2. Accomplishments

2.1 Numerical method

The solver used in the current work is based on the method developed by Choi *et al.* (1992). Previous simulations (Mittal, 1995) had shown that due to the relatively low accuracy of the second-order central difference scheme, the flow in the near wake of the circular cylinder was under-resolved in the spanwise directions, and as a result of this the downstream development of the flow was not simulated accurately. In order to increase the resolution in the spanwise direction, a Fourier discretization method was introduced, and this was found to be a cost effective alternative to increasing the number of grid points. The spanwise velocity is collocated at the pressure node, and dealiasing is performed using the $(2/3)^{rd}$ rule in order to stabilize the computations. Other significant changes to the code include a new line-zebra scheme for the iterative pressure Poisson solver, which incorporates full coupling across the branch cut resulting in significant acceleration of convergence. When used in conjunction with a multigrid scheme, acceptable reduction in residual can be achieved with less than 10 iterations for each spanwise wavenumber.

2.2 Flow past a circular cylinder

A C -mesh is used for the present simulation. The inflow, outflow, and far field boundaries are located at $19\mathcal{D}$, $17\mathcal{D}$, and $25\mathcal{D}$ respectively (\mathcal{D} is the cylinder diameter). Uniform freestream velocity is prescribed at the inflow and far field boundaries, and a convective boundary condition is employed at the outflow boundary in order to smoothly convect the disturbances out of the computational domain. Previous simulations were carried out on domains that only extended to about $10\mathcal{D}$ from the cylinder in the vertical direction, and this resulted in significant streamwise acceleration of the flow at the edge of the wake region. In the current simulation the far field boundary is extended to about $25\mathcal{D}$, and this reduces the confinement effect of

¹ Present address: University of Florida, Dept. of Mechanical Engr., Gainesville, FL

the boundaries to an acceptable level. The spanwise domain size of πD is chosen, which was found to be adequate for this flow by Beaudan & Moin. The simulation has been carried out on a $401 \times 120 \times 48$ mesh with 140 points on the cylinder surface, 129 streamwise points along the wake centerline, 120 points in the wall normal direction, and 48 points along the spanwise direction. A non-dimensional time step size ($U_\infty \Delta t / D$) of about 0.007 was used, which corresponds to a maximum CFL number of about 1.5. The solver takes about 70 seconds per time step on the CRAY C-90, and simulating one shedding cycle requires about 13 CPU hours. All the statistics for the current simulations have been averaged over about 12 shedding cycles. Furthermore, all of the results of Beaudan & Moin used here are from the simulation that employed the 5th-order upwind biased scheme.

Some of the key wall and near wake statistics are summarized in Table 1 where $\overline{C_{pb}}$, $\overline{C_D}$, $\overline{\theta_s}$, and St are the mean base pressure coefficient, mean drag coefficient, mean separation angle, and Strouhal number respectively. It can be seen that the wall statistics obtained from the current simulation are in good agreement with experiments and with the simulations of Beaudan & Moin (1994). Since the drag and base pressure coefficients depend strongly on the accurate prediction of near wake features like vortex rollup and formation of streamwise vortical structures, good prediction of these quantities implies that the development and evolution of the vortical structures in the near wake is being simulated reasonably accurately.

	Central Diff.	Upwind Biased	Experiments
$\overline{C_{pb}}$	-0.93	-0.95	-0.9 ± 0.05 ★
$\overline{C_D}$	1.0	1.0	0.98 ± 0.05 ★
$\overline{\theta_s}$	86.9°	85.8°	$85^\circ \pm 2^\circ$ †
St	0.207	0.203	0.215 ± 0.005 ‡
mean bubble length	$1.4D$	$1.36D$	$1.33D \pm 0.3D$ ‡

Table 1. Wall Statistics. ★ Norberg, 1987; † Son and Hanratty, 1969; ‡ Cardell, 1993.

Figure 1a shows the mean streamwise velocity profiles at four different streamwise stations in the near wake. In this and subsequent figures, profiles obtained from simulations of Beaudan & Moin (1994) and experiments are also plotted whenever available. Furthermore, the profiles have been suitably shifted along the y -axis to fit multiple profiles in one plot. It is found that the streamwise velocity profiles obtained from the current simulations are in reasonable agreement with the experiments. Furthermore, the profiles are found to match closely with Beaudan & Moin (1994). Figure 1b shows the mean vertical velocity profiles at three streamwise locations in the recovery region. It is found that the agreement with the experiments at the first two locations is in general not good, and both simulations over-predict the peak vertical velocity. However, there is a good match with the profiles of Beaudan & Moin (1994). Also at $x/D = 3.0$, both simulations match the experimental

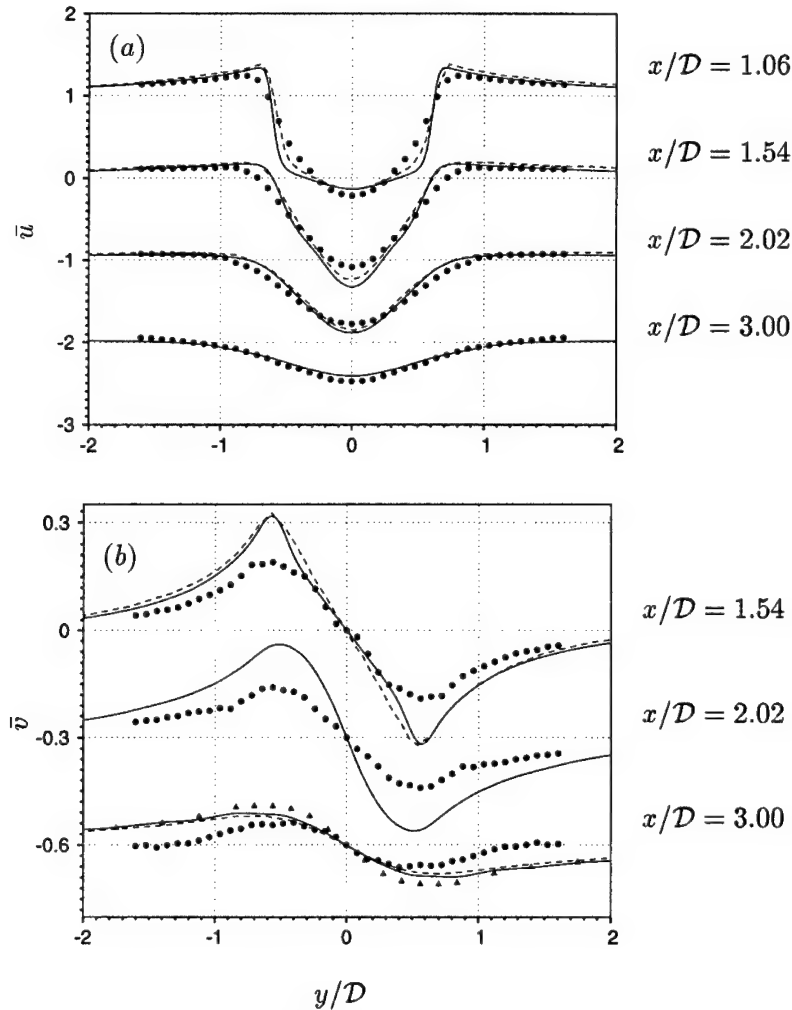


FIGURE 1. Mean velocity profiles in the near wake region. — Current simulation, ---- Beaudan & Moin, • Lourenco & Shih, ▲ Ong & Wallace. (a) Streamwise velocity (b) Vertical velocity.

profiles of Ong & Wallace (1993) quite well. Beaudan & Moin (1994) noted significant symmetry errors in the vertical velocity profiles of Lourenco & Shih (1993), and this could possibly account for the disagreement between the simulations and their experiment.

From the above comparison of mean velocity profiles, we find that the current simulation produces results which compare reasonably well in the near wake region with the experiments and with the simulations of Beaudan & Moin (1994). The bubble length seems to be better predicted by the simulations of Beaudan & Moin (1994). This is probably due to the fact that for the current simulation, the streamwise grid spacing in this region is roughly the same as that used by Beaudan & Moin (1992), which results in a relatively lower resolution due to the lower order

method used here. However, the mean velocity profiles from the two simulations are in reasonable agreement with each other, and we therefore expect that differences in the downstream evolution of the flow in the two simulations will be solely due to differences in the in-plane resolution, and thus comparison of the statistics in the downstream portion of the wake should allow us to compare the performance of the different schemes.

A comparison shows that the streamwise grid spacing in the current simulation is 20–30% better between $x/D = 4$ and 7 than the simulations of Beaudan & Moin. However, at $x/D = 10.0$ both simulations have roughly the same streamwise grid spacing. The difference in the streamwise grid spacing cannot be avoided since the grid cannot be stretched in the streamwise direction as fast in the central difference simulation as was done in the upwind-biased simulations (Mittal, 1995). It should be pointed out that a comparison of the modified wavenumber (Beaudan & Moin, 1994) for the schemes suggests that roughly twice the number of grid points are needed for a second-order central difference scheme to match the resolution of these higher-order upwind biased schemes at low-wavenumbers. Thus, the smaller grid spacing is required in the current simulations in order to adequately resolve the energy containing scales in the wake.

In Fig. 2 we have plotted the one-dimensional frequency spectra, E_{11} , at three locations in the downstream region of the wake. Spectra from both simulations and experiment (Ong & Wallace, 1996) are plotted together for comparison. The streamwise grid spacing limits the highest frequency that can be locally resolved in the simulation, and this corresponds to the implicit “grid-filter”. The vertical lines in the plots indicate the grid cutoffs for the two simulations. The experimental spectra shows about half a decade of inertial range extending from about $\omega/\omega_{st} = 2$ to 7. Figure 2a clearly shows that the spectra from the current simulation matches the experimental spectra much better than the simulation of Beaudan & Moin (1994). A closer look at the spectra at the three locations obtained from the upwind-biased simulation of Beaudan & Moin (1994) shows that only the energy in the lower 20–25% of the resolved wavenumbers matches with the experiment. On the other hand, in the current simulation the damping at the higher wavenumbers is not as severe, and spectra in the lower 40–50% of the resolved wavenumber range matches well with the experiment. The marginal performance of the upwind-biased schemes in the downstream wake region was attributed to the dominance of numerical dissipation. Thus, given the fact that the spectra for the current simulation shows better agreement with the experiment than Beaudan & Moin, it is reasonable to expect that the turbulence statistics obtained from current simulation will also be better predicted in the current simulation.

Figure 3 shows velocity profiles at three selected locations in this region. We observe that the streamwise and vertical velocity profiles obtained from both simulations agree reasonably well with the experiment. Figure 4 shows the Reynolds stress profiles at these locations. The comparison in Fig. 4a indicates enhanced level of streamwise normal stress at the first two streamwise locations. The simulation of Beaudan & Moin (1994) predicts the peak streamwise normal stress at $x/D = 4.0$

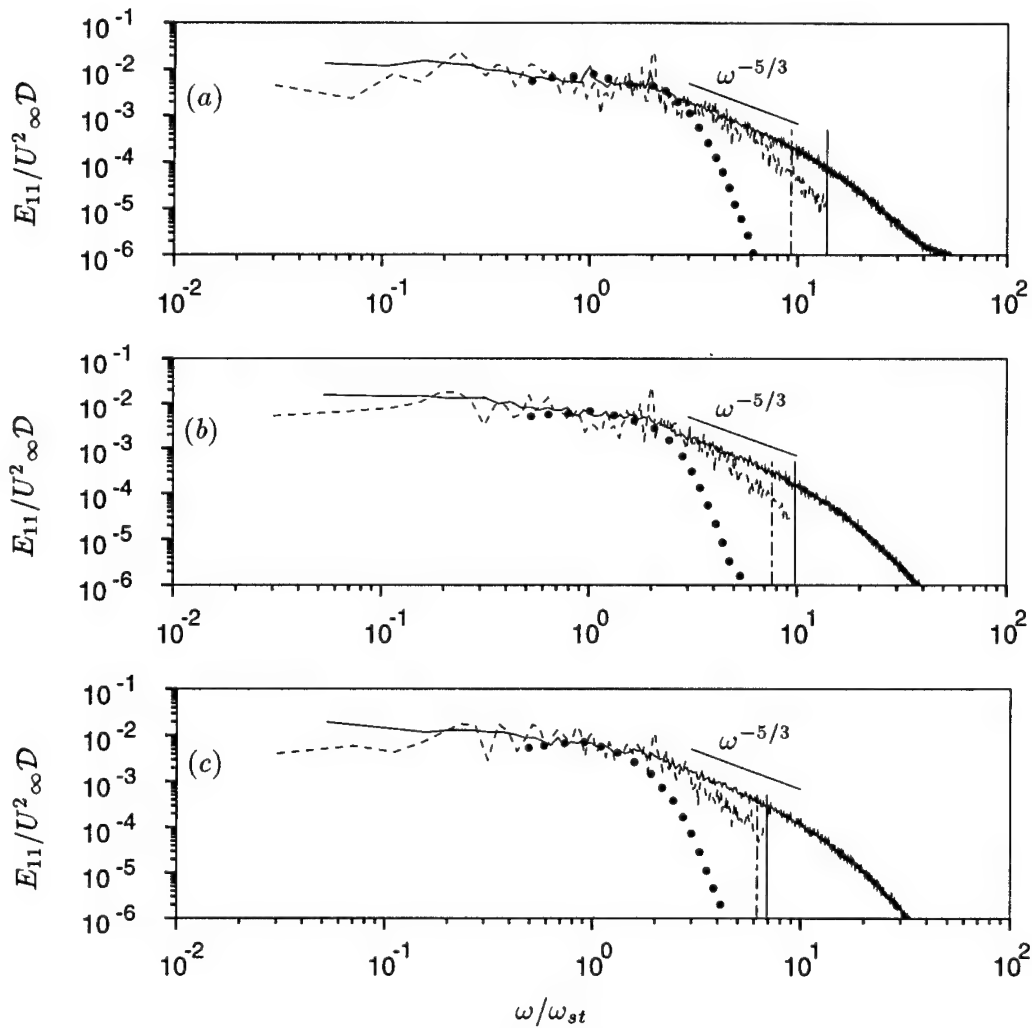


FIGURE 2. One dimensional spectra E_{11} along the wake centerline. — Ong & Wallace, ---- Current simulation, • Beaudan & Moin. Grid cutoffs are shown by vertical lines: — Current simulation, ---- Beaudan & Moin. (a) $x/D = 5.00$ (b) $x/D = 7.00$ (c) $x/D = 10.00$.

quite well and the current simulation over-predicts the peak streamwise normal stress. At $x/D = 7.0$ the simulation of Beaudan & Moin (1994) under-predicts the peak streamwise normal stress significantly, whereas the current simulation shows better agreement in both the magnitude of the peak stress and shape of the stress profile. At $x/D = 10.0$ streamwise stress profiles from both the simulations match quite well and both under-predict the experimental stress level significantly. Since streamwise Reynolds stress at the wake centerline is directly related to the area underneath the curves shown in Fig. 4, it is somewhat surprising that the current simulation does not predict a streamwise stress level which is significantly higher

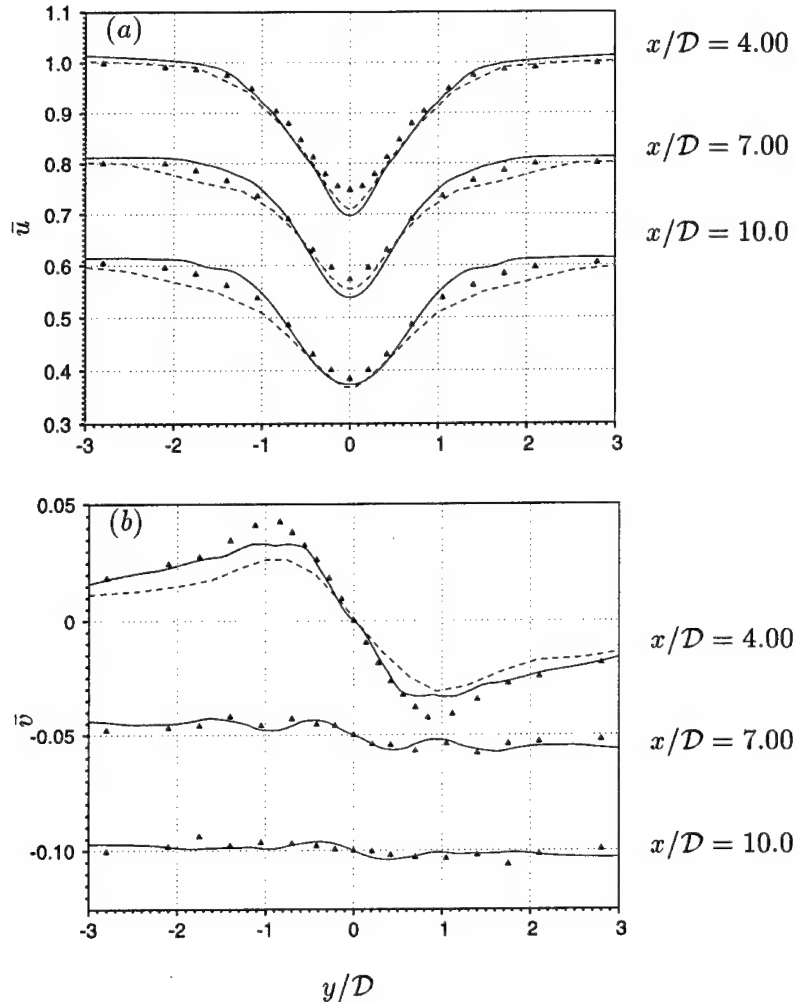


FIGURE 3. Mean velocity profiles downstream of the recovery region. — Current simulation, ---- Beaudan & Moin, \blacktriangle Ong & Wallace. (a) Mean streamwise velocity (b) Mean vertical velocity.

than the simulation of Beaudan & Moin. However, this can be explained by noting that for this flow most of the contribution to the Reynolds stress come from fluctuations in a narrow frequency band extending from about $0.5\omega_{st}$ to $3.0\omega_{st}$, and in this frequency band the energy in both the simulations is comparable. Thus, even though the simulations of Beaudan & Moin exhibit significant damping of the higher frequencies, this does not have a significant impact on the low-order turbulence statistics.

Figure 4b shows the vertical normal stress profiles at these three locations. Again, a slightly enhanced level of stress is observed at $x/D = 4.0$; however, overall the predictions from the two simulations at the first two locations are quite similar. At $x/D = 10.0$ the two simulations predict roughly the same peak stress level; however,

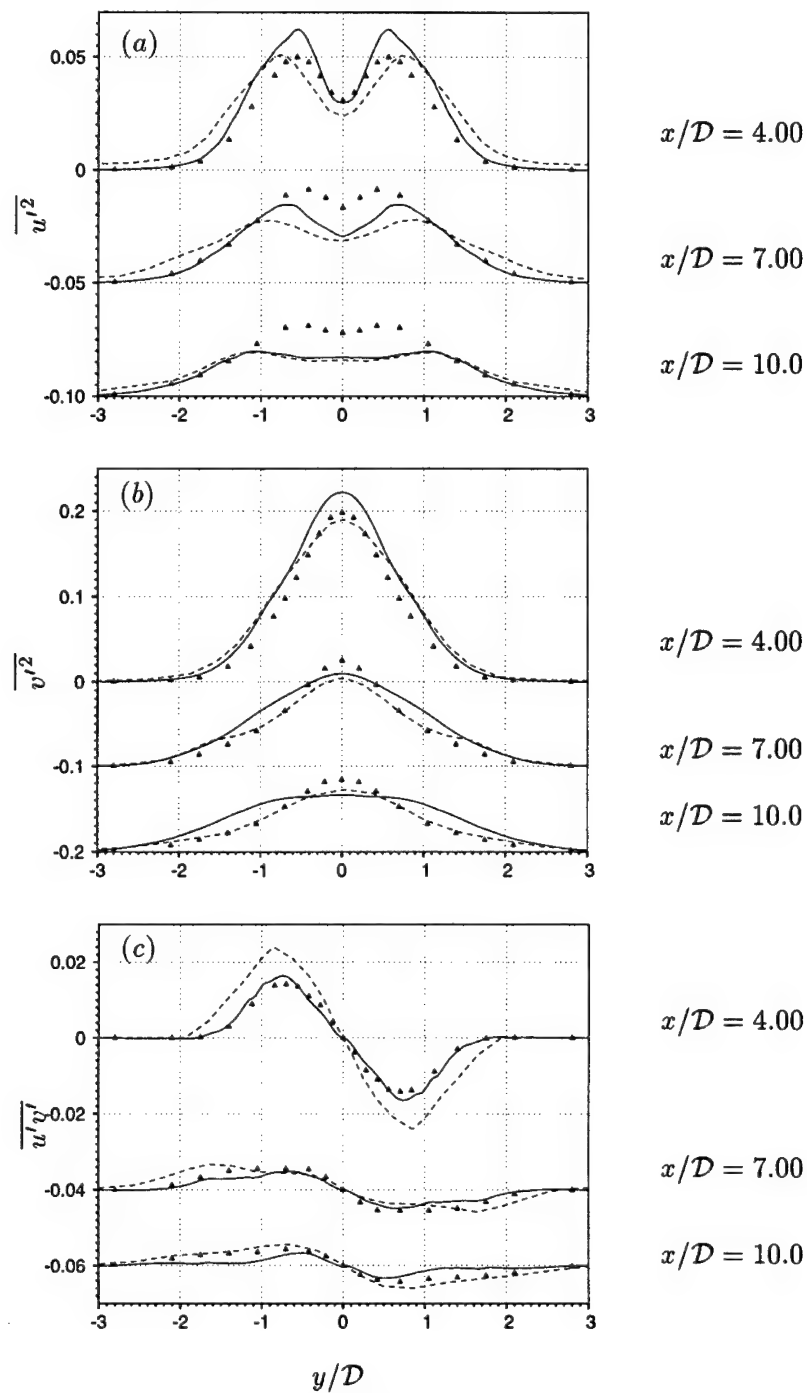


FIGURE 4. Reynolds stress profiles downstream of the recovery region. — Current simulation, ---- Beaudan & Moin, Δ Ong & Wallace. (a) Streamwise Reynolds normal stress (b) Vertical Reynolds normal stress. (c) Reynolds shear stress.

the shape of the experimental profile matches the profile of Beaudan & Moin (1994) better than it does for the current simulation. Figure 4c shows the Reynolds shear stress profiles at these three locations. It is observed that the current simulation shows better agreement with the experiments than Beaudan & Moin (1994) at $x/D = 4.0$. At the two other downstream locations, predictions from both the simulation are comparable and in reasonable agreement with the experiments.

Thus, it is found that in the downstream portion of the wake where the grid is relatively coarse, the numerical dissipation inherent in the higher-order upwind-biased scheme removes energy from roughly three-quarters of the resolved wavenumber range. In the central-difference simulation, since there is no numerical dissipation, the smaller scales are more energetic, and we find that the spectra agrees well with the experiment up to about half of the resolved wavenumber range. However, the enhanced energy in the small scales has no significant effect on the low order statistics, and mean velocity and Reynolds stress profiles in this region obtained from the two simulations are comparable. This is due to the fact that most of the stress contribution comes from fluctuations whose frequency is centered in a narrow band around the shedding frequency, and change in the energy of the small scales does have any significant effect on the magnitude of the Reynolds stresses. It should be pointed out that in applications such as flow generated noise and reactive flows, small scales play a crucial role, and it is therefore critical to retain the energy in these scales. In such applications energy conservative schemes would be clearly preferable over upwind schemes.

In addition, we find that with about a 20-30% smaller grid spacing, the second-order central difference scheme gives results that are comparable to those obtained by the high-order upwind biased schemes. The higher-order upwind based solver is more expensive on a per-point basis than the second-order central difference solver, and this partially offsets the additional cost of the increased resolution required by the second-order method. A drawback of the second-order central scheme is that the simulations are sensitive to numerical aspects such as grid discontinuities and outflow boundary conditions, and thus grids and boundary conditions have to be designed with extreme care.

In future work we plan to use kinetic energy conserving central difference schemes whenever possible. Work is continuing on the development of higher order central difference schemes with the expectation that these will allow for accurate simulation results on meshes coarser than currently required for the second order scheme.

REFERENCES

- BEAUDAN, P. & MOIN, P. 1994 Numerical Experiments on the Flow Past a Circular Cylinders at Sub-Critical Reynolds Numbers. *Report No. TF-62*, Thermosciences Div., Dept. of Mech. Engr., Stanford Univ.
- CARDELL, G. S. 1993 Flow Past a Circular Cylinder With a Permeable Splitter Plate. *Ph.D. Thesis*, Graduate Aeronautical Laboratories, California Institute of Technology.

- CHOI, H., MOIN, P. & KIM, J. 1992 Turbulent Drag Reduction: Studies of Feedback Control and Flow Over Riblets. *Report No. TF-55*, Thermosciences Div., Dept. of Mech. Engr., Stanford Univ.
- LOURENCO, L. M. & SHIH, C. 1993 Characteristics of the Plane Turbulent Near Wake of a Circular Cylinder. A Particle Image Velocimetry Study. *Private Communication*.
- MITTAL, R. 1995 Large-Eddy Simulation of Flow Past a Circular Cylinder. *Annual Research Briefs*. Center for Turbulence Research, NASA Ames/Stanford Univ., 107-116.
- NORBERG, C. 1987 Effects of Reynolds Number and Low-Intensity Freestream Turbulence on the Flow Around a Circular Cylinder. *Publications No. 87/2*, Department of Applied Thermodynamics and Fluid Mechanics, Chalmers University of Technology, Gothenburg, Sweden.
- ONG, L., & WALLACE, J. 1996 The Velocity Field of the Turbulent Very Near Wake of a Circular Cylinder. *Exp. Fluids*. **20**(6).
- RAI, M. M. & MOIN, P. 1993 Direct Numerical Simulation of Transition and Turbulence in a Spatially Evolving Boundary Layer. *J. Comp. Phys.* **109**(2), 169-192.
- SON, J. & HANRATTY, T. J. 1969 Velocity Gradients at the Wall for Flow Around a Cylinder at Reynolds Numbers from 5×10^3 to 10^5 . *J. Fluid Mech.* **35**, 353-368.

Experimental investigation of flow through an asymmetric plane diffuser

By Carl U. Buice AND John K. Eaton¹

1. Motivation and objectives

There is a need for experimental measurements in complex turbulent flows that originate from very well-defined initial conditions. Testing of large-eddy simulations and other higher-order computation schemes requires inlet boundary condition data that are not normally measured. The use of fully developed upstream conditions offers a solution to this dilemma in that the upstream conditions can be adequately computed at any level of sophistication. Unfortunately, experimenters have only recently been sensitized to this issue and there are relatively few appropriate data sets.

The plane diffuser experiment by Obi *et al.* (1993) has received a lot of attention because it has fully-developed inlet conditions and it includes separation from a smooth wall, subsequent reattachment, and redevelopment of the downstream boundary layer. Each of these features offers challenges for modern turbulence models. In particular, Durbin, Kaltenbach, and Mittal of CTR have devoted considerable effort in developing several different computations of the flow. Unfortunately, they found that the experiment had several deficiencies as they began careful comparison to the data. The most glaring problem is the fact that the data set does not appear to satisfy mass conservation, a problem that is most likely due to three-dimensional effects in the diffuser.

The objective of this study is to provide careful qualification and detailed measurements in a re-creation of the Obi experiment. The work will include extensive documentation of the flow two-dimensionality and detailed measurements required for testing of flow computations. Also important to this study is the close interaction of the experimental and computational groups to improve the utility of the data obtained and the accuracy of computation.

2. Accomplishments

The diffuser geometry as specified by Obi *et al.* is shown in Fig. 1. The expected flow includes flow separation approximately one third of the way along the diffuser followed by reattachment in the tailpipe. The problem with this flow is that separation is likely to occur on the end-walls, causing an acceleration of the mid-plane flow. Our approach has been to modify an existing blower wind-tunnel to accommodate a very high aspect ratio version of the diffuser in hopes of minimizing end-wall effects. Unfortunately, the separated regions on the end-wall can be quite large and

¹ Mechanical Engineering Department, Stanford University

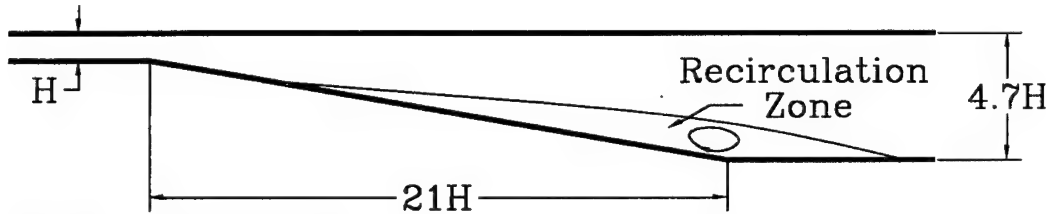


FIGURE 1. Plane diffuser.

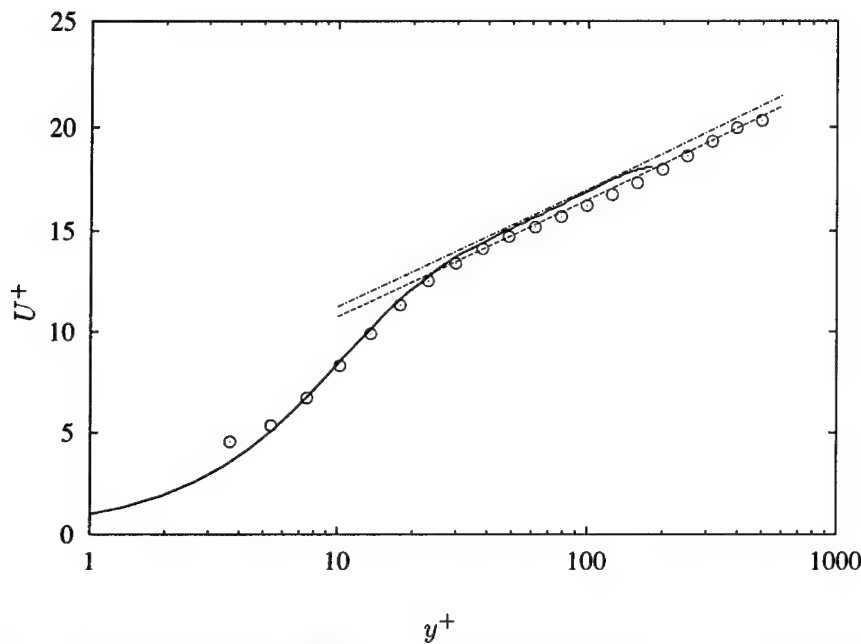


FIGURE 2. Mean-velocity profiles: \circ , current experiment; —, DNS from Kim *et al.*; ----, law of the wall with constant = 5.0; - · - ·, law of the wall with constant = 5.5.

have a significant effect on the mid-plane flow. After construction, the majority of our efforts have been in controlling the end-wall boundary layer separation.

The experimental facility is described in last year's CTR briefs (Buice and Eaton 1995). The facility has an upstream channel width ($H = 2\delta$) of 1.5cm. The experiment is being conducted at a channel Reynolds number ($U_{cl}H/\nu$) of 20,000.

2.1 Tunnel qualification

Our basic approach for qualification of this experiment was to first verify that the inlet conditions corresponded to those of a known fully developed turbulent channel flow. In Fig. 2, the inlet velocity profile for this experiment is compared to the turbulent channel profile produced by the DNS calculation performed by Kim *et al.* The primary difference between these two profiles is the additive constant in the log law. While our profile follows the log law with the traditional additive constant of 5.0, the DNS follows the log law with a value of 5.5. According to Kim

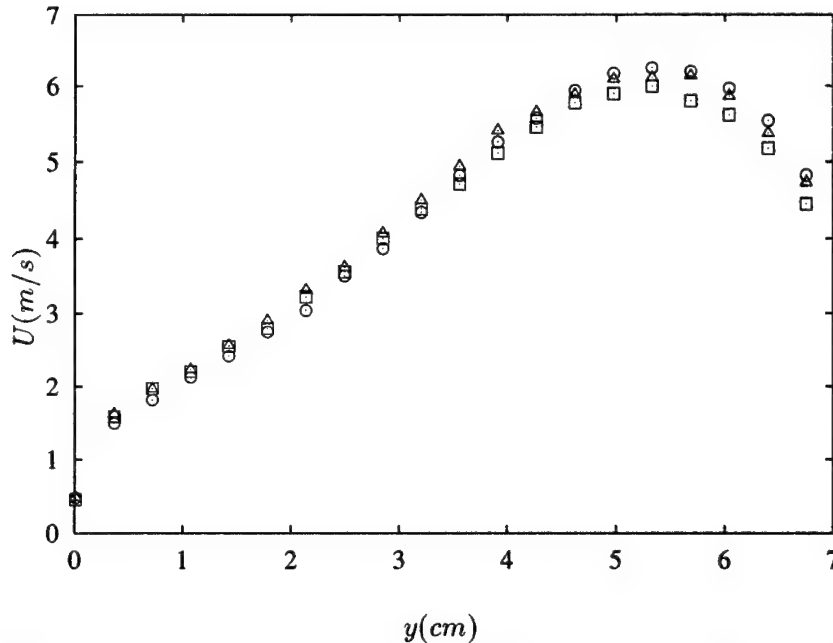


FIGURE 3. Mean-velocity profiles at $x/\delta = 59$: o, centerline; Δ , near end-wall; \square , far end-wall.

et al. the higher constant is a low Reynolds number effect, $Re_\tau = 180$, for the DNS compared with $Re_\tau = 490$ for our experiment.

The second step in the tunnel qualification process was to verify that mean velocity profiles taken near the end-walls closely matched the centerline profile. Figure 3 shows three similar mean velocity profiles taken just downstream of the reattachment point at the centerline and two stations approximately 1/6 of the span away from the two end-walls. The final qualification step is the integration of the mean velocity profiles to verify that the conservation of mass holds throughout the measurement region. Although this step is not complete because we lack the final pulsed-wire data in the recirculation region, the preliminary results look very good. The profiles before and after the separation integrate to within 3% of the initial mass flow at the inlet of the diffuser. The primary difficulty with the results of Obi *et al.* was the 15% increase in mass-flow along the core section of the diffuser downstream of $x = 40\delta$, see Kaltenbach (1995), which was most likely due to secondary flow produced by end-wall separation.

2.2 Preliminary results

We have completed single-wire and cross-wire surveys outside of the separation region throughout the measurement domain, from $12H$ upstream of the beginning of the diffuser to $77H$ downstream of the inlet. We have also taken frequency spectra at a number of locations in the recovery region along with the associated time records. The thermal tuft was used to determine the separation location and will be used in the near future to determine the reattachment location. The pressure

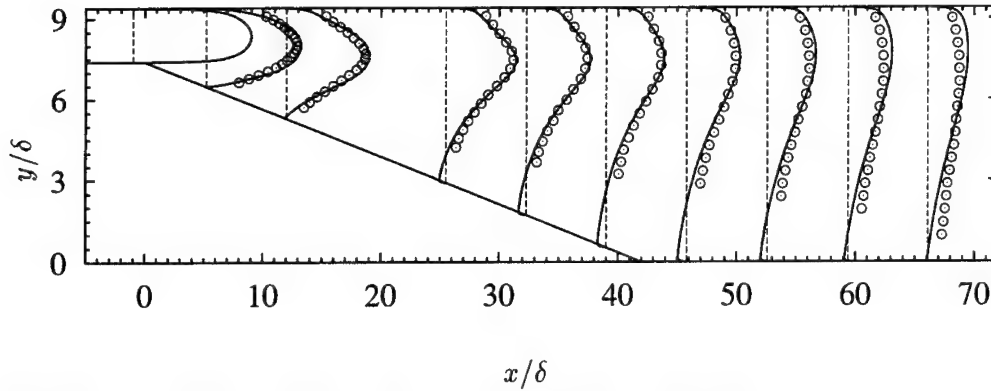


FIGURE 4. Mean velocity $U/U_{cl,in}$: \circ , current experiment; —, $k - \epsilon - v^2$. Where $U/U_{cl,in} = 1.0 = 10\delta$.

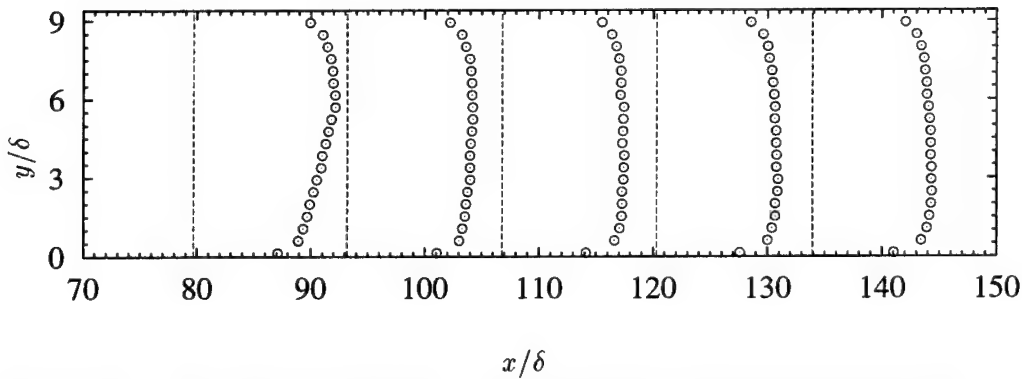


FIGURE 5. Mean velocity $U/U_{cl,in}$: \circ , current experiment. Where $U/U_{cl,in} = 1.0 = 60\delta$.

distribution along the upper and lower walls has been measured.

2.2.1 Mean flow data

Figure 4 shows the mean velocity profiles taken using a single-wire anemometer compared to the results from a calculation performed using Durbin's $k - \epsilon - v^2$ model. They compare favorably until the region after reattachment where the computed recovery lags the measured recovery. The mean velocity profiles from the redevelopment section of the experiment are shown in Fig. 5 and on a different scale than the previous figure. Near the end of the measurement region, the flow has almost returned to fully developed turbulent channel flow.

Using the thermal tuft, the mean separation point was found to be $6H$ downstream of the beginning of the diffuser, which corresponds well to the $7H$ found in the Durbin calculation and differs significantly from the experiment performed by Obi *et al.*, which found that the flow separated at $11H$. End-wall separation would be expected to relieve the adverse pressure gradient and delay separation.

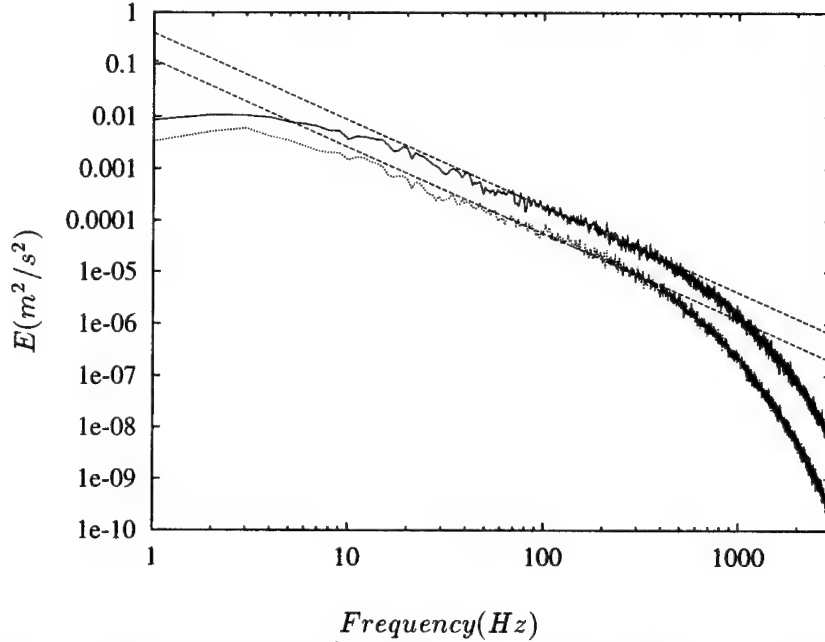


FIGURE 6. Energy spectra at $y^+ = 300$: —, $x/\delta = 93.2$; ·····, $x/\delta = 133.9$; ----, Kolmogorov's $-5/3$ law.

2.2.2 Turbulence statistics

We have measured Reynolds stresses and triple products in the region of the flow outside of the recirculating region. The pulsed-wire is currently being used to measure the mean and fluctuating components of the streamwise velocity. We have calculated the frequency spectra using velocity measurements recorded by a single wire at two locations in the boundary layer, $y^+ = 30$ and $y^+ = 300$, at various stations in the recovery region downstream of the diffuser. Figure 6 shows the frequency spectra at two stations, $x/\delta = 93.2$ and $x/\delta = 133.9$. Also plotted are two lines with the $-5/3$ slope given by Kolmogorov's law for the inertial subrange. The decay in turbulent kinetic energy as the flow recovers from separation is apparent.

3. Future work

We are now in the final stages of the experiment. The pulsed-wire data is nearly complete and preliminary spatial correlation measurements have been made. The tunnel will require some minor modification to get the final spatial correlations with the two-point correlation probe and the skin-friction data using the pulsed-wall probe.

REFERENCES

- BUICE, C., & EATON, J. 1995 Experimental investigation of flow through an asymmetric plane diffuser, *Annual Research Briefs-1995*, Center for Turbulence Research, Stanford Univ./NASA Ames. 117-120.

- KALTENBACH, H.-J. 1994 Large-eddy simulation of flow through a plane, asymmetric diffuser, *Annual Research Briefs-1994*, Center for Turbulence Research, Stanford Univ./NASA Ames. 175-184.
- KIM, J., MOIN, P. & MOSER, R. 1987 Turbulence statistics in fully developed channel flow at low Reynolds number. *J. Fluid Mech.* **177**, 133-166.
- OBI, S., AOKI, K. & MASUDA, S. 1993 Experimental and computational study of turbulent separating flow in an asymmetric plane diffuser; in: *Ninth Symposium on Turbulent Shear Flows*, Kyoto, Japan, August 16-19, 1993. p 305.

Progress in the large-eddy simulation of an asymmetric plane diffuser

By Massimiliano Fatica & Rajat Mittal¹

1. Motivation and objectives

The flow through a plane asymmetric diffuser is a good test case for assessing the capability of LES since it contains features such as large scale unsteady separation and strong intermittency which are difficult to capture using conventional modeling approaches. Previous attempts to simulate this flow (Kaltenbach, 1994) have significantly underpredicted the extent of separation.

The objective of the present research is to understand why the previous simulations did not predict the flow separation correctly. This study focuses on mesh refinement and matching of the inlet velocity profile. In order to perform this study, the flow solver of Kaltenbach (1994) was modified to increase its accuracy and efficiency. The improved algorithm allows for better resolution at affordable CPU cost. The present results are compared with those of Kaltenbach (1994) and the experimental data of Obi *et al.* (1993).

2. Accomplishments

2.1 Numerical method

Although previous simulations used a fully implicit method (Kaltenbach 1994, Choi *et al.* 1992), the time-step in this flow is limited mainly by the turbulence time-scale in the inlet and not by numerical stability considerations. This fact implies that much of the potential benefit of using the implicit scheme is not fully realized in this case. In the current study, the semi-implicit solver used for the simulations of flow past the circular cylinder (see Mittal, this volume) has been modified for solving flow through the diffuser. The direct inversion of the momentum equations coupled with the fast iterative pressure Poisson solver results in an extremely efficient algorithm. The Fourier discretization method provides better spanwise resolution, and it was found to be a cost effective alternative to increasing the number of grid points. The spanwise velocity is collocated at the pressure node, and dealiasing is performed using the $(2/3)^{rd}$ rule in order to guarantee kinetic energy conservation. The increased efficiency allows us to use a finer mesh and to accumulate statistics over a longer period than has been possible before.

2.2 LES of flow in an asymmetric planar diffuser

The flow configuration consists of a asymmetric planar diffuser with a 10° angle and expansion ratio of 4.7. The turbulent inflow corresponds to a fully developed

¹ Present address: University of Florida, Dept. of Mechanical Engr., Gainesville, FL

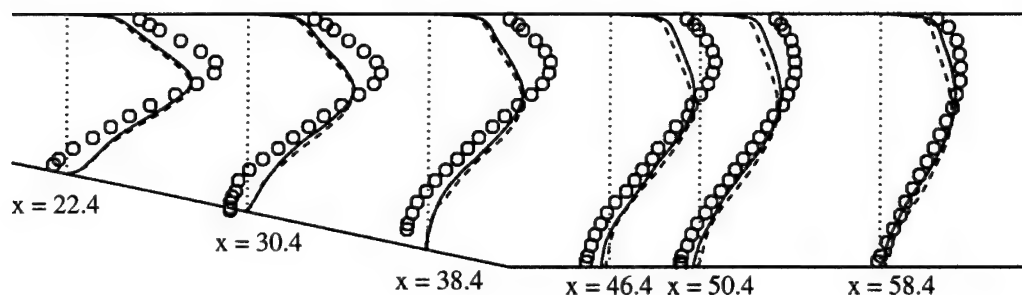


FIGURE 1. Mean velocity profiles $x + 10U/U_b$ in the exit section of the diffuser. Effect of spanwise resolution. — Run A ; ---- Kaltenbach (1994); o Experimental data by Obi *et al.* (1993).

channel flow with a bulk Reynolds number $Re_b = 9000$. The bulk Reynolds number is defined as $Re_b = hU_b/\nu$ where h , U_b , and ν are the inlet half-channel height, inlet bulk velocity, and kinematic viscosity, respectively. The spanwise domain size is $4h$.

The disparity in the length and time-scales in the inlet and exit sections of the diffuser imposes significant demands on the computational resources. The sensitivity of the flow to inflow/outflow conditions also causes difficulties for experimental measurements, and a parallel experimental effort is currently underway (Buice & Eaton, 1995) to provide reliable data for validation purposes.

Previous LES studies (Kaltenbach, 1994) have under-predicted the extent of separation, and our objective is to investigate the reason for this discrepancy. Possible causes include mismatch of upstream and/or downstream conditions, low streamwise/spanwise resolution, and small spanwise domain size.

2.3 Results

To investigate the effect of spanwise resolution, one simulation of this flow has been carried out on the same $163 \times 65 \times 64$ (streamwise \times vertical \times spanwise) grid that was used by Kaltenbach (1994), but with the better resolution in the spanwise direction provided by the spectral discretization (this simulation will be hereafter referred as Run A).

Kaltenbach realized that the simulation was under-resolved on this mesh, but could not afford better resolution with his less efficient, fully implicit code. He could afford better resolution in the separate channel flow simulation used to produce the inflow data, however, and consequently he used 128 points in the span for this purpose. The increased accuracy associated with the 128 points for the inflow generation can not be sustained on the 64 point diffuser mesh, and thus the solution is assumed to degrade with increasing distance downstream from the inlet. Inflow data for our run A was generated with Fourier collocation in the spanwise direction using 64 points. The statistics from this simulation were found to be nearly identical to Kaltenbach's full finite difference calculation done on 128 points. The main

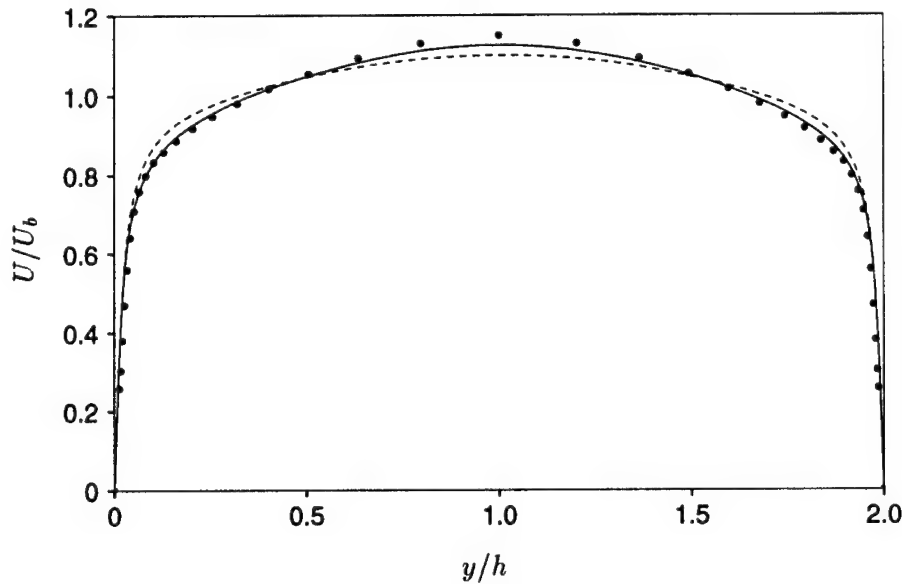


FIGURE 2. Comparison of inflow profiles with experiments: ---- Inlet condition for Run A ($\Delta x_{in}^+ = 100$); — Inlet condition for Run B ($\Delta x_{in}^+ = 50$); • Experimental data by Buice & Eaton (1996).

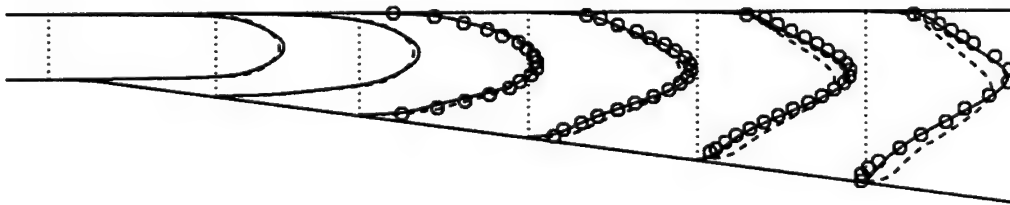


FIGURE 3. Mean velocity profiles $x + 5U/U_b$ in the inlet section of the diffuser. Effect of streamwise resolution. — Run B; ---- Kaltenbach (1994); o Experimental data by Obi *et al.* (1993).

difference is that Fourier collocation was also used in the diffuser simulation, which means the quality of the inflow data should be preserved throughout the domain.

The statistics from Run A have been accumulated over a period of about $1200U_b/h$, which corresponds to about 50 exit inertial time scales. Mean streamwise velocity profiles in the downstream section of the diffuser are shown in Fig. 1. The results of Run A are nearly identical to those of Kaltenbach at the first station in Fig. 1.

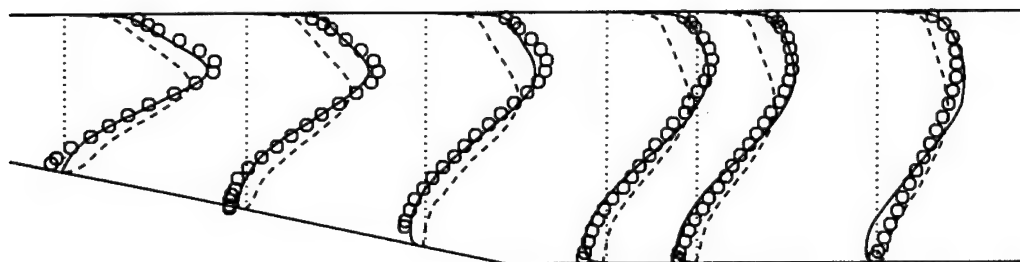


FIGURE 4. Mean velocity profiles $x + 10U/U_b$ in the exit section of the diffuser. Effect of streamwise resolution. — Run B ; ---- Kaltenbach (1994); o Experimental data by Obi *et al.* (1993).

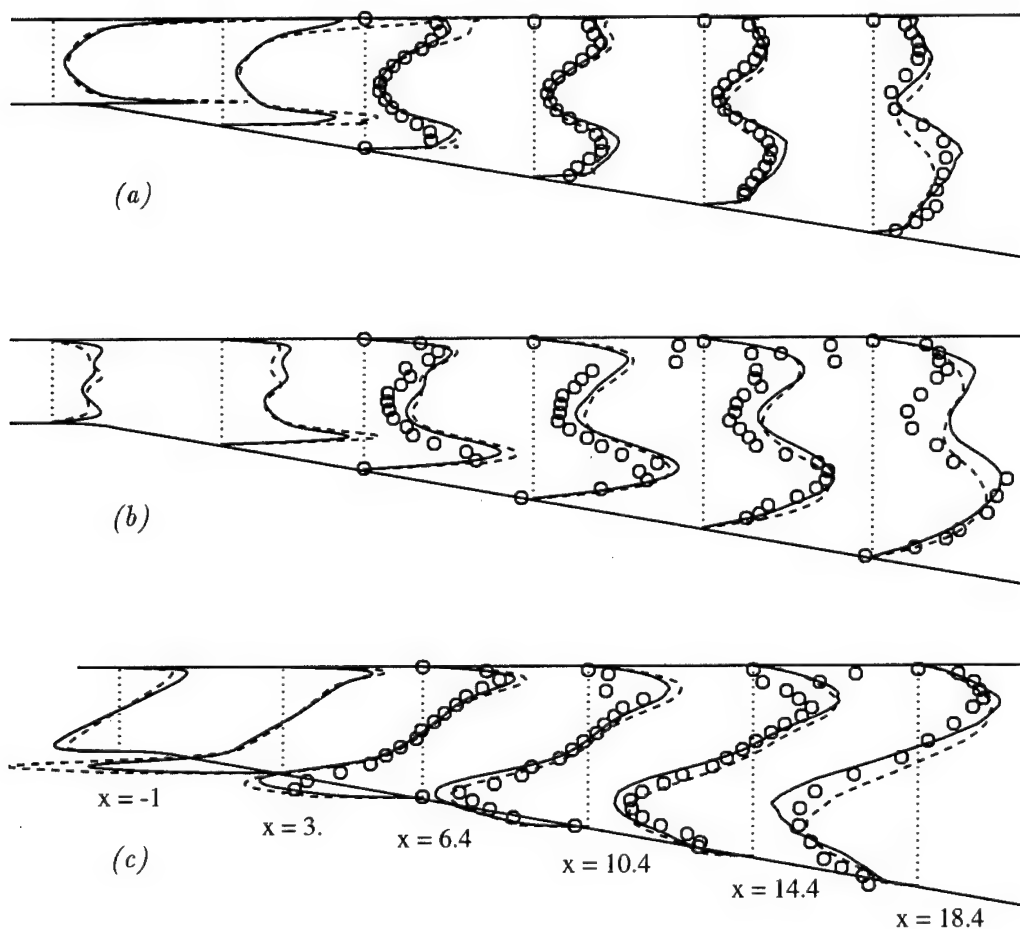


FIGURE 5. Variances $x + 150\overline{uu}/U_b^2$ (a), $x + 500\overline{vv}/U_b^2$ (b) and shear stress $x + 750\overline{uv}/U_b^2$ (c) in the first half of diffuser. — Run B ---- Kaltenbach (1994); o Obi *et al.* (1993).

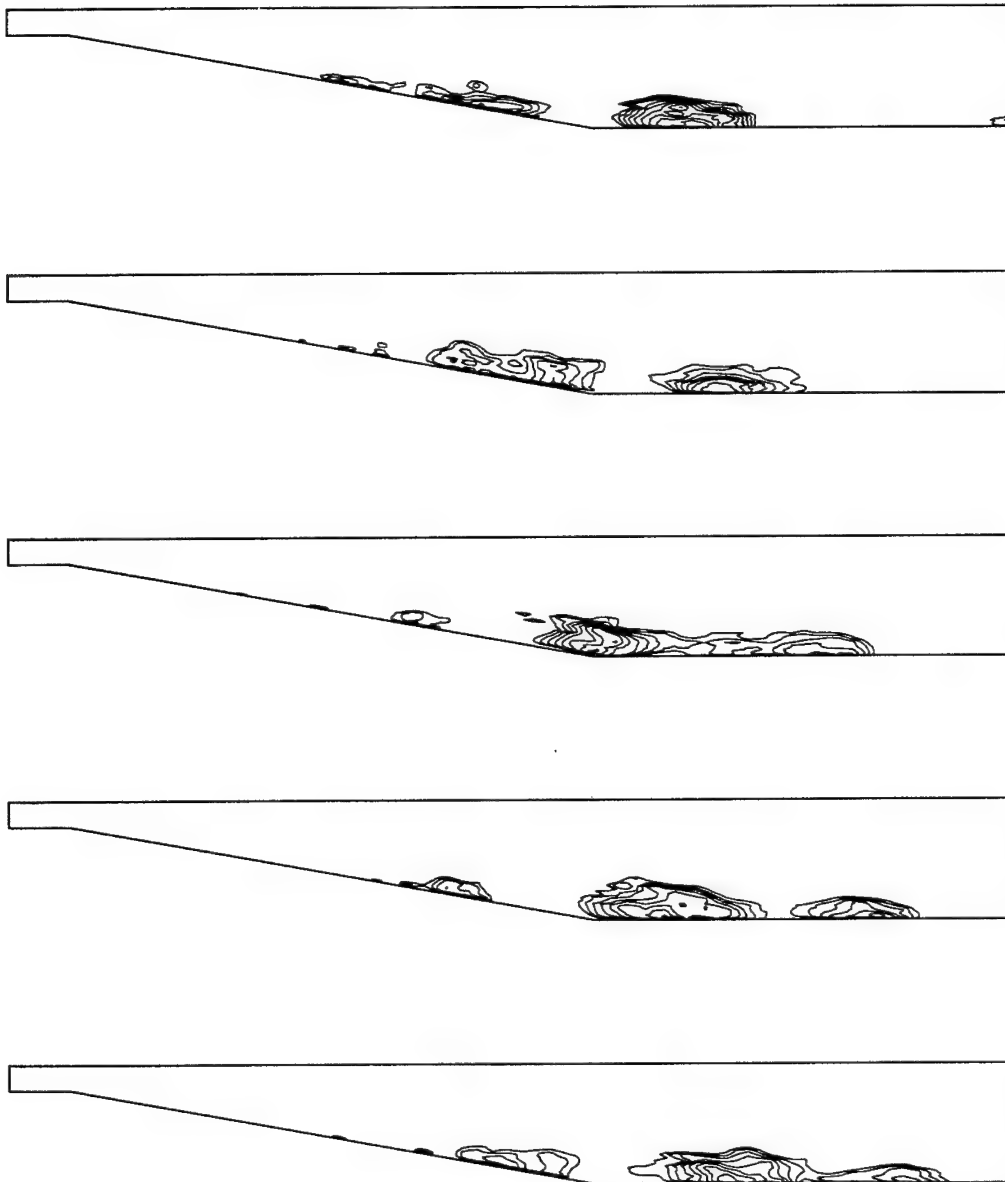


FIGURE 6. Contour line of negative streamwise velocity averaged in the spanwise direction. Time increment among frames is approximately $30U_b/h$.

Small differences can be observed over the next three stations with Run A producing a slightly larger separated region. Overall the differences are slight, however, and Run A is still in considerable disagreement with the experimental data.

The current mismatch with the experimental data appears to be related to the streamwise resolution. Both Kaltenbach's and the Run A simulation are under-resolved in the streamwise direction which results in mean velocity profiles upstream of the diffuser that are noticeably fuller near the wall as compared with the experimental data. As shown in Fig. 2, doubling the number of streamwise mesh points in the inflow generation ($\Delta x_{in}^+ = 50$ compared to the previous $\Delta x_{in}^+ = 100$) has shown to lead to profiles that agree well with the experimental data.

A new simulation with improved streamwise resolution has been started. This simulation, referred to as Run B, has a streamwise mesh spacing of $\Delta x_{in}^+ = 50$ at the inlet and contains $273 \times 65 \times 64$ points. Although the statistics have not yet converged, some preliminary results will be presented below. Due to the disparity in the time-scales in the inlet and outlet section, the statistics converge more slowly in the outlet section. Thus the results near the inlet are probably trustworthy while those near the outlet may change as the simulation is run further in time. The figures shown are obtained using statistics accumulated over a period of about 400 inlet inertial time scales (U_b/h). Measured in terms of exit inertial time scales, however, the averaging time is only about 18 units.

It can now be observed in Figs. 3 and 4 that there is good agreement between the LES computation and the experimental data in all the stations except the last one. This can be an effect of insufficient average time. In Fig. 5 velocity fluctuations are plotted in the first half of the diffuser. Also, for these quantities, better agreement with the experiment is found.

Using LES, not only statistical quantities can be obtained, but also instantaneous information. We are interested in understanding the dynamics of the separation: that there is in this flow a very unsteady and intermittent process as can be noticed from Fig. 6. A computer animation is being generated to visualize the process.

3. Future plans

From the result of the fine simulation (Run B), it seems pretty clear that the previous disagreement between LES and experiments was due to inadequate streamwise resolution. The current simulation will be continued until the statistics are fully converged. A detailed comparison of the results will be made with both the data of Obi *et al.* (1993) and that of Buice and Eaton (1996).

Acknowledgment

The fine simulation has been performed on the Aeronautical Systems Center Cray C90 under the ASC MSRC Pioneer Program.

REFERENCES

- BUICE, C. U. & EATON, J. K. 1995 Experimental Investigation of Flow Through an Asymmetric Plane Diffuser. *Annual Research Briefs*. Center for Turbulence Research, NASA Ames/Stanford Univ., 117-121.
- CHOI, H., MOIN, P. & KIM, J. 1992 Turbulent drag reduction: studies of feedback control and flow over riblets. *Report No. TF-55*, Thermosciences Div., Dept. of Mech. Engr., Stanford Univ.
- KALTENBACH, H-J. 1994 Large-eddy simulation of flow through a plane, symmetric diffuser. *Annual Research Briefs*. Center for Turbulence Research, NASA Ames/Stanford Univ., 175-184.
- OBI, S., AOKI, K. & MASUDA, S. 1993 Experimental and computational study of turbulent separating flow in an asymmetric plane diffuser. *Ninth Symposium on Turbulent Shear Flows*, Kyoto, Japan, 305.

A numerical study of self-similarity in a turbulent plane wake using large-eddy simulation

By Sandip Ghosal¹ AND Michael M. Rogers²

1. Motivation and objectives

Turbulent wakes are known to develop self-similarly sufficiently far downstream from obstacles that generate them. It has long been assumed that the spreading rate of the wake in the self-similar regime is independent of the details of the body generating the wake, being dependent only on the total drag (or momentum deficit). This assumption seems to be in contradiction with some recent experiments. In this study we attempt to complement these experimental investigations through a numerical study of a time-developing wake. A numerical study has the advantage of eliminating many of the uncontrolled factors present in experiments and allowing precise control of initial conditions. Large-eddy simulations employing the recently developed dynamic localization model are used to extend previous results from direct numerical simulations. The large-eddy simulation results are compared to the direct numerical simulation database, wherever such comparisons are feasible, as a check of the method. Like the experiments, the large-eddy simulations suggest that non-unique self-similar states, characterized by different spreading rates and turbulent statistics, are possible and that they can be maintained for significant time periods. The study also demonstrates the predictive capability of the dynamic localization subgrid model.

2. Introduction

A turbulent flow is said to be self-similar when some or all of its statistical properties depend only on certain combinations of the independent variables rather than on each independent variable individually. The consequence of this is that the number of independent variables in the problem is reduced, thus greatly facilitating its solution. Geometrically, a self-similar flow possesses a certain symmetry; for example the flow pattern on any two cross sections perpendicular to a given axis may be identical except for a scale factor. The property of self similarity has been used on many occasions in fluid dynamics to derive elegant solutions to otherwise very difficult problems (such as the structure of turbulent boundary layers, jets, and wakes). Recently, George (1989) presented a critical analysis of the self-similarity argument in the context of certain apparent discrepancies of self-similar solutions with experimental results on jets and wakes. He argued that in the traditional analysis, in

1 Present address: LMFN-INSA Rouen URA-CNRS 230-CORIA, Mont-St-Aignan 76821, France

2 Nasa Ames Research Center

addition to the assumption of self-similarity, one often invokes additional restrictions inspired by the dictum "turbulence forgets its initial conditions". For example, in the case of the turbulent plane wake, one requires that the growth rate sufficiently far from the source can depend only on the momentum deficit of the wake (which is proportional to the drag on the obstacle producing the wake). Dimensional analysis then implies "universal" solutions that do not depend on the nature of the obstacle or the details of the initial conditions. George argued that when such additional restrictions are removed, one obtains a wider class of self-similar solutions that are no longer "universal". Thus, for a plane wake, these solutions will depend on the nature of the obstacle and not just on the total drag. These conclusions seem to be in agreement with the experiments of Wygnanski *et al.* (1986) and Marasli *et al.* (1992). However, conditions in experiments are difficult to control precisely and some doubt remains about whether the results indicate the existence of multiple self-similar states or if this is an artifact of experimental uncertainties.

To address this issue further, direct numerical simulations (DNS) of plane wakes have been generated by Moser and Rogers (1994) and Moser, Rogers, and Ewing (1996). Such numerical simulations are free from various uncontrollable extraneous factors that complicate the interpretation of experiments and should complement the experimental results already available (see Wygnanski 1986, Marasli 1992, and references therein). However, such simulations are very costly since all scales of turbulent motion must be accurately resolved. In practice this limits the Reynolds numbers and the extent of flow evolution that can be simulated. This suggests that large-eddy simulation (LES) might be a better tool than direct numerical simulation to study high-Reynolds-number fully developed wake turbulence over long evolution times, particularly if small-scale information is not desired. In LES one explicitly solves a coarse-grained version of the Navier-Stokes equations. The collective effect of the small scales on the large scales is taken into account through a "subgrid model". Although LES can be computationally much less expensive, it has the disadvantage that it leaves open the possibility of significant errors resulting from the approximation of the unknown subgrid stress by a model.

In order to achieve the longest possible simulation of a high-Reynolds-number self-similar plane wake, we have resorted to LES of the temporally evolving flow, as was done in the DNS. First, the LES methodology is validated by comparison to existing DNS for cases that are less computationally intensive. The limitations of the DNS can then in turn be addressed by the use of new LES results in larger computational domains. This complementary use of both LES and DNS bolsters confidence in the simulation results and facilitates better understanding of the self-similar behavior of the plane wake.

Three DNS of temporally evolving plane wakes have been documented in Moser, Rogers, and Ewing (1996). These wakes differ from each other in the level of initial two-dimensional turbulent fluctuations. The "unforced" case is initiated from two realizations of a fully developed turbulent boundary layer with no added disturbances. In the other "weakly forced" and "strongly forced" cases, additional

two-dimensional fluctuation energy has been added to the boundary layer turbulence. This is achieved by multiplying the streamwise and cross-stream velocity components associated with the two-dimensional Fourier modes in the computation by factors of 5 and 20, respectively. The resulting evolution of the unforced and weakly forced cases shows convincing evidence of self-similar evolution, although the growth rates and Reynolds stress levels for the two cases are different. The strongly forced case, on the other hand, shows irregularities in the shapes of mean velocity and Reynolds stress profiles and exhibits at most a short period of approximate self-similar evolution (with a very high growth rate and large levels of Reynolds stress).

The flow structure in this strongly forced case has an underlying pattern of a few large-scale motions, and it was speculated in Moser, Rogers, and Ewing (1996) that the poor self-similarity resulted from an inadequate sample of large-scale turbulent eddies in the computational domain. In order to confirm this, an LES of nominally the same flow in a domain that is twice as large in the streamwise direction and four times as large in the spanwise direction has been generated and compared to both DNS and LES of the small-domain case. Of primary interest is whether a self-similar state does indeed exist in this strongly forced flow and what the growth rate and Reynolds stress levels are if such a period exists. This allows us to better address the issue of whether or not multiple initial-condition-dependent self-similar states exist for the turbulent plane wake.

The LES is performed using a fully spectral code and a recently developed subgrid model known as the "dynamic localization model" (DLM). In a previous paper (Ghosal 1995), the theoretical development leading to the dynamic localization model for large-eddy simulation was presented. The method has been successfully applied to isotropic turbulence (Ghosal 1995, Carati *et al.* 1995), channel flow (Cabot 1993), and the flow over a backward-facing step (Akselvoll 1993a, Akselvoll 1993b). Two attractive features of this model are:

- (1) The magnitude of the eddy viscosity does not need to be prescribed in an ad hoc manner but the algorithm itself chooses an optimum value based on a certain well-defined optimization procedure.
- (2) The subgrid model parameter ("Smagorinsky coefficient") is a function of space and time and automatically adjusts itself to the intensity of the turbulence. In particular, it goes to zero near walls and vanishes in those regions of space and time where the flow is laminar.

The present study, in addition to investigating the issue of self-similarity in plane wakes, also provides another test of the predictive capability of the dynamic localization model. This includes both the ability to predict turbulent statistics as well as flow structure. In Moser, Rogers, and Ewing (1996), forcing was found to significantly affect both statistics and flow structure in the plane wake, with forcing increasing the level of organized large-scale motions in the flow. Since it seems that these differences in flow structure are linked to the differences in turbulent statistics it may be essential that the subgrid model preserve the character of the filtered vorticity field for accurate prediction of the statistics. The local character

of the subgrid model employed in this work would seem to offer a greater likelihood of achieving this. The level of correspondence between the vortex structures in the LES and the DNS is also of interest for flow control and understanding mechanisms of turbulent mixing.

In Section 3 certain general properties of plane wakes are reviewed and the problem to be solved numerically is defined. In Section 4 the computational methods used, including the subgrid model, are briefly discussed. The LES results for the unforced wake are presented and compared with the DNS database in Section 5. LES computations of the forced case in two different domain sizes (the smaller for comparison to the DNS, the larger to address limitations of the DNS and to study the long-time evolution of the forced case) are considered in Section 6. In the conclusion (Section 7), the results and their significance are discussed.

3. Formulation of the problem

In a temporally developing wake the flow is statistically homogeneous in the streamwise (x) and spanwise (z) directions and inhomogeneous in the cross-stream (y) direction. The governing equations are the incompressible Navier-Stokes equations with periodic boundary conditions in x and z . In the y direction the domain is infinite and the velocity field is assumed to asymptotically approach the free-stream velocity, which can be taken as zero in a suitably chosen reference frame. This flow becomes equivalent to the physically more relevant spatially developing wake in the limit of a small wake deficit. If one imagines a “box” being advected downstream at the “free-stream” velocity in a spatially developing wake, then the motion of the fluid in the imaginary box approximates a temporally developing wake. The integrated mass flux deficit

$$\mu = - \int_{-\infty}^{+\infty} \delta U(y) dy \quad (1)$$

is conserved in a temporally developing wake, as opposed to the momentum flux deficit

$$\mu_* = - \int_{-\infty}^{+\infty} (U_\infty + \delta U(y)) \delta U(y) dy, \quad (2)$$

which is conserved for a spatially developing wake. Clearly, if the mean velocity deficit δU is small compared to the free stream velocity U_∞ , then $\mu_* \approx U_\infty \mu$. A suitable scale for the velocity is the initial centerplane velocity deficit $\delta U_0 = -(\delta U(0))_{t=0}$ and a suitable length scale is $\mu/\delta U_0$. The associated time scale is $\mu/(\delta U_0)^2$. Most of the results given below are quoted in these units.

4. Computational methods

The numerical method used is a spectral method in vorticity variables. Both the velocity and vorticity are periodic in the x and z directions and can, therefore, be expanded in a basis of trigonometric functions for these variables. The y direction is somewhat more difficult to deal with since the domain is infinite in y . One

method is to choose a basis of functions that have an infinite support (such as the Jacobi polynomials coupled with a mapping to the infinite interval) for the y direction (Spalart *et al.* 1991). However, here we use an artifice that results in a simpler numerical code. We take advantage of the fact that in a wake the vorticity field is much more confined in the y direction than the velocity field. One then expands the vorticity in a trigonometric series in y defined over (y_{min}, y_{max}) with periodic boundary conditions. This is permissible provided that the vorticity is narrowly confined around $y = 0$ and effectively decays to zero at the boundaries y_{min} and y_{max} . The velocity field is not so confined and cannot be represented in terms of these trigonometric functions. But once the vorticity field is determined, the correct velocity field may be obtained by adding a potential “correction” to the periodic velocity field so as to match the boundary conditions at $y = \pm\infty$. Further details of the computational method may be found in Corral and Jiménez (1995).

We use the “dynamic method” for computing the coefficient $C(\mathbf{x}, t)$ in the generalization of Smagorinsky’s subgrid model

$$\tau_{ij} - \frac{1}{3}\delta_{ij}\tau_{kk} = -2C(\mathbf{x}, t)\Delta^2|\bar{S}|\bar{S}_{ij} \quad (3)$$

where τ_{ij} is the subgrid stress, \bar{S}_{ij} is the resolved rate of strain, $|\bar{S}|^2 = 2\bar{S}_{ij}\bar{S}_{ij}$, and Δ is the LES filter-width (taken equal to the grid spacing). We will consider two variants of the dynamic method for determining C . The first, the Dynamic Model (DM), can be considered as a special case of the more general DLM discussed below for flows that are homogeneous in one or more directions. For the wake flow the coefficient C is considered a function of y and t only in DM and is given by

$$C(y, t) = \frac{\langle m_{ij}L_{ij} \rangle_{xz}}{\langle m_{kl}m_{kl} \rangle_{xz}} \quad (4)$$

where the angular brackets denote averaging over the homogeneous $x - z$ planes.

Here $L_{ij} = \widehat{\bar{u}_i\bar{u}_j} - \widehat{\bar{u}_i}\widehat{\bar{u}_j}$ is the Leonard term and $m_{ij} = \Delta^2|\widehat{\bar{S}}|\widehat{\bar{S}}_{ij} - \widehat{\Delta^2|\bar{S}|}\widehat{\bar{S}}_{ij}$, where \bar{u}_i is the filtered velocity and the $\widehat{}$ denotes the “test filtering” operation:

$$\hat{f}(\mathbf{x}) = \int G(\mathbf{x}, \mathbf{y}) f(\mathbf{y}) d\mathbf{y}. \quad (5)$$

The “test-level” filter-width is $\hat{\Delta}$ ($\hat{\Delta} > \Delta$), and $G(\mathbf{x}, \mathbf{y})$ is the test filter kernel.

The second method, DLM, is applicable to arbitrary homogeneous flows but imposes the constraint $C \geq 0$. It is the more general of the two but requires more computation. The constraint $C \geq 0$ can be relaxed. This is done either by introducing an additional equation for the subgrid energy, k (Ghosal 1995) or by adding a “stochastic backscatter” term (Carati *et al.* 1995). In DLM one obtains $C(\mathbf{x}, t)$ as a function of position at each time-step by solving an integral equation

$$C(\mathbf{x}) = \left[f(\mathbf{x}) + \int \mathcal{K}(\mathbf{x}, \mathbf{y}) C(\mathbf{y}) d\mathbf{y} \right]_+ \quad (6)$$

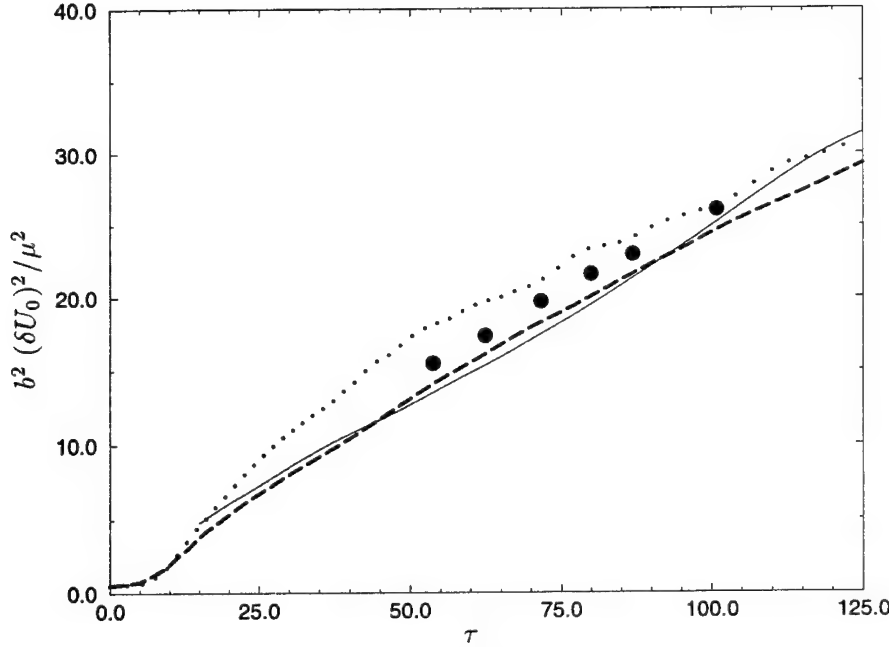


FIGURE 1. The square of the wake-width as a function of time using DLM —; DM — —; No model ·····; filtered DNS •.

where the suffix “+” indicates the positive part and

$$f(\mathbf{x}) = \frac{1}{\alpha_{kl}(\mathbf{x})\alpha_{kl}(\mathbf{x})} \left[\alpha_{ij}(\mathbf{x})L_{ij}(\mathbf{x}) - \beta_{ij}(\mathbf{x}) \int L_{ij}(\mathbf{y})G(\mathbf{y}, \mathbf{x})d\mathbf{y} \right], \quad (7)$$

$$\mathcal{K}(\mathbf{x}, \mathbf{y}) = \frac{\mathcal{K}_A(\mathbf{x}, \mathbf{y}) + \mathcal{K}_A(\mathbf{y}, \mathbf{x}) - \mathcal{K}_S(\mathbf{x}, \mathbf{y})}{\alpha_{kl}(\mathbf{x})\alpha_{kl}(\mathbf{x})}, \quad (8)$$

$$\mathcal{K}_A(\mathbf{x}, \mathbf{y}) = \alpha_{ij}(\mathbf{x})\beta_{ij}(\mathbf{y})G(\mathbf{x}, \mathbf{y}), \quad (9)$$

and

$$\mathcal{K}_S(\mathbf{x}, \mathbf{y}) = \beta_{ij}(\mathbf{x})\beta_{ij}(\mathbf{y}) \int G(\mathbf{z}, \mathbf{x})G(\mathbf{z}, \mathbf{y})d\mathbf{z}. \quad (10)$$

In these expressions $G(\mathbf{x}, \mathbf{y})$ is the “test filter”, $\alpha_{ij} = -2\hat{\Delta}^2|\hat{S}|\hat{S}_{ij}$, $\beta_{ij} = -2\Delta^2|\bar{S}|\bar{S}_{ij}$, and L_{ij} is the Leonard term. The method of numerically solving the integral equation to determine the coefficient C has been described elsewhere (Ghosal *et al.* 1995). The test filter width in these computations was taken to be twice the grid-filter width, $\hat{\Delta} = 2\Delta$, and a “top-hat” filter was used with a Simpson’s rule quadrature.

5. Validation of the LES for the unforced wake

In this section we attempt to establish confidence in the predictive capability of the subgrid model by reproducing, using LES, the results for the “unforced”

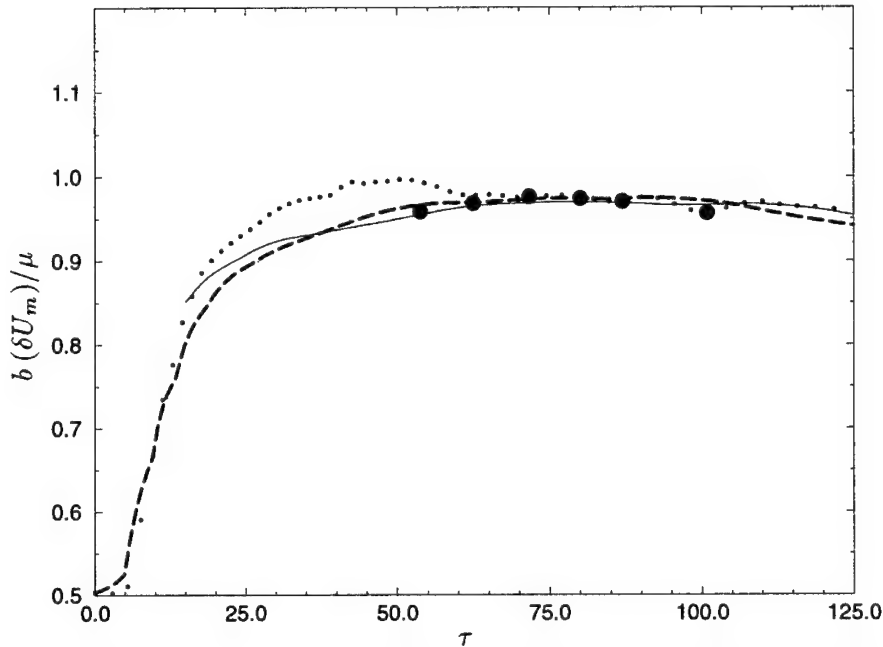


FIGURE 2. The product of the wake-width and the maximum velocity deficit as a function of time using DLM —; DM — —; No model ·····; filtered DNS •.

plane wake generated by DNS in Moser and Rogers (1994) and Moser, Rogers, and Ewing (1996). The initial conditions for the DNS were generated by taking two realizations of “turbulence over a flat plate” from DNS data generated by Spalart (1988) and “fusing” them together to produce a wake. Physically this corresponds to a situation in which two independent boundary layers exist on either side of a rigid plate and the plate is instantaneously “dissolved” without disturbing the surrounding fluid.

This initial DNS data field was then interpolated onto the coarser LES grid to generate the initial conditions for the LES. All the parameters in the LES described in this section were chosen to correspond to those used in the DNS.

The LES reported here were performed on a grid of size $N_x = 64$, $N_y = 48$, and $N_z = 16$. By contrast the DNS required up to $N_x = 512$, $N_y = 195$, and $N_z = 128$ modes. The half-size of the y -domain was set to $Y_0 = 16$. To compare the LES results to the DNS, all DNS data must first be “filtered” to the same resolution as the LES. This is done by truncating the DNS data in Fourier space to the same number of modes retained in the LES for the x and z directions. For the y direction, the DNS data is interpolated onto the coarser LES grid. This filtering procedure is applied to the initial conditions as well as to all DNS data with which we wish to compare the LES results. The “filtered DNS” represents the theoretical best that can be achieved by any LES. Since the mean velocity is given by the $k_x = k_z = 0$ Fourier-mode, the mean profile is unaffected by filtering in x - z planes. Also, since the mean profile varies very little over a single grid-length, filtering in the y direction does not have any observable effect on the mean velocity. This, however, is not the

case for second-order statistics of velocity and vorticity, and there explicit filtering must be applied to the DNS data for comparison with the LES. The LES with DM took about 11 minutes of CPU time for the entire simulation to be completed. For the DLM the CPU time depended on the level of convergence required for the solution of the integral equation. We measured the degree of convergence by the rms error in satisfying the integral equation normalized by the maximum value of $\langle C \rangle$, where $\langle \rangle$ denote averaging over x - z planes. When it was required that the error as defined above should not exceed 10^{-4} , the DLM used about 18 minutes of CPU time. To test if this level of convergence was adequate, the simulation was rerun with the convergence criterion set at 10^{-9} . There were no observable differences in any of the computed statistics. For comparison, the high resolution DNS of the same flow over the same physical time interval by Moser and Rogers (1994) required about 200 CPU hours. All computations were performed on a CRAY C90.

The gross features of the wake are characterized by the maximum wake deficit δU_m of the mean velocity profile and the wake half-width b . The half-width is defined here as the distance between the two points at which the mean velocity deficit is half its maximum value. Fig. 1 shows b^2 plotted as a function of the dimensionless time $\tau = t(\delta U_0)^2/\mu$ for the LES using both the DM and DLM models, the filtered DNS, and LES with the subgrid model turned off. The width grows as $b \sim \sqrt{t}$ in the self-similar region ($\tau \approx 50 - 100$) as expected. Fig. 2 shows the product $b(\delta U_m)$ as a function of τ . All curves exhibit plateaus during the self-similar periods. Note that the Reynolds number $Re_b = b\delta U_m/\nu$ is constant and just under 2000 in the self-similar period because $\mu/\nu = 2000$. The results of all the LES computations agree reasonably well with the filtered DNS. A somewhat surprising result is that even the LES with zero eddy viscosity gives a reasonable prediction for the spreading rate despite the simulation being grossly underresolved. Flow visualization of the instantaneous flow field and plots of energy spectra show large accumulations of small-scale fluctuations at the smallest resolved scales for this “no-model” case, as is expected in an underresolved simulation. However, even this gross error does not affect the growth rate much except to make it more “wiggly”. This is in sharp contrast to past experience in isotropic turbulence. In that flow, the absence of an eddy-viscosity would prevent energy decay of free turbulence and make a steady state impossible in forced turbulence, rendering comparisons with experiments impossible.

Fig. 3 shows the mean velocity profile plotted in self-similar coordinates $\delta U_* = \delta U/\delta U_m$ and $y_* = y/b$ for $\tau \approx 50 - 100$. In all cases very good self-similar collapse is observed (even with the subgrid model turned off!). Thus, like the growth rate, the mean velocity profile is quite insensitive to the subgrid model.

The second-order velocity statistics $\langle u^2 \rangle$, $\langle v^2 \rangle$, $\langle w^2 \rangle$, and $\langle uv \rangle$ normalized by $(\delta U_m)^2$ are shown in Fig. 4. Here u , v , and w are the velocities in the x , y , and z directions, respectively, with the mean velocity subtracted out. The angular brackets denote averaging over x - z planes. In all cases it is observed that both the DM and the DLM predict the filtered second-order statistics well. Except for the $\langle uv \rangle$ profile, the quality of the predictions deteriorates if the model is turned off.

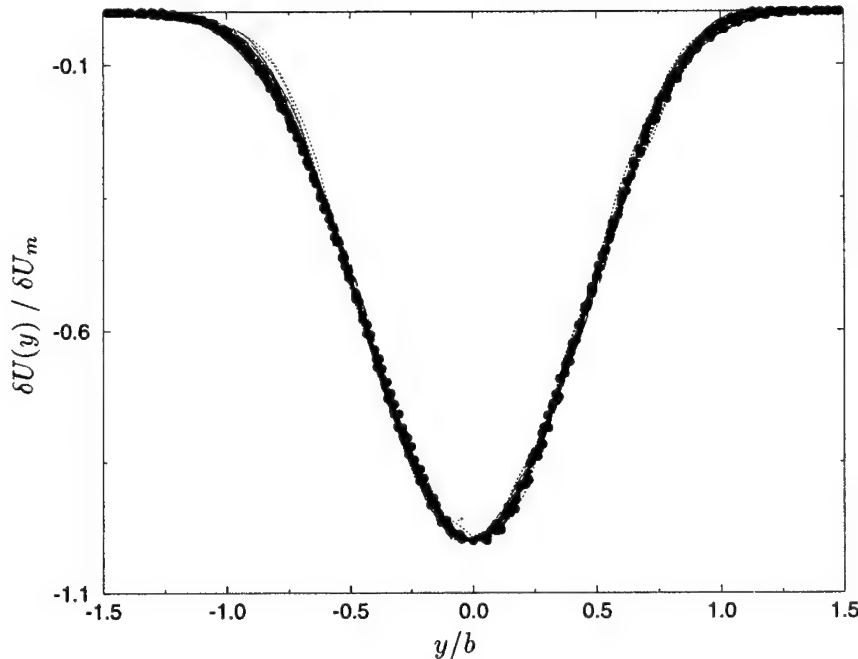


FIGURE 3. The mean wake velocity deficit in self-similar coordinates using DLM —; DM — —; No model ·····; filtered DNS •.

The better agreement for the $\langle uv \rangle$ profile is expected since it is directly linked to the mean velocity profile $\delta U(y)$ through the x -component of the momentum equation, and it has already been seen that $\delta U(y)$ is insensitive to the subgrid model.

The second-order vorticity statistics $\langle \omega_x^2 \rangle$, $\langle \omega_y^2 \rangle$, $\langle \omega_z^2 \rangle$, and $\langle \omega_x \omega_y \rangle$ normalized by $Re_b \delta U_m^2$ are shown in Figure 5. Here ω_x , ω_y , and ω_z are the vorticities in the x , y , and z directions, respectively, with the mean vorticity subtracted out. As before, the angular brackets denote averaging over $x - z$ planes. The agreement of both the DM and the DLM predictions with the filtered DNS is seen to be good. The quality of the predictions is significantly degraded when the model is turned off, in which case the magnitudes of the enstrophy components are about four or five times the corresponding filtered DNS levels. Vorticity statistics are a sensitive measure of the scales close to the threshold of the resolution of the LES. The fact that even vorticity statistics are captured by the LES suggests that all of the resolved scales, and not just the lowest wavenumber modes, are faithfully represented in the simulation. Thus, we use vorticity statistics as a “quality indicator” of the LES rather than as a quantity of practical importance (note that much of the vorticity resides at subgrid scales and the levels found in the LES or filtered DNS are much less than those observed in the DNS).

In Figs. 4 and 5 it is apparent that the self-similar collapse is not perfect but that there is a systematic variation between the curves at different times in the simulation, even when scaled in self-similar variables. This is the case not only for the LES, but also for the filtered DNS. This is an artifact of the filtering procedure

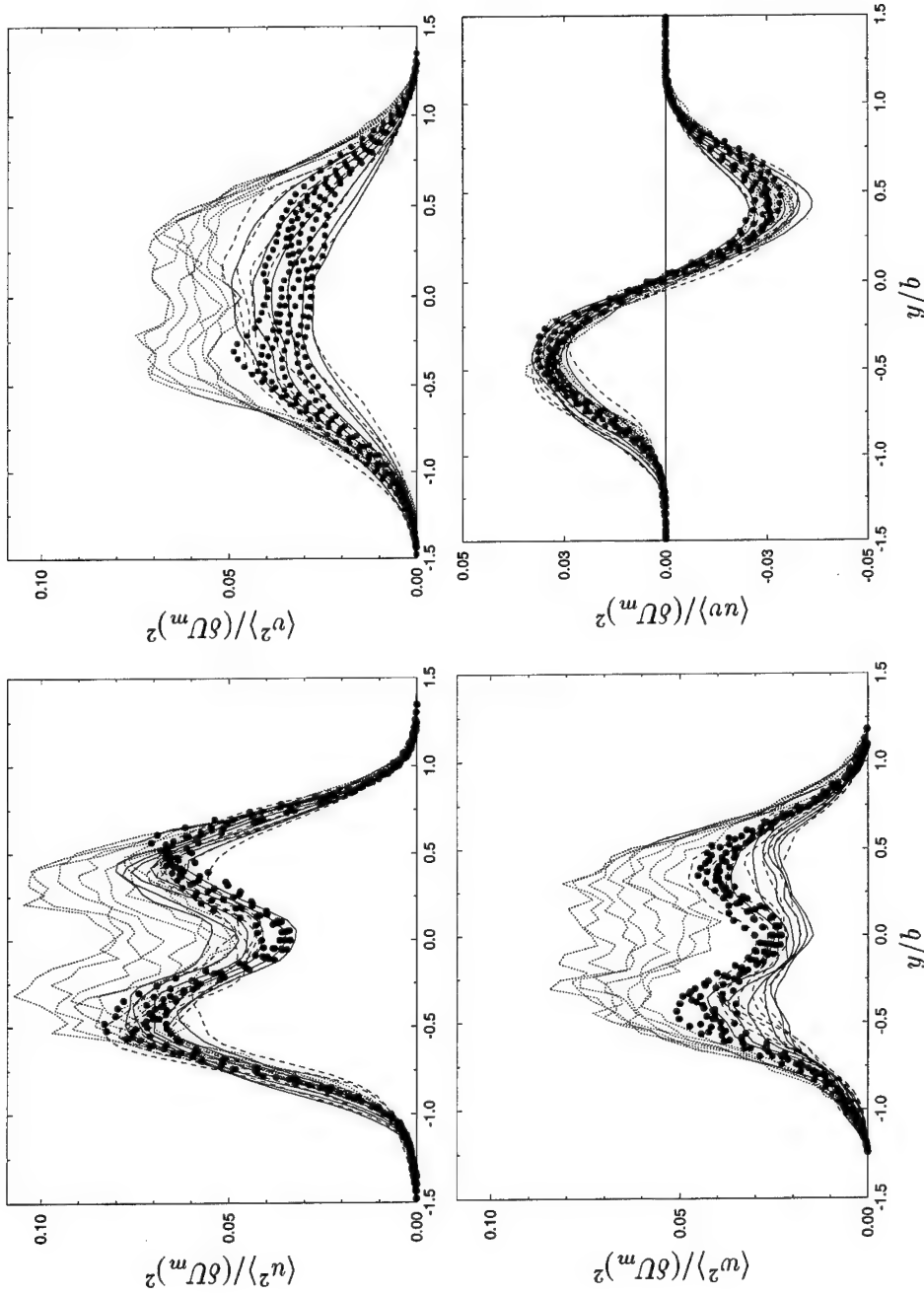


FIGURE 4. Normalized velocity statistics in self-similar coordinates using DLM —; DM — —; No model; filtered DNS ••. The figures are (clockwise from top left) $\langle u \rangle$, $\langle v \rangle$, $\langle w \rangle$, and $\langle u^2 \rangle$.

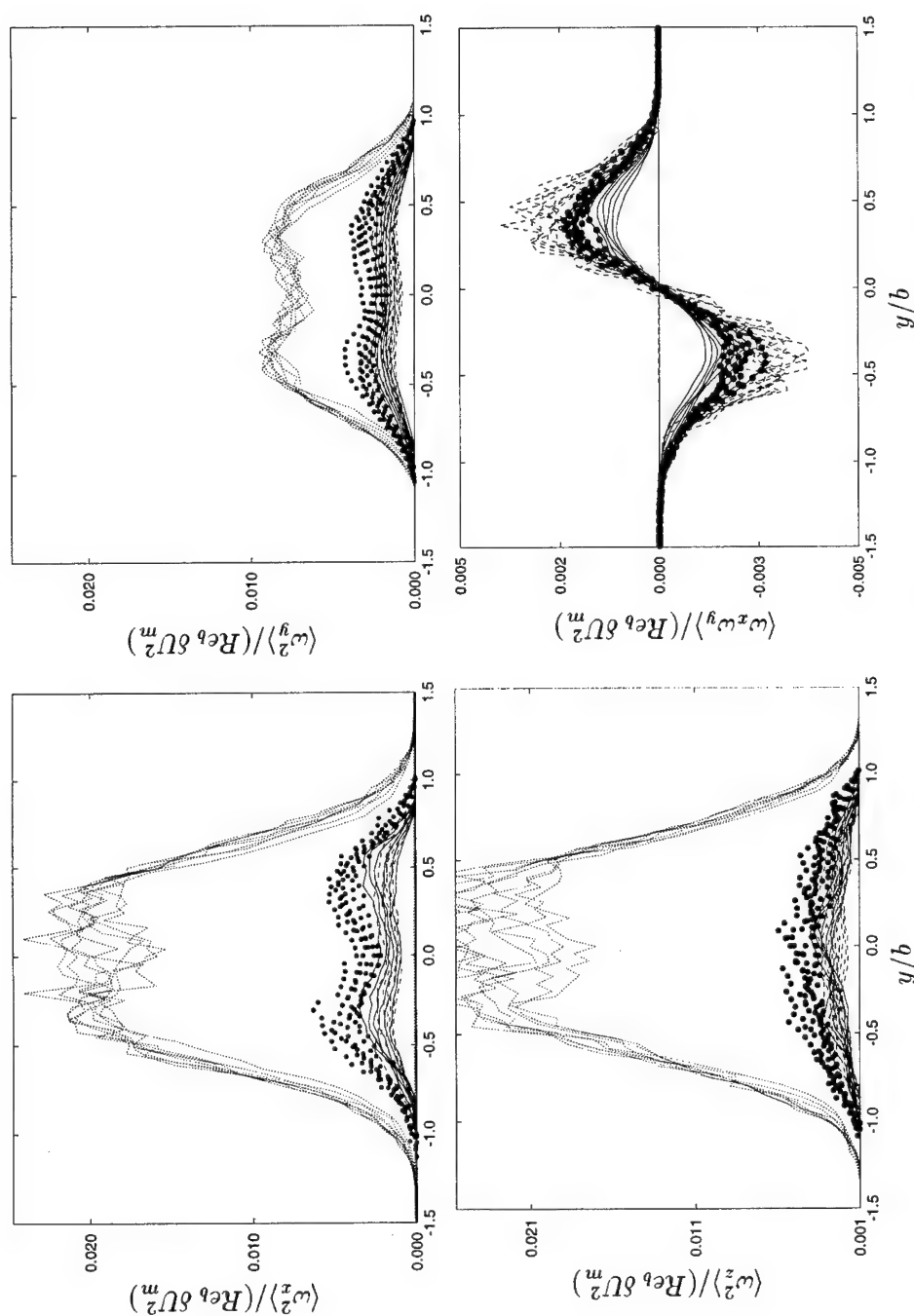


FIGURE 5. Vorticity statistics in self-similar coordinates using DLM —; DM - - -; No model; filtered DNS •••••. The figures are (clockwise from top left) $\langle \omega_x^2 \rangle$, $\langle \omega_y^2 \rangle$, $\langle \omega_x \omega_y \rangle$, and $\langle \omega_z^2 \rangle$.

itself and can be understood in the following way. The flow evolves self-similarly at constant Reynolds number $Re_b = b(\delta U_m)/\nu$ (see Fig. 2) in the self-similar region but the length scales increase in time. Thus, as the flow evolves, the energy spectrum shifts to the left. Since the grid size is held fixed, this implies that more and more of the energy becomes “resolved” as the spectrum shifts to lower wavenumbers past $\bar{k} = 2\pi/\Delta$. Therefore, the resolved part of the second-order statistics increases with time. This is precisely what is observed in the LES and filtered DNS data and is responsible for the systematic increasing trend during the self-similar period. The problem here could be remedied by adding the subgrid part of the stress, that is by plotting $\langle uv \rangle + \tau_{12}$ instead of $\langle uv \rangle$. This cannot be done, however, for the turbulent intensities $\langle u^2 \rangle$, $\langle v^2 \rangle$, and $\langle w^2 \rangle$ because the diagonal components of the subgrid stress τ_{11} , τ_{22} , and τ_{33} are absorbed into the pressure and not modeled in the present LES. They could be obtained in a more elaborate model such as the DLM with the k -equation (Ghosal *et al.* 1995), but in this study we have used the simpler version of the DLM that models only the deviatoric part of the stress.

In addition to obtaining quantitative predictions, one also hopes to gain some qualitative understanding of the large-scale flow structures from an LES. Thus, it is of interest to see if the model is able to generate structures that look realistic. As an example, typical contour plots of the u -velocity at a time during the self-similar period are presented in Fig. 6 over an $x - y$ plane. It is seen that Fig. 6(c) and Fig. 6(d) (LES with model) bear an overall resemblance to Fig. 6(b) (filtered DNS) in the sense that they have a similar number of “eddies” of approximately similar size and shape. However, Fig. 6(e) (LES without model) looks qualitatively different from Fig. 6(b) in that it has a profusion of poorly resolved small-scale structures. A similar statement can be made about the other flow variables.

In summary, mean normalized velocity profiles plotted in self-similar coordinates are insensitive to the choice of subgrid models. The prediction of the self-similar growth of the wake width is improved by the subgrid model, but the results with no model are nevertheless good. Second-order velocity and vorticity statistics are predicted well by both the DM and DLM, but the predictions of these statistics without a model are poor. The flow structures in the LES have a strong visual resemblance to those of the corresponding filtered DNS, but this is not the case if the LES is performed with no subgrid model. The LES results in a very significant savings in CPU time over the corresponding DNS. The results presented here suggest that LES can provide accurate predictions for turbulent free shear flows when information related to small-scale structures is not required.

6. An alternate self-similar state resulting from forcing

In this section we investigate the time evolution of a “forced” wake that has the same mass flux deficit as the “unforced” wake in the previous section. Using LES, we first attempt to reproduce the DNS results for the “strongly forced” wake of Moser and Rogers (1994) and Moser, Rogers, and Ewing (1996). Next we attempt to extend the DNS results in time with a new LES simulation in a larger computational domain in an effort to observe a definitive self-similar regime. In the

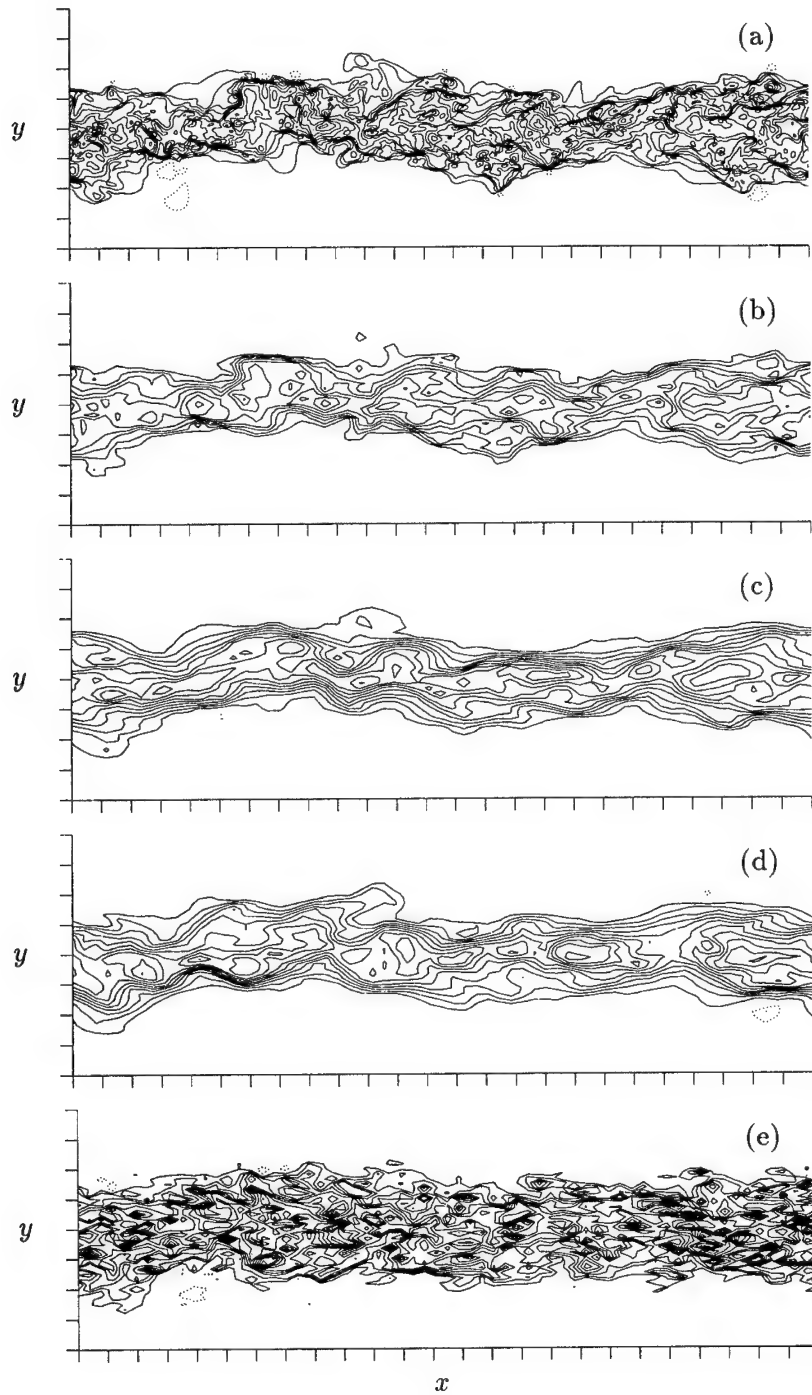


FIGURE 6. Contour plots of streamwise velocity fluctuation u for (a) DNS, (b) filtered DNS, (c) DLM LES, (d) DM LES, and (e) no model LES at $\tau = 71.7$. Tick marks are at $2\mu/\delta U_0$, solid contours are negative, dotted contours are positive, and the contour level is $0.03\delta U_0$.

DNS no sustained self-similar period was achieved for the strongly forced wake, although there was a fairly brief period of approximate self-similarity that was used to generate time-averaged similarity profiles.

The initial conditions used in the DNS of the “forced” wake were generated from the same two turbulent boundary layer realizations used for the unforced flow, but with additional two-dimensional disturbance energy added to them. In order to maintain a $t^{1/2}$ spreading rate, all of the two-dimensional Fourier modes in the computation were amplified instead of just a few particular wavelengths. For the forced case considered here, both the streamwise and cross-stream velocity fluctuations (u' and v') of the two-dimensional Fourier modes were multiplied by a factor of 20 at $\tau = 0$. This amplification is large, increasing the initial disturbance energy by an order of magnitude. The initial conditions for the corresponding LES computation were generated by filtering the evolved DNS field at $\tau = 9.56$. This field was chosen rather than that at $\tau = 0.0$ to allow the initial cusped mean profile to smooth out somewhat before trying to resolve it on the LES grid. The subgrid model used is DLM. Although this is computationally more expensive than the DM, it is preferred because of its wider applicability.

6.1 Reproducing the DNS results

The square of the wake width as a function of time in the DLM LES is shown by the dashed line in Fig. 7a. The size of the LES is $N_x = 64$, $N_y = 64$ or 96 , $N_z = 16$, and Y_0 ranges from 14.0 initially to 64.0 at the end of the simulation, where N_x , N_y , and N_z are the number of modes in the x , y , and z directions, respectively, and Y_0 is the half-width of the y -domain. (The DNS uses up to $N_x = 600$, $N_y = 260$, and $N_z = 160$.) The LES results agree well with the DNS up to the point where both computations become constrained by the computational domain size. After $\tau \approx 65$ both the DNS and the LES computed in the same domain size exhibit decreasing wake widths instead of reaching the expected sustained self-similar growth. The LES is also no longer as good at predicting the wake width after this point, with the LES width decreasing somewhat more rapidly than that of the DNS.

As with the unforced case, contours of u velocity show good agreement between the LES (Fig. 8c) and the filtered DNS (Fig. 8b). When no subgrid scale model is used, the computation has an excessive level of small-scale structure owing to inadequate energy dissipation (Fig. 8d). Note that at the time shown ($\tau = 26.3$), the sample of large-scale eddies in the computational domain is becoming somewhat limited. As the wake continues to spread, it is thus quite probable that the computational domain size will become inadequate and the simulation will no longer be a good representation of an unbounded turbulent flow.

In order to demonstrate that the turbulence in these two computations is constrained by the computational domain size (rather than simply being in a transient non-self-similar state), another LES computation in a domain with twice the streamwise extent and four times the spanwise extent of the computations described above was performed. It should be noted that performing a DNS in this expanded domain size is infeasible with the computational capabilities currently available.

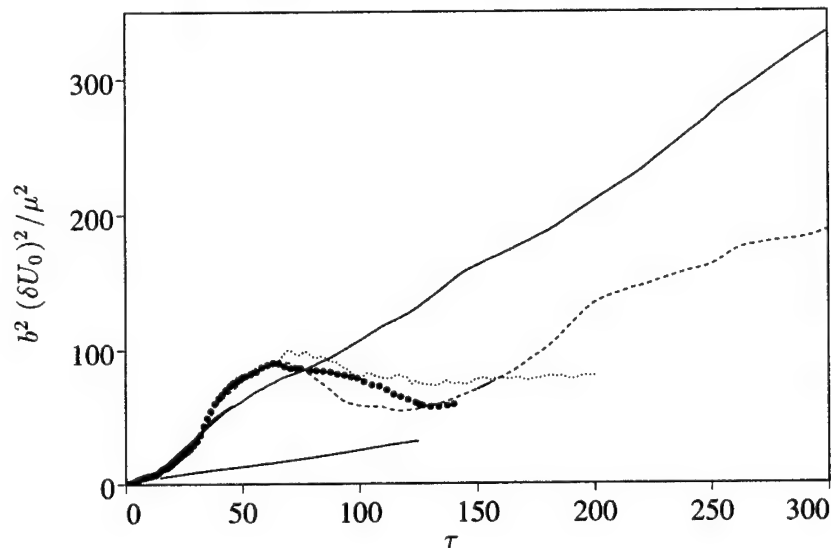


FIGURE 7A. The square of the wake-width as a function of time for the forced wake: \bullet DNS, $--$ DLM LES, \cdots no-model LES, $---$ DLM LES of the forced wake extended to the larger domain (upper curve), and $---$ DLM LES of the unforced wake (lower curve).

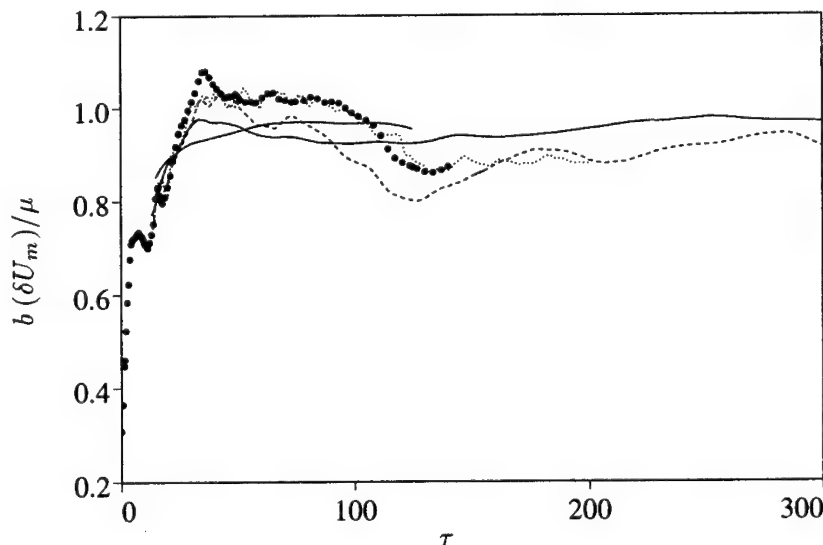


FIGURE 7B. The product of the wake-width and the maximum velocity deficit as a function of time: \bullet DNS, $--$ DLM LES, \cdots no-model LES, $---$ DLM LES of the forced wake extended to the larger domain (long curve), and $---$ LES of the unforced wake using DLM (short curve).

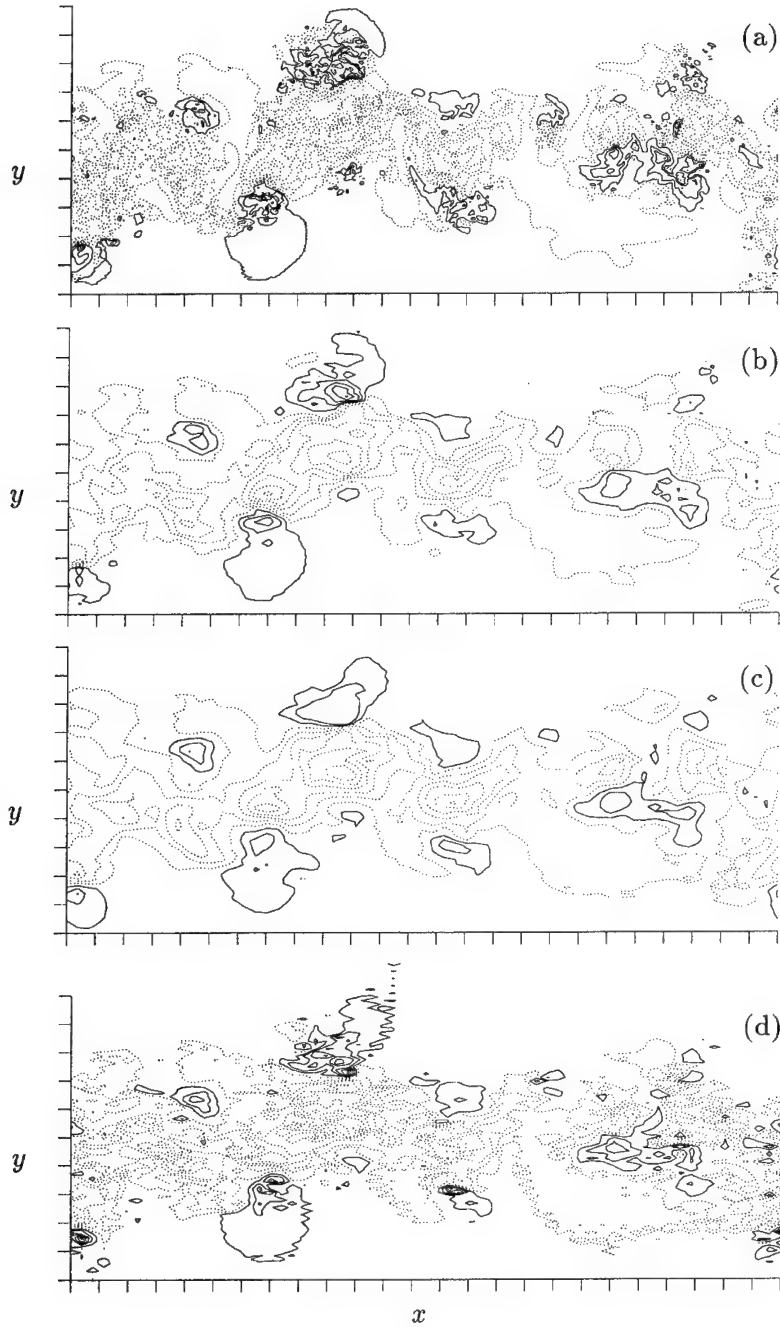


FIGURE 8. Contour plots of spanwise vorticity ω_z for (a) DNS, (b) filtered DNS, (c) DLM LES, and (d) no model LES for the forced wake in the smaller domain at $\tau = 26.3$. Tick marks are at $2\mu/\delta U_0$, solid contours are positive, dotted contours are negative, and the contour level is $0.10\delta U_0$.

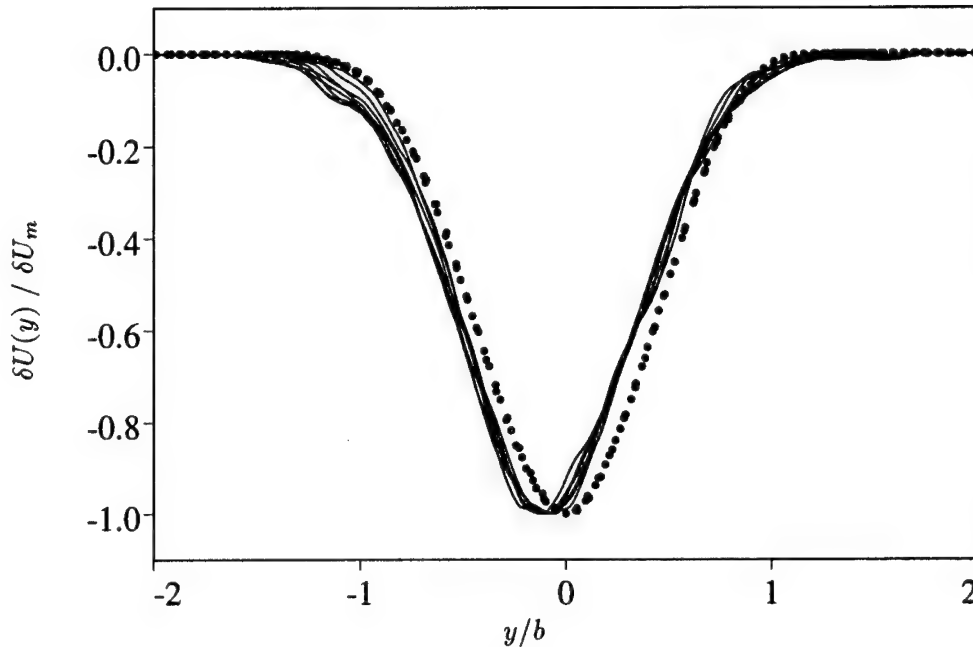


FIGURE 9. The mean wake velocity deficit in self-similar coordinates for — the forced (large-domain) LES at various times during the period $73 < \tau < 300$ and for • the unforced flow at $\tau = 62, 72$, and 86 .

6.2 Extending the DNS results to a larger flow domain

Generating the initial conditions for the expanded-domain computation requires some care. Ideally we would like to be simulating the same flow, but simply replicating the periodic flow field used previously will not change the flow evolution at all since the initial periodic symmetry will be maintained by the Navier-Stokes equations. It is thus necessary to break this symmetry in the periodically extended initial conditions. Considering the streamwise direction, if the initial computational wavenumbers are scaled to be integers, then the periodic doubling of the streamwise direction will introduce new wavenumbers that are odd multiples of one half; these wavenumbers have zero energy. To break the initial periodic symmetry, these Fourier modes must be seeded with some energy. While adding energy to any single one of the wavenumbers would break the symmetry, the time required for nonlinear interactions to transfer energy to the rest of them would be long, and the size of the large-scale motions would approach the size of the computational domain before the spectra smoothed out. In order to minimize this transient development time, we have chosen to initialize energy in nearly all of the newly generated wavenumbers. This has been accomplished by simply taking the disturbance energy in wavenumber k_x and putting the same energy (randomizing the phase of the disturbance) in the new wavenumber $k_x + \frac{1}{2}$. The only exception is the $k_x = \frac{1}{2}$ wavenumber, which does not initially receive any energy from the $k_x = 0$ mode. After this, the entire field is rescaled to have the same disturbance energy density as the original

computation. The same procedure is used in the spanwise direction, although since the domain is four times as large, the content of k_z is propagated to $k_z + \frac{1}{4}$, $k_z + \frac{1}{2}$, and $k_z + \frac{3}{4}$ (again with randomized phase for each new mode).

The initial flow field generated by the above procedure is thus unphysical, unlike the initial field used for the original computations, which were generated from DNS of a turbulent boundary layer. However, it is hoped that this flow will be similar to the previous computation since the initial energy spectra, mean profiles, relative importance of two-dimensional disturbances, and other features are the same between the two flows (the mean velocity profiles are identical). The correspondence between the results from this new simulation and the previous forced simulations up to $\tau \approx 35$ provides some evidence that this is indeed the case (see, for example, Fig. 7a).

As with the original forced LES calculation, the initial field for the large-domain LES computation was generated (using the above procedure) from the DNS field at $\tau = 9.56$. The large-domain LES was begun with $N_x = 128$, $N_y = 64$, $N_z = 64$, and $Y_0 = 14$. The y -domain is periodically remeshed, increasing both Y_0 and N_y in such a way as to keep the y -resolution approximately constant. The choice of Y_0 at each remesh is such that it is large enough to contain all the vorticity in the flow but not so large that CPU time is wasted computing regions of little activity.

The evolution of the square of the wake width for the LES in the extended domain is shown in Fig. 7a. It shows significant deviation from the previous computation beyond $\tau \approx 35$ and achieves a sustained period of linear growth, unlike the forced case in the small domain. It is interesting to note that the growth rate during this apparently self-similar period in the large-domain case is about the same as that during the brief approximately self-similar period of the original LES and DNS computations, although the "virtual origins" of the flows are different (i.e. the width curves are parallel but shifted vertically relative to each other in Fig. 7a). This difference in virtual origins of the flows is presumably a consequence of the initialization procedure. Because the large-domain computation does achieve a sustained linear growth period of the squared wake width, it is likely that the previous computations were indeed constrained by the size of the computational domain by $\tau \approx 65$ if not sooner.

The product of the wake width and centerline velocity deficit for the large-domain LES is plotted along with the previous LES and DNS results in Fig. 7b. The product is quite constant beyond $\tau \approx 50$, consistent with self-similar evolution. In the original LES and the DNS, the product is not as constant.

It should be noted that although the large-domain forced LES and the unforced LES both exhibit sustained periods of apparent self-similar evolution, these self-similar periods are characterized by markedly different growth rates. The computations are thus indeed supportive of the idea that alternative initial condition-dependent, self-similar states are possible as suggested by the analysis of George (1989) and the experiments of Wignanski *et al.* (1986) and Marasli *et al.* (1992). Two-dimensional forcing is seen to result in a sustained significant increase in wake

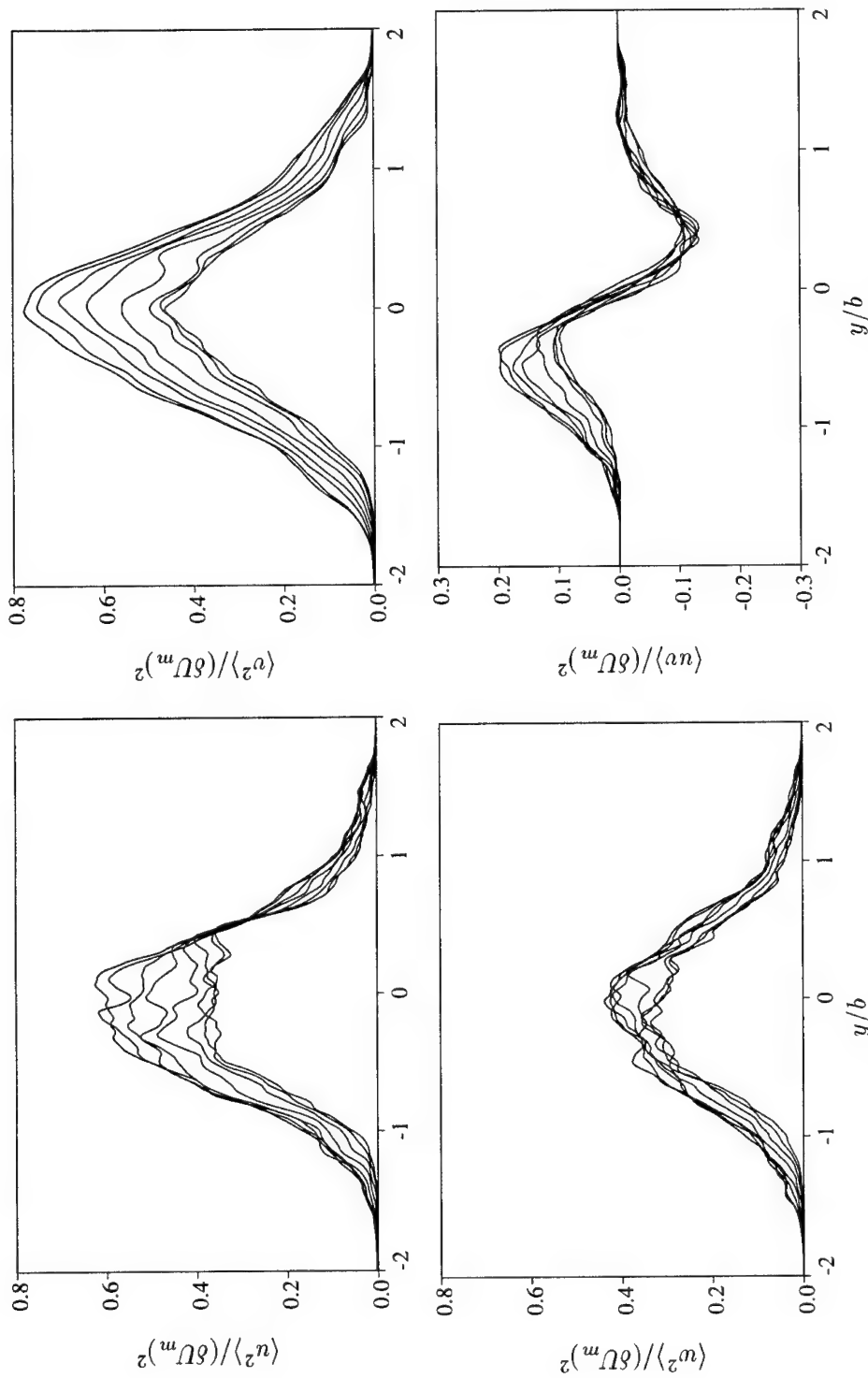


FIGURE 10. Reynolds stress profiles in self-similar coordinates for the LES of the forced wake in the large domain during the period $73 < \tau < 300$ (curves generally decreasing in time). The figures are (clockwise from top left) $\langle u'^2 \rangle$, $\langle v'^2 \rangle$, $\langle u'v' \rangle$, and $\langle w'^2 \rangle$.

growth rate. The linear region in Fig. 7a is well approximated by

$$\frac{b^2 (\delta U_0)^2}{\mu^2} = \alpha \frac{(\delta U_0)^2}{\mu} (t - t_0) \quad (11)$$

where $\alpha = 0.26$, $t_0 = 3.1$ in the unforced case but $\alpha = 1.02$ and $t_0 = -5.9$ in the forced case. The dimensionless growth rate β used in Moser, Rogers, and Ewing (1996) can be calculated from α by

$$\beta = \frac{\alpha}{2} \frac{\mu}{b (\delta U_m)} , \quad (12)$$

resulting in $\beta = 0.13$ and $\beta = 0.54$ for the unforced and forced cases, respectively. Note that the value of 0.54 for the forced case is close to the value of 0.58 calculated from the approximate self-similar period in the DNS of Moser, Rogers, and Ewing (1996), and significantly larger than the value of 0.21 quoted for the “weakly forced” case of that work.

The mean velocity profiles plotted in self-similar coordinates for both the large-domain forced LES and the unforced LES are plotted in Fig. 9. For the forced flow the profiles are obtained from a sequence of approximately equispaced times during the period $73 < \tau < 300$. The circles for the unforced case are taken from three times during the self-similar period. It is seen that the velocity profiles at different times for the forced case collapse onto a single curve as they do for the unforced flow examined previously. Furthermore, even though the forced wake has a significantly different growth rate, the mean velocity profile (when plotted in self-similar coordinates) has the same form as the corresponding profile from the unforced case. There is, however, a small lateral shift in the forced mean profile relative to the unforced case that results from a shift present in the initial conditions (and maintained by the Navier-Stokes equations). This comes about as a result of the initialization procedure used, which involves large amplification of particular modes and their propagation to nearby uninitialized Fourier modes. This universality of the mean velocity profile shape is consistent with the experiments (Wynanski *et al.* 1986, Marasli *et al.* 1992) and the arguments by George (1989), as discussed in Section 2.

The linear growth of the squared wake width in Fig. 7a appears to begin at $\tau \approx 75$ and continue until $\tau \approx 220$, after which the growth rate appears to increase further. The collapse of the scaled mean velocity profiles is good throughout this period, and it thus appears that the flow may be evolving self-similarly during this period. Reynolds stress profiles at times varying from $t = 73$ to $\tau = 300$ in the large-domain forced LES computation are shown in Fig. 10. The different curves correspond to the same times used in Fig. 9. Although the collapse of the curves is greatly improved by using the self-similar scalings, the $\langle u^2 \rangle$, $\langle v^2 \rangle$, and lower half of the $\langle uv \rangle$ profiles show a systematic decrease in magnitude until about $\tau \approx 220$, when the growth rate appears to be changing. This suggests that the flow is not yet completely self-similar. Presumably it takes a while for the high levels of $\langle u^2 \rangle$ and $\langle v^2 \rangle$ present in the initial conditions to come into complete equilibrium with the

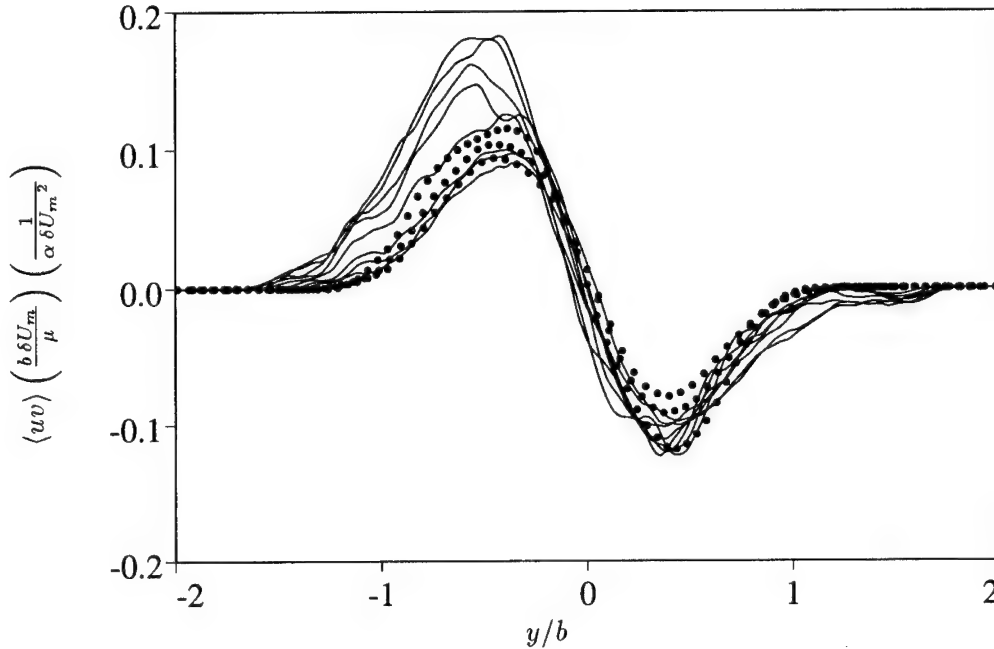


FIGURE 11. Normalized Reynolds shear stress in self-similar coordinates for the LES using DLM; —: forced wake, •; unforced wake.

rest of the flow. For the cross-stream resolution used in this forced flow, the subgrid contribution to $\langle uv \rangle$ is negligible and the collapse of the resolved component of $\langle uv \rangle$ is good. In the unforced simulation described in Section 5 the subgrid contribution to $\langle uv \rangle$ decreased from 17% of the resolved amount at $\tau = 24.9$ to 3.5% at $\tau = 125.0$.

The scaled Reynolds stress profiles are not identical in the forced and unforced cases as is evident by comparing Fig. 10 and Fig. 4. First, there is a large difference in magnitude, with the levels in the forced case being up to an order of magnitude larger than those in the unforced flow. Second, the form of the curves is different. The discrepancy cannot be removed by a simple scaling factor, as can be seen from the fact that the $\langle u^2 \rangle$ and $\langle w^2 \rangle$ profiles are not “double-peaked” in the forced case. This is in agreement with the arguments of George (1989) and contrary to what is expected in the classical theory (Tennekes and Lumley 1972). It is also in agreement with the experimental results of (Wynanski *et al.* 1986, Marasli *et al.* 1992).

Since the Reynolds shear stress profile is related to the mean velocity profile, it can be shown (Moser and Rogers 1994, Moser, Rogers, and Ewing 1996) that the $\langle uv \rangle$ profile should be identical for all (inviscid) wakes when scaled with the quantity $(\alpha \delta U_m^2)(\mu/b\delta U_m)$ instead of with $(\delta U_m)^2$. In Fig. 11 the Reynolds shear stress $\langle uv \rangle$ has been plotted with this new scaling. The collapse of the profiles for the two flows is quite good once the high levels of $\langle uv \rangle$ on the lower side of the layer stop decreasing at $\tau \approx 160$. The curves for the unforced case increase in time, partly owing to the decreasing fraction of $\langle uv \rangle$ that is associated with the “sub-grid” scales. By comparing Fig. 10 and Fig. 4, it is seen that the ratio $\langle uv \rangle/\delta U_m^2$

is about four times larger in the forced wake than in the unforced flow, so including the layer growth rate in the scaling, as in Fig. 11, does remarkably well in bringing the profiles into agreement.

7. Discussion

Large-eddy simulations of temporally evolving wakes were performed using the “dynamic localization” subgrid model. Comparison of growth rates, profiles of first- and second-order statistics, and flow structures show good agreement with the DNS results. This, together with previous tests of the subgrid model on other flows, gives us confidence in the method as an accurate and efficient tool for simulations of unbounded turbulent flows.

LES was performed for both unforced and forced wakes and the hypothesis of universal self-similarity was examined in the light of the data from the simulations. It was found that although flow statistics from each simulated wake exhibited self-similar behavior, the wake spreading rates depended on the initial conditions. This is in contrast to the classical picture (Tennekes and Lumley 1972), which assumes that all wakes with the same momentum deficit asymptotically approach the same self-similar state. The results of this investigation support the theoretical arguments of George (1989) for the existence of “multiple self-similar states” and the experimental results (Wyganski *et al.* 1986, Marasli *et al.* 1992), and others. The numerical and experimental work complement each other well since the inherent strengths and weaknesses of the two approaches are different. An agreement between the two approaches provides a strong indication that the observed effect is indeed real.

Strictly speaking, asymptotic results are exact only after the flow has evolved for an infinitely long time. Numerical simulations can only be run for a limited time period and this makes statements about asymptotic states based on simulation results somewhat tentative; we can really only speculate on the plausibility of different proposed asymptotic states. There is no guarantee that if the flow evolved long enough it would not reach the “classical self-similar state”. However, even if this were the case, the present results show that there exists at least a significant intermediate period during which there is self-similar evolution with growth rates depending on initial conditions, as predicted by the analysis of George (1989).

Acknowledgments

During the final preparation of this manuscript one of the authors (S. G.) was supported by CNLS, Los Alamos National Laboratory, USA and by LMFN-INSA Rouen URA-CNRS 230 - CORIA, France. The computer time required for these simulations was provided by the NAS program at the NASA-Ames Research Center.

REFERENCES

- AKSELVOLL, K. AND MOIN, P. 1993a Large-eddy simulation of a backward facing step flow. *2nd international symposium on engineering turbulence modeling and measurements*, Florence, Italy.
- AKSELVOLL, K. AND MOIN, P. 1993b Application of the dynamic localization model to large-eddy simulation of turbulent flow over a backward facing step. *ASME Fluids engineering conference*, Washington D. C.
- CABOT, W. 1993 Dynamic localization and second-order subgrid-scale models in large-eddy simulations of channel flow. *Annual Research Briefs-1993* Center for Turbulence Research, Stanford Univ./NASA Ames, 129-144.
- CARATI, D., GHOSAL, S., AND MOIN, P. 1995 On the representation of backscatter in dynamic localization models. *Phys. of Fluids* **7**, 606.
- CORRAL, R. AND JIMÉNEZ, J. 1995 Fourier/Chebyshev methods for the incompressible Navier-Stokes equations in infinite domains. *J. Comp. Phys.* **121**, 261.
- GEORGE, W. K. 1989 The self preservation of turbulent flows and its relation to initial conditions and coherent structure. *Advances in Turbulence (1989)*, Ed. W. K. George and R. Arndt (Hemisphere, New York).
- GHOSAL, S., LUND, T. S., MOIN, P., AND AKSELVOLL, K. 1995 A dynamic localization model for large-eddy simulation of turbulent flows. *J. Fluid Mech.* **286**, 229. [Corrigendum: *J. Fluid Mech.* **297**, 402 (1995).]
- MARASLI, B., CHAMPAGNE, F. H., AND WYGNANSKI, I. 1992 Effect of traveling waves on the growth of a plane turbulent wake. *J. Fluid Mech.* **235**, 511.
- MOSER, R. D. AND ROGERS, M. M. 1994 Direct simulation of a self-similar plane wake. *NASA Tech. Mem* 108815.
- MOSER, R. D. ROGERS, M. M. AND EWING, D. W. 1996 Self-similarity of Time-Evolving Plane Wakes. Submitted to *J. Fluid Mech.*
- SPALART, P. R., MOSER, R. D., AND ROGERS, M. M. 1991 Spectral methods for the Navier-Stokes equations with one infinite and two periodic directions. *J. Comp. Phys.* **96**, 297.
- SPALART, P. R. 1988 Direct simulation of a turbulent boundary layer up to $Re_\theta = 1410$. *J. Fluid Mech.* **187** 61.
- TENNEKES AND LUMLEY, 1972 A first course in turbulence. MIT Press.
- WYGNANSKI, I., CHAMPAGNE, F., AND MARASLI, B. 1986 On the large-scale structures in two-dimensional, small-deficit, turbulent wakes. *J. Fluid Mech.* **168**, 31.

On the generation of turbulent inflow conditions for boundary layer simulations

By T. S. Lund, X. Wu¹, AND K. D. Squires¹

1. Motivation and objectives

Turbulent flows that exhibit inhomogeneities in the streamwise direction pose a particular challenge to numerical simulation approaches due to the need to prescribe time-dependent turbulent inflow conditions. In most cases the flow downstream is more or less "driven" by the conditions at the inlet, making it necessary to specify realistic turbulent fluctuations that are in equilibrium with the assumed mean flow. This requirement often dictates that the inflow data should satisfy the Navier-Stokes equations, which in turn implies that an independent simulation be used to generate them. Detailed simulations for the purpose of creating inflow conditions can be costly and thus certain levels of approximation are desirable. In this paper we shall focus on an approximate yet accurate method for generating inflow conditions for spatially-developing boundary layer simulations. The proposed method is essentially a simplification of the method of Spalart and Leonard (1985), who devised an ingenious transformation that allows for the calculation of spatially-evolving boundary layers in conjunction with periodic boundary conditions applied in the streamwise direction. While this method is elegant and highly accurate, it is more complicated than is necessary for the purpose of generating inflow data. A few key approximations are used in this work to arrive at a "modified Spalart method" that is very easy to implement and efficient to use. The new method is shown to yield results that compare well with the computations of Spalart (1988). When used as a means of generating inflow data, the modified Spalart method is shown to be superior to existing approaches.

2. Accomplishments

2.1 Review of Spalart's original method

The basic idea behind the method of Spalart and Leonard (1985) is to define a set of coordinate lines along which the streamwise inhomogeneity associated with the boundary layer growth is minimized. When the Navier-Stokes equations are transformed into this coordinate system, the velocity field is approximately homogeneous in the streamwise direction and is thus amenable to periodic boundary conditions. The periodic boundary condition allow for a "self-contained" simulation that does not require external inputs for the upstream and downstream boundaries. In addition, periodic boundary conditions allow for the use of a highly-accurate Fourier

¹ University of Vermont, Mechanical Engineering Department, Burlington, VT 05405

representation of the velocity field in the streamwise direction. While the advantages of periodic boundary conditions are apparent, they come at the expense of a more complicated set of equations to solve. The coordinate transformation introduces new terms to the Navier-Stokes equations that account for the inhomogeneity in the streamwise direction. These so-called "growth terms" are both numerous and complicated in form. Spalart was able to show that a few of the terms are of higher order and therefore could be neglected. Several terms still remain, however, and these involve streamwise gradients of the mean flow variables, which must be supplied externally. In his 1988 work, Spalart advocates deducing these quantities from two or more simulations performed at different Reynolds numbers.

2.2 Proposed modification to Spalart's method

The main disadvantage of Spalart's method is the need evaluate the growth terms. The presence of these terms require a special flow solver along with possibility of having to perform multiple simulations in order to estimate streamwise gradients of the mean flow quantities. In this section we propose a modification of Spalart's method that effectively eliminates the need to deal with the growth terms. This is achieved by electing to transform only the boundary conditions as opposed to the entire solution domain. In effect, the proposed method computes a spatially-evolving boundary layer in a Cartesian coordinate system but makes use of the ideas of Spalart and Leonard to create a quasi-periodic boundary condition in the streamwise direction. This approach has the advantage that an existing Cartesian inflow-outflow simulation code can be adapted for the purpose of inflow generation by straightforward modifications to the streamwise boundary conditions. Furthermore, the spatial development of the boundary layer is computed directly and only a single empirical relation is required to relate the wall shear at the inlet boundary to the solution downstream.

Our simplifications come at the expense of the loss of strict periodic boundary conditions in the streamwise direction and therefore the inability to use a Fourier representation. This is not a concern in the context of inflow generation, however, since the recipient spatially-evolving simulation will invariably use discrete operators. There is little to be gained from generating inflow data with a numerical method that is significantly more accurate than what is to be used in the main simulation. In fact, our experience has been that non-physical transients often arise near the inlet boundary when inflow data generated with a high fidelity method are subjected to the increased numerical errors associated with the use of lower-order approximations in the inflow-outflow simulation.

The heart of our method is a means of estimating the velocity at the inlet plane based on the solution downstream. This is accomplished through the use of classical scaling laws for an equilibrium turbulent boundary layer. The procedure is to extract the velocity from a plane near the domain exit, rescale it, and then reintroduce it as a boundary condition at the inlet. Following Spalart & Leonard (1985), we first decompose the velocity into a mean and fluctuating part and then apply the appropriate scaling laws to each component separately.

The decomposition is achieved by defining the mean (denoted by upper case) as

an average in the spanwise direction and in time. The velocity fluctuation is then defined as

$$u'_i(x, y, z, t) = u_i(x, y, z, t) - U_i(x, y). \quad (1)$$

In an effort to simplify the notation, the overline denoting the LES filter is omitted on u_i throughout this section.

The mean flow is rescaled according to the law of the wall in the inner region and the defect law in the outer region. The law of the wall reads

$$U^{\text{inner}} = u_\tau(x) f_1(y^+), \quad (2)$$

where $u_\tau = \sqrt{\nu(\partial u / \partial y)_{\text{wall}}}$ is the friction velocity, $y^+ = (u_\tau y) / \nu$ is the wall coordinate, and f_1 is a universal function to be determined. The defect law is

$$U_\infty - U^{\text{outer}} = u_\tau(x) f_2(\eta), \quad (3)$$

where $\eta = y / \delta$ is the outer coordinate (δ is the boundary layer thickness), U_∞ is the free-stream velocity, and f_2 is a second universal function to be determined. Let U_{recy} and U_{inlt} denote the mean velocity at the downstream station to be recycled, and at the inlet respectively. The law of the wall, (2), and the defect law, (3), dictate that U_{recy} and U_{inlt} are related in the inner and outer regions via

$$U_{\text{inlt}}^{\text{inner}} = \gamma U_{\text{recy}}(y_{\text{inlt}}^+) \quad (4)$$

and

$$U_{\text{inlt}}^{\text{outer}} = \gamma U_{\text{recy}}(\eta_{\text{inlt}}) + (1 - \gamma) U_\infty, \quad (5)$$

where

$$\gamma = \left(\frac{u_{\tau, \text{inlt}}}{u_{\tau, \text{recy}}} \right). \quad (6)$$

The independent variables in (4) and (5), y_{inlt}^+ and η_{inlt} , are the inner and outer coordinates of the grid nodes at the inlet station. Thus, $U_{\text{recy}}(y_{\text{inlt}}^+)$ is the mean velocity at the recycle station, expressed as a function of y^+ , and evaluated at the inner coordinate of the mesh at the inlet. This evaluation requires an interpolation since the inner coordinates for the grid nodes at the recycle and inlet stations will, in general, be different. A linear interpolation was found to be sufficiently accurate for this purpose. A similar interpolation is required for the outer coordinate.

The mean vertical velocity in the inner and outer regions is assumed to scale as

$$V^{\text{inner}} = U_\infty f_3(y^+), \quad (7)$$

and

$$V^{\text{outer}} = U_\infty f_4(\eta), \quad (8)$$

where f_3 and f_4 are assumed to be universal functions. Applied between the recycle and inlet stations, the above scaling laws lead to

$$V_{\text{inlt}}^{\text{inner}} = V_{\text{recy}}(y_{\text{inlt}}^+), \quad (9)$$

and

$$V_{\text{inlt}}^{\text{outer}} = V_{\text{recy}}(\eta_{\text{inlt}}) . \quad (10)$$

The spanwise velocity should be zero in the mean and thus no scaling relations are required.

The velocity fluctuations in the inner and outer regions are decomposed further to give

$$(u'_i)^{\text{inner}} = u_\tau(x)g_i(x, y^+, z, t) , \quad (11)$$

and

$$(u'_i)^{\text{outer}} = u_\tau(x)h_i(x, \eta, z, t) . \quad (12)$$

The purpose of this decomposition is to isolate the streamwise inhomogeneity through the explicit dependence on u_τ . The functions g_i and h_i are then approximately homogeneous in the streamwise direction and are therefore amenable to periodic boundary conditions. In Spalart & Leonard (1985) and Spalart (1988), periodic boundary conditions are assumed at this stage. The procedure here is different since we have elected to retain an inflow-outflow structure. The fundamental difference in the present approach is that the “periodic” condition provides only one-way coupling between the recycle station and the inlet. The velocity fluctuations at the downstream station will be related to those at the inlet using (11) and (12), but there is no downstream transfer of information from the inlet via boundary conditions. A convective outflow condition applied at the domain exit provides the necessary downstream boundary condition.

Assuming the functions g_i and h_i to be “periodic” the velocity fluctuations at the inlet are related to those at the recycle station via

$$(u'_i)^{\text{inner}}_{\text{inlt}} = \gamma(u'_i)_{\text{recy}}(y_{\text{inlt}}^+, z, t) , \quad (13)$$

and

$$(u'_i)^{\text{outer}}_{\text{inlt}} = \gamma(u'_i)_{\text{recy}}(\eta_{\text{inlt}}, z, t) . \quad (14)$$

Equations (4), (5), (6), (9), (10), (13), and (14) provide a means of rescaling the mean and fluctuating velocity for both the inner and outer regions of the boundary layer. A composite profile that is approximately valid over the entire layer is obtained by forming a weighted average of the inner and outer profiles:

$$(u_i)_{\text{inlt}} = \left[(U_i)^{\text{inner}}_{\text{inlt}} + (u'_i)^{\text{inner}}_{\text{inlt}} \right] [1 - W(\eta_{\text{inlt}})] + \left[(U_i)^{\text{outer}}_{\text{inlt}} + (u'_i)^{\text{outer}}_{\text{inlt}} \right] W(\eta_{\text{inlt}}) . \quad (15)$$

The weighting function $W(\eta)$ is defined as

$$W(\eta) = \frac{1}{2} \left\{ 1 + \frac{\tanh \left[\frac{\alpha(\eta-b)}{(1-2b)\eta+b} \right]}{\tanh(\alpha)} \right\} , \quad (16)$$

where $\alpha = 4$ and $b = 0.2$. The weighting function is zero at $\eta = 0$, 0.5 at $\eta = b$, and unity at $\eta = 1$. The parameter α controls the width of the region over which

the function transitions from 0 to 1. For $\alpha \rightarrow \infty$ the distribution becomes a step function centered at $\eta = b$. As $\alpha \rightarrow 0$ the transition is spread across the entire boundary layer. The values of α and b quoted above were determined through analysis of an independent spatially-evolving boundary layer simulation.

The rescaling operation requires the scaling parameters u_τ and δ both at the recycle station and at the inlet. These quantities can be determined from the mean velocity profile at the rescale station, but must be specified at the inlet. It turns out that the problem is over determined if both u_τ and δ are fixed independently at the inlet, and thus an additional relation is needed to connect one of these parameters at the inlet to the solution on the interior. While several suitable relations exist, we have obtained the best results by fixing δ at the inlet and computing u_τ via

$$u_{\tau, \text{inlt}} = u_{\tau, \text{resc}} \left(\frac{\theta_{\text{resc}}}{\theta_{\text{inlt}}} \right)^{1/[2(n-1)]}; \quad n = 5, \quad (17)$$

where θ is the momentum thickness. The above relation is similar to the Ludwig-Tillmann (1949) correlation and can be derived from the standard power-law approximations $C_f \sim R_x^{-1/n}$, $\theta/x \sim R_x^{-1/n}$. In many cases it is more advantageous to control the inlet momentum thickness than the inlet boundary layer thickness. This can be done with a little extra effort by iteratively adjusting the inlet boundary layer thickness until the target inlet momentum thickness is achieved.

2.3 Numerical method

A second order finite difference method on a staggered mesh is used to discretize the incompressible Navier-Stokes equations (see Harlow & Welch, 1965). The fractional step method (e.g., see Chorin 1967, Kim & Moin 1985) is used to enforce the incompressibility constraint through the solution of a Poisson equation for the pressure. The discrete system is time advanced in a semi-implicit fashion where all terms with gradients in the wall-normal direction are treated implicitly with the Crank-Nicholson method while the remaining terms are treated explicitly with a third-order Runge-Kutta scheme.

The boundary conditions on the top surface of the computational domain are

$$\frac{\partial \bar{u}}{\partial y} = 0, \quad \bar{v} = U_\infty \frac{d\delta^*}{dx}, \quad \frac{\partial \bar{w}}{\partial y} = 0, \quad (18)$$

where δ^* is the boundary layer displacement thickness. The derivative $d\delta^*/dx$ is evaluated from the mean velocity field. At the exit plane a convective boundary condition of the form $\partial \bar{u}_i / \partial t + c \partial \bar{u}_i / \partial x = 0$ is applied (c is the local bulk velocity, Han *et al.* 1983).

The dynamic Smagorinsky model is used to model the effect of the unresolved motions. The equations for the model coefficient are averaged in the spanwise direction, and test filtering is performed in planes parallel to the wall (see Ghosal *et al.*, 1995 for more details).

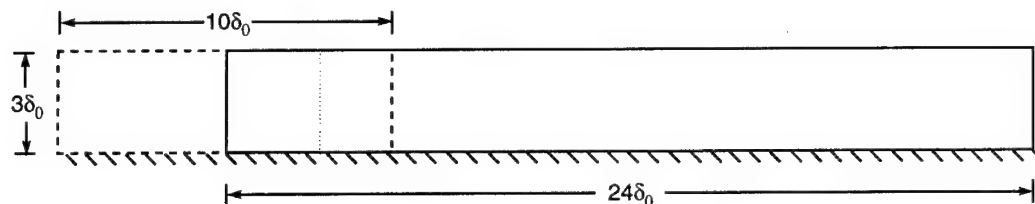


FIGURE 1. Arrangement of the computational domains. The solid lines represent the boundaries of the (inflow-outflow) boundary layer simulation while the dashed lines represent the inflow calculation using the modified Spalart method. The dotted line denotes the location of the recycle station in the inflow calculation.

2.4 Results

The methodology described above was used to simulate a zero pressure gradient turbulent boundary layer over a momentum thickness Reynolds number range of $R_\theta=1400$ -1640. As an example of use of this method for inflow generation, a time series of velocity data was extracted from the mid plane of the simulation and used as an inflow condition for an inflow-outflow simulation of a zero pressure gradient boundary layer. The latter simulation extends from $R_\theta=1530$ to 2150. Due to the fact that the inflow data is extracted from the central plane of inflow generation simulation, the two domains overlap as depicted in Fig. 1. This feature provides a critical test for the inflow generation technique; the results should be nearly identical in the region of overlap, and no changes in the streamwise evolution of boundary layer statistics should occur as the flow develops further downstream.

In order to fully evaluate the inflow condition obtained using the modified Spalart method, calculations were also performed using inflow obtained from two simpler methods. The first of these is achieved by extracting velocity information from a parallel-flow boundary layer simulation. This simulation is similar to the modified Spalart method, except that strict periodic boundary conditions are applied in the streamwise direction. In addition, a no-stress condition is applied at the upper boundary along with the condition that the (instantaneous) vertical velocity vanish there. These boundary conditions are very easy to implement but result in a boundary layer that is void of spatial growth. This method has been used by Lund and Moin (1996) to generate inflow data for a boundary layer over a curved surface.

The second alternative set of inflow data was fabricated through the use of a random number generator. In this approach, both the mean and second order velocity statistics were constrained to match the profiles obtained from the modified Spalart method calculation. The random fluctuations are decorrelated in space and thus the synthetic velocity field lacks turbulent structure. A similar method has been used by Le and Moin (1994) and Akselvoll and Moin (1995) to produce inflow conditions for simulations of a backward-facing step.

The computational domains for the inflow generation and the recipient spatially-evolving simulation have dimensions $10\delta_0 \times 3\delta_0 \times (\pi/2)\delta_0$ and $24\delta_0 \times 3\delta_0 \times (\pi/2)\delta_0$ in the streamwise, wall-normal, and spanwise directions, respectively, where δ_0 is the

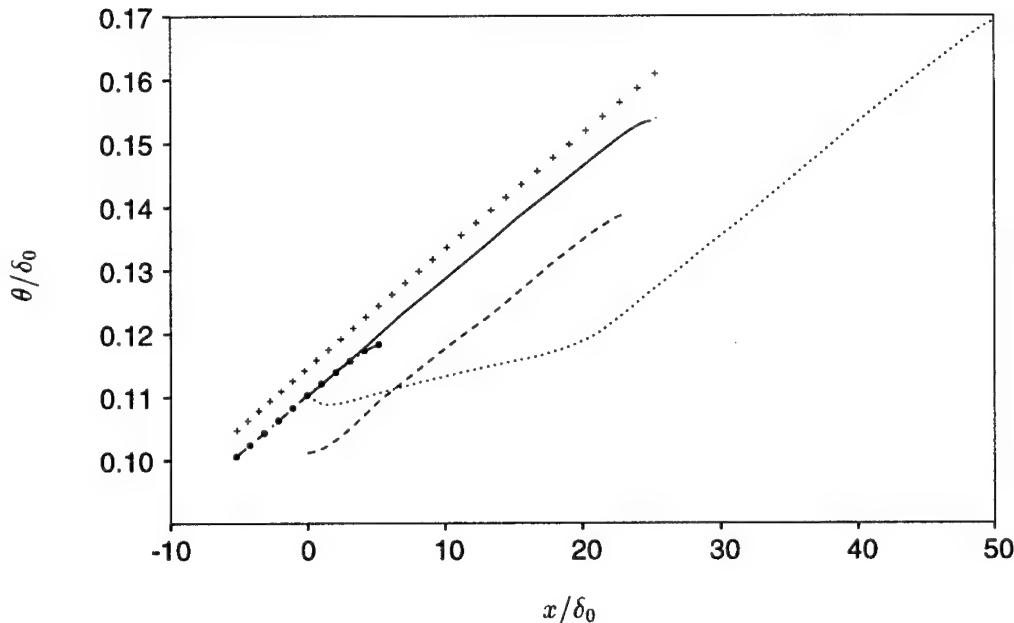


FIGURE 2. Evolution of the momentum thickness in the inflow-outflow simulations. —, inflow generated with the modified Spalart method; ----, inflow generated with the parallel-flow boundary layer method; ·····, inflow generated with the random fluctuation inflow method; ●—●, momentum thickness from the inflow calculation using the modified Spalart method; +, momentum integral estimate.

99% boundary layer thickness at the inlet of the main simulation. The two meshes contains $100 \times 45 \times 64$ and $240 \times 45 \times 64$ points in the streamwise, wall-normal, and spanwise directions. The mesh spacings are the same for the two grids and have the following dimensions in wall units: $\Delta x^+ \approx 64$, $\Delta y_{\text{wall}}^+ \approx 1.2$, and $\Delta z^+ \approx 15$. The mesh is uniform in the streamwise and spanwise directions while a hyperbolic tangent stretching is used in the normal direction to cluster points near the wall.

Once the modified Spalart and parallel-flow boundary layer simulations had reached a statistically stationary state, a time sequence of two-dimensional velocity fields was extracted from the central $x-z$ (streamwise-spanwise) plane and written to disk. The inflow-outflow calculations were then performed by reading one plane of inflow data per time step. The inflow-outflow simulations were run for an initial period of 70 inertial time units (U_∞/δ_0), or equivalently 2.9 flow through times (U_∞/X_L), to eliminate starting transients. Statistics were then accumulated over a period of 1400 inertial time units.

Figure 2 shows the evolution of the momentum thickness for the three inflow-outflow simulations as well as the modified Spalart method calculation. For reference, the predictions of a momentum integral estimate (White, 1974) are also included. The first thing to notice is that the results from the modified Spalart method calculation and its corresponding inflow-outflow simulation agree quite well

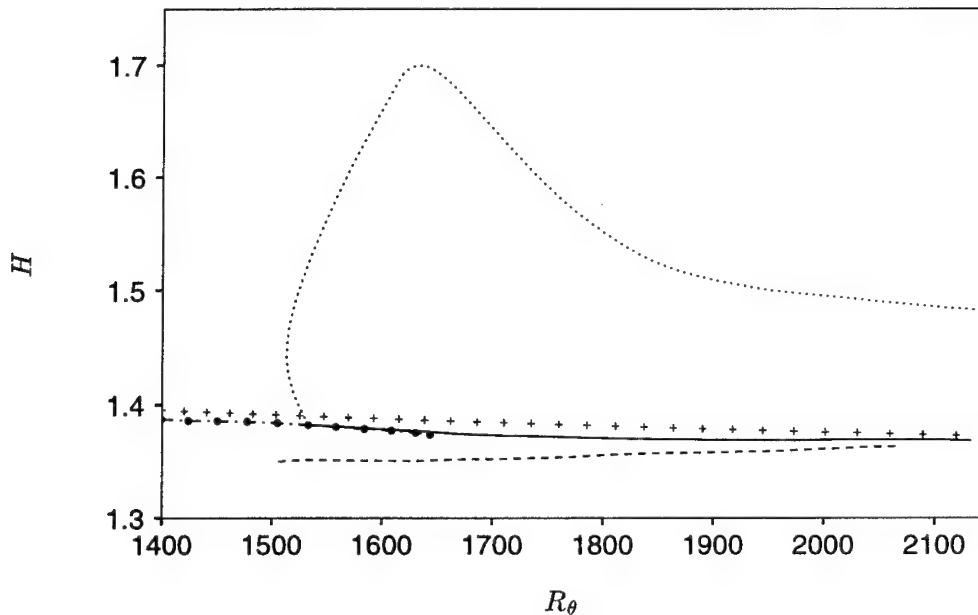


FIGURE 3. Evolution of the shape factor in the inflow-outflow simulations. —, inflow generated with the modified Spalart method; ----, inflow generated with the parallel-flow boundary layer method; ·····, inflow generated with the random fluctuation inflow method; ◆—◆, shape factor from the inflow calculation using the modified Spalart method; +, momentum integral estimate.

in region of overlap ($x/\delta_0 = 0 - 5$). The small deviation near the downstream end of the inflow calculation ($x/\delta_0 \simeq 5$) is due to errors produced by the exit boundary condition. A similar decrease in slope is noted near the end of the main simulation. Aside from this small deviation, the momentum thickness evolution shows no sign of readjustment with downstream distance and agrees well with the momentum integral estimate. The parallel-flow method yields a momentum thickness distribution that is reasonable although there is a noticeable transient near the inlet. The agreement with the momentum integral analysis is also not as good as compared with the case using the modified Spalart inflow data.

While the modified Spalart method and the parallel-flow method produce reasonable results, the random fluctuation method is seen to lead to a very pronounced transient where the initial growth rate is almost a factor of four too small. This feature is due to the fact that the pseudo-turbulence produced by the random fluctuations is not a solution to the Navier-Stokes equations. The fluctuations decay under the influence of viscosity until physical instabilities organize the disturbances into realistic turbulence. This process results in a transition of sorts that is responsible for the change in slope of the momentum thickness at $x/\delta_0 \simeq 20$. Once this transition is past, the growth rate is greatly improved and is comparable to the results of the other simulations. Note that the computational domain for the

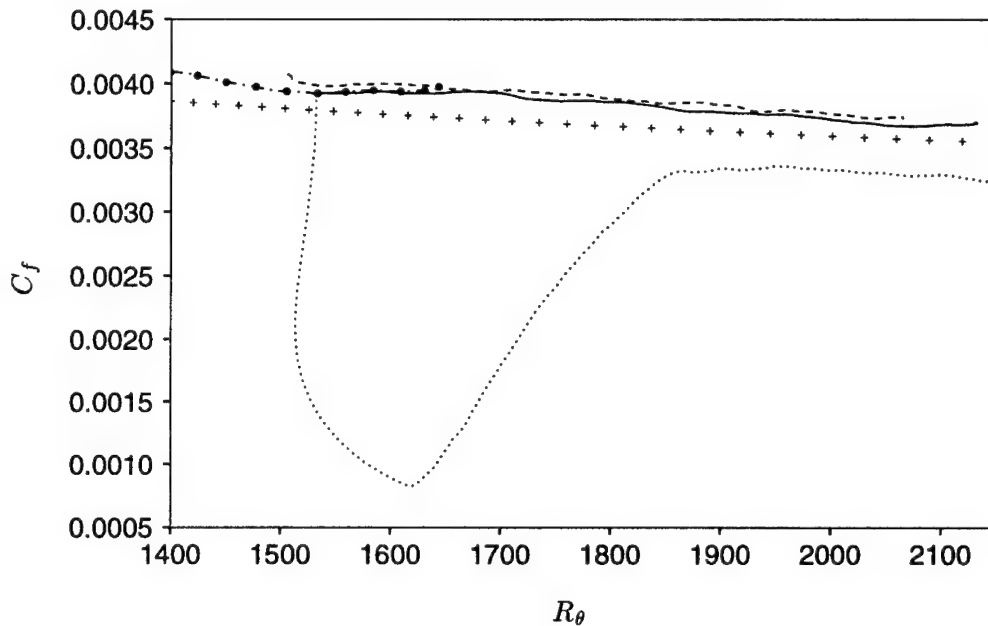


FIGURE 4. Evolution of the skin friction in the inflow-outflow simulations. —, inflow generated with the modified Spalart method; ----, inflow generated with the parallel-flow boundary layer method; ·····, inflow generated with the random fluctuation inflow method; -·-·-, skin friction from the inflow calculation using the modified Spalart method; +, momentum integral estimate.

random fluctuation inflow case extends more than twice as far downstream as the other two cases ($x/\delta_0 = 50$ as opposed to $x/\delta_0 = 50$). This was done in order to compensate for the initial slow growth in the momentum thickness so that all three simulations cover roughly the same momentum thickness Reynolds number range.

The shape factor (ratio of displacement to momentum thickness) evolution is shown in Fig. 3. As in the case of the momentum thickness, the modified Spalart calculation and its corresponding inflow-outflow simulation are in good agreement within the overlap region. The results are also in very good agreement with the momentum integral estimate. When the parallel-flow method is used, the shape factor is a few percent low at the inlet but this error diminishes with increasing streamwise distance. The results from the random fluctuation method are again poor. The shape factor increases initially toward the laminar value of 2.6, then following "transition" relaxes back toward more reasonable values for a turbulent boundary layer. Note however that the 50 boundary layer thicknesses of spatial evolution are not sufficient to produce a canonical turbulent boundary layer when this method is used.

Figure 4 shows the computed skin friction. Once again the results from the modified Spalart simulation and its inflow-outflow counterpart are seen to be in good agreement within the region of overlap. They are also in reasonable agreement

with the momentum integral estimate. The parallel-flow method produces a small initial transient, followed by an acceptable skin friction evolution. The random fluctuation method exhibits an initial sharp drop in skin friction followed by an increase once the flow develops realistic turbulent structure.

Mean velocity profiles for three streamwise locations are shown in Fig. 5. The simulation with inflow obtained using the modified Spalart method (Fig. 5a) yields canonical mean profiles as the flow evolves downstream. In particular, the viscous sublayer and logarithmic region collapse very well when plotted in wall units, while the expected Reynolds number dependence is displayed in the wake region. The results also agree well with the computations of Spalart (1988), except at the beginning of the logarithmic region where the mean velocity is overpredicted slightly. This defect is a common feature of simulations using finite-difference methods on relatively coarse meshes and is not related to the rescaling approach used in the inflow generation process. In support of this claim, we include the results of Rai & Moin (1993) which display a very similar discrepancy in the same region of the profile.

The simulation with the parallel-flow method (Fig. 5b) is seen to produce a small transient where the initial profile shape changes in the logarithmic and wake regions. The parallel-flow method produces a profile that has a larger deviation in the logarithmic region. This discrepancy diminishes with increasing streamwise distance and the profiles at the last two stations collapse in the logarithmic region. These latter two profiles are also nearly identical to the corresponding pair in the case with the modified Spalart method inflow (Fig. 5a).

The random fluctuation method (Fig. 5c) leads to rather anomalous behavior where the profile experiences a large transient as it evolves downstream. At the second plotting station, the mean velocity is underpredicted in the logarithmic region and an unusually large wake develops. The profile then starts to relax back to the expected shape with an increase of the velocity in the logarithmic region and a reduction in the wake. The apparent agreement with the standard logarithmic law (between $y^+ = 30$ and 60) for the third plotting station is fortuitous; profiles further downstream show an overprediction in this region similar to that in the other two simulations. Consistent with this observation is the fact that the profiles do not reach a self-similar state by the domain exit, although it is roughly 50 initial boundary layer thicknesses downstream of the inlet.

Figure 6 shows velocity fluctuation and shear stress profiles for three streamwise locations. When inflow from the modified Spalart method is used (Fig. 6a), the profiles collapse reasonably well for the three Reynolds numbers and the results are in good agreement with the computations of Spalart (1988).

Simulations performed using the parallel-flow inflow (Fig. 6b) also results in profiles that yield an acceptable degree of collapse. The largest discrepancy occurs in the outer region of the streamwise and spanwise profiles where the values from the first station are too large. This is a side effect of the boundary conditions used in the inflow generation simulation. When the parallel-flow method is used, the

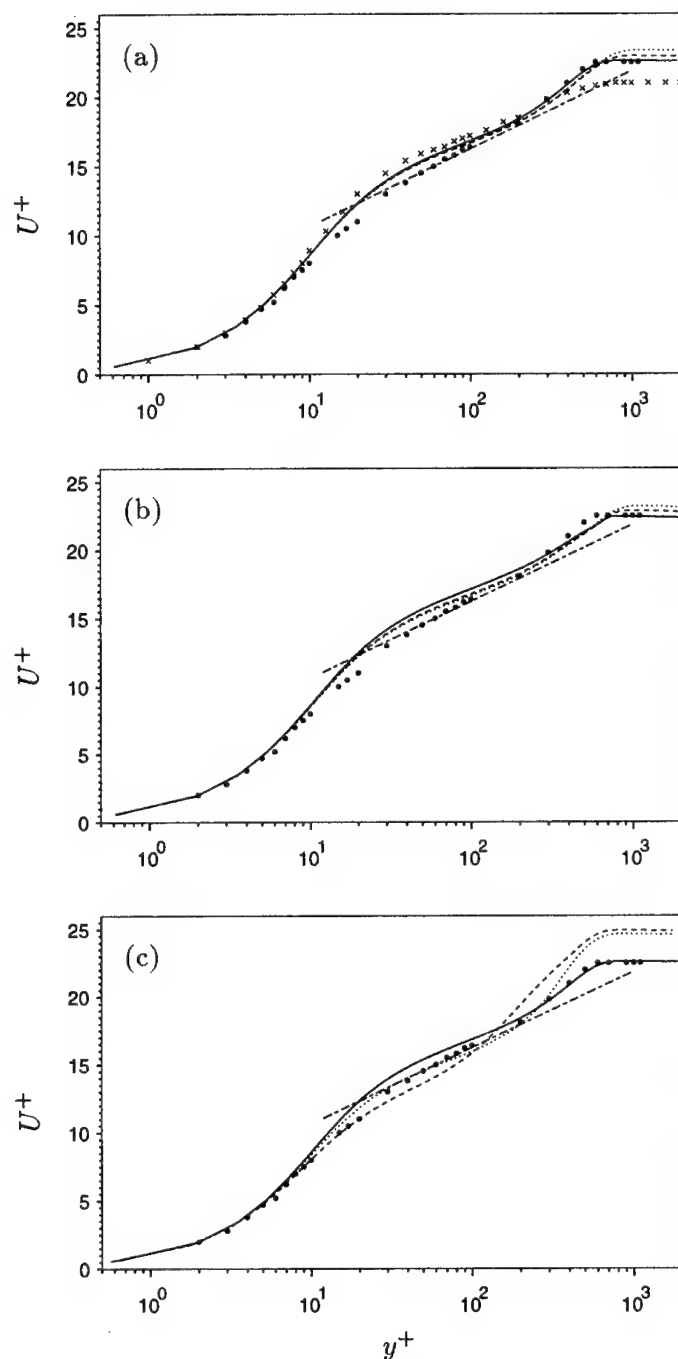


FIGURE 5. Mean velocity profiles in the inflow-outflow simulations. (a), inflow generated with the modified Spalart method; (b), inflow generated with the parallel-flow boundary layer method; (c), inflow generated with the random fluctuation method. —, $R_\theta = 1530$; ----, $R_\theta = 1850$; ·····, $R_\theta = 2050$; •, Spalart (1988), $R_\theta = 1410$; ×, Rai & Moin (1993), $R_\theta = 1350$.

boundary layer edge is rigidly defined as the position where the no stress, zero normal velocity boundary conditions are applied. This condition forces v' to vanish at the boundary layer edge and results in a redistribution of the wall-normal fluctuation energy into u' and w' . Another side effect of this approach is that there are no naturally occurring fluctuations in the region between the boundary layer edge and the upper boundary of the computational domain at the inflow plane. In an attempt to remedy this, random fluctuations were superimposed on the free-stream velocity in this region. The scaling of these disturbances is rather arbitrary, and in this case, the isotropic distribution $u'_i = 0.1U_\infty \exp[-2(y/\delta - 1)]$ was used. The high-frequency random disturbances decay rapidly, and after a few boundary layer thicknesses of spatial evolution, roughly the correct level of free-stream fluctuations are obtained. Aside from the problems near the boundary layer edge, the remainder of the profiles collapse reasonably well and are in acceptable agreement with Spalart (1988).

As in the case of the mean velocity profile, the results from the simulation using the random fluctuation method (Fig. 6c) are poor. The velocity fluctuations in the outer region of the profile are seen to decay initially and then rebuild as the streamwise distance is increased. The transient process is seen to be slow with the fluctuations not returning to equilibrium by the third plotting station which is roughly 35 initial boundary layer thicknesses downstream of the inlet.

3. Conclusions and future work

The proposed simplification to Spalart's method is seen to produce an accurate description a turbulent boundary layer. When used as a means of generating turbulent inflow data for inflow-outflow simulations of spatially-developing boundary layers, the method proves to be very effective at producing simulation results that are free of transients near the inlet boundary. A comparison of this method with the simpler parallel-flow or random fluctuation methods shows that it is superior to both of these techniques. The differences between the modified Spalart method and the parallel flow method are not so great, however, and the latter method may be acceptable in certain cases. The random fluctuation method, on the other hand, appears to be a very rough procedure when compared to the other two methods. Although the inflow data can be generated with minimal computational effort when this scheme is used, the resulting velocity field lacks turbulent structure. This fact implies that the inflow data must be allowed to evolve for a substantial streamwise distance before it can be subjected to an inhomogeneity. When the random fluctuation method has been used in the past, the inlet of the computational domain was displaced 10 to 20 boundary layer thickness upstream of the region of interest (Le and Moin, 1994; Akselvoll and Moin, 1995). The need to extend the mesh for the inflow-outflow simulation increases the overall cost, which obscures any savings in the generation of the inflow data. In fact, the incremental cost of enlarging the main simulation domain will probably exceed the cost to generate more accurate inflow in most cases.

In the future, the modified Spalart method will be generalized to allow for inclusion of a streamwise pressure gradient. This feature is useful for inflow-outflow

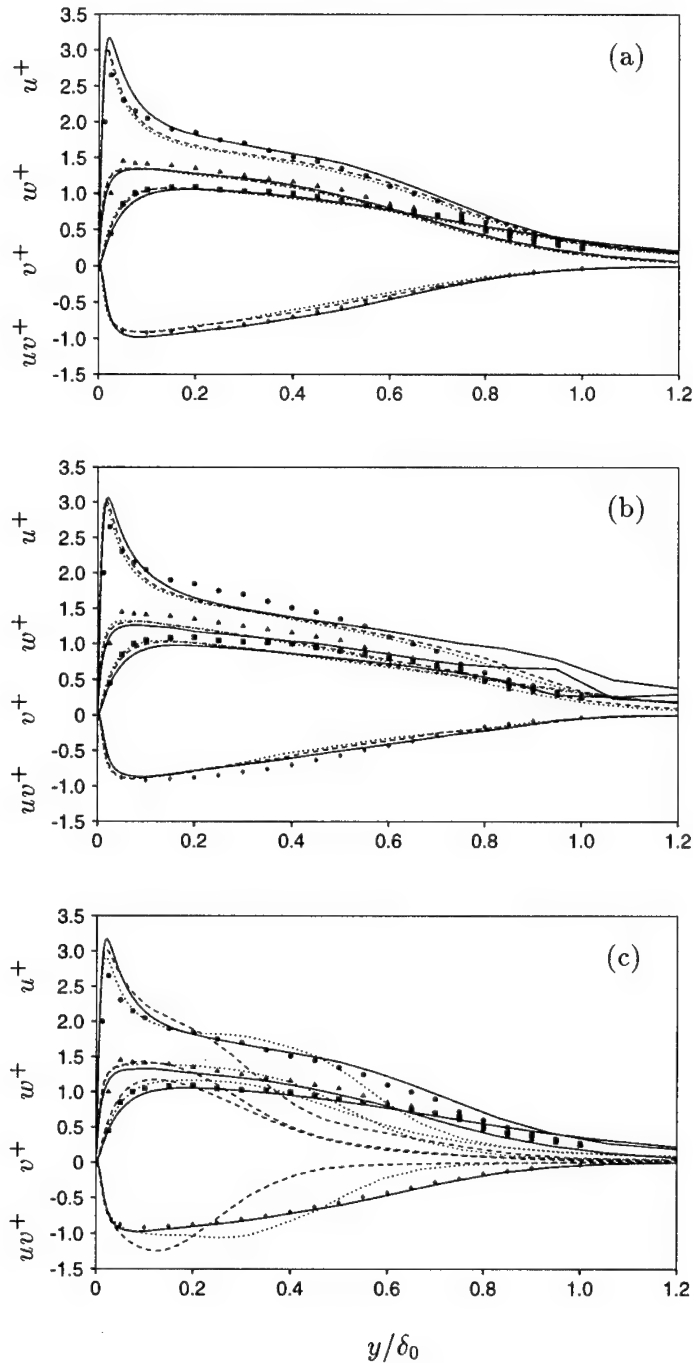


FIGURE 6. Velocity fluctuation and shear stress profiles in the inflow-outflow simulations. (a), inflow generated with the modified Spalart method; (b), inflow generated with the parallel-flow boundary layer method; (c), inflow generated with the random fluctuation method. —, $R_\theta = 1530$; ----, $R_\theta = 1850$; ·····, $R_\theta = 2050$. Filled symbols are data from the simulations of Spalart at $R_\theta = 1410$.

simulations where the inflow boundary is located in a region of significant pressure gradient. One relevant example is in the computation of the aft section of an airfoil. Previous attempts to simulate this flow (Kaltenbach and Choi, 1995; Jansen 1995) have shown that the computations are both costly and very sensitive to the details of the laminar-turbulent transition that takes place near the leading edge. Both of these problems can be minimized by electing to simulate only the aft section of the airfoil, since it is flow separation in this region that is of primary interest. Such a strategy has been adopted by Wang (this volume). In Wang's case the airfoil is at zero angle of attack and thus the pressure gradients are mild at the position where the inflow data are prescribed. At high angles of attack, however, the pressure gradients will be large at the inflow plane and it is desirable to have this effect captured in the inflow computation.

Preliminary study indicates that the modified Spalart method can be extended to account for a restricted class of equilibrium boundary layers that develop under power-law pressure gradients. Under these circumstances the same scaling laws described in this work continue to apply, and the required changes involve only a modification of the friction velocity computation at the inlet and the vertical velocity distribution at the upper boundary. These modifications will be made and the generalized method will be validated in one or more test cases before being used to generate inflow data for the truncated airfoil simulation.

REFERENCES

- AKSELVOLL, K. & MOIN, P. 1995 Large eddy simulation of turbulent confined coannular jets and turbulent flow over a backward facing step. Rep. TF-63, Thermosciences Div., Dept. Mech. Eng., Stanford University, Stanford, CA.
- CHORIN, A.J. 1967 A numerical method for solving incompressible viscous flow problems. *J. Comp. Phys.* **2**, 745-762.
- GHOSAL, S., LUND, T.S., MOIN, P. & AKSELVOLL, K. 1995 A dynamic localization model for large-eddy simulation of turbulent flows. *J. Fluid Mech.* **286**, 229-255.
- HAN, T.Y., MENG, J.C.S. & INNIS, G.E. 1983 An open boundary condition for incompressible stratified flows. *J. Comp. Phys.* **49**, 276-297.
- HARLOW, F.H. & WELCH, J.E. 1965 Numerical calculation of time-dependent viscous incompressible flow of fluid with free surface. *Phys. Fluids*. **8**, 2182-2189.
- JANSEN, K. 1995 Preliminary large eddy simulation of flow around a NACA 4412 airfoil using an unstructured mesh. In *Annual Research Briefs 1995*, Center for Turbulence Research, Stanford Univ./NASA Ames, 61-72.
- KALTENBACH, H.-J. & CHOI, H. 1995 Large eddy simulation of flow around an airfoil on a structured mesh. In *Annual Research Briefs 1995*, Center for Turbulence Research, Stanford Univ./NASA Ames, 51-60.

- KIM, J. & MOIN, P. 1985 Application of a fractional-step method to incompressible Navier-Stokes equations. *J. Comp. Phys.* **59**, 308-323.
- LE, H. & MOIN, P. 1994 Direct numerical simulation of turbulent flow over a backward-facing step, Rep. TF-58, Thermosciences Div., Dept. Mech. Eng., Stanford University, Stanford, CA 94305.
- LUDWIG, H. & TILLMANN, W. 1949 Untersuchungen uber die wandschubspannung turbulenter reibungsschichten. *Ing.-Arch.* **17**, 288-299. (trans. as NACA *Tech. Mem.* 1285 (1949)).
- LUND, T.S. & MOIN, P. 1996 Large eddy simulation of a concave wall boundary layer. *Int. J. of Heat and Fluid Flow.* **17**, 290-295.
- RAI, M.M. & MOIN, P. 1993 Direct numerical simulation of transition and turbulence in a spatially evolving boundary layer. *J. Comp. Phys.* **109**, 169-192.
- SPALART, P.R. & LEONARD, A. 1985 Direct numerical simulation of equilibrium turbulent boundary layers, in *Proc. 5th Symp. on Turbulent Shear Flows*, Ithaca, NY, August 7-9, 1985. Bound volume published by Springer-Verlag, Berlin, 1987.
- SPALART, P.R. 1988 Direct simulation of a turbulent boundary layer up to $Re_\theta = 1410$. *J. Fluid Mech.* **187**, 61-98.
- WHITE, F.M., 1974 *Viscous Fluid Flow*, McGraw-Hill, New York.

A new class of finite difference schemes

By K. Mahesh

1. Motivation and objectives

Fluid flows in the transitional and turbulent regimes possess a wide range of length and time scales. The numerical computation of these flows therefore requires numerical methods that can accurately represent the entire, or at least a significant portion, of this range of scales. The inaccurate representation of small scales is inherent to non-spectral schemes. This can be detrimental to computations where the energy in the small scales is comparable to that in the larger scales, e.g. large-eddy simulations of high Reynolds number turbulence. The inaccurate numerical representation of the small scales in these large-eddy simulations can result in the numerical error overwhelming the contribution of the subgrid-scale model (Kravchenko & Moin 1996).

Recently, Lele (1992) introduced a family of implicit (also called compact) finite difference schemes for the spatial derivatives. The implicit schemes equate a weighted sum of the nodal derivatives to a weighted sum of the function, e.g., $f'_{i-1} + 4f'_i + f'_{i+1} = 3(f_{i+1} - f_{i-1})/h$, and $f''_{i-1} + 10f''_i + f''_{i+1} = 12(f_{i+1} - 2f_i + f_{i-1})/h^2$. Throughout this paper, f_i and f_i^k denote the values of the function and its k^{th} derivative respectively, at the node $x = x_i$, and h denotes the uniform mesh spacing. These schemes have better small scale accuracy than explicit schemes with the same stencil width. The most popular of the implicit schemes (also called Padé schemes due to their earlier derivation from Padé approximants) appear to be the symmetric fourth and sixth order versions. There have been several recent computations of compressible flows that have used the Padé schemes. The flows computed, include transitional boundary layers, turbulent flows and flow-generated noise. The Padé schemes have been less popular in incompressible computations, presumably due to the Poisson equation generating sparse matrices when there is more than one inhomogeneous direction.

This report presents a related family of finite difference schemes for the spatial derivatives. The proposed schemes are more accurate than the standard Padé schemes, while incurring essentially the same computational cost. The objective of this report is to present these schemes as an attractive alternative to the standard Padé schemes.

This work is discussed in detail by Mahesh (1996); this report only summarizes the more prominent results.

2. Accomplishments

For the same stencil width, the standard Padé schemes are two orders higher in accuracy and have better spectral representation than the corresponding symmetric, explicit schemes. For example, $f'_{i-1} + 4f'_i + f'_{i+1} = 3(f_{i+1} - f_{i-1})/h$ is fourth

order accurate, while $f'_i = (f_{i+1} - f_{i-1})/2h$ is only second order accurate. The implicit relation between the derivatives in the Padé schemes yields additional degrees of freedom that allow higher accuracy to be achieved. It is therefore to be expected, that including the second derivatives in the implicit expression would further increase the degrees of freedom, and thereby the accuracy that can be obtained. Additional motivation to solve for the first and second derivatives simultaneously, is provided by the Navier-Stokes equations requiring both derivatives of most variables. This suggests a numerical scheme of the form[†] :

$$a_1 f'_{i-1} + a_0 f'_i + a_2 f'_{i+1} + h(b_1 f''_{i-1} + b_0 f''_i + b_2 f''_{i+1}) = \frac{1}{h}(c_1 f_{i-2} + c_2 f_{i-1} + c_0 f_i + c_3 f_{i+1} + c_4 f_{i+2}). \quad (1)$$

Hermitian expressions involving functions and their first, and higher derivatives have been suggested in the literature (see Mahesh, 1996 for references). However, the development was not completed to a point where the resulting schemes could be used for solving partial differential equations. The objective of this paper is to develop this family of schemes, and assess their potential for computations of the Navier-Stokes equations. The schemes will be referred to as the 'coupled-derivative', or 'C-D' schemes to distinguish them from the standard Padé schemes.

2.1 The interior scheme

Simultaneous solving for f'_i and f''_i , implies that the number of unknowns is equal to $2N$. A total of $2N$ equations are therefore needed to close the system. Equation 1 may be used to derive two linearly independent equations at each node. This is done as follows. Both sides of Eq. 1 are first expanded in a Taylor series. The resulting coefficients are then matched, such that Eq. 1 maintains a certain order of accuracy. Note that Eq. 1 has eleven coefficients, of which one is arbitrary, i.e., Eq. 1 may be divided through by one of the constants, without loss of generality. A convenient choice of the normalizing constant, is either of a_0 or b_0 . It will be seen that the equation obtained by setting a_0 equal to 1, is linearly independent of the equation obtained when b_0 is set equal to 1. The two equations may therefore be applied at each node, and the resulting system of $2N$ equations solved for the nodal values of the first and second derivative.

The details of this process are discussed by Mahesh (1996) and are not repeated here. Expressions ranging from second through eighth order may be obtained, depending upon the choice of coefficients. The sixth order C-D scheme has the same stencil width as the fourth order Padé scheme, while the eighth order scheme has the same stencil width as the sixth order Padé scheme. The sixth, and eighth order C-D schemes are summarized below. Note that the schemes are restricted to be symmetric. The standard Padé schemes are also presented, for completeness.

[†] The schemes are developed on uniform meshes. It is assumed that computations with non-uniform grids can define analytical mappings between the non-uniform grid and a corresponding uniform grid. The metrics of the mapping may then be used to relate the derivatives on the uniform grid to those on the non-uniform grid.

Sixth order C-D scheme ($c_1 = c_4 = 0$)

$$7f'_{i-1} + 16f'_i + 7f'_{i+1} + h(f''_{i-1} - f''_{i+1}) = \frac{15}{h}(f_{i+1} - f_{i-1}). \quad (2a)$$

$$9(f'_{i+1} - f'_{i-1}) - h(f''_{i-1} - 8f''_i + f''_{i+1}) = \frac{24}{h}(f_{i-1} - 2f_i + f_{i+1}). \quad (2b)$$

Eighth order C-D scheme

$$51f'_{i-1} + 108f'_i + 51f'_{i+1} + 9h(f''_{i-1} - f''_{i+1}) = \frac{107}{h}(f_{i+1} - f_{i-1}) - \frac{f_{i+2} - f_{i-2}}{h}. \quad (3a)$$

$$138(f'_{i+1} - f'_{i-1}) - h(18f''_{i-1} - 108f''_i + 18f''_{i+1}) = -\frac{f_{i+2} + f_{i-2}}{h} + \frac{352}{h}(f_{i+1} + f_{i-1}) - \frac{702}{h}f_i. \quad (3b)$$

Standard fourth order Padé

$$f'_{i-1} + 4f'_i + f'_{i+1} = \frac{3}{h}(f_{i+1} - f_{i-1}). \quad (4a)$$

$$f''_{i-1} + 10f''_i + f''_{i+1} = \frac{12}{h^2}(f_{i-1} - 2f_i + f_{i+1}). \quad (4b)$$

Standard sixth order Padé

$$f'_{i-1} + 3f'_i + f'_{i+1} = \frac{7}{3h}(f_{i+1} - f_{i-1}) + \frac{f_{i+2} - f_{i-2}}{12h}. \quad (5a)$$

$$2f''_{i-1} + 11f''_i + 2f''_{i+1} = \frac{12}{h^2}(f_{i-1} - 2f_i + f_{i+1}) + \frac{3}{4h^2}(f_{i-2} - 2f_i + f_{i+2}). \quad (5b)$$

Fourier analysis and the concept of the 'modified wavenumber' shows that the C-D schemes are noticeably more accurate than the standard Padé schemes. Expressions for the modified wavenumber are given by Mahesh (1996). The modified wavenumbers for the first derivative are shown in Fig. 1. The C-D schemes are seen to follow the exact solution more closely than the standard Padé schemes. Recall that the sixth order C-D scheme has the same stencil width as the fourth order Padé, while the eighth order C-D scheme has the same stencil width as the sixth order Padé. In spite of its smaller stencil, the sixth order C-D scheme is seen to have lower error than the sixth order Padé. Of the different compact schemes considered by Lele (1992), the only scheme that outperforms the eighth order C-D scheme is the pentadiagonal tenth order scheme (designated 'i' by Lele). The pentadiagonal scheme, however, has a stencil of five points on the left hand side, and seven on the right.

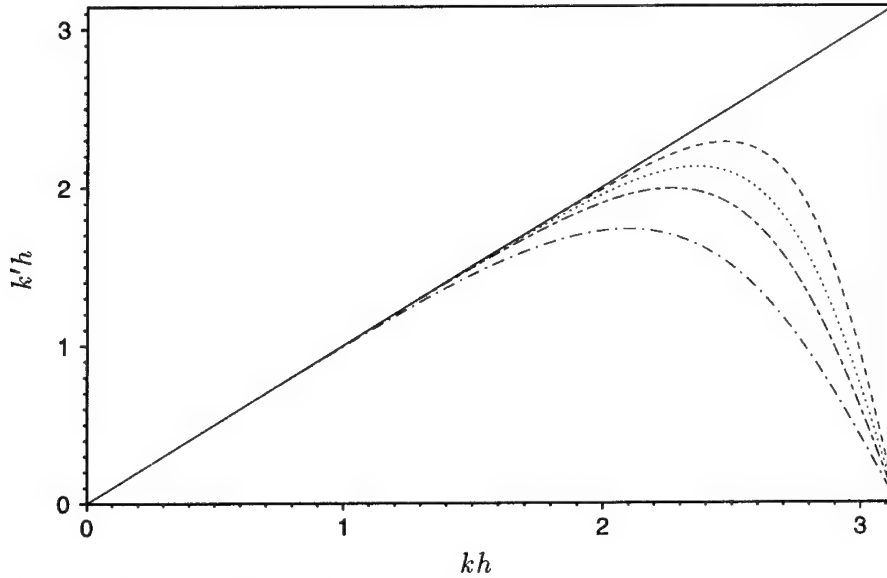


FIGURE 1. The modified wavenumber for the first derivative. The C-D schemes are compared to the standard Padé schemes. — (Exact), ---- (C-D: eighth order), (C-D: sixth order), - - - (Padé: sixth order), — · — (Padé: fourth order).

	$N = 4$	$N = 8$
Padé 4	4.51 %	2.3×10^{-1} %
Padé 6	0.97 %	1.2×10^{-2} %
C-D 6	0.36 %	3.1×10^{-3} %
C-D 8	0.06 %	1.1×10^{-4} %

TABLE 1. The percentage error in the first derivative, as a function of the number of points per wave (N). The C-D schemes are compared to the standard Padé schemes.

The modified wavenumber may be used to determine the error as a function of the resolution. Consider the case where $k = 1$; i.e., we have one wave of wavelength $\lambda = 2\pi$. The mesh spacing, h is given by $h = 2\pi/N = \lambda/N$. kh is therefore equal to λ/N , the reciprocal of the number of points per wavelength. Table 1 documents the percentage error in the first derivative, for resolutions of 4 and 8 points per wave. The C-D schemes are seen to represent even four delta waves with an accuracy of 0.4% and 0.06%, respectively.

Modified wavenumbers for the second derivative are shown in Fig. 2. The C-D schemes are seen to be noticeably more accurate at the higher wavenumbers. Interestingly, $k''^2 h^2$ for the C-D schemes is greater than the exact solution for

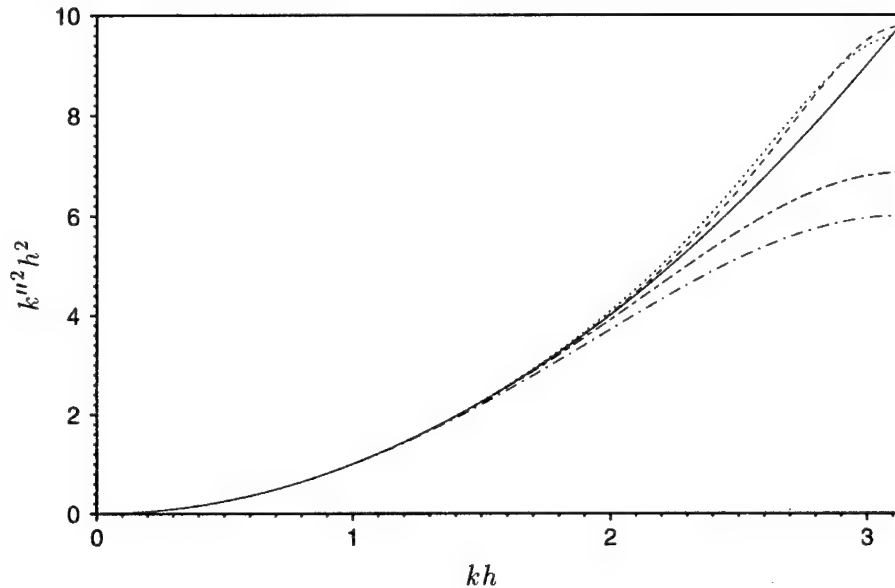


FIGURE 2. The modified wavenumber for the second derivative. The C-D schemes are compared to the standard Padé schemes. — (Exact), ---- (C-D: eighth order), (C-D: sixth order), - - - (Padé: sixth order), - · - (Padé: fourth order).

	$N = 4$	$N = 8$
Padé 4	2.73 %	1.6×10^{-1} %
Padé 6	0.52 %	7.41×10^{-3} %
C-D 6	0.44 %	6.16×10^{-3} %
C-D 8	0.09 %	2.84×10^{-4} %

TABLE 2. The percentage error in the second derivative, as a function of the number of points per wave (N). The C-D schemes are compared to the standard Padé schemes.

certain wavenumbers. This is in contrast to the standard Padé schemes, whose modified wavenumber is always less than the exact solution. Table 2 shows the percentage error in the second derivative, as a function of the resolution. As was observed for the first derivative, the sixth and eighth order C-D schemes represent even four-delta waves, to an accuracy of about 0.4% and 0.1% respectively.

2.2 The boundary schemes

Consider a spatial domain that is discretized by using N points (including those at the boundaries). Equations 2 and 3 show that the sixth order C-D scheme can be

applied from $j = 2$ to $N - 1$, while the eighth order scheme can be applied from $j = 3$ to $N - 2$. For problems with periodic boundary conditions, the periodicity of the solution may be used to apply the same equations at the boundary nodes. However, for non-periodic problems, additional expressions are needed at the boundary nodes to close the system. These expressions are derived below.

Consider $j = 1$. The following general expression may be written for f'_1 and f''_1 :

$$a_0 f'_1 + a_1 f'_2 + h(b_0 f''_1 + b_1 f''_2) = \frac{1}{h}(c_1 f_1 + c_2 f_2 + c_3 f_3 + c_4 f_4). \quad (6)$$

The corresponding equation at $j = N$ would be given by:

$$a_0 f'_N + a_1 f'_{N-1} - h(b_0 f''_N + b_1 f''_{N-1}) = -\frac{1}{h}(c_1 f_N + c_2 f_{N-1} + c_3 f_{N-2} + c_4 f_{N-3}). \quad (7)$$

The width of the stencil on the left hand side of the above equation is restricted to two. This ensures that the number of bands in the left-hand side matrix is still seven. As was done for the interior scheme, the constants in Eq. 6 may be obtained by expanding the terms in a Taylor's series, and matching expressions of the same order. Recall that we need two independent equations at each node. For the interior schemes, we saw that b_0 was equal to 0 if a_0 was equal to 1, and vice-versa. This yielded the two independent equations. This relationship between a_0 and b_0 for the interior schemes is a natural consequence of their symmetry. However for the boundary schemes, it turns out that setting a_0 to 1 does not imply that b_0 is zero. The equation obtained when $a_0 = 1$, is the same as that obtained when $b_0 = 1$. The following procedure is therefore used to obtain two independent equations. When matching the terms in the Taylor table, (a_0, b_0) is first explicitly set equal to $(1, 0)$. This yields the first equation. Next, (a_0, b_0) is set equal to $(0, 1)$, and the terms in the Taylor table are matched. This yields the second equation.

Expressions of order ranging from three to five were derived, and are outlined by Mahesh (1996). The boundary expressions were then combined with the interior scheme, and hyperbolic stability of the complete differencing scheme was examined. Numerical solutions of the one-dimensional wave equation, and eigenvalue analysis were used for this purpose. The higher order boundary closures were found to yield asymptotically unstable schemes. The following boundary closures were found to yield stable schemes, when combined with both sixth and eight order interior schemes. Note that the following equations are applied at $j = 1$. Equation 7 may be used to obtain the corresponding expressions at $j = N$. Also, recall that the sixth order interior scheme may be applied from $j = 2$ to $N - 1$, while the eighth order interior scheme may be applied from $j = 3$ to $N - 2$. In this report, the sixth order scheme is used at $j = 2$ and $N - 1$ if the eighth order scheme is used in the interior. The stable boundary closures are as follows:

(3,4) boundary closure

The third order expression for the first derivative is combined with a fourth order expression for the second derivative.

$$f'_1 + 2f'_2 - \frac{h}{2}f''_2 = \frac{3}{h}(f_2 - f_1) \quad (8a)$$

$$-\frac{5}{2}f_2' + h(f_1'' + \frac{17}{2}f_2'') = \frac{1}{h}(\frac{34}{3}f_1 - \frac{83}{4}f_2 + 10f_3 - \frac{7}{12}f_4) \quad (8b)$$

(3,3) boundary closure

The third order expression for the first derivative is combined with a third order expression for the second derivative.

$$f_1' + 2f_2' - \frac{h}{2}f_2'' = \frac{3}{h}(f_2 - f_1) \quad (9a)$$

$$-6f_2' + h(f_1'' + 5f_2'') = \frac{3}{h}(3f_1 - 4f_2 + f_3) \quad (9b)$$

(3,2) boundary closure

The third order expression for the first derivative is combined with a second order expression for the second derivative.

$$f_1' + 2f_2' - \frac{h}{2}f_2'' = \frac{3}{h}(f_2 - f_1) \quad (10a)$$

$$-6f_2' + h(f_1'' + 2f_2'') = \frac{6}{h}(f_1 - f_2) \quad (10b)$$

2.3 Cost comparison

The computational cost of the C-D schemes is compared to that of the standard Padé schemes, in this section. The standard Padé schemes and the C-D schemes are both of the form,

$$\mathbf{A} \tilde{\mathbf{f}} = \mathbf{B} \mathbf{f} \quad (11)$$

where $\mathbf{f} = [\dots f_{i-1}, f_i, f_{i+1}, \dots]^T$, and \mathbf{A} and \mathbf{B} are constant matrices that depend on the scheme. For the standard Padé schemes, the vector $\tilde{\mathbf{f}}$ is of length N , and is either equal to $[\dots f_{i-1}', f_i', f_{i+1}' \dots]^T$, or $[\dots f_{i-1}'', f_i'', f_{i+1}'' \dots]^T$. Also, the matrix \mathbf{A} is tridiagonal with a band-length of N . For the C-D schemes, $\tilde{\mathbf{f}}$ is of length $2N$, and is equal to $[\dots f_{i-1}', f_{i-1}'', f_i', f_i'', f_{i+1}', f_{i+1}'', \dots]^T$. The matrix \mathbf{A} now has seven bands, each of length equal to $2N$.

At first glance, it might appear as if the C-D schemes would be significantly more expensive. However, this is not the case. When the cost of computing both derivatives is estimated, the C-D schemes are seen to incur essentially the same cost as the standard Padé schemes. This is illustrated below.

In using schemes of the form given by Eq. 11, the common practice is to perform *LU* decomposition of the matrix \mathbf{A} only once, and store the L and U matrices. Computation of the derivatives therefore involves computing the right-hand side ($\mathbf{B} \mathbf{f}$), followed by forward and back substitution. The operation count associated with computing the right-hand side, and solving the resulting system of equations is tabulated in Table 3. When the cost of computing both derivatives is estimated, the C-D schemes are seen to involve the same number of divides, and add/subtracts

	<i>RHS</i>	<i>LU</i> solve	Total
Padé 4: 1 st der.	$1 + 1 + 0 = 2$	$2 + 2 + 1 = 5$	$3 + 3 + 1 = 7$
Padé 4: 2 nd der.	$2 + 2 + 0 = 4$	$2 + 2 + 1 = 5$	$4 + 4 + 1 = 9$
Padé 6: 1 st der.	$2 + 3 + 0 = 5$	$2 + 2 + 1 = 5$	$4 + 5 + 1 = 10$
Padé 6: 2 nd der.	$4 + 5 + 0 = 9$	$2 + 2 + 1 = 5$	$6 + 7 + 1 = 14$
Padé 4: both ders.	$3 + 3 + 0 = 6$	$4 + 4 + 2 = 10$	$7 + 7 + 2 = 16$
Padé 6: both ders.	$6 + 8 + 0 = 14$	$4 + 4 + 2 = 10$	$10 + 12 + 2 = 24$
C-D 6	$3 + 3 + 0 = 6$	$12 + 4 + 2 = 18$	$15 + 7 + 2 = 24$
C-D 8	$3 + 7 + 0 = 10$	$12 + 4 + 2 = 18$	$15 + 11 + 2 = 28$

TABLE 3. The operation count per node to compute the first and second derivative. The entries are of the form, 'number of multiplies + adds/subtracts + divides = total'. The overall cost is obtained by multiplying the entries by the total number of points, N .

as the standard Padé schemes with the same stencil width. The only increase in the number of operations involves the number of multiplies: the eighth order scheme has 1.5 times the number of multiplies as the sixth order Padé, while the sixth order scheme has twice the number of multiplies as the fourth order Padé. A numerical evaluation of the derivatives (Mahesh, 1996) shows this increase in the number of multiplies is not very significant.

3. Conclusions

A new class of finite difference schemes for the first and second derivatives of smooth functions was proposed. The schemes are Hermitian, symmetric, and solve for the first and second derivatives simultaneously. They are two orders higher in accuracy than the standard Padé schemes with the same stencil width, and have noticeably better spectral representation. The computational cost of computing both derivatives is essentially the same as the Padé schemes. The proposed schemes are attractive alternatives to the Padé schemes, for Navier-Stokes computations.

Acknowledgments

This work was supported by the AFOSR under Contract F49620-92-J-0128 with Dr. Len Sakell as technical monitor. I am grateful to Prof. Parviz Moin, Dr. Karim Shariff, and Mr. Jon Freund for useful discussions.

REFERENCES

- KRAVCHENKO, A. G. & MOIN, P. 1996 On the effect of numerical errors in large eddy simulations of turbulent flows. *CTR Manuscript 160*, To appear in *J. Comp. Phys.*
- LELE, S. K. 1992 Compact finite difference schemes with spectral-like resolution. *J. Comp. Phys.* **103**, 16-42.
- MAHESH, K. 1996 A family of finite difference schemes with good spectral resolution. *CTR Manuscript 162*, Submitted to *J. Comp. Phys.*

Appendix

ROSTER

<u>NAME/TERM</u>		<u>AREA OF RESEARCH</u>
POSTDOCTORAL FELLOWS		
BASTIN, Dr. Francois 10/95-present	(Ph.D. Aeroacoustics, 1995, Ecole Centrale Paris)	Aeroacoustics
FATICA, Dr. Massimiliano 10/95-present	(Ph.D. Fluid Mechanics, 1995, University of Rome)	Large eddy simulation
IM, Dr. Hong Geun 10/94-9/96	(Ph.D. Mechanical & Aerospace Engr., 1994, Princeton University)	Turbulent combustion
JANSEN, Dr. Kenneth 9/93-8/96	(Ph.D. Mechanical Engr., 1993, Stanford)	Large eddy simulation
KOUMOUTSAKOS, Dr. Petros 8/94-present	(Ph.D. Aeronautics & Applied Mathematics, 1992, California Institute of Technology)	Flow control/vortex methods
MAHESH, Dr. Krishnan 6/96-present	(Ph.D., Mechanical Engr., 1996, Stanford)	High speed flows
MITTAL, Dr. Rajat 6/95-9/96	(Ph.D. Theoretical & Applied Mechanics, 1995, U. Illinois)	Large eddy simulation
OBERLACK, Dr. Martin 4/95-present	(Ph.D., Technical Mechanics, 1994, RWTH-Aachen)	Turbulence modeling and theory

PARNEIX, Dr. Sacha 12/95-present	(Ph.D., 1995, University of Bordeaux)	Turbulence modeling
RUETSCH, Dr. Gregory 9/93-present	(Ph.D. Applied Mathematics, 1991, Brown University)	Turbulent combustion
SMITH, Dr. Nigel S. A. 10/94-8/96	(Ph.D. Mechanical & Mechatronic Engr., 1994, University of Sydney)	Turbulent combustion
WANG, Dr. Meng 9/92-present	(Ph.D. Mechanical Engr., 1989, Univ. of Colorado)	Aerodynamic noise

RESEARCH ASSOCIATES

CABOT, Dr. William H. 3/88-present	(Ph.D. Physics, 1983, University of Rochester)	Large eddy simulation
DRESSELHAUS, Dr. Eliot 9/91-5/96	(Ph.D. Applied Mathematics, 1991, Columbia University)	Postprocessing and computer languages
LUND, Dr. Thomas S. 11/90-present	(Ph.D. Aero-Astro, 1987, Stanford)	Large eddy simulation

SR. VISITING FELLOWS

BEHNIA, Prof. Masud	University of New South Wales	Turbulence modeling
CAMBON, Dr. Claude 8/96	Ecole Centrale Lyon	Rotating turbulence
CHOI, Prof. Haecheon 7/96	Seoul National University	Turbulence control
CHUNG, Prof. Myung Kyoan 9/95-1/96	KAIST	Turbulence modeling
GODEFERD, Dr. Fabien 8/96	Ecole Centrale Lyon	Rotating turbulence/ EDQMN modeling

HAMBA, Dr. Fujihiro 2/96-7/96	University of Tokyo	Turbulence modeling
HORIUTI, Prof. Kiyosi 2/96-4/96	Tokyo Institute of Technology	Subgrid-scale modeling
MORINISHI, Dr. Youhei 3/95-1/96	Nagoya Institute of Technology	Large eddy simulation
ORLANDI, Prof. Paolo 6/96-8/96	University of Rome	Turbulence physics
TEMAM, Prof. Roger 7/96	University of Paris, SUD	Turbulence control

SR. RESEARCH FELLOWS

BROADWELL, Dr. James E. 1/94-present		Turbulent combustion
DURBIN, Prof. Paul 1/90-1/96		Turbulence modeling
JIMENEZ, Prof. Javier 6/96-8/96		Small scales in turbulence
YAGLOM, Prof. Akiva 7/95-present		Writing of 2nd edition, "Statistical Fluid Mechanics"

GRADUATE STUDENTS

BUICE, Carl 7/95 - present		Measurements in an asymmetric plane diffuser
-------------------------------	--	--

1996 ADVISORY COMMITTEE

Dr. Ronald Bengelink
Boeing Commercial Airplane Group

Prof. John L. Lumley
Cornell University

Dr. Richard G. Bradley, Jr.
Lockheed

Dr. James M. McMichael
Air Force Office of Scientific Research

Prof. Eugene Covert
Massachusetts Institute of Technology

Prof. Norbert Peters
RWTH - Aachen

Dr. Spiro Lekoudis
Office of Naval Research

Dr. John Howe (Ex-officio)
NASA Ames Research Center

1996 STEERING COMMITTEE

Prof. Paul A. Durbin
Professor, Mechanical Engineering,
Stanford

Dr. Charles A. Smith
Acting Chief, Aeronautical Technologies
Division,
NASA Ames Research Center

Dr. Dochan Kwak
Chief, Computational Algorithms and
Applications Branch,
NASA Ames Research Center

Prof. Parviz Moin
Director, Center for Turbulence Research
Professor, Mechanical Engineering, Stanford
Sr. Staff Scientist, NASA Ames Research
Center

Dr. N. N. Mansour
Turbulence Physics Section,
NASA Ames Research Center

Prof. William C. Reynolds
Program Coordinator, Center for Turbulence
Research
Professor, Mechanical Engineering, Stanford
Sr. Staff Scientist, NASA Ames Research
Center

Mr. Joseph G. Marvin
Chief, Modeling & Experimental
Validation Branch, NASA Ames Research
Center